UNIVERSITY OF NAPLES FEDERICO II
SCHOOL OF MEDICINE
DEPARTMENT OF PHARMACY

PhD program in Pharmaceutical Sciences

Title
Development of epigenetic modulators

PhD student
Simona Barone

Tutor
Prof. MARGHERITA BRINDISI

Coordinator
Prof. ROSARIA MELI

XXXVIII CYCLE (a.y. 2024/2025)

Abstract

This PhD thesis aimed at the identification of novel epigenetic modulators to address major health burden diseases, including oncological and infectious diseases, inflammatory states related to persistent bacterial and fungal infections, and rare diseases. In this context, compelling new evidence linked histone deacetylase 6 (HDAC6) activity to a wide range of biological processes, including cell cycle regulation, apoptotic and autophagic events, stress response and protein quality control, immune system modulation and cytoskeletal dynamics. Accordingly, HDAC6 aberrant activity or expression has been linked to the onset and progression of several pathological states, including cancer, rare diseases and inflammatory disorders. Moreover, unlike other members of HDAC family, HDAC6 presents unique structural features (e.g. the presence of two tandem catalytic domains) and predominantly cytoplasmic localization, enabling it to exert its activity on non-histone proteins (e.g. tubulin, HSPs, ubiquitin, cortactin) involved in key physiological and pathological processes. Thereby, selectively targeting HDAC6 is emerging as a promising strategy for the treatment of pathological states with a strong epigenetic component driven by HDAC6, while minimizing side effects related to pan HDAC inhibition. Accordingly, during my PhD I was involved in the design of novel spiro-capped HDAC6 inhibitors, in order to both improve selectivity and potency – in comparison to available inhibitors - while improving pharmacokinetic properties and safety profile. Driven by *in silico* studies, we first identified *1,3,8-triazaspiro[4,5]decan-4-one* as a suitable capping group for preferential interaction within HDAC6 catalytic surface, while the canonical hydroxamic acid was initially selected as the zinc binding group (ZBG). All synthesised compounds displayed high potency towards HDAC6 and high selectivity over HDAC1 and HDAC8 (as representative of other HDAC classes), while showing efficacy in activating both pro- apoptotic and autophagic pathways, as well as

inhibiting cell migration and epithelial-to-mesenchymal transition (EMT) in both monolayer and 3D cellular cultures (spheroids) of MDA-MB-231 triple negative breast cancer (TNBC) cells. Starting from these promising results, we sought to perform a linker inversion on the newly conceived cap group, in order to exploit the different cap group geometry to enhance binding affinity within HDAC6, also by targeting uncommon binding sites on the enzyme. In collaboration with Professor David W. Christianson (University of Pennsylvania), compound **7b** (*Chapter 4*) was co-crystallized within HDAC6 revealing its ability to interact with S531 in L2 loop (a unique structural portion, very rarely targeted by available HDAC6 inhibitors), thus validating our hypothesis for linker overturning to generate more potent and selective inhibitors. During the second year of my PhD, I had the opportunity to spend six months in Finn K. Hansen research group (University of Bonn) working on the introduction of TMFOs and DFMOs ZBGs on a newly conceived *1-thia-4,8-diazaspiro[4.5]decan-3-one* cap group. Moreover, proprietary selective HDAC6is presented in this thesis work showed efficacy in modulating *P. aeruginosa* and *C. albicans* virulence, thereby offering a new glimpse in the treatment of resistant bacterial and fungal infections. In parallel, in the field of infectious diseases, I took part in the design and synthesis of novel pyrazole-isoxazole antifungal agents in synergy with voriconazole in *C. albicans* strains resistant to voriconazole itself.

Abbreviations

$(NH_4)_2CO_3$ = ammonium carbonate

2D = two-dimensional

3D = three-dimensional

5mC = 5-methylcytosine

AcCl = acetylchloride

ACLY = ATP-Citrate Lysase

AcOH = acetic acid

ACS2 = acetyl-coenzyme A synthase 2SET

AcuC = Histone deacetylase-like protein C

ALL = acute lymphoblastic leukemia

AML = acute myeloid leukemia

AO = acridine orange

ApaH = Histone deacetylase-like protein

AURKA = serine/threonine-protein kinase 6

BC = breast cancer

BCAA = branched-chain amino acid synthesis

BDNF = Brain-Derived Neurotrophic Factor

BRG1 = biofilm regulator 1

CD = catalytic domain

CDKN = cyclin-dependent kinase inhibitor

CF = Cystic fibrosis

CFTR = cystic fibrosis transmembrane regulator

CIDEA = Cell Death Inducing DFFA Like Effector A

CMT = Charcott-Marie-Tooth Disease

CSCs = cancer stem-like cells

DCM = dichloromethane

DFAA = difluoroacetic anhydride

DFMO = difluoro 1,3,4-oxadiazole

DIPEA = diisopropyl ethyl amine

DMB = dynein motor binding region

DMF = *N,N*-dimethylformamide

DMSO = dimetylsulphoxide

DNA = deoxyribonucleic acid

DNMTs = DNA methyltransferases

DOT1-L = Disruptor of Telomeric Silencing 1-like

EB = ethidium bromide

ED = electron-donating

eIFs = eukaryotic initiation factors

EMT = ephitelial-mesenchimal transition

ENaC = epithelial sodium channel

EPS = exopolysaccharide

ER = estrogen receptor

Et_2O = diethyl ether

EtOAc = ethyl acetate

EW = electron-withdrawing

FAD = flavin adenine dinucleotide

FDA = food and drug administration

FICI = fractional inhibitory concentration index

FICI = fractional inhibitory concentration index

Fsp^3 = fraction of sp^3 hybridized carbons

GLDH = glutamate dehydrogenase

GlyRS = glycil-tRNA synthetase

HATs = histone acetylases

HBTU = *N,N,N′,N′*-Tetramethyl-*O*-(1*H*-benzotriazol-1-yl)uronium hexafluorophosphate

HCC = hepatocellular carcinoma

HDA1 = yeast Histone Deacetylase 1

HDACis = HDAC inhibitors

HDACs = histone deacetylases

HDLP = histone deacetylase-like protein

HDMs = histone demethylases

HER2 = human epidermal growth factor receptor 2

Hex = hexane

HFT = high-fat-diet

HMTs = histone methyltransferases

HPLC = high performance liquid chromatography

HSF1 = heat-shock factor 1

Hsp = heat-shock protein

HSPB1 = small heat shock protein B1

IBCF = isobutylchloroformate

IDH2 = isocitrate dehydrogenase 2

IPF = idiopathic pulmonary fibrosis

***i*PrOH** = isopropanol

KHMDS = potassium bis(trimethylsilyl)amide

KMTs = lysine methyltransferases

KOH = potassium hydroxide

LDM = lanosterol-α-demethylase

$LiAlH_4$ = litium aluminium hydride

lncRNAs = long non coding RNAs

LPS = lipopolysaccharide

m1A = 1-methyladenosine

m3C = 3-methylcytidine

m6A = *N*6-methyladenosine (m6A)

m7G = 7-methylguanosine

MALAT1 = non-coding RNA metastasis-associated lung adenocarcinoma transcript 1

MAT2A = methionine adenosyl-transferase 2A

***m*CPBA** = *m*-chloroperbenzoic acid

MeCP2 = Methyl-CpG-binding protein 2

MeOH = methanol

METTL = methyl-transferase-like protein

MIC = minimal inhibitory concentration

MIC = minimum inhibitory concentration

MTase = methyltransferase

MTD = methyltransferase domain

mTNBCOs = axillary lymph node metastases

MTOC = microtubule-organizing center

$NaBH_3CN$ = sodium cyanoborohydride

NAFLD = non-alcoholic fatty liver disease

NCoR = nuclear receptor corepressor

NES = nuclear export signal

NF-κB = kappa-light-chain-enhancer of activated B cells

NH_2OH = hydroxylamine

NH_4OH = ammonium hydroxide

NMM = *N*-methyl morpholine

NuRD = nucleosome remodeling and deacetylase complex

PARP = adenosine diphosphate ribose polymerase

PD-1 = programmed cell death protein 1

PD-L1 = programmed death ligand 1

PDOs = patient-derived organoids

PE = petroleum ether

PHD = Plant Homeodomain

PI = propidium iodide

PMDA = Japanese Pharmaceuticals and Medicals Devices Agency

piRNAs = piwi-interacting RNAs

PMTs = post-translational modifications

PPEC = putative product exit channel

PR = progesterone receptor

Prdx = peroxiredoxins

PRMTs = protein arginine methyltransferases

QS = quorum sensing

RING = Really Interesting New Gene

RNA = ribonucleic acids

ROS = reactive oxygen species

RTT = Rett syndrome

SAH = S-adenosyl-L-homocysteine

SAM = S-Adenosyl Methionine

SCD_1 = stearoyl-Coenzyme A desaturase 1

SEC = substrate entry channel

Set3C = Set3 histone deacetylase complex

SETD = SET containing domain

siRNAs = short-interfering RNA

SMRT = retinoid and thyroid hormone receptors

sncRNAs = short non coding RNAs

SOGA1 = Suppressor Of Glucose Autophagy Associated 1

TEA = triethylamine

TFAA = trifluoroacetic anhydride

TFMO = trifluoromethyl 1,2,4-oxadiazole

TfR1 = transferrin receptor 1

TGF = tumor growth factor

THF = tetrahydrofuran

TMSCN = trimethylsilyl cyanide

TNBC = triple negative breast cancr

TsCl = tosyl chloride

UHRF1 = RING finger domains 1

UV = ultraviolet

VRC = vertebrates conserved regions

Chapter 1

Introduction – Part 1: Epigenetics and epigenetic modifications

1.1 DNA methylation

1.2 non-coding RNAs

1.3 Histone modifications

1.3.1 HDAC family: structure and function

1.3.2 HDAC inhibitors

1.4 *HDAC6: a unique isoenzyme among HDAC family*

1.4.1 HDAC6 structure

1.4.2 HDAC6 catalytic deacetylase mechanism

1.4.3 HDAC6 substrate specificity

1.5 HDAC6 in pathological states

1.5.1 HDAC6 role in rare diseases

1.5.2 HDAC6 in oncological diseases

Introduction – Part 2: Rational Design of HDAC6is

Introduction - Part 3: Epitrascriptomics and epitranscriptomic modifications. Insights into Methyl-Transferase-Like Protein 16 (METTL16) protein structure and biological role.

1.6 METTL16 structure

1.6.1 METTL16 substrate specificity

1.7 METTL16 in pathological states

1.7.1 METTL16 role in non-oncological states

1.7.2 METTL16 role in oncological diseases

1.8 METTL16 inhibitors

Introduction – Part 4: Escape from flatland: how spirofused compounds are reshaping medicinal chemistry.

References

Chapter 2

PhD work: aims and general methods

Chapter 3

Design, synthesis, in silico studies and biological validation of potent and selective HDAC6 inhibitors for the treatment of Triple Negative Breast Cancer.

3.1 Results and discussion

3.1.1 Chemistry

3.1.2 Crystallographic studies in complex with zHDAC6 CD2

3.1.3 Identification of 1,3,8-triazaspiro[4,5]decan-4-one cap group

3.1.4 Investigation of structure-activity relationships

3.2 Conclusions

3.3 Experimental section

3.3.1 Chemistry

3.3.2 Supporting Figures

References

Chapter 4

Selective HDAC6 Inhibition by Mesinostat Impairs Tumor Growth and Stemness in Triple-Negative Breast Cancer

4.1 Results and discussion

4.1.1 Mesinostat exerts antitumoral activity on MDA-MB-231 TNBC cells

4.2 Conclusions

4.3 Experimental section

4.3.1 Cell culture and reagents

4.3.2 Organoid Culture

4.3.3 LIVE/DEAD Viability assay on organoids

4.3.4 Western blot analysis

4.3.5 RNA purification and quantitative real-time PCR

4.3.6 Proliferation assay

4.3.7 Flow Cytometry analysis

4.3.8 Wound healing assay

4.3.9 Clonogenic assay

4.3.10 3D culture

4.3.11 Organoid clonogenic assay

4.3.12 Statistical analysis

References

Chapter 5

Unlocking L2 Pocket Interactions: Linker Inversion Enables the Design of Next-Generation Selective HDAC6 Inhibitors.

5.1 Results and discussion

5.1.1 Chemistry

5.1.2 Linker overturning of 1,3,8-triazaspiro[4,5]decan-4-one cap group enabled the interaction within L2 on HDAC6 catalytic rim

5.2 Conclusions

5.3 Experimental section

5.3.1 Chemistry

5.3.2 Supporting Figures

Chapter 6

Isoform-Selective HDAC6 Inhibition via Spirocyclic Capping and Heterocyclic Zinc-Binding Group Modulation (Finn K. Hansen Research Group)

6.1 Results and discussion

6.1.1 Chemistry

6.1.2 Investigation of novel TFMO and DFMO ZBGs on 1,3,8-triazaspiro[4,5]decan-4-one cap group

6.1.3 Exploration of a thia-diazaspiro[4.5]decane cap group

6.1.4 Target engagement by Western Blot analysis

6.1.5 Target engagement by NanoBRET assay on HDAC6

6.1.6 Kinetic studies

6.1.7 Biological assessment in human bladder carcinoma T24 cell lines

6.2 Conclusions

6.3 Experimental section

6.3.1 Chemistry

6.3.2 Supporting Figures

References

Chapter 7

Selective HDAC6 inhibitors disrupt P. aeruginosa virulence factor production and biofilm production.

7.1 Results and discussion

7.1.1 Chemistry

7.1.2 Identification of compound 15a as high potent and selective HDAC6 inhibitor.

7.1.3 Compound 15a modulates Pseudomonas aeruginosa virulence and biofilm formation.

7.1.4 Structure-activity relationship studies on compound 15a

7.1.5 Crystallographic studies of compund 15b in complex with zHDAC6 CD2

7.1.6 Enzymatic assays on PA3774

7.2 Conclusions

7.3 Experimental section

7.3.1 Chemistry

7.3.2 Supporting Figures

Chapter 8

Synergistic antifungal activity of selective HDAC6 inhibitor in combination with Voriconazole agains azole-resistant C. albicans strains

8.1 Results and discussion

8.1.1 Compound 15a in combination with Voriconazole inhibits C. albicans cells

8.1.2 Compound 15a in combination with Voriconazole inhibits C. albicans yeast-to-hyphae

8.1.3 Compound 56a in combination with Voriconazole modulates the expression of genes involved in morphogenesis and azole resistance

8.1.4 Compound 15a in combination with Voriconazole modulates the expression of ERG11 gene

8.2 Conclusions

8.3 Experimental section

8.3.1 Candida strains and culture conditions

8.3.2 Antifungal susceptibility testing

8.3.3 Checkerboard assay

8.3.4 Yeast-to-hyphae morphology studies

8.3.5 Azoles fungistatic effect determination

8.3.6 RNA isolation and real time PCR

References

Chapter 9

Discovery of the first-in-class pyrazole isoxazole based synergistic antifungal agent in combination with voriconazole

9.1 Results and discussion

9.1.1 Chemistry

9.1.2 In vitro antifungal activity

9.1.3 Candida albicans morphological transition

9.1.4 The combination SL-38/VRC modulates gene associated with resistance in Candida albicans

9.1.5 SL-38 assessment in LDM inhibition assay

9.1.6 In silico studies on SL-38 within LDM active site

9.1.7 In vivo efficacy of the combination SL-38/VRC

9.1.6 In silico studies on SL-38 within LDM active site

9.1.8 Biocompatibility profile of SL-38

9.2 Conclusions

9.3 Experimental section

9.3.1 Chemistry

9.3.2 Supporting Figures

References

Chapter 10

Conclusions

Chapter 1 - Introduction

Part 1: Epigenetics and epigenetic modifications

The central dogma of molecular biology – which states the unidirectional transfer of genetic information from DNA to RNA and proteins - has long served as the framework for understanding how genetic information is stored, transmitted, and expressed along living organisms [1,2]. Indeed, all somatic cells belonging to the same organism contain the identic DNA sequence, while displaying remarkable diversity in structure and function. Historically, the establishment of genome expression has been attributed to transcription factors, proteins which bind to specific DNA sequences, therefore activating or repressing the transcription of specific cell-lineage genes. Nowadays, the complex regulatory machinery underlying the expression of distinct phenotypes - despite being encoded by the same genotype - is increasingly well understood. This regulation depends on a multitude of factors which play a pivotal role in fine-tuning gene expression at various levels, including chromatin accessibility, transcriptional activity, RNA processing, translation, and stability [3–9]. Among these, the concepts of *epigenetics* and *epitranscriptomics* have gained particular interest in biology and precision medicine.

The term *epigenetics* was coined in 1942 by Conrad Waddington referring to "*the branch of biology which studies the causal interactions between genes and their products which bring the phenotype into being*" [10–12]. Among the most common epigenetic modifications, we acknowledge DNA methylation and histone modifications (e.g. methylation, acetylation and phosphorylation), while non-coding RNAs contribute to epigenetic regulation by modulating gene silencing. Epigenetic modifications are reversible processes, catalysed by enzymes with opposite role, respectively clustered as *writers* and *erasers*, while *readers* are enzymes able to recognize such modifications and convert them into cellular responses. Epigenetic writers, like DNA methyltransferases (DNMTs)

and histone methyltransferases (HMTs) and acetylases (HATs), catalyse the transfer of the epigenetic mark from a co-factor to, respectively, DNA or histone proteins. Epigenetic marks introduced by *writers* can be recognized by epigenetic readers, usually chromatin modifiers presenting protein domains able to recognize and bind covalent modifications occurring on DNA or histone proteins [13]. Among them, Methyl CpG binding proteins recognize methylated CpG dinucleotides, and recruit chromatin remodelling proteins leading to transcriptional repression [14]. For instance, Ubiquitin-like, PHD (Plant Homeodomain) and RING (Really Interesting New Gene) finger domains 1 (UHRF1) bears a tandem tudor domain able to recognizes trimethylated lysine 9 on histone 3 (H3K9me3) [15], while bromodomains are protein specialized in recognizing ε-N-acetylated lysine residues on histone proteins [16]. *Erasers*, including histone demethylases (HDMs) and histone deacetylases (HDACs), remove epigenetic marks introduced by *writers*, thereby restoring chromatin structure and modulating gene expression.

1.1 DNA methylation

DNA methylation is one of the most studied epigenetic marks in eukaryotic genomes. It involves the addition of a methyl group on the C-5 position of the cytosine ring, predominantly within CpG dinucleotides of somatic cells [17–19]. In contrast, during embryonic development, about a quarter of all DNA methylation occurs in stem cells in non-CpG contexts (e.g. CpA, CpT and CpC dinucleotides), thereby affecting the expression of genes involved in normal development, such as X-chromosome silencing, genome imprinting, and several huma pathologies (e.g. cancer and neurodegenerative disorders) [20,21].

In mammalians, enzymes involved in the covalent addition of methyl groups on DNA sequence are known as DNMTs [22,23].This enzyme family comprises isoenzymes DNMT1, DNMT2, DNMT3A, DNMT3B, and DNMT3L, typically distinguished for their functional activity and sequence homology. DNMT1,

DNMT3A and DNMT3B are catalytically active members of this family. They possess a conserved C-terminal methyltransferase domain, which binds the co-factor *S*-adenosyl methionine (SAM),and catalyse the transfer of a methyl group from SAM to the 5-C position of the cytosine ring within the DNA. The methylation reaction results in the formation of 5-methylcytosine (5mC) and the byproduct *S*-adenosyl-L-homocysteine (SAH) [22,23].

DNMT3A and DNMT3B are *de novo* methyltransferases which preferentially recognize unmethylated CpG dinucleotides during development, thus they introduce new covalent modifications independently to pre-existing methylation marks[24,25]. On the contrary, DNMT1 is a maintenance methyltransferase, able to recognize hemi-methylated CpG sites on DNA single strands during replication. DNMT1 strictly cooperates with DNA replication machinery, copying DNA methyl marks from parental DNA strand and ensuring faithful transition of the epigenetic information during somatic cells replication [23]. Despite DNMT3L shares structural similarity to DNMT3A and DNMT3B, it lacks catalytic activity, due to the absence of a functional C-terminal methyltransferase domain. DNMT3L serves as an enhancer of *de novo* methyltransferases activity, by increasing their ability to bind SAM, promoting effective DNA methylation[26–28]. DNMT2, also known as TRDMT1, is the most evolutionarily conserved member of DNMTs. Initially considered a DNA methyltransferase due to the high structural homology to canonical DNMTs, nowadays it is recognized as a tRNA methyltransferase, specifically involved in the methylation of cytosine 38 in the anticodon loop of tRNA^Asp [29–31].

1.2 Non-coding RNAs (ncRNAs)

The majority of human genome encodes for RNA sequences which are not translated into proteins, namely non-coding RNAs[32–35]. A wide range of non-coding RNAs have been identified nowadays, labelled according to sequence length and composition into two main groups: short ncRNAs (<30 nucleotides)

and long ncRNAs (>200 nucleotides), both groups mainly involved in heterochromatin formation, DNA rearrangements, gene silencing, and other RNAs (e.g. mRNA) processing and regulation.

Short ncRNAs

Among short ncRNAs, **miRNAs** (19-25 nucleotides) regulate mRNA expression by interacting with the latter, accordingly to the complementarity between miRNA and its target mRNA[36,37]. Canonically, miRNAs bind to 3'-UTR of target mRNA, activating its degradation or translational repression, while few evidence report miRNA ability to enhance translational activation, thus affecting pivotal cellular functions, such as proliferation, differentiation, and embryonal development[38,39].

Short-interfering RNAs (**siRNAs**, 20-25 nucleotides) are double stranded short ncRNAs serving as gene silencing tool through RNA interference mechanism. Once incorporated into the RNA-induced silencing complex (RISC), the siRNA is unwound and the guide strand – single siRNA strand complementary to a specific mRNA – binds to the mRNA to be degraded, thus resulting in the corresponding gene silencing. Moreover, several studies have linked siRNA-mediated transcriptional silencing to the promotion of H3K9 methylation, with consequent chromatin condensation and transcriptional repression [35,40].

Piwi-interacting RNAs (**piRNAs**, 21-35 nucleotides) specifically interact with Piwi proteins (RNA binding proteins essential in maintaining genome integrity in germline cells). piRNA-piwi protein complex primary function is the suppression of transposon movement, to preserve genome stability in both germline and somatic cells[41].

Long ncRNAs

Long ncRNAs a highly heterogeneous class of transcripts (more than 200 nucleotides) which do not encode for proteins. Unlike short ncRNAs, a common and unequivocal mechanism of action has not been identified so far, however

lncRNAs are broadly classified for their capability to interact with mRNA, DNA and DNA-associated proteins, or miRNAs to regulate gene expression at multiple levels [42].

Furthermore, in the last decade, a new mechanism was proposed, called "sponge effect": lncRNAs may regulate miRNA-dependent gene silencing, by competing with endogenous RNAs to bind their miRNAs, thereby sequestering the latter. This mechanism could be effective in contrasting lncRNAs overexpression. Indeed, lncRNAs - such as PolIII-transcribed RNAs - can serve as "molecular scaffolds" for targeting ribonucleoprotein complexes, thus affecting chromatin structure and gene expression [43]. Also, XIST is essential for X-chromosome inactivation in female mammals [44], while HOTAIR regulates gene expression by guiding histone methylation and, consequently, gene silencing [45].

1.3 Histone modifications

In the nucleus of the eukaryotic cells, genomic DNA is organized into highly structured complexes, called chromatin, which undergo different levels of folding and compaction. Chromatin is a dynamic polymer consisting of DNA tightly bound to histones, small and positively charged proteins able to interact with the negative charge of DNA phosphate groups. The different levels of DNA packaging into chromatin are primarily guided by the core histones (H2A, H2B, H3 and H4) and the linker histone H1 (Figure 1) [46]. The first level of DNA packaging involves the association of DNA with an octamer of core histones (two copies each of H2A, H2B, H3 and H4) and the formation of the nucleosome core particle, the structural unit of chromatin. As mentioned, histones are small basic proteins consisting of a globular domain and a more flexible and positively charged NH_2-terminus, the so-called *histone tail*, which protrudes from the nucleosome, and can undergo several covalent modifications which contribute to alter chromatin structure by influencing histone-DNA and histone-histone interaction [46]. As a result, histone modifications play a pivotal role in

controlling the degree of chromatin compaction. Indeed, histone proteins undergo reversible post-translational modifications (PTMs) which regulate protein-protein interactions, thereby allowing the switch between "euchromatin" (relaxed chromatin structure, transcriptionally active) and "heterochromatin" (highly compacted, transcriptionally inactive form), and, consequently, DNA accessibility to transcriptions factors, controlling gene expression by promoting either gene activation or repression [47–49].

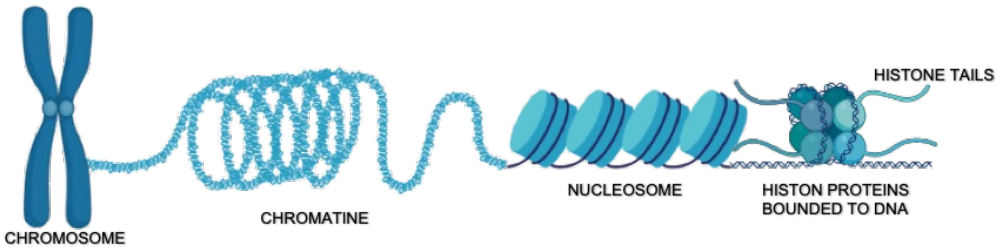


Figure 1. Organization of genetic code from chromosome to DNA. Imagine created using biorender.com.

Histone PTMs can be found in both the histones terminal tails and their globular domains. Among PTMs, acetylation and methylation occurring on lysine or arginine residues of histone tails are the most representative, and their role in regulating gene expression is well established. Also, phosphorylation on globular residues (e.g. serine, threonine or tyrosine) plays a key role in DNA repair and condensation, while histone ubiquitination is either related to gene expression activation or repression.

Histone methylation and demethylation

Histone methylation, which usually occurs on all basic amino acid residues (arginine, lysine and, rarely, histidine) of histone H3 and H4, is one of the most important and common PTMs. Lysine can be mono-methylated, di-methylated or tri-methylated on its ε-amine group, while arginine can be found in monomethylated form or it can be di-methylated symmetrically or asymmetrically, on its guanidyl group. The most studied histone methylation

events are H3 lysine 4 (H3K4), H3K9, H3K27, H3K36, H3K79 and H4K20, and arginine (R) methylation sites include H3R2, H3R8, H3R17, H3R26 and H4R3, while histidine methylation has not been deeply characterized. Interestingly, depending on the residue involved and the degree of methylation, histone methylation can both activate or repress gene transcription. For instance, H3K4, H3K36, and H3K79 are considered as active marks which occupy the actively transcribed gene regions in chromatin (Figure 2). H3K9, H3K27, and H4K20 are repressive marks that are usually associated with the silenced gene expression and condensed chromatin (Figure 2).

Enzymes responsible for the transfer of methyl groups from co-factor SAM to the histone to be methylated are named histone methyltransferases (HMTs), further labelled into histone lysine methyltransferases (KMTs) and protein arginine methyltransferases (PRMTs) [50].

1. **KMTs**: most KMTs share a conserved site of about 130 amino acids, SET domain (named after Su(var)3-9, Enhancer of zeste, and Trithorax), which facilitates the transfer of methyl groups from SAM to specific lysine residues on histones. H3K4 methylation - generally associated with gene expression - is catalyzed by SETD (SET Domain Containing)1A, SETD1B, MLL1 (KMT2A), MLL2 (KMT2B), MLL3 (KMT2C) and MLL4 (KMT2D) complexes. H3K9 methylation is pivotal in the formation of heterochromatin, and consequent gene repression. This PTM is catalysed by G9a, SUV39H1, SUV39H2, SETDB1. Notably, G9a is also responsible for H327 methylation, a key epigenetic marker in gene silencing. H3K36 methylation (ASH1L, SETD2) is associated with gene activation, promoting transcription elongation and splicing. Among KMTs, DOT1-L (Disruptor of Telomeric Silencing 1-like) is the only member of KMTs which did not present SET domain. DOT1-L is a H3K79 methyltransferase involved in transcriptional regulation and genome stability [51].

2. **PRMTs**: to date nine different PRTM isoforms have been identified, seven of them involved in mono- or di-methylation of histone arginine residues. While Type I PRMTs (PRMT1, PRMT2, PRMT3, PRMT4 or CARM1, PRMT6, and PRMT8) catalyze asymmetric arginine methylation, PRMTs belonging to type II (PRMT5 and PRMT9) symmetrically methylate arginine residues [52], and PRMT7 (type III) is involved in arginine monomethylation reactions [53]. Methylation reactions promoted by PRMT1 and PRMT4 always result in gene expression activation, while PRMT5 activity is related to heterochromatin formation and gene silencing.

Despite histone methylation was originally thought to be irreversible, the discovery of the demethylases (*erasers* responsible for the removal of methyl group, reverting PTMs cellular effects) revealed methylation events are controlled by a balance between enzymes that catalyze the addition and removal of a given modification.

Demethylases can be labelled into two different families:

1. **Amine oxidases**: remove methyl groups from lysine or arginine residues of histones by an oxidation reaction, using flavin adenine dinucleotide (FAD) as cofactor. LSD1 is the first enzyme belonging to this family identified as a lysine-specific demethylase with substrate specificity for K4-methylated histone H3. It is a flavin-containing protein, which, binding the co-factor FAD, can catalyze the amine oxidation, characterized by oxidative cleavage of the alfa-carbon bond of the substrate to form an imine intermediate, which, is hydrolyzed to form an aldehyde and amine via a nonenzymatic process. In a complete catalytic cycle, the cofactor FAD is reduced to FADH2 and then is likely to be re-oxidized by oxygen releasing hydrogen peroxide [54].

2. **Jumonji (JmjC)- domain-containing, iron dependent dioxygenases:** Fe(II)- and α-ketoglutarate- dependent histone demethylases, involved in lysine demethylation through oxidative mechanism [55].

Histone acetylation and deacetylation

Histone acetylation consists in the introduction of an acetyl moiety on the ε-amino group of a lysine residue. This modification reduces the positive charge of the amino acid and inhibits the binding between histone tails and negatively charged DNA resulting in a less compacted chromatin structure. Thus, while histone methylation can result in both transcription activation and inactivation, histone acetylation is usually considered as promoters of gene expression, and it can also act as a methylation antagonist (Figure 2) [47,49]. Indeed, the acetyl mark on histone tails neutralizes lysine positive charge, thus decreasing the electrostatic interactions between histone lysine tails negatively charged DNA, resulting in more opened chromatin conformation which enhance DNA accessibility to transcriptional machinery (Figure 2).

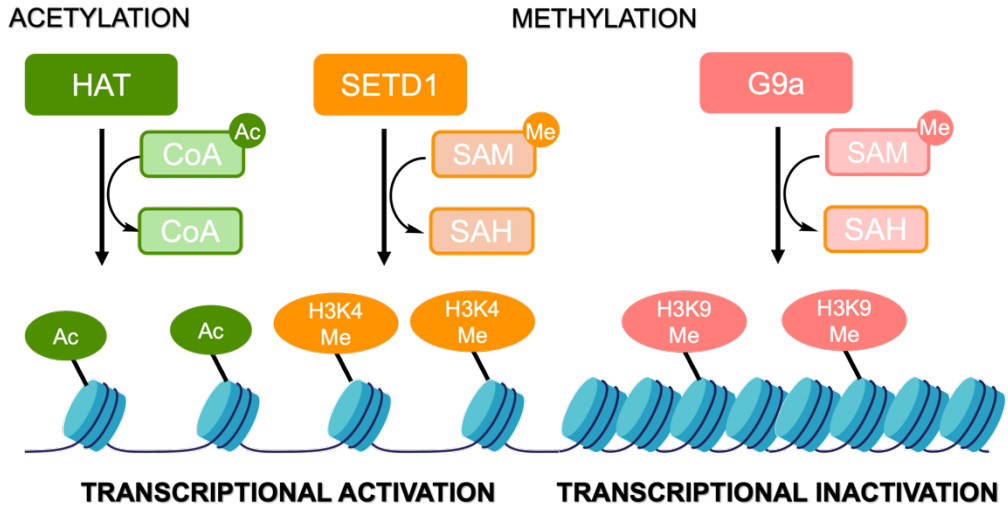


Figure 2. Transcriptional activation/inactivation mediated by histone PTMs. HAT = acetyltransferases, SETD1 = SET Domain Containing 1A, G9a = Euchromatic Histone-Lysine N-methyltransferase 2.

Since histone acetylation is a reversible mark, it is regulated by the balance between two families of enzymes with opposite function:

1. **Histone acetyltransferases (HATs)**: They catalyze the transfer of an acetyl group from the co-factor acetyl-CoA to the ε-amino group of lysine placed within histone tails [56]. Historically, HATs are classified as s type-A and type-B. Type A HATs comprises a diverse family of enzymes located into cell nucleus, and classified at least into three separate groups, depending on amino-acid sequence homology and conformational structure. Type A comprises Gcn5/PCAF, MYST, and Rtt109 enzymes. While the Gcn5/PCAF and MYST families have homologs from yeast to humans[57–59], p300/CBP is metazoan-specific, and Rtt109 is fungal-specific[60]. Type-B HATs are predominantly cytoplasmic, acetylating free histones, but not those already deposited into chromatin. Type-B HATs family members are highly conserved, presenting high sequence homologues [61,62].
2. **Histone deacetylases (HDACs)**: This family of enzymes counteracts the effects of HATs thus reverting lysine acetylation, thus stabilizing the local chromatin architecture, and resulting in transcriptional repression. Structure, function, and involvement in pathological states of HDAC family will be in-depth discussed in the following paragraphs.

1.3.1 HDAC family: structure and function

As discussed in the previous paragraph, enzymes belonging to HDAC family catalyze the removal of the acetyl group from acetylated lysine residues, thus restoring the transcriptionally repressed form of chromatin structure. According to the structure of their active site and, consequently, their mechanism of action, HDACs are labelled in two families, namely: (i) Zn^{2+}-dependent deacetylases, which comprises Class I, IIa, IIb, IV; (ii) NAD^{+}-dependent deacetylases (Class III HDACs), also known as sirtuins.

In the mammalian cells, 18 different HDAC isoforms have been identified so far, divided into four classes based on their sequence similarity to yeast counterparts (Figure 3).

1. Class I HDACs: it comprises HDAC1, HDAC2, HDAC3 and HDAC8. Class I HDACs are ubiquitously expressed in cell nucleus and display high homology to the yeast HDAC Rpd3. For their cellular localization, they are mainly involved in gene transcription regulation exerting their activity on histone proteins through the removal of acetyl marks. Class I HDACs often function as part of multifactorial complexes. For instance, HDAC1 and HDAC2 are part of nucleosome remodeling and deacetylase complex (NuRD), one of the major chromatin modeling complexes in cells [63]. In its active form, HDAC3 was found in complex with silencing mediator for retinoid and thyroid hormone receptors (SMRT) and nuclear receptor corepressor (NCoR), which facilitates HDAC3 catalytic activity[64]. HDAC8 is a muscle-specific isoenzyme able to deacetylase cohesin regulating cell cycle. Its activity is modulated by autoacetylation (K202), which inhibits its deacetylase activity, thereby fine-tuning its role in cohesin complex regulation and chromatin remodeling [65]. Class I HDACs were also found to target a wide range of non-histone proteins, such as transcriptional factors (p53, STAT3) or AMP-activated protein kinase, thereby modulating key cellular processes involved in cell cycle regulation, DNA repair and metabolic activity.
2. Class II HDACs: enzymes belonging to this class are homologous to the yeast Histone Deacetylase 1 (HDA1) and are both expressed in cell nucleus and cytoplasm. Class II is further divided in two subclasses, namely Class IIa (HDAC4, HDAC5, HDAC7 and HDAC9), and Class IIb (HDAC6 and HDAC10). Class IIa HDACs differs from other isoenzymes for the presence of a long N-terminal domain able to interact

with several transcription factors (e.g. MEF2, NFAT, Runx2), thus serving as signal transducers. N-terminal tails are also characterized by the presence of conserved serine residues, susceptible to reversible and signal-dependent phosphorylation. In normal conditions, unphosphorylated Class IIa HDACs are stably located into cell nucleus, where they bind their target genes and inhibit their expression. In response to specific signals, serine phosphorylation allows Class IIa HDACs export to cell cytoplasm, thereby dissociating them from target genes and allowing their transcriptional activation. Interestingly, probably due to the replacement of catalytic tyrosine with a histidine residue, Class IIa HDACs display a negligible intrinsic deacetylase activity in comparison to Class I, exerted only in complex with HDAC3/SMRT. Thus, Class IIa HDACs have been suggested to act as bromodomains, recognizing acetylated lysine in a sequence-dependent context and recruiting chromatin-modifying enzymes to regulate transcription [66–68]. On the other and, Class IIb HDACs are mainly expressed in cell cytoplasm and bear two tandem catalytic domains. HDAC10 is not effective as lysine deacetylase, mainly due to the presence of a glutamate gatekeeper (replacing the lysine gatekeeper of HDAC6) and to a sterically constricted active site, which confer specificity for acetylpolyamine substrates over acetyl lysine hydrolysis [69]. Insights into the unique structural and mechanistic characteristics of HDAC6 will be discussed in *Paragraph 1.4.*

3. Class III HDACs: it comprises seven NAD^+-dependent HDACs (sirtuins) derived by the homologs yeast Sir2 [70]. They are broadly expressed in human tissues and are involved in the regulation of DNA repair, metabolism, oxidative stress, and aging. SIRT1 is mainly located in cell nucleus, where deacetylases several transcription factors (e.g. p53), but it

can also be shuttled in cytoplasm, where it is involved in deacetylase the cytoplasmic transcription factor p65, a subunit of nuclear factor kB (NF-kB), thus indirectly regulating the expression of NF-kB-dependent genes [71]. SIRT2 is expressed in both the nucleus and cytoplasm, where it plays distinct roles. In cell nucleus, it regulates G2-M transition during cell cycle, while, when expressed in cell cytoplasm, SIRT2 is able to deacetylase α-tubulin, contributing to microtubule dynamics [72–74]. SIRT3, mainly expressed in cell mitochondria, plays a pivotal role in regulating cell energy metabolism, through deacetylase activity exerted on acetyl-coenzyme A synthase 2 (ACS2), glutamate dehydrogenase (GLDH), isocitrate dehydrogenase 2 (IDH2), and the electron transport complex I [75]. In a similar manner, SIRT4 is involved in lipid metabolism by deacetylating malonyl CoA decarboxylase. SIRT5 is involved in SIRT5 PMTs such as lysine succinylation, malonylation, or glutarylation[76]. SIRT6 and SIRT7 are expressed in cell nucleus. They regulate inflammatory response and macrophage activation, and regulates RNA polymerase I transcription, respectively[70].

4. Class IV HDACs: HDAC11 is the only isoform belonging to this class. Recent studies suggest its role in fine-tuning immune system activation or tolerance through its inhibitory effect on interleukin 10 (IL-10) expression [77].

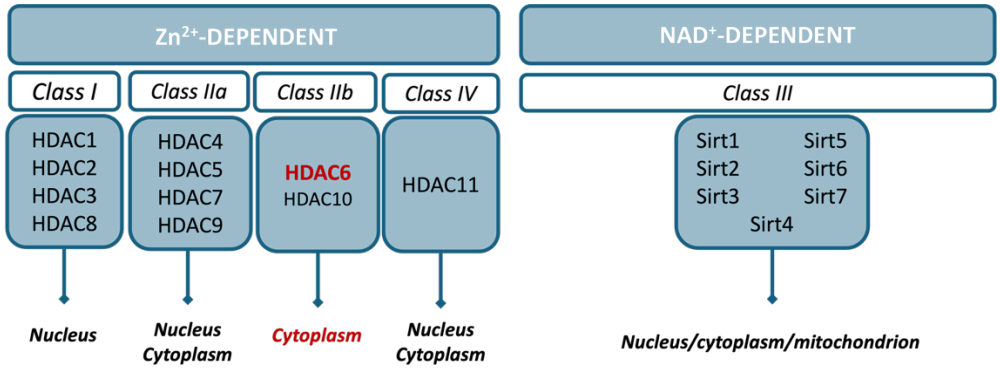


Figure 3. HDAC family enzyme classification.

1.3.2 HDAC inhibitors

HDAC inhibitors (HDACis) general structure can be summarized in three main portions, namely: (i) a cap group, which interacts whit enzymatic catalytic surface; (ii) a zinc binding group (ZBG) responsible for the inhibitory activity through the coordination of the catalytic zinc ion; (iii) an aromatic or aliphatic linker which connects the cap group to the ZBG (Figure 4) [78].



Figure 4. General structure of HDACis.

According to the nature of the ZBG, currently developed HDACis can be labelled in different chemical classes, often exhibiting different degrees isoform selectivity. The current state of the art in HDAC inhibitor development, including their chemical diversity and selectivity profiles, will be discussed in the present paragraph.

Hydroxamic acid derivatives

Hydroxamic acid derivatives are the most studied class of HDACis for the high ability of this functional group in coordinating, in a bidentate fashion, a wide spectrum of metal ions including zinc, which is the most frequently occurring metal in metalloenzymes such as HDACs. Finnin et al. described the bidentate

coordination mode of the hydroxamate moiety, referring to the crystal structure of the histone deacetylase-like protein (HDLP) in complex with Trichostatin A (TSA, **1**, Figure 6) and Vorinostat (SAHA, **2**, Figure 6). In this canonical binding mode, the hydroxamate group of TSA coordinates the catalytic zinc ion in a bidentate fashion, resulting in the formation of a pentacoordinated Zn^{2+} complex [79]. Interestingly, the hydroxamic acid moiety is also involved in hydrogen bonds with charge-relay H131 and H132, and the Y297 hydroxyl group, while it displaces the zinc-bound water molecule of the active structure with its hydroxyl group (Figure 5A) [79]. In line with the well-established binding mode of this structural class of inhibitors, most of approved pan-HDACis bear the hydroxamate ZBG, including Vorinostat (SAHA, **2**, Figure 6), Panobinostat (**3**, Figure 6), Belinostat (**4**, Figure 6), Givinostat (**5**, Figure 6), while several selective hydroxamate-based inhibitors - such as Ricolinostat (**6**, Figure 6), Citarinostat (**7**, Figure 7), KA2507 (**8**, Figure 8) - are currently enrolled in clinical trials.

With the resolution of the X-Ray crystal structures of HDAC6 CD2 from human (*h*HDAC6) and HDAC6 CD1 and CD2 from zebrafish (*z*CD1, *z*CD2), which presents high sequence homology with *h*HDAC6, Christianson et al. showed an unusual hydroxamate-zinc ion coordination mode at the basis of isozyme-specific inhibition. The X-Ray structure of the complex between the HDAC6i HPOB (**9**, Figure 6) and *z*CD2 (Figure 5B) revealed the hydroxamate group coordinated to Zn^{2+} only through its hydroxyl group, without displacing the zinc-bound water molecule. This monodentate coordination model is linked to the short and bulky linker of HPOB (**9**, Figure 6) unable to insert deeply into HDAC6 active site [80]. Consistently, the introduction of bulky and rigid cap groups in the structure of phenyl-hydroxamate inhibitors generally leads to monodentate Zn^{2+} coordination, suggesting the insertion of bulky and rigid cap groups modulate the equilibrium between bidentate and monodentate metal ion coordination mode.

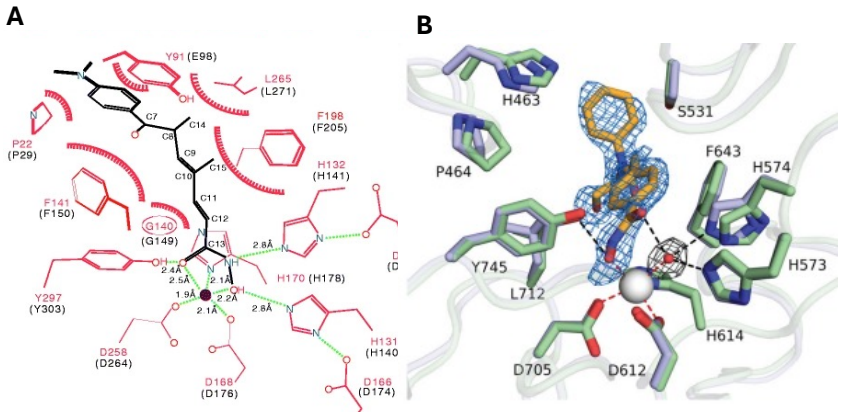


Figure 5. (A) Binding mode of TSA within HDLP active site (PDB: 1C3R). (B) Binding mode of HPOB within *z*CD2 (PDB: 5WJK) [79].

The first acknowledged HDACi is TSA (**1**, Figure 6), a natural compound isolated from the bacterium *Streptomyces hygroscopicus [81]*. It selectively inhibits class I and II HDACs and SIRT6, leading to cell cycle arrest and the activation of pro-apoptotic events. TSA (**1**, Figure 6) has demonstrated antitumoral activity both *in vitro* and *in vitro*, primarily inducting the hyperacetylation of histone and non-histone proteins (e.g. ERα)[82–84]. Despite its potent biological activity, TSA (**1**, Figure 6) has not received FDA approval for clinical use due to its poor drug-like properties and toxicity. Indeed, it has served as pharmacological tool in the development of novel HDACis, guiding the development of more effective and clinically relevant inhibitors, such as Vorinostat (**2**, Figure 6), which in 2006 became the first FDA-approved HDACi, for the treatment of cutaneous T-cell lymphoma (CTCL) refractory to other treatments[85]. It has also been implicated in other cancer types, as brain metastasis, refractory colorectal, advanced solid tumors, melanoma, pancreatic, lung cancer and multiple myeloma. Vorinostat (**2**, Figure 6) was designed to retain the pan-HDAC inhibitory potency of TSA, while improving drug like properties such as bioavailability and stability. Vorinostat (**2**, Figure 6), is a Class

I and II inhibitor but it did not showed activity against Class III HDACs. Vorinostat (**2**, Figure 6) modulates the expression of genes related to tumor suppression, thus regulating cell cycle arrest, apoptosis, angiogenesis inhibition and the downregulation of immunosuppressive interleukins[86].

Panobinostat (**3**, Figure 6) have received FDA approval in 2015 for the treatment of multiple myeloma. It showed potent inhibitory activity against Class I, II and IV HDAC enzymes at nanomolar concentration, it induces tumor cell-specific cytotoxicity and has demonstrated anti-tumor activity in several *in vivo* tumor models [87]. Belinostat (**4**, Figure 6) is a close structural analogue of Panobinostat (**3**, Figure 6). It has been approved by FDA in 2014 for the treatment of patients with relapsed or refractory peripheral T-cell lymphoma (PTCL) [88].

In 2024, FDA approved Givinostat (**5**, Figure 6) for the treatment of Duchenne Dystrophy in patients aged from 6 years. It significantly slows the course of the disease by promoting motor function recovery and limiting tissue inflammation and necrosis. Givinostat (**5**, Figure 6) is also the first approved non-steroidal drug for the treatment of this pathology [89].

While several hydroxamate pan-HDACis have been approved, no selective HDAC6is have been approved so far. To date, several HDAC6is have been entered in Phase I and II clinical trials, although most of their chemical structures remain undisclosed. Among most relevant inhibitors, we acknowledge Ricolinostat (**6**, Figure 6), Citarinostat (**7**, Figure 6) and KA2507 (**8**, Figure 6).

Ricolinostat (**6**, Figure 6) is an orally bioavailable HDAC6i with nanomolar potency, considered to possess a more than 10-fold selectivity over HDAC isoforms 1, 2 and 3 [90]. However, high concentrations of Ricolinostat (**6**, Figure 6) induce both tubulin and histone hyperacetylation, thus confirming the lack of selectivity of this drug among HDACs. Accordingly, a very recent study, published in June 2023, pointed out Ricolinostat (**6**, Figure 6) anti-cancer activity is conserved even in HDAC6 genetic depletion models, thus confirming its

therapeutic effects are also mediated by other target proteins and highlighting the lack of strict selectivity on HDAC6 [91].

Citarinostat (**7**, Figure 6) displays slightly improved HDAC6 inhibitory potency and isoform selectivity (13 to 18 folds) with respect to Ricolinostat (**6,** Figure 6), which may be attributed to the presence of the electron-withdrawing chlorine substituent on the phenyl ring [92].

HPOB (**9**, Figure 6) is a selective HDAC6i bearing a bulky and rigid aromatic linker, and a phenyl-based linker, which attributes to this inhibitor more than 30-fold selectivity for HDAC6 over other isoforms. The short phenyl linker of HPOB (**9**, Figure 6) also prevents the cap group from interacting with the L1 loop, which is essential for the binding of HDACis to isoforms 1, 2 and 3, but not for interaction within HDAC6 binding site, thus explaining the high selectivity profiles of HPOB (**9**, Figure 6) for HDAC6 [93].

Nexturastat A (NextA, **10**, Figure 6) is an ureidic derivative with more than 190-fold selectivity over HDAC6 [94]. Very recently, an interesting study revealed a key correlation between the accumulation of phosphorylated HDAC6 condensate in cells nuclei and liquid-liquid phase separation, directly responsible for aberrant chromatin packaging, metastatic events and aggressive cancer behaviour [95,96]. Interestingly, among assessed HDAC6is, NextA (**10**, Figure 6) demonstrated the unique ability to disrupt phospho-HDAC6 condensate formation and promote HDAC6 dephosphorylation through its release from the condensate phase to the liquid one, accompanied by apoptotic events and significant tumor growth inhibition [97]. Genome analysis revealed HDAC6 dephosphorylation induced by NextA (**10**, Figure 6) altered chromatin structure, leading to the upregulation of tumor suppressor genes, downregulation of proto-oncogenes, and activation of immunomodulatory pathways.

Due to the presence of a highly lipophilic cap group, consisting of six aromatic rings, Tubacin (**11**, Figure 6) exhibits a remarkable selectivity toward HDAC6 over other HDAC isoforms. Tubacin (**11**, Figure 6) has been shown to disrupt the interaction between HDAC6 and dynein, a motor protein complex involved in microtubule-dependent intracellular transport, consequently leading to a dose-dependent accumulation of polyubiquitinated proteins, consistent with HDAC6 role in aggresome formation and protein homeostasis regulation [98]. Despite its promising selectivity profile, Tubacin (**11**, Figure 6) is affected by high lipophilicity, suboptimal pharmacokinetic properties, and synthetic complexity, which have limited its potential as a therapeutic agent. As a result, its application has been primarily restricted to the chemical biology field, where it serves as a chemical probe for elucidating the biological functions of HDAC6 and investigating its role in neurodegenerative diseases, cancer, and protein degradation pathways.

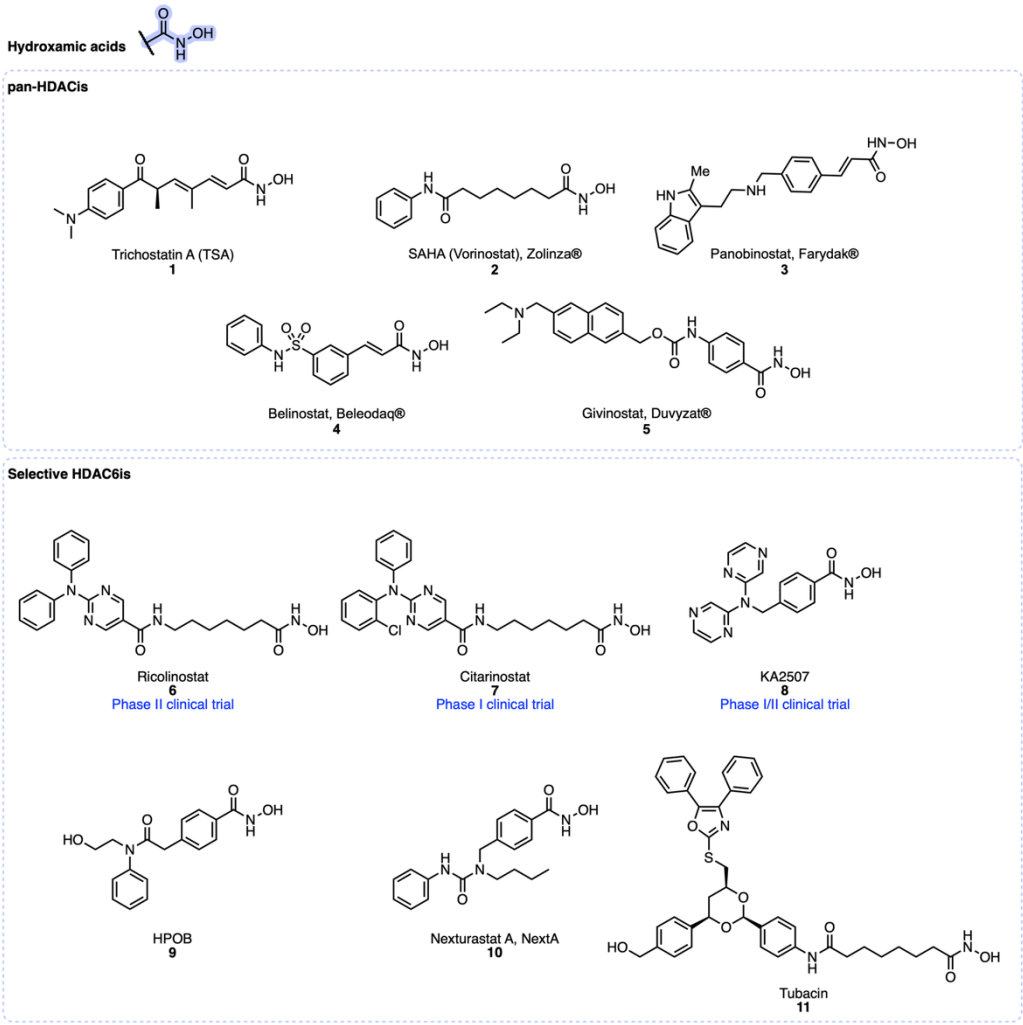


Figure 6. Structures of hydroxamate HDACis **1-11**.

Although the hydroxamic group represents a well-established and highly effective zinc-coordinating group, which ensures strong inhibition of HDAC enzymes family, many concerns remain regarding its potential mutagenic liability [99]. This issue is primarily associated with the generation of reactive intermediates during metabolic processing, which pose safety concerns in long-term therapeutic applications. Indeed, hydroxamic acids can undergo Lossen rearrangement *in vivo,* supposed to be the main mechanism underlying

mutagenicity of this chemical class. Indeed, in the presence of a base, the hydroxamate moiety generates a transient, unstable anionic intermediate, which rapidly rearranges to yield isocyanate species, highly reactive chemical species capable of readily binding to nucleophilic DNA nucleobases (Figure 6) [100]. The interaction between the isocyanate and DNA results in the formation of ureido adducts, which compromise the integrity of the genetic material, thereby interfering with normal DNA replication and repair processes, potentially contributing to genetic mutations and genomic stability, recognized drivers in carcinogenesis underlying hydroxamic acids toxicity. The second proposed *in vivo* rearrangement mechanism involves a zinc-triggered reaction. As previously described, hydroxamates are capable of coordinating zinc ions with high affinity. Their low acidity suggests hydroxamic acids reach the active sites as neutral molecules, and the deprotonation reaction, to form a strongly chelating hydroxamate anion, takes place after the chelation of the zinc cation. Hydrogen migration from the nitrogen atom to the hydroxy group leads to the formation of an unsaturated complex in which zinc bears anionic aceto-hydroxamate, water, and acetylnitrene as ligands. The nitrene can undergo rearrangement to yield a more stable isocyanate species (Figure 7) [100].

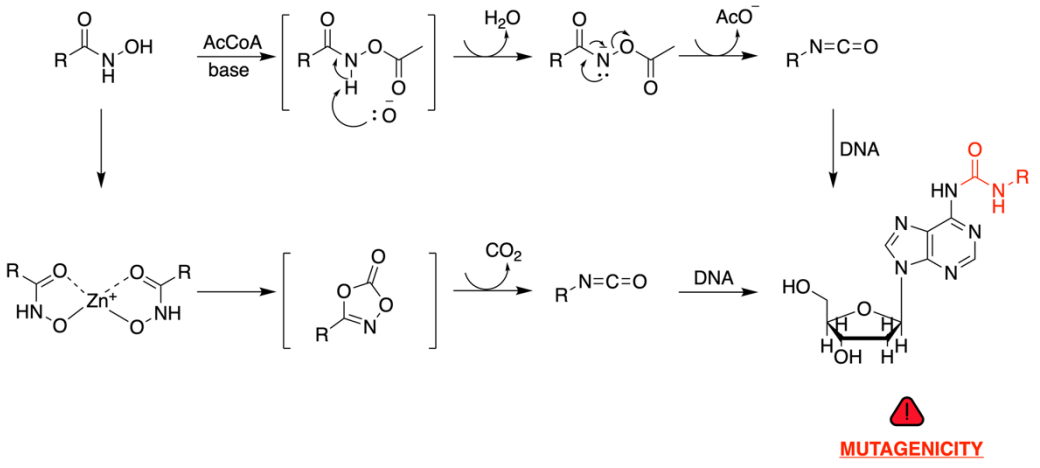


Figure 7. Base-mediated (upper part) and zinc-triggered (lower part) Lossen rearrangement occurring on hydroxamic acids *in vivo*.

Consistently, hydroxamate HDACis on the market, such as Vorinostat, are Ames positive and cause chromosomal aberrations in rodent cells. Indeed, most HDACis are approved for cancer treatment or diseases considered to be life threatening, since compounds displaying genotoxic effects are unsuitable for a chronic use, considering the risk of secondary complications such as the onset of oncological disorders or DNA damage. Therefore, in diseases requiring prolonged use of HDACis, it would be highly preferable to develop new inhibitors with less toxic effects.

Benzamide derivatives

Benzamide based inhibitors are selective for Class I HDACs. They inhibit HDACs through the coordination of the catalytic Zn^{2+} ion involving the *o*-aminoanilide group. Despite the high selectivity of this ZBG for isoenzymes belonging to Class I, the benzamide group has been related to *in vivo* toxicity, thus no benzamide derivatives have been approved by FDA so far.

Tucidinostat (**12**, Figure 8) is a Class I (HDAC1, 2 and 3) and Class IIb (HDAC10) inhibitor, approved by the Chinese FDA for the treatment of PTCL. In 2021, Tucidinostat (**12**, Figure 8) has been approved by Japanese Pharmaceuticals and Medicals Devices Agency (PMDA) for relapsed or refractory adult T-cell leukemia-lymphoma [101].

Entinostat (**13**, MS-275, Figure 8) has received FDA approval in 2015 for treatment of hestrogen receptor positive breast cancer subtypes. It is a Class I selective inhibitor which showed efficacy in different hematological malignancies and solid tumors through the modulation of genes involved in cell cycle control, apoptosis, immune modulation, and differentiation[102,103].

Similarly, Mocetinostat (**14**, MGCD0103, Figure 8) is currently enrolled in Phase I/II clinical trials for the treatment of hematological malignancies [104].

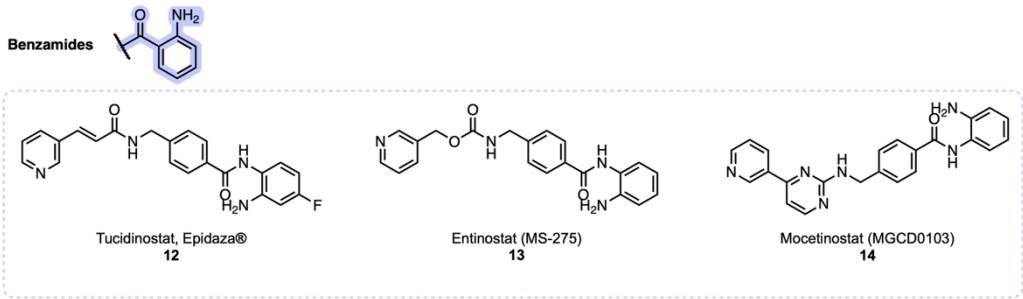


Figure 8. Structures of benzamide HDACis **12-14**.

Cyclic peptides

Romidepsin (**15**, Figure 9) is a bicyclic depsipeptide originally isolated by *Chromobacterium violaceum*. It has been approved by FDA for patients affected by CTCL and PTCL which have received prior systemic therapies. Romidepsin (**15**, Figure 9) specifically inhibits Class I and II HDACs, inducing cell cycle arrest and apoptotic events in malignant cells. It is the only HDACi administrated as prodrug. Upon administration, the disulfide bridge is reduced *in vivo* by glutathione reductase, converting it into the pharmacologically active thiol derivative **16** (Figure 9), able to coordinate the catalytic zinc ion [105].

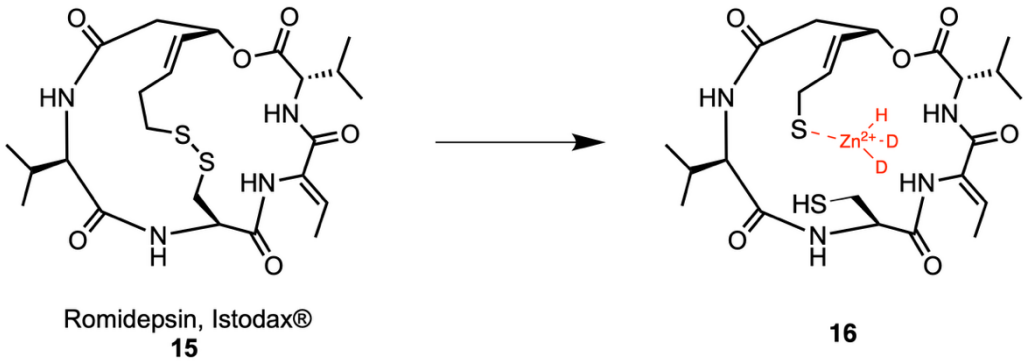


Figure 9. Structure of Romidepsin **15** and its active form **16** coordinating a Zn^{2+} ion.

Trifluoro 1,2,4-oxadiazoles

In 2013, the trifluoromethyl 1,2,4-oxadiazole (TFMO) moiety was disclosed as novel ZBG with high isoform specificity for Class IIa HDACs. TFMOs mediate enzyme inhibition the coordination of the catalytic Zn^{2+} ion through one of the oxadiazole ring oxygens and a fluorine atom in the CF_3 group [106]. Despite the promising pharmacological outcome of this chemical class, only a limited number of studies involving TFMO-based inhibitors appeared since 2021, when Scott and coworkers disclosed promising preclinical data for a novel class of TMFO-based class IIa HDACis in Huntington Disease, while in 2024 TFMO-based inhibitors were reported for oncological application [107,108]. In 2023, novel TFMOs derivatives featuring pyrrolo-pyrimidine and purine cap groups were reported as selective Class IIa and HDAC6is [109]. Although limited, these studies underscore the importance of fine-tuning the combination of the cap group and the ZBG to achieve potency and isoform selectivity within HDAC family (Figure 10).

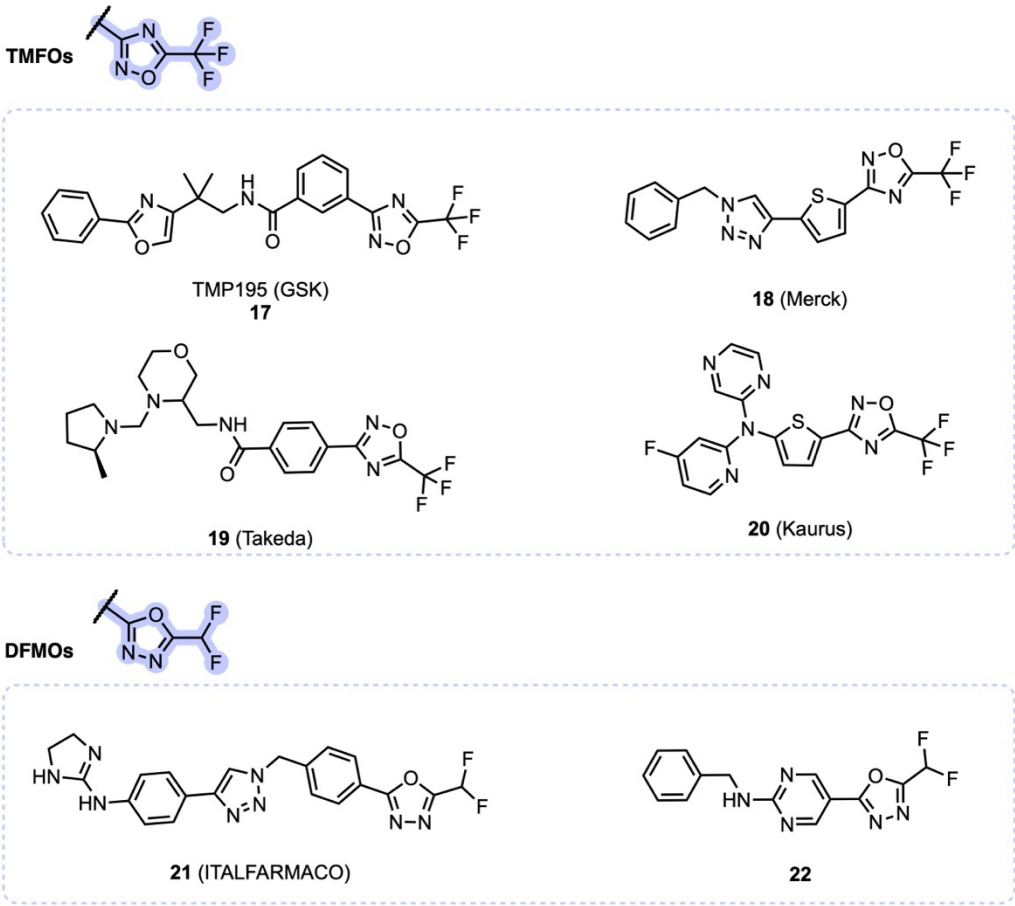


Figure 10. Structures of representative TFMO and DFMO based HDACis.

Difluoro 1,3,4-oxadiazoles

In 2017, difluoro 1,3,4-oxadiazoles (DMFOs) have been unveiled as novel ZBG for the selective inhibition of HDAC6 isoenzyme (Figure 10). Despite DMFOs showed a potent inhibitory profile, their underlying mechanism of action remained unclear until 2020, when the first detailed biochemical studies, independently reported by Hansen and Steinkühler research groups, confirmed DMFOs as mechanism-based inhibitors, which undergo an enzyme-catalysed ring opening to form the corresponding acetyl-hydrazide, in turn able to tightly bind Zn^{2+} ion in HDAC6 active site, thereby resulting in irreversible inhibition [110,111].

In 2023, König et al. demonstrated DFMOs act as slow-binding inhibitors, following a two-step and substrate-dependent inhibition mechanism [110]. Crystal structure of compound **22** (Figure 11) in complex within *h*HDAC6 revealed that the zinc-bounded water molecule in HDAC6 catalytic site mediates a nucleophilic attack on oxadiazole ring, thus catalysing its enzyme-mediated hydrolysis. This reaction generates the corresponding difluoroacetyl hydrazide, which tightly coordinates the catalytic zinc ion. Additionally, the difluoroacetic moiety occupies a pocket defined by P571 residue - a unique feature of HDAC6 - thus contributing to high isoform selectivity and essentially irreversible inhibition. Accordingly, the corresponding trifluoro 1,3,4-oxadiazole did not undergo ring-opening in the same conditions, likely due its lower nucleophilicity. Furthermore, structural analysis revealed that the introduction of the trifluoroacetyl moiety turned in steric clash with the backbone carbonyl of G582, contributing to a reduced binding affinity and overall weaker inhibitory activity compared to the DFMO analogue **22** [110].

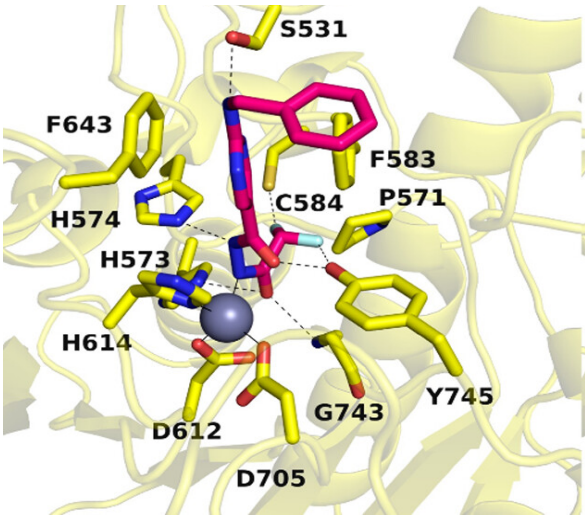


Figure 11. Binding mode of **22** within *z*HDAC6 CD2 (PDB: 8GD4) [110].

In parallel, Steinkühler et al. provided key mechanistic insights into the selective inhibition profile of DFMOs towards HDAC6is. Kinetic studies demonstrated that the inhibitory activity of compound **21** increased during the time course of the assay, consistent with a slow-binding inhibition mechanism for this class of compounds. Furthermore, co-crystallographic studies of compound **21** within *z*HDAC6-CD2 revealed an electron density of the bound ligand not compatible with the DFMO structure. This observation strongly suggested an enzyme-mediated ring-opening reaction had occurred, in agreement with the mechanism proposed by König et al. for compound **22**. In the first proposed pathway, the zinc-bound water molecule mediates a nucleophilic attack on the oxadiazole ring, leading to ring opening and formation of the corresponding difluoroacetyl hydrazide (C2, Figure 12), which transiently dissociates from the enzyme active. Upon rebinding, intermediate C2 may undergo a second hydrolysis step, that further stabilizes its interaction with the catalytic Zn^{2+} ion, resulting in tight-binding and HDAC6 irreversible inhibition [111]. The second hypothesized mechanism involves the initial binding of the DFMO within HDAC6 catalytic site. Catalytic Zn^{2+} ion could enhance the electrophilic behaviour of the sp^2-hybridized carbon in the oxadiazole ring, facilitating the nucleophilic attack by the zinc-bound water molecule. The corresponding hydrated DFMO intermediate B (Figure 12) forms hydrogen bonds with the catalytic histidine dyad, also preserving the original interaction with Y745. However, this intermediate is instable and can undergo a subsequent ring-opening reaction to yield the corresponding difluoroacetyl hydrazide, which irreversibly coordinates catalytic Zn^{2+} ion[111,112].

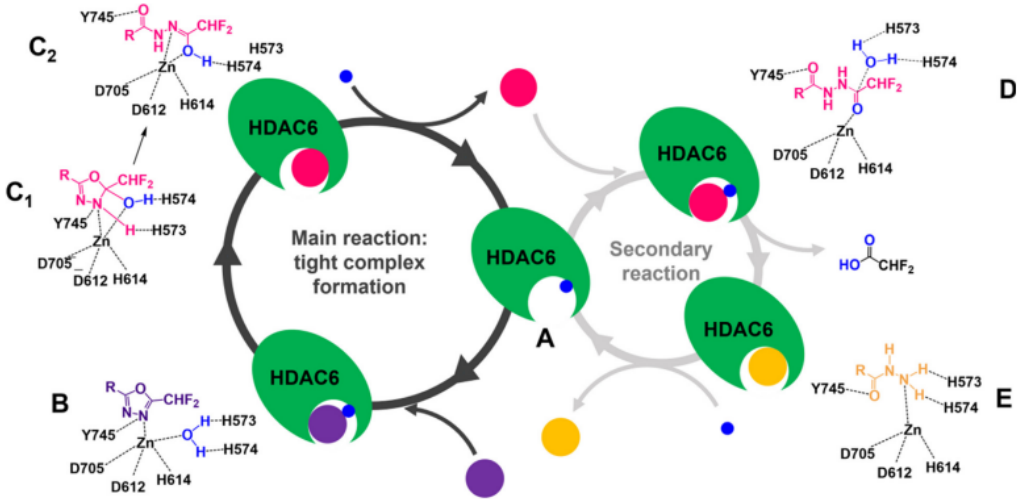


Figure 12. Proposed inhibition mechanism of DFMOs [111,112].

1.4 HDAC6: a unique isoenzyme among HDAC family

1.4.1 HDAC6 structure

As mentioned, HDAC6 is a member of the Class IIb histone deacetylase family, predominantly localized in the cytoplasm, with high tissue-specificity in heart, liver, kidney, and pancreas. HDAC6 stands out for the presence, in its structure, of two homologous, highly conserved, tandem catalytic domains (CD1 and CD2). Structurally, five domains can be identified in HDAC6 structure (Figure 13) [113–115]:

1) N-terminal end (a.a:1-87). It contains a Ser-Glu tetradecapeptide (SE14) motifs and a leucine-rich nuclear export signal (NES), which play a crucial role in the retainment of human HDAC6 in the cytoplasm.

2) The catalytic domains CD1 (a.a: 88-447) and CD2 (a.a: 482-800). At first was assumed that both catalytic domains of HDAC6 possess independent activities and contribute independently to the activity of HDAC6. However, some studies have shown that the activity of HDAC6 relies solely on CD2, while the integrity of both HDAC6 catalytic domains is indispensable for the whole tubulin

deacetylase activity of the enzyme. A zinc ion, present at the bottom of the catalytic pocket of HDAC6 is required for the deacetylase function of HDAC6.

3) The dynein motor binding region (DMB) in between CD1 and CD2. It helps HDAC6 to bind dynein and to transport the cargo of ubiquitinated proteins along microtubules (MTs).

4) The C-terminal region containing a zinc finger ubiquitin binding domain (ZnF-UBP, a.a: 1131-1192). It is involved in ubiquitination process in protein clearance and degradation *via* aggresome pathway.

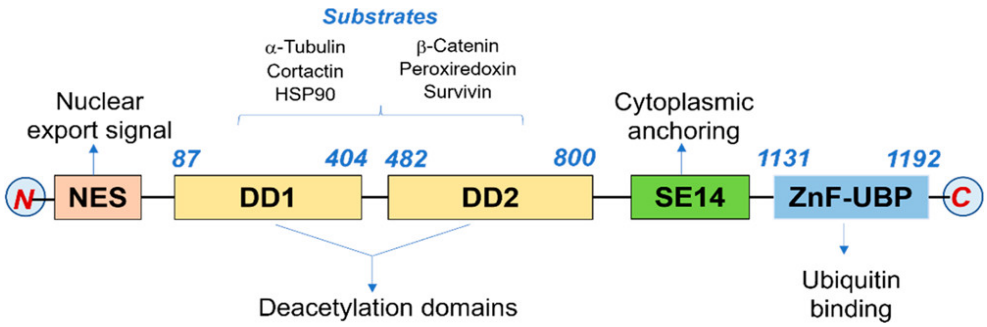


Figure 13. HDAC6 structural domains [114].

1.4.2 HDAC6 catalytic deacetylase mechanism

The first solved HDAC structure is the crystal structure of histone deacetylase-like protein (HDLP) from *Aquifex aeolicus*. HDLP shares significant structural and functional homology with eukaryotic HDACs, thus Finnin et al. proposed a catalytic mechanism for Class I and II HDACs according to X-ray structures of HDLP in complex with Trichostatin A (**1**, TSA, Figure 6) and Vorinostat (**2**, SAHA, Figure 6)[79]. According to the established catalytic mechanism, the Zn^{2+} ion in the active site is coordinated by one histidine and two aspartate residues, and a water molecule. Zn^{2+} ion binds the oxygen of the acetyl group to be hydrolysed, and the oxygen of a water molecule. These interactions polarize the

carbonyl group of the acetylated lysine rendering it more electrophilic, while the water molecule becomes more nucleophilic due the additional interaction with the H131. The water molecule performs a nucleophilic attack on the carbon of the carbonyl group leading to the formation of a tetrahedral oxyanion intermediate that is stabilized by the interactions with the Zn^{2+} ion and with the oxygen of Y297. At the end, breakage of the carbon-nitrogen bond would occur, and a proton would be transferred from H132 to the nitrogen atom with the release of both the acetate group and deacetylated lysine (Figure 14) [79].

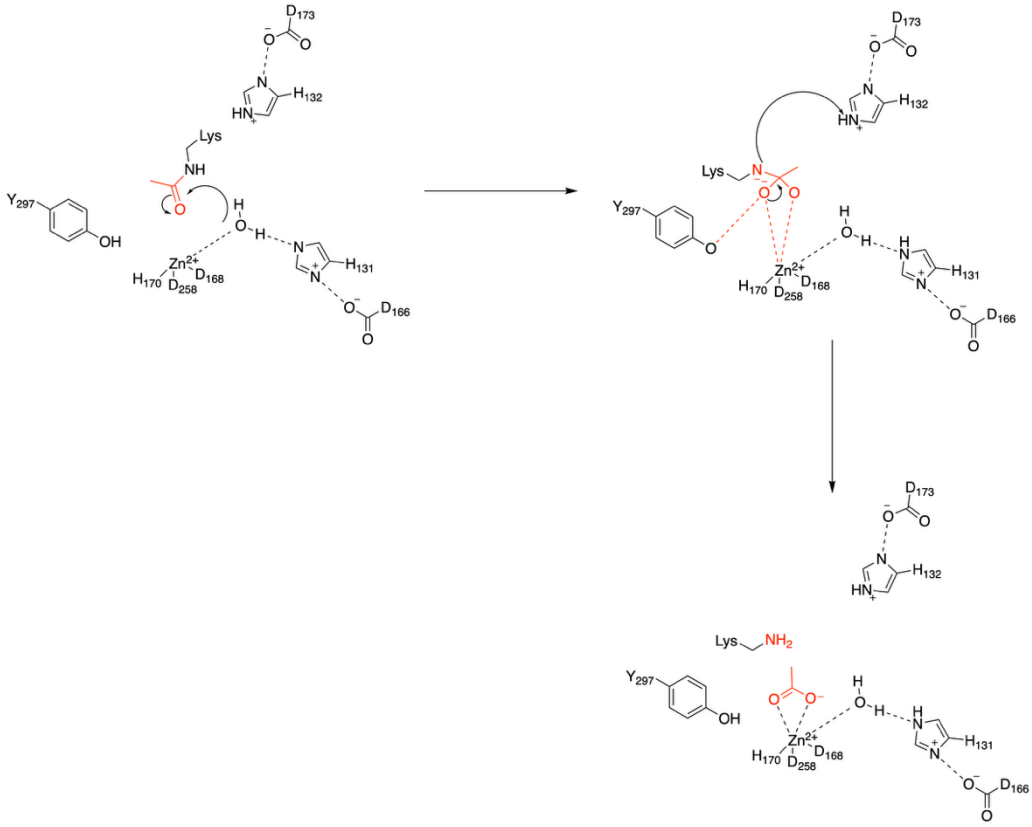


Figure 14. Catalytic hydrolysis mechanism proposed by Finnin et al.

1.4.3 HDAC6 substrate specificity

For its localization, HDAC6 is mainly involved in regulating the function of several non-histone proteins, such as α-tubulin, Hsp90, cortactin, retinoic acid-

inducible gene I, beta-catenin and many more. Also, HDAC6 can interact with nuclear proteins such as the DNA repair factor KU70.

HDAC6 and α-tubulin

The first identified and best studied HDAC6 substrate is tubulin. In particular, acetylation on K40 residue is one of the most common PTMs occurring on tubulin, strictly related to microtubule stability, cellular resistance to mechanical stress and intracellular transport[116]. HDAC6 was found to catalyze the opposite reaction, affecting overall tubulin assembly and stability. Indeed, α-tubulin monomers electrostatically interact with each other, contributing to protofilaments stability within the microtubule lattice. K40 acetylation occurring on α-tubulin leads to the loss of these electrostatic interactions, thereby reducing inter-protofilament interactions and leading to increased microtubule flexibility under mechanic stress. Thus, when HDAC6 exerts its deacetylase activity restore microtubule dynamics by reducing tubulin stability. Impaired HDAC6 activity has been found in several pathological states, leading to unbalanced degree of α-tubulin acetylation. For instance, HDAC6 overexpression leads to α-tubulin hypoacetylation, with increased cell motility and chemotactic behaviour (Figure 15)[117]. α-tubulin hypoacetylation induced by HDAC6 has also been linked to reduced axonal transport, due to reduced binding affinity of kinesin-1 to microtubules, directly affecting cargos transport along microtubules and protein aggregate accumulation in neurodegenerative diseases[118–122]. In addition to microtubule-dependent cell motility, HDAC6 is also implicated in cytoskeletal remodeling, through the interaction with the F-actin binding protein cortactin. Under physiological conditions, cortactin recruits Arp2/3 complex and promotes actin polymerization, thus promoting cytoskeleton stability. By deacetylating cortactin, HDAC6 enhances the association affinity between cortactin and F-actin, while cortactin hyperacetylation prevents its translocation to the cell periphery, and blocks its association with F-actin, impairing cell motility[123].

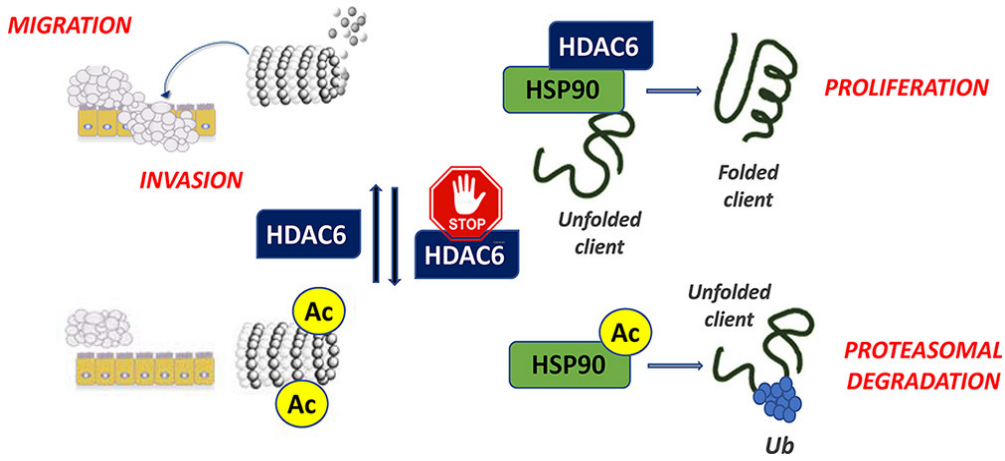


Figure 15. HDAC6 interaction with α-tubulin and Hsp90 [115].

HDAC6 and Hsp-90

Under normal conditions, cell maintains protein homeostasis through a tightly regulated network involving Heat-shock protein (Hsp90), an ATP-dependent molecular chaperone which plays a pivotal role in both detecting ubiquitinated cell aggregates (Figure 15), and regulating folding and function of many client proteins, such as hormone receptors. Under physiological conditions, HDAC6 forms a multi-protein complex with VCP/p97 (an ATPase involved in protein degradation and trafficking), Hsp90 and heat-shock factor 1 (HSF1, a transcription factor inactive when associated with Hsp90). Under stress conditions, HDAC6 dissociates from this complex - as a result of cytoplasmic accumulation of misfolded proteins - resulting in HSF1 activation. In its active form, HSF1 forms a trimer able to bind heat shock elements, resulting in the activation of the transcription of heat shock factors (e.g. Hsp70 and Hsp40), which counteract proteotoxic conditions ensuring cell survival [124].

HDAC6 and ubiquitin

Due to the presence of its C-terminal ZnF-UBP, HDAC6 is also able to directly bind polyubiquitinated proteins. Indeed, in addition to the regulation of protein clearance mediated through its interaction with Hsp90, HDAC6 plays a crucial

role in the recognition, binding, and transport of misfolded ubiquitinated proteins (Figure 16). Thus, ubiquitinated proteins aggregates bind HDAC6 and are bind to dynein motor complex, facilitating their transport on microtubules toward the microtubule-organizing center (MTOC), where they form aggresomes – specialized structures for sequestering misfolded protein by autophagy pathways [125]. Also, VCP/p97 – previously mentioned as HDAC6 binding complex - was found to be involved in ubiquitin-proteasome degradation pathway. Indeed, when VCP/p97 chaperone binds HDAC6, it negatively regulates excessive polyubiquitin chain assembly and accumulation promoted by HDAC6 itself. Under stress conditions, VCP/p97 dissociates from HDAC6, thus allowing its interaction with polyubiquitinated proteins and their transport towards microtubules [126]. These data are further corroborated by experiments conducted on HDAC6-deficient cells, in which protein clearance is impaired resulting in the accumulation of protein aggregates.

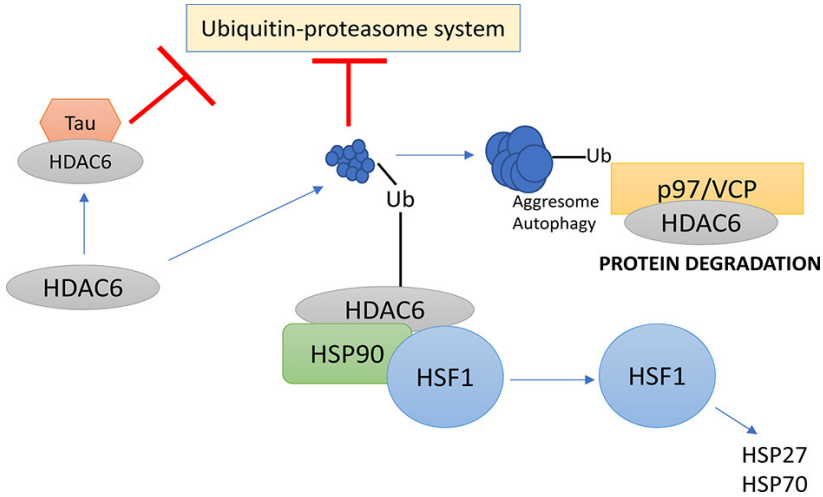


Figure 16. HDAC6 interaction with ubiquitin and tau protein [115].

HDAC6 and peroxiredoxin

Peroxiredoxin are a family of cysteine-based antioxidant enzymes involved in the regulation of redox reactions in cells, thereby modulating important cellular

functions such as cell proliferation and apoptosis. Among the six identified mammalian peroxiredoxins (Prdx I–VI), several have been shown to undergo reversible acetylation, which influences their enhances its reducing activity, its resistance to super-oxidation and its resistance to high-molecular-mass complexes. Therefore, HDAC6 deacetylase activity on PrxI and II was suggested to enhance their ability to reduce H_2O_2 rather than their non acetylated form, suggesting the possibility to inhibit HDAC6 to counteract oxidative stress in many pathological states [127,128].

HDAC6 and Tau

Tau proteins family comprises six distinct tau isoforms located into the brain and acting as neuronal microtubules stabilizers, thereby playing a crucial role in axonal transport and cytoskeletal integrity. HDAC6 was found to bind tau proteins both *in vitro* and brain tissue derived by patients through the interaction of HDAC6 SE14 domain and microtubule-binding repeat domain on tau. This interaction facilitates the transport of tau toward aggresome-like compartments, particularly under proteasomal stress. For instance, in cells treated with the proteasome inhibitor MG132, HDAC6 was found co-localized with tau in perinuclear inclusions, strongly suggesting the role of HDAC6 in tau sequestration and degradation *via* aggresome pathway [129]. Interestingly, the inhibition or catalytic inactivation of HDAC6 did not impair its interaction with tau, while decreasing its phosphorylation on T231, thus suggesting HDAC6 catalytic activity is not necessary for binding tau protein [130]. On the contrary, HDAC6 inhibition resulted in Hsp hyperacetylation, thereby promoting its release from HDAC6-Hsp90 complex and ubiquitination of phosphorylated tau proteins (Figure 16) [131].

HDAC6 and TFG-β

TFG-β1 is a key hallmark and the main regulator in ephitelial-mesenchila-transition (EMT), a cellular process whereby epithelial cells loss their adhesion

properties, while acquiring mesenchymal and migratory ones [132]. This process is strictly related to organ fibrosis (e.g. idiopathic fibrosis) and metastatic events in cancer. When TFG-β1 binds its receptors, it activates downstream signalling pathways, including the SMAD-dependent one. SMAD proteins are transcriptional factors which, when activated by TFG-β1, translocate into the nucleus and promote the transcription of EMT-related genes. Notably, EMT induced by TFG-β1impairs HDAC6 deacetylase activity on α-tubulin, thus affecting microtubules stability and prompting cell motility and invasiveness (Figure 17). Accordingly, HDAC6 inhibition downregulates TFG-β1 induced signaling and increases SMAD3 acetylation, thereby reducing SMAD2/3 phosphorylation, nuclear translocation, and transcriptional activity [133,134].

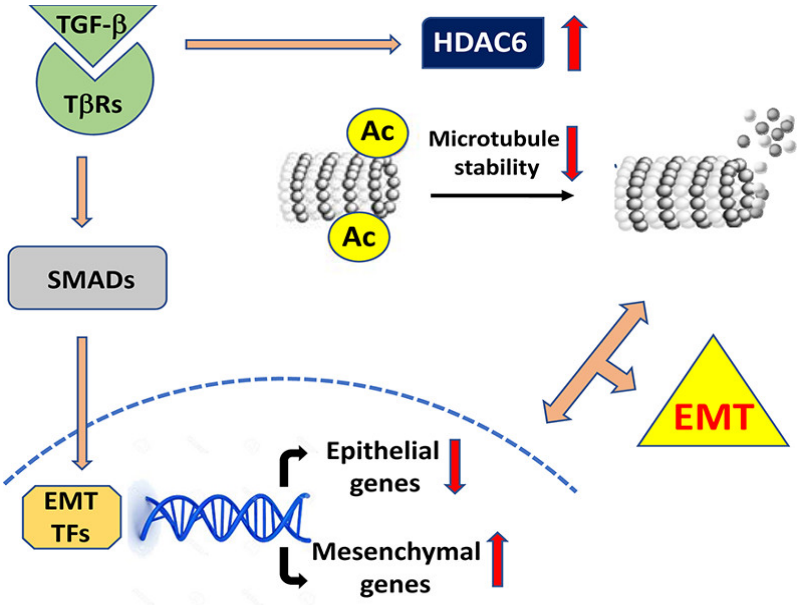


Figure 17. EMT activation mediated by HDAC6 and TGF-β [115].

1.5 HDAC6 in pathological states

1.5.1 HDAC6 role in rare diseases

Rare diseases are chronic and life-threatening disorders affecting a small percentage of population and characterized by a wide diversity of symptoms. Although rare diseases have been typically attributed by single-gene mutations, the arising knowledge in the field of epigenetics revealed crucial insights in both the onset and development of these kinds of disorders. In this context, HDAC6 abnormal activity has been implicated in the pathogenesis of several neurodegenerative and inflammatory disorders. Thereby, the role of HDAC6 in rare disease phenotype will be discussed in the present *Paragraph.*

Cystic Fibrosis

Cystic Fibrosis (CF) is an inherited autosomal recessive disease caused by mutations in cystic fibrosis transmembrane regulator (CFTR) gene, which encodes for a cAMP-regulated chloride channel, located on the apical surface of epithelial cells [114]. CFTR protein is mainly expressed in lungs, pancreas, liver, sweat glands and reproductive tract, whereby it promotes the expulsion of chloride from cells and inhibits the epithelial sodium channel (ENaC), thus regulating the osmotic balance between the intracellular and extracellular environments. Nowadays, about 2000 CFTR mutations have been recognized, responsible for impaired protein function and defective ion transport across apical membranes of the epithelial cells [135]. CFTR ΔF508 mutation is the most common in CF, accounting for approximately 70% of all CF alleles worldwide. ΔF508 mutation is associated with defects in CFTR transport from the nucleus to the cell membrane, and with reduced stability of the channel in the cell membrane itself. In turn, CFTR mutations lead to an excess of mucin relative to salt and water in the airway surface liquid, thereby impairing ciliary and cough-dependent clearance, ultimately resulting in mucus stasis and organ obstruction. In lungs, thickened mucus accumulation impairs mucociliary clearance, causing inflammation and creating a favourable environment for persistent bacterial

infections, which in turns worsen inflammatory state, leading to lung damage, fibrosis, and loss-of-function. Recent studies have shown that defective CFTR itself impairs autophagy mediated by reactive oxygen species (ROS), contributing to increased oxidative stress in the respiratory tract [136,137]. Therefore, the absence of CFTR on the surface of epithelial cells triggers pro-inflammatory signalling mediated by nuclear factor kappa-light-chain-enhancer of activated B cells (NF-κB) and IL-8 dependent neutrophil chemotaxis, resulting in a chronic inflammatory state [138]. Abnormal mucus production, accompanied by reduced respiratory clearance, also facilitates the onset of bacterial and fungal infections (e.g. *Pseudomonas aeuruginosa*, *Candida albicans*) difficult to eradicate. Primary infections caused by *P. aeruginosa* easily become chronic due to the onset of chemoresistant strains, making the choose of *ad persona* treatments essential for patient survival. Moreover, sticky mucus creates areas of low oxygen tension, which are well known to promote biofilm formation by pathogens (particularly *P. aeruginosa*), which is one of the main causes of antibiotic resistance in bacterial infections [139]. Taken together, the onset and persistence of lung infections and the overactivation of inflammatory response represent one of the main causes of morbidity and mortality in patients affected by CF. For these reasons, currently available CF treatments comprise a multidrug approach to address the various aspects of the disease, including CFTR modulators (enhancers, correctors, or amplifiers) in combination with antibiotics, bronchodilators, mucolytics, anti-inflammatory agents, and nutritional supplements, such as pancreatic enzymes and vitamins. Despite the role of epigenetics in CF has not yet been entirely unveiled, several studies have pointed out the involvement of DNA methylation and histone modifications in CFTR gene regulation and protein activity [140–142]. For instance, CFTR expression was found to be directly influenced by DNA methylation at CFTR gene CpG islands. In CF epithelial cells – where ROS-mediated autophagy is triggered by

impaired CFTR function – hypermethylation in CFTR was found, thus suggesting a direct correlation between CFTR expression and this epigenetic modification [143]. Similarly, the involvement of HDAC6 in the activation of key pathological mechanisms in CF has been validated by various studies conducted on both cellular and murine models, which mimic CF pathological state. In the context of inflammation, HDACis showed efficacy in reducing key inflammatory markers, such as various cytokines and interleukins. In mice lacking both copies of the CFTR gene and infected with *P. aeruginosa* lipopolysaccharide (LPS), Vorinostat (**2**, Figure 6) administration significantly reduced of IL-8 and NF-κB activity [144]. Similarly, selective HDAC6is such as MC2780 (**23**, Figure 20) and Tubastatin A (TubA, **24**, Figure 22) showed efficacy, respectively, in reducing IL-1β expression in epithelial fibroblast and the expression of IL-6 in an arthritis mouse model [145]. Also, both pan-HDAC and selective HDAC6 inhibition influenced CCL-4 expression, as well as the genetic depletion of HDAC6 was found to suppress activity of $FoxP3^+$ regulatory T-cells in inflammation models. Taken together, these data strongly support the involvement of HDAC6 in regulating inflammatory state related to CF (Figure 18)[146].

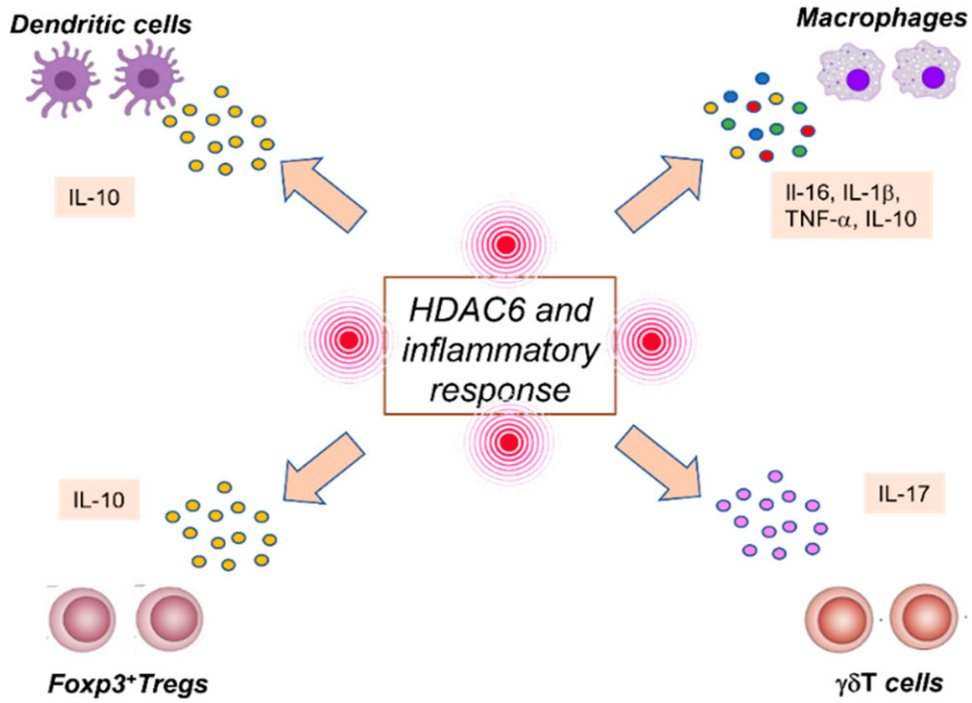


Figure 18. HDAC6 role in the regulation of inflammatory markers [114].

As previously described, in CF patients, inflammatory states are often accompanied and worsen by the persistence of chronic infections – most commonly by multidrug resistant *P. Aeruginosa* strains. Recent studies have pointed out how certain bacteria can disrupt epigenetic mechanisms governing host system inflammatory response, thus suggesting the use of epigenetic modulators – such as HDACis - as a novel and non-canonical therapy to counteract difficult-to-treat bacterial infections. In this context, HDAC1 affinity for immunity gene promoters was found to decrease during the course of *Anaplasma phagocytophilum* infection in granulocyte models, while both HDAC1 silencing and pharmacological inhibition induced by siRNA restored the expression of genes related to host immune defence, significatively reducing bacterial load [147]. In 2016, it was demonstrated that the *P. aeruginosa* quorum-sensing signal 2-aminoacetophenone prompted the expression of HDAC1 in human THP-1 monocytes, in turn resulting in H3K18 hypoacetylation and

reduced induction of inflammatory cytokines and chemokines (e.g. TNF and IL-β). Interestingly, HDAC1 inhibition completely reverted its overexpression induced by 2-aminoacetophenone, thus confirming the pivotal role of HDACs in bacterial virulence [148].

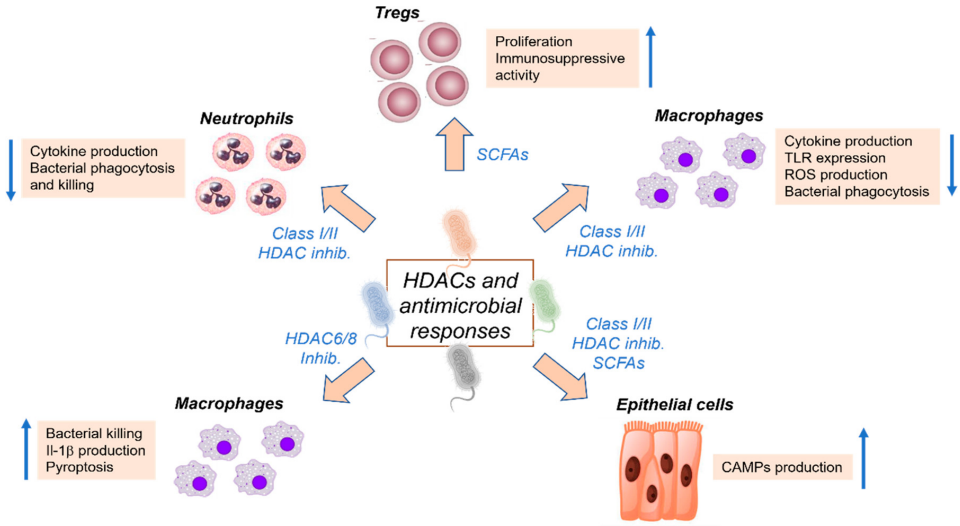


Figure 19. Modulation of antimicrobial response mediated by HDACs [114].

Also, anaerobic bacteria produce short chain fatty acids (SCFAs) as metabolites. Among them, propionic acid (**25**, Figure 20) and butyric acid (**26**, Figure 20) both act as Class I/II HDACis (due to the coordination of the catalytic Zn^{2+} ion mediated by the carboxylic acid moiety)[149]. Accordingly, the suppression of HDAC6 and HDAC9 mediated by butyrate showed a suppressive role in $FoxP3^{+}$ induction, thereby increasing the suppressive function of T cells [150]. Similarly, valproic acid (VPA, **27**, Figure 20) – an anticonvulsant drug – and TSA (**1**, Figure 6) were found to act as repressors of cytokine production in macrophages (Figure 19). *In vivo*, VPA (**27**, Figure 20) increased the mortality of mice affected with non-severe infections by *Klebsiella pneumoniae* or *Candida albicans* [151], while reducing phagocytosis and killing of *Escherichia coli* in bone-marrow derived macrophages [152].

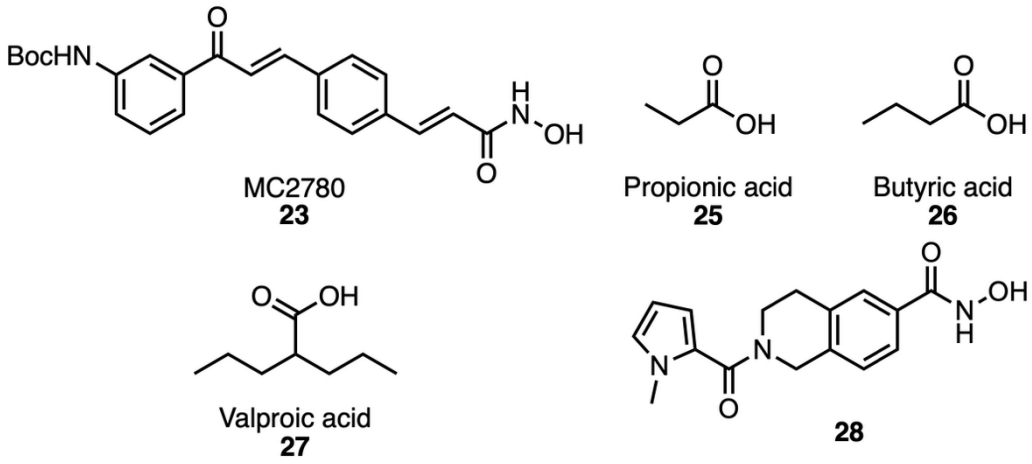


Figure 20. Structures of HDACis which showed efficacy in CF-related anti-inflammatory and antimicrobial response.

More interestingly, while pan-HDACis - such as VPA - impaired host system ability to fight bacterial infections, selective HDAC6 inhibition mediated by Tubstatin A (TubA, **24**, Figure 26) enhanced macrophages bacterial killing, thus prompting bacterial clearance. Also, TubA reduced pro-inflammatory cytokine production, restored innate immune cell populations in the bone marrow, and improved *in vivo* survival in sepsis models (Figure 19) [153–155]. HDAC genetic depletion was also found to enhance bacterial clearance in an *in vivo* model of *P. Aeruginosa* infection recapitulating CF airway, thus further highlining HDAC6 is a pivotal player in phenotypes related to CFTR impaired function, and corroborating the use of selective HDAC6is in CF patients.

Interestingly, CF fibroblasts are more sensitive to growth factors and exhibit an excessive release of TGF-β1, which in turns activates the epithelial-to-mesenchymal transition (EMT) pathway. As previously described, HDAC6 is a key player in EMT mediated by TGF/SMAD signalling [134,156]. Accordingly, the correlation between TGF-β1 and HDAC-dependent tubulin deacetylation in pulmonary epithelial cells has been outlined, confirming HDAC6 inhibition is able to reduce the expression of EMT markers induced by TGF-β1 in fibrotic

remodelling. Moreover, nasal epithelial cells from patients with double CFTR gene depletion displayed about a 40% reduction of acetylated α-tubulin compared to wild-type cells, which in turn leads to altered intracellular trafficking, and accumulation of cholesterol in endosomes and lysosomes [157]. Enhancing microtubule acetylation *via* HDAC6 inhibition restored cholesterol transport to levels comparable with wild-type cells[158,159]. Another important concern closely linked to CF morbidity is the presence of growth defects and weight loss. It has been shown that HDAC6 knockout mice exhibit increased growth in both length and weight. These finding demonstrated for the first time the potential to correct growth defects associated with CF, thus suggesting CF patients may benefit from the therapeutical use of selective HDAC6is [160,161].

Given the compelling new evidence for HDAC6 role in the dysregulation of proinflammatory phenotype in CF, as well as in the immune response to persistent bacterial infections, we sought to investigate the efficacy of selective HDAC6 inhibition in contrasting the pro-inflammatory phenotype in a mouse model of chronic *P. aeruginosa* respiratory infection. Upon selection and in-house re-profiling of literature potent and selective HDAC6is, we engaged the best performing compound **28** (Figure 20) to be investigated the *in vivo* infection model[162]. Compound **28 (**Figure 20) demonstrated *in vivo* a significant reduction of leukocyte recruitment in the airways, in particular neutrophils. Also, quantitative immunoassays confirmed a significant reduction of chemokines and cytokines in lung homogenate upon treatment with compound **28 (**Figure 20), accompanied by a modest reduced bacterial load compared to the vehicle. Thereby, we provided the first *in vivo* proof-of-concept for the efficacy of HDAC6 pharmacological inhibition in a chronic infection model of *P. Aeruginosa* miming CF phenotype [162].

<u>Idiopathic pulmonary fibrosis</u>

Idiopathic pulmonary fibrosis (IPF) is a chronic and progressive lung disease characterized by lung fibrosis in absence of a known triggering cause. The main hallmark in IPF is the aberrant activation of fibroblasts, including excessive proliferation, tissue invasiveness, myofibroblast transformation, and extracellular matrix overproduction [163]. After the diagnosis, the average life expectancy is of approximatively 5 years, while common symptoms include persistent cough, tiredness, and shortness of breath. Nowadays, nintedanib (tyrosine kinase inhibitor) and pirfenidone (antifibrotic and antinflamamtory drug) are the only drugs approved for the treatment of IPF. They showed efficacy in reducing fibrotic progress and pulmonary failure, delaying disease progression without reversing lung damage. However, their mechanism of action is still unclear, making the treatment of IPF still challenging [164,165]. As in part discussed in the previous section about the role of HDAC6 in CF physiopathology, several evidence have been provided supporting HDAC6 role in fibrotic degeneration in IPF[166]. Indeed, fibroblast accumulation active ates TGF-β1 signalling, which in turn promotes EMT. Mesenchymal cells acquire invasive, profibrotic and proinflammatory characteristics - by secreting extracellular mediators - overall contributing to lung tissue remodelling and fibrotic phenotype in IPF [167]. As previously discussed, TGF-β/SMAD3 signalling is tightly controlled by HDAC6, thereby suggesting the potential therapeutic value of HDCA6is in IPF-related fibrosis. Accordingly, both the selective HDAC6i Tubacin (**11**, Figure 6) and the pan-HDACi Vorinostat (**2**, Figure 6) respectively decreased the expression of EMT-related markers [168] – namely type-1 collagen and VEGF - and fibroblast differentiation and proliferation [169]. TGF-β1 also mediates the activation of COX-2 and, consequently, the production of prostaglandin E_2, an important antifibrotic mediator. In IPF cells, histone hypoacetylation reduced the expression of COX-2. Accordingly, the treatment with pan-HDACis restored COX-2 mediated

inflammatory response, thus counteracting fibroblast activation [170–172]. Aberrant expression of HDAC enzyme have been also proved in basal cells of IPF lungs, contributing to apoptosis resistance, due to the downregulation of Fas protein - a tumor-necrosis factor receptor [173]. Interestingly, increased histone acetylation levels were detected in the Fas promoter. The treatment with pan-HDACis restored Fas expression, while resulting in the upregulation of the pro-apoptotic gene Bak and downregulation of the antiapoptotic gene Bcl-xL, ultimately leading to fibroblasts apoptosis [174]. Taken together, these findings strongly support the efficacy of HDAC inhibition as potential therapeutic approach in IPF. In particular, targeting HDAC6 may provide significant advantages in countraacting EMT and fibrogenesis, while minimizing off-target effects in chronic treatments related to histone acetylation dysregulation mediated by pan-HDAC inhibition.

Rett syndrome

Rett syndrome (RTT) is a rare neurodegenerative disorder, primary affecting females. A common early symptom of the pathology is the regression of spoken language, with progression by various neurological, motor, and behavioural impairments, including growth failure, abnormal muscular tone and psychomotor development, and so on. Currently, there is no cure for RTT, with life expectancy of 50 years [175]. In 2023, Trofinetide – a synthetic analogue of glycine-proline-glutammate tripeptide - was approved by FDA as the first pharmacological treatment for RTT clinical manifestations, showing *in vivo* efficacy in reducing respiratory and motor symptoms [176]. RTT is caused by mutations in Methyl-CpG-binding protein 2 (MeCP2) gene, located on the X chromosome, which encodes the MeCP2 protein, essential for the correct development of nervous system. MeCP2 interacts with methylated DNA within CpG islands, acting as a transcriptional repressor by modulating chromatin remodelling [177]. MeCP2 abnormalities have been linked to defective Brain-Derived Neurotrophic Factor

(BDNF) – which is essential for growth, survival and differentiation of neurons in the brain - vesicle transport and microtubule dynamics. MeCP2 regulates BDNF expression through its binding to the BDNF promoter. Accordingly, reduced protein and mRNA levels of BDNF have been observed in MeCP2-deficient mice and RTT patients. Also, MeCP2-defective neurons exhibit a reduced number of synapses and defective calcium signalling when compared to controls. These phenotypic alterations are entirely consistent with those observed in RTT mouse models and post-mortem brain tissue from patients. Recent studies have shown MeCP2 defects results in hypoacetylation of α-tubulin, a well-known substrate for HDAC6. In brain, the correct balance of the degree of acetylated α-tubulin is essential for correct neurons migration, thereby promoting synaptic plasticity. Also, both MeCP2-mutated fibroblasts derived by patients and astrocytes from RTT mice showed significant impairment in microtubule dynamics, strictly related to tubulin hypoacetylation. In this context, the HDAC6i TubA (**24**, Figure 26) has demonstrated a strong ability in increasing levels of acetylated tubulin, leading to improved microtubule stability in fibroblasts from RTT patients [178]. HDAC6 inhibition restored defects in neuron axonal transport of BNDF in several neurological disorders characterized by impaired microtubule transport, such as Amyotrophic Lateral Sclerosis, Hung Huntington's Disease, Charcot-Marie-Tooth Type 2F, and so on [179–185]. These data strongly support the role HDAC6 as disease-modifying target, thereby prompting the use of HDAC6is as potential target to improve axonal transport and synaptic defects in RTT patients.

HDAC6 and Charcott-Marie-Tooth Disease

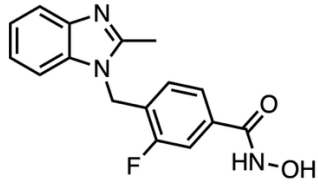
Charcott-Marie-Tooth Disease (CMT), also called hereditary motor and sensory neuropathy, comprises a heterogenous group of inherited disorders affecting peripheral nervous system. CMT early symptoms include muscle weakness in the lower limbs, dizziness and balance disorders, impaired sensorial responses

[186,187]. In most cases, as the pathology progresses, these symptoms lead to muscle atrophy and fatigue. To date, several gene mutations (e.g. MFN2, MPZ, HSPB1) have been identified as cause of different CMT subtypes, each of them leading to different clinical manifestations. For instance, CMT1 subtype is characterized by demyelination, causing reduced motor nerve conduction velocities, while CMT2 features axonal loss. Despite the genetic heterogeneity of this pathology, all CMT subtypes share common phenotypical features, arising from impaired axonal transport and cytoskeleton defects [188–190]. More in detail, the small heat shock protein B1 (HSPB1) is involved in many cellular processes, such as cytoskeleton protection, axonal viability and apoptosis. HSPB1 is also involved in the formation of neurofilaments, in the regulation of cells redox state and in preventing the formation of misfolded protein aggregates. Mutations in N-terminal tail of HSPB1 are associated to CMT2F subtype, resulting in reduced chaperone-activity of this protein, ultimately leading to neurofilaments aggregation and subsequent motoneuron degeneration and death [191].

Also, CMT2D subtype has been linked to mutations in glycil-tRNA synthetase (GlyRS), involved in covalently linking glycine to its conjugated tRNA during proteic synthesis. Mutations in GlyRS lead to peripheral axons degeneration and, consequently, deficits in distal motor function [192].

Despite the pan HDACi VPA (**27**, Figure 20) showed efficacy in CMT2B subtype by promoting neurites outgrowth in *Rab7* mutants independently from its pan-HDAC inhibitory activity [193], several HDAC6is significantly restored mitochondria motility and axonal transport, consistent with the role of this unique isoenzyme in regulating acetylated α-tubulin levels in microtubule dynamics. Indeed, in HSPB1 mutant dorsal root ganglion neurons (DRG), both the pan-HDACi TSA and selective HDAC6is TubA (**24**, Figure 26) and tubacin (**11**, Figure 6) increased mitochondria number [194]. However, only selective

HDAC6is were able to increase mitochondria motility, thereby highlighting the role of HDAC6 in neuronal transport impairments. *In vivo*, increased levels of acetylated α-tubulin upon treatment with TubA (**24**, Figure 26) and tubacin (**11**, Figure 6) significantly improved peripheral motorial functions. Accordingly, Kozikowski and coworkers identified compound **29** (Figure 21) as a high selective HDAC6i [195].



29

Figure 21. Structure of HDAC6i **29** which showed efficacy in CMT.

In HSPB1 mutant DRG, compound **29** (Figure 21) enhanced mitochondrial transport, increasing acetylated α-tubulin levels, while not affecting the degree of H3 acetylation, thus confirming both its selectivity profile and suggesting its efficacy in restoring axonal transport is likely due to HDAC6 inhibition. Consistently, HSPB1 mutant DRG derived from CMT mice showed increased motility and total number of mitochondria upon treatment with HDCA6is ACY738 and ACY775 – close structural analogues of the clinical candidate Ricolinostat (**6**, Figure 6) – in comparison to untreated neurons. *In vivo*, both ACY738, ACY775 and Ricolinostat showed efficacy in increasing both neuromuscular junction innervation and motor and sensory nerve conduction [196]. An elegant study published in 2018 also demonstrated HDAC6 interacts with mutant GlyRS in CMT2D models, resulting in HDAC6 overactivation, the decrease acetylated α-tubulin levels and, consequently, impaired axonal transport [197]. *In vivo*, HDAC6 inhibition completely rescued axonal transport in CMT2D mice models. These data unequivocably link HDAC6 inhibition, and the consequent increase in α-tubulin acetylation degree, in stabilizing cytoskeletal network and cargo motility, thereby enhancing CMT neurons activity.

Accordingly, co-immunoprecipitation assays revealed that TubA (**24**, Figure 26) is able to disrupt GlyRS-HDAC6 inhibition.

Taken together, these findings strongly support the use of selective HDAC6is to restore cytoskeleton stability and axonal transport in CMT.

HDAC6 and Inherited Retinal Diseases

Inherited Retinal Diseases (IRDs) are a heterogenous group of retinal disorders characterized by progressive degeneration of photoreceptors or retinal pigment epithelial cells, ultimately leading to blindness. Currently, the therapeutic approaches comprise gene therapy to slowdown disease progression[198]. Compelling evidence have pointed out the involvement of aberrant Class I/II HDAC activity in photoreceptors degeneration *in vivo* [199,200].

In cone-like cells 661W, selective HDAC6i TubA (**24**, Figure 26) protected cells from oxidative stress induced by H_2O_2, promoting the expression of Hsp70 and Hsp25, thereby activating HSF1, which counteract protein-damage in stress conditions. Moreover, the pretreatment with TubA (**24**, Figure 26) was able to prevent the inactivation of Prx1 – a key HDAC6 substrate which catalyses the reduction of hydrogen peroxide in oxidative stress[201]. In dye^{ucd6} zebrafish models – miming retinal degeneration – TubA (**24**, Figure 26) rescued locomotor activity in response to light and eye saccades on treated dye larvae, accompanied by increased levels of α-tubulin, thereby confirming the role of HDAC6 in protecting retinal cells from degeneration in IRD [201].

1.5.2 HDAC6 in oncological diseases

Tumorigenesis is a complex multifactorial process characterized by abnormal cell growth, leading to a loss of cell differentiation and, consequently, organ loss of function. Multiple subtypes of malignancy have been identified, sharing common genetic features, which are nowadays considered cancer hallmarks. Indeed, genetic mutations commonly control cancer cells phenotype, mainly

regarding the ability to escape programmed cell death signalling, promoting genome instability and mutations, and proliferative signalling [202]. Interestingly, nearly 6 million coding mutations have been identified in 1.4 million tumor samples[203]. Different mutations widely influence cancer phenotype and patient outcome, thereby making challenging the treatment of this complex pathology, and underscoring the urgent need for novel *ad personam* therapeutical approaches. Beyond genetic mutations, epigenetic dysregulations play a key role in cancer phenotype onset and maintenance[204,205]. As abovementioned, DNA or histone modifications affect chromatin structure and, consequently, gene expression, thereby both promoting the expression of oncogenes and the silencing of tumor suppressor genes, overall contributing to cancer development [206]. Among epigenetic players, HDACs aberrant activity is often observed in both solid tumors and haematological malignancies [207–211].

The first evidence for HDACis efficacy as anticancer agents occurred through an empirical screening for agents able to induce tumor cell differentiation. Butyrate (**26**, Figure 20), Vorinostat (**2**, Figure 6), and TSA (**1**, Figure 6) were identified for their ability to induce cancer cells apoptosis [212,213]. This finding opened new frontiers for the discovery of innovative therapeutical options targeting HDAC enzymes in cancer treatment, which aberrant expression was confirmed in several cancer types.

Therefore, an *epigenetic vulnerability* has been postulated in transformed cells, suggesting they rely on specific epigenetic pathways to maintain the expression of oncogenes. Accordingly, four pan-HDACis have been approved by the American FDA for the treatment of different kind of cancers such as cutaneous T-cell lymphoma, peripheral T-cell lymphoma, and multiple myeloma, namely Vorinostat (**2**, Figure 6), Panobinostat (**3**, Figure 6), Belinostat (**4**, Figure 6) and Romidepsin (**15**, Figure 9). Despite the well-established role of pan-HDACis in

key cancer-related pathways, their application in solid tumors concerns many challenges mainly ascribable to significant toxicity, which impacts drug exposure and could contribute to limited clinical activity [214]. Additionally, tumor microenvironment can limit drug penetration and metabolism impacting the accessibility of tumor cells to HDACis, while genotype remodelling usually leads to drug resistance phenomena, involving efflux pumps upregulation or the activation of compensatory signalling pathways [215]. Another key issue is the lack of a complete and clear picture about chemoresistance to this therapeutic class. Current advancements in drug delivery systems, such as nanoparticle-based delivery, could help overcoming some of the depicted limitations, improving drug bioavailability and allowing the proper use of HDACis. Furthermore, the use of combinatorial therapies can be envisaged, in order to sensitize tumor cells to therapy. For instance, the combination of HDACis with immune checkpoint inhibitors, chemotherapy, or targeted therapies could enhance their efficacy by sensitizing tumor cells to other treatments [216,217]. Another crucial point to be considered is the heterogenicity of tumor cells, which poses a significant challenge in cancer treatment, leading to treatment failure and cancer maintenance. In this scenario, HDAC6 has been found to be overexpressed in many cancer types, thereby it emerged as a key player in many cancer-related pathways (Figure 22). HDAC6 overexpression promotes α-tubulin and cortactin deacetylation, thus enhancing microtubule dynamics and facilitating cell migration and tissue invasion [116]. Similarly, by TGFβ/SMAD pathway, HDAC6 promotes EMT in metastatic events [218].

Also, by deacetylating Hsp90, HDAC6 ensures the stability of oncogenic client proteins, included several kinases and glucocorticoid receptors, essential for cell survival and proliferation [219–221]. Interestingly, HDAC6 ensures cell survival in oncogenic stress conditions, facilitating misfolded proteins clearance by ubiquitin-proteasome machinery. On the other and, HDAC6 deacetylase activity

on F-actin facilitates autophagosome maturation in protein degradation [222]. Furthermore, HDAC6 overexpression has be found to play a key role in cancer cells immune evasion, through the regulation of immune checkpoint pathways, including PD-1 singalling in T-cells and cytokine production [223,224]. Taken together, these data strongly support the use of selective HDAC6is in cancer treatment, as they allow to specifically target pro-oncogenic pathways directly regulated by HDAC6 activity. This approach may offer new glimpse in precision medicine and cancer therapy, aimed to overcome pan-HDAC inhibition disadvantages, such as the onset of chemoresistance phenomena (e.g. drug efflux pump expression), and systemic toxicity, likely due to broad epigenetic reprogramming [225–229].

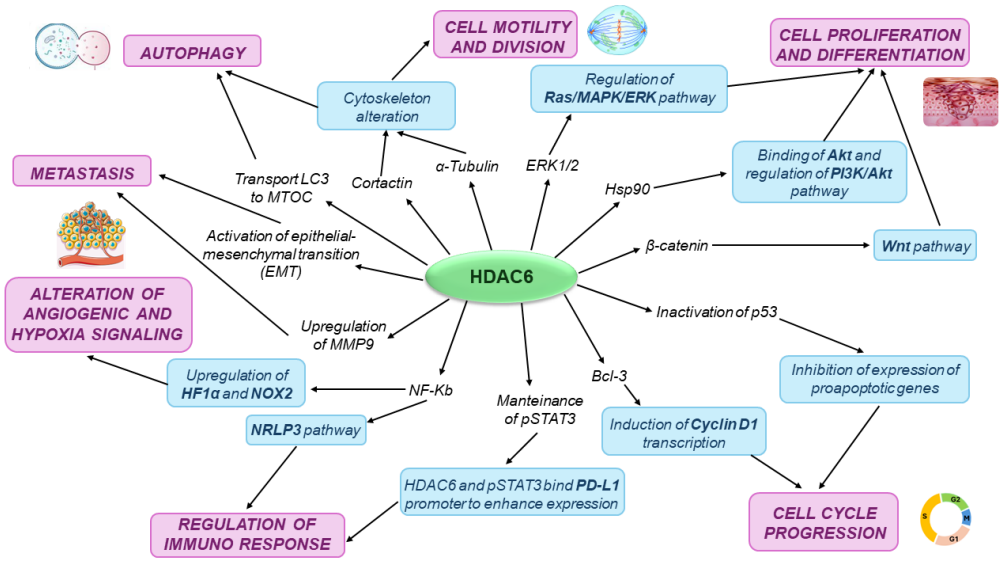


Figure 22. HDAC6 involvement in cancer pathways [230].

This Paragraph will specifically analyse the role of HDAC6 in triple negative breast cancer (TNBC) and urothelial bladder carcinoma (Bc), both of which are central to the focus of this thesis.

HDAC6 and Triple Negative Breast Cancer

Breast cancer (BC) is the most spread cancer among females worldwide [231]. According to expression of hormone receptors, BC be clustered into different subtypes [232], namely:

1. Luminal A: it is the most common BC subtype, characterized by the expression of both estrogen receptor (ER) and progesterone receptor (PR) positive, while lacking for HER2 expression.
2. Luminal B: cancer cells belonging to this subtype express both ER, PR and HER2 receptors.
3. HER2-Enriched: it is characterized by the overexpression of HER2 receptors, while it lacks the expression of ER and PR.
4. Basal-like or Triple Negative: it is the most aggressive BC subtype, characterized by the lack of ER, PR and HER2.

TNBC display an aggressive behaviour linked to its high tendency to give rise to distant metastasis and to a poorly responsivity to canonical therapeutical approaches. The main drawback in TNBC treatment is the lack of expression of ER, PR and HER2, which makes specific endocrine therapies – a gold therapeutic standard in BC – ineffective. Therefore, chemotherapy has become the main approach for the treatment of TNBC. However, a common trend in TNBC phenotype is the onset of chemoresistance phenomena, which make commonly used chemotherapeutics effective only in a small subset of patients, while the majority of individuals is refractory to this therapeutical approach with poorer survival rates. Several evidence revealed metabolic rewiring as one of the most spread mechanisms underlying chemoresistance, in which glycolytic metabolism plays a key role in T-cell activation and drug resistance [233] (Figure 23).

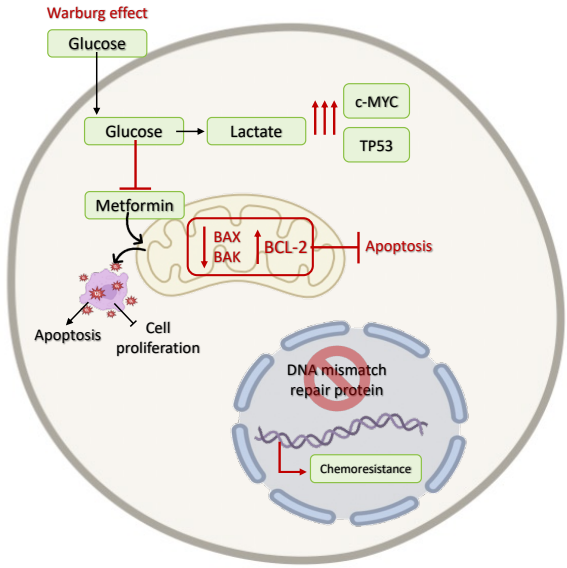


Figure 22. Most common chemoresistance phenomena in TNBC [230].

Aerobic glycolysis involves the conversion of glucose to pyruvate, and subsequently lactate, in the presence of an abundant supply of oxygen. The dependence of cancer cells on aerobic glycolysis has been directly associated with the activation of oncogenes such as c-MYC and RAS [234,235], as well as mutant suppressor genes. TNBC cell lines and patient samples are characterized by heightened glycolysis, accompanied by c-MYC amplification and TP53 mutation, especially in the relapsed setting (Figure 23). It has been suggested that the glycolytic potential of TNBC is associated with chemotherapeutic resistance, as exposing TNBC cells to increasing levels of glucose decreases the efficacy of metformin-induced apoptosis [233,236]. Also, according to previous research, mitochondria play an essential role in the activation of apoptotic pathway in response to various cytotoxic stimuli, included chemotherapies. DNA damage or microtubule stabilization ultimately lead to modifications in the BCL-2 protein family. As response to DNA damage, the proapoptotic proteins BAX and BAK oligomerize at the mitochondrion, resulting in mitochondrial outer membrane permeabilization and programmed cell death. Chemoresistance is strictly

dependent on the deregulation of expression of the antiapoptotic members of the BCL-2 family, resulting from both genetic and epigenetic mechanisms. Several evidence suggest MCL-1 (belonging to the BCL-2 family) amplification occurs in patient samples with TNBC after neoadjuvant chemotherapy, thereby underlying *in vivo* chemoresistance [237–239] (Figure 23).

TNBC treatment poses a significant challenge due to its poor responsiveness to endocrine therapy and multiple resistance mechanisms making ineffective classic chemotherapy. Thus, the urgency to improve survival rates in TNBC patients, resulted in many research efforts aimed to unveil new molecular targets and treatment strategies. Given the involvement of epigenetic modifications in driving tumorigenesis, the role of HDAC enzymes in modulating TNBC phenotype have been elucidated, thereby highlighting the potential role of HDACis in regulating tumor angiogenesis, survival and metastasis. The pan-HDACi Vorinostat (**2**, Figure 6) and Panobinostat (**3**, Figure 6) exerted antiproliferative and pro-apoptotic activity in TNBC cell lines MDA-MB-231, 4T1 and BT-549, by the modulation of multiple pathways involved in cellular metastasis and growth [240]. Indeed, the treatment with both Vorinostat (**2**, Figure 6) and Panobinostat (**3**, Figure 6) resulted in the block of EMT, and in the downregulation of the growth factor FOXA1. Moreover, Vorinostat impairs BC cell migration and invasion *via* the inhibition of matrix metallo-proteinase 9 (MMP9), involved in tissue remodeling, inflammation, and cancer progression [241]. Furthermore, both the treatment with TSA (**1**, Figure 6) and the Class I selective HDACi Entinostat (**13**, Figure 8) converte ER-negative tumors to ER-positive pehnotype, thereby sensitizing TNBC to letrozole treatment [242].

Despite the promising outcome of pan-HDACis in TNBC treatment, they did not showed efficacy in clinical trials against solid tumors such as TNBC, with several mechanisms contributing to their clinical ineffectiveness as standalone treatments. Thus, deeper studies are required in order to fully elucidate the role

of HDAC enzymes in driving TNBC phenotype, which could allow the identification of targeted and combinatorial therapies to enhance the efficacy of HDACis in refractory TNBC subtypes.

In this context, a promising strategy could be the development of selective HDACis, in order to avoid side toxic effects and enhance therapeutic efficacy. In the last years, HDAC6 isoenzyme has gained attention for its potential implication in TNBC cell survival, metastasis and drug resistance.

Very recently, BAS-2 (**30**, Figure 24) was discovered as a potent HDAC6i selectively killing apoptotic-resistant TNBC cells, inducing alterations in their glycolytic metabolism [243,244].

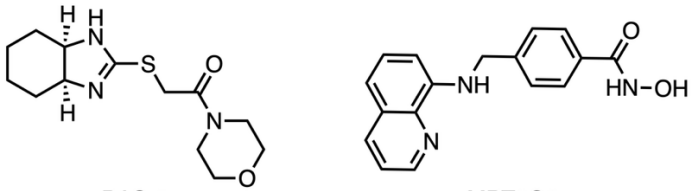


Figure 24. Structures of selective HDAC6is **30** and **31** which showed efficacy in TNBC.

Through a screening of more than 30,000 small molecules, performed on both MDA-MB-231 TNBC cells and MCF10a breast epithelial cells, Downling et al identified BAS-2 (**30**, Figure 24) which selectively killed breast and lung cancer cells irrespective of BAX/BAK status more readily than normal cells [245]. To confirm BAS-2 selectivity for cancer cells, an *in vitro* model was performed to examine the tumorigenic conversion of human mammary epithelial cells (HMECs). HMEC LER transformed cells were more sensitive to BAS-2 rather than non-transformed HMEC and HMEC LE cells, thereby confirming the selectivity of BAS-2 (**30**, Figure 24) effects towards cancer cells. After BAS-2 pro-apoptotic effect in cancer cells was confirmed, its molecular target was investigated using a functional genetic approach, which revealed BAS-2

possesses a mechanism of action ascribable to the pan-HDACi Vorinostat (**2**, Figure 6). Thereby, BAS-2 (**30**, Figure 24) was assessed in enzymatic assays on different HDAC isoforms, confirming it acts as a selective HDAC6i (IC_{50} = 76 nM). *In vitro*, this data was confirmed by increased levels of acetylated α-tubulin, with not detectable changes in acetylated H4, substrate for nuclear HDAC isoforms [245].

To elucidate the mechanisms underlying its anti-cancer effects, BAS-2 (**30**, Figure 24), acetylome was measured in MDA 231 cells upon treatment with BAS-2 or HDAC6 knockdown, leading to the identification of altered activity and acetylation in two glycolytic enzymes aldolase and glyceraldehyde-3-phosphate dehydrogenase (GAPDH) [245].

Furthermore, it was demonstrated that both pan-HDACi Vorinostat (**2**, Figure 6) and selective HDAC6i Ricolinostat (**6**, Figure 6) enhance the antitumor effect of eribulin - an inhibitor of microtubule dynamics effective in reverting EMT – likely due HDAC6 inhibition, which in turn lead to increased levels of acetylated α-tubulin, linked to to microtubule stabilization and consequent apoptosis[246].

Furthermore, selective HDAC6i MPT0G21 (**31**, Figure 24) is able to inhibit TNBC cell migration both *in vitro* e *in vivo* conditions *via* the regulation of the HSP90-aurora A-cofilin-F-actin complexes and cortactin pathways, Accordingly, the combination of MPT0G211 (**31**, Figure 24) with paclitaxel enhanced the anti-tumor effect of the latter [247].

Moreover, as very recently a key correlation between the accumulation of phosphorylated HDAC6 condensate in cells nuclei and liquid-liquid phase separation phenomenon was found, directly responsible for aberrant chromatin packaging, metastatic events and aggressive cancer behavior[248,249]. HDAC6 and its phosphorylated form are overexpressed in most TNBCs compared to other cancer types, reinforcing the pivotal role of HDAC6 in metastatic progression and advanced disease stages. Interestingly, among assessed HDAC6is, NextA

(**10**, Figure 6) demonstrated the unique ability to disrupt phospho-HDAC6 condensate formation and promote HDAC6 dephosphorylation through its release from the condensate phase to the liquid one, accompanied by apoptotic events and significant tumor growth inhibition. Genome analysis revealed HDAC6 dephosphorylation induced by NextA (**10**, Figure 6) altered chromatin structure, leading to the upregulation of tumor suppressor genes, downregulation of proto- oncogenes, and activation of immunomodulatory pathways [97].

HDAC6 and Bladder Urothelial Carcinoma

Bladder urothelial carcinoma is the most common malignancy of the urinary tract. Bladder carcinoma main treatments comprise surgery, chemotherapy and radiotherapies, and immunotherapy [250,251]. In 2020, FDA approved checkpoint blockade therapy for the treatment of bladder carcinoma patients, however this cancer subtype is characterized by high recurrence rates and muscle invasion after initial treatments, making cystectomy the gold therapy in the treatment of invasive bladder carcinoma, thereby novel effective therapeutic treatments are required. In this context, many studies have pointed out patients affected with bladder carcinoma express increased levels of HDAC enzymes, including both Class I (HDAC 1, 2 and 3) and Class IIb HDAC6 isoenzyme. A study reported in 2018 showed the pan-HDACi Vorinostat (**2**, Figure 6) exerts antiproliferative and pro-apoptotic effects in bladder carcinoma cells [252]. Accordingly, Class I HDACs overexpression has been frequently observed in urothelial bladder carcinoma phenotypes related to poor prognosis and increased tumor aggressiveness [253]. On the other and selective inhibition of Class IIa HDAC4 isoenzyme exerted limited efficacy in comparison to pan-HDACi Vorinostat (**1**, Figure 1), thereby strongly supporting the role of Class I HDACs in tumor phenotype maintenance [252]. This data may reflect the strict cancer-subtype dependent expression and function of Class IIa HDACs, while enzymes belonging to Class I are ubiquitously expressed and widely upregulated across

solid tumors, including bladder carcinoma. Similarly, Vorinostat derivatives showed *in vitro* efficacy in arresting cell cycle and inducing ROS-mediated apoptosis in bladder carcinoma cells [254]. *In vivo*, Vorinostat derivatives significantly relayed tumor growth in comparison to cyproheptadine – a first generation antihistamine which showed antitumoral efficacy in models.32 Both siRNA-mediated gene silencing and pharmacological inhibition of HDAC1/2 led to the suppression of cells proliferation and clonogenic properties of various bladder carcinoma cell lines [255]. Interestingly, individual knockdown of HDAC1 or HDAC2 resulted less effective, probably due to compensatory upregulation of unsilenced isoform. These findings strongly highlight the importance of targeting HDACs at multiple levels to exploit the potential therapeutical effect of HDACis in bladder carcinoma. Also, HDAC6 promotes the migration and invasion of bladder carcinoma cells by regulating the degree of acetylated cortactin, a well-established HDAC6 substrate involved in actin dynamics. Reduced levels of acetylated cortactin facilitates cytoskeletal reorganization necessary to acquire a migratory phenotype, thereby enhancing the metastatic potential of neoplastic cells. In a similar manner, cortactin is also a substrate of Class III HDAC SIRT2. Notably, the treatment with HDAC6i Tubacin suppressed bladder carcinoma cells migration and invasion. Tubacin efficacy was further enhanced in SIRT2 silenced cells, thus indicating the synergistic role of these two enzymes in promoting tumor aggressiveness and confirming HDAC6 role in modulating bladder carcinoma invasiveness is dependent on its deacetylase activity on cortactin [74]. On the contrary, despite bladder carcinoma cells derived by patients may express increased levels of HDAC6 protein – thereby suggesting its activity may be associated with specific molecular subtypes - gene silencing did not affect bladder carcinoma cells viability, suggesting other cellular mechanism may play a more dominant role in driving bladder carcinoma cell survival [256,257]. Despite the controversial

nature of this data, unlike pan-HDAC6is, selective HDAC6 inhibition increased bladder carcinoma cells sensitivity to radiotherapy, by enhancing induced CXCL2 expression. Similarly, HDAC6 inhibition in bladder carcinoma cell lines significantly decreased PD-L1 levels [258]. These findings strongly support the rationale of combinatory therapeutic strategies in bladder carcinoma to enhance the efficacy of currently available treatments by the use of selective HDAC6is. Interestingly, western blot analysis on RT4 bladder carcinoma cells revealed HDAC6 is expressed in both its unphosphorylated and phosphorylated forms, whereas the latter was linked to increased deacetylase activity [259]. Taken together, these findings support the relevance of selective HDAC6is in bladder carcinoma treatment. However, while pan-HDACis have consistently showed efficacy in bladder carcinoma cell survival, literature evidence regarding the efficacy for selective HDAC6is in bladder carcinoma remain still limited. This discrepancy suggests pan HDAC inhibition may be more effective in targeting bladder carcinoma oncogenic pathways, while selective HDAC6 inhibition might be more suitable for combinatory therapies.

Introduction – Part 2: Rational Design of HDAC6is

As discussed in the previous section, HDAC6 exhibits unique structural features, including two tandem catalytic domains, a ZnF-UBP domain for the interaction of ubiquitinated proteins, and a cytoplasmic retention signal, all of which contribute to its distinct cellular functions. Moreover, its involvement in several pathological conditions, through the regulation of its cytoplasmic substrates, makes HDAC6 an attractive target in medicinal chemistry [114,115,230]. In the last decade, the development of selective HDAC6 aimed to exploit its therapeutical efficacy, while minimizing side and toxic effects related to pan-HDAC inhibition.

As described, the general structure of a HDACi is composed by three main portions, namely:

(i) The cap group, which interacts with the rim of HDACs catalytic site.

(ii) A linker, which interacts with the catalytic channel allowing the correct orientation of the ZBG.

(iii) A ZBG, which coordinates the catalytic Zn^{2+} ion, thereby inhibiting HDACs catalytic activity.

Recent advancement highlighted the importance of fine-tuning each of these structural components in order to achieve high potency on HDAC6 while minimizing off-target effects. The cap group engages unique aminoacidic residues on HDAC6 surface, thereby driving selectivity, while linker length and rigidity affect the accessibility of the catalytic channel for the ZBG. Furthermore, as discussed in *Paragraph 1.3.2*, ZBG modulation strictly influence isoform selectivity and safety profiles of designed inhibitor. For instance, while the majority of pan-HDACis bear the hydroxamic acid as ZBG, benzamide derivatives preferentially inhibit Class I HDACs, while DFMOs exhibit high isoform selectivity for HDAC6, independently from the structure of the cap-linker portion [260,261].

In this section, structural insights into the design of the cap group and linker moieties for achieving selective HDAC6 inhibition will be provided, focusing on HDAC6 unique structural features which contribute to improve binding affinity and, consequently, isoform selectivity.

Cap group

Before the resolution of *h*HDAC1 and *h*HDAC6 crystal structures, Kozikowski and coworkers carried protein homology studies to predict the three-dimensional structure of HDAC6 catalytic domain in comparison to HDAC1, employing solved HDACs crystal structures as templates [262]. It is worth considering that HDAC1 is often used as a representative of nuclear HDACs - useful in the comparison with the cytoplasmic isoform HDAC6 - since it belongs to a different

HDAC Class and predominantly involved in histone deacetylation and chromatin remodelling.

While the active site is highly conserved, the size of the catalytic channel rim notably differs between the two isozymes. The catalytic channel rim can be figured by four regions A-D (Figure 25).

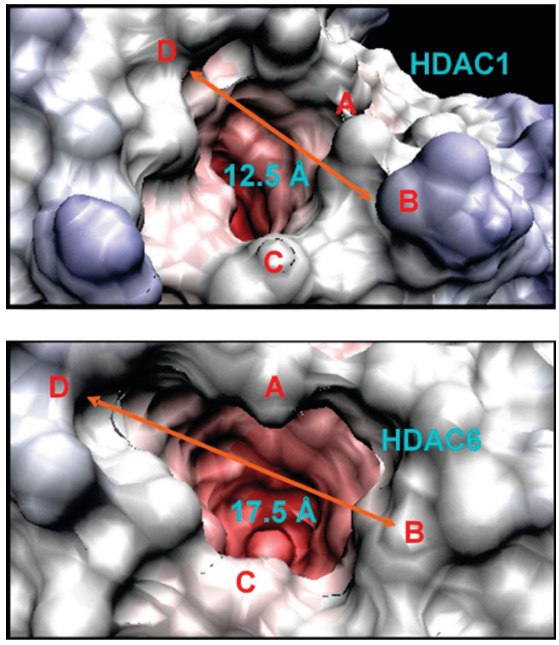


Figure 25. Active sites of HDAC1 (top) and HDAC6 (bottom) from protein homology studies. Letters A-D outline catalytic site channel rim [262].

In the homology model of HDAC6, aminoacidic variations at the D region are translated in a significantly wider channel rim – 17.5 Å versus 12.5 Å in HDAC1 - a structural feature which can be exploited for the design of selective HDAC6is (*Table 1*).

Table 1. Aminoacidic variation identified in regions A-D of HDAC1 and HDAC6 catalytic sites.

	A	B	C	D
HDAC1	Pro32	Leu271 Tyr204	Asp99 Phe205	Gln26 Gly27 Met30

				Lys31
HDAC6	Pro501	Leu749 Phe679	Asp567 Phe680	Ser498 His500 Glu502 Val503

Thereby, this area of structural diversity could be targeted with both large and rigid chemical templates, namely the "*cap group*", which nicely accommodate in the rim region of HDAC6, while being not suitable for the appropriate binding to the smaller HDAC1 surface groove. Starting from these key insights into HDAC6 catalytic structure, Kozikowski et al. developed TubA (**24**, Figure 26A), the first example of a rational designed selective HDAC6i [262]. In 2016, with the resolution of HDAC6 catalytic domains by Christianson et al., protein homology studies have been confirmed, further fostering the structure-based design of selective HDAC6is [113].

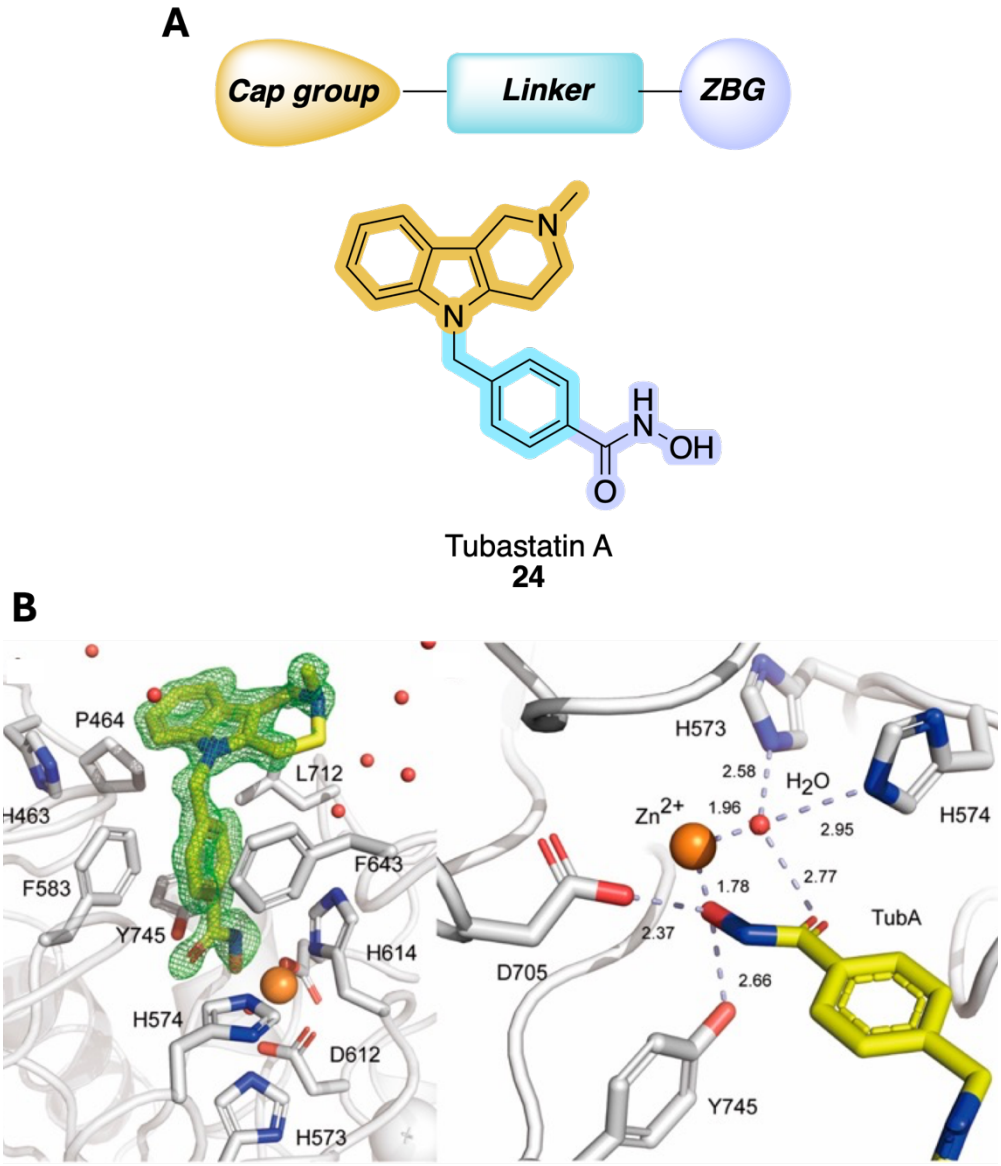


Figure 26. (A) Structure of TubA (**24**). (B) Crystal structure of TubA in complex with CD2 of *z*HDAC6 [263].

TubA (**24**, Figure 26A) bears a tetrahydro-γ carboline as cap group, which is engaged in hydrophobic interaction within the L1 loop shaping the catalytic rim on HDAC6. While the indole moiety establishes hydrophobic interactions with

H463, P464, F583, and L712 residues in L1 pocket, the methyl-piperidine ring is projected toward a more solved exposed region, thereby establishing weaker Van der Waals interaction with F643 and L712 residues (Figure 26B) [263]. Regarding the phenyl linker, it is inserted in the aromatic crevice shaped by F583, F643, and H614 residues forming HDAC6 catalytic channel[263]. The orientation of the linker allows the interaction of the hydroxamate ZBG with the catalytic Zn^{2+} ion in a monodentate fashion, consistent with the observed binding mode for inhibitors featuring bulky and rigid cap groups (*Paragraph 1.3.2*, *Hydroxamic acids*).

More in detail, the mouth of HDAC6 catalytic cleft is defined by L1 and L2 loops, the former shaped by H463, P464, F853, and L712 residues, highly conserved across *z*HDAC6 and *h*HDAC6 [264]. Notably, this aminoacidic composition makes L1 loop highly hydrophobic and conformationally rigid, allowing the accommodation of bulky and rigid cap groups, with minimal enzyme conformational rearrangement upon inhibitor binding. Except from few reported examples [265–268] (Figure 27), most of designed inhibitors interacts with L1 pocket at the entrance of HDAC6 active site. Despite this approach has yielded several potent inhibitors, L1 pocket shares some structural similarities across HDAC isoenzymes, which may make challenging the design of selective inhibitors, and increasing the risk of off-target effects. On the contrary, L2 pocket (G640-N645) flanks the entrance of the catalytic tunnel and possesses unique structural features among HDACs. Notably, the unique presence of a S531 residue in *z*HDAC6 (corresponding to S568 in *h*DCA6) is replaced by an aspartate residue in all other HDAC isoforms, making the design of inhibitors able to bind L2 pocket very attractive in medicinal chemistry [113,269].

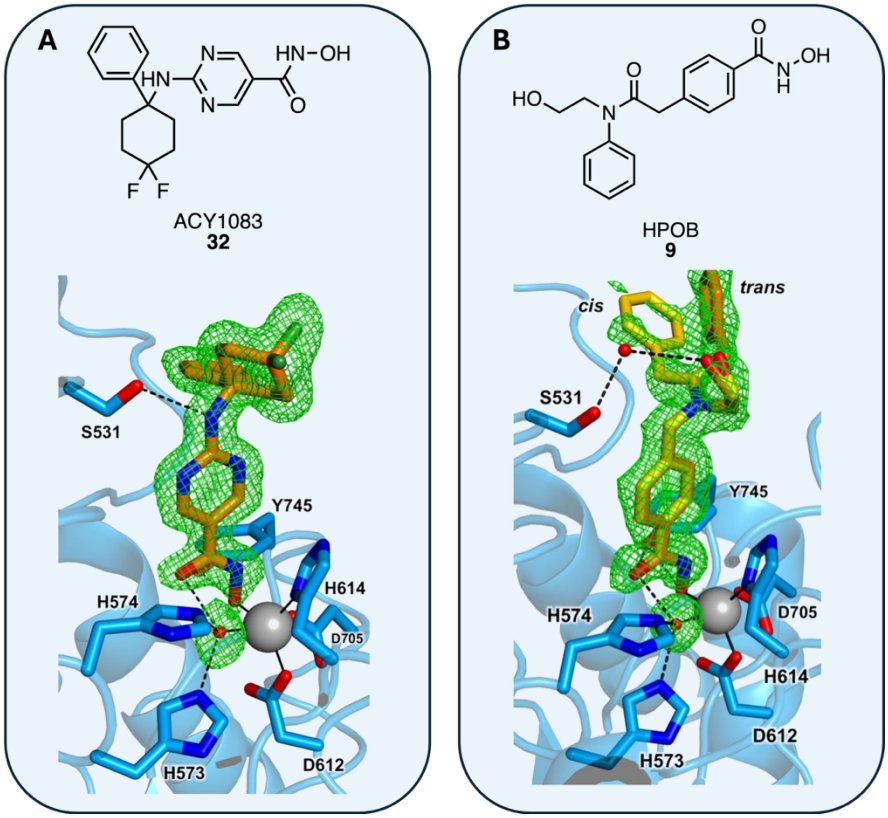


Figure 27. Examples of HDAC6is interacting with L2 loop. (A) Interaction of the secondary amino group of ACY1093 with S531. (B) Water-mediated interaction between the hydroxyl group of HPOB and S531. [270]

Linker

After the disclosure of TubA (**24**, Figure 26A) as potent and selective HDAC6i, followed by the resolution of HDAC6 crystal structure, the optimal orientation and length of the linker moiety – which allow the correct positioning of the ZBG, while orientating the cap group toward L1 loop - have been elucidated. HDAC enzymes share an aromatic crevice – shaped by Phe-Phe, Thr-Phe, or Tyr-Phe residues – adjacent to the catalytic Zn^{2+} ion [113]. Most of hydroxamate inhibitors bearing aliphatic linkers – such as Vorinostat - do not exhibit

isoenzyme selectivity, likely due to linker conformational flexibility, which does not allow the correct Zn^{2+} ion positioning (resulting in weaker inhibitory activity) neither the correct engagement of isoform-specific structural determinants (e.g. L1 loop in HDAC6). In HDAC6, the aromatic crevice is shaped by F583-F643 residues. The introduction of an aromatic, heteroaromatic or alkyl-aryl linker facilitates π-π interaction within this hydrophobic pocket in HDAC6 CD2, thereby enhancing binding affinity and isoform selectivity. This interaction allows the linker moiety to be *sandwiched* between these two phenylalanine residues, thus correctly positioning the ZBG for the interaction with the catalytic Zn^{2+} [73,113,271].

Over years, the introduction of fluorinated motifs in small molecules has emerged as an important tool in order to improve bioavailability and pharmacokinetic properties of drugs (Figure 28) [272]. Indeed, owing to fluorine high electronegativity, its introduction in designed molecules can strongly influence p*K*a properties and polarity, thereby enhancing pharmacokinetic properties. For instance, fluorinated molecules display increased lipophilicity, which in turn reflects into enhanced cell permeability and bioavailability [273–275]. The high electronegativity of fluorine may also influence the polarity of other functional groups within a molecule. Also, fluorine ability to form weak halogen bonds have been documented, thereby offering new opportunities for non-canonical interactions with the target enzyme [272]. Also, increased metabolic stability was demonstrated, ascribable to the higher strength of C-F bond compared to C-H one. Accordingly, the introduction of trifluoromethyl or difluoromethyl functionalities showed to significantly reduce oxidative metabolism by CYP450 [276–278].

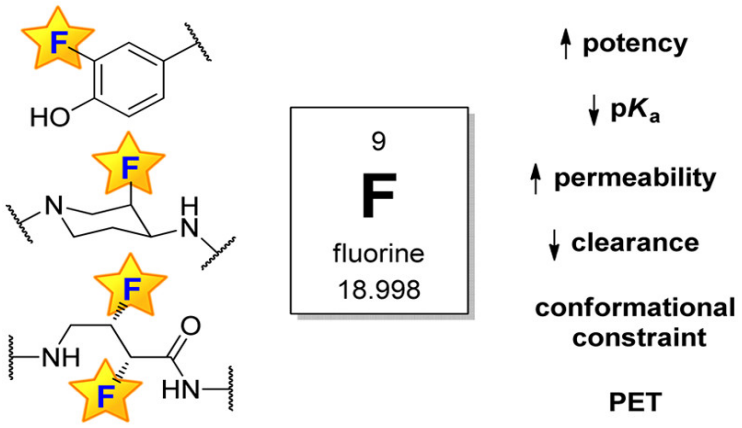


Figure 28. Role of fluorination in medicinal chemistry [272].

Despite ongoing concerns remain about the possibility of *in vivo* C–F bond cleavage, more than 20% of marketed drugs contains a fluorine atom, with many reported pharmacodynamic and pharmacokinetic advantages in comparison to their not-fluorinated analogues [279,280]. Accordingly, many reported HDAC6is bear fluorinated linkers. Recently, Stevenazzi and coworkers demonstrated the positive impact of *m*-fluoro and *m*-difluoro substituted aromatic linkers in the design of selective HDAC6is [281]. Despite *m*-fluorination can be ineffective in modulating HDAC6is potency, this strategy resulted in the increased selectivity over HDAC6, mainly due to a decreased interaction with HDAC1 isoform. The X-ray crystal structure of compound IT3985 (**33**, Figure 29A, PDB: 7O2R) in complex with HDAC6 revealed the fluorine atom in the meta position of the benzyl linker is oriented toward S531 on loop L2 of HDAC6, resulting in steric repulsion in HDAC1 catalytic channel, featuring an aspartate residue at the same position [282]. The *m*-difluorophenyl linker makes favorable π-π interactions in the aromatic crevice as well as weak interaction between one of the C−F groups and S531 [281,283]. Further studies demonstrate that the *m*-fluorine substitution is sterically favourite over para-substitution for optimally binding HDAC6 CD2 active site. A similar binding mode has been described for peptoid-capped

HDAC6is. Co-crystal structure of compound **34** (Figure 29B, PDB: 7U8Z) within *z*HDAC6 CD2 revealed the m-fluorobenzyl linker is sandwiched between the conserved F583-F643 residues, while the fluorine atom is projected toward the hydroxyl group of S531 [284]. Similarly, Bavarostat (**35**, Figure 29C) is a high selective HDAC6i. Its crystal structure in complex within *z*HDAC6 CD2 (Figure 29C, PDB: 6DVO) showed that the hydroxamate ZBG coordinates the Zn^{2+} ion in a bidentate fashion, while the *m*-fluorobenzyl linker is inserted into the aromatic crevice and projected towards the methylene group of S531 [80].

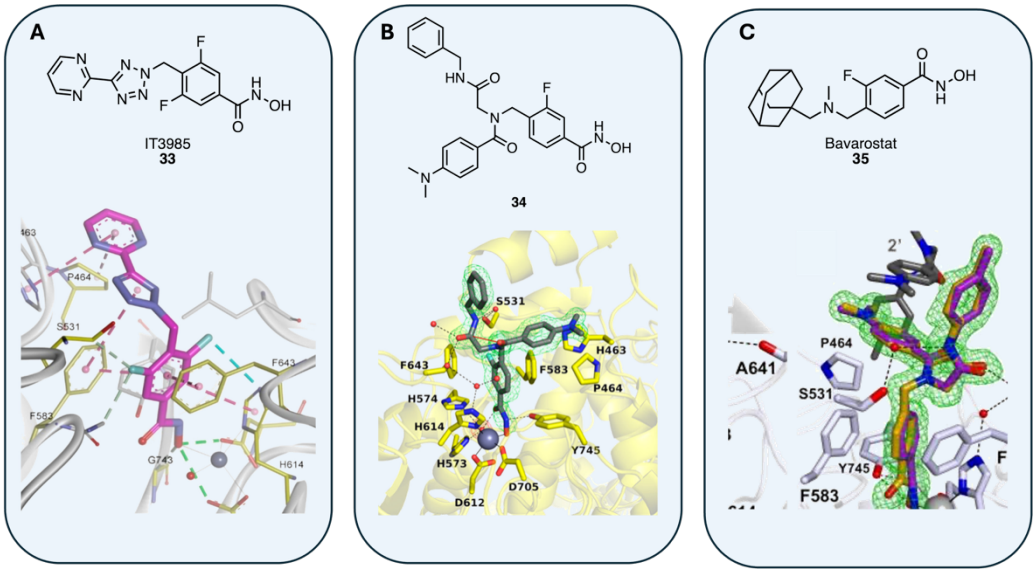


Figure 29. Examples of HDAC6is bearing a *m*-fluorinated benzyl linker for the interaction of S531 residue. (A) X-ray structure of compound **33** within HDAC6 (PDB: 7O2R). The *m*-difluorophenyl linker π-π interactions with the aromatic crevice is shown as dashed magenta lines. The *m*-fluorine atom of interaction with S531 residue is high shown as dashed grey lines. (B) X-ray structure of compound **34** within HDAC6 (PDB: 7U8Z). The *m*-fluorine interaction with S531 is shown as dashed black lines. (C) X-ray structure of compound **35** within

HDAC6 (PDB: 6DVO). The *m*-fluorine atom of interaction with S531 residue is high shown as dashed black lines.

Introduction - Part 3: Epitrascriptomics and epitranscriptomic modifications. Insights into Methyl-Transferase-Like Protein 16 (METTL16) protein structure and biological role.

RNA is the genetic code keeper responsible for various cellular activities, such as development, differentiation, and changing in response to the environment. During or after the transcription process, RNAs undergo modifications on bases or ribose units. The study of the chemical modifications targeting RNA is known as epitranscriptomics [285]. To date, 172 epitranscriptomic modifications have been identified [286], including covalent addition of functional groups (methyl, acyl, thioalkyl, and glycosyl groups), such as bases modification to form *N*6-methyladenosine (m6A) [287], 1-methyladenosine (m1A) [288], 3-methylcytidine (m3C) [289], and 7-methylguanosine (m7G) [290] or post-transcriptional isomerization and nucleoside exchange, including adenosine-to-inosine editing, isomerization of uridine to pseudouridine (Ψ) (the so-called *fifth nucleoside*) [291], splicing, and polyadenylation. Methylation originating m6A is among the most commonly arising post-transcriptional modification on yeast, plants, flies, bacteria, humans, and other mammals' mRNA. Epitranscriptomic modifications regulate mRNA expression through splicing, export, localization, stability, degradation, and translation [292–297].

m6A is a reversible modification occurring on a specific site and catalyzed by three sets of proteins responsible for opposite functions (Figure 30). Writers (e.g. methyl-transferase-like protein (METTL) 3/METTL14 complex [298], METTL16) introduce the methyl group on adenosine *N*-6, by transferring the methyl group from the methyl donor *S*-adenosyl-methionine (SAM) to the substrate; readers (such as YTHDC1) recognize the modified site converting this

modification in a cellular response, and erasers (e.g. ALBKHs, FTO [299]) allow to exert reversible regulation of mRNA metabolism, by removing the methyl group on adenosine *N*-6.

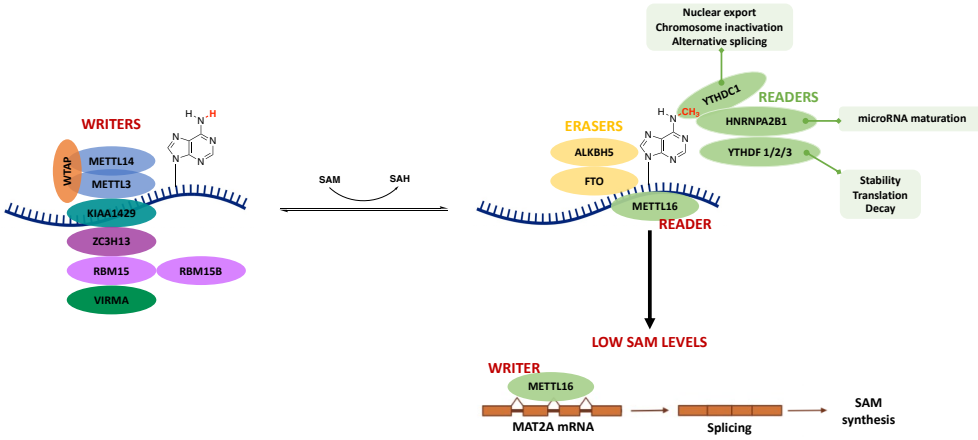
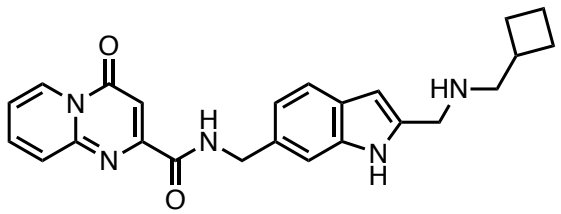


Figure 30. Schematic representation of m6A modification occurring on mRNA and consequent cellular responses [300].

Despite epitranscriptomic modifications are well known since more than four decades, only in the last years the knowledge more detailed information became available on structural features of key epitranscriptomic players, as well as their crucial involvement in several physio-pathological pathways. Based on this growing information, the design and generation of novel chemical entities behaving as epitranscriptomic modulators has started, opening a huge glimmer for drug discovery in the field [301]. In this context, METTL3 has become the first epitranscriptomic player targeted by drug design efforts. METTL3 is a m6A writer, catalytic component of the heterodimer METTL3/METTL14. In the last years, METTL3/METTL14 complex has been widely explored. The full-length crystallographic resolution of METTL3 (5L6D) [302] unveiled structural details, thus triggering subsequent design activity which led to the generation of several

patents and research papers reporting the development of new modulators, thus supporting the role of METTL3 as a promising biological target.

In parallel, the biological role of METTL3/METTL14 complex was increasingly unveiled, thus underlying its involvement in several pathologies such as cardiovascular, neurologic, and oncological diseases, as well as viral infections. However, a full picture of the functions of METTL3/METTL14 complex is still not available, and its physio- and patho-logical role remains unclear and controversial for some aspects [303–306]. In the last two years, new molecules were identified and developed acting as direct METTL3/METTL4 catalytic methyl transferase domain (MTD) inhibitors, degraders, or allosteric inhibitors. The first comprehensive review reporting medicinal chemistry approaches towards novel METTL3 modulators was recently published[307]. In November 2022, STC-15, METTL3 inhibitor developed by Storm therapeutics, was approved in a Phase I clinical trial for the treatment of acute myeloid leukaemia (AML) and other solid cancers, representing the first-in-class inhibitor targeting an RNA methyltransferase. Only in July 2023 the structure of STC-15 was disclosed (**36**, Figure 31) [308].



STC-15
36

Figure 31. Structure of STC-15 (1), a METTL3/METTL14 inhibitor in Phase I clinical trial.

Despite the rapidly advancing drug discovery progress on METTL3/METTL14, the METTL16 m6A writer has been very poorly explored so far, from both the structural and biological points of view. Accordingly, a second aim within the present thesis work was to identify novel structural determinants for METTL16 inhibition, to address a critical gap in the field which could open new avenue for structure-based drug design of METTL16 inhibitors.

1.6 METTL16 structure

METTL16 is a conserved protein with analogues in vertebrates and bacteria and displaying nuclear and cytoplasmic localization. METTL16 acts as a writer in the cell nucleus, contributing to fine tune the equilibrium of RNA methylome, while in the cytosol it behaves as a key player in translation, independently from its methyltransferase (MTase) activity [309,310]. From the structural point of view, METTL16 is composed by 562 residues, with the MTD domain located at N-terminal extension, followed by C-terminal VCR 1 and 2 (spanning residues 289-400 and 514-562), which are connected by an unstructured region (Figure 32).

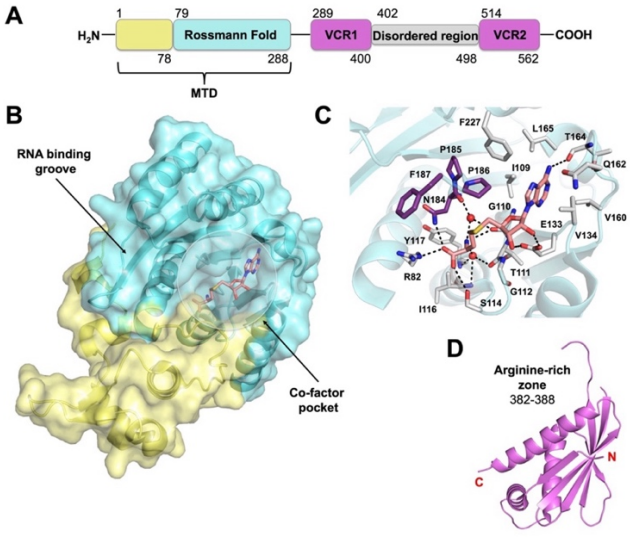


Figure 32. Structure of METTL16. (A) Schematic diagram outlining the domain organization of human METTL16. (B) The 3D structure of METTL16 MTD (PDB 6GFN) represented as ribbons under a semitransparent surface, color-coded as in panel A. The bound SAH is displayed as salmon sticks. (C) Zoom-in of the co-factor binding pocket. The key residues forming the pocket are displayed as white sticks and labeled; the NPPF catalytic motif is displayed as purple sticks; the water molecules are displayed as red spheres. H-bonds are depicted as dashed black lines. (D) The 3D structure of vertebrates conserved regions (VCRs) located in the C-terminal domain of METTL16 containing the arginine-rich zone [300].

Unlike methyltransferase heterodimeric complex METTL3/METTL14, which is required to exert METTL3 catalytic activity [311,312], METTL16 was found to exist in both the homodimer and the monomer form[313]. Size-exclusion chromatography of both METTL16 full length protein and MTD confirmed METTL16 as a homodimer, while METTL16 MTD was found in monomeric form, suggesting the key role of C-terminal VCR in the polymerization process.

MTD domain

METTL16 MTD interacts with the substrate RNA and the SAM cofactor; subsequently, methylated RNA and the co-product SAH are dissociated from the complex. To elucidate the binding mode, apo MTD and (PDB: 6GFN) MTD in complex with SAH (PDB: 6B92) crystals were solved [313], revealing the presence of a type I Rossmann fold composed by seven β-sheets alternated by α and 3_{10} (η) helixes creating a superstructure in which binding sites for SAM/SAH and for the RNA to be methylated can be recognized (Figure 32B). β6 is linked to α8 through a cardinal $_{184}$NPPF$_{187}$ motif (Asn184-Phe187) corresponding to $_{395}$DPPW$_{398}$ motif in METTL3/METTL14 complex [314,315]. The comparison

between apo-METTL16-MTD and SAH-MTD crystal structures revealed a *trans* conformation between Pro185 and Pro186 of $_{184}$NPPF$_{187}$ motif, which undergoes a conformational change when SAH binds METTL16 MTD, positioning the two residues in a *cis*-conformation more prone to accommodate the co-factor [313]. Interestingly, these unique structural features explain why METTL3/METTL14 complex and METTL16 are able to recognize different substrates (e.g., METTL3/METTL14 complex binds single-stranded RNAs and mainly methylates exons, while METTL16 methylation sites are mainly located on pre-mRNA intronic sequences)[316]. Moreover, while METTL3/METTL14 complex recognizes specific consensus sequences called DRACH motif (D=A, G or U; H=A, C or U) at the 3′-UTRs of mRNAs [317], the identified METTL16 targets share a nonameric UAC**A**GARAA sequence where the adenosine undergoing methylation is highlighted in bold font. This sequence is located in proximity of hairpins (hps) suggesting METTL16 role in RNA translation. Notably, METTL16 possesses a unique region, outlined by the N-terminal residues 1-78, preceding the Rossmann fold and featuring three α-helices and two short β-strands (Figure 32A). This region has been reported to be critical for the interaction with specific RNA substrates [313,318]. Rossmann fold β-strands are stabilized by Cys183 and Cys247 residues forming a disulfide bridge, with a positively charged surface (Figure 33) for the binding with RNA substrate constituted by Arg82, Lys251, Lys 252, Arg279 and Arg282 residues and Lys5, Lys14, Arg41 and Lys47 residues in the N-terminal tail, contributing for the RNA substrate specificity of METTL16. Lys47 and Arg279 residues form a pocket on the surface accommodating a phosphate group.

The co-factor SAM (and SAH in a similar way) binds METTL16 MTD through non-covalent interactions within the Rossmann fold (Figure 3B). Adenine is recognized by Val160 and the binding stabilized by a hydrophobic pocket

composed by Ile109, Val134, Val160, Leu165 and Phe227 residues. Both hydroxyl groups of ribose, and sulfur group are recognized by Glu133, Asn184 and Pro186 (Figure 32C). The GXG motif (corresponding to residues Gly110-Thr111-Gly112 in METTL16), which is conserved in other MTases [319,320], contributes to shape the co-factor binding pocket and canonically interacts with the homocysteine/methionine moieties of SAH/SAM, either directly or via a water molecule.

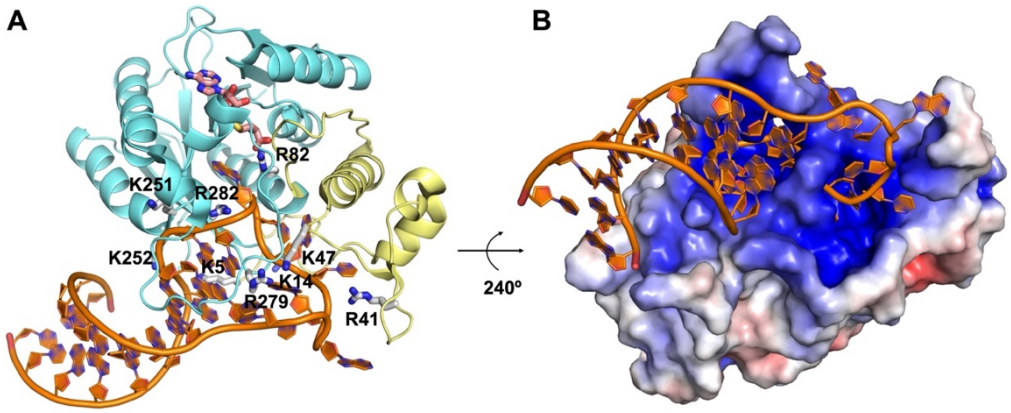


Figure 33. METTL16 MTD in complex with an RNA substrate. (A) Overall structure of METTL16 MTD in complex with MAT2A optimized hairpin 1 (hp1x) (PDB 6DU4) represented as ribbons and color-coded as in Figure 3 panel A. SAH is superimposed from the structure 6GFN and shown as salmon thick sticks. Key positively charged residues are shown as white thick sticks and labeled. RNA is shown in orange. (B) Surface charge representation of METTL16 MTD/hp1x complex showing a positively charged (blue) groove [300].

In order to understand the role of these residues in catalyzing MTase process, single point mutations were introduced[321]. P185A-P186A mutant leads to the loss of the enzymatic activity, suggesting the importance of these residues in

catalyzing the methyl transfer process. Also, mutations in the positively charged groove can reduce or abolish METTL16 activity. Respectively, single point mutations K47E and R279E reduce methyltransferase activity, while the double mutation K47E and R279E, and single point mutations R82E, R282E, and R74E abrogate enzymatic activity, confirming the importance of the positive groove in the recognition of the RNA to be methylated. Phe187 targets RNA adenine bringing the adenine to be methylated, explaining why Phe187 mutants are not capable to recognize MAT2A mRNA *in vivo* [321,322].

For the presence of the Rossmann fold at the N-terminal MTD, METTL16 is labeled among class I SAM-dependent MTase. Methyltransferases belonging to this group are known to transfer the methyl group to a great variety of nucleophiles adopting a SN_2 mechanism (Figure 34). A mechanism was proposed for methyl transfer catalyzed by METTL16. As described above, adenosine undergoing methylation inserts in MTD through hydrophobic interactions, blocking the substrate in the catalytic site. Asn184 and Pro185 are fundamental residues in starting the SN_2 process, polarizing 6A to be methylated. 6A strong nucleophilicity allows nucleophilic attack on the S-methyl group of the co-factor SAM, and the N^6-methylaminocation is stabilized in MTD, leading to the release from the complex of the m6A-RNA and the SAH side-product of reaction.

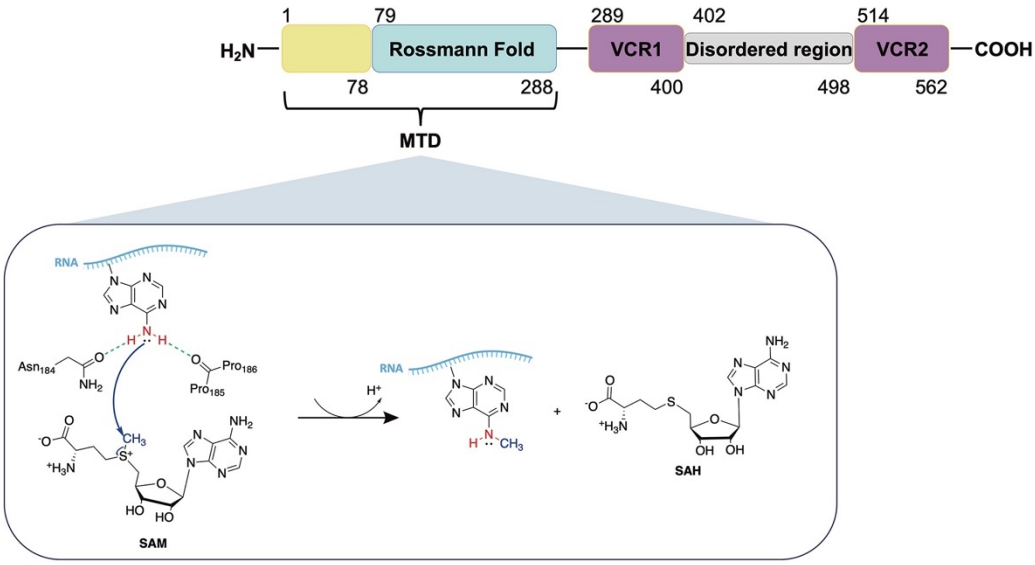


Figure 34. METTL16 MTase activity catalyzed by MTD domain [300].

VRC domain

METTL16 C-terminal region contains a VCR domain in which two regions (VCR1, including residues 289–400, and VCR2, including residues 514–562) are divided by a central disordered region (residues 411-508). The first available crystal structure of VCR domain dates back to 2020 [323]. Interestingly, VCR domain structure displays high homology with C-terminal kinase-associated 1 (KA1) domain of terminal uridylyl-transferase (TUT) 1 protein [324,325], involved in the maturation of U6 snRNA, which is an identified target for METTL16 discussed in the following paragraph. Protein crystallization achieved by the removal of the disordered region which links VCR1 to VCR2 revealed five stranded anti-parallel β-sheets and three α-helices, containing an arginine-rich zone corresponding to residues 382–388 (RRR domain), constituted by RRKKRER residues and corresponding to the RRR region in KA1 domain of

TUT1 protein [323]. The importance of these residues in assisting the catalytic activity of METTL16 will be discussed in the following *Paragraph.*

1.6.1 METTL16 substrate specificity

METTL16 is responsible for the m6A on different substrates, including the methylation of mRNA methionine adenosyl-transferase (MAT) 2A, as response to low SAM cellular levels. Furthermore, non-coding RNA metastasis-associated lung adenocarcinoma transcript 1 (MALAT1) and U6 snRNA are also targets of the enzyme. m6A modifications are widely spread in eukaryotic cells in almost all tissues, pointing out the relevance of this epitranscriptomic modification in several processes with particular reference to processes such as translation, mRNA stability and splicing. In the following paragraphs physio-pathological states in which the role of METTL16 as a writer has been elucidated will be discussed, highlighting the potential role of METTL16 as biological targets for development of therapeutic option to treat several diseases.

MAT2A mRNA methylation

SAM is the main methyl donor in eukaryotic cells, and it is involved in several processes such as epigenetic modifications, amino acid and polyamine synthesis and so on. Methionine and ATP are building blocks for the synthesis of SAM catalyzed by MAT enzymes. Mammalian MAT1 isozyme is mainly expressed in hepatocytes while MAT2 was ubiquitously found.

In particular, such isozymes are encoded by three genes, MAT1A, MAT2A, and MAT2B, with the first two acting as catalytic subunits. The catalytic subunits are 85% identical at the amino acid level, and derive from the MAT1A and MAT2A genes, respectively [326] .

MAT2A catalytic subunit is in complex with the regulatory subunit MAT2B. Several evidence link the catalytic activity of METTL16 to the regulation of SAM homeostasis by the activation of MAT2A pre-mRNA splicing in m6A independent manner [327]. The 3' UTR of vertebrates MAT2A mRNA contains six hps where the sequence UAC**A**GARAA can be recognized by METTL16 following in MAT2A mRNA stabilization and in pre-mRNA splicing, confirmed by MAT2A mRNA early degradation in 3' UTR mutants [328]. Reliably, low SAM levels affect METTL16 turnover, increasing the residence time of the enzyme on the hp1 of MAT2A pre-mRNA, lied in proximity of the stop codon, and inducing a conformational change leading to splicing and the production of the mature MAT2A protein (Figure 6) [322].

On the other hand, METTL16 binding on hps triggers the stabilization of MAT2A mRNA dependently on m6A levels (Figure 35). Methylation on the fourth adenosine of the motif UAC**A**GARAA in hps 2-6 leads to MAT2A mRNA degradation, confirmed by hypomethylation of the same hps in low SAM level conditions.

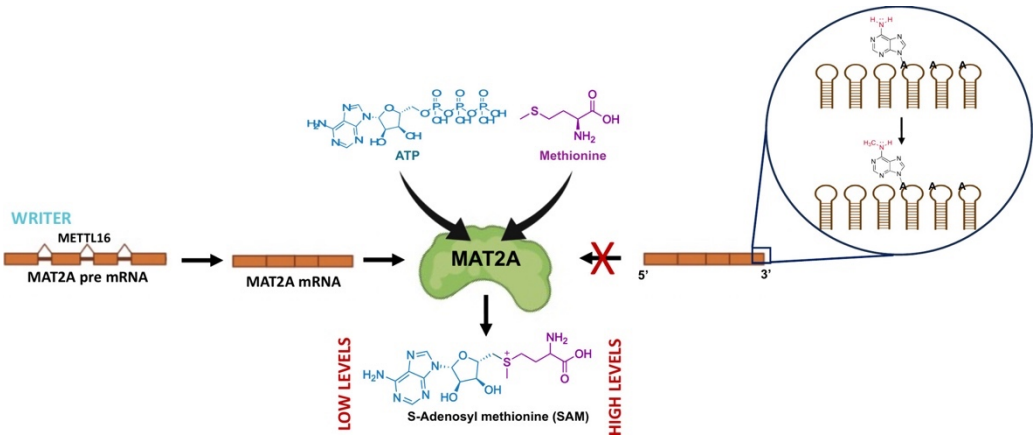


Figure 35. SAM homeostasis regulation [300].

Through a CRISPR knockout (KO) model, Scarborough et al. [329] proved that the cleavage factor I_m complex (CFI_m)25 also regulates MAT2A splicing, but it is still unknown the way CFI_m25 and METTL16 cooperate in maintaining SAM homeostasis.

Non-coding RNA MALAT1

A wide portion (about 98%) of the human genetic code consists of non-coding genes. Non-coding RNA can be classified in short non-coding (snc) RNA and long non-coding (lnc) RNA based on nucleotide sequence length. LncRNAs are responsible for several functions: they bind transcriptional factors, causing their (in)activation, and are involved in mRNA turnover, regulating stability, splicing, or translation. MALAT1, also known as nuclear-enriched abundant transcript 2 (NEAT2), is a lncRNA (>8000 nucleotides) widely conserved and expressed among mammalians. MALAT1 3' terminal presents an element for nuclear expression (ENE) containing a U-rich internal loop. This domain can interact with a downstream A-rich tract to form a triple helix composed of nine UAU, CGC, CG motifs, and probably accountable for its longest half-life compared with other lncRNAs. A study on different cell lysate revealed a panel of proteins interacting with MALAT1, among which METTL16 is capable to bind MALAT1 3' triple helix in cell-type independent manner [330], differently from other RNA-binding proteins which usually recognize only single or double stranded RNAs[330]. To validate MALAT1 as a relevant substrate for METTL16, an *in vitro* immunofluorescence cell based assay on both HeLa and HEK293T cells was performed, thus unveiling METTL16-MALAT1 interaction with increased levels of endogenous methylated RNAs [331]. To confirm MALAT1 is a substrate of METTL16 *in vivo* and whether METTL16 is able to specifically recognize MALAT1 3' triple helix, a Cross-Linking Immunoprecipitation coupled with quantitative-PCR (CLIP-qPCR) analysis was performed in

presence of both MALAT1-ENE and multiple endocrine neoplasia β lnRNA-ENE reporters, highlighting enriched levels of MALAT1-ENE in presence of immunoprecipitated METTL16. This data, coupled with RNA-proximity ligation assay, confirmed METTL16 directly interacts with the MALAT1 triple helix *in vivo* [331]. Although MALAT1 triple helix was confirmed as METTL16 substrate, experimental proofs of MALAT1 specific methylation are still lacking, as also confirmed by an elegant kinetic study reported in 2022 on a label of 30 adenosines, in which the authors did not detect any methylation signal, concluding that MALAT1 3' triple helix is a METTL16 substrate in the *in vitro* settings [332] independently from its catalytic activity. Certainly, deeper studies are required to fully elucidate the interplay between MALAT1 and METTL16 enzyme, and whether other proteins are involved, potentially uncovering new regulatory mechanisms and therapeutic targets in many pathological states involving lnRNAs, like cancer, neurological disorders, atherosclerosis and so on.

U6 snRNA

Spliceosome is a complex machinery containing proteins and six small nuclear (sn) RNAs, involved in pre-mRNA maturation by the removal of non-coding sequences between exons. U6 snRNA is the catalytic subunit of spliceosome machinery. Even if the discovery of a m6A site (adenosine 43, A43) on U6 snRNA dates to four decades ago [333], only few years ago the methylation reaction occurring on this site was ascribed to METTL16 enzymatic activity (Figure 36). To first elucidate METTL16 role in splicing mechanism, a study was conducted on *Schizosaccharomyces pombe (S. pombe)* METTL16 knockdown and wild type (WT) strains[334]. This yeast strain was selected since m6A modified sites were not identified in RNA sequence and because *S. pombe* MAT2A analogue doesn't contain hairpins recognized by METTL16, rendering U6 snRNA the only possible methylation site. In WT *S. pombe* m6A site was

detected on adenosine 37 (A37), at the 5' introns splicing site, while in knockdown strains m6A37 modification was absent. Moreover, fainty levels of m6A37 were detected even in absence of SAM, thus evidencing this co-factor could be endogenously present in METTL16 active site. Alterations in intron retention were found in strains lacking of m6A37, suggesting the importance of METTL16 in the regulation of the splicing machinery [334].

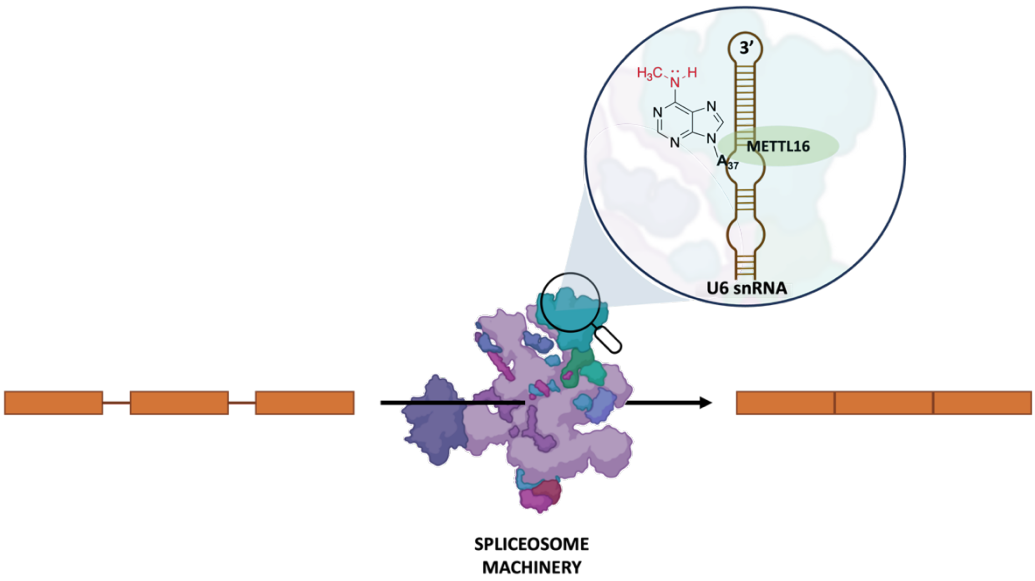


Figure 36. Effects of METTL16-catalyzed m6A on spliceosome machinery assembly [300].

However, vertebrate splicing machinery is much more complex involving a huge number of introns; therefore, it is more difficult to assume METTL16 is a structural component of the spliceosome machinery. A recent study demonstrated the importance of METTL16 in early embryonic mice development, comparing METTL16$^{-/-}$ and WT fertilized cells [332]. After their growth to the stage of blastocyst, cells were implanted in fertile female mice, showing the arrest in the growth of METTL16$^{-/-}$ embryos. MAT2A displayed a 5-fold downregulation in

the KO embryos with decreased distribution of MAT2A mRNA exons sequences, leading to decreased levels of SAM and consequent alterations in methylation reactions mandatory for embryonic development. Furthermore, kinetic studies were also performed in order to elucidate the methylation mechanism ascribed to U6 snRNA [332], concluding that U6 snRNA must bind first to METTL16, followed by SAM to start the catalytic process. Also, the role of VCR domain in the interaction of METTL16 with U6 snRNA was investigated, displaying a more efficient methylation process for METTL16 full protein rather than purified MTD, suggesting that VCR domain enhances U6 snRNA methylation increasing the MTase affinity for the protein [323]. Indeed, VCR deleted-RRR mutant showed a reduction in methylation activity on U6 snRNA, due to the 12-fold increased K_m for the binding between METTL16 and the same U6 snRNA [323]. The same data was pointed out in MAT2A splicing activation enhanced by METTL16, justified by the fact that the two proteins share the same recognition sequence.

1.7 METTL16 in pathological states

1.7.1 METTL16 role in non-oncological states

While m6A modifications have been mainly studied in the context of cancer, emerging research suggests their role in several non-oncological diseases as well. In the last years, compelling new evidence suggested the importance of m6A regulators METTL3/METTL14, YTHDF2 and YTHDF3 in managing viral infections spread (e.g., HIV, SARS-CoV-2) cardiovascular and metabolic diseases, hypertension, cell cycle, neurological degeneration, and cancer [335–348].

<u>Neurological disorders</u>

In brain, m6A is fundamental in the regulation of synaptic plasticity related to memory and learning processing [349–351]. In 2022, Zhang et al. proved METTL16 is the most upregulated MTase protein in mice hippocampal through behavioral experiments of learning and memory, confirming the epitranscriptomic mechanism underlying molecular modifications involved in synaptic plasticity [328]. Knockdown (KD) METTL16 mice in Y-maze and Morrison water maze tests showed significant memory deficit (e.g., discrimination of new objects and the time spent in every arm of the maze) without affecting emotional state of the mouse. This trend was reverted in knockdown METTL16 mice with MAT2A overexpressed protein. KD METTL16 cause an overall reduction of m6A levels, maybe due to reduced levels of MAT2A protein and consequent low SAM co-factor. Thus, overexpressed MAT2A can increase m6A levels, improving memory and learning processes (Figure 37).

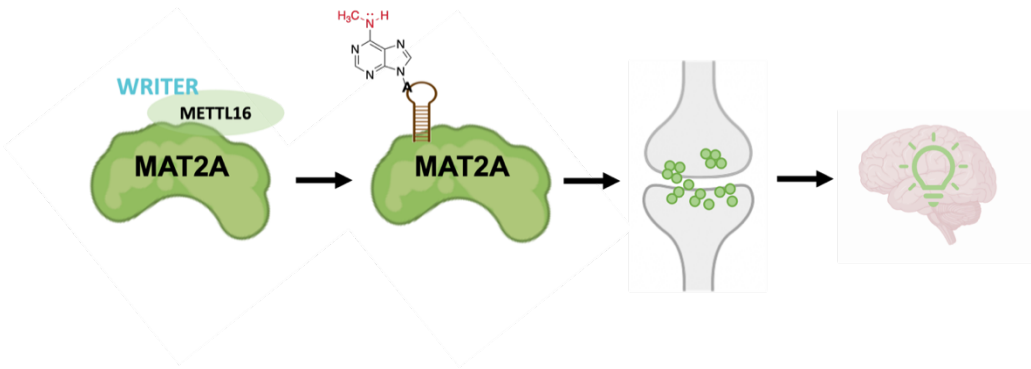


Figure 37. METTL16 stimulates memory and learning processes trough the methylation of MAT2A mRNA [300].

Metabolic diseases

Non-alcoholic fatty liver disease (NAFLD) is a condition caused by the accumulation of fat in the liver, strictly related to obesity and type 2 diabetes.

NAFLD is a complex and multifactorial pathology, leading to liver fibrosis, cirrhosis, and loss-of-function. m6A modulator METTL3/METTL14 is a confirmed pathological marker in NAFLD via regulating ATP-Citrate Lysase (ACLY) and stearoyl-Coenzyme A desaturase 1 (SCD_1) proteins expression [352]. In 2022 also METTL16 was confirmed as a trigger for NAFDL progression in high-fat-diet (HFD) murine models [353]. First, mRNA abundance analysis in HFD mice showed high levels of METTL16 compared to others m6A regulators, comprising METTL3/METTL14 complex. Then, Kegg Pathway Database analysis on HFD mice revealed a hypermethylated set of proteins involved in regulating triglyceride and fructose metabolism, and in chronic inflammation onset. Otherwise, genes responsible for triglyceride catabolism, such as lipid digestion and insulin-resistance pathways, resulted in hypomethylation, suggesting m6A modifications can worsen NAFDL clinical picture enhancing fatty-acids synthesis and inflammatory response. Cell Death Inducing DFFA Like Effector A (CIDEA) gene, a well-known trigger in driving fatty acids synthesis and the consequent hepatic steatosis [354,355], resulted the most methylated gene in HFD mice liver. To confirm CIDEA expression is influenced by m6A activity, silenced models for METTL16 were built on HepG2 cell. As expected, METTL16 overexpression resulted in a surge of CIDEA expressed protein, while METTL16 KD models dramatically affect CIDEA expression.

4.3.2 METTL16 role in *role in safeguarding genome integrity*

Red blood cells (erythropoiesis) production occurs mainly in bone narrow, where hematopoietic stem cells rapidly undergo differentiation and duplication devoted to deliver a large number of new erythrocytes, crucial for the transport of oxygen throughout the body. Given the rapidity of hematopoietic stem cells replication and differentiation cycles, errors in red blood cells differentiation can naturally

occur. A fine-tuned repair machinery is in place to remove genome damaged cells or repair these damages. When the repair system fails, defects in erythropoiesis can lead to several blood disorders, such as anemia or hematological malignances. A key process in red blood cells production is the incorporation by cells of the transferrin-bound iron from the blood stream, necessary for the formation of hemoglobin, and mediated by transferrin receptor (TfR1), which was found to be overexpressed in human hematopoietic progenitor cells. Both epigenetics and epitranscriptomics were supposed to regulate this process [356,357], but only recently METTL16 was found to regulate TfR1 expression via its catalytic m6a activity [358]. Yoshinaga et al. clearly highlighted the critical role of METTL16 in erythroid differentiation controlling genome integrity both in *in vitro* and *in vivo* models [358]. CRISPR interference methodology was applied to K562 erythroleukemia cell lines showing METTL16 ablation negatively affected both TfR1 and hemin-induced HBG mRNA (a marker for K562 cells differentiation) expression. Also, in K562 cells WT for METTL16, but not in METTL16 catalytic death mutants, both the expression of TfR1 and hemin-induced HBG mRNA was restored, thus confirming METTL16 catalytic m6a activity is necessary in erythroid differentiation [358]. To validate these findings and further investigate METTL16 molecular mechanism involved in erythropoiesis, an *in vivo* model of METTL16 deficient mice was studied, confirming the failure in erythroblasts differentiation marked by both the presence of micronuclei, sign of DNA damage, and the extended activation of apoptotic pathways, confirmed by elevated levels of cleaved caspase 3. Also, caspase-mediate cleavage of GATA-1 – an essential transcription factor for TfR1 expression – was detected, suggesting METTL16 acts as a pivotal safeguard in genome integrity during erythroblasts differentiation. Given the role of METTL16 in RNA m6a regulation, RNA immunoprecipitation sequencing assay was performed on METTL16 KD mice, revealing hypomethylation on ACAGAR

sites (attributable to specific METTL16 methylation sites, also recognized on U6 snRNA and MAT2A mRNAs) of several proteins involved in DNA damage repair and cell cycle control, confirming RNA methylation induced by METTL16 is crucial for their proper expression. Since the expression of mRNAs involved in these processes is regulated by MTR4 helicase, whether METTL16 would be able to interact with this protein was investigated, finding MTR4 depletion completely restored the normal expression of METTL16 mRNAs substrate. Taken together, these data strongly support the involvement of METTL16 regulation in DNA damage repair, cellular life cycle and erythropoiesis. In our opinion, this study provides a fundamental starting point for investigating the potential role of epitranscriptomics and the METTL16 network in conjunction with protein machinery involved in DNA damage repair. Accordingly, METTL16 aberrant expression may be linked to impaired cellular functions in cancers, hematological disorders, and genetic pathologies.

1.7.2 METTL16 role in oncological diseases

m6A modification controls RNA metabolism and related cellular activities, such as the stress response and DNA damages repair. Disrupted methylome is accountable for tumoral cells proliferation, differentiation, invasion, and drug resistance. The role of protein synthesis in cancer progression was widely explored, but only in 2022 the role of METTL16 as enhancer of the translation process was pointed out [359]. The MTD residues 79-289 allow the interaction of METTL16 with mRNA 5'-cap, suggesting it is involved in translation initiation. Western blot and co-immunoprecipitation assay confirmed METTL16 interaction with eukaryotic initiation factors (eIFs) 3a and 3b, responsible for the recruitment of mRNA, 40S ribosomal subunit and other translation factors needful at the early stages of protein synthesis. Interestingly, knocking-out METTL16 dramatically suppresses translation even in presence of overexpressed

METTL3/METTL14 complex. These results underscore the benefits of selectively targeting METTL3/METTL14 complex or METTL16 based on therapeutic needs, thus reducing off-target effects.

Hepatocellular Carcinoma

METTL16 and eIFs are overexpressed in hepatocellular carcinoma (HCC) [360,361]. Suppressing METTL16 induces a decrease in proliferation, migration, and invasion of liver cancer cells, while the expression of MTD domain completely rescues transcription and cellular growth, apart from m6A cell levels [309]. Also, serine/threonine-protein kinase 6 (AURKA) is overexpressed in HCC. AURKA is an oncogene, triggering cellular cycle activation [360]. LncRNA AC079360.1 (transcript that induces AURKA lysosomal degradation, TIALD), responsible for AURKA lysosomal degradation, is downregulated in HCC with respect to healthy cells and fosters invasion and proliferation through the activation of epithelial-mesenchymal transition (EMT). Indeed, the *in vitro* TIALD knockdown promotes the expression of N-cadherin decreasing expressed E-cadherin, two relevant markers in EMT [362]. A mouse lung metastatic model confirmed the data collected in the *in vitro* assay: TIALD overexpression led to E-cadherin increased level and significant metastatic cells spread, while TIALD knockdown mice group showed a lower number of metastatic nodules. Furthermore, the levels of METTL16 and TIALD levels display a mutual dependence, since METTL16 overexpression in HCC causes TIALD degradation, through the recognition of the RNA secondary structure and its m6A modification, confirmed by increased TIALD stability in absence of YTHDF2 and YTHDC1 readers. Overexpressed METTL16 in HCC also downregulates RB11B-AS1 lnRNA, promoting cellular migration, invasion, and proliferation, associated to HCC poor life expectation [362].

Breast Cancer

Although METTL16 role in BC progression has not been fully elucidated yet, its overexpression was confirmed in several BC cell lines [363]. METTL16 suppression significantly arrests cell growth, with detectable high levels of Fe^{2+} species, responsible for the activation of ferroptosis process. On the other hand, GXP4 overexpression restored Fe^{2+} cell levels, reverting cell proliferation. These data, compared to the reduced methylation sites on GPX4 in absence of METTL16, suggest the role of MTase process, catalyzed by METTL16 protein, in the regulation of BC cell viability, triggering ferroptosis programmed cell-death process. However, the molecular basis of GPX4 methylation ascribed to METTL16 is still unclear and requires further investigation.

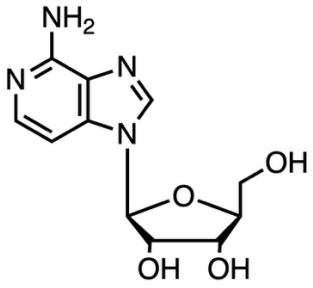
Leukemogenesis

AML is a type of blood cancer characterized by the uncontrolled growth and accumulation of abnormal myeloid cells in the bone marrow. Several studies have reported dysregulation of METTL3 expression and m6A RNA methylation patterns in different types of leukemia, including AML and acute lymphoblastic leukemia (ALL) [364–366]. More recently, METTL16 has been found to play a pivotal role in regulating the m6A modification of specific target genes in AML, potentially contributing to leukemogenesis [367]. METTL16 knockdown or knockout in both mouse and human xenograft models showed engraftment of leukemia cells, prolonged survival, and promoted myeloid differentiation, completely reverted by METTL16 restored activity [367] . In order to gain further insight into the role of METTL16 in AML progression, m6A RNA sequencing was conducted. This analysis revealed that the genes encoding for branched chain amino acid transaminase (BCAT) 1 and 2, leucyl-tRNA synthetase 1 (LARS1), and isoleucyl-tRNA synthetase 1 (IARS1) were downregulated in parallel with METTL16 knockdown. The observed downregulation of these genes aligns with the progression of AML induced by METTL16, as previous studies have indicated that the branched-chain amino acid synthesis (BCAA) pathway is

essential in AML progression [368]. Moreover, METTL16 knockdown significantly reduces BCAT1/2 stability in AML cells, completely restored by the expression of the WT protein but not of METTL16 catalytically inactive mutants (PP185/186AA and F187G), suggesting m6A methylation by METTL16 enhances the stability of BCAT1/2 mRNAs.

Gastric cancer

Consistently with what reported in literature, m6A modifications are also related to increased cell proliferation and migration in gastric cancer (GC) [369]. METTL16 high levels in GC was related to implemented cell replication, confirmed by the block of cell cycle at G1/S phase for GC cells in response to METTL16 knockdown, with a significant reduction in cyclin D1 expression (G1/S transition checkpoint in complex with cyclin-dependent kinases CDK 4 and 6). Mechanistic insights for the regulation of cell cycle by METTL16 protein were performed on GC cell lines, knockdown or WT for METTL16 protein, treated with actynomicin D, resulting in faster degradation of cyclin D1 mRNA in knockdown cells rather than WT cell lines. Furthermore, 3-deazaadenosine (**36**, Figure 38) treatment significantly inhibits the expression of cyclin D1, confirming the regulation of cyclin D1 by METTL16 RNA MTase activity [370].



36

Figure 38. Structure of 3-deazaadenosine, S-adenosylhomocysteine hydrolase inhibitor.

In vivo METTL16 depletion confirmed reduced tumor growth, volume, and mass, supporting the hypothesis of METTL16 overexpression involvement in promoting cancer progression.

Pancreatic carcinoma

As mentioned in the above paragraphs, METTL16 moves between the nucleus and the cytoplasmic environment, where it can exert its role both exploiting or not its MTase activity. METTL16 was found overexpressed in the cytoplasm of several cancer cell lines, suggesting its involvement in cancer progression independently from the MTase activity. On the contrary, METTL16 writer activity demonstrated an onco-suppressor role in pancreatic adenocarcinoma cancer via regulation of the cyclin-dependent kinase inhibitor (CDKN) 1A (p21) pathway [371]. Accordingly, pancreatic adenocarcinoma tissues were demonstrated to express lower METTL16 levels compared to health tissues. Interestingly, lower levels of METTL16 protein were linked to higher tumoral cells size and weight, but there was no correlation with migration and invasion phenomena, which instead are increased in cell types expressing METTL16 in the cytoplasmic medium. Several pancreatic adenocarcinoma cell lines showed promoted cell replication, while when METTL16 was overexpressed cell-cycle resulted blocked at G1 phase. The transcriptome analysis revealed that p21 expression was strongly influenced by METTL16 MTase activity. Silenced METTL16 cells showed reduced p21 expression, while its levels significantly increased in overexpressed MELLT16 conditions. To better understand how METTL16 regulates cell-cycle, PANC-1 and CFPAC-1 pancreatic adenocarcinoma cell lines were treated with the S-adenosylhomocysteine hydrolase inhibitor 3-deazaadenosine (**2**, Figure 9), and the m6A modifications were mapped, disclosing the presence of a m6A site on p21 mRNA stop codon. These data suggest METTL16 inhibits pancreatic adenocarcinoma cells

proliferation, promoting the synthesis of the cell-suppressor protein p21 thanks to the presence of a recognized methylation site on the mRNA codifying for this protein [371].

Colorectal carcinoma

Colorectal carcinoma (CRC) is one of the most arising and lethal malignancy spread worldwide and the third cause of cancer-related death in United States [372]. In the last decades, epigenetic bases (including DNA and histone modifications) have been confirmed to drive the differentiation of CRC cells occurring on distal or proximal colon. Programmed death ligand-1 (PD-L1) is an immune-checkpoint blocking immune response through inhibiting cytokines release and promoting T-cells apoptosis. Current CRC therapy includes anti-programmed cell death protein 1 (PD-1)/ PD-L1 immunotherapy, which showed promising results in CRC phenotypes with high grade of microsatellite instability. However, about 90% of CRC patients presents high degrees of stable microsatellite, with very low response to immunotherapy. In this context, a very recent study highlighted a tight correlation between METTL16 expression and the capability of CRC cells to elude immune system via the regulation of PD-L1 pathway [373]. Clinical CRC cells express PD-L1 protein but very low levels of METTL16 protein compared with healthy tissues. To understand how METTL16 can affect cancer phenotype, SW480 and SW620 CRC cells were transfected with METTL16 siRNA. Overexpressed METTL16 was accompanied by a significant increase in E-cadherin levels, while a reduction in Vimentin was observed, confirming the suppression of CRC cells proliferation, migration and invasion. Furthermore, T-cells apoptosis was observed in co-cultures with METTL16-overexpressed CRC cells, thus suggesting METTL16 regulates immune response. Also, PD-L1 m6A RNA was quantified, confirming METTL16-overexpression enhances PD-L1 degradation. Accordingly, these preliminary results encourage further studies of METTL16-mediated immune

response, as a new potential therapeutic option in drug-resistant CRC cancer [373]. Another relevant study reported in 2023 showed METTL16 promotes CRC initiation and progression via regulating aerobic glycolysis[374]. Suppressor Of Glucose Autophagy Associated 1 (SOGA1) mRNA presents a m6A site recognized by METTL16, while the expression of IGF2BP1 m6A reader significantly induce metastatic states, suggesting it is responsible in recognizing methylated SOGA1 m6A mRNA. Indeed, SOGA1 promotes PDK4 expression, related to aggressiveness and therapy resistance in multiple malignancies**.** Wei and collaborators also proved enfeeble METTL16 expression in *in vivo* conditions of PDK4 and SOGA1 knockdown [374], with the consequent reduction of CRC tumor size, thus confirming METTL16 as a reliable marker in CRC phenotype. Moreover, a very recent study reported in October 2023 confirmed METTL16 also as a key regulator in cholangiocarcinoma cancer progression. Indeed, METTL16 is responsible for the m6A methylation of fibroblast growth factor receptor 4 (FGFR4), a recognized marker for cholangiocarcinoma. METTL16 KD and KO models confirmed the inhibition in cholangiocarcinoma cells proliferation, through the reduction in the expression of PR/SET domain 15 protein (PRDM15), which promotes FGFR4 mRNA translation [375].

1.8 METTL16 inhibitors

Due to the poor structural information and the still ongoing progress in the identification of METTL16 biological role and molecular targets, the medicinal chemistry efforts for the design and development of new molecules targeting METTL16 are still in their infancy. Nonetheless, a few sets of molecules worthy of note have been developed and they can represent the groundwork for further structural elaboration and optimization. In this paragraph, we report an overview on these newly generated structural templates as well as compounds arising from

repurposing approaches. The molecules reported so far are targeting the METTL16 MTD binding side. The first reported inhibitors date back 2021, and they were proposed as an innovative therapeutic option for oncologic pathologies characterized by high levels of expressed METTL16 protein, with particular reference to acute myeloid leukemia (AML) and liver cancer line cells [376]. Compounds reported in *Table 1* are representative derivatives of this newly conceived series of compounds, characterized by nanomolar inhibitory activity (IC_{50} calculated in function of AML cell viability between 1 and 700 nM). The direct interaction with METTL16 and the reduction of the expression of METTL16 target genes was demonstrated for all compounds reported in *Table 2*.

All compounds present a pyrrolo-[3,2-f]quinazoline-1,3 diamine scaffold (general structure **A**, Figure 39) differing only for the alkyl substituent on the indole nitrogen.

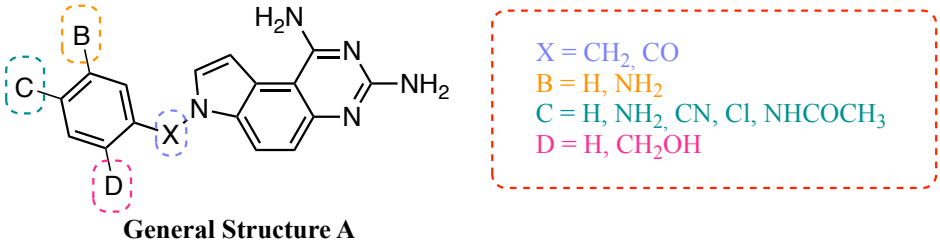
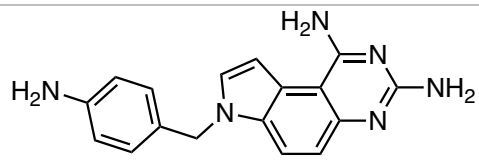
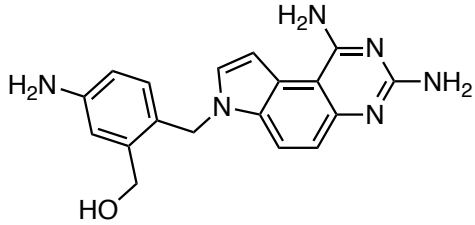
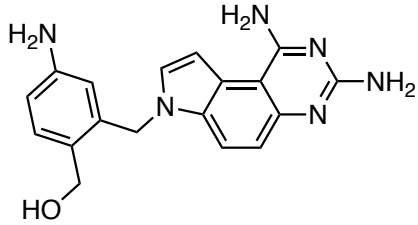
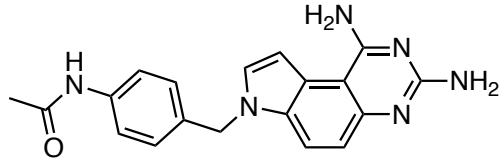
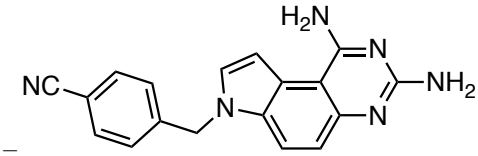
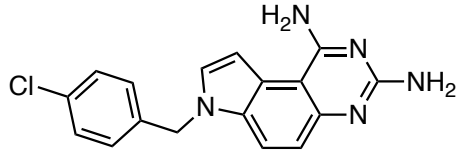
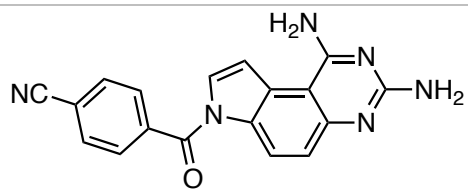


Figure 39. General structure **A** of compounds **37-43** [300].

Table 2. Structure and activity for compounds of general structure **A**.

Compound name	Compound number	Structure	**IC_{50} nM** NOMO-1 Cell viability
CDH24	**37**		N.R.
CDH24-6	**38**		N.T.
CDH24-7	**39**		55
CDH24-16	**40**		1.39
CDH24-18	**41**		20.59
CDH24-20	**42**		1.55

CDH24-21	**43**		736.1

N.R. = not reported. N.T. = not tested against NOMO-1 cell line.

CDH24 (**37**, *Table 2*) is the representative chemical template of the series, and its putative binding mode and interactions with METTL16 MTD are reported in Figure 11. The aromatic ring of 4-aminobenzyl group is engaged in a π-staking with Phe227, while its amine group interact with Thr164 CO backbone via hydrogen bond. Phe227 in turn also engages a further π-stacking with the pyrroloquinazoline moiety of the ligand. The amino group in position 3 is H-bonded with both side chain and CO backbone of Asn184. The aromatic skeleton of the molecule is involved in hydrophobic interactions with Leu165, Val134, Phe227, while positions 12 e 13 are solvent exposed [376].

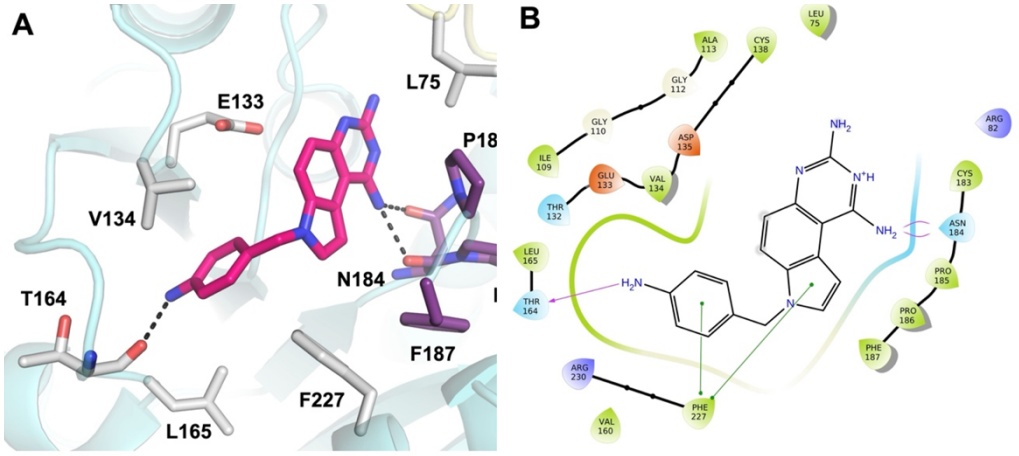
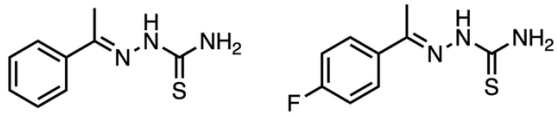


Figure 40. Putative binding mode of compound CDH24 (**37**) (A, magenta sticks) into METTL16 MTD represented as ribbon model. Key residues discussed in the text are displayed (white sticks) and labeled; the NPPF catalytic motif is displayed as purple sticks. H-bonds discussed in the text are depicted as dashed

black lines. (B) 2D ligand interaction diagram of compound CDH24 (**37**) into METTL16 MTD. Positively charged amino acids are represented with dark blue drops, negatively charged amino acids are represented with red drops, polar amino acids are represented with light blue drops and hydrophobic amino acids are represented with green drops. H-bonds are depicted with purple arrows. Straight green lines represent π-stacking interactions [300].

A second series was published in June 2021 by Chemestmed Ltd, following a high-throughput virtual screening approach on 130000 compounds from the ZINC database (*in vivo* subset) against METTL16 MTD. The virtual screening procedure and subsequent biological evaluation led to the selection of compounds **44** and **45** with nanomolar activity (Figure 41)[377,378]. The relative inhibitory effect of the compounds on METTL16 activity was assessed by measuring the METTL16 induced RNA m6A methylation by means of a biotin-marked RNA oligonucleotide. Interestingly, no inhibitory activity on METTL3/14 was detected (even though these results were not shown). Binding of the two compounds was also confirmed by microscale thermophoresis (MST) experiments, obtaining K_d values of 3.31 ± 0.61 μM and 2.84 ± 0.94 μM for compounds **44** and **45**, respectively. The authors hypothesized that the higher Kd values observed, as compared to the IC_{50} values, might be due to the different proteins employed, namely the full-length METTL16 protein in the enzyme inhibition experiment and the catalytic subunit in the MST experiment [377,378].



44
$IC_{50\ nM}$ = 25.82 ± 17.19

45
$IC_{50\ nM}$ = 60.91 ± 2.75

Figure 41. Structure and IC_{50} values for compounds **44, 45**.

Compounds did not show cytotoxic activity under 100 μM on HEK293T line cells. Furthermore, cytotoxic activity on HL-60 (adult acute myeloid leukemia)

and CCRF-CEM (Childhood T- cell acute lymphoblastic leukemia) cells was evaluated. On HL-60 cell lines both compounds **44** and **45** showed cell growth inhibition (up to 40% of inhibition at the concentration of 0.1 μM) linked to cell division inhibition, however the inhibitory activity did not show a dose-dependent behavior. In CCFR-CEM cells the effect of compounds **44** and **45** on cell viability was smaller, with no dose dependency. Moreover, compound **44** significantly reduced the level of m_6A as compared to unmodified adenosine in the HL-60 cell mRNAs. The binding mode of compounds **44** and **45** in the METTL16 MTD was also predicted by *in silico* studies (Figure 42), revealing some differences in comparison with compound **3** belonging to the General Structure A described above. The thio-semicarbazide moiety of both compounds **44** and **45** establish tight H-bonds with the residues Arg82, Gly110, and Asn184. Their aromatic portions, although quite solvent-exposed, could still engage hydrophobic interactions with Leu75, Pro186, Phe187 (Figure 12). While compound **37** (*Table 2*) strongly engaged Asn184 by interacting with both residue's side chain and CO backbone, the smaller compounds **44** and **45** are able to get closer to Arg82 (which is known to be involved in RNA substrate binding) and only interact with Asn184 side chain.

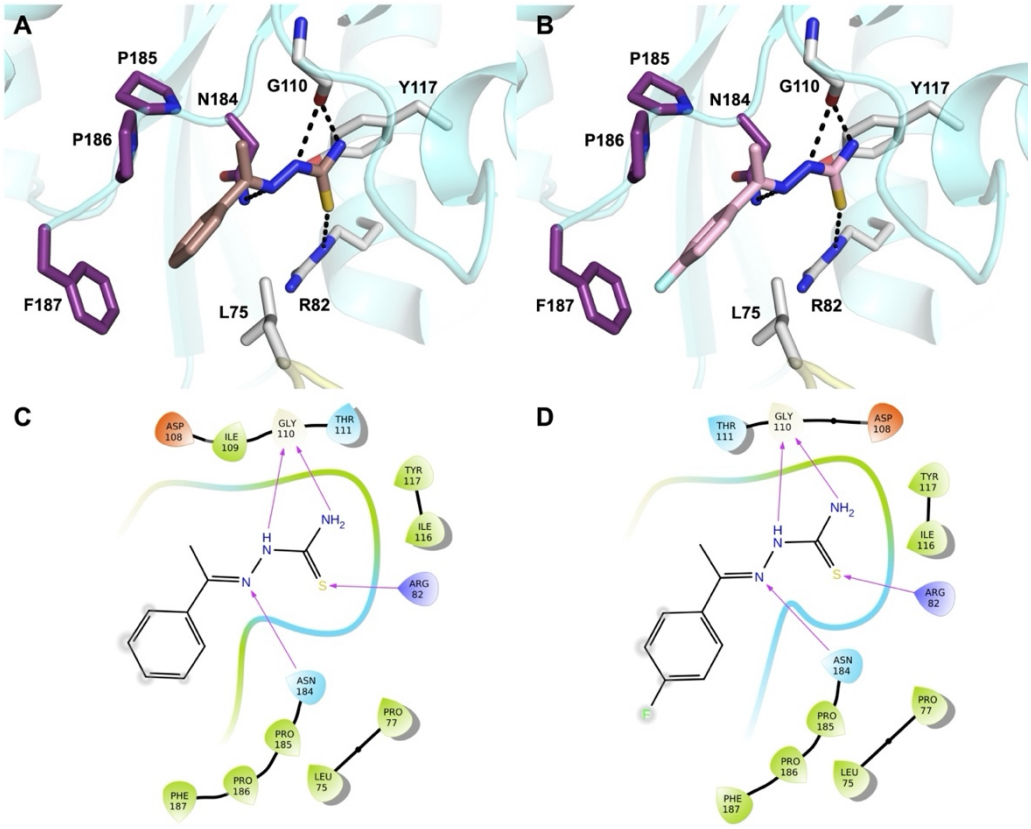


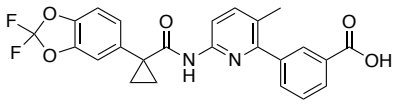
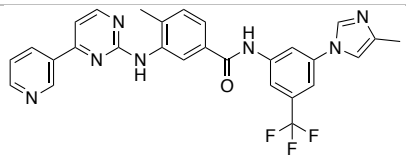
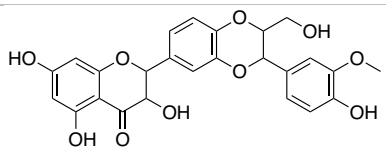
Figure 42. Putative binding mode of compounds **44** (A, dark salmon sticks) and **45** (B, pink sticks) into METTL16 MTD represented as ribbon model. Key residues discussed in the text are displayed (white sticks) and labeled; the NPPF catalytic motif is displayed as purple sticks. H-bonds discussed in the text are depicted as dashed black lines. 2D ligand interaction diagram of compounds 44 (C) and **45** (D) into METTL16 MTD. Positively charged amino acids are represented with dark blue drops, negatively charged amino acids are represented with red drops, polar amino acids are represented with light blue drops and hydrophobic amino acids are represented with green drops. H-bonds are depicted with purple arrows. Straight green lines represent π-stacking interactions [300].

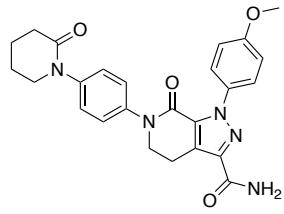
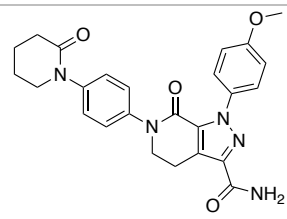
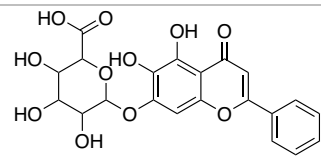
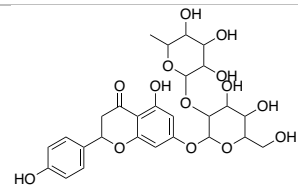
According with the unique binding mode reported for compounds **44**, **45** in comparison with compounds with General Structure A (Figure 39, *Table 2*), solving the crystal structure of compounds **44**, **45** in complex with METTL16

MTD could unveil new hints for the structure-based development of selective METTL16 inhibitors targeting METLL16 catalytic function [377,378].

More recently, in January 2023, a virtual screening approach was pursued by Mitra A. et al [104] with the objective of identifying potential drugs to be repurposed as METTL16 inhibitors. Specifically, a set of 682 drug molecules was virtually screened on the co-factor binding pocket. Promising compounds were prioritized on the basis of the docking score values (by applying a cut-off of -9 kcal/mol, corresponding to the docking score of SAH docked back into the protein structure). Eight compounds (*Table 3*) were selected according to the score [379].

Table 3. Top compounds as potential competitive inhibitors for METTL16 SAM binding pocket.

Compound name	Compound number	Structure	Current use
Lumacaftor, VX-809	**46**		Cystic fibrosis treatment in combination with Ivacaftor
Nilotinib	**47**		Chronic myeloid leukemia treatment
Silymarin	**48**		Food supplement

Etoposide	**49**		Refractory testicular tumor treatment; small cell lung cancer, in combination with cisplatin
Apixaban	**50**		Oral anticoagulant
Baicalin	**51**		Food supplement
Naringin	**52**		-

The eight selected compounds were further shortlisted on the basis of predicted toxicity and theoretically calculated inhibition constant (*K*i). Finally, compounds **46** and **47** (*Table 3*) were proposed as the best candidates for further *in silico* investigations, by docking and molecular dynamic simulation studies (Figure 13). Molecular modeling studies suggested that both compounds **46** and **47** could potentially fit within the SAH binding site, mostly establishing hydrophobic interactions through their bulky hydrophobic scaffolds. Moreover, both compounds are at favorable distance to interact with Arg230, located at the edge of the hydrophobic site where the adenine moiety of SAH lies. Regarding

compound **46**, the 2,2-difluoro-1,3-benzodioxol portion looks quite solvent exposed, even though it might still be able to engage hydrophobic interactions with residues of NPPF catalytic motif, in particular Phe187 and Pro186. This latter is juxtaposed against the ligand's methyl pyridine ring. In addition, Phe227 and Val134 "clamp" the benzoic acid portion of **46**. In a similar fashion, compound **47** establishes a π-stacking interaction with Phe227 through its pyrimidine ring, which, together with the terminal pyridine, appear rather solvent-exposed. The amide portion of **47** donates a H-bond to the side chain of Glu133, whereas the remainder of the ligand extends toward a hydrophobic area, enclosed by Leu75 and Arg74 (Figure 43) [379].

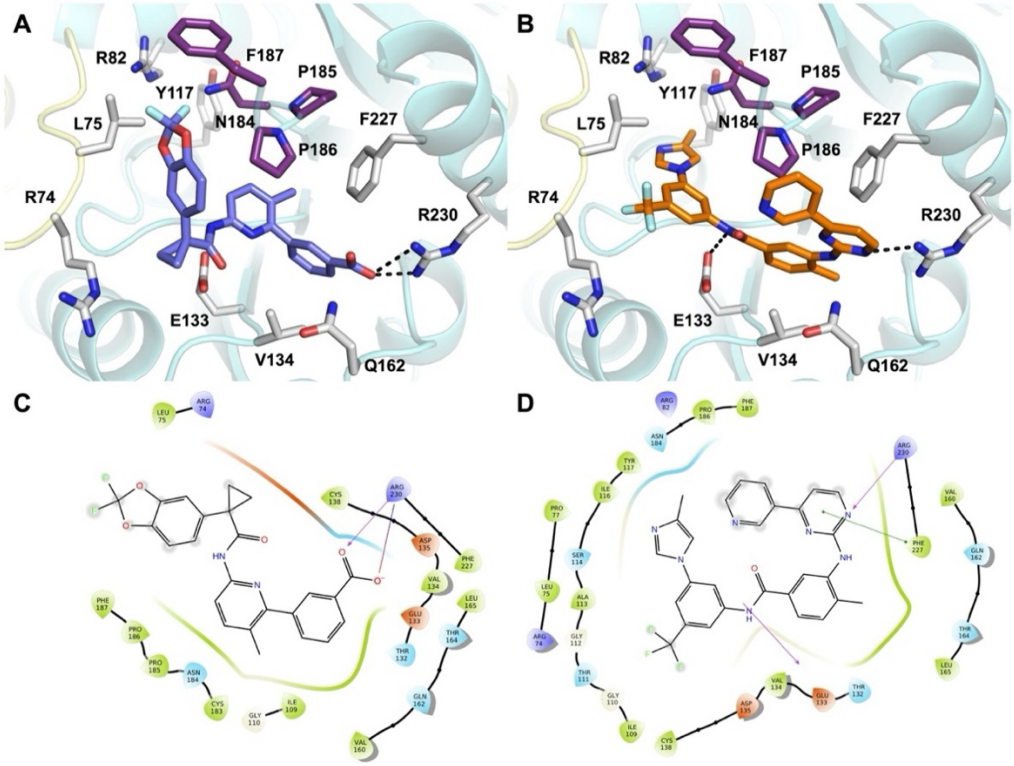


Figure 43. Putative binding mode of compounds **46** (A, slate sticks) and **47** (B, orange sticks) into METTL16 MTD represented as ribbon model. Key residues discussed in the text are displayed (white sticks) and labeled; the NPPF catalytic

motif is displayed as purple sticks. H-bonds discussed in the text are depicted as dashed black lines. 2D ligand interaction diagram of compounds **46** (C) and **47** (D) into METTL16 MTD. Positively charged amino acids are represented with dark blue drops, negatively charged amino acids are represented with red drops, polar amino acids are represented with light blue drops and hydrophobic amino acids are represented with green drops. H-bonds are depicted with purple arrows. Straight green lines represent π-stacking interactions [300].

The first consistent study highlighting SAR in the design of METTL16 inhibitors was published in March 2024. Liu et al. identified first-in-class aminothiazolone inhibitors able to disrupt the METTL16−MAT2A-hp1 mRNA interaction [380]. Through the screening of an in-house library comprising about 25000 compounds, the authors identified the hit compound **54** displaying μM activity against METTL16 (Figure 44) [380] .

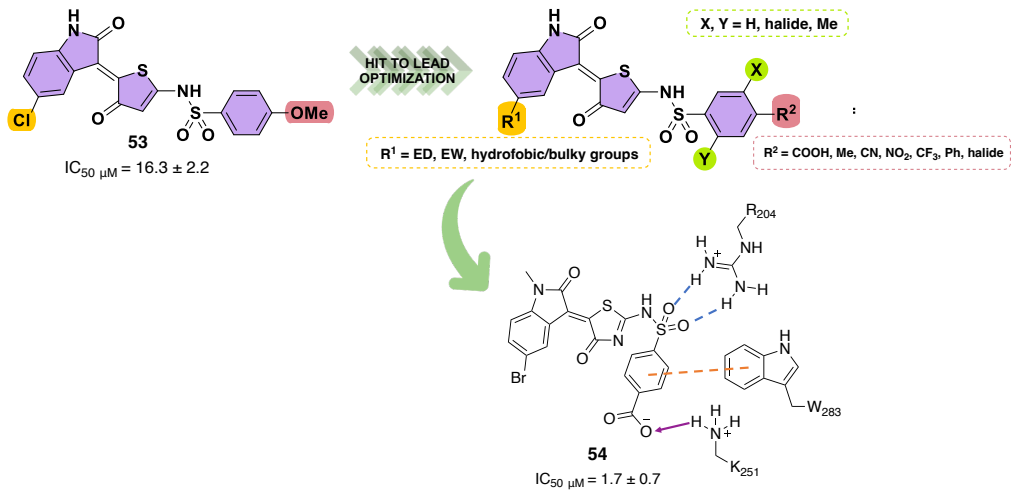
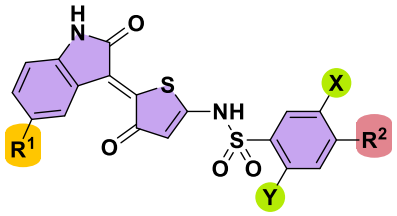
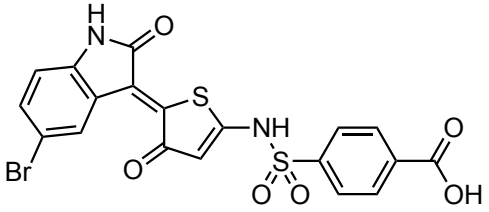
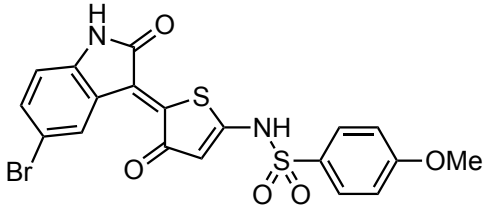
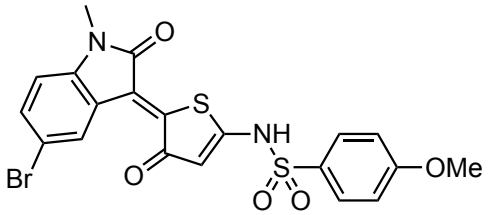
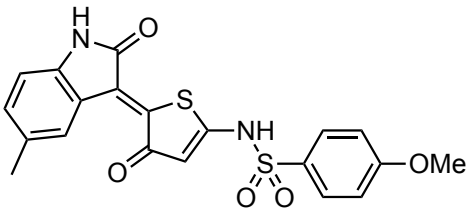
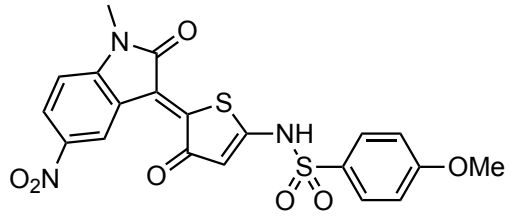
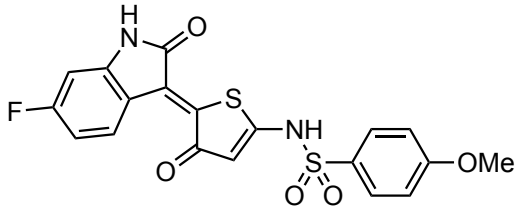
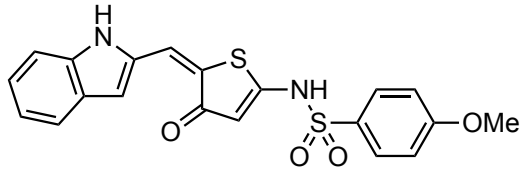
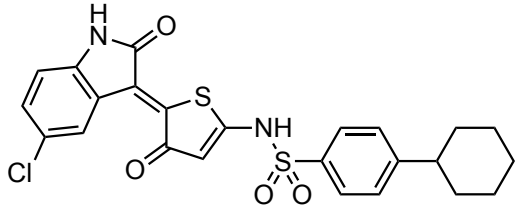
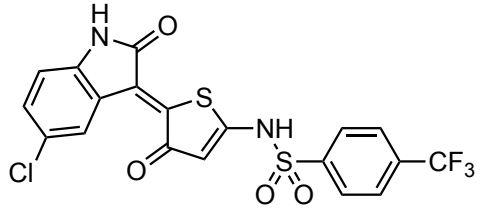


Figure 44. Hit to lead identification of aminothiazolone-based METTL16 inhibitors. ED = electron-donating; EW = electron-withdrawing [300].

Table 3. Structure and activity of representative aminothiazolone METTL16 inhibitors.



Compound number	Structure	IC_{50} µM
54		1.7 ± 0.7
55		12.4 ± 2.8
56		6.8 ± 0.45
57		24.3 ± 5.3

58		6.8 ± 1.0
59		NA
60		23.2 ± 2.7
61		NA
62		13.6 ± 3.6

NA = not active

Various substitutions (e.g. halide, methyl group, nitro group) on the position 5 of the oxindole ring, as well as the methylation of the nitrogen, were well-tolerated and did not significantly affect the activity of resulting compounds **55**, **56**, **57, 58** (*Table 4*) in comparison with hit compound **53** (Figure 44), while the introduction of an halogen in position 6 (**59**, *Table 4*) or 7 was detrimental for the activity. A

second screening was performed keeping the R^1 substituent of the hit compound **53** (R^1 = Cl), while the sulfonamide portion role was investigated. Interestingly, analogues lacking the sulfonamide resulted in the complete loss of activity, suggesting the importance of this group in the RNA binding site of METTL16. In a similar trend, the replacement of the oxindole scaffold with the analogue indole ring was detrimental for the activity (**60**, *Table 4*) [380]. Also, the introduction of bulky groups (e.g. tert-butyl, phenyl, cyclohexyl) on R^2 moiety resulted in the complete loss of activity (**61,** Table 4), while the insertion of polar groups (**53**, Figure 44, *Table 4*; **62**, *Table 4*) was helpful in the reduction of IC_{50} values in comparison with compound **53**. This data perfectly aligns with previous published literature about the importance of carboxylic acids in small molecules binding RNA-binding proteins [381–384], presenting a positive charged lysing-rich region devoted to the binding with RNA negatively charged groove. Moreover, competition assays were performed incubating the enzyme both with the inhibitor and increasing concentration of SAM, METTL16 substrate. The presence of SAM at any concentration did not affect the inhibitory activity of tested compound, showing a non-competitive inhibition profile. This study represents a significant advancement in the discovery of METTL16 inhibitors, given all the few inhibitors generated so far are supposed to bind the SAM pocket in METTL16 MTD[376–380] and their inhibitory profiles remain elusive. This work provided the first coherent set of structure-relationship data for METTL16 inhibition, thereby strongly supporting the feasibility of a rational design campaign to target this epitranscriptomic player and opening a new avenue in structure-based optimization for METTL16 inhibitors [380].

Introduction – Part 4: Escape from flatland: how spirofused compounds are reshaping medicinal chemistry.

Achieving the optimal balance between the biological activity of a drug and its pharmacokinetic properties is a major challenge in medicinal chemistry. For

instance, aromatic motifs are the most recurrent substructures in approved drugs for their synthetic versability, allowing a wide platform of chemical diversity. Also, aromatic systems are naturally occurring in amino acids and nucleotides, thereby their incorporation in designed drugs represents a useful tool to achieve drug-target interaction [385,386]. The limited degrees of freedom in Csp^2 systems allows a lower ligand-receptor binding energy, thereby increasing compound potency [387].

Unlikely, the planar nature of these systems is linked to non-specific hydrophobic interactions, allowing the binding with multiple targets and undesirable off-target effects [388]. Suboptimal *aromatic ring count* (number of aromatic rings in a molecule) can significantly affect drug-like properties of a molecule. Indeed, high aromatic ring count reduces water solubility while increasing the lipophilicity and plasma protein binding. Also, high aromatic ring count has been linked to increased inhibition of CYP450 and hERG ion channel, thus limiting drug developability [388].

Accordingly, the replacement of aromatic systems with saturated frameworks has gained growing interest as a viable strategy to enhance molecular complexity, exploring three-dimensional space, without significantly increasing molecular weight. In this context, the introduction of saturated and spirofused systems proved to be a valuable strategy to *escape from flatland* and increase drug-like properties of designed molecules [389,390]. In recent years, the number of approved drugs bearing spirofused cores has been steadily increasing, thereby underscoring the validity of such structural motifs to achieve success in clinical development [391].

According to IUPAC, *spirofused ring systems have two or more rings linked by one common atom* [392]. These systems are valuable tools in medicinal chemistry, since they offer the opportunity to enhance metabolic stability, while optimizing target interaction and selectivity, and ADME properties [393,394].

For instance, the rigid three-dimensional architecture of spirocycles can be exploited to lock the molecule in a conformation which resembles the bioactive one, thereby increasing target-affinity and avoiding off-target effects due to aspecific interactions (Figure 45) [395–397]. Similarly, spirocyclic systems have proved increased metabolic stability and improved *in vivo* half-lives in comparison to their planar analogues, strongly supporting the positive impact of constrained geometry to slow down metabolic reactions (Figure 30) [398,399].

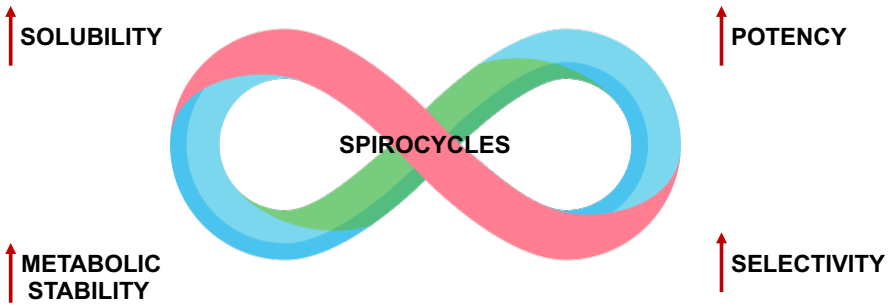


Figure 45. Schematic representation of advantages of the application of spirocyclic systems in drug discovery.

More interestingly, the introduction of spirocyclic cores is related to an increase of the *fraction of sp^3 hybridized carbo*ns (Fsp^3), defined as:

$$Fsp3 = \frac{\text{number of sp}^3\text{ hybridized carbons}}{total\ carbon\ count}$$

Fsp^3 is considered a valuable parameter in the design of drug candidates, since in turn it correlates with improved drug-like properties. Accordingly, more than 80% of marketed drugs exhibits the ideal value of $Fsp^3 \geq 0.42$. The importance of high Fsp^3 values stands in the abovementioned possibility to increase target-ligand interaction exploiting molecule three-dimensionality, by introducing out-of-plane substituents and explore a wider chemical space [400]. Furthermore,

high Fsp^3 values also correlates to increased water solubility and ADME properties [389], key factors for the development of successful drugs. Thereby, considering successful stories of clinical candidates (Figure 46), the introduction of spirocyclic cores in designed molecules is an innovative approach in the design of molecules with improved Fsp^3 and, consequently physiochemical properties, as well as the possibility to fine-tune the interaction with the selected target in comparison to flat analogues, making these molecular motifs attractive in the design of novel drugs.

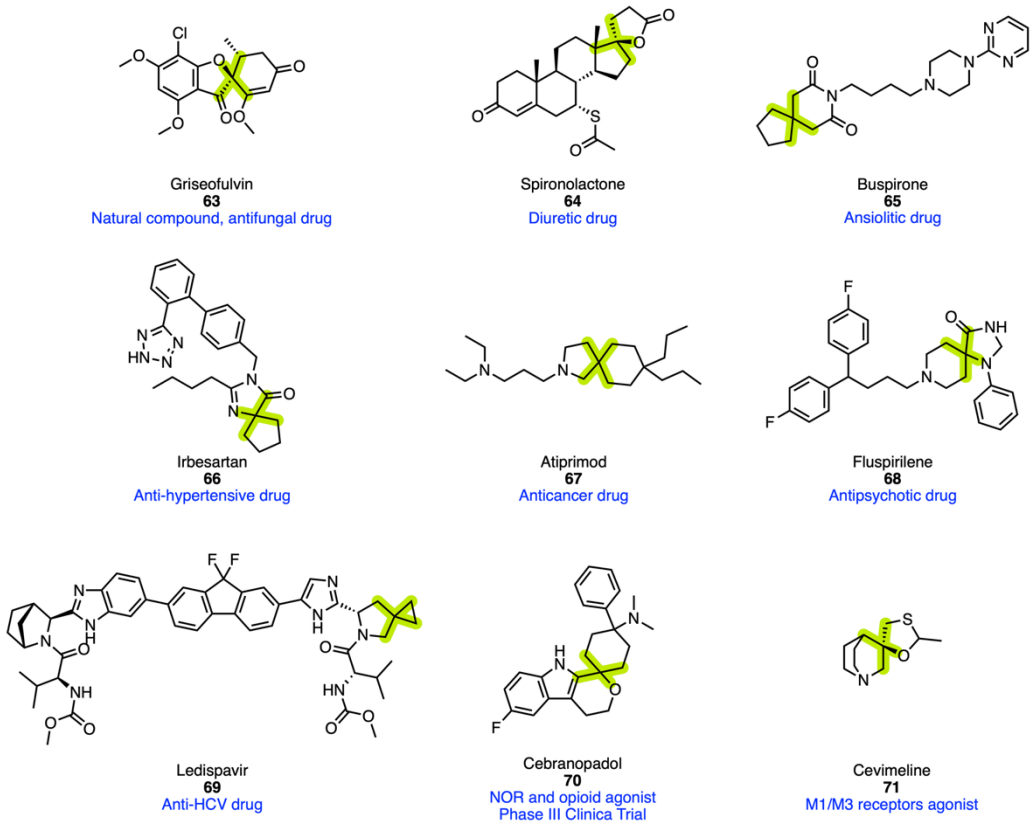


Figure 46. Examples of approved drugs containing spirocyclic motifs and their application. The junction of the spirocyclic motif is highlighted in green.

In line with the rising relevance of spirocyclic systems in drug design, these motifs frequently occur within this thesis work – particularly in the design of HDAC6is. This strategy allowed us to modulate potency, selectivity and drug-

like properties of designed compounds, thereby demonstrating spirofused cores are versatile frameworks able to optimize both the biological activity and pharmacodynamic properties of designed molecules,

References

[1] F. Crick, Nature 227 (1970) 561–563.

[2] J. Füllrabe, W.S. Gosal, P. Creed, S. Liu, C.K. Lumby, D.J. Morley, T.W.B. Ost, A.J. Vilella, S. Yu, H. Bignell, P. Burns, T. Charlesworth, B. Fu, H. Fordham, N.J. Harding, O. Gandelman, P. Golder, C. Hodson, M. Li, M. Lila, Y. Liu, J. Mason, J. Mellad, J.M. Monahan, O. Nentwich, A. Palmer, M. Steward, M. Taipale, A. Vandomme, R.S. San-Bento, A. Singhal, J. Vivian, N. Wójtowicz, N. Williams, N.J. Walker, N.C.H. Wong, G.N. Yalloway, J.D. Holbrook, S. Balasubramanian, Nat Biotechnol 41 (2023) 1457–1464.

[3] M.C. Thomas, C.-M. Chiang, Crit Rev Biochem Mol Biol 41 (2006) 105–178.

[4] S. Hahn, Nat Struct Mol Biol 11 (2004) 394–403.

[5] P.R. Andersen, L. Tirian, M. Vunjak, J. Brennecke, Nature 549 (2017) 54–59.

[6] Y. Xie, J.Y.S. Lim, W. Liu, C. Gilbreath, Y.J. Kim, S. Wu, bioRxiv (2025).

[7] Y. Chen, R. Liang, Y. Li, L. Jiang, D. Ma, Q. Luo, G. Song, Signal Transduct Target Ther 9 (2024) 340.

[8] E.T. Friman, C. Deluz, A.C. Meireles-Filho, S. Govindan, V. Gardeux, B. Deplancke, D.M. Suter, Elife 8 (2019), e50087.

[9] L.A. Passmore, S. Zhang, Nat Struct Mol Biol 31 (2024) 730–731.

[10] C.H. Waddington, Int J Epidemiol 41 (2012) 10–13.

[11] C.H. Waddington, Genetic Assimilation of the Bithorax Phenotype 10, (1956), 1-13

[12] C.H. Waddington, Nature 150, (1942), 563–565

[13] S. Biswas, C.M. Rao, Eur J Pharmacol 837 (2018) 8–24.

[14] B.C. Buchmuller, B. Kosel, D. Summerer, Sci Rep 10 (2020) 4053.

[15] L. Gu, Y. Fu, X. Li, Epigenetics Chromatin 17 (2024) 15.

[16] P. Filippakopoulos, S. Picaud, M. Mangos, T. Keates, J.-P. Lambert, D. Barsyte-Lovejoy, I. Felletar, R. Volkmer, S. Müller, T. Pawson, A.-C. Gingras, C.H. Arrowsmith, S. Knapp, Cell 149 (2012) 214–231.

[17] L.A. Uroshlev, E.T. Abdullaev, I.R. Umarova, I.A. Il'icheva, L.A. Panchenko, R. V. Polozov, F.A. Kondrashov, Y.D. Nechipurenko, S.L. Grokhovsky, Sci Rep 10 (2020) 8635.

[18] O.A. Stefansson, B.D. Sigurpalsdottir, S. Rognvaldsson, G.H. Halldorsson, K. Juliusson, G. Sveinbjornsson, B. Gunnarsson, D. Beyter, H. Jonsson, S.A. Gudjonsson, T.A. Olafsdottir, S. Saevarsdottir, M.K. Magnusson, S.H. Lund, V. Tragante, A. Oddsson, M.T. Hardarson, H.P. Eggertsson, R.L. Gudmundsson, S. Sverrisson, M.L. Frigge, F. Zink, H. Holm, H. Stefansson, T. Rafnar, I. Jonsdottir, P. Sulem, A. Helgason, D.F. Gudbjartsson, B. V. Halldorsson, U. Thorsteinsdottir, K. Stefansson, Nat Genet 56 (2024) 1624–1631.

[19] H. Jang, W. Shin, J. Lee, J. Do, Genes (Basel) 8 (2017) 148.

[20] M. Bartas, M. Petrovič, V. Brázda, O. Trenz, A. Ďurčanský, J. Šťastný, Journal of Biological Chemistry 301 (2025) 108537.

[21] S. Pinney, Biology (Basel) 3 (2014) 739–751.

[22] D.J. Kim, Current Oncology 32 (2025).

[23] A. Kikuchi, H. Onoda, K. Yamaguchi, S. Kori, S. Matsuzawa, Y. Chiba, S. Tanimoto, S. Yoshimi, H. Sato, A. Yamagata, M. Shirouzu, N. Adachi, J. Sharif, H. Koseki, A. Nishiyama, M. Nakanishi, P.A. Defossez, K. Arita, Nat Commun 13 (2022).

[24] T.H. Xu, M. Liu, X.E. Zhou, G. Liang, G. Zhao, H.E. Xu, K. Melcher, P.A. Jones, Nature 586 (2020) 151–155.

[25] M. Okano, D.W. Bell, D.A. Haber, E. Li, DNA Methyltransferases Dnmt3a and Dnmt3b Are Essential for De Novo Methylation and Mammalian Development, 1999.

[26] M.S. Kareta, Z.M. Botello, J.J. Ennis, C. Chou, F. Chédin, Journal of Biological Chemistry 281 (2006) 25893–25902.

[27] N. Veland, Y. Lu, S. Hardikar, S. Gaddis, Y. Zeng, B. Liu, M.R. Estecio, Y. Takata, K. Lin, M.W. Tomida, J. Shen, D. Saha, H. Gowher, H. Zhao, T. Chen, Nucleic Acids Res 47 (2019) 152–167.

[28] A. Basu, A. Tomar, V. Dasari, R.K. Mishra, S. Khosla, Sci Rep 6 (2016).

[29] H. Li, H. Liu, D. Zhu, C. Dou, B. Gang, M. Zhang, Z. Wan, Pharmacol Res 205 (2024).

[30] A. Dong, J.A. Yoder, X. Zhang, L. Zhou, T.H. Bestor, X. Cheng, Structure of Human DNMT2, an Enigmatic DNA Methyltransferase Homolog That Displays Denaturant-Resistant Binding to DNA, 2001.

[31] A. Jeltsch, A. Ehrenhofer-Murray, T.P. Jurkowski, F. Lyko, G. Reuter, S. Ankri, W. Nellen, M. Schaefer, M. Helm, RNA Biol 14 (2017) 1108–1123.

[32] L.J. Collins, B. Schönfeld, X.S. Chen, Mol genet genomic med 4 (2011), 49-61.

[33] S. Panni, R.C. Lovering, P. Porras, S. Orchard, Biochim Biophys Acta Gene Regul Mech 1863 (2020), 194417.

[34] L.J. Collins, X.S. Chen, RNA Biol 6 (2009) 495–502.

[35] S.E. Castel, R.A. Martienssen, Nat Rev Genet 14 (2013) 100–112.

[36] W. Filipowicz, S.N. Bhattacharyya, N. Sonenberg, Nat Rev Genet 9 (2008) 102–114.

[37] T. Kaucsár, Z. Rácz, P. Hamar, Adv Drug Deliv Rev 62 (2010) 1390–1401.

[38] W.S. Park, W. Do Heo, J.H. Whalen, N.A. O'Rourke, H.M. Bryan, T. Meyer, M.N. Teruel, Mol Cell 30 (2008) 381–392.

[39] S. Vasudevan, Y. Tong, J.A. Steitz, Science (1979) 318 (2007) 1931–1934.

[40] A. Fire, S. Xu, M. Montgomery, S.A. Kostas, S.E. Driver, C.C. Mello, Nature 391 (1998), 806–811.

[41] D.M. Ozata, I. Gainetdinov, A. Zoch, D. O'Carroll, P.D. Zamore, Nat Rev Genet 20 (2019) 89–108.

[42] J.S. Mattick, P.P. Amaral, P. Carninci, S. Carpenter, H.Y. Chang, L.-L. Chen, R. Chen, C. Dean, M.E. Dinger, K.A. Fitzgerald, T.R. Gingeras, M. Guttman, T. Hirose, M. Huarte, R. Johnson, C. Kanduri, P. Kapranov, J.B. Lawrence, J.T. Lee, J.T. Mendell, T.R. Mercer, K.J. Moore, S. Nakagawa, J.L. Rinn, D.L. Spector, I. Ulitsky, Y. Wan, J.E. Wilusz, M. Wu, Nat Rev Mol Cell Biol 24 (2023) 430–447.

[43] H. Täuber, S. Hüttelmaier, M. Köhn, J Mol Cell Biol 11 (2019) 880–885.

[44] G. Pintacuda, A.N. Young, A. Cerase, Front Mol Biosci 4 (2017).

[45] R.A. Gupta, N. Shah, K.C. Wang, J. Kim, H.M. Horlings, D.J. Wong, M.-C. Tsai, T. Hung, P. Argani, J.L. Rinn, Y. Wang, P. Brzoska, B. Kong, R. Li, R.B. West, M.J. van de Vijver, S. Sukumar, H.Y. Chang, Nature 464 (2010) 1071–1076.

[46] C.W. Carter, Proceedings of the National Academy of Sciences 75 (1978) 3649–3653.

[47] V. Cavalieri, Genes (Basel) 12 (2021) 1596.

[48] R. Liu, J. Wu, H. Guo, W. Yao, S. Li, Y. Lu, Y. Jia, X. Liang, J. Tang, H. Zhang, MedComm (Beijing) 4 (2023), 161.

[49] G. Millán-Zambrano, A. Burton, A.J. Bannister, R. Schneider, Nat Rev Genet 23 (2022) 563–580.

[50] E.L. Greer, Y. Shi, Nat Rev Genet 13 (2012) 343–357.

[51] S. Park, J.H. Cho, J.-H. Kim, J.-A. Kim, Exp Mol Med 56 (2024) 2127–2144.

[52] M.I. Maron, A.D. Casill, V. Gupta, J.S. Roth, S. Sidoli, C.C. Query, M.J. Gamble, D. Shechter, Elife 11 (2022), e72867.

[53] C.I. Zurita-Lopez, T. Sandberg, R. Kelly, S.G. Clarke, Journal of Biological Chemistry 287 (2012) 7859–7870.

[54] Y. Shi, F. Lan, C. Matson, P. Mulligan, J.R. Whetstine, P.A. Cole, R.A. Casero, Y. Shi, Cell 119 (2004) 941–953.

[55] Md.S. Islam, M.A. McDonough, R. Chowdhury, J. Gault, A. Khan, E. Pires, C.J. Schofield, Journal of Biological Chemistry 294 (2019) 11637–11652.

[56] A.J. Bannister, T. Kouzarides, Cell Res 21 (2011) 381–395.

[57] V. Sapountzi, J. Côté, Cellular and Molecular Life Sciences 68 (2011) 1147–1156.

[58] E. Koutelou, A.T. Farria, S.Y.R. Dent, Biochimica et Biophysica Acta (BBA) - Gene Regulatory Mechanisms 1864 (2021) 194609.

[59] J.E. Herrera, M. Bergel, X.-J. Yang, Y. Nakatani, M. Bustin, Journal of Biological Chemistry 272 (1997) 27253–27258.

[60] S. D'Arcy, K. Luger, Curr Opin Struct Biol 21 (2011) 728–734.

[61] A. Haigney, M.D. Ricketts, R. Marmorstein, Journal of Biological Chemistry 290 (2015) 30648–30657.

[62] M.R. Parthun, Oncogene 26 (2007) 5319–5328.

[63] Y. Zhang, D. Remillard, U. Onubogu, B. Karakyriakou, J.N. Asiaban, A.R. Ramos, K. Bowland, T.R. Bishop, P.A. Barta, S. Nance, A.D.

Durbin, C.J. Ott, M. Janiszewska, B.F. Cravatt, M.A. Erb, Nat Struct Mol Biol 30 (2023) 1160–1171.

[64] T. Ishizuka, M.A. Lazar, Mol Cell Biol 23 (2003) 5122–5131.

[65] C. Sang, X. Li, J. Liu, Z. Chen, M. Xia, M. Yu, W. Yu, EMBO Rep 25 (2024) 3925–3943.

[66] K. Das Gupta, M.R. Shakespear, J.E.B. Curson, A.M.V. Murthy, A. Iyer, M.P. Hodson, D. Ramnath, V.A. Tillu, J.B. von Pein, R.C. Reid, K. Tunny, D.M. Hohenhaus, S.V. Moradi, G.M. Kelly, T. Kobayashi, J.H. Gunter, A.J. Stevenson, W. Xu, L. Luo, A. Jones, W.A. Johnston, A. Blumenthal, K. Alexandrov, B.M. Collins, J.L. Stow, D.P. Fairlie, M.J. Sweet, Cell Rep 30 (2020) 2712-2728.e8.

[67] A. Clocchiatti, C. Florean, C. Brancolini, J Cell Mol Med 15 (2011) 1833–1846.

[68] X.-J. Yang, S. Grégoire, Mol Cell Biol 25 (2005) 2873–2884.

[69] Y. Hai, S.A. Shinsky, N.J. Porter, D.W. Christianson, Nat Commun 8 (2017) 15368.

[70] Q.-J. Wu, T.-N. Zhang, H.-H. Chen, X.-F. Yu, J.-L. Lv, Y.-Y. Liu, Y.-S. Liu, G. Zheng, J.-Q. Zhao, Y.-F. Wei, J.-Y. Guo, F.-H. Liu, Q. Chang, Y.-X. Zhang, C.-G. Liu, Y.-H. Zhao, Signal Transduct Target Ther 7 (2022) 402.

[71] F. Yeung, J.E. Hoberg, C.S. Ramsey, M.D. Keller, D.R. Jones, R.A. Frye, M.W. Mayo, EMBO J 23 (2004) 2369–2380.

[72] A. Vaquero, M.B. Scher, D.H. Lee, A. Sutton, H.-L. Cheng, F.W. Alt, L. Serrano, R. Sternglanz, D. Reinberg, Genes Dev 20 (2006) 1256–1261.

[73] L. Sinatra, A. Vogelmann, F. Friedrich, M.A. Tararina, E. Neuwirt, A. Colcerasa, P. König, L. Toy, T.Z. Yesiloglu, S. Hilscher, L. Gaitzsch, N. Papenkordt, S. Zhai, L. Zhang, C. Romier, O. Einsle, W. Sippl, M.

Schutkowski, O. Gross, G. Bendas, D.W. Christianson, F.K. Hansen, M. Jung, M. Schiedel, J Med Chem 66 (2023) 14787–14814.

[74] Q. Zuo, W. Wu, X. Li, L. Zhao, W. Chen, Oncol Rep 3 (2011), 819-824.

[75] L.W.S. Finley, M.C. Haigis, Trends Mol Med 18 (2012) 516–523.

[76] G. Laurent, N.J. German, A.K. Saha, V.C.J. de Boer, M. Davies, T.R. Koves, N. Dephoure, F. Fischer, G. Boanca, B. Vaitheesvaran, S.B. Lovitch, A.H. Sharpe, I.J. Kurland, C. Steegborn, S.P. Gygi, D.M. Muoio, N.B. Ruderman, M.C. Haigis, Mol Cell 50 (2013) 686–698.

[77] A. Villagra, F. Cheng, H.-W. Wang, I. Suarez, M. Glozak, M. Maurin, D. Nguyen, K.L. Wright, P.W. Atadja, K. Bhalla, J. Pinilla-Ibarz, E. Seto, E.M. Sotomayor, Nat Immunol 10 (2009) 92–100.

[78] K. V. Butler, J. Kalin, C. Brochier, G. Vistoli, B. Langley, A.P. Kozikowski, J Am Chem Soc 132 (2010) 10842–10846.

[79] M.S. Finnin, J.R. Donigian, A. Cohen, V.M. Richon, R.A. Rifkind, P.A. Marks, R. Breslow, N.P. Pavletich, Nature 401 (1999) 188–193.

[80] N.J. Porter, J.D. Osko, D. Diedrich, T. Kurz, J.M. Hooker, F.K. Hansen, D.W. Christianson, J Med Chem 61 (2018) 8054–8060.

[81] N. TSUJI, M. KOBAYASHI, K. NAGASHIMA, Y. WAKISAKA, K. KOIZUMI, J Antibiot (Tokyo) 29 (1976) 1–6.

[82] A. Matsuyama, EMBO J 21 (2002) 6820–6831.

[83] M. Wood, S. Rymarchyk, S. Zheng, Y. Cen, Arch Biochem Biophys 638 (2018) 8–17.

[84] C. Sharma, D. Donu, A.M. Curry, E. Barton, Y. Cen, RSC Adv 13 (2023) 11771–11781.

[85] B.S. Mann, J.R. Johnson, M.H. Cohen, R. Justice, R. Pazdur, Oncologist 12 (2007) 1247–1252.

[86] J. Lee, S. Huang R, Chemotherapy 2 (2013).

[87] J.P. Laubach, P. Moreau, J.F. San-Miguel, P.G. Richardson, Clinical Cancer Research 21 (2015) 4767–4773.

[88] H.Z. Lee, V.E. Kwitkowski, P.L. Del Valle, M.S. Ricci, H. Saber, B.A. Habtemariam, J. Bullock, E. Bloomquist, Y.L. Shen, X. Chen, J.Brown, N. Mehrotra, S. Dorff, R. Charlab, R.C. Kane, E. Kaminskas, R. Justice, A.T. Farrell, R. Pazdur, CCR 21 (2015), 2666–2670.

[89] L. Bello, V. Sansone, R. Masson, C. Bruno, Acta Myol 43 (2024) 114–115.

[90] D.T. Vogl, N. Raje, S. Jagannath, P. Richardson, P. Hari, R. Orlowski, J.G. Supko, D. Tamang, M. Yang, S.S. Jones, C. Wheeler, R.J. Markelewicz, S. Lonial, Clinical Cancer Research 23 (2017) 3307–3315.

[91] G. Médard, J.M. Sheltzer, Nat Cancer 4 (2023) 807–808.

[92] M.S. Gordon, G.I. Shapiro, J. Sarantopoulos, D. Juric, B. Lu, A. Zarotiadou, J.N. Connarn, Y. Le Bruchec, C.D. Dumitru, R.D. Harvey, Front Oncol 11 (2022).

[93] J.-H. Lee, A. Mahendran, Y. Yao, L. Ngo, G. Venta-Perez, M.L. Choy, N. Kim, W.-S. Ham, R. Breslow, P.A. Marks, Proceedings of the National Academy of Sciences 110 (2013) 15704–15709.

[94] J.A. Bergman, K. Woan, P. Perez-Villarroel, A. Villagra, E.M. Sotomayor, A.P. Kozikowski, J Med Chem 55 (2012) 9891–9899.

[95] B. Wang, L. Zhang, T. Dai, Z. Qin, H. Lu, L. Zhang, F. Zhou, Signal Transduct Target Ther 6 (2021) 290.

[96] M. Saito, D. Hess, J. Eglinger, A.W. Fritsch, M. Kreysing, B.T. Weinert, C. Choudhary, P. Matthias, Nat Chem Biol 15 (2019) 51–61.

[97] B. Lu, R. Qiu, J. Wei, L. Wang, Q. Zhang, M. Li, X. Zhan, J. Chen, I.-Y. Hsieh, C. Yang, J. Zhang, Z. Sun, Y. Zhu, T. Jiang, H. Zhu, J. Li, W. Zhao, Nat Cancer 5 (2024) 1622–1640.

[98] M. Namdar, G. Perez, L. Ngo, P.A. Marks, Proceedings of the National Academy of Sciences 107 (2010) 20003–20008.

[99] S. Shen, A.P. Kozikowski, ChemMedChem 11 (2016) 15–21.

[100] M. Thomas, J. Alsarraf, N. Araji, I. Tranoy-Opalinski, B. Renoux, S. Papot, Org Biomol Chem 17 (2019) 5420–5427.

[101] A. Utsunomiya, K. Izutsu, T. Jo, S. Yoshida, K. Tsukasaki, K. Ando,Iì I. Choi, Y. Imaizumi, K. Kato, M. Kurosawa, S. Kusumoto, T. Miyagi, E. Ohtsuka, O. Sasaki, H. Shibayama, K. Shimoda, Y. Takamatsu, K. Takano, K. Yonekura, S. Makita, J. Taguchi, M. Gillings, H. Onogi, K. Tobinai, Cancer Sci 113 (2022), 2778-2787.

[102] J. Knipstein, L. Gore, Expert Opin Investig Drugs 20 (2011) 1455–1467.

[103] R.M. Connolly, M.A. Rudek, R. Piekarz, Future Oncology 13 (2017) 1137–1148.

[104] M.L. Johnson, J. Strauss, M.R. Patel, E.B. Garon, K.D. Eaton, T. Neskorik, J. Morin, R. Chao, B. Halmos, Clin Lung Cancer 24 (2023) 218–227.

[105] C. Grant, F. Rahman, R. Piekarz, C. Peer, R. Frye, R.W. Robey, E.R. Gardner, W.D. Figg, S.E. Bates, Expert Rev Anticancer Ther 10 (2010) 997–1008.

[106] M. Lobera, K.P. Madauss, D.T. Pohlhaus, Q.G. Wright, M. Trocha, D.R. Schmidt, E. Baloglu, R.P. Trump, M.S. Head, G.A. Hofmann, M. Murray-Thompson, B. Schwartz, S. Chakravorty, Z. Wu, P.K. Mander, L. Kruidenier, R.A. Reid, W. Burkhart, B.J. Turunen, J.X. Rong, C. Wagner, M.B. Moyer, C. Wells, X. Hong, J.T. Moore, J.D. Williams, D. Soler, S. Ghosh, M.A. Nolan, Nat Chem Biol 9 (2013) 319–325.

[107] Y. Asfaha, L.M. Bollmann, A.J. Skerhut, F. Fischer, N. Horstick, D. Roth, M. Wecker, C. Mammen, S.H.J. Smits, G. Fluegen, M.U. Kassack, T. Kurz, Eur J Med Chem 263 (2024) 115907.

[108] A.J. Stott, M.C. Maillard, V. Beaumont, D. Allcock, O. Aziz, A.H. Borchers, W. Blackaby, P. Breccia, G. Creighton-Gutteridge, A.F. Haughan, R.E. Jarvis, C.A. Luckhurst, K.L. Matthews, G. McAllister, S. Pollack, E. Saville-Stones, A.J. Van de Poël, H.D. Vater, J. Vann, R. Williams, D. Yates, I. Muñoz-Sanjuán, C. Dominguez, ACS Med Chem Lett 12 (2021) 380–388.

[109] D. Moi, D. Bonanni, S. Belluti, P. Linciano, A. Citarella, S. Franchini, C. Sorbi, C. Imbriano, L. Pinzi, G. Rastelli, Eur J Med Chem 260 (2023) 115730.

[110] B. König, P.R. Watson, N. Reßing, A.D. Cragin, L. Schäker-Hübner, D.W. Christianson, F.K. Hansen, J Med Chem 66 (2023) 13821–13837.

[111] E. Cellupica, G. Caprini, P. Cordella, C. Cukier, G. Fossati, M. Marchini, I. Rocchio, G. Sandrone, M.A. Vanoni, B. Vergani, K. Źrubek, A. Stevenazzi, C. Steinkühler, Journal of Biological Chemistry 299 (2023) 102800.

[112] E. Cellupica, A. Gaiassi, I. Rocchio, G. Rovelli, R. Pomarico, G. Sandrone, G. Caprini, P. Cordella, C. Cukier, G. Fossati, M. Marchini, A. Bebel, C. Airoldi, A. Palmioli, A. Stevenazzi, C. Steinkühler, B. Vergani, Int J Mol Sci 25 (2024) 5885.

[113] Y. Hai, D.W. Christianson, Nat Chem Biol 12 (2016) 741–747.

[114] S. Barone, E. Cassese, A.I. Alfano, M. Brindisi, V. Summa, J Med Chem 65 (2022) 3080–3097.

[115] M. Brindisi, A.P. Saraswati, S. Brogi, S. Gemma, S. Butini, G. Campiani, J Med Chem 63 (2020) 23–39.

[116] C. Hubbert, A. Guardiola, R. Shao, Y. Kawaguchi, A. Ito, A. Nixon, M. Yoshida, X.-F. Wang, T.-P. Yao, Nature 417 (2002) 455–458.

[117] J.R. Cabrero, J.M. Serrador, O. Barreiro, M. Mittelbrunn, S. Naranjo-Suárez, N. Martín-Cófreces, M. Vicente-Manzanares, R. Mazitschek, J.E.

Bradner, J. Ávila, A. Valenzuela-Fernández, F. Sánchez-Madrid, Mol Biol Cell 17 (2006) 3435–3445.

[118] C. Simões-Pires, V. Zwick, A. Nurisso, E. Schenker, P.-A. Carrupt, M. Cuendet, Mol Neurodegener 8 (2013) 7.

[119] S.H. Berth, T.E. Lloyd, Journal of Clinical Investigation 133 (2023).

[120] W. Guo, M. Naujock, L. Fumagalli, T. Vandoorne, P. Baatsen, R. Boon, L. Ordovás, A. Patel, M. Welters, T. Vanwelden, N. Geens, T. Tricot, V. Benoy, J. Steyaert, C. Lefebvre-Omar, W. Boesmans, M. Jarpe, J. Sterneckert, F. Wegner, S. Petri, D. Bohl, P. Vanden Berghe, W. Robberecht, P. Van Damme, C. Verfaillie, L. Van Den Bosch, Nat Commun 8 (2017) 861.

[121] S. Sun, Z. Xu, L. He, Y. Shen, Y. Yan, X. Lv, X. Zhu, W. Li, W.-Y. Tian, Y. Zheng, S. Lin, Y. Sun, L. Li, Nat Commun 15 (2024) 8377.

[122] J.W. Hammond, C.-F. Huang, S. Kaech, C. Jacobson, G. Banker, K.J. Verhey, Mol Biol Cell 21 (2010) 572–583.

[123] X. Zhang, Z. Yuan, Y. Zhang, S. Yong, A. Salas-Burgos, J. Koomen, N. Olashaw, J.T. Parsons, X.-J. Yang, S.R. Dent, T.-P. Yao, W.S. Lane, E. Seto, Mol Cell 27 (2007) 197–213.

[124] C. Boyault, Y. Zhang, S. Fritah, C. Caron, B. Gilquin, S.H. Kwon, C. Garrido, T.-P. Yao, C. Vourc'h, P. Matthias, S. Khochbin, Genes Dev 21 (2007) 2172–2181.

[125] T. Simms-Waldrip, A. Rodriguez-Gonzalez, T. Lin, A.K. Ikeda, C. Fu, K.M. Sakamoto, Mol Genet Metab 94 (2008) 283–286.

[126] C. Boyault, B. Gilquin, Y. Zhang, V. Rybin, E. Garman, W. Meyer-Klaucke, P. Matthias, C.W. Müller, S. Khochbin, EMBO J 25 (2006) 3357–3366.

[127] S. Petri, M. Kiaei, K. Kipiani, J. Chen, N.Y. Calingasan, J.P. Crow, M.F. Beal, Neurobiol Dis 22 (2006) 40–49.

[128] E. Hockly, V.M. Richon, B. Woodman, D.L. Smith, X. Zhou, E. Rosa, K. Sathasivam, S. Ghazi-Noori, A. Mahal, P.A.S. Lowden, J.S. Steffan, J.L. Marsh, L.M. Thompson, C.M. Lewis, P.A. Marks, G.P. Bates, Proceedings of the National Academy of Sciences 100 (2003) 2041–2046.

[129] J. Park, Y. Park, I. Ryu, M.-H. Choi, H.J. Lee, N. Oh, K. Kim, K.M. Kim, J. Choe, C. Lee, J.-H. Baik, Y.K. Kim, Nat Commun 8 (2017) 15730.

[130] H. Ding, P.J. Dolan, G.V.W. Johnson, J Neurochem 106 (2008) 2119–2130.

[131] H. Ding, P.J. Dolan, G.V.W. Johnson, J Neurochem 106 (2008) 2119–2130.

[132] J.P. Thiery, J.P. Sleeman, Nat Rev Mol Cell Biol 7 (2006) 131–142.

[133] B. Shan, T. Yao, H.T. Nguyen, Y. Zhuo, D.R. Levy, R.C. Klingsberg, H. Tao, M.L. Palmer, K.N. Holder, J.A. Lasky, Journal of Biological Chemistry 283 (2008) 21065–21073.

[134] S. Zhu, P.J. Goldschmidt-Clermont, C. Dong, Circ Res 94 (2004) 617–625.

[135] S.D. Varkki, R. Aaron, A. Chapla, S. Danda, P. Medhi, N. Jansi Rani, G.R. Paul, The Lancet Regional Health - Southeast Asia 27 (2024) 100434.

[136] A. Luciani, V.R. Villella, S. Esposito, N. Brunetti-Pierri, D. Medina, C. Settembre, M. Gavina, L. Pulze, I. Giardino, M. Pettoello-Mantovani, M. D'Apolito, S. Guido, E. Masliah, B. Spencer, S. Quaratino, V. Raia, A. Ballabio, L. Maiuri, Nat Cell Biol 12 (2010) 863–875.

[137] A. Poghosyan, J.K. Patel, R.L. Clifford, A.J. Knox, Biochem Biophys Res Commun 476 (2016) 431–437.

[138] M. Bodas, N. Vij, Discov Med 9 (2010) 346–56.

[139] S. Malhotra, D. Hayes, D.J. Wozniak, Clin Microbiol Rev 32 (2019).

[140] A. Bergougnoux, I. Rivals, A. Liquori, C. Raynal, J. Varilh, M. Magalhães, M.-J. Perez, N. Bigi, M. Des Georges, R. Chiron, A.S. Squalli-Houssaini, M. Claustres, A. De Sario, Epigenetics 9 (2014) 1007–1017.

[141] R. Bartoszewski, A. Rab, G. Twitty, L. Stevenson, J. Fortenberry, A. Piotrowski, J.P. Dumanski, Z. Bebök, Journal of Biological Chemistry 283 (2008) 12154–12165.

[142] C.J. Ott, M. Suszko, N.P. Blackledge, J.E. Wright, G.E. Crawford, A. Harris, J Cell Mol Med 13 (2009) 680–692.

[143] N. Sirinupong, Z. Yang, Curr Drug Targets 16 (2015) 976–987.

[144] M. Bodas, S. Mazur, T. Min, N. Vij, Respir Res 19 (2018) 2.

[145] R. Di Liddo, S. Valente, S. Taurone, C. Zwergel, B. Marrocco, R. Turchetta, M.T. Conconi, C. Scarpa, T. Bertalot, S. Schrenk, A. Mai, M. Artico, Autoimmunity 49 (2016) 155–165.

[146] E.F. de Zoeten, L. Wang, K. Butler, U.H. Beier, T. Akimova, H. Sai, J.E. Bradner, R. Mazitschek, A.P. Kozikowski, P. Matthias, W.W. Hancock, Mol Cell Biol 31 (2011) 2066–2078.

[147] J.C. Garcia-Garcia, N.C. Barat, S.J. Trembley, J.S. Dumler, PLoS Pathog 5 (2009) e1000488.

[148] A.M. Grabiec, J. Potempa, Crit Rev Microbiol 44 (2018) 336–350.

[149] R. Corrêa-Oliveira, J.L. Fachi, A. Vieira, F.T. Sato, M.A.R. Vinolo, Clin Transl Immunology 5 (2016).

[150] U.H. Beier, L. Wang, R. Han, T. Akimova, Y. Liu, W.W. Hancock, Sci Signal 5 (2012).

[151] T. Roger, J. Lugrin, D. Le Roy, G. Goy, M. Mombelli, T. Koessler, X.C. Ding, A.-L. Chanson, M.K. Reymond, I. Miconnet, J. Schrenzel, P. François, T. Calandra, Blood 117 (2011) 1205–1217.

[152] M. Mombelli, J. Lugrin, I. Rubino, A.-L. Chanson, M. Giddey, T. Calandra, T. Roger, J Infect Dis 204 (2011) 1367–1374.

[153] T. Zhao, Y. Li, B. Liu, B. Pan, X. Cheng, P. Georgoff, H.B. Alam, Journal of Trauma and Acute Care Surgery 80 (2016) 34–41.

[154] Y. Li, T. Zhao, B. Liu, I. Halaweish, R. Mazitschek, X. Duan, H.B. Alam, Journal of Trauma and Acute Care Surgery 78 (2015) 378–385.

[155] J.K. Ariffin, K. das Gupta, R. Kapetanovic, A. Iyer, R.C. Reid, D.P. Fairlie, M.J. Sweet, Antimicrob Agents Chemother 60 (2016) 1521–1529.

[156] A. Osseni, A. Ravel-Chapuis, E. Belotti, I. Scionti, Y.-G. Gangloff, V. Moncollin, L. Mazelin, R. Mounier, P. Leblanc, B.J. Jasmin, L. Schaeffer, Nat Commun 13 (2022) 7108.

[157] S.M. Rymut, A. Harker, D.A. Corey, J.D. Burgess, H. Sun, J.P. Clancy, T.J. Kelley, American Journal of Physiology-Lung Cellular and Molecular Physiology 305 (2013) L419–L431.

[158] R.C. RUBENSTEIN, P.L. ZEITLIN, Am J Respir Crit Care Med 157 (1998) 484–490.

[159] O. Ammerpohl, A. Trauzold, B. Schniewind, U. Griep, C. Pilarsky, R. Grutzmann, H.-D. Saeger, O. Janssen, B. Sipos, G. Kloppel, H. Kalthoff, Br J Cancer 96 (2007) 73–81.

[160] S.M. Rymut, D.A. Corey, D.M. Valerio, B.O. Erokwu, C.A. Flask, T.J. Kelley, C.A. Hodges, Sci Rep 7 (2017) 3676.

[161] J. Rosenjack, C.A. Hodges, R.J. Darrah, T.J. Kelley, Sci Rep 9 (2019) 10282.

[162] M. Brindisi, S. Barone, A. Rossi, E. Cassese, N. Del Gaudio, Á.J. Feliz Morel, G. Filocamo, A. Alberico, I. De Fino, D. Gugliandolo, M. Babaei, G. Bove, M. Croce, C. Montesano, L. Altucci, A. Bragonzi, V. Summa, Eur J Pharmacol 936 (2022) 175349.

[163] T.S. Prior, N. Hoyer, J.R. Davidsen, S.B. Shaker, M.P. Hundahl, S. Lomholt, B.W. Deleuran, E. Bendstrup, T.W. Kragstrup, Scand J Immunol 100 (2024).

[164] L. Richeldi, R.M. du Bois, G. Raghu, A. Azuma, K.K. Brown, U. Costabel, V. Cottin, K.R. Flaherty, D.M. Hansell, Y. Inoue, D.S. Kim, M. Kolb, A.G. Nicholson, P.W. Noble, M. Selman, H. Taniguchi, M. Brun, F. Le Maulf, M. Girard, S. Stowasser, R. Schlenker-Herceg, B. Disse, H.R. Collard, New England Journal of Medicine 370 (2014) 2071–2082.

[165] L. Richeldi, H.R. Collard, M.G. Jones, The Lancet 389 (2017) 1941–1952.

[166] M. Korfei, P. Mahavadi, A. Guenther, Cells 11 (2022) 1626.

[167] R. Niayesh-Mehr, M. Kalantar, G. Bontempi, C. Montaldo, S. Ebrahimi, A. Allameh, G. Babaei, F. Seif, R. Strippoli, Cell Communication and Signaling 22 (2024) 542.

[168] S. Saito, Y. Zhuang, B. Shan, S. Danchuk, F. Luo, M. Korfei, A. Guenther, J.A. Lasky, PLoS One 12 (2017) e0186615.

[169] Z. Wang, C. Chen, S.N. Finger, S. d/o Kwajah M.M, M. Jung, H. Schwarz, N. Swanson, R.R. Lareu, M. Raghunath, European Respiratory Journal 34 (2009) 145–155.

[170] W.R. Coward, C.A. Feghali-Bostwick, G. Jenkins, A.J. Knox, L. Pang, The FASEB Journal 28 (2014) 3183–3196.

[171] A. Pasini, O.J. Brand, G. Jenkins, A.J. Knox, L. Pang, Biochimica et Biophysica Acta (BBA) - Gene Regulatory Mechanisms 1861 (2018) 463–472.

[172] K.M. P, K. Sivashanmugam, M. Kandasamy, R. Subbiah, V. Ravikumar, Life Sci 266 (2021) 118883.

[173] M. Korfei, D. Stelmaszek, B. MacKenzie, S. Skwarna, S. Chillappagari, A.C. Bach, C. Ruppert, S. Saito, P. Mahavadi, W. Klepetko, L. Fink, W. Seeger, J.A. Lasky, S.S. Pullamsetti, O.H. Krämer, A. Guenther, PLoS One 13 (2018) e0207915.

[174] S.K. Huang, A.M. Scruggs, J. Donaghy, J.C. Horowitz, Z. Zaslona, S. Przybranowski, E.S. White, M. Peters-Golden, Cell Death Dis 4 (2013) e621–e621.

[175] K. Bricker, B. V. Vaughn, Frontiers in Sleep 3 (2024).

[176] S.J. Keam, Drugs 83 (2023) 819–824.

[177] X. Nan, F.J. Campoy, A. Bird, Cell 4 (1997), 471-481.

[178] W.A. Gold, T.A. Lacina, L.C. Cantrill, J. Christodoulou, J Mol Med 93 (2015) 63–72.

[179] R. Fazal, S. Boeynaems, A. Swijsen, M. De Decker, L. Fumagalli, M. Moisse, J. Vanneste, W. Guo, R. Boon, T. Vercruysse, K. Eggermont, B. Swinnen, J. Beckers, D. Pakravan, T. Vandoorne, P. Vanden Berghe, C. Verfaillie, L. Van Den Bosch, P. Van Damme, EMBO J 40 (2021).

[180] L. Van Helleputte, M. Kater, D.P. Cook, C. Eykens, E. Rossaert, W. Haeck, T. Jaspers, N. Geens, P. Vanden Berghe, C. Gysemans, C. Mathieu, W. Robberecht, P. Van Damme, G. Cavaletti, M. Jarpe, L. Van Den Bosch, Neurobiol Dis 111 (2018) 59–69.

[181] R. Adalbert, A. Kaieda, C. Antoniou, A. Loreto, X. Yang, J. Gilley, T. Hoshino, K. Uga, M.T. Makhija, M.P. Coleman, ACS Chem Neurosci 11 (2020) 258–267.

[182] X. Xu, A.P. Kozikowski, L. Pozzo-Miller, Front Cell Neurosci 8 (2014).

[183] E.R. Rhymes, R.L. Simkin, J. Qu, D. Villarroel-Campos, S. Surana, Y. Tong, R. Shapiro, R.W. Burgess, X.-L. Yang, G. Schiavo, J.N. Sleigh, Neurobiol Dis 195 (2024) 106501.

[184] J.P. Dompierre, J.D. Godin, B.C. Charrin, F.P. Cordelières, S.J. King, S. Humbert, F. Saudou, The Journal of Neuroscience 27 (2007) 3571–3583.

[185] W. Guo, M. Naujock, L. Fumagalli, T. Vandoorne, P. Baatsen, R. Boon, L. Ordovás, A. Patel, M. Welters, T. Vanwelden, N. Geens, T. Tricot, V. Benoy, J. Steyaert, C. Lefebvre-Omar, W. Boesmans, M. Jarpe, J.

Sterneckert, F. Wegner, S. Petri, D. Bohl, P. Vanden Berghe, W. Robberecht, P. Van Damme, C. Verfaillie, L. Van Den Bosch, Nat Commun 8 (2017) 861.

[186] C. d'Ydewalle, V. Benoy, L. Van Den Bosch, Int J Biochem Cell Biol 44 (2012) 1299–1304.

[187] C. d'Ydewalle, V. Benoy, L. Van Den Bosch, Int J Biochem Cell Biol 44 (2012) 1299–1304.

[188] C. Alberti, F. Rizzo, A. Anastasia, G. Comi, S. Corti, E. Abati, Neurobiol Dis 193 (2024) 106467.

[189] E.M. Yiu, P. Bray, J. Baets, S.K. Baker, N. Barisic, K. de Valle, T. Estilow, M.A. Farrar, R.S. Finkel, J. Haberlová, R.A. Kennedy, I. Moroni, G.A. Nicholson, S. Ramchandren, M.M. Reilly, K. Rose, M.E. Shy, C.E. Siskind, S.W. Yum, M.P. Menezes, M.M. Ryan, J. Burns, J Neurol Neurosurg Psychiatry 93 (2022) 530–538.

[190] Y. Okamoto, H. Takashima, Genes (Basel) 14 (2023) 1391.

[191] E. Abati, S. Magri, M. Meneri, G. Manenti, D. Velardo, F. Balistreri, C. Pisciotta, P. Saveri, N. Bresolin, G. Pietro Comi, D. Ronchi, D. Pareyson, F. Taroni, S. Corti, Ann Clin Transl Neurol 8 (2021) 1158–1164.

[192] W. He, G. Bai, H. Zhou, N. Wei, N.M. White, J. Lauer, H. Liu, Y. Shi, C.D. Dumitru, K. Lettieri, V. Shubayev, A. Jordanova, V. Guergueltcheva, P.R. Griffin, R.W. Burgess, S.L. Pfaff, X.-L. Yang, Nature 526 (2015) 710–714.

[193] J. Yamauchi, T. Torii, S. Kusakawa, A. Sanbe, K. Nakamura, S. Takashima, H. Hamasaki, S. Kawaguchi, Y. Miyamoto, A. Tanoue, J Neurosci Res 88 (2010) 3189–3197.

[194] C. d'Ydewalle, J. Krishnan, D.M. Chiheb, P. Van Damme, J. Irobi, A.P. Kozikowski, P. Vanden Berghe, V. Timmerman, W. Robberecht, L. Van Den Bosch, Nat Med 17 (2011) 968–974.

[195] S. Shen, V. Benoy, J.A. Bergman, J.H. Kalin, M. Frojuello, G. Vistoli, W. Haeck, L. Van Den Bosch, A.P. Kozikowski, ACS Chem Neurosci 7 (2016) 240–258.

[196] V. Benoy, P. Vanden Berghe, M. Jarpe, P. Van Damme, W. Robberecht, L. Van Den Bosch, Neurotherapeutics 14 (2017) 417–428.

[197] Z. Mo, X. Zhao, H. Liu, Q. Hu, X.-Q. Chen, J. Pham, N. Wei, Z. Liu, J. Zhou, R.W. Burgess, S.L. Pfaff, C.T. Caskey, C. Wu, G. Bai, X.-L. Yang, Nat Commun 9 (2018) 1007.

[198] Y. Nuzbrokh, S.D. Ragi, S.H. Tsang, Ann Transl Med 9 (2021) 1278–1278.

[199] C. Daly, J. Yin, B.N. Kennedy, in: 2016, pp. 455–461.

[200] J. Sancho-Pelluz, M. V Alavi, A. Sahaboglu, S. Kustermann, P. Farinelli, S. Azadi, T. van Veen, F.J. Romero, F. Paquet-Durand, P. Ekström, Cell Death Dis 1 (2010) e24–e24.

[201] J. Leyk, C. Daly, U. Janssen-Bienhold, B.N. Kennedy, C. Richter-Landsberg, Cell Death Dis 8 (2017) e3028–e3028.

[202] M. Sinkala, Sci Rep 13 (2023) 12742.

[203] https://cancer.sanger.ac.uk.

[204] M. Schnekenburger, C. Florean, M. Dicato, M. Diederich, Curr Top Med Chem 16 (2015) 745–776.

[205] X. Yu, H. Zhao, R. Wang, Y. Chen, X. Ouyang, W. Li, Y. Sun, A. Peng, Cell Death Discov 10 (2024) 28.

[206] T.C. Dakal, B. Dhabhai, A. Pant, K. Moar, K. Chaudhary, V. Yadav, V. Ranga, N.K. Sharma, A. Kumar, P.K. Maurya, J. Maciaczyk, I.G.H. Schmidt-Wolf, A. Sharma, MedComm (Beijing) 5 (2024).

[207] P. Wang, Z. Wang, J. Liu, Mol Cancer 19 (2020) 5.

[208] L.F. Peterson, D.-E. Zhang, Oncogene 23 (2004) 4255–4262.

[209] I. Rettig, E. Koeneke, F. Trippel, W.C. Mueller, J. Burhenne, A. Kopp-Schneider, J. Fabian, A. Schober, U. Fernekorn, A. von Deimling, H.E. Deubzer, T. Milde, O. Witt, I. Oehme, Cell Death Dis 6 (2015) e1657–e1657.

[210] T. Sudo, M. Mimori, N. Nishida, R. Kogo, T. Iwaya, F. Tanaka, K. Shibata, H. Fujita, K- Shirouzu, M. Mori, Oncol Rep 4 (2011), 777-782.

[211] A.C. West, R.W. Johnstone, Journal of Clinical Investigation 124 (2014) 30–39.

[212] K.J. Falkenberg, R.W. Johnstone, Nat Rev Drug Discov 13 (2014) 673–691.

[213] M.G. RIGGS, R.G. WHITTAKER, J.R. NEUMANN, V.M. INGRAM, Nature 268 (1977) 462–464.

[214] M.-Q. Shi, Y. Xu, X. Fu, D.-S. Pan, X.-P. Lu, Y. Xiao, Y.-Z. Jiang, J Hematol Oncol 17 (2024) 37.

[215] M. Minisini, M. Mascaro, C. Brancolini, Cancer Drug Resistance (2024).

[216] L. Nolan, P.W.M. Johnson, A. Ganesan, G. Packham, S.J. Crabb, Br J Cancer 99 (2008) 689–694.

[217] A. Suraweera, K.J. O'Byrne, D.J. Richard, Front Oncol 8 (2018).

[218] Y. Jiang, J. Zhang, J. Yu, W. Luo, Q. Du, W. Liu, Q. Xu, X. Li, H. Liu, D. Huang, T. Qin, NPJ Precis Oncol 9 (2025) 150.

[219] R. Benedetti, M. Di Crosta, M.S. Gilardini Montani, G. D'Orazi, M. Cirone, Cell Death Discov 11 (2025) 162.

[220] J.J. Kovacs, P.J.M. Murphy, S. Gaillard, X. Zhao, J.-T. Wu, C. V. Nicchitta, M. Yoshida, D.O. Toft, W.B. Pratt, T.-P. Yao, Mol Cell 18 (2005) 601–607.

[221] Z. WANG, F. TANG, P. HU, Y. WANG, J. GONG, S. SUN, C. XIE, Oncol Rep 36 (2016) 589–597.

[222] J.-Y. Lee, H. Koga, Y. Kawaguchi, W. Tang, E. Wong, Y.-S. Gao, U.B. Pandey, S. Kaushik, E. Tresse, J. Lu, J.P. Taylor, A.M. Cuervo, T.-P. Yao, EMBO J 29 (2010) 969–980.

[223] T. Knox, E. Sahakian, D. Banik, M. Hadley, E. Palmer, S. Noonepalle, J. Kim, J. Powers, M. Gracia-Hernandez, V. Oliveira, F. Cheng, J. Chen, C. Barinka, J. Pinilla-Ibarz, N.H. Lee, A. Kozikowski, A. Villagra, Sci Rep 9 (2019) 6136.

[224] S. Moufarrij, A. Srivastava, S. Gomez, M. Hadley, E. Palmer, P.T. Austin, S. Chisholm, N. Diab, K. Roche, A. Yu, J. Li, W. Zhu, M. Lopez-Acevedo, A. Villagra, K.B. Chiappinelli, Sci Rep 10 (2020) 3470.

[225] O. Khan, S. Fotheringham, V. Wood, L. Stimson, C. Zhang, F. Pezzella, M. Duvic, D.J. Kerr, N.B. La Thangue, Proceedings of the National Academy of Sciences 107 (2010) 6532–6537.

[226] W. Yeo, H.C. Chung, S.L. Chan, L.Z. Wang, R. Lim, J. Picus, M. Boyer, F.K.F. Mo, J. Koh, S.Y. Rha, E.P. Hui, H.C. Jeung, J.K. Roh, S.C.H. Yu, K.F. To, Q. Tao, B.B. Ma, A.W.H. Chan, J.H.M. Tong, C. Erlichman, A.T.C. Chan, B.C. Goh, Journal of Clinical Oncology 30 (2012) 3361–3367.

[227] S. Fotheringham, M.T. Epping, L. Stimson, O. Khan, V. Wood, F. Pezzella, R. Bernards, N.B. La Thangue, Cancer Cell 15 (2009) 57–66.

[228] V.R. Fantin, A. Loboda, C.P. Paweletz, R.C. Hendrickson, J.W. Pierce, J.A. Roth, L. Li, F. Gooden, S. Korenchuk, X.S. Hou, E.A. Harrington, S. Randolph, J.F. Reilly, C.M. Ware, M.E. Kadin, S.R. Frankel, V.M. Richon, Cancer Res 68 (2008) 3785–3794.

[229] A.A. Ruefli, D. Bernhard, K.M. Tainton, R. Kofler, M.J. Smyth, R.W. Johnstone, Int J Cancer 99 (2002) 292–298.

[230] A. Guadagni, S. Barone, A.I. Alfano, S. Pelliccia, I. Bello, E. Panza, V. Summa, M. Brindisi, Eur J Med Chem 279 (2024) 116884.

[231] https://www.who.int/news-room/fact-sheets/detail/breast-cancer.

[232] F. Borri, A. Granaglia, Semin Cancer Biol 72 (2021) 136–145.

[233] B.N.M. Zordoky, D. Bark, C.L. Soltys, M.M. Sung, J.R.B. Dyck, Biochimica et Biophysica Acta (BBA) - General Subjects 1840 (2014) 1943–1957.

[234] H. Shim, Y.S. Chun, B.C. Lewis, C. V. Dang, Proceedings of the National Academy of Sciences 95 (1998) 1511–1516.

[235] J. Yun, C. Rago, I. Cheong, R. Pagliarini, P. Angenendt, H. Rajagopalan, K. Schmidt, J.K. V. Willson, S. Markowitz, S. Zhou, L.A. Diaz, V.E. Velculescu, C. Lengauer, K.W. Kinzler, B. Vogelstein, N. Papadopoulos, Science (1979) 325 (2009) 1555–1559.

[236] S.R. Lord, W.-C. Cheng, D. Liu, E. Gaude, S. Haider, T. Metcalf, N. Patel, E.J. Teoh, F. Gleeson, K. Bradley, S. Wigfield, C. Zois, D.R. McGowan, M.-L. Ah-See, A.M. Thompson, A. Sharma, L. Bidaut, M. Pollak, P.G. Roy, F. Karpe, T. James, R. English, R.F. Adams, L. Campo, L. Ayers, C. Snell, I. Roxanis, C. Frezza, J.D. Fenwick, F.M. Buffa, A.L. Harris, Cell Metab 28 (2018) 679-688.e4.

[237] J.T. Opferman, A. Kothari, Cell Death Differ 25 (2018) 37–45.

[238] S. Maji, S. Panda, S.K. Samal, O. Shriwas, R. Rath, M. Pellecchia, L. Emdad, S.K. Das, P.B. Fisher, R. Dash, in: 2018, pp. 37–75.

[239] L. Nocquet, J. Roul, C.C. Lefebvre, L. Duarte, M. Campone, P.P. Juin, F. Souazé, Sci Rep 14 (2024) 14177.

[240] S. Wu, Z. Luo, P.-J. Yu, H. Xie, Y.-W. He, Biol Chem 397 (2016) 75–83.

[241] H.-W. Chiu, Y.-L. Yeh, Y.-C. Wang, W.-J. Huang, Y.-A. Chen, Y.-S. Chiou, S.-Y. Ho, P. Lin, Y.-J. Wang, PLoS One 8 (2013) e76340.

[242] G.J. Sabnis, O. Goloubeva, S. Chumsri, N. Nguyen, S. Sukumar, A.M.H. Brodie, Cancer Res 71 (2011) 1893–1903.

[243] C. Maccallini, A. Ammazzalorso, B. De Filippis, M. Fantacuzzi, L. Giampietro, R. Amoroso, Pharmaceuticals 15 (2022).

[244] C.M. Dowling, K.E.R. Hollinshead, A. Di Grande, J. Pritchard, H. Zhang, E.T. Dillon, K. Haley, E. Papadopoulos, A.K. Mehta, R. Bleach, A.U. Lindner, B. Mooney, H. Düssmann, D. O'connor, J.H.M. Prehn, K. Wynne, M. Hemann, J.E. Bradner, A.C. Kimmelman, J.L. Guerriero, G. Cagney, K.-K. Wong, A.G. Letai, T. Ní Chonghaile, Multiple Screening Approaches Reveal HDAC6 as a Novel Regulator of Glycolytic Metabolism in Triple-Negative Breast Cancer, 2021.

[245] C.M. Dowling, K.E.R. Hollinshead, A. Di Grande, J. Pritchard, H. Zhang, E.T. Dillon, K. Haley, E. Papadopoulos, A.K. Mehta, R. Bleach, A.U. Lindner, B. Mooney, H. Düssmann, D. O'Connor, J.H.M. Prehn, K. Wynne, M. Hemann, J.E. Bradner, A.C. Kimmelman, J.L. Guerriero, G. Cagney, K.-K. Wong, A.G. Letai, T.N. Chonghaile, Sci Adv 7 (2021).

[246] T. Oba, M. Ono, H. Matoba, T. Uehara, Y. Hasegawa, K. Ito, (2020).

[247] Y.-L. Hsieh, H.-J. Tu, S.-L. Pan, J.-P. Liou, C.-R. Yang, Biochimica et Biophysica Acta (BBA) - Molecular Cell Research 1866 (2019) 992–1003.

[248] B. Wang, L. Zhang, T. Dai, Z. Qin, H. Lu, L. Zhang, F. Zhou, Signal Transduct Target Ther 6 (2021) 290.

[249] S. Mehta, J. Zhang, Nat Rev Cancer 22 (2022) 239–252.

[250] L. Dyrskjøt, D.E. Hansel, J.A. Efstathiou, M.A. Knowles, M.D. Galsky, J. Teoh, D. Theodorescu, Nat Rev Dis Primers 9 (2023) 58.

[251] P. Su, Y. Yang, H. Zheng, Discover Oncology 16 (2025) 424.

[252] A. Kaletsch, M. Pinkerneil, M.J. Hoffmann, A.A. Jaguva Vasudevan, C. Wang, F.K. Hansen, C. Wiek, H. Hanenberg, C. Gertzen, H. Gohlke, M.U. Kassack, T. Kurz, W.A. Schulz, G. Niegisch, Clin Epigenetics 10 (2018) 100.

[253] C. Poyet, B. Jentsch, T. Hermanns, D. Schweckendiek, H.-H. Seifert, M. Schmidtpeter, T. Sulser, H. Moch, P.J. Wild, G. Kristiansen, BMC Clin Pathol 14 (2014) 10.

[254] C.-H. Shen, J.-Y. Wu, S.-C. Wang, H.-T. Liu, P.-X. Wu, K.-W. Chan, S.-W. Huang, M.-Y. Lee, Y.-W. Liu, Biomedicine & Pharmacotherapy 187 (2025) 118108.

[255] M. Pinkerneil, M.J. Hoffmann, R. Deenen, K. Köhrer, T. Arent, W.A. Schulz, G. Niegisch, Mol Cancer Ther 15 (2016) 299–312.

[256] A.F. Giannopoulou, A.D. Velentzas, E.G. Konstantakou, M. Avgeris, S.A. Katarachia, N.C. Papandreou, N.I. Kalavros, V.E. Mpakou, V. Iconomidou, E. Anastasiadou, I.K. Kostakis, I.S. Papassideri, G.E. Voutsinas, A. Scorilas, D.J. Stravopodis, Int J Mol Sci 20 (2019) 1291.

[257] L. Rosik, G. Niegisch, U. Fischer, M. Jung, W.A. Schulz, M.J. Hoffmann, Cancer Biol Ther 15 (2014) 742–757.

[258] Y.-C. Tsai, T.-Y. Wang, C.-L. Hsu, W.-C. Lin, J.-Y. Chen, J.-H. Li, Y.-S. Pu, A.-L. Cheng, J.C.-H. Cheng, S.-F. Su, Br J Cancer 128 (2023) 1753–1764.

[259] H. Kuroki, T. Anraku, A. Kazama, Y. Shirono, V. Bilim, Y. Tomita, Oncol Lett 21 (2020) 64.

[260] S. Geurs, D. Clarisse, K. De Bosscher, M. D'hooghe, J Med Chem 66 (2023) 7698–7729.

[261] B. König, F.K. Hansen, ACS Pharmacol Transl Sci 7 (2024) 899–903.

[262] K. V. Butler, J. Kalin, C. Brochier, G. Vistoli, B. Langley, A.P. Kozikowski, J Am Chem Soc 132 (2010) 10842–10846.

[263] S. Shen, M. Svoboda, G. Zhang, M.A. Cavasin, L. Motlova, T.A. McKinsey, J.H. Eubanks, C. Bařinka, A.P. Kozikowski, ACS Med Chem Lett 11 (2020) 706–712.

[264] N.J. Porter, J.D. Osko, D. Diedrich, T. Kurz, J.M. Hooker, F.K. Hansen, D.W. Christianson, J Med Chem 61 (2018) 8054–8060.

[265] N. Reßing, M. Sönnichsen, J.D. Osko, A. Schöler, J. Schliehe-Diecks, A. Skerhut, A. Borkhardt, J. Hauer, M.U. Kassack, David.W. Christianson, S. Bhatia, F.K. Hansen, J Med Chem 63 (2020) 10339–10351.

[266] J.D. Osko, N.J. Porter, P.A. Narayana Reddy, Y.-C. Xiao, J. Rokka, M. Jung, J.M. Hooker, J.M. Salvino, D.W. Christianson, J Med Chem 63 (2020) 295–308.

[267] P. Linciano, R. Benedetti, L. Pinzi, F. Russo, U. Chianese, C. Sorbi, L. Altucci, G. Rastelli, L. Brasili, S. Franchini, Bioorg Chem 106 (2021) 104462.

[268] A.P. Saraswati, N. Relitti, M. Brindisi, J.D. Osko, G. Chemi, S. Federico, A. Grillo, S. Brogi, N.H. McCabe, R.C. Turkington, O. Ibrahim, J. O'Sullivan, S. Lamponi, M. Ghanim, V.P. Kelly, D. Zisterer, R. Amet, P. Hannon Barroeta, F. Vanni, C. Ulivieri, D. Herp, F. Sarno, A. Di Costanzo, F. Saccoccia, G. Ruberti, M. Jung, L. Altucci, S. Gemma, S. Butini, D.W. Christianson, G. Campiani, ACS Med Chem Lett 11 (2020) 2268–2276.

[269] N.J. Porter, D.W. Christianson, Curr Opin Struct Biol 59 (2019) 9–18.

[270] N.J. Porter, A. Mahendran, R. Breslow, D.W. Christianson, Proceedings of the National Academy of Sciences 114 (2017) 13459–13464.

[271] Y. Miyake, J.J. Keusch, L. Wang, M. Saito, D. Hess, X. Wang, B.J. Melancon, P. Helquist, H. Gut, P. Matthias, Nat Chem Biol 12 (2016) 748–754.

[272] E.P. Gillis, K.J. Eastman, M.D. Hill, D.J. Donnelly, N.A. Meanwell, J Med Chem 58 (2015) 8315–8359.

[273] N.A. Meanwell, J Med Chem 61 (2018) 5822–5880.

[274] P. Richardson, Expert Opin Drug Discov 11 (2016) 983–999.

[275] G. Chandra, D.V. Singh, G.K. Mahato, S. Patel, Chemical Papers 77 (2023) 4085–4106.

[276] A.S. Nair, A.K. Singh, A. Kumar, S. Kumar, S. Sukumaran, V.P. Koyiparambath, L.K. Pappachen, T.M. Rangarajan, H. Kim, B. Mathew, Processes 10 (2022) 2054.

[277] S. Saphier, Y. Zafrani, Future Med Chem 16 (2024) 1181–1184.

[278] B.K. Park, N.R. Kitteringham, P.M. O'Neill, Annu Rev Pharmacol Toxicol 41 (2001) 443–470.

[279] Y. Pan, ACS Med Chem Lett 10 (2019) 1016–1019.

[280] Y. Du, Y. Bian, D. Baecker, G. Dhawan, A. Semghouli, L. Kiss, W. Zhang, A.E. Sorochinsky, V.A. Soloshonok, J. Han, Chemistry – A European Journal 31 (2025).

[281] G. Sandrone, C.D. Cukier, K. Zrubek, M. Marchini, B. Vergani, G. Caprini, G. Fossati, C. Steinkühler, A. Stevenazzi, ACS Med Chem Lett 12 (2021) 1810–1817.

[282] G. Sandrone, C.D. Cukier, K. Zrubek, M. Marchini, B. Vergani, G. Caprini, G. Fossati, C. Steinkühler, A. Stevenazzi, ACS Med Chem Lett 12 (2021) 1810–1817.

[283] K. Zrubek, G. Sandrone, C.D. Cukier, A. Stevenazzi, Worldwide Protein Data Bank (2023).

[284] N. Reßing, J. Schliehe-Diecks, P.R. Watson, M. Sönnichsen, A.D. Cragin, A. Schöler, J. Yang, L. Schäker-Hübner, A. Borkhardt, D.W. Christianson, S. Bhatia, F.K. Hansen, J Med Chem 65 (2022) 15457–15472.

[285] S. Kumar, T. Mohapatra, Front Cell Dev Biol 9 (2021).

[286] P. Boccaletto, F. Stefaniak, A. Ray, A. Cappannini, S. Mukherjee, E. Purta, M. Kurkowska, N. Shirvanizadeh, E. Destefanis, P. Groza, G. Avşar, A. Romitelli, P. Pir, E. Dassi, S.G. Conticello, F. Aguilo, J.M. Bujnicki, Nucleic Acids Res 50 (2022) D231–D235.

[287] D. Dominissini, S. Moshitch-Moshkovitz, S. Schwartz, M. Salmon-Divon, L. Ungar, S. Osenberg, K. Cesarkas, J. Jacob-Hirsch, N. Amariglio, M. Kupiec, R. Sorek, G. Rechavi, Nature 485 (2012) 201–206.

[288] D. Dominissini, S. Nachtergaele, S. Moshitch-Moshkovitz, E. Peer, N. Kol, M.S. Ben-Haim, Q. Dai, A. Di Segni, M. Salmon-Divon, W.C. Clark, G. Zheng, T. Pan, O. Solomon, E. Eyal, V. Hershkovitz, D. Han, L.C. Doré, N. Amariglio, G. Rechavi, C. He, Nature 530 (2016) 441–446.

[289] K.E. Bohnsack, N. Kleiber, N. Lemus-Diaz, M.T. Bohnsack, Trends Biochem Sci 47 (2022) 596–608.

[290] V.H. Cowling, Biochem J 425 (2009) 295–302.

[291] X. Li, S. Ma, C. Yi, Curr Opin Chem Biol 33 (2016) 108–116.

[292] J. Mauer, X. Luo, A. Blanjoie, X. Jiao, A. V. Grozhik, D.P. Patil, B. Linder, B.F. Pickering, J.-J. Vasseur, Q. Chen, S.S. Gross, O. Elemento, F. Debart, M. Kiledjian, S.R. Jaffrey, Nature 541 (2017) 371–375.

[293] Y. Wang, Y. Li, J.I. Toth, M.D. Petroski, Z. Zhang, J.C. Zhao, Nat Cell Biol 16 (2014) 191–198.

[294] M.N. Flamand, K.D. Meyer, Nucleic Acids Res 50 (2022) 4464–4483.

[295] X. Wang, Z. Lu, A. Gomez, G.C. Hon, Y. Yue, D. Han, Y. Fu, M. Parisien, Q. Dai, G. Jia, B. Ren, T. Pan, C. He, Nature 505 (2014) 117–120.

[296] W. Xiao, S. Adhikari, U. Dahal, Y.-S. Chen, Y.-J. Hao, B.-F. Sun, H.-Y. Sun, A. Li, X.-L. Ping, W.-Y. Lai, X. Wang, H.-L. Ma, C.-M. Huang, Y. Yang, N. Huang, G.-B. Jiang, H.-L. Wang, Q. Zhou, X.-J. Wang, Y.-L. Zhao, Y.-G. Yang, Mol Cell 61 (2016) 507–519.

[297] X. Wang, B.S. Zhao, I.A. Roundtree, Z. Lu, D. Han, H. Ma, X. Weng, K. Chen, H. Shi, C. He, Cell 161 (2015) 1388–1399.

[298] W. Zhang, Y. Qian, G. Jia, Journal of Biological Chemistry 297 (2021) 100973.

[299] G. Jia, Y. Fu, X. Zhao, Q. Dai, G. Zheng, Y. Yang, C. Yi, T. Lindahl, T. Pan, Y.-G. Yang, C. He, Nat Chem Biol 7 (2011) 885–887.

[300] S. Barone, C. Cerchia, V. Summa, M. Brindisi, J Med Chem 67 (2024) 14786–14806.

[301] Y.-N. Qi, Z. Liu, L.-L. Hong, P. Li, Z.-Q. Ling, J Hematol Oncol 16 (2023) 89.

[302] P. Śledź, M. Jinek, Elife 5 (2016).

[303] S. Zhao, J. Liu, P. Nanga, Y. Liu, A.E. Cicek, N. Knoblauch, C. He, M. Stephens, X. He, Nat Commun 10 (2019) 3399.

[304] X. Li, J. Tang, W. Huang, F. Wang, P. Li, C. Qin, Z. Qin, Q. Zou, J. Wei, L. Hua, H. Yang, Z. Wang, Oncotarget 8 (2017) 96103–96116.

[305] I. Barbieri, K. Tzelepis, L. Pandolfini, J. Shi, G. Millán-Zambrano, S.C. Robson, D. Aspris, V. Migliori, A.J. Bannister, N. Han, E. De Braekeleer, H. Ponstingl, A. Hendrick, C.R. Vakoc, G.S. Vassiliou, T. Kouzarides, Nature 552 (2017) 126–131.

[306] L.P. Vu, B.F. Pickering, Y. Cheng, S. Zaccara, D. Nguyen, G. Minuesa, T. Chou, A. Chow, Y. Saletore, M. MacKay, J. Schulman, C. Famulare, M. Patel, V.M. Klimek, F.E. Garrett-Bakelman, A. Melnick, M. Carroll, C.E. Mason, S.R. Jaffrey, M.G. Kharas, Nat Med 23 (2017) 1369–1376.

[307] F. Fiorentino, M. Menna, D. Rotili, S. Valente, A. Mai, J Med Chem 66 (2023) 1654–1677.

[308] G. Feng, Y. Wu, Y. Hu, W. Shuai, X. Yang, Y. Li, L. Ouyang, G. Wang, J Hematol Oncol 17 (2024), 30.

[309] R. Su, L. Dong, Y. Li, M. Gao, P.C. He, W. Liu, J. Wei, Z. Zhao, L. Gao, L. Han, X. Deng, C. Li, E. Prince, B. Tan, Y. Qing, X. Qin, C. Shen, M. Xue, K. Zhou, Z. Chen, J. Xue, W. Li, H. Qin, X. Wu, M. Sun, Y. Nam, C.W. Chen, W. Huang, D. Horne, S.T. Rosen, C. He, J. Chen, Nat Cell Biol 24 (2022) 205–216.

[310] D.J. Nance, E.R. Satterwhite, B. Bhaskar, S. Misra, K.R. Carraway, K.D. Mansfield, PLoS One 15 (2020) e0227647.

[311] J. Liu, Y. Yue, D. Han, X. Wang, Y. Fu, L. Zhang, G. Jia, M. Yu, Z. Lu, X. Deng, Q. Dai, W. Chen, C. He, Nat Chem Biol 10 (2014) 93–95.

[312] X. Wang, J. Feng, Y. Xue, Z. Guan, D. Zhang, Z. Liu, Z. Gong, Q. Wang, J. Huang, C. Tang, T. Zou, P. Yin, Nature 534 (2016) 575–578.

[313] A. Ruszkowska, M. Ruszkowski, Z. Dauter, J.A. Brown, Sci Rep 8 (2018).

[314] S. Oerum, V. Meynier, M. Catala, C. Tisné, Nucleic Acids Res 49 (2021) 7239–7255.

[315] X. Wang, J. Feng, Y. Xue, Z. Guan, D. Zhang, Z. Liu, Z. Gong, Q. Wang, J. Huang, C. Tang, T. Zou, P. Yin, Nature 534 (2016) 575–578.

[316] A.S. Warda, J. Kretschmer, P. Hackert, C. Lenz, H. Urlaub, C. Höbartner, K.E. Sloan, M.T. Bohnsack, EMBO Rep 18 (2017) 2004–2014.

[317] J. Liu, Y. Yue, D. Han, X. Wang, Y. Fu, L. Zhang, G. Jia, M. Yu, Z. Lu, X. Deng, Q. Dai, W. Chen, C. He, Nat Chem Biol 10 (2014) 93–95.

[318] M. Mendel, K.-M. Chen, D. Homolka, P. Gos, R.R. Pandey, A.A. McCarthy, R.S. Pillai, Mol Cell 71 (2018) 986-1000.e11.

[319] T. Malone, R.M. Blumenthal, X. Cheng, J Mol Biol 253 (1995) 618–632.

[320] J. Martin, Curr Opin Struct Biol 12 (2002) 783–793.

[321] M. Mendel, K.M. Chen, D. Homolka, P. Gos, R.R. Pandey, A.A. McCarthy, R.S. Pillai, Mol Cell 71 (2018) 986-1000.e11.

[322] K.E. Pendleton, B. Chen, K. Liu, O. V. Hunter, Y. Xie, B.P. Tu, N.K. Conrad, Cell 169 (2017) 824-835.e14.

[323] T. Aoyama, S. Yamashita, K. Tomita, Nucleic Acids Res 48 (2020) 5157–5168.

[324] Y. Yashiro, K. Tomita, Front Genet 9 (2018).

[325] S. Yamashita, Y. Takagi, T. Nagaike, K. Tomita, Nat Commun 8 (2017) 15788.

[326] G.D. Markham, M.A. Pajares, Cellular and Molecular Life Sciences 66 (2009) 636–648.

[327] J.E. Mermoud, Genes (Basel) 13 (2022).

[328] R. Zhang, Y. Zhang, F. Guo, G. Huang, Y. Zhao, B. Chen, C. Wang, C. Cui, Y. Shi, S. Li, H. Cui, Cell Death Discov 8 (2022).

[329] A.M. Scarborough, J.N. Flaherty, O. V. Hunter, K. Liu, A. Kumar, C. Xing, B.P. Tu, N.K. Conrad, Elife 10 (2021).

[330] N. Amodio, L. Raimondi, G. Juli, M.A. Stamato, D. Caracciolo, P. Tagliaferri, P. Tassone, J Hematol Oncol 11 (2018).

[331] J.A. Brown, C.G. Kinzig, S.J. Degregorio, J.A. Steitz, Proc Natl Acad Sci U S A 113 (2016) 14013–14018.

[332] K. Breger, J.A. Brown, Biochemistry 62 (2023) 494–506.

[333] P. Epstein, R. Reddy, D. Henning, H. Busch, Journal of Biological Chemistry 255 (1980) 8901–8906.

[334] Y. Ishigami, T. Ohira, Y. Isokawa, Y. Suzuki, T. Suzuki, Nat Commun 12 (2021).

[335] J. Chen, Y. Ning, H. Zhang, N. Song, Y. Gu, Y. Shi, J. Cai, X. Ding, X. Zhang, Life Sci 239 (2019) 117034.

[336] Y.-C. Hou, C.-L. Lu, T.-H. Yuan, M.-T. Liao, C.-T. Chao, K.-C. Lu, Int J Mol Sci 21 (2020) 980.

[337] D. Jian, Y. Wang, L. Jian, H. Tang, L. Rao, K. Chen, Z. Jia, W. Zhang, Y. Liu, X. Chen, X. Shen, C. Gao, S. Wang, M. Li, Theranostics 10 (2020) 8939–8956.

[338] X.-Q. Gao, Y.-H. Zhang, F. Liu, M. Ponnusamy, X.-M. Zhao, L.-Y. Zhou, M. Zhai, C.-Y. Liu, X.-M. Li, M. Wang, C. Shan, P.-P. Shan, Y. Wang, Y.-H. Dong, L.-L. Qian, T. Yu, J. Ju, T. Wang, K. Wang, X.-Z. Chen, Y.-H. Wang, J. Zhang, P.-F. Li, K. Wang, Nat Cell Biol 22 (2020) 1319–1331.

[339] L. Li, N. Xu, J. Liu, Z. Chen, X. Liu, J. Wang, Front Genet 13 (2022).

[340] L.E. Dorn, L. Lasman, J. Chen, X. Xu, T.J. Hund, M. Medvedovic, J.H. Hanna, J.H. van Berlo, F. Accornero, Circulation 139 (2019) 533–545.

[341] T. Berulava, E. Buchholz, V. Elerdashvili, T. Pena, M.R. Islam, D. Lbik, B.A. Mohamed, A. Renner, D. Lewinski, M. Sacherer, K.E. Bohnsack, M.T. Bohnsack, G. Jain, V. Capece, N. Cleve, S. Burkhardt, G. Hasenfuss, A. Fischer, K. Toischer, Eur J Heart Fail 22 (2020) 54–66.

[342] H.M. Burgess, D.P. Depledge, L. Thompson, K.P. Srinivas, R.C. Grande, E.I. Vink, J.S. Abebe, W.P. Blackaby, A. Hendrick, M.R. Albertella, T. Kouzarides, K.A. Stapleford, A.C. Wilson, I. Mohr, Genes Dev 35 (2021) 1005–1019.

[343] M. Lu, Z. Zhang, M. Xue, B.S. Zhao, O. Harder, A. Li, X. Liang, T.Z. Gao, Y. Xu, J. Zhou, Z. Feng, S. Niewiesk, M.E. Peeples, C. He, J. Li, Nat Microbiol 5 (2020) 584–598.

[344] N.S. Gokhale, A.B.R. McIntyre, M.J. McFadden, A.E. Roder, E.M. Kennedy, J.A. Gandara, S.E. Hopcraft, K.M. Quicke, C. Vazquez, J. Willer, O.R. Ilkayeva, B.A. Law, C.L. Holley, M.A. Garcia-Blanco, M.J. Evans, M.S. Suthar, S.S. Bradrick, C.E. Mason, S.M. Horner, Cell Host Microbe 20 (2016) 654–665.

[345] Y. Wu, L. Xie, M. Wang, Q. Xiong, Y. Guo, Y. Liang, J. Li, R. Sheng, P. Deng, Y. Wang, R. Zheng, Y. Jiang, L. Ye, Q. Chen, X. Zhou, S. Lin, Q. Yuan, Nat Commun 9 (2018) 4772.

[346] H. Song, X. Feng, H. Zhang, Y. Luo, J. Huang, M. Lin, J. Jin, X. Ding, S. Wu, H. Huang, T. Yu, M. Zhang, H. Hong, S. Yao, Y. Zhao, Z. Zhang, Autophagy 15 (2019) 1419–1437.

[347] M. Kobayashi, M. Ohsugi, T. Sasako, M. Awazawa, T. Umehara, A. Iwane, N. Kobayashi, Y. Okazaki, N. Kubota, R. Suzuki, H. Waki, K.

Horiuchi, T. Hamakubo, T. Kodama, S. Aoe, K. Tobe, T. Kadowaki, K. Ueki, Mol Cell Biol 38 (2018).

[348] Y. Yang, J. Cai, X. Yang, K. Wang, K. Sun, Z. Yang, L. Zhang, L. Yang, C. Gu, X. Huang, Z. Wang, X. Zhu, Molecular Therapy 30 (2022) 2342–2353.

[349] J. Widagdo, J.J.-L. Wong, V. Anggono, Semin Cell Dev Biol 125 (2022) 110–121.

[350] J. Widagdo, V. Anggono, J Neurochem 147 (2018) 137–152.

[351] Z. Zhang, M. Wang, D. Xie, Z. Huang, L. Zhang, Y. Yang, D. Ma, W. Li, Q. Zhou, Y.-G. Yang, X.-J. Wang, Cell Res 28 (2018) 1050–1061.

[352] Y. Yang, J. Cai, X. Yang, K. Wang, K. Sun, Z. Yang, L. Zhang, L. Yang, C. Gu, X. Huang, Z. Wang, X. Zhu, Molecular Therapy 30 (2022) 2342–2353.

[353] J. Tang, X. Zhao, W. Wei, W. Liu, H. Fan, X. ping Liu, Y. Li, L. Wang, J. Guo, PeerJ 10 (2022).

[354] J. Cheng, D. Xu, L. Chen, W. Guo, G. Hu, J. Liu, S. Fu, J Agric Food Chem 70 (2022) 11324–11335.

[355] L. Zhou, L. Xu, J. Ye, D. Li, W. Wang, X. Li, L. Wu, H. Wang, F. Guan, P. Li, Hepatology 56 (2012) 95–107.

[356] T. Maeda, Int J Hematol 104 (2016) 310–323.

[357] T. Moriguchi, M. Yamamoto, Int J Hematol 100 (2014) 417–424.

[358] M. Yoshinaga, K. Han, D.W. Morgens, T. Horii, R. Kobayashi, T. Tsuruyama, F. Hia, S. Yasukura, A. Kajiya, T. Cai, P.H.C. Cruz, A. Vandenbon, Y. Suzuki, Y. Kawahara, I. Hatada, M.C. Bassik, O. Takeuchi, Nat Commun 13 (2022).

[359] Y. Yang, B.-F. Sun, W. Xiao, X. Yang, H.-Y. Sun, Y.-L. Zhao, Y.-G. Yang, Sci Bull (Beijing) 60 (2015) 21–32.

[360] R. Du, C. Huang, K. Liu, X. Li, Z. Dong, Mol Cancer 20 (2021) 15.

[361] Y. zhang Dai, Y. da Liu, J. Li, M. ting Chen, M. Huang, F. Wang, Q. song Yang, J. hang Yuan, S. han Sun, Cell Mol Biol Lett 27 (2022).

[362] C.-Y. Loh, J. Chai, T. Tang, W. Wong, G. Sethi, M. Shanmugam, P. Chong, C. Looi, Cells 8 (2019) 1118.

[363] F. Ye, J. Wu, F. Zhang, Biochem Biophys Res Commun 638 (2023) 1–6.

[364] L.P. Vu, B.F. Pickering, Y. Cheng, S. Zaccara, D. Nguyen, G. Minuesa, T. Chou, A. Chow, Y. Saletore, M. MacKay, J. Schulman, C. Famulare, M. Patel, V.M. Klimek, F.E. Garrett-Bakelman, A. Melnick, M. Carroll, C.E. Mason, S.R. Jaffrey, M.G. Kharas, Nat Med 23 (2017) 1369–1376.

[365] I. Barbieri, K. Tzelepis, L. Pandolfini, J. Shi, G. Millán-Zambrano, S.C. Robson, D. Aspris, V. Migliori, A.J. Bannister, N. Han, E. De Braekeleer, H. Ponstingl, A. Hendrick, C.R. Vakoc, G.S. Vassiliou, T. Kouzarides, Nature 552 (2017) 126–131.

[366] H. Weng, H. Huang, H. Wu, X. Qin, B.S. Zhao, L. Dong, H. Shi, J. Skibbe, C. Shen, C. Hu, Y. Sheng, Y. Wang, M. Wunderlich, B. Zhang, L.C. Dore, R. Su, X. Deng, K. Ferchen, C. Li, M. Sun, Z. Lu, X. Jiang, G. Marcucci, J.C. Mulloy, J. Yang, Z. Qian, M. Wei, C. He, J. Chen, Cell Stem Cell 22 (2018) 191-205.e9.

[367] L. Han, L. Dong, K. Leung, Z. Zhao, Y. Li, L. Gao, Z. Chen, J. Xue, Y. Qing, W. Li, S.P. Pokharel, M. Gao, M. Chen, C. Shen, B. Tan, A. Small, K. Wang, Z. Zhang, X. Qin, L. Yang, M. Wunderlich, B. Zhang, J.C. Mulloy, G. Marcucci, C.W. Chen, M. Wei, R. Su, J. Chen, X. Deng, Cell Stem Cell 30 (2023) 52-68.e13.

[368] A. Hattori, M. Tsunoda, T. Konuma, M. Kobayashi, T. Nagy, J. Glushka, F. Tayyari, D. McSkimming, N. Kannan, A. Tojo, A.S. Edison, T. Ito, Nature 545 (2017) 500–504.

[369] T. Liu, S. Yang, J. Sui, S. Xu, Y. Cheng, B. Shen, Y. Zhang, X. Zhang, L. Yin, Y. Pu, G. Liang, J Cell Physiol 235 (2020) 548–562.

[370] X.K. Wang, Y.W. Zhang, C.M. Wang, B. Li, T.Z. Zhang, W.J. Zhou, L. jia Cheng, M.Y. Huo, C.H. Zhang, Y.L. He, J Cell Mol Med 25 (2021) 6602–6617.

[371] F. Wang, J. Zhang, X. Lin, L. Yang, Q. Zhou, X. Mi, Q. Li, S. Wang, D. Li, X.M. Liu, J. Zhou, Cell Rep 42 (2023).

[372] M. Fleming, S. Ravula, S.F. Tatishchev, H.L. Wang, J Gastrointest Oncol 3 (2012) 153–73.

[373] Wang A, Sun Y, Wang X, Yan Z, Wang D, Zeng L, Lu Q. m6A methyltransferase METTL16 mediates immune evasion of colorectal cancer cells via epigenetically regulating PD-L1 expression. Aging (Albany NY). 2023 Aug 29;15(16):8444-8457. d

[374] W. Wei, Z.Y. Zhang, B. Shi, Y. Cai, H.S. Zhang, C.L. Sun, Y.F. Fei, W. Zhong, S. Zhang, C. Wang, B. He, G.M. Jiang, H. Wang, Journal of Experimental and Clinical Cancer Research 42 (2023).

[375] N. Liu, J. Zhang, W. Chen, W. Ma, T. Wu, Journal of Experimental and Clinical Cancer Research 42 (2023).

[376] WO2021035045A1.

[377] S. Selberg, L. Ivanova, M. Kotli, K. Herodes, D. Blokhina, E. Kankuri, N. Seli, I. Ilves, I. Teino, M. Saarma, M. Karelson, bioRxiv (2023).

[378] WO2021116477A1.

[379] A. Mitra, S. Manna, R. Kundu, D. Hazra, A. Roychowdhury, IEEE/ACM Trans Comput Biol Bioinform (2023) 1–8.

[380] Y. Liu, G.L. Goebel, L. Kanis, O. Hastürk, C. Kemker, P. Wu, JACS Au 4 (2024) 1436–1449.

[381] P. Wu, Nat Rev Chem 4 (2020) 441–458.

[382] L. Borgelt, F. Li, P. Hommen, P. Lampe, J. Hwang, G.L. Goebel, S. Sievers, P. Wu, ACS Med Chem Lett 12 (2021) 893–898.

[383] L. Borgelt, F. Huang, L. Hohnen, X. Qiu, G.L. Goebel, P. Hommen, P. Wu, ChemBioChem 24 (2023).

[384] G.L. Goebel, L. Hohnen, L. Borgelt, P. Hommen, X. Qiu, H. Lightfoot, P. Wu, Eur J Med Chem 228 (2022) 114014.

[385] D.A. Dougherty, Science (1979) 271 (1996) 163–168.

[386] G.B. McGaughey, M. Gagné, A.K. Rappé, Journal of Biological Chemistry 273 (1998) 15458–15463.

[387] T.J. Ritchie, S.J.F. Macdonald, J Med Chem 57 (2014) 7206–7215.

[388] T.J. Ritchie, S.J.F. Macdonald, Drug Discov Today 14 (2009) 1011–1020.

[389] F. Lovering, J. Bikker, C. Humblet, J Med Chem 52 (2009) 6752–6756.

[390] H. Gunaydin, M.D. Bartberger, ACS Med Chem Lett 7 (2016) 341–344.

[391] E. Benedetti, L. Micouin, Expert Opin Drug Discov 3 (2024) 263-266.

[392] G.P. Moss, Pure and Applied Chemistry 71 (1999) 531–558.

[393] M.T. Varela, G.G. Dias, L.F.N. de Oliveira, R.G. de Oliveira, F.D. Aguiar, J.P. Nogueira, L.R. Cruz, L.C. Dias, Eur J Med Chem 287 (2025) 117368.

[394] K. Hiesinger, D. Dar'in, E. Proschak, M. Krasavin, J Med Chem 64 (2021) 150–183.

[395] Y.-J. Zheng, C.M. Tice, Expert Opin Drug Discov 11 (2016) 831–834.

[396] O.O. Grygorenko, P. Babenko, D.M. Volochnyuk, O. Raievskyi, I. V. Komarov, RSC Adv 6 (2016) 17595–17605.

[397] J. Meyers, M. Carter, N.Y. Mok, N. Brown, Future Med Chem 8 (2016) 1753–1767.

[398] E. Benedetti, L. Micouin, Expert Opin Drug Discov 19 (2024) 263–266.

[399] V.F. Batista, D.C.G.A. Pinto, A.M.S. Silva, Expert Opin Drug Discov 17 (2022) 603–618.

[400] W. Wei, S. Cherukupalli, L. Jing, X. Liu, P. Zhan, Drug Discov Today 25 (2020) 1839–1845.

Chapter 2 – PhD work: aims and general methods

The aim of this PhD thesis work was the development of novel epigenetic modulators for the treatment of pathological states characterized by a strong epigenetic component. According to the growing knowledge in molecular underpinnings driving these regulatory mechanisms, this work aimed to identify novel chemical entities able to restore physiological pathways strictly depending on epigenetics interplay – such as those involved in cancer and rare diseases - to address a critical gap in currently available treatments. The main objective was to identify novel potent and selective HDAC6is with improved pharmacokinetic properties with respect to already known inhibitors. According, to date there are not approved selective HDAC6is, while most of HDAC6is in clinical trials, considered to be selective, fail to achieve a satisfying selectivity index in order to dissect whether their efficacy stands on HDAC6 activity over nuclear isoforms. To address this challenge, the present work explored the use of spirofused cores as cap groups, which were decorated with different linkers and ZBGs to achieve high potency towards HDAC6 and high selectivity over nuclear HDACs. Designed compounds have been assessed in different cellular models (including patient-derived organoids), demonstrating efficacy in inhibiting several cancer-related pathways, as well as bacterial and fungal virulence, underscoring their potential to address multidrug resistant infection diseases.

All starting materials and solvents were purchased from commercial suppliers and used without further purification. For ^{1}H NMR and ^{13}C NMR measurements an accurately weighed amount of analyte (about 5.0 - 10.0 mg) was dissolved in 600 μL of deuterated chloroform (CDCl3) or dimethyl sulfoxide (DMSO-d6). The mixture was transferred into a 5 mm NMR tube and the spectra were acquired on a Bruker Advance 400 MHz or 700 MHz spectrometers by using the residual signal of the deuterated solvent as internal standard. Splitting patterns are described as singlet (s), doublet (d), triplet (t), quartet (q) and broad (br); the

values of chemical shifts (δ) are given in ppm and coupling constants (J) in Hertz (Hz). NMR data were processed with MestreNova (Version 8.1.1, Mestrelab Research). ESI-MS spectra analysis was carried out on a mass spectrometer LTQ-XL. Spectra were recorded by infusion into the ESI source using MeOH as solvent. Column chromatography was performed using 70-230 mesh, 60 Å pore diameter silica gel. TLC analysis was conducted using 5x20 aluminum foil supported thin-layer silica gel chromatography plates (F254 indicator) with a thickness of 0.25 mm, using the UV as detection method (225 nM) and ninhydrin, ferric chloride and phosphomolybdic acid as staining agents. Optical rotation values were measured at room temperature operating at λ = 589 nm, corresponding to the sodium D line, and were determined in a Jasco P-200 (Jasco Europe s.r.l., Cremella, Italy) polarimeter using a microcell (1 mg sensitivity) containing the compound dissolved in 1 mL of chloroform or methanol.

Chapter 3

Design, synthesis, in silico studies and biological validation of potent and selective HDAC6 inhibitors for the treatment of Triple Negative Breast Cancer.

As reported in *Chapter 1*, TNBC is a highly aggressive and invasive BC subtype, for which a gold standard therapy has to be still defined. Compelling new evidence highlighted about 30% of BC subtype can benefit from HDAC6 inhibition, including TNBC [1]. Thereby, our aim was to identify novel potent and selective HDAC6is to be assessed in TNBC models. We disclosed a novel class of spiro-fused compounds acting as potent and selective HDAC6is. Structure-based optimization led to derivatives **16c** and **17c** with high potency and selectivity towards HDAC6 *in vitro* and in cell-based settings. Following our observation that mRNA expression level of HDAC6 was significantly higher in MDA-MB-231, we have evaluated the effect of the compounds on cell viability. Moreover, we have unveiled for compounds **16c** and **17c** the

involvement of the autophagic machinery in cell death induction. Scratch assay revealed for the newly conceived compounds a very potent effect on inhibiting the migration process in MDA-MB-231 cells. Our results underscore the key role of HDAC6 in TNBC progression, providing a solid groundwork to reshape TNBC therapy [2].

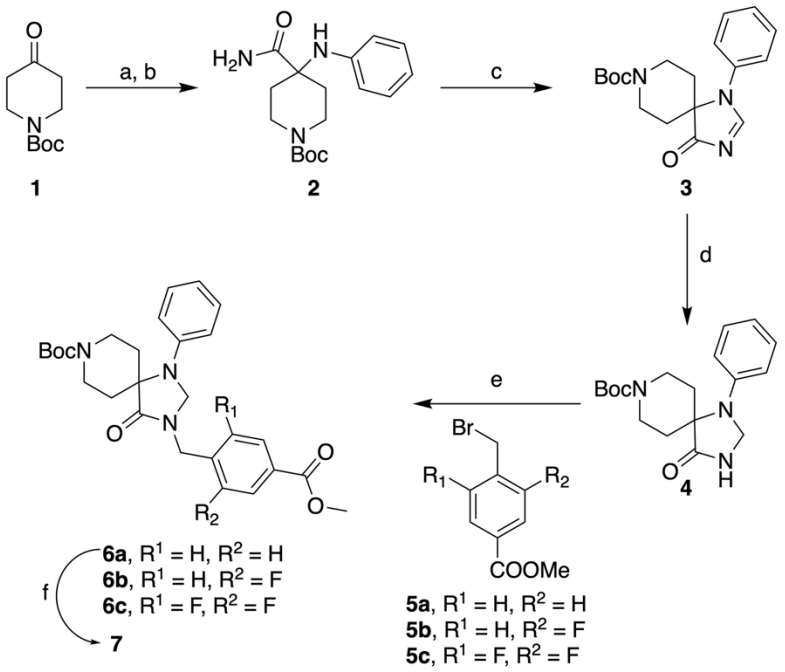
3.1 Results and discussion

3.1.1 Chemistry

Spirofused core **4** was synthesized as reported in Scheme 1 following a previously described procedure. Commercially available N-Boc-piperidone **1** was converted into the corresponding α-aminonitrile by a Strecker reaction performed in presence of aniline and trimethylsilyl cyanide (TMSCN) in acidic environment. The following nitrile hydrolysis by 1 N aqueous NaOH in the presence of hydrogen peroxide provided the amide intermediate **2**. The latter amide was subsequently treated with triethyl orthoformate in presence of acetic acid to give the intermediate **3**, subjected to the treatment with sodium borohydride to afford the desired product **4** in 63% yield over two steps.

Intermediate **4** was then subjected to an alkylation reaction with methyl-4-bromomethyl-benzoate (**5a**), methyl-4-(bromomethyl)-3-fluorobenzoate (**5b**), or 4-(bromomethyl)benzonitrile (**5c**) respectively, using sodium hydride as base, in anhydrous THF at 25 °C, to provide the corresponding methyl esters **6a-c**, with yields ranging from 30% to 83%. Compound **6a** underwent a reaction with 50% aqueous hydroxylamine in presence of 4 N methanolic KOH using DCM/MeOH (2:1) as solvent mixture, to provide final compound **7**.

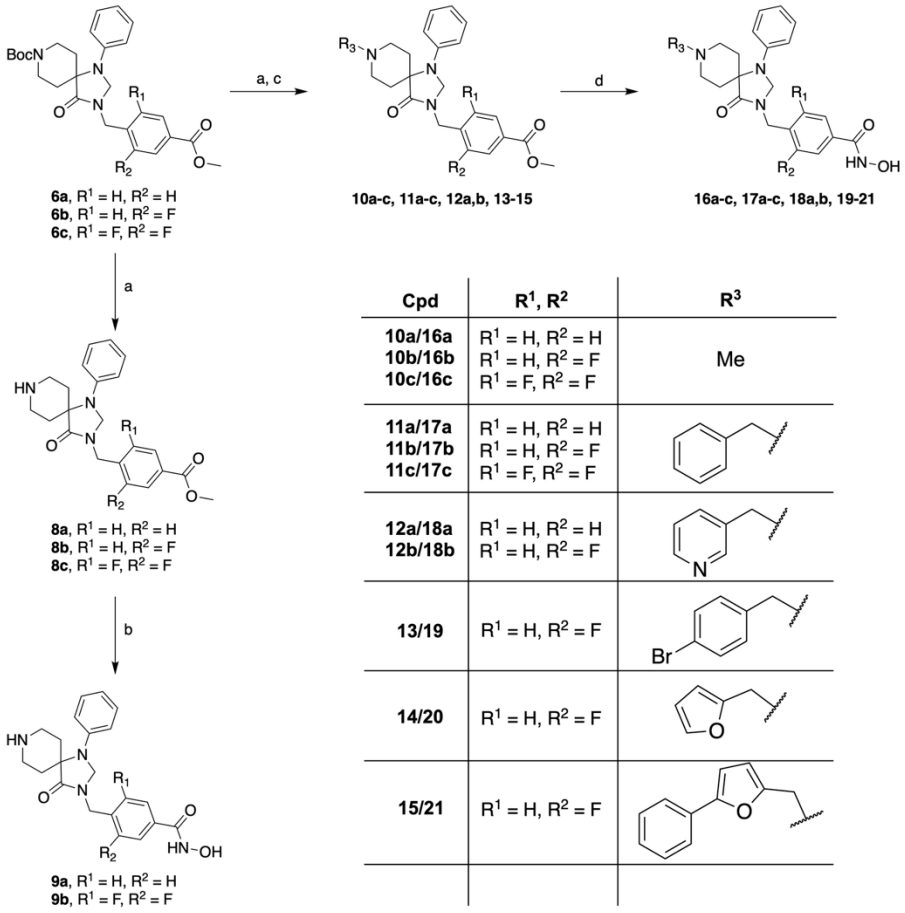
Scheme 1. Synthetic route for the synthesis of key tert-butyl 4-oxo-1-phenyl-1,3,8-triazaspiro[4.5]decane based derivatives **6a-c** and final compound **7**.[a]



[a]Reagents and conditions: (a) Aniline, AcOH, 0 °C, TMSC, 18 h, 25 °C, quant; (b) 1 M NaOH, MeOH, 15 min, H_2O_2, 18 h, 25 °C, 60%; (c) $CH(OEt)_3$, AcOH, 18 h; reflux, quant.; (d) $NaBH_4$, MeOH, 0 °C to rt, 30 min, 64%; (e) NaH 60 % oil dispersion, dry THF, 24 h, 25 °C, 53% (**6a**), 68% (**6b**), 30% (**6c**) ; (f) 50% aq. NH_2OH, 4 M KOH in MeOH, DCM/MeOH (2:1), 1 h, 25 °C, 83%.

To explore further functionalization on the nitrogen in position 1 of the spirocyclic cap group, the Boc group was removed in acidic conditions (Scheme 2) providing the intermediates **8a-c** in quantitative yields. Free amines **8a,b** were also converted into their hydroxamic acid derivatives **9a,b**. Amine derivatives **8a-c** were also subjected to reductive amination with the appropriate aldehydes in presence of acetic acid as catalyst and sodium cyanoborohydride ($NaBH_3CN$) as reductant, and then treated with 50% aqueous hydroxylamine and methanolic KOH to provide the final hydroxamic acid derivatives **16a-c**, **17a-c**, **18a,b** and **19-21.**

Scheme 2. Synthetic route for N^1-amine capped derivatives **9a,b, 16a-c**, **17a-c**, **18a,b** and **19-21**.[a]



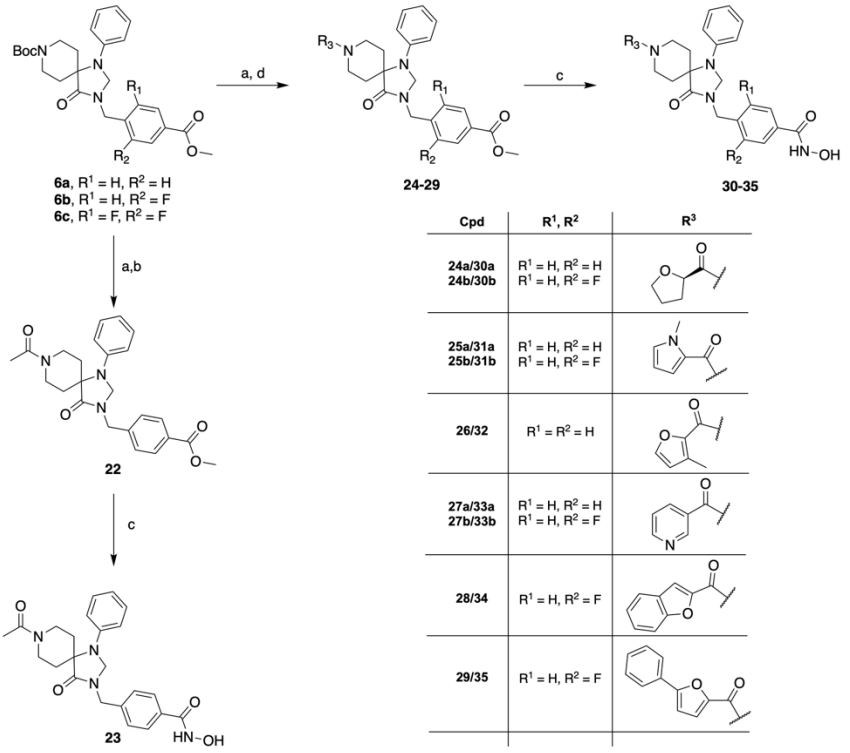
Cpd	R^1, R^2	R^3
10a/16a **10b/16b** **10c/16c**	R^1 = H, R^2 = H R^1 = H, R^2 = F R^1 = F, R^2 = F	Me
11a/17a **11b/17b** **11c/17c**	R^1 = H, R^2 = H R^1 = H, R^2 = F R^1 = F, R^2 = F	
12a/18a **12b/18b**	R^1 = H, R^2 = H R^1 = H, R^2 = F	
13/19	R^1 = H, R^2 = F	
14/20	R^1 = H, R^2 = F	
15/21	R^1 = H, R^2 = F	

[a]Reagents and conditions: (a) 4 N HCl in dioxane, DCM, 1 h, 25 °C or AcCl, MeOH, 1 h, 25 °C, quant,; (b) 50% aq. NH_2OH, 4 M KOH in MeOH, DCM/MeOH (2:1), 1 h, 25 °C, 60% (**16a**), 50% (**16b**); (c) aldehyde, AcOH, MeOH, 1 h, 25 °C, $NaBH_3CN$, 18 h, 25 °C, 93-61%; (d) 50% aq. NH_2OH, 4 M KOH in MeOH, DCM/MeOH (2:1), 1 h, 25 °C, 83-15%.

Scheme 3 describes the synthesis of N^1-amide capped compounds. Compound **22** was obtained from **6a** by sequential Boc deprotection, N-acetylation and conversion into the corresponding hydroxamic acid derivative. Intermediates **31-36** were obtained from compounds **13a,b** after Boc deprotection and coupling

reaction with the appropriate carboxylic acid, in presence of N-methyl morpholine as base and HBTU as coupling agent in anhydrous DCM at 25 °C, to provide the corresponding desired amide products with yields ranging from 37% to 96%. Subsequent treatment with 50% aqueous hydroxylamine in presence of 4 N methanolic KOH, using DCM/MeOH (2:1) as solvent, led to the desired final products **37-42**.

Scheme 3. Synthetic route for N^1-amide capped derivatives **30** and **37-42**[a].



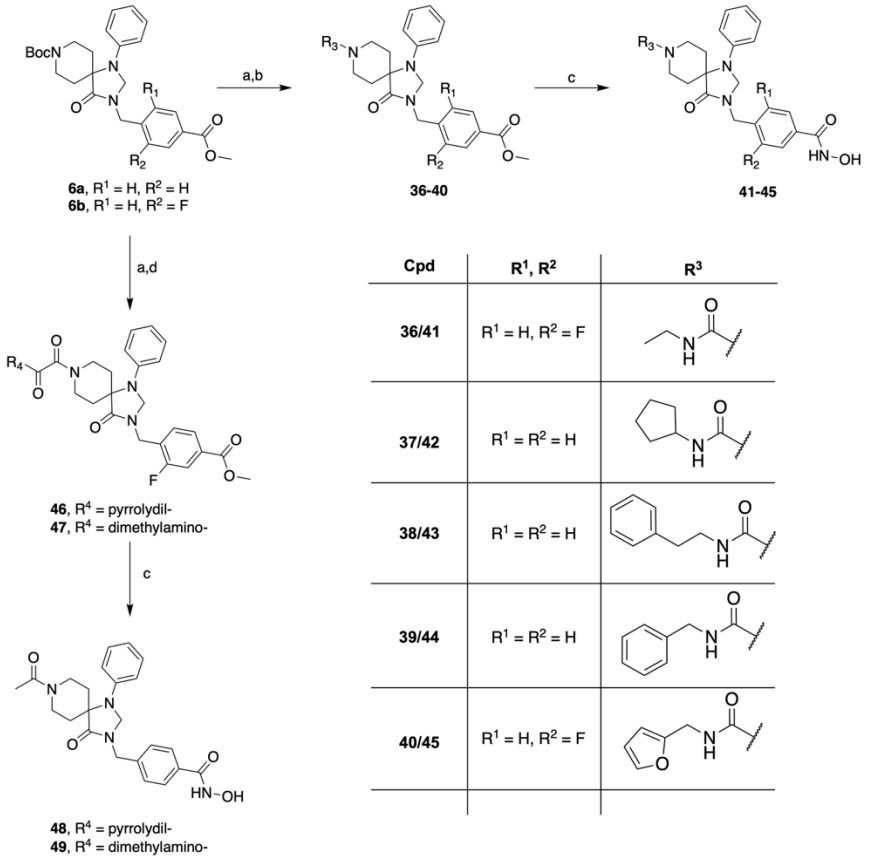
Cpd	R^1, R^2	R^3
24a/30a 24b/30b	R^1 = H, R^2 = H R^1 = H, R^2 = F	
25a/31a 25b/31b	R^1 = H, R^2 = H R^1 = H, R^2 = F	
26/32	R^1 = R^2 = H	
27a/33a 27b/33b	R^1 = H, R^2 = H R^1 = H, R^2 = F	
28/34	R^1 = H, R^2 = F	
29/35	R^1 = H, R^2 = F	

[a]Reagents and conditions: (a) 4 N HCl in dioxane, DCM, 1 h, 25 °C or AcCl, MeOH, 1 h, 25 °C, quant.; (b) AcCl, MeOH, 1 h, 0 °C, 76%; (c) 50% aq. NH_2OH, 4M KOH in MeOH, DCM/MeOH (2:1), 1 h, 25 °C; (d) carboxylic acid, NMM, HBTU, dry DCM, 25 °C, 24 h, 93-14%.

As described in Scheme 4, compounds **36-40** were synthesized treating amine intermediates with the proper isocyanate, in the presence of triethylamine as base, with high yields. Similarly, intermediates **46** and **47** were synthesized treating the

free amine of **6b** with oxalyl chloride in presence of pyrrolidine or dimethylamine, respectively. As described above, final compounds **41-45** and **48,59** were obtained converting the methyl esters into their corresponding hydroxamic acids counterparts using 50% aqueous hydroxylamine in presence of methanolic KOH.

Scheme 4. Synthetic route for N^1-urea and N^1-oxalamide capped derivatives **41-45** and **48,49**[a].



Cpd	R^1, R^2	R^3
36/41	R^1 = H, R^2 = F	
37/42	R^1 = R^2 = H	
38/43	R^1 = R^2 = H	
39/44	R^1 = R^2 = H	
40/45	R^1 = H, R^2 = F	

[a]Reagents and conditions: (a) AcCl, MeOH, 1 h, 0 °C; (b) isocyanide, TEA, DCM, 1 h, 0 °C; (iii) 50% aq. NH_2OH, 4M KOH in MeOH, DCM/MeOH (2:1), 1 h, 25 °C; (d) oxalyl chloride, pyrrolidine or dimethylamine, TEA, DCM, 2 h, 0 °C to rt.

3.1.2 Identification of 1,3,8-triazaspiro[4,5]decan-4-one cap group

For the rational design of novel selective HDAC6is, we first considered the general features for HDACs inhibition, namely: i) a cap group to interact with the enzyme surface, ii) a linker and iii) a ZBG for metal-binding group interacting with the catalytic Zn^{2+} ion [3,4]. Accordingly, we focused on the design of a cap group able to efficiently accommodate in the HDAC binding site while also targeting a specific lipophilic pocket identified in HDAC6 and shaped by L749, F679 and F680, while in the HDAC1 homolog the F679 is replaced by Y204 residue (*Table 1*, Chapter 2) [4]. Such different aminoacidic composition may represent a further handhold for gaining potency and selectivity on HDAC6 over HDAC1 isoform.

Preliminary computational studies performed by our research group led to the identification of the 1,3,8-triazaspiro[4,5]decan-4-one core (Figure 1) as a novel optimal and versatile cap-group for the design of potent and selective HDAC6is, able to establish extensive interactions with HDAC6 external surface, and displaying increased Fsp^3 in comparison to already existing cap groups. Indeed, our driving hypothesis was to increase the cap group level of saturation, in order to enhance the binding affinity within enzyme surface and improve potency and selectivity of designed HDAC6is, while also increasing solubility, a key parameter in the development of clinical candidates [2].

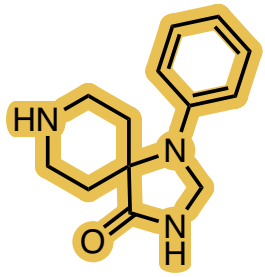
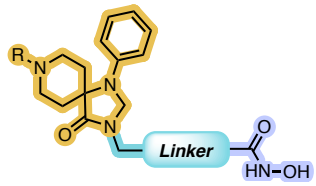


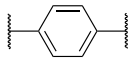
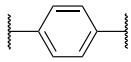
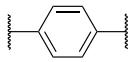
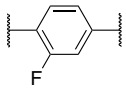
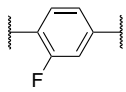
Figure 1. Structure 1,3,8-triazaspiro[4,5]decan-4-one core selected as novel cap group.

In our design, we kept the canonical benzyl, *m*-fluoro or *m*-difluorobenzyl linker, while the hydroxamic acid ZBG was an attractive choice for both for its synthetic feasibility and its high capability to coordinate zinc ions, with respect to other classes of ZBGs.

Therefore, the primary objective of our design was to evaluate whether the novel identified cap group **4** conformed to the structural requirements necessary for selective interaction within the catalytic surface of HDAC6, thereby conferring selectivity over nuclear isoforms. First, a simple *p*-phenyl hydroxamic acid moiety was explored as linker-ZBG combination, while the piperidine nitrogen in spirofused cap group was exploited to interrogate the effect of various substitutions. In a first design, unsubstituted piperidine (**9a**), as well the introduction of a methyl (**16a**) or a bulkier benzyl group (**17a**) on piperidine ring were interrogated. On the next stage, in order to rapidly interrogate whether structural modifications on the linker moiety portion could modulate both potency and selectivity profiles, compounds **16b** and **17b** were designed, based on the speculation that the insertion of a fluorine atom in the linker moiety could be responsible for a key alogen-bond interaction specifically established in HDAC6 isoform with S531(*Table 1*). All compounds were assessed in enzymatic assays on HDAC6, and their selectivity profiles were evaluated through their assessment on HDAC1 as a representative of nuclear isoforms [2].

Table 1. Structures and Inhibitory Activities of inhibitors **9a**, **16a,b** and **17a,b**.



Cpd	R	Linker	IC_{50} HDAC6 (nM)	IC_{50} HDAC1 (nM)	SI
9a	H		23.3	1230	53
16a	Me		13.3	832	63
17a	Bn		12.9	1370	106
16b	Me		7.7	2118	275
17b	Bn		17.6	7373.2	419

Interestingly, all compounds displayed low nM IC_{50} towards HDAC6 in enzymatic assays, while the introduction of bulkier benzyl group in compound **17a** resulted in slight increase of selectivity toward HDAC1, thereby confirming the suitability of novel conceived 1,3,8-triazaspiro[4,5]decan-4-one cap group for the preferential interaction with HDAC6. The introduction of a *m*-fluorine atom in the linker moiety of compounds **16b**,**17b** resulted in a significant gain of potency on HDAC6, thus increasing the selectivity over the nuclear isoform HDAC1. To provide insights into the potential binding mode of the investigated

compounds and provide a rational interpretation of these preliminary structure-activity relationships, molecular modeling studies were undertaken by means of Glide (Glide, Schrödinger, LLC, New York, NY, 2021). Docking of **16a**, bearing a methyl group as substituent on the nitrogen atom of the piperidine moiety, showed that it interacts with the catalytic Zn^{2+} ion through the hydroxamic acid moiety, establishing a bidentate coordination, with the carbonyl oxygen accepting an additional H-bond from the side chain of Y782 (Figure 2A). The benzyl linker engaged favorable π-π stacking interactions with F620, H651, and F680 within the aromatic crevice in the substrate binding channel, whereas the terminal piperidine on the cap group formed and additional cation- π interaction with H500, lining the L1 loop (Figure 2A) [2].

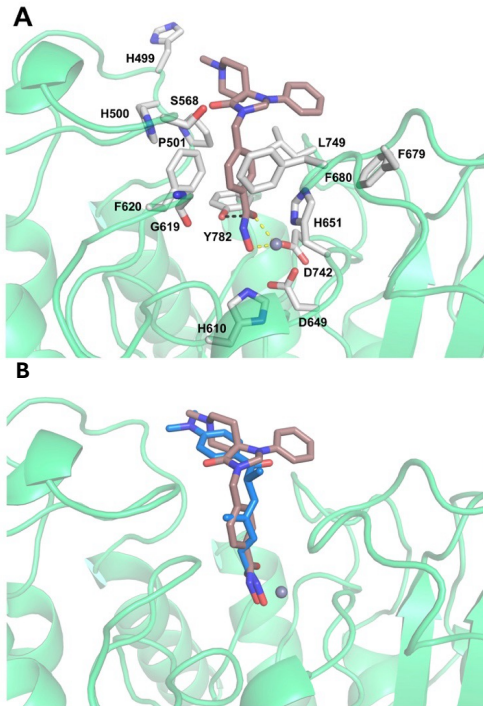


Figure 2. (A) Docking pose of compound **16a** within *h*HDAC6 active site (PDB 5EDU) represented as green transparent ribbon model. (B) Superimposition of compound **16a** with TSA into *h*HDAC6. Residues in the active site are displayed

as white sticks and labeled. H-bonds discussed in the text are depicted as dashed black lines. The catalytic Zn^{2+} ion is represented as a gray sphere; metal coordination is shown as dashed yellow lines [401]. In addition, the 1-phenyl group formed extensive hydrophobic interactions with L749. The overlay of **16a** with TSA co-crystallized into *h*HDAC6 (PDB: 5EDU; Figure 2B). This explains the nanomolar affinity of compound **16a** towards HDAC6 (IC_{50} = 13.3 nM) although with only a moderate selectivity over HDAC1 isoform (SI = 63). The binding mode of **17a**, bearing a benzyl group as substituent on the nitrogen atom of the piperidine moiety, was overall very similar to its parent compound **17a** (Figure 3), consistent with their similar inhibitory activity (IC_{50} = 12.9 nM). Moreover, compound the bulkier benzyl cap group approached more closely the L1 loop, forming additional hydrophobic interactions with H499 (Figure 3). The bulky cap group, combined with the benzyl linker, most likely prevent these compounds from properly adapting into HDAC1 active site [2].

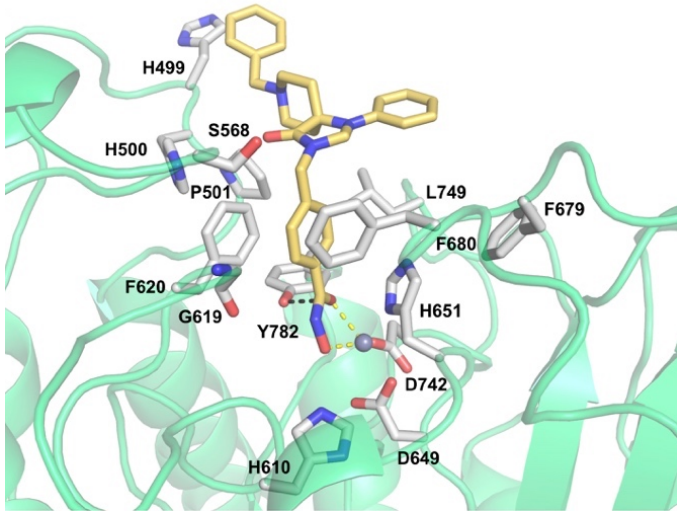


Figure 3. Docking pose of compound **17a** within *h*HDAC6 active site (PDB: 5EDU) [2].

Accordingly, both **16a** and **17a** were not able to coordinate the catalytic Zn^{2+} ion in HDAC1 active site. The only interactions observed were π-π stacking with

F150 and H178, with **16a** forming an additional one with H28 through its 1-phenyl on the cap group (Figure 4).

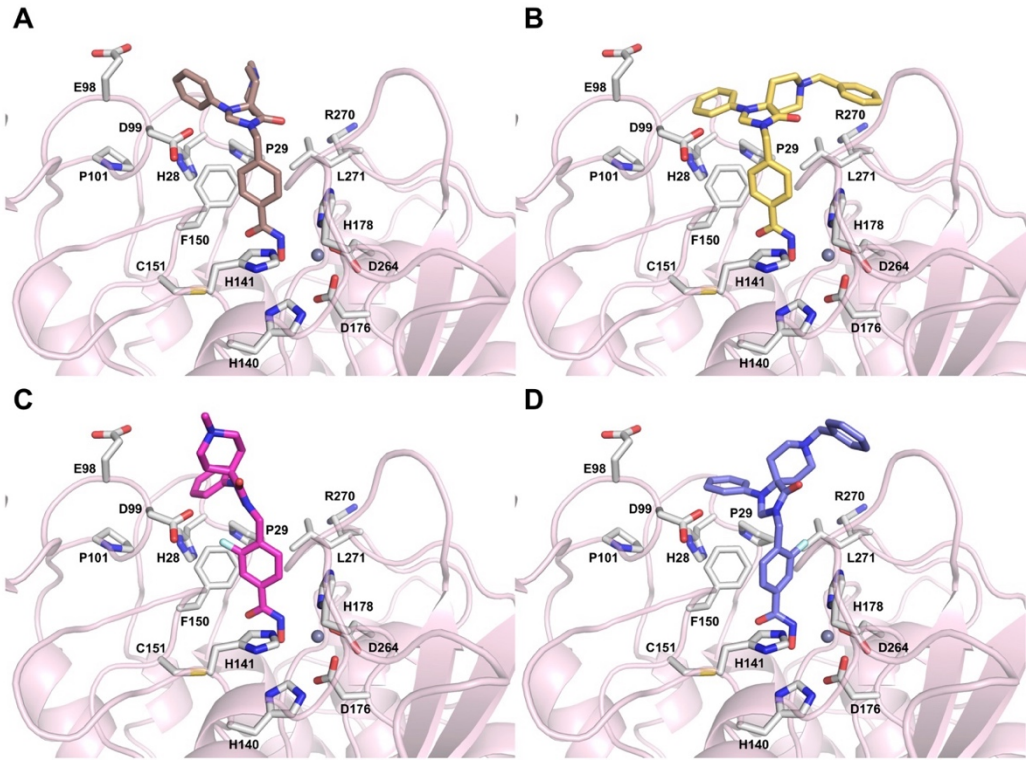


Figure 4. Docking poses of **16a** (A, dirty violet sticks), **17a** (B, yellow sticks), **16b** (C, magenta sticks) and **17b** (D, slate sticks) within *h*HDAC1 active site (PDB: 4BKX) represented as pink transparent ribbon model. Residues in the active site are displayed as white sticks and labeled. The catalytic Zn2+ ion is represented as a gray sphere [2].

The introduction of a *m*-fluorobenzyl linker in compound **16b** (HDAC6 IC_{50} = 7.7 nM, SI = 275) induced a very slight rearrangement of the ligand within the HDAC6 crevice, which resulted in a monodentate coordination of the Zn^{2+} ion and the formation of a H-bond between the hydroxamate nitrogen and the main chain carbonyl of G619 (Figure 5A). The fluorine atom was positioned at a distance of 3 Å from the side chain of S568, which is a favorable distance to promote interactions within this key residue, as also reported previously. In

addition, the ligand engaged a π- π stacking interaction with F679 through its 1-phenyl group, whereas the methylpiperidine moiety formed hydrophobic contacts with L749 (Figure 5A).

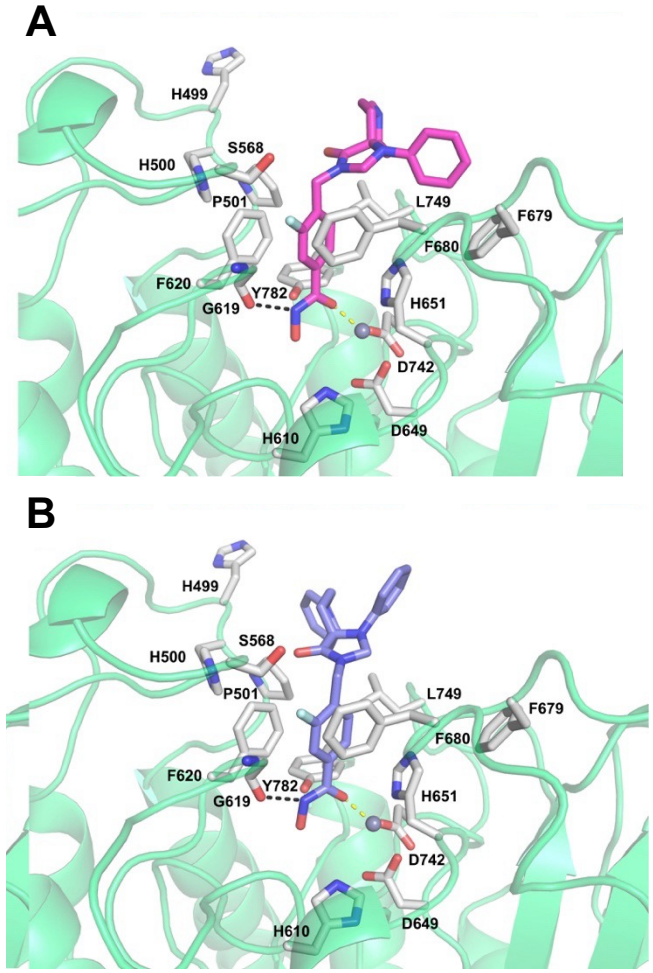


Figure 5. (A) Docking pose of compound **16b** (slate sticks) within *h*HDAC6 active site (PDB 5EDU) represented as green transparent ribbon model. (B) Docking pose of compound **17b** within *h*HDAC6 active site represented as green transparent ribbon model. Residues in the active site are displayed as white sticks and labeled. H-bonds discussed in the text are depicted as dashed black lines. The catalytic Zn^{2+} ion is represented as a gray sphere; metal coordination is shown as dashed yellow lines [2].

Compound **17b** (HDAC6 IC_{50} = 17.6 nM, SI = 419), bearing a *m*-fluorobenzyl linker and the N-benzyl-substituted cap group, maintained the monodentate Zn^{2+} coordination, also projecting the fluorine atom towards S568 (Figure 5B). The aromatic linker was able to form multiple π- π stacking interactions, with F680, F620 and H651. Differently from the N-methyl capped compound **16b**, the bulkier cap group was positioned in a more solvent exposed area, probably accounting for the slight drop in potency with respect to **16b**.

In general, both compounds **16b** and **16b** showed an improved selectivity towards HDAC6, compared to their unsubstituted benzyl analogues, with compound **16b** becoming also the most potent HDAC6 inhibitor of this focused series.

We further evaluated the selective specificity of comounds **9a**, **16a,b** and **17a,b** (*Table 1*) by assessing their activity in the acetylation of a HDAC6-specific target (α-tubulin) compared to a class I HDAC-specific target (H3 histone, a substrate of nuclear HDAC isoforms) in a cell-based assay (Figure 6). HeLa cells were treated for 16 h with serial dilutions of the five selected compounds, cell lysates were collected and the acetylation levels of both tubulin and H3 were evaluated by western blot analysis as markers for selective inhibition of HDAC6. As The potent pan-HDACi LAQ824 was ass in parallel as reference. For normalization both GAPDH and Vinculin proteins were immunodetected. Acetyl-tubulin and acetyl-H3 signals detected in western blot were quantified and normalized to signals of vinculin, to obtain an acetyl-tubulin to acetyl-H3 ratio in each sample As shown in Figure 6A, all selected compounds, except for **9a**, showed a dose-response inhibition of HDAC6, indicated by the increase in the amount of acetylated tubulin. On the other side, H3 acetylation increase appeared much lower, especially in comparison to that obtained with the pan-HDAC inhibitor LAQ824. Moreover, **9a** showed almost no effect on either substrate protein, while **16b** and **17b** showed the best ratio of tubulin to H3 acetylation, and a much

higher specificity versus HDAC6 in comparison to LAQ824 reference compound. These data indicated their selective inhibitory activity on HDAC6 enzyme.

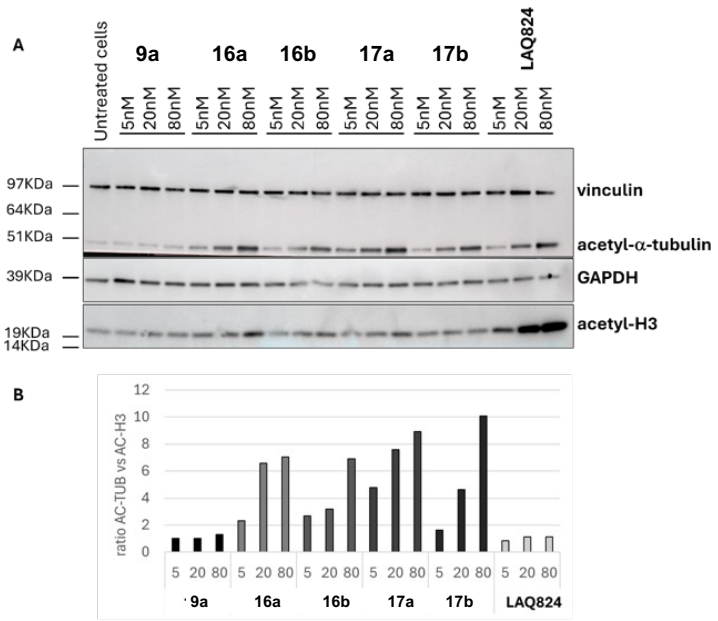


Figure 6. (A) Western blot analysis of acetylated α-tubulin and acetylated histone H3 (AC H3) levels in HeLa Cells treated with 5, 20, 80 nM of the indicated compounds for 16 h at 37 °C. Vinculin served as a loading control. (B) Bands detected with anti-acetyl-tubulin and anti-acetyl-H3 antibodies were quantified and normalized to signals of vinculin, and the ratio of AC α-TUB: AC H3 was calculated and shown [2].

We also analysed the toxicity profiles of designed compounds in HeLa cells, in comparison to the reference compound LAQ824. A viability assay was performed by treating HeLa cells with a dose curve of compounds **9a**, **16a,b**, and **17a,b** and LAQ824 for 72 h. While the reference compound LAQ824 showed an CC50 = 30 nM, all selective HDAC6is showed no significant toxicity, with a maximum activity of 30% inhibition by 24a when tested at 900 nM. Interestingly, compound **17b**, which exhibited the highest HDAC6 specificity in the acetylation

assay (Figure 6A), also emerged as the top performer in the viability assay (Figure 7). Taken together, the cell data converge on the selective HDAC6 target engagement upon treatment with the selected analogues.

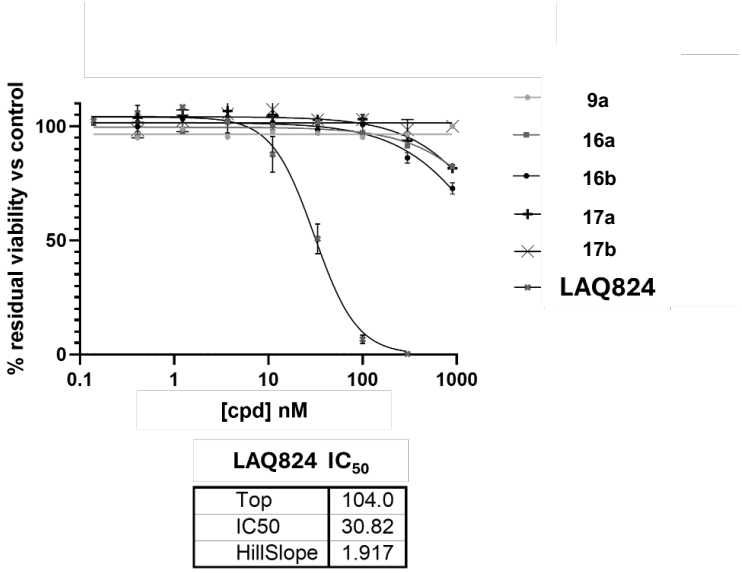


Figure 7. Viability assay of HeLa cells treated with the indicated compounds for 72 h at 37 °C [2].

Once validate the efficacy of the novel 1,3,8-triazaspiro[4,5]decan-4-one cap group, together with the selectivity and safety profiles of our candidates, we aimed to evaluate pharmacokinetic parameters of designed compounds to identify a suitable candidate to be assessed in TNBC models. In particular, designed compounds display an increased Fsp^3 value in comparison to already published inhibitors, which, as discussed in *Chapter 1*, is a key parameter in drug design, able to influence drug physiochemical characteristics such as solubility. Accordingly, as shown in *Table 2*, **17b**, beyond its high potency and selectivity, displays the higher Fsp^3 fraction and, as expected, exhibited the best experimentally determined solubility [2].

Table 2. Fsp^3 quote and experimentally determined solubility for inhibitors **9a**,**b 16b** and **17b**.

Cpd	Fsp^3 quote	Experimental Solubility (µM)
Tubastatin	0.125	< 1 mg/mL (insoluble)
9a	0.333	341
9b	0.364	213
16b	0.364	280
17b	0.286	78

3.1.2 Investigation of structure-activity relationships

In order to further improve the potency and selectivity profile of our newly identified HDAC6is, we embarked a parallel activity of structure-activity relationships studies (*Table 3*). Several derivatives were designed and synthesized to unveil the structural determinants of potency and selectivity for this novel class of inhibitors. We decided to explore several structural decorations on the piperidine nitrogen atom, through the assessment of a variety of functional groups and aryl/alkyl appendages, with the final aim of interrogating the interaction capability and potential further chemical handles for gaining potency and selectivity on HDAC6 over other isoforms.

Based on the chemical nature of the appendages that we anchored to the piperidyl nitrogen we clustered the compounds into three subseries, namely: i) amines subseries, ii) amide subseries and iii) urea, carbamate and oxalamide subseries. Also, three different linkers were selected namely: benzyl, *m*-fluorobenzyl and *m*-difluorobenzyl linkers (Figure 8) [2].

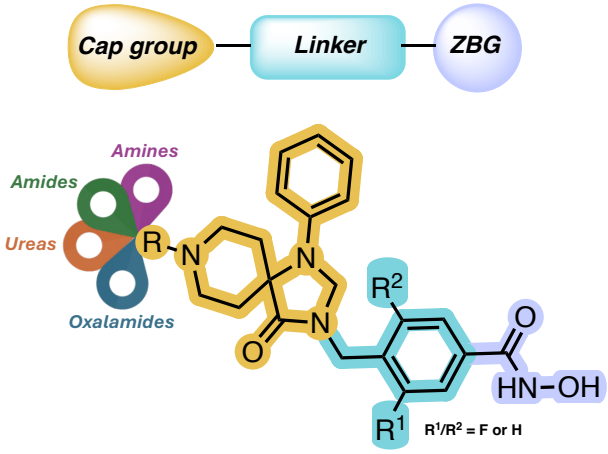


Figure 8. General structures of novel selective HDAC6is bearing 1,3,8-triazaspiro[4,5]decan-4-one cap group.

i) Amine subseries

First, we sought to investigate the outcome of a *m*-difluorobenzyl linkers on the first hit of the series. Therefore, **9b**, **16c** and **17c** were designed as analogues of **9a**, **16a,b** and **17a,b**, respectively. Compound **17c**, featuring the *m*-difluorobenzyl linker, displayed a conserved binding mode in comparison with **17b**; a nice overlap with the fluorinated ligand ITF3985 (PDB ID: 7O2R) could also be observed (Figure 9).

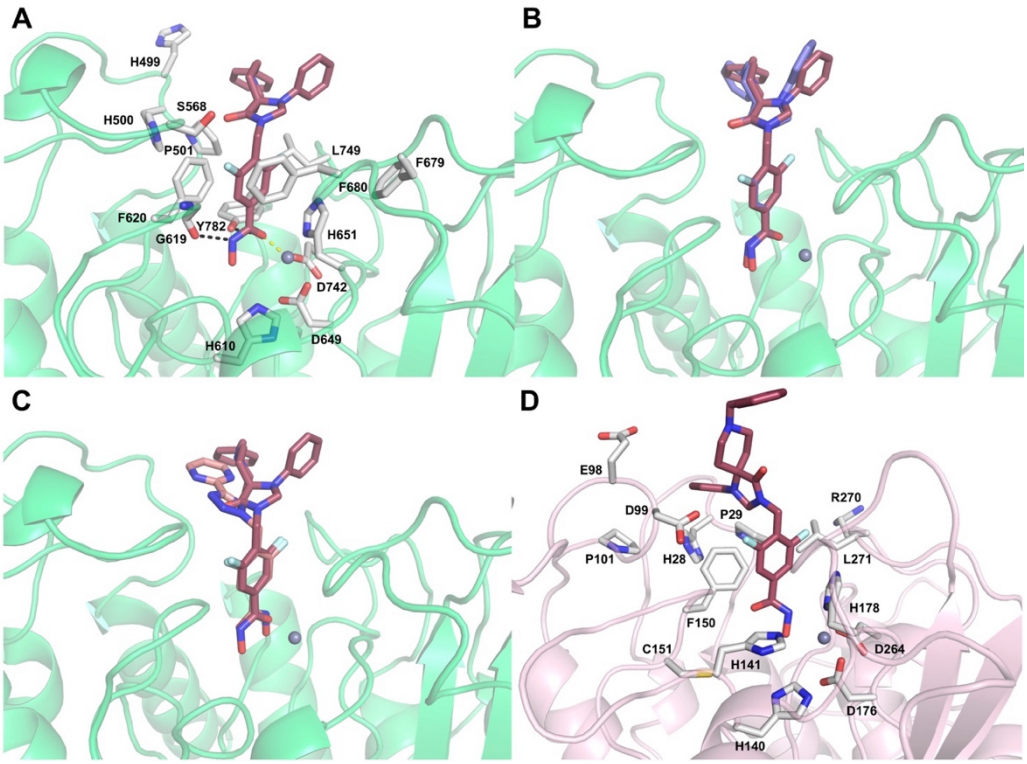


Figure 9. (A) Predicted binding mode of **17c** within *h*HDAC6 active site (PDB 5EDU) represented as green transparent ribbon model. Residues in the active site are displayed as white sticks and labeled. H-bonds discussed in the text are depicted as dashed black lines. The catalytic Zn^{2+} ion is represented as a gray sphere; metal coordination is shown as dashed yellow lines. Overlay of **17c** docked pose with **17b** (B, slate sticks) and ligand ITF3985 (C, salmon sticks) bound to *z*HDAC6 (PDB 7O2R). (D) Predicted binding mode of **17c** within the *h*HDAC1 (PDB: 4BKX) represented as pink transparent ribbon model [2].

As reported in *Table 3*, **17c** displays the highest SI among the series ($IC_{50\ HDAC6}$ = 9.5 nM, Selectivity index (1/6) = 776), likely due to the presence of the di-fluorinated linker group, in combination with the bulky cap group, which further impairs the interaction with the catalytic metal ion in HDAC1, thus explaining the exceptional selectivity profile. Indeed, as previously discussed (*Chapter 1, Introduction – Part 2*) HDAC6 active site is characterized by an aromatic crevice

defined as "*fluorophilic*" by Watson et al., in which the C−F group preferentially binds instead of being oriented out toward the solvent, lined by residues F620 and F680 (F583−F643 in *z*HDAC6, respectively) [113,262]. Aromatic linker fluorination, instead, substantially impairs binding to HDAC1, as compound **17c** docked pose displayed only hydrophobic interactions within this isoform active site (Figure 9).

The exploration of a 3-pyridyl methyl moiety (compounds **18a,b**) on the spiropiperidine nitrogen led to a slight increase in the potency and confirmed the role of linker fluorination for increasing selectivity (**18a**, $IC_{50\ HDAC6}$ = 7.9 nM, Selectivity index (1/6) = 62; **18b**, $IC_{50\ HDAC6}$= 4.6 nM, Selectivity index (1/6) = 337). On the other and, the introduction of *p*-bromo benzyl, a 2-furanylmethyl and a 5-phenyl-2-furanylmethyl, in compounds **19-21** respectively, did not lead to a striking increase of potency nor selectivity (**19**, $IC_{50\ HDAC6}$ = 18.5; **20**, $IC_{50\ HDAC6}$ = 8.4, **21**, $IC_{50\ HDAC6}$ = 18.9 nM).

ii) Amide subseries

In order to evaluate how further modifications could be made at the R level of the general structure, we interrogated a series of amide linkages to the spiropiperidyl nitrogen. An acetamide moiety, although keeping the nanomolar potency, was detrimental for the selectivity (**23**, $IC_{50\ HDAC6}$= 4.6 nM, Selectivity index (1/6) = 50). When investigated a stereochemically defined 2-tetrahydrofuranyl amide moiety, we could again maintain the nanomolar potency and confirm the role of linker fluorination in driving isoform selectivity on HDAC6 (**30a**, $IC_{50\ HDAC6}$= 15.4 nM, Selectivity index (1/6) = 38; **30b**, $IC_{50\ HDAC6}$= 13.1 nM, Selectivity index (1/6) = 189), although to a lesser extent with respect to the amine series. We also designed compounds **31a,b**, in which *N*-methylpyrrolo-2-carboxamide substitution - already explored for the development of potent HDAC6 inhibitors - was interrogated. According to other compounds outcome, the insertion of a fluorine containing linker strongly

boosted the selectivity profile (**31a**, $IC_{50\ HDAC6}$= 12.3 nM, Selectivity index (1/6) = 79; **31b**, $IC_{50\ HDAC6}$= 5.6 nM, Selectivity index (1/6) = 324).

The insertion of a 3-methylfurane-2-carboxamide in combination with a simple benzyl linker (**32**) led to a comparable outcome of the pyrrole containing compound **31a** (**32**, $IC_{50\ HDAC6}$= 12.1 nM, Selectivity index (1/6) = 7). Similarly, the nicotinamide containing derivatives **33a,b** do not deviate from the general trend of potency and selectivity in absence and in presence of the fluoro substituted linker moiety (**33a**, $IC_{50\ HDAC6}$= 27.7 nM, Selectivity index (1/6) = 60; **33b**, $IC_{50\ HDAC6}$= 5.9 nM, Selectivity index (1/6) = 249). The 2-benzofuranyl carboxamide derivative **34** also maintained superimposable potency and selectivity values ($IC_{50\ HDAC6}$= 7.8 nM, Selectivity index (1/6) = 308), while the exploration of a 5-phenyl-2-furanyl carboxamide led to a considerable drop in potency (**35**, $IC_{50\ HDAC6}$= 176.4 nM).

iii) Carbamate, urea and oxalamide subseries

Despite the mutagenicity of the carbamate group and its metabolic liability, making its presence undesirable in medicinal chemistry, compound **7** was reasonably tested since it was derived from a key synthetic intermediate. Compound **7** showed displayed moderate potency and selectivity ($IC_{50\ HDAC6}$= 19.1 nM, Selectivity index (1/6) = 130) probably ascribable to the ability of the carbonyl oxygen placed on the *tert*-butyl carbamate group to accept a key hydrogen bond by Asp497 in the L1 loop of enzyme pocket.

Additionally, with the aim to further explore the interaction between the cap group and the HDAC6 pocket, other compounds bearing different functionalities on the R group, were designed (Figure 8). In particular, compounds bringing an urea-based capping group are particularly interesting, since urea moiety has been demonstrated to confer potency and selectivity, as demonstrated in NextA, a HDAC6 inhibitor designed by Kozikowski et al. A cyclopentyl, phenethyl and benzyl urea derivatives (compounds **42**, **43** and **44**, respectively) in combination

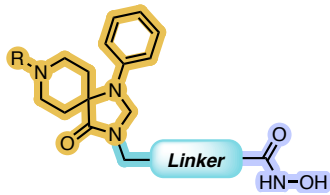
with a simple benzyl linker were first interrogated, demonstrating notable potency, although with only moderate selectivity (**42**, $IC_{50\ HDAC6}$= 15.7 nM, Selectivity index (1/6) = 72; **43**, $IC_{50\ HDAC6}$= 11.5 nM, Selectivity index (1/6) = 106; **44**, $IC_{50\ HDAC6}$= 12.3 nM, Selectivity index (1/6) = 100). A smaller ethyl urea, in combination with a fluoro containing linker, surprisingly led to a substantial loss of selectivity (**41**, $IC_{50\ HDAC6}$= 18.1 nM, Selectivity index (1/6) = 22.7), while selectivity was restored with a 2-furanylmethyl urea containing capping group (**45**, $IC_{50\ HDAC6}$= 26.7 nM, Selectivity index (1/6) = 375).

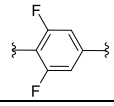
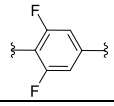
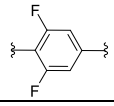
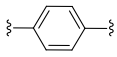
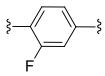
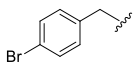
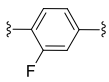
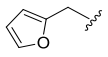
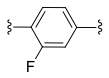
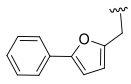
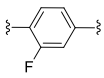
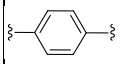
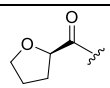
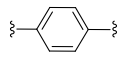
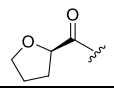
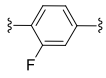
As a further structural decoration, we sought to explore compounds featuring an oxalamide-based capping group, since this functionality could guarantee a multiple contact point for establishing polar interactions within HDAC6 binding site. Compounds **48** and **49**, bearing a pyrrolidyl and dimethyl oxalamide respectively, in combination with a *m*-fluorobenzyl linker, were synthesized demonstrating a slight loss in potency with respect to their urea counterparts and only moderate selectivity (**48**, $IC_{50\ HDAC6}$= 34.5 nM, Selectivity index (1/6) = 195.3; **49**, $IC_{50\ HDAC6}$= 25.2 nM, Selectivity index (1/6) = 184.8).

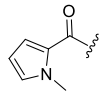
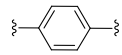
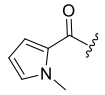
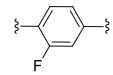
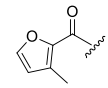
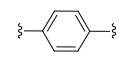
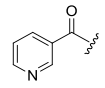
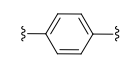
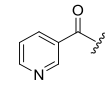
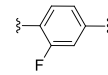
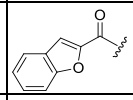
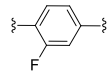
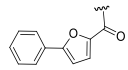
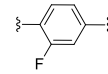
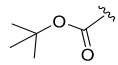
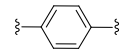
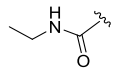
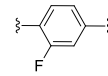
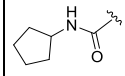
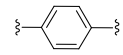
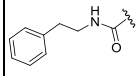
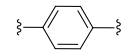
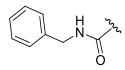
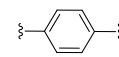
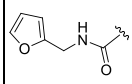
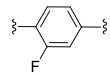
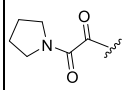
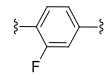
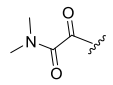
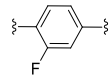
In general, carbamates, ureas and oxalamides, being more constrained, due to the augmented planarity and reduced rotational freedom, might well lose the occasional hydrogen bond interactions that are observed between capping group and protein atoms, the majority of which are reported to be mediated by intervening water molecules.

Consistently with *in vitro* potency and selectivity data, pharmacokinetic profile and outcome on cellular settings, compound **10c** and **11c** were selected to be engaged in efficacy studies on TNBC models.

Table 3. Structures and inhibitory activities (HDAC6 and HDAC1) of designed inhibitors.



Cpd class	Cpd	R	Linker	IC_{50} HDAC6 (nM)	IC_{50} HDAC1 (nM)	SI
Amines	**9b**	H		58.2	39% @ 10uM	N.D
	16c	Me		10.4	6101.3	587
	17c	Bn		9.5	7374.5	776
	18a			7.9	486	62
	18b			4.6	1548	337
	19			18.5	5767.5	312
	20			8.4	1454.6	173
	21			18.9	60% @ 10uM	ND
Amides	**23**			19.9	1058	50
	30a			15.4	577	38
	30b			13.1	2475.9	189

	31a			12.3	969	79
	31b			5.6	1814.9	324
	32			12.1	927.5	77
	33a			27.7	1667.3	60
	33b			5.9	1467.2	249
	34			7.8	2398.7	308
	35			176.4	48% @ 10uM	ND
Carbamates ureas and oxalamides	**7**			19.1	2473	130
	41			18.1	410.9	22.7
	42			15.7	1131.2	72
	43			11.5	1219	106
	44			12.3	1235.1	100
	45			26.7	41% @ 10uM	ND
	48			25.2	4662.0	184.8
	49			34.5	6743.0	195.3

SI = selectivity index; ND = not determined

3.1.3 Crystallographic studies in complex with zHDAC6 CD2

In collaboration with Professor David W. Christianson (University of Pennsylvania), we were able to obtain X-ray crystal structures of compounds **16b** and **18b** in complex with *z*HDAC6 CD2, further corroborating *in silico* binding studies (*unpublished data*). The hydroxamate group of **16b** coordinates to the catalytic Zn^{2+} ion with monodentate geometry through its carbonyl group (Zn^{2+}•••O separation = 2.3 Å) and does not displace the zinc-bound water molecule (Figure 10). Moreover, the hydroxamate group is tending toward a bidentate coordination interaction, but the hydroxamate hydroxyl group is 2.9 Å from the Zn^{2+} ion, which is too long for inner-sphere metal coordination. Possibly, the observed binding mode represents an intermediate state on the pathway to fully bidentate coordination. In addition to Zn^{2+} coordination by the hydroxamate carbonyl group, the hydroxamate hydroxyl group forms a hydrogen bond with Y745 and the hydroxamate NH group makes a van der Waals contact with the Zn^{2+}-bound water molecule. The Zn^{2+}-bound water molecule (Zn^{2+}•••O separation = 1.8 Å) is hydrogen bonded to H573 and H574, as observed in the unliganded enzyme (Figure 10).

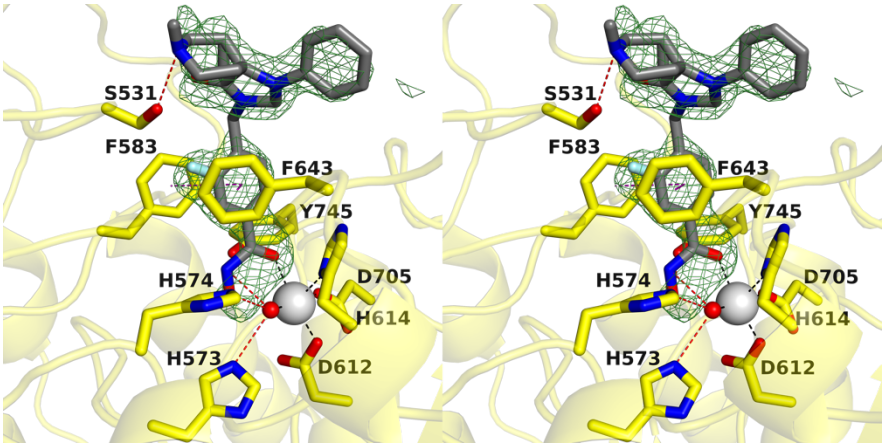


Figure 10. Stereoscopic view of polder omit map contoured at 3σ showing the binding of **16b** in the active site of *z*HDAC6 CD2 (PDB no deposited yet).

The aromatic linker of **16b** binds in the aromatic crevice formed by F583 and F643, where it engages in offset π-π stacking interactions. The electron density map (Figure 10) clearly reveals that the fluorine substituent on the aromatic ring preferentially binds in the aromatic crevice rather than being oriented out toward solvent. This binding preference has been previously observed for other monofluorinated aromatics rings (e.g. Bavarostat, *Chapter 1, **35**, Figure 29c*), so the F583-F643 aromatic crevice is *fluorophilic* in nature. Electron density for the spiro linkage in the capping group is partially incomplete, perhaps reflecting some disordered binding in the outer active site cleft. The best fit to the electron density indicates that the capping group adopts slightly different conformations in monomers A and B in the asymmetric unit. The 6-membered piperidine ring adopts a favorable chair conformation and forms a hydrogen bond with S531 in monomer A (Figure 10). In monomer B, the capping group does not make direct contacts with any nearby residues. The lack of specific interactions to anchor the capping group in place is consistent with the apparent conformational flexibility and disorder.

According to their structural similarity (N-methylpyridine group in place of the N-methyl substituent in compound **16b**), the hydroxamate carbonyl group of compund **18b** coordinates to Zn^{2+} and does not displace the Zn^{2+}-bound water molecule. Also, the capping group of **18b** is largely characterized by weak or missing electron density, suggestive of conformational flexibility and disorder (Figure 11).

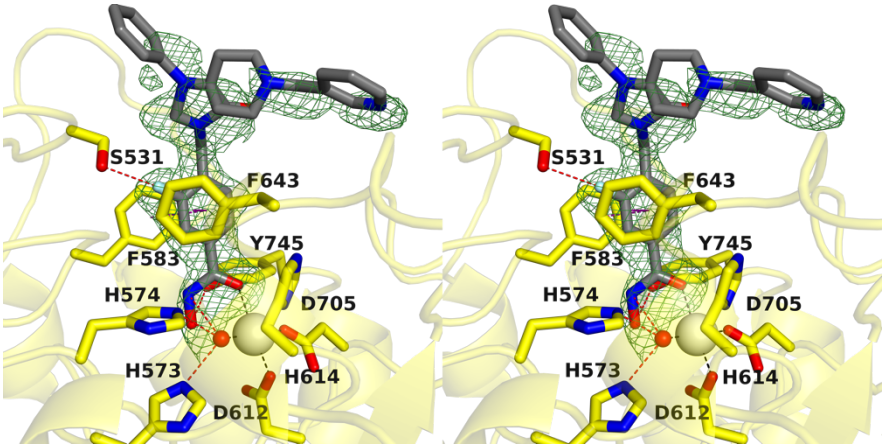


Figure 11. Stereoscopic view of polder omit map contoured at 3σ showing the binding of **18b** in the active site of *z*HDAC6 CD2 (PDB no deposited yet).

*3.1.4 Biological Studies on optimized derivatives **16c** and **17c***

*- Target engagement studies by Western Blot analysis for **16c** and **17c** and Hela cells viability*

Based on *in vitro* potency, selectivity data, and pharmacokinetic profile among all the above-described compounds, **16c** and **17c** were selected for further cell-based studies.

First, to further characterize the behaviour of selected compounds, we also assessed the potency of the optimized compounds **16c** and **17c** on Class I HDAC8, since it is able to both recognize histone and non-histone substrates and it is ubiquitously expressed in nucleus and cytoplasm. As reported in *Table 4*, both **16c** and **17c** confirmed their selective profile towards HDAC6 enzyme (for **23c**, Selectivity index (8/6) = 347; for **24c**, selectivity index (8/6) = 343).

Table 4. Inhibitory Activities of Inhibitors **16c** and **17c** on HDAC8 in comparison with pan-HDACis Panobinostat and LAQ824.

Cpd	16c	17c	Panobinostat	LAQ824
IC50 HDAC8 (nM)	3613	3258	1182	90.70

Moreover, similarly to what already done on the first set of compounds, we repeated the cell-based acetylation assay in HeLa cells for compounds **16c** and **17c**. As previously described, HeLa cells were treated with serial dilutions of compounds **16c** and **17c** for 16 h at 37 °C, in parallel to a dose curve of the reference pan-HDACi LAQ824. Cell lysates were loaded on a 4-12% acrylamide gel for western blot analysis of the acetylated HDAC targets a-tubulin and H3 histone. As shown in Figure 10, both compounds showed a clear increase in the acetylation of tubulin, higher than that observed with LAQ824. Notably, the two new compounds showed a complete absence of H3 acetylation induction.

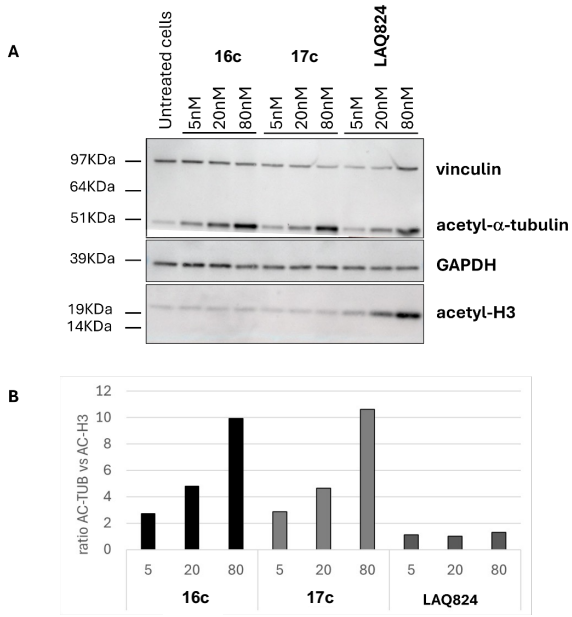


Figure 12. (A) Western blot analysis of acetylated α-tubulin and acetylated histone H3 levels in HeLa Cells treated with 5, 20, 80 nM of the indicated compounds for 16 h at 37 ºC. Vinculin served as a loading control. (B) Bands detected with anti-acetyl-tubulin and anti-acetyl-H3 antibodies were quantified and normalized to signals of vinculin, and the ratio of AC α-TUB: AC H3 was calculated and shown [2].

Compounds **16c** and **17c** were also tested in a viability assay to control their possible toxicity. As expected, none of them induced cell death, while the pan-HDACi LAQ824 showed a CC_{50} around 30 nM (Figure 13).

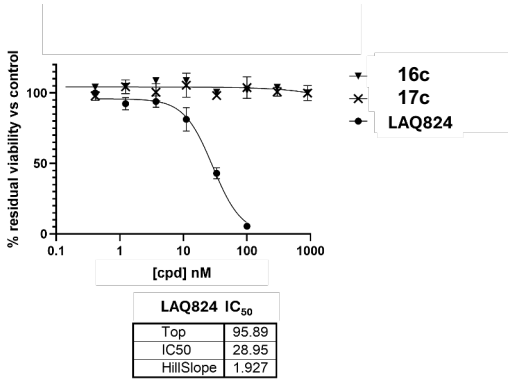


Figure 13. Viability assay of HeLa cells treated with compounds **16c** and **17c** for 72 h at 37 ˚C [2].

Taken together, these data showed that optimized compounds **16c** and **17c** were highly specific for HDAC6 and completely clean in the cell-based toxicity assay and encouraged us to engage the compounds in efficacy studies on TNBC models.

- *Compounds **16c** and **17c** exert antiproliferative effect on MDA-MB-231 cells through selective inhibition of HDAC6*

In order to select the breast cancer cell line for the assessment of our newly conceived HDAC6is, we first analyzed the expression levels of HDAC6 in normal human breast cells (MCF10-A), as well as in two distinct human triple-negative breast cancer cell lines (MDA-MB-231 and MDA-MB-468) and a human estrogen/progesterone receptor-positive breast cancer cell line (MCF-7) using real-time qPCR. As shown in Figure 14A, the mRNA expression level of HDAC6 was significantly increaed in MDA-MB-231 in comparison to other breast cell lines. Therefore, we therefore investigated the effect of the optimized HDAC6is **16c** and **17c** on the proliferation of the human TNBC cells MDA-MB-231. MDA-MB-231 cells were treated with **16c** and **17c** at various concentrations

for 48 h and the cell viability was measured using colorimetric MTT assay (Figure 14B). Compounds **16c** and **17c** decreased the cell viability of MDA-MB-231 cells in a concentration-dependent manner, with an IC_{50} of 25.02 μM and 26.97 μM for **16c** and **17c**, respectively. More in detail, MDA-MB-231 cells were treated with both **16c** and **17c** (at 3 and 10 μM) or the pan-HDACi LBH-589 (3 μM) for 24 h, and whole-cell lysates were subjected to Western Blot analysis in order to quantify the levels of acetyl α-tubulin and acetyl histone H3 (Figure 14C). As shown, the treatment of MDA-MB-231 cells with **16c** and **17c** concentration-dependently increased the acetylation of α-tubulin, thus confirming direct inhibition of HDAC6 also in TNBC cell lines and the molecular mechanism underlying **16c** and **17c** antiproliferative effect on TNBC cells. In addition, conversely to the pan-HDACi LBH-589, compounds **16c** and **17c** did not affect the H3 acetylation, thus supporting their selective inhibitory profile on HDAC6 isoform activity (Figure 14D,E). Comparison between the two selective inhibitors highlights stronger effect of **17c** with respect to compound **16c** in increasing the levels of acetylated α-tubulin.

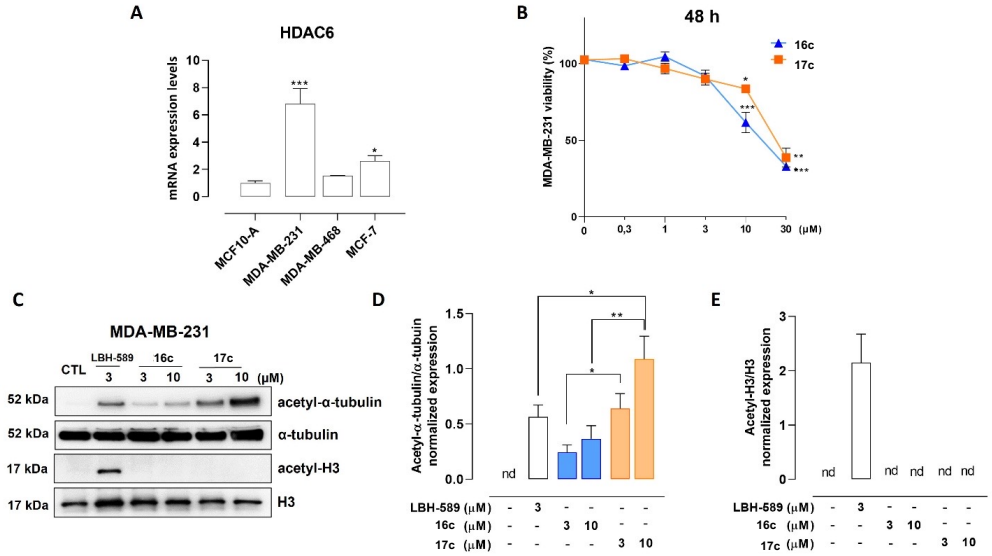


Figure 14. 16c and **17c** affect MDA-MB-231 cell proliferation through the selective inhibition of HDAC6. (A) mRNA expression levels of HDAC6 in non-tumorigenic epithelial cell line (MCF-10A), triple negative (MDA-MB-231, MDA-MB-468) and estrogen/progesterone receptor positive (MCF-7) breast cancer cell lines was evaluated by qPCR analysis. Data are expressed as $2^{-\Delta\Delta ct}$ relative to ribosomal protein S16. *$p < 0.1$, ***$p < 0.001$ vs. MCF-10A; (B) MTT proliferation assay performed in MDA-MB-231 cells exposed or not to **16c** or **17c** (0.3-30 μM) for 48 h. (C) Representative blots of acetyl-α-tubulin, α-tubulin and acetyl-H3. MDA-MB-231 cells were treated with **16c**, **17c** (3 and 10 μM) or the pan-HDAC inhibitor LBH-589 (3 μM) for 24 h and whole-cell lysates were subjected to western blotting analysis. (D-E) Normalized quantitative analysis of acetyl-α-tubulin and acetyl-H3 in MDA-MB-231 were obtained using total α-tubulin and H3 as loading control, respectively. Each point is the mean ± SEM of three independent experiments (*n=3*) with similar results. nd indicates when a protein was not detected. *$p < 0.1$, **$p < 0.01$, ***$p < 0.001$ vs CTL [2].

- *Compounds **16c** and **17c** induce autophagy in MDA-MB-231 cells*

In the next step, we explored whether the inhibition of HDAC6 using compounds **16c** and **17c** could modulate autophagy flux in MDA-MB-231 cells. To further examine autophagy in response to compound treatment, a transcriptomic analysis using quantitative PCR (qPCR) was carried out on MDA-MB-231 cells exposed to **16c** and **17c** at 10 μM for 6 h. We found that the mRNA expression of autophagy-related genes, including ULK1, BNIP3, Lamp1 and Beclin1, was significantly increased by both compounds (Figure 15).

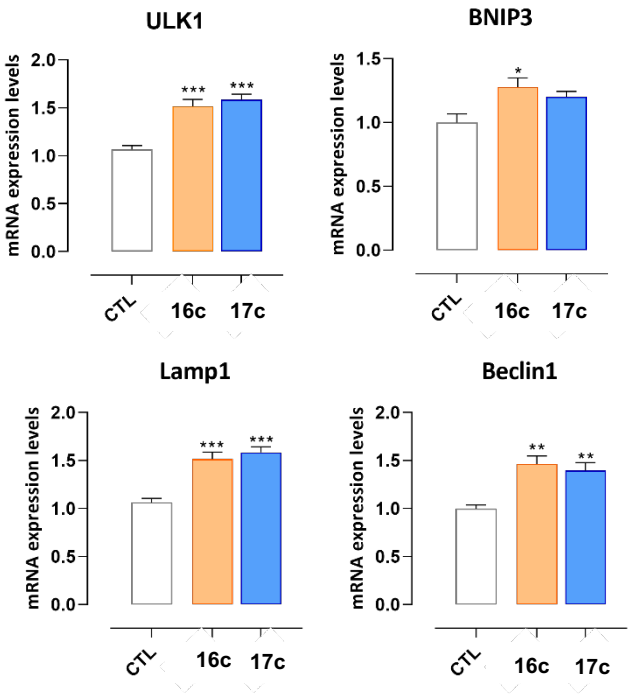


Figure 15. mRNA expression levels of autophagy markers ULK1, BNIP3, Lamp1 and Beclin1 in MDA-MB-231 human triple negative breast cancer cells following the treatment with **16c** and **17c** (10 μM) for 6 h. Data are expressed as $2\Lambda^{-\Delta\Delta ct}$ relative to ribosomal protein S16. Each data point represents the mean ± SEM of three independent experiments ($n=3$). *$p < 0.1$, **$p < 0.01$, ***$p < 0.001$ vs. CTL [2].

- *Compounds **16c** and **17c** inhibit migration in MDA-MB-231 cells*

Starting from these results and to better characterize the potential anticancer activity of **16c** and **17c**, we investigated their effects on MDA-MB-231 cell migration performing a wound healing assay. For this purpose, cells were treated with non-cytotoxic concentration of **16c** or **17c** (1 and 3 μM) and quantitatively evaluated in terms of percentage of the wound coverage after 24 and 48 h of treatment in comparison to untreated cells (Figure 16A). Our results showed that the wound healing ability of cells treated with both HDAC6 selective

inhibitors decreased significantly compared to that observed in the control. If after 24 h of treatment the wound coverage for both was around 30%, after 48 h **16c** seemed to be more potent maintaining the wound coverage at around 30% against the 50% for **17c** (Figure 16B).

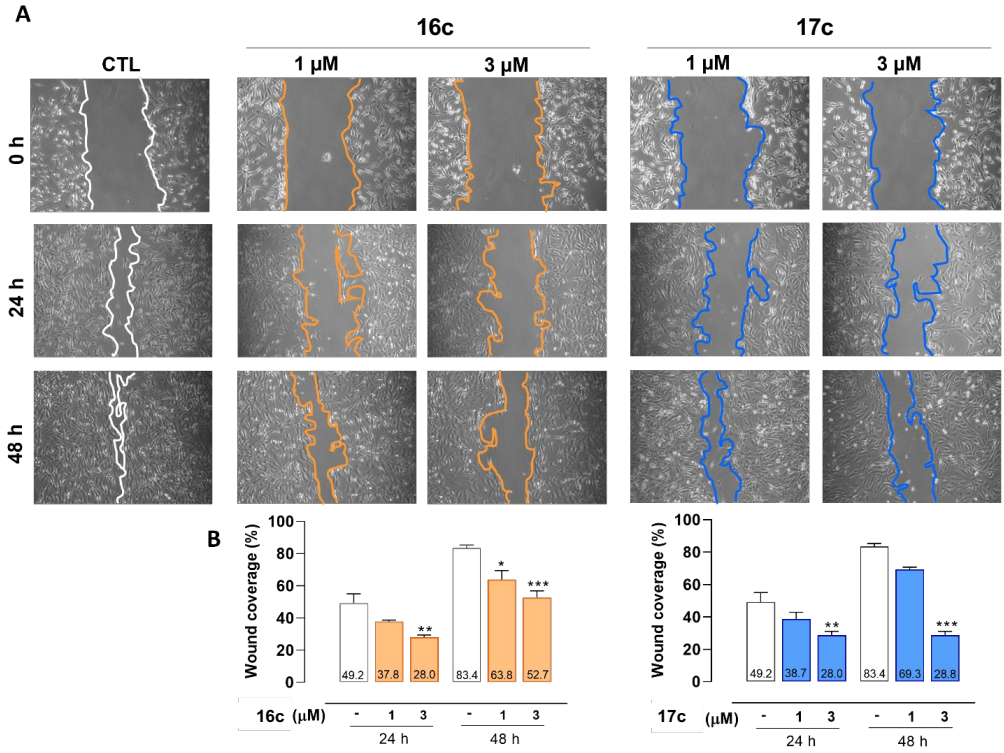


Figure 16. Effect of **16c** and **17c** on MDA-MB-231 cell migration. (A) Images were captured at 0 h and after 24 and 48 h of treatment with or without **16c** and **17c** (1 and 3 μM). (B) The percentage of the wound coverage was quantified measuring the scratch area at each time and concentration and expressed using the formula $\frac{100-A}{A_0}$ x 100 (A= scratch area of tested condition at each time; A_0= scratch area of same condition at 0 h). Each point represents the mean ± SEM of three independent experiments. *$p < 0.1$, **$p < 0.01$, ***$p < 0.001$ vs. CTL [2].

3.2 Conclusions

We disclosed a novel class of spiro-fused compounds acting as potent and selective HDAC6is bearing a novel spirofused cap-group, namely 1,3,8-triazaspiro[4,5]decan-4-one core, which showed optimum 3D features for preferential HDAC6 inhibition. After determination of HDAC6 potency, selectivity over HDAC1 isoform, experimental solubility and target engagement in HeLa cells, we embarked a structure-based optimization based on the information deriving from this focused set of HDAC6is. Accordingly, three different subsets of compounds were designed, based on structural modifications on N^1 of piperidine ring, namely (i) amine, (ii) amides, and (iii) carbamates, ureas and oxalamides, and bearing hydroxamate as ZBG. All compounds displayed nM potency on HDAC6 and high selectivity towards nuclear HDAC1 and HDAC8 (assessed for most performing compounds **16c** and **17c**), thereby confirming the suitability of the novel conceived spirofused cap group coupled with phenyl-hydroxamate linker-ZBG moieties.

Upon detection of higher mRNA levels of HDAC6 in MDA-MB-231 human TNBC cells, we have evaluated the effects of compounds **16c** and **17c** on the viability of the same cell line. Further, we have registered the increase of mRNA expression of ULK1, BNIP3, Lamp1 and Beclin1 autophagic markers in MDA-MB-231 cells upon treatment with compounds **16c** and **17c** (at 10 μM for 6h), thus supporting the hypothesis of the involvement of the autophagic machinery in cell death induction upon selective HDAC6 inhibition. Scratch assay revealed for the newly conceived compounds a very potent effect on inhibiting the migration process in MDA-MB-231 cells. Taken together, our results underscore the key role of HDAC6 in TNBC tumorigenesis and cancer progression, providing a solid groundwork to reshape classical chemotherapeutic approaches and enrich the armamentarium of therapeutic options to face this aggressive type of cancer.

3.3 Experimental section

3.3.1 Chemistry

General procedure for the alkylation of tert-butyl 4-oxo-1-phenyl-1,3,8-triazaspiro[4.5]decane-8-carboxylate (**4**). To a suspension of **4** in dry THF, 60 % mineral oil dispersion NaH (1.5 eq) was added and the resulting solution was allowed to stir at 25 °C. After 30 min, the corresponding alkyl bromide (1.5 eq, **5a**, **5b** or **5c**) was added. The reaction mixture was allowed to stir at 25 °C for 24 h, then concentrated under reduced pressure. The residue was dissolved in EtOAc and washed with $NaHCO_3$ saturated solution for three times. Organic layer was dried over Na_2SO_4 and evaporated under reduced pressure. Crude material was purified by Biotage® ISOLERA flash chromatography (EP/EtOAc 75:25 v/v to 50:50 v/v).

General procedure for Boc group deprotection. *General procedure A*. To a stirred solution of the corresponding Boc protected amine (0.1 mmol) in MeOH (6 mL), acetyl chloride (2 mL) was added, and the resulting reaction mixture allowed to stir at 25 °C. After 1 h, the reaction mixture was concentrated under reduced pressure, the residue dissolved in EtOAc and washed with $NaHCO_3$ saturated solution for three times. Organic layer was dried over Na_2SO_4 and evaporated under reduced pressure. The obtained residue was used in the next synthetic step without further purification. *General procedure B.* To a stirred solution of the corresponding Boc protected amine in DCM, 4 M HCl in dioxane was added (10 eq) and the resulting solution allowed to stir at 25 °C. After 1 h, the reaction mixture was concentrated under vacuum, the residue was dissolved in EtOAc and washed with $NaHCO_3$ saturated solution for three times. Organic layer was dried over Na_2SO_4 and evaporated under reduced pressure. The obtained deprotected amine was used in the next synthetic step without further purification.

General procedure for coupling reaction. To a solution of the corresponding amine (**8a**, **8b**, or **8c**, 1 eq) and the opportune carboxylic acid (1.15 eq) in dry

DCM, NMM (1.5 eq) was added followed by HBTU (1.5 eq) and the resulting mixture was allowed to stir at 25 °C for 24 h.

General procedure for the synthesis of urea-capped derivatives. To a cooled solution of the corresponding amine (**8a**, **8b**, or **8c**, 1 eq) in DCM, TEA (1.1 eq) was added followed by the opportune isocyanate (1.05 eq). The resulting mixture was stirred at 25 °C for 2 h, then quenched with saturated aqueous NH_4Cl solution and extracted with DCM. Organic layer was washed with $NaHCO_3$ saturated solution and brine, dried over Na_2SO_4 and evaporated under reduced pressure.

General procedure for reductive amination. To a stirred solution of the corresponding amine (**8a**, **8b**, or **8c** 1 eq) in MeOH, a catalytic amount of acetic acid was added followed by the opportune aldehyde (1.2 eq) and the reaction mixture allowed under stirring at 25 °C. After 1 h, $NaBH_3CN$ (1.6 eq) was added and the resulting mixture allowed under stirring for 18 h at 25 °C. MeOH was evaporated under vacuum, the residue dissolved in EtOAc and washed with distilled H_2O for three times. Organic layer was dried over Na_2SO_4 and evaporated under reduced pressure.

General procedure for the synthesis of hydroxamic acids. To a stirring solution of the corresponding methyl ester in a mixture of DCM/MeOH (1:1), 50% aqueous hydroxylamine (100 eq) was added followed by methanolic 4 M potassium hydroxide (50 eq). After 1 h, the reaction mixture was quenched by the addition of 6 N HCl and concentrated under vacuum. Crude material was purified by silica gel column chromatography (DCM/MeOH/NH_4OH 20:1:0.05 v/v to 20:1:1 v/v) giving desired hydroxamic acids.

tert-Butyl 4-carbamoyl-4-(phenylamino)piperidine-1-carboxylate (2). *Step 1.* To a cooled solution of aniline (5.02 mmol, 0.46 mL) and N-Boc-piperidone (5.02 mmol, 1g) in AcOH (4 mL), TMSCN was added (5.12 mmol, 0.640 mL) and the resulting mixture allowed to stir for 24 h at 25 °C. Saturated aqueous NH_4Cl solution was added, the mixture was filtered and the filter cake dried under

reduced pressure to afford *tert-butyl 4-cyano-4-(phenylamino)piperidine-1-carboxylate* with 66 % of yield (1.002 g). *Step 2*. To a solution of *tert-butyl 4-cyano-4-(phenylamino)piperidine-1-carboxylate* (3.34 mmol, 1 g) in MeOH (4 mL) 1 M aqueous sodium hydroxide was added (6 mL). After 15 min, 30 % aqueous hydrogen peroxide solution (0.400 mL) was added dropwise, and the reaction mixture was stirred for 18 h at 25 °C. The mixture was dried under reduced pressure, and the residue partitioned between H_2O (20 mL) and EtOAc (20 mL). Organic layer was dried over Na_2SO_4 and evaporated under reduced pressure. The reaction crude was purified by silica gel column chromatography (DCM, DCM/MeOH 98:2 v/v to 95:5 v/v), giving the desired product 9 with 60% yield (642.7 mg).

^{1}H NMR (700 MHz, CDCl3) δ 7.11 (t, J = 7.9 Hz, 2H), 6.82–6.76 (m, 3H), 3.86–3.73 (m, 2H), 3.15–3.09 (m, 2H), 2.15–2.10 (m, J = 13.4 Hz, 2H), 1.67–1.61 (m, 2H), 1.33 (s, 9H).

^{1}H NMR (400 MHz, DMSO-d6) δ 7.11–7.04 (m, J = 10.4, 5.4 Hz, 2H), 6.63–6.56 (m, J = 7.7 Hz, 2H), 3.63–3.55 (m, 1H), 3.16–3.05 (m, 1H), 1.86 (m, J = 30.1, 20.1, 9.1 Hz, 3H), 1.40 (s, 6H).

tert-Butyl 4-oxo-1-phenyl-1,3,8-triazaspiro[4.5]dec-2-ene-8-carboxylate (3). A mixture of intermediate 10 (2 mmol, 642 mg) and triethyl orthoformate (7.5 mL) was stirred at 150 °C for 12 h in presence of a catalytic amount of acetic acid. The reaction mixture was concentrated under reduced pressure to remove volatile components, and the brown solid reaction crude was employed in the next step without further purification.

tert-Butyl 4-oxo-1-phenyl-1,3,8-triazaspiro[4.5]decane-8-carboxylate (4). To a cooled solution of intermediate 10 (1.56 mmol, 513.86 mg) in MeOH (6 mL), sodium borohydride (2.028 mmol, 76.72 mg) was added, and the resulting mixture allowed under stirring for 30 min at 25 °C. The solvent was removed under reduced pressure and the residue partitioned between H_2O (15 mL) and

EtOAc (20 mL). The organic layer was collected, and the aqueous layer extracted three times with ethyl acetate. The combined organic layers were dried over anhydrous Na_2SO_4 and concentrated under reduced pressure. The residue was purified by silica gel column chromatography (Hex/EtOAc 75:25 v/v) to afford the desired product **4** as a pale yellow solid with 64 % yield (328 mg).

^{1}H NMR (400 MHz, CDCl3) δ 7.28–7.27 (m, 2H), 7.24–7.22 (m, 3H), 6.92 (s, 4H), 6.86 (t, J = 7.3 Hz, 6H), 6.77–6.73 (m, J = 8.0 Hz, 10H), 4.76 (s, 11H), 4.13–3.94 (m, J = 28.3, 21.2 Hz, 10H), 3.60–3.45 (m, J = 21.6 Hz, 10H), 2.61–2.48 (m, 10H), 1.75–1.66 (m, J = 13.6 Hz, 12H), 1.51 (s, 49H).

tert-Butyl 3-(4-(methoxycarbonyl)benzyl)-4-oxo-1-phenyl-1,3,8-triazaspiro[4.5]decane-8-carboxylate (6a). Compound **6a** was synthesized following the generical procedure for the alkylation of *tert-butyl 4-oxo-1-phenyl-1,3,8-triazaspiro[4.5]decane-8-carboxylate* (**4**, 3.06 mmol, 1 g) providing compound **6a** with 53 % yield (780 mg)

MS (ESI) m/z calc. $[M+H]^+$ for $C_{27}H_{34}N_3O_5^+$: 480.25; found: 480.0.

^{1}H NMR (700 MHz, CDCl3) δ 8.04 (d, J = 8.3 Hz, 2H), 7.35 (d, J = 7.9 Hz, 2H), 7.21 (t, J = 7.2 Hz, 2H), 6.83 (t, J = 7.3 Hz, 1H), 6.69 (d, J = 8.4 Hz, 2H), 4.67–4.63 (m, 2H), 4.57 (s, 2H), 4.13 (s, 1H), 4.01 (d, J = 19.5 Hz, 1H), 3.92 (s, 3H), 3.61 (d, J = 45.3 Hz, 2H), 2.57 (d, J = 38.0 Hz, 2H), 1.66 (s, 2H), 1.51 (s, 9H).

tert-Butyl 3-(2-fluoro-4-(methoxycarbonyl)benzyl)-4-oxo-1-phenyl-1,3,8-triazaspiro[4.5]decane-8-carboxylate (6b). Compound **6b** was synthesized following the generical procedure for the alkylation of *tert-butyl 4-oxo-1-phenyl-1,3,8-triazaspiro[4.5]decane-8-carboxylate* (**4**, 1.21 mmol, 400 mg) providing compound **6b** with 68% yield (408 mg).

MS (ESI) m/z calc. $[M+H]^+$ per $C_{27}H_3F_3N_3O_5^+$: 498.24; found: 498.0.

^{1}H NMR (400 MHz, CDCl3) δ 7.84 (dd, J = 7.9, 1.6 Hz, 1H), 7.76 (dd, J = 10.3, 1.6 Hz, 1H), 7.41 (t, J = 7.6 Hz, 1H), 7.25–7.19 (m, 2H), 6.85 (tt, J = 7.4, 1.0 Hz,

1H), 6.75–6.67 (m, 2H), 4.72 (s, 2H), 4.63 (s, 2H), 4.14–3.99 (m, 2H), 3.93 (s, 3H), 3.58 (s, 2H), 2.54 (s, 2H), 1.69–1.59 (m, 2H), 1.51 (s, 9H).

tert-Butyl 3-(2,6-difluoro-4-(methoxycarbonyl)benzyl)-4-oxo-1-phenyl-1,3,8-triazaspiro[4.5]decane-8-carboxylate (6c). Compound **6c** was synthesized following the generical procedure for the alkylation of *tert-butyl 4-oxo-1-phenyl-1,3,8-triazaspiro[4.5]decane-8-carboxylate* (**4**, 1.32 mmol, 471 mg). Crude material was purified by silica gel column chromatography (EP/EtOAc 70:30 v/v) providing compound **6c** with 30% yield (220 mg).

^{1}H NMR (700 MHz, CDCl3): δH 7.54 (2H, d, J = 7.2 Hz), 7.15 (2H, t, J = 7.6 Hz), 6.77 (1H, t, J = 7.2 Hz), 6.64 (2H, d, J = 8.1 Hz), 4.71 (2H, s), 4.53 (2H, s), 4.02–3.96 (1H, m), 3.87 (3H, s), 3.58–3.42 (2H, m), 2.45–2.34 (2H, m), 1.58–1.52 (3H, m), 1.43 (9H, s).

tert-Butyl 3-(4-(hydroxycarbamoyl)benzyl)-4-oxo-1-phenyl-1,3,8-triazaspiro[4.5]decane-8-carboxylate (7). Compound **7** was prepared starting from intermediate **6a** (0.181 mmol, 71 mg). following the general procedure for the preparation of hydroxamic acids with 83% yield (30 mg).

(ESI) m/z calc. $[M+H]^+$ for $C_{26}H_{33}N_4O_5^+$: 481.24; found: 481.0.

^{1}H NMR (400 MHz, DMSO-d6) δ 7.76 (d, J = 7.8 Hz, 2H), 7.38 (d, J = 8.1 Hz, 2H), 7.19 (d, J = 8.1 Hz, 2H), 6.78 (t, J = 7.3 Hz, 1H), 6.69 (d, J = 9.1 Hz, 2H), 4.67–4.58 (m, 4H), 3.96–3.83 (m, 2H), 3.53–3.37 (m, 2H), 2.47–2.37 (m, 2H), 1.71–1.63 (m, 2H), 1.46 (s, 9H).

^{13}C NMR (101 MHz, DMSO) δ 173.3, 163.9, 154.4, 142.5, 139.3, 132.1, 129.1, 127.5, 118.3, 114.2, 78.9, 62.7, 59.6, 43.5, 28.1.

Methyl 4-((4-oxo-1-phenyl-1,3,8-triazaspiro[4.5]decan-3-yl)methyl)benzoate (8a). Compound **8a** was obtained following the general procedure for Boc group deprotection starting from the corresponding Boc-protected derivative **6a** (1.62 mmol, 780 mg). The reaction product was used in the next step without further purification.

Methyl 3-fluoro-4-((4-oxo-1-phenyl-1,3,8-triazaspiro[4.5]decan-3-yl)methyl)benzoate (8b). Compound **8b** was obtained following the general procedure for Boc group deprotection starting from the corresponding Boc-protected derivative **6b** (0.819 mmol, 408 mg). The reaction product was used in the next step without further purification.

Methyl 3,5-difluoro-4-((4-oxo-1-phenyl-1,3,8-triazaspiro[4.5]decan-3-yl)methyl)benzoate (8c). Compound **8c** was obtained following the general procedure for Boc group deprotection starting from the corresponding Boc-protected derivative **6c** (0.427 mmol, 220 mg). The desired reaction product was used in the next step without further purification.

N-Hydroxy-4-((4-oxo-1-phenyl-1,3,8-triazaspiro[4.5]decan-3-yl)methyl)benzamide (9a). Compound **9a** was prepared starting from intermediate **8a** (0.135 mmol, 51 mg) following the general procedure for the preparation of hydroxamic acids with 60 % yield (54 mg).

MS (ESI) m/z calc. $[M+H]^+$ for $C_{21}H_{25}N_4O_3^+$: 381.19; found: 381.3.

^{1}H NMR (400 MHz, DMSO-d6) δ 7.77 (d, J = 8.2 Hz, 2H), 7.39 (d, J = 8.0 Hz, 2H), 7.22 (t, J = 7.0 Hz, 3H), 7.02 (d, J = 8.2 Hz, 2H), 6.80 (t, J = 7.3 Hz, 1H), 4.64 (d, J = 11.4 Hz, 4H), 3.61–3.50 (m, 2H), 3.32–3.28 (m, 2H), 2.93–2.80 (m, 2H), 1.90–1.82 (m, 2H).

^{13}C NMR (176 MHz, DMSO-d6) δ 172.9, 164.3, 142.7, 139.5, 132.5, 129.6, 127.9, 118.7, 114.9, 63.3, 58.7, 44.1, 40.5, 26.0.

3,5-Difluoro-N-hydroxy-4-((4-oxo-1-phenyl-1,3,8-triazaspiro[4.5]decan-3-yl)methyl)benzamide (9b). Compound **9b** was prepared starting from compound **8b** (0.120 mmol, 50 mg) following the general procedure for the preparation of hydroxamic acids with 50 % yield (25 mg).

^{1}H NMR (700 MHz, DMSO) δ 7.51 (d, J = 7.8 Hz, 1H), 7.47 (d, J = 8.5 Hz, 1H), 7.21–7.16 (m, 2H), 6.95 (t, J = 8.2 Hz, 2H), 6.81–6.76 (m, 1H), 4.69 (d, J = 9.4

Hz, 2H), 4.62 (d, J = 13.8 Hz, 2H), 3.53–3.44 (m, 3H), 2.72–2.65 (m, 2H), 2.52–2.51 (m, 1H), 1.78–1.72 (m, 2H).

^{13}C NMR (176 MHz, DMSO-d6) δ 22.5, 26.0, 29.5, 30.3, 30.8, 31.6, 33.0, 34.8, 34.9, 35.0, 35.1, 58.6, 63.0, 112.5, 115.3, 118.9, 119.1, 124.8, 128.9, 129.6, 139.7, 142.6, 145.8, 147.6, 160.4, 161.1, 161.8, 172.3.

Methyl 4-((8-methyl-4-oxo-1-phenyl-1,3,8-triazaspiro[4.5]decan-3-yl)methyl)benzoate (10a). Compound **10a** was prepared following the general procedure of reductive amination in presence of paraformaldehyde starting from intermediate **8a** (0.254 mmol, 96 mg). Crude material was purified by liquid chromatography (DCM, DCM/MeOH 98:2 v/v) giving compound **10a** as a white solid (32 % yield, 22 mg).

MS (ESI) m/z calc. $[M+H]^+$ for $C_{23}H_{28}N_3O_3^+$: 394.21; found: 394.3.

^{1}H NMR (400 MHz, CDCl3) δ 7.97 (d, J = 6.6 Hz, 2H), 7.29 (d, J = 8.3 Hz, 2H), 7.20 (s, 1H), 7.19–7.15 (m, 1H), 6.88–6.63 (m, 3H), 4.58 (s, 2H), 4.51 (s, 2H), 3.85 (s, 3H), 3.07–2.91 (m, 2H), 2.89–2.71 (m, 4H).

Methyl 3-fluoro-4-((8-methyl-4-oxo-1-phenyl-1,3,8-triazaspiro[4.5]decan-3-yl)methyl)benzoate (10b). Compound **10b** was prepared following the general procedure of reductive amination in presence of paraformaldehyde starting from intermediate **9b** (0.199 mmol, 79 mg). Crude material was purified by silica gel column chromatography (DCM, DCM/MeOH 98:2 v/v) giving compound **10b** as a white solid (61 % yield, 50 mg).

(ESI) m/z calc. $[M+H]^+$ per $C_{23}H_{27}FN_3O_3^+$: 412.20; trovato: 394.3.

^{1}H NMR (400 MHz, CDCl3) δ 7.76 (d, J = 1.6 Hz, 1H), 7.68 (d, J = 1.6 Hz, 1H), 7.34 (t, J = 7.6 Hz, 1H), 7.19–7.18 (m, 1H), 7.16 (s, 1H), 6.83–6.73 (m, 3H), 4.63 (s, 2H), 4.55 (s, 2H), 3.86 (s, 3H), 2.93–2.80 (m, 2H), 2.81–2.57 (m, 4H), 2.33 (s, 3H), 2.19–1.66 (m, 1H).

Methyl 3,5-difluoro-4-((8-methyl-4-oxo-1-phenyl-1,3,8-triazaspiro[4.5]decan-3-yl)methyl)benzoate (10c). Compound **10c** was

prepared following the general procedure of reductive amination in presence of paraformaldehyde starting from intermediate **9c** (0.214 mmol, 52 mg). Crude material was purified by silica gel column chromatography (PE/EtOAc 80:20 v/v to 70:30 v/v) giving compound **10c** as a white solid (81 %, 74.4 mg).

^{1}H NMR (700 MHz, CDCl3): δH 7.54 (2H, d, J = 7.4 Hz), 7.17 (2H, t, J = 5.3, 4.2 Hz), 6.81 (2H, d, J = 8.2 Hz), 6.77 (1H, t, J = 7.3 Hz), 4.70 (2H, s), 4.53 (2H, s), 3.87 (3H, s), 2.97–2.84 (2H, m), 2.82–2.73 (2H, m), 2.72–2.61 (2H, m), 2.34 (3H, s), 1.60 (2H, d, J = 13.8 Hz).

Methyl 4-((8-benzyl-4-oxo-1-phenyl-1,3,8-triazaspiro[4.5]decan-3-yl)methyl)benzoate (11a). Compound **11a** was prepared following the general procedure of reductive amination in presence of benzaldehyde (0.402 mmol, 0.041 mL). Crude material was purified by silica gel column chromatography (DCM, DCM/MeOH 98:2 v/v) giving compound **11a** as a white solid (61 % yield, 36 mg).

^{1}H NMR (400 MHz, CDCl3) δ 8.07–7.87 (m, 2H), 7.34–7.24 (m, 5H), 7.22–7.16 (m, 4H), 6.82–6.75 (m, 3H), 4.58 (s, 2H), 4.49 (s, 2H), 3.84 (s, 3H), 3.55 (s, 2H), 2.87–2.74 (m, 4H), 2.71–2.56 (m, 2H).

Methyl 4-((8-benzyl-4-oxo-1-phenyl-1,3,8-triazaspiro[4.5]decan-3-yl)methyl)-3-fluorobenzoate (11b). Compound **11b** was prepared following the general procedure of reductive amination in presence of benzaldehyde (0.240 mmol, 0.024 mL). Crude material was purified by silica gel column chromatography (DCM/MeOH 98:2 v/v) giving compound **11b** as white solid (41 %, 40 mg).

^{1}H NMR (700 MHz, CDCl3) δ 7.82 (d, J = 7.9 Hz, 1H), 7.75 (d, J = 10.2 Hz, 1H), 7.42–7.35 (m, 5H), 7.33 (t, J = 7.5 Hz, 2H), 7.29–7.26 (m, 1H), 6.89 (d, J = 8.1 Hz, 2H), 6.86 (t, J = 7.3 Hz, 1H), 4.70 (s, 2H), 4.61 (s, 2H), 3.92 (s, 3H), 3.60 (s, 2H), 2.89–2.79 (m, 4H), 2.73–2.63 (m, 2H), 1.66 (d, J = 13.8 Hz, 2H).

Methyl 4-((8-benzyl-4-oxo-1-phenyl-1,3,8-triazaspiro[4.5]decan-3-yl)methyl)-3,5-difluorobenzoate (11c). Compound **11c** was prepared following the general procedure of reductive amination in presence of benzaldehyde (0.213 mmol, 0.022 mL). Crude material was purified by silica gel column chromatography (Hex/EtOAc 60:40 v/v) giving compound **11c** as a white solid (56 % yield, 61 mg).

^{1}H NMR (700 MHz, CDCl3) δ 7.55–7.51 (m, 1H), 7.31–7.28 (m, 1H), 7.25 (t, J = 7.6 Hz, 1H), 7.22–7.15 (m, 2H), 6.83–6.77 (m, 1H), 4.70 (s, 1H), 4.52 (s, 1H), 3.87 (s, 1H), 3.52 (s, 1H), 2.78 (td, J = 11.9, 2.9 Hz, 1H), 2.72 (dd, J = 11.0, 4.8 Hz, 1H), 2.55 (td, J = 13.3, 5.2 Hz, 1H), 1.62–1.49 (m, 2H).

Methyl 4-((4-oxo-1-phenyl-8-(pyridin-2-ylmethyl)-1,3,8-triazaspiro[4.5]decan-3-yl)methyl)benzoate (12a). Compound **12a** was prepared following the general procedure of reductive amination in presence of pyridine-3-carboxaldehyde (0.336 mmol, 0.031 mL). Crude material was purified by silica gel column chromatography (DCM/MeOH/NH4OH 200:10/0.001 v/v) giving compound **12a** as a white solid (41% yield, 54 mg).

^{1}H NMR (700 MHz, CDCl3) δ 8.63 (s, 1H), 8.53–8.48 (m, 1H), 8.02 (d, 2H), 7.70 (d, 1H), 7.35 (d, J = 7.9 Hz, 2H), 7.29–7.23 (m, 4H), 6.85 (d, J = 4.8 Hz, 3H), 4.65 (s, 2H), 4.56 (s, 2H), 3.91 (d, J = 1.7 Hz, 3H), 3.62 (s, 2H), 2.96–2.86 (m, 2H), 2.86–2.73 (m, 2H), 2.73–2.64 (m, 2H), 1.76–1.64 (m, 2H).

Methyl 3-fluoro-4-((4-oxo-1-phenyl-8-(pyridin-2-ylmethyl)-1,3,8-triazaspiro[4.5]decan-3-yl)methyl)benzoate (12b). Compound **12b** was prepared following the general procedure of reductive amination in presence of pyridine-3-carboxaldehyde (0.337 mmol, 0.032 mL). Crude material was purified by silica gel column chromatography (DCM/MeOH 99:1 v/v) giving compound **12b** as white solid (32%, 43 mg).

^{1}H NMR (700 MHz, CDCl3): δH 8.58 (1H, s), 8.45 (1H, d, J = 5.6 Hz), 8.04 (2H, d, J = 7.8 Hz), 8.01 (2H, d, J = 4.5 Hz), 7.76 (1H, d, J = 7.1 Hz), 7.68 (1H, d, J =

10.1 Hz), 7.57 (1H, q, J = 4.5 Hz), 7.34 (1H, t, J = 7.6 Hz), 7.23 (2H, t, J = 7.9 Hz), 6.83 (3H, t, J = 7.4 Hz), 6.84–6.78 (3H, m), 6.80 (3H, d, J = 8.3 Hz), 4.63 (2H, d, J = 12.6 Hz), 4.56 (2H, s), 3.86 (3H, s), 2.96–2.91 (2H, m), 2.68–2.65 (2H, m), 2.63–2.56 (2H, m), 1.64 (2H, d, J = 14.0 Hz).

Methyl 4-((8-(4-bromobenzyl)-4-oxo-1-phenyl-1,3,8-triazaspiro[4.5]decan-3-yl)methyl)-3-fluorobenzoate (13). Compound **13** was prepared following the general procedure of reductive amination in presence of 4-bromobenzaldehyde (0.261 mmol, 48.4 mg). Crude material was purified by silica gel column chromatography (Hex/EtOAc 70:30 v/v) giving compound **13** as white solid (56%, 40 mg).

^{1}H NMR (700 MHz, CDCl3) δ 7.75 (dd, J = 8.0, 1.4 Hz, 1H), 7.67 (dd, J = 10.2, 1.3 Hz, 1H), 7.36 (t, J = 8.6 Hz, 2H), 7.33 (t, J = 7.6 Hz, 1H), 7.22–7.16 (m, 4H), 6.79 (dd, J = 14.5, 7.5 Hz, 3H), 4.62 (s, 2H), 4.54 (s, 2H), 3.84 (s, 3H), 3.46 (s, 2H), 2.78 (t, J = 10.6 Hz, 2H), 2.70 (d, J = 6.4 Hz, 2H), 2.63–2.52 (m, 2H), 1.60 (t, J = 12.5 Hz, 2H).

Methyl 3-fluoro-4-((8-(furan-2-ylmethyl)-4-oxo-1-phenyl-1,3,8-triazaspiro[4.5]decan-3-yl)methyl)benzoate (14). Compound **14** was prepared following the general procedure of reductive amination in presence of furan-2-carbaldehyde (0.302 mmol, 0.025 mL). Crude material was purified by silica gel column chromatography (DCM/MeOH 99:1 v/v) giving compound **14** as white solid (93%, 112 mg).

^{1}H NMR (700 MHz, CDCl3): δ 7.75 (1H, d, J = 1.4, 7.9 Hz), 7.67 (1H, d, J = 1.3, 10.2 Hz), 7.35–7.30 (2H, m), 7.19–7.16 (3H, m), 6.82–6.77 (3H, m), 6.28–6.25 (1H, m), 4.62 (2H, s), 4.53 (2H, s), 3.85 (3H, s), 3.62 (2H, s), 2.81–2.81 (4H, m), 2.69–2.49 (2H, m), 1.63 (2H, d, J = 13.7 Hz).

Methyl 3-fluoro-4-((4-oxo-1-phenyl-8-((5-phenylfuran-2-yl)methyl)-1,3,8-triazaspiro[4.5]decan-3-yl)methyl)benzoate (15). Compound **15** was prepared following the general procedure of reductive amination in presence of 5-

phenylfuran-2-carbaldehyde (0.452 mmol, 0.065 mL). Crude material was purified by silica gel column chromatography (DCM/MeOH 99:1 v/v) giving compound **15** as white solid (44 %, 91 mg).

^{1}H NMR (600 MHz, CDCl3) δ 7.73 (d, 1H), 7.66 (d, 1H), 7.59 (d, 2H), 7.34–7.29 (m, 1H), 7.29–7.25 (m, 2H), 7.19–7.13 (m, 3H), 6.81–6.78 (m, 2H), 6.78–6.73 (m, 1H), 6.51 (s, 1H), 6.23 (s, 1H), 4.61 (s, 2H), 4.52 (s, 2H), 3.83 (s, 3H), 3.62 (s, 2H), 2.93–2.86 (m, 2H), 2.86–2.80 (m, 2H), 2.64–2.56 (m, 2H), 1.65–1.58 (m, 2H).

N-Hydroxy-4-((8-methyl-4-oxo-1-phenyl-1,3,8-triazaspiro[4.5]decan-3-yl)methyl)benzamide (16a). Compound **16a** was prepared starting from compound **10a** (0.181 mmol, 71 mg) following the general procedure for the preparation of hydroxamic acids with 46 % yield (33 mg).

MS (ESI) m/z calc. $[M+H]^+$ for $C_{22}H_{27}N_4O_3^+$: 395.20; found: 395.43.

^{1}H NMR (400 MHz, DMSO-d6) δ 11.15 (bs, 1H), 9.04 (bs, 1H), 7.76 (d, J = 9.0 Hz, 2H), 7.37 (d, J = 8.5 Hz, 2H), 7.23 (dd, J = 2246.4, 7.6 Hz, 2H), 6.83 (d, J = 8.6 Hz, 2H), 6.76 (t, J = 7.3 Hz, 1H), 4.59 (d, J = 4.1 Hz, 4H), 2.71–2.65 (m, 4H), 2.65–2.55 (m, 2H), 2.24 (s, 3H), 1.63–1.56 (m, 2H).

^{13}C NMR (176 MHz, DMSO-d6) δ 174.1, 164.3, 143.2, 139.4, 132.5, 129.6, 127.8, 118.4, 114.7, 63.1, 59.4, 51.9, 46.6, 43.7, 28.9.

3-Fluoro-N-hydroxy-4-((8-methyl-4-oxo-1-phenyl-1,3,8-triazaspiro[4.5]decan-3-yl)methyl)benzamide (16b). Compound **16b** was prepared starting from compound **10b** (0.122 mmol, 50 mg) following the general procedure for the preparation of hydroxamic acids with 57 % yield (29 mg).

(ESI) m/z calc. $[M+H]^+$ for $C_{22}H_{26}FN_4O_3^+$: 413.19; found: 413.3.

^{1}H NMR (400 MHz, DMSO-d6) δ 7.65–7.55 (m, 2H), 7.42 (t, J = 7.7 Hz, 1H), 7.24 (t, J = 7.2 Hz, 2H), 6.85 (d, J = 8.2 Hz, 2H), 6.78 (t, J = 7.3 Hz, 1H), 4.64 (d, J = 7.8 Hz, 4H), 2.75–2.66 (m, 4H), 2.66–2.54 (m, 2H), 2.25 (s, 3H), 1.67–1.57 (m, 2H).

^{13}C NMR (101 MHz, DMSO-d6) δ 174.0, 162.9, 160.4 (d, J = 246.4 Hz), 143.2, 134.8, 130.3, 129.6, 126.6, 123.7, 118.6, 115.0, 63.2, 59.4, 51.9, 46.5, 38.3, 28.9.

3,5-Difluoro-N-hydroxy-4-((8-methyl-4-oxo-1-phenyl-1,3,8-triazaspiro[4.5]decan-3-yl)methyl)benzamide (16c). Compound **16c** was prepared starting from compound 17c (0.173 mmol, 74.4 mg) following the general procedure for the preparation of hydroxamic acids with 14 % yield (10 mg).

(ESI) m/z calc. $[M+H]^+$ for $C_{22}H_{24}F_2N_4O_3^+$: 430.18; found: 431.2.

^{1}H NMR (700 MHz, DMSO-d6) δ 11.46 (bs, 1H), 9.36 (bs, 1H), 7.56 (d, J = 7.9 Hz, 2H), 7.31 (t, 2H), 6.89 (d, J = 8.2 Hz, 2H), 6.83 (t, J = 7.3 Hz, 1H), 4.73 (s, 2H), 4.64 (s, 2H), 2.81–2.66 (m, 4H), 2.29 (s, 3H), 1.59 (d, J = 13.6 Hz, 3H), 1.39–1.26 (m, J = 14.2 Hz, 2H).

^{13}C NMR (176 MHz, DMSO-d6) δ 172.9, 161.5 (d, J = 7.6 Hz), 161.1, 160.1 (d, J = 8.3 Hz), 142.7, 135.1, 129.1, 118.2, 114.6, 110.3 (d, J = 27.3 Hz), 62.5, 58.9, 51.3, 46.0, 32.4, 28.2.

4-((8-Benzyl-4-oxo-1-phenyl-1,3,8-triazaspiro[4.5]decan-3-yl)methyl)-N-hydroxybenzamide (17a). Compound 24a was prepared starting from compound **11a** (0.181 mmol, 71 mg) following the general procedure for the preparation of hydroxamic acids with 87% yield (31 mg).

MS (ESI) m/z calc. [M+H]+ for C_{28}H31N4O3+: 471.24; found: 471.3.

^{1}H NMR (400 MHz, MeOD) δ 7.67 (d, 2H), 7.35–7.24 (m, 7H), 7.14 (dd, J = 2149.6, 8.6 Hz, 2H), 6.91–6.86 (m, 2H), 6.79 (t, J = 7.4 Hz, 1H), 4.56 (d, J = 7.9 Hz, 4H), 3.77 (s, 2H), 3.17–3.10 (m, 2H), 2.98–2.91 (m, 2H), 2.54–2.46 (m, 2H), 1.78–1.72 (m, 2H).

^{13}C NMR (176 MHz, DMSO-d6) δ 173.9, 166.5, 154.9, 143.0, 142.2, 130.1, 129.6, 128.2, 118.7, 114.6, 79.4, 63.2, 60.0, 52.6, 44.0, 28.5.

4-((8-Benzyl-4-oxo-1-phenyl-1,3,8-triazaspiro[4.5]decan-3-yl)methyl)-3-fluoro-N-hydroxybenzamide (17b). Compound **17b** was prepared starting from

compound **11b** (0.082 mmol, 40 mg) following the general procedure for the preparation of hydroxamic acids with 62% yield (25 mg).

MS (ESI) m/z calc. $[M+H]^+$ for $C_{28}H_{29}FN_4O_3^+$: 489.23; found: 489.2.

^{1}H NMR (700 MHz, DMSO-d6) δ 7.67 (d, J = 1.7 Hz, 1H), 7.63 (d, 2H), 7.47 (t, J = 7.7 Hz, 1H), 7.44–7.39 (m, 3H), 7.34–7.29 (m, 2H), 6.93 (d, J = 8.1 Hz, 2H), 6.86 (t, J = 7.3 Hz, 2H), 4.74–4.67 (m, 4H), 3.60 (s, 2H), 2.82–2.76 (m, 3H), 2.61 (s, 4H), 1.72–1.67 (m, 2H).

^{13}C NMR (700 MHz, DMSO-d6) 29.1, 49.6, 55.4, 60.0, 63.2, 63.3, 79.6, 115.3, 118.8, 127.3, 128.7, 129.2, 129.6, 130.1, 143.3.

4-((8-Benzyl-4-oxo-1-phenyl-1,3,8-triazaspiro[4.5]decan-3-yl)methyl)-3,5-difluoro-N-hydroxybenzamide (17c). Compound **17c** was prepared starting from compound **11c** (0.121 mmol, 61 mg) following the general procedure for the preparation of hydroxamic acids with 53% yield (37 mg).

MS (ESI) m/z calc. $[M+H]^+$ for $C_{28}H_{28}F_2N_4O_3^+$: 507.22; found: 507.2.

^{1}H NMR (600 MHz, DMSO-d6) δ 11.41 (bs, 1H), 9.30 (bs, 1H), 7.50 (d, J = 7.9 Hz, 2H), 7.38–7.30 (m, 4H), 7.26 (t, J = 7.7 Hz, 3H), 6.87 (d, J = 8.1 Hz, 2H), 6.80 (t, J = 7.4 Hz, 1H), 4.67 (s, 2H), 4.59 (s, 2H), 3.56 (s, 2H), 2.76–2.71 (m, 3H), 2.50–2.43 (m, 1H), 1.57 (d, J = 13.5 Hz, 2H).

^{13}C NMR (176 MHz, DMSO-d6) δ 173.4, 161.2 (d, J = 256.9 Hz), 143.2, 135.4, 129.6, 129.3, 128.7, 127.4, 119.0, 115.6, 110.7, 63.0, 62.5, 60.0, 49.5, 32.8, 28.9.

N-Hydroxy-4-((4-oxo-1-phenyl-8-(pyridin-3-ylmethyl)-1,3,8-triazaspiro[4.5]decan-3-yl)methyl)benzamide (18a). Compound **18a** was prepared starting from compound **12a** (0.11 mmol, 36 mg) following the general procedure for the preparation of hydroxamic acids with 35% yield (19 mg).

MS (ESI) m/z calc. $[M+H]^+$ for $C_{27}H_{30}N_5O_3^+$: 472.57; found: 472.46.

^{1}H NMR (700 MHz, DMSO-d6) δ 11.21 (bs, 1H), 9.04 (bs, 1H), 8.56 (s, 1H), 8.50–8.47 (m, 1H), 7.79–7.77 (m, 1H), 7.75 (d, J = 7.9 Hz, 2H), 7.41–7.35 (m, 3H), 7.27–7.24 (m, 2H), 6.86 (d, J = 8.1 Hz, 2H), 6.79 (t, J = 7.3 Hz, 1H), 4.60

(d, J = 9.8 Hz, 4H), 3.60 (s, 1H), 2.83–2.72 (m, 4H), 2.59–2.55 (m, 2H), 1.67–1.61 (m, 2H).

^{13}C NMR (176 MHz, DMSO-d6) δ 174.0, 164.4, 150.5, 148.7, 143.3, 140.0, 137.0, 134.3, 129.6, 127.9, 127.82, 123.9, 115.1, 63.1, 59.9, 59.7, 49.5, 43.9, 29.2.

3-Fluoro-N-hydroxy-4-((4-oxo-1-phenyl-8-(pyridin-3-ylmethyl)-1,3,8-triazaspiro[4.5]decan-3-yl)methyl)benzamide (18b). Compound **18b** was prepared starting from compound **12b** (0.051 mmol, 25 mg) following the general procedure for the preparation of hydroxamic acids with 70% yield (18 mg).

(ESI) m/z calc. $[M+H]^+$ for $C_{27}H_{29}FN_5O_3^+$: 490.56; found: 490.37.

^{1}H NMR (600 MHz, DMSO-d6) δ 11.30 (bs, 1H), 9.17 (bs, 1H), 8.54 (s, 1H), 8.47 (d, J = 4.8 Hz, 1H), 7.76 (d, J = 7.8 Hz, 1H), 7.60 (d, J = 8.0 Hz, 1H), 7.57 (d, J = 10.8 Hz, 1H), 7.42–7.35 (m, 2H), 7.25 (t, J = 7.7 Hz, 2H), 6.86 (d, J = 8.2 Hz, 2H), 6.79 (t, J = 7.3 Hz, 1H), 4.63 (d, J = 10.4 Hz, 4H), 3.58 (s, 2H), 2.79–2.70 (m, 4H), 2.57–2.51 (m, 2H), 1.66–1.60 (m, 2H).

^{13}C NMR (176 MHz, DMSO-d6) δ 173.9, 163.0, 160.4 (d, J = 246.5 Hz), 150.5, 148.7, 143.3, 137.0, 134.8 (d, J = 6.7 Hz), 134.4, 130.3 (d, J = 4.4 Hz), 129.6, 126.5 (d, J = 15.1 Hz), 123.9, 123.7, 118.7, 115.2, 114.4 (d, J = 23.0 Hz), 63.2, 59.9, 59.7, 49.5, 38.3 (d, J = 3.8 Hz), 29.1.

4-((8-(4-Bromobenzyl)-4-oxo-1-phenyl-1,3,8-triazaspiro[4.5]decan-3-yl)methyl)-3-fluoro-N-hydroxybenzamide (**19**). Compound **19** was prepared starting from compound **1** (0.082 mmol, 40 mg) following the general procedure for the preparation of hydroxamic acids with 67% yield (27 mg).

(ESI) m/z calc. $[M+H]^+$ for $C_{28}H_{29}BrFN_4O_3^+$: 568.47; found: 569.30.

^{1}H NMR (700 MHz, DMSO-d6) δ 7.67 (d, J = 6.3 Hz, 1H), 7.63 (d, J = 10.8 Hz, 1H), 7.58 (d, J = 8.4 Hz, 2H), 7.46 (t, J = 7.8 Hz, 1H), 7.38 (d, J = 8.4 Hz, 2H), 7.32 (d, J = 16.3 Hz, 2H), 6.92 (d, J = 8.2 Hz, 2H), 6.85 (t, J = 7.3 Hz, 1H), 4.69

(s, 2H), 4.68 (s, 2H), 3.58 (s, 2H), 2.83–2.74 (m, 4H), 2.62–2.58 (m, 2H), 1.71–1.64 (m, 2H).

^{13}C NMR (176 MHz, DMSO-d6) δ 174.0, 163.0, 160.4 (d, J = 246.4 Hz), 143.3, 138.5, 134.8 (d, J = 7.0 Hz), 131.6, 131.4, 130.3, 129.6, 126.52 (d, J = 15.0 Hz), 123.7, 120.3, 118.9, 115.4, 114.4 (d, J = 23.3 Hz), 63.3, 61.7, 60.0, 49.5, 38.3 (d, J = 4.4 Hz), 29.2.

3-Fluoro-4-((8-(furan-2-ylmethyl)-4-oxo-1-phenyl-1,3,8-triazaspiro[4.5]decan-3-yl)methyl)-N-hydroxybenzamide (20). Compound **20** was prepared starting from compound **14** (0.235 mmol, 112 mg) following the general procedure for the preparation of hydroxamic acids with 61% yield (71 mg).

^{1}H NMR (700 MHz, DMSO-d6) δ 7.63–7.59 (m, 2H), 7.59–7.56 (m, 1H), 7.41 (t, J = 7.8 Hz, 1H), 7.27–7.19 (m, 2H), 6.84 (d, J = 8.1 Hz, 2H), 6.78 (t, J = 7.3 Hz, 1H), 6.41 (s, 1H), 6.31 (s, 1H), 4.69–4.54 (m, 4H), 3.34 (s, 2H), 2.80–2.74 (m, 3H), 2.56–2.52 (m, 1H), 1.65–1.58 (m, 2H).

^{13}C NMR (176 MHz, DMSO-d6) δ 173.9, 162.9, 160.4 (d, J = 246.2 Hz), 152.5, 152.5, 143.3, 142.8, 142.7, 129.6, 123.7, 118.7, 115.2, 110.7, 110.7, 109.1, 63.2, 59.9, 54.6, 49.3, 38.3, 29.1.

3-Fluoro-N-hydroxy-4-((4-oxo-1-phenyl-8-((5-phenylfuran-2-yl)methyl)-1,3,8-triazaspiro[4.5]decan-3-yl)methyl)benzamide (21). Compound **21** was prepared starting from compound **15** (0.082 mmol, 40 mg) following the general procedure for the preparation of hydroxamic acids with 53% yield (37 mg).

(ESI) *m/z* calc. $[M+H]^+$ for $C_{32}H_{32}FN_4O_4^+$: 492.60; found: $[M+Na]^+$ 555.39.

^{1}H NMR (700 MHz, DMSO-d_6): δH 11.41 (1H, bs), 9.22 (1H, bs), 7.67 (2H, d, J = 8.0 Hz), 7.64 (2H, d, J = 10.6 Hz), 7.51-7.46 (6H, m), 7.35 (2H, t, J = 7.1 Hz), 7.30 (3H, t, J = 7.9 Hz), 6.84 (2H, s), 4.69 (1H, s), 3.72 (1H, s), 3.14-3.10 (1H, m), 2.95-2.89 (4H, m), 1.72-1.72 (2H, m).

^{13}C NMR (176 MHz, DMSO-d_6) δ 173.9, 162.8, 160.4 (d, *J* = 246.2 Hz), 152.5, 143.3, 134.8, 130.9, 130.3, 129.6, 129.3, 127.7, 123.7, 118.7, 115.2, 111.5, 107.0, 63.2, 59.9, 54.6, 49.2, 40.5, 29.2.

Methyl 4-((8-acetyl-4-oxo-1-phenyl-1,3,8-triazaspiro[4.5]decan-3-yl)methyl)benzoate (22). To a cooled stirring solution of intermediate **6a** (0.313 mmol, 115 mg) in THF (1.5 mL), a catalytic amount of DMAP and TEA (0.809 mmol, 0.112 mL) were subsequently added, followed by acetyl chloride. The resulting reaction mixture was allowed under stirring at 0 °C for 1 h. Volatile components were removed under reduced pressure and the crude residue dissolved in EtOAc (10 mL) and washed with distilled water for three times (10 mL x3). Organic layer was dried over Na2SO4 and evaporated under reduced pressure. Crude material was purified by silica gel column chromatography (DCM, DCM/Acetone 99:1 v/v to 90:10 v/v) giving the desired compound **22** with 76% yield (101 mg).

^{1}H NMR (400 MHz, CDCl3) δ 7.98 (d, J = 8.9 Hz, 2H), 7.29 (d, 2H), 7.19–7.11 (m, 2H), 6.80 (tt, J = 7.3, 1.0 Hz, 1H), 6.63 (d, J = 8.4, 2H), 4.60 (s, 2H), 4.57–4.50 (m, 3H), 4.51 (s, 2H), 3.94 (td, J = 13.2, 3.3 Hz, 1H), 3.85 (s, 3H), 3.75–3.62 (m, 1H), 3.42 (td, J = 13.0, 3.5 Hz, 1H), 2.41 (m, 2H), 2.09 (s, 3H), 1.77–1.64 (m, 2H), 1.59 (s, 1H).

4-((8-Acetyl-4-oxo-1-phenyl-1,3,8-triazaspiro[4.5]decan-3-yl)methyl)-N-hydroxybenzamide (23). Compound **23** was prepared starting from compound **22** (0.240 mmol, 101 mg) following the general procedure for the preparation of hydroxamic acids with 67% yield (68 mg).

MS (ESI) *m/z* calc. $[M+H]^+$ for $C_{23}H_{26}N_4O_4^+$: 422.49; found: $[M+Na]^+$ 445.25.

^{1}H NMR (400 MHz, DMSO-d_6) δ 11.17 (bs, 1H), 9.04 (bs, 1H), 7.76 (d, *J* = 7.8 Hz, 2H), 7.39 (d, *J* = 7.8 Hz, 2H), 7.23 (d, *J* = 8.8 Hz, 2H), 6.80 (t, *J* = 7.3 Hz, 1H), 6.75 (d, *J* = 8.2 Hz, 2H), 4.64 (d, *J* = 5.9 Hz, 4H), 4.39 – 4.30 (m, 1H), 3.87

– 3.73 (m, 2H), 3.30 – 3.22 (m, 1H), 2.45 (d, *J* = 0.0 Hz, 1H), 2.35 – 2.25 (m, 1H), 2.08 (s, 3H), 1.80 – 1.65 (m, 2H).

^{13}C NMR (101 MHz, DMSO-d_6) δ 173.7, 168.8, 143.2, 139.8, 132.6, 129.7, 128.0, 127.8, 119.1, 115.4, 63.2, 60.4, 44.0, 42.7, 37.7, 29.9, 28.9, 21.7.

Methyl (R)-4-((4-oxo-1-phenyl-8-(tetrahydrofuran-2-carbonyl)-1,3,8-triazaspiro[4.5]decan-3-yl)methyl)benzoate (24a). Compound **24a** a was synthesized following the general coupling procedure starting from R-tetrahydrofuran-2-carboxylic acid (0.296 mmol, 112 mg). Crude material was purified by liquid chromatography (DCM, DCM/MeOH 99:1 v/v) giving compound **24a** as a white solid (65% yield, 92 mg).

^{1}H NMR (700 MHz, CDCl3) δ 7.97 (d, 2H), 7.29 (d, J = 8.2 Hz, 2H), 7.17–7.11 (m, 2H), 6.75 (t, J = 7.3 Hz, 1H), 6.65–6.59 (m, 2H), 4.67–4.62 (m, 1H), 4.62–4.59 (m, 2H), 4.51 (d, J = 6.7 Hz, 2H), 4.02–3.97 (m, 1H), 3.96–3.88 (m, 2H), 3.86–3.84 (m, 3H), 3.84–3.79 (m, 1H), 3.50–3.37 (m, 1H), 2.73–2.68 (m, 1H), 2.53–2.33 (m, 2H), 2.09–1.95 (m, 2H), 1.88 (dq, J = 9.5, 6.5 Hz, 1H).

Methyl (R)-3-fluoro-4-((4-oxo-1-phenyl-8-(tetrahydrofuran-2-carbonyl)-1,3,8-triazaspiro[4.5]decan-3-yl)methyl)benzoate (24b). Compound **24b** was synthesized following the general coupling procedure starting from R-tetrahydrofuran-2-carboxylic acid (0.330 mmol, 131 mg). Crude material was purified by silica gel column chromatography (DCM, DCM/MeOH 99:1 v/v to 98:2 v/v) giving compound **24b** as a white solid (93% yield, 168 mg).

^{1}H NMR (700 MHz, CDCl3) δ 7.77 (d, J = 1.6 Hz, 1H), 7.69 (d, J = 1.6 Hz, 1H), 7.37–7.32 (m, 1H), 7.18–7.12 (m, 2H), 6.77 (t, J = 7.3 Hz, 1H), 6.67–6.61 (m, 2H), 4.67–4.65 (m, 2H), 4.58–4.55 (m, 2H), 4.52–4.47 (m, 1H), 4.00–3.95 (m, 1H), 3.93–3.88 (m, 2H), 3.86 (s, 3H), 3.84–3.79 (m, 2H), 2.72–2.65 (m, 1H), **2.52–2.44 (m, 1H), 2.02–1.93 (m, 2H), 1.90–1.82 (m, 1H), 1.71–1.60 (m, 3H).**

Methyl 4-((8-(1-methyl-1H-pyrrole-2-carbonyl)-4-oxo-1-phenyl-1,3,8-triazaspiro[4.5]decan-3-yl)methyl)benzoate (25a). Compound **25a** was

synthesized following the general coupling procedure starting from 1-methyl-1H-pyrrole-2-carboxylic acid (0.304 mmol, 38 mg). Crude material was purified by silica gel column chromatography (PE/EtOAc 75:25 v/v) giving compound **25a** with 41% yield (52 mg).

1H NMR (700 MHz, CDCl3) δ 8.05 (d, J = 7.9 Hz, 2H), 7.36 (d, J = 7.9 Hz, 2H), 7.22 (t, J = 7.7 Hz, 2H), 6.85 (t, J = 7.3 Hz, 1H), 6.77–6.70 (m, 3H), 6.43–6.31 (m, 1H), 6.09 (t, J = 3.2 Hz, 1H), 4.68 (s, 2H), 4.59 (s, 2H), 4.48 (s, 2H), 3.92 (s, 4H), 3.83 (s, 4H), 2.81–2.76 (m, 2H), 2.7–2.47 (m, 2H), 1.85–1.72 (m, 4H).

Methyl 3-fluoro-4-((8-(1-methyl-1H-pyrrole-2-carbonyl)-1-oxo-4-phenyl-2,8-diazaspiro[4.5]decan-2-yl)methyl)benzoate (**25b**). Compound **25b** a was synthesized following the general coupling procedure starting from 1-methyl-1H-pyrrole-2-carboxylic acid (0.280 mmol, 35 mg). Crude material was purified by silica gel column chromatography (PE/EtOAc 75:25 v/v to 50:50 v/v) giving compound **25b** as a white solid (87% yield, 107 mg).

Methyl 4-((8-(3-methylfuran-2-carbonyl)-4-oxo-1-phenyl-1,3,8-triazaspiro[4.5]decan-3-yl)methyl)benzoate (26). Compound **26** was synthesized following the general coupling procedure starting from 3-methylfuran-2-carboxylic acid (0.400 mmol, 150 mg). Crude material was purified by silica gel column chromatography (PE/EtOAc 50:50 v/v) giving compound **26** as a white solid (54% yield, 91 mg).

^{1}H NMR (700 MHz, CDCl3) δ 8.05 (d, 2H), 7.36 (d, 2H), 7.33 (d, J = 1.8 Hz, 1H), 7.22 (t, 2H), 6.84 (t, 1H), 6.72 (d, 2H), 6.34 (d, J = 1.7 Hz, 1H), 4.68 (s, 2H), 4.59 (s, 2H), 4.23–4.14 (m, 1H), 4.05–3.96 (m, 1H), 3.92 (s, 3H), 3.71–3.60 (m, 1H), 2.73–2.62 (m, 2H), 2.31 (s, 2H), 1.84–1.74 (m, 2H).

Methyl 4-((8-nicotinoyl-1-oxo-4-phenyl-2,8-diazaspiro[4.5]decan-2-yl)methyl)benzoate (27a). Compound **27a** was synthesized following the general coupling procedure starting from nicotinic acid (0.450 mmol, 56.11 mg). Crude material was purified by silica gel column chromatography (DCM,

DCM/MeOH 99:1 v/v to 98:2 v/v) giving compound **27a** as a white solid (37 % yield, 144 mg).

^{1}H NMR (700 MHz, CDCl3) δ 7.98 (d, J = 4.1 Hz, 2H), 7.29 (d, J = 8.0 Hz, 2H), 7.18–7.15 (m, 2H), 6.81 (t, J = 7.3 Hz, 2H), 6.66 (d, 4H), 4.60 (s, 2H), 4.52 (s, 2H), 3.97–3.89 (m, 2H), 3.85 (s, 3H), 3.75–3.66 (m, 2H), 2.47–2.35 (m, 3H), 1.75–1.67 (m, 2H).

Methyl 3-fluoro-4-((4-oxo-1-phenyl-8-picolinoyl-1,3,8-triazaspiro[4.5]decan-3-yl)methyl)benzoate (27b). To a stirring solution of nicotinic acid (0.210 mmol, 26 mg) in dry DMF (1 mL), COMU (0.210 mmol, 90 mg) and OXYMA (0.210 mmol, 30 mg) were added. After 10 min, DIPEA (0.420 mmol, 0.071 mL) was added followed by amine **27b** (0.252 mmol, 100 mg), and the resulting mixture was allowed to stir at 25 °C for 18 h. The reaction mixture was diluted with water (10 mL) and extracted with EtOAc (10 mL). Organic layer was dried over Na2SO4 and evaporated under vacuum. Crude material was purified by silica gel column chromatography (DCM/MeOH/NH4OH 99:1:0.01 v/v) to effort compound **27b** as a white solid (59% yield, 75 mg).

^{1}H NMR (700 MHz, CDCl3) δ 8.56 (s, 1H), 8.48–8.42 (m, 1H), 7.96 (d, 2H), 7.64 (d, 1H), 7.28 (d, J = 7.9 Hz, 2H), 7.23–7.15 (m, 3H), 6.79–6.77 (m, 2H), 4.58 (s, 2H), 4.49 (s, 2H), 3.84 (d, J = 1.7 Hz, 3H), 2.90–2.80 (m, 2H), 2.76–2.70 (m, 2H), 2.66–2.57 (m, 2H), 1.65–1.58 (m, 2H).

Methyl 4-((8-(benzofuran-2-carbonyl)-4-oxo-1-phenyl-1,3,8-triazaspiro[4.5]decan-3-yl)methyl)-3-fluorobenzoate (28). Compound **28** was synthesized following the general coupling procedure starting from benzofuran-2-carboxylic acid (0.289 mmol, 47 mg). Crude material was purified by liquid chromatography (PE/EtOAc 75:15 v/v to 50:50 v/v) giving compound **35** as a white solid (96%, 76.4 mg).

^{1}H NMR (700 MHz, CDCl3) δ 7.77 (d, 1H), 7.70–7.66 (m, 1H), 7.59–7.55 (m, 1H), 7.44–7.40 (m, 1H), 7.35 (t, J = 7.6 Hz, 1H), 7.32–7.28 (m, 1H), 7.20 (t, J = 7.5 Hz, 1H), 7.17 (t, 2H), 6.79 (t, J = 6.4 Hz, 1H), 6.69 (d, J = 8.2 Hz, 1H), 4.67 (s, 2H), 4.62–4.59 (m, 1H), 4.58 (s, 2H), 4.42–4.35 (m, 1H), 4.07–3.98 (m, 1H), 3.84 (s, 3H), 3.72–3.61 (m, 1H), 2.61–2.53 (m, 2H).

Methyl 3-fluoro-4-((1-oxo-4-phenyl-8-(5-phenylfuran-2-carbonyl)-2,8-diazaspiro[4.5]decan-2-yl)methyl)benzoate (29). Compound **29** a was synthesized following the general coupling procedure starting from 5-phenylfuran-2-carboxylic acid (0.260 mmol, 31 mg). Crude material was purified by silica gel column chromatography (DCM, DCM/MeOH 99:1 v/v) giving compound **29** as a white solid (71% yield, 91 mg).

^{1}H NMR (700 MHz, CDCl3) δ 7.78 (d, J = 1.6 Hz, 1H), 7.70 (d, J = 1.6 Hz, 1H), 7.59 (d, 2H), 7.37 (t, J = 7.5 Hz, 1H), 7.30 (t, J = 7.0 Hz, 2H), 7.23 (t, 1H), 7.17 (t, 2H), 7.07 (d, J = 3.6 Hz, 1H), 6.79 (t, J = 7.3 Hz, 1H), 6.71 (d, 2H), 6.67 (d, J = 3.6 Hz, 1H), 4.68 (s, 2H), 4.60 (s, 2H), 4.56 (dd, J = 6.4, 4.4 Hz, 2H), 4.11–3.97 (m, 1H), 3.86 (s, 3H), 3.77–3.54 (m, 1H), 2.68–2.56 (m, 2H), 1.81–1.73 (m, 2H).

(R)-N-Hydroxy-4-((4-oxo-1-phenyl-8-(tetrahydrofuran-2-carbonyl)-1,3,8-triazaspiro[4.5]decan-3-yl)methyl)benzamide (30a). Compound **30a** was prepared starting from compound **24a** (0.219 mmol, 107 mg) following the general procedure for the preparation of hydroxamic acids with 39% yield (36 mg).

MS (ESI) *m/z* calc. $[M+H]^+$ for $C_{26}H_{30}N_4O_5^+$: 478.55; found: $[M+Na]^+$ 501.37.

^{1}H NMR (700 MHz, DMSO-d_6) δ 7.76 (d, *J* = 2.1 Hz, 2H), 7.39 (d, *J* = 2.1 Hz, 2H), 7.24 – 7.17 (m, 2H), 6.81 – 6.75 (m, 1H), 6.74 – 6.69 (m, 2H), 4.80 – 4.72 (m, 1H), 4.66 – 4.59 (m, 4H), 4.37 – 4.32 (m, 1H), 4.07 – 4.02 (m, 1H), 3.83 – 3.69 (m, 4H), 2.71 – 2.61 (m, 1H), 2.40 – 2.31 (m, 1H), 2.23 – 2.17 (m, 1H), 2.11 – 2.04 (m, 1H), 1.97 – 1.90 (m, 2H), 1.89 – 1.82 (m, 1H), 1.73 – 1.65 (m, 1H).

^{13}C NMR (176 MHz, DMSO-d_6) δ 173.9, 169.7, 164.3, 142.8, 139.8, 132.5, 129.6, 127.9, 127.8, 118.6, 114.60, 79.6, 79.5, 75.4, 68.7, 63.2, 60.1, 44.0, 39.0, 27.9, 26.0.

(*R*)-3-Fluoro-*N*-hydroxy-4-((4-oxo-1-phenyl-8-(tetrahydrofuran-2-carbonyl)-1,3,8-triazaspiro[4.5]decan-3-yl)methyl)benzamide (30b). Compound **30b** was prepared starting from compound **24b** (0.352 mmol, 168 mg) following the general procedure for the preparation of hydroxamic acids with 13% yield (25 mg).

(ESI) *m/z* calc. $[M+H]^+$ for $C_{26}H_{30}FN_4O_5^+$: 497.55; found: $[M+Na]^+$ 519.38.

^{1}H NMR (700 MHz, DMSO-d_6) δ 11.26 (bs, 1H), 9.19 (bs, 1H), 7.63 (d, *J* = 7.9 Hz, 1H), 7.59 (d, *J* = 10.8 Hz, 1H), 7.45 (t, *J* = 7.7 Hz, 1H), 7.25 – 7.18 (m, 2H), 6.82 – 6.76 (m, 1H), 6.75 – 6.71 (m, 2H), 4.80 – 4.73 (m, 1H), 4.70 – 4.63 (m, 4H), 4.37 – 4.31 (m, 1H), 4.06 – 4.01 (m, 1H), 3.84 – 3.77 (m, 2H), 3.77 – 3.67 (m, 2H), 2.66 – 2.59 (m, 1H), 2.46 – 2.40 (m, 1H), 2.37 – 2.29 (m, 1H), 2.22 – 2.17 (m, 1H), 2.11 – 2.03 (m, 1H), 1.97 – 1.89 (m, 2H), 1.87 – 1.81 (m, 1H).

^{13}C NMR (176 MHz, DMSO-d_6) δ 173.9, 169.7, 163.0, 160.4, 152.5, 142.9, 134.9, 130.4, 129.7, 126.4, 123.7, 118.7, 115.3, 114.7, 75.4, 68.7, 63.3, 60.1, 55.4, 40.5, 29.7, 26.0, 21.9.

***N*-Hydroxy-4-((8-(1-methyl-1*H*-pyrrole-2-carbonyl)-4-oxo-1-phenyl-1,3,8-triazaspiro[4.5]decan-3-yl)methyl)benzamide (31a).** Compound **31a** was prepared starting from compound **25a** (0.103 mmol, 50 mg) following the general procedure for the preparation of hydroxamic acids with 68% yield (34 mg).

^{1}H NMR (700 MHz, DMSO-d_6) δ 11.20 (bs, 1H), 9.04 (bs, 1H), 7.76 (d, *J* = 8.0 Hz, 2H), 7.39 (d, *J* = 7.9 Hz, 2H), 7.23 (t, *J* = 7.8 Hz, 2H), 6.92 (s, 1H), 6.79 (t, *J* = 7.2 Hz, 1H), 6.75 (d, *J* = 8.1 Hz, 2H), 6.39 – 6.37 (m, 1H), 6.06 – 6.02 (m, 1H), 4.65 (s, 2H), 4.63 (s, 2H), 4.33 – 4.27 (m, 2H), 3.73 (s, 4H), 3.72 – 3.63 (m, 2H), 2.49 – 2.46 (m, 2H), 1.79 – 1.74 (m, 2H).

^{13}C NMR (176 MHz, DMSO-d$_6$) δ 173. 3, 162.6, 142.6, 129.2, 127.5, 126.4, 125.0, 118.4, 114.4, 111.8, 106.7, 62.8, 59.9, 43.5, 35.1, 21.4.

3-Fluoro-*N*-hydroxy-4-((8-(1-methyl-1*H*-pyrrole-2-carbonyl)-4-oxo-1-phenyl-1,3,8-triazaspiro[4.5]decan-3-yl)methyl)benzamide (31b). Compound **31b** was prepared starting from compound **25b** (0.219 mmol, 107 mg) following the general procedure for the preparation of hydroxamic acids with 28% yield (30 mg).

(ESI) *m/z* calc. $[M+H]^+$ for $C_{27}H_{29}FN_5O_4^+$: 506.22; found: 506.2; $[M+Na]^+$ 528.1.

^{1}H NMR (700 MHz, DMSO-d$_6$) δ 7.69 (d, *J* = 1.6 Hz, 1H), 7.65 (d, *J* = 1.6 Hz, 1H), 7.51 (t, *J* = 7.8 Hz, 1H), 7.29 (t, 2H), 6.99 – 6.97 (m, 1H), 6.86 (t, *J* = 7.3 Hz, 1H), 6.82 (d, *J* = 8.2 Hz, 2H), 6.44 – 6.42 (m, 1H), 6.12 – 6.08 (m, 1H), 4.73 (d, *J* = 10.5 Hz, 4H), 4.37 – 4.30 (m, 2H), 3.79 (s, 3H), 3.77 – 3.68 (m, 2H), 2.54 – 2.48 (m, 2H), 1.86 – 1.78 (m, 2H).

^{13}C NMR (176 MHz, DMSO-d$_6$) δ 173.2, 162.6, 160.0 (d, *J* = 246.2 Hz), 142.6, 129.9, 129.2, 126.4, 125.0, 118.5, 114.6, 111.8, 106.7, 62.8, 59.9, 48.6, 38.0, 35.1, 28.9.

***N*-Hydroxy-4-((8-(3-methylfuran-2-carbonyl)-4-oxo-1-phenyl-1,3,8-triazaspiro[4.5]decan-3-yl)methyl)benzamide (32).** Compound **32** was prepared starting from compound **26** (0.214 mmol, 91 mg) following the general procedure for the preparation of hydroxamic acids with 77% yield (81 mg).

^{1}H NMR (700 MHz, DMSO-d$_6$) δ 9.11 (bs, 1H), 7.82 (d, *J* = 7.4 Hz, 2H), 7.79 – 7.74 (m, 1H), 7.45 (d, *J* = 8.1 Hz, 2H), 7.27 (t, *J* = 7.3 Hz, 2H), 6.84 (t, *J* = 7.3 Hz, 1H), 6.79 (d, *J* = 9.2 Hz, 2H), 6.58 – 6.56 (m, 1H), 4.69 (d, *J* = 11.7 Hz, 4H), 2.55 – 2.51 (m, 2H), 2.26 (s, 3H), 1.88 – 1.84 (m, 2H).

^{13}C NMR (176 MHz, DMSO-d$_6$) δ 173.3, 160.0, 152.0, 143.1, 142.7, 142.5, 139.3, 132. 1, 129.2, 127.5, 127.4, 125.7, 118.5, 114.6, 114.5, 114.4, 62.8, 59.9, 43.6, 14.6, 10.8, 10. 8.

***N*-Hydroxy-4-((8-nicotinoyl-4-oxo-1-phenyl-1,3,8-triazaspiro[4.5]decan-3-yl)methyl)benzamide (33a).** Compound **33a** was prepared starting from compound **27a** (0.144 mmol, 70 mg) following the general procedure for the preparation of hydroxamic acids with 53% yield (37 mg).

(ESI) *m/z* calc. $[M+H]^+$ for $C_{27}H_{28}N_5O_4^+$: 486.55; found: 486.37; $[M+Na]^+$ 508.37.

^{1}H NMR (700 MHz, DMSO-d$_6$) δ 11.21 (bs, 1H), 9.06 (bs, 1H), 8.71 – 8.69 (m, 1H), 8.69 – 8.64 (m, 1H), 7.94 – 7.90 (m, 1H), 7.76 (d, *J* = 8.0 Hz, 2H), 7.53 – 7.49 (m, 1H), 7.39 (d, *J* = 7.9 Hz, 2H), 7.28 (t, *J* = 7.6 Hz, 2H), 6.84 – 6.79 (m, 3H), 4.67 – 4.60 (m, 4H), 4.52 – 4.45 (m, 1H), 3.89 – 3.83 (m, 1H), 3.63 – 3.56 (m, 2H), 2.61 – 2.55 (m, 1H), 2.45 – 2.39 (m, 1H), 1.88 – 1.82 (m, 1H), 1.73 – 1.67 (m, 1H).

^{13}C NMR (176 MHz, DMSO-d$_6$) δ 173.2, 167.4, 164.0, 150.5, 147.5, 142.7, 139.3, 134.8, 132.0, 129.4, 127.6, 127.4, 123.8, 118.6, 114.7, 62.9, 60.0, 43.6.

3-Fluoro-*N*-hydroxy-4-((8-nicotinoyl-4-oxo-1-phenyl-1,3,8-triazaspiro[4.5]decan-3-yl)methyl)benzamide (33b). Compound **33b** was prepared starting from compound **26b** (0.149 mmol, 75 mg) following the general procedure for the preparation of hydroxamic acids with 40% yield (30 mg).

(ESI) *m/z* calc. $[M+H]^+$ for $C_{27}H_{27}FN_5O_4^+$: 504.54; found: 486.37; $[M+Na]^+$ 526.38.

^{1}H NMR (700 MHz, DMSO-d$_6$) δ 8.65 (d, *J* = 1.6 Hz, 1H), 8.01 (t, *J* = 1.7 Hz, 1H), 7.69 (t, *J* = 7.6 Hz, 2H), 7.64 (d, *J* = 10.8 Hz, 1H), 7.56 – 7.53 (m, 1H), 7.50 (t, *J* = 7.7 Hz, 1H), 7.31 (t, *J* = 8.2 Hz, 2H), 6.90 – 6.84 (m, 3H), 4.78 – 4.69 (m, 4H), 4.58 – 4.54 (m, 1H), 3.84 – 3.73 (m, 2H), 3.61 – 3.55 (m, 1H), 2.67 – 2.60 (m, 2H), 1.93 – 1.87 (m, 1H), 1.77 – 1.72 (m, 1H).

^{13}C NMR (176 MHz, DMSO-d$_6$) δ 173.2, 167.0, 160.0 (d, *J* = 246.0 Hz), 148.5, 142.6, 137.5, 129.9, 129.3, 124.6, 123.0, 118.6, 114.8, 62.9, 59.8, 43.2, 38.5, 38.0, 29.2, 28.5.

4-((8-(Benzofuran-2-carbonyl)-4-oxo-1-phenyl-1,3,8-triazaspiro[4.5]decan-3-yl)methyl)-3-fluoro-*N*-hydroxybenzamide (34). Compound **34** was prepared starting from compound **28** (0.141 mmol, 76.4 mg) following the general procedure for the preparation of hydroxamic acids with 20% yield (15 mg).

(ESI) *m/z* calc. $[M+H]^+$ for $C_{30}H_{28}FN_4O_5^+$: 543.57; found: $[M+Na]^+$ 565.40.

^{1}H NMR (400 MHz, DMSO-d$_6$) δ 7.76 (d, *J* = 1.0 Hz, 1H), 7.71 – 7.55 (m, 3H), 7.50 – 7.42 (m, 3H), 7.37 – 7.31 (m, 1H), 7.25 (t, *J* = 8.4 Hz, 2H), 6.80 (d, *J* = 8.0 Hz, 3H), 4.69 (d, *J* = 5.9 Hz, 4H), 4.49 – 4.28 (m, 2H), 2.60 – 2.52 (m, 1H), 1.90 – 1.82 (m, 2H).

^{13}C NMR (101 MHz, DMSO-d$_6$) δ 173.6, 162.9, 160.4 (d, *J* = 246.3 Hz), 159.7, 154.4, 148.8, 143.1, 130.4, 129.8, 127.2, 127.0, 124.2, 122.9, 119.2, 115.5, 112.3, 111.1, 63.4, 60.4, 38.5.

3-Fluoro-*N*-hydroxy-4-((4-oxo-1-phenyl-8-(5-phenylfuran-2-carbonyl)-1,3,8 triazaspiro[4.5]decan-3-yl)methyl)benzamide (35). Compound **35** was prepared starting from compound **29** (0.160 mmol, 91 mg) following the general procedure for the preparation of hydroxamic acids with 38% yield (35 mg).

^{1}H NMR (400 MHz, DMSO-d$_6$) δ 7.84 – 7.79 (m, 2H), 7.70 – 7.62 (m, 2H), 7.56 – 7.47 (m, 3H), 7.45 – 7.39 (m, 1H), 7.32 – 7.26 (m, 2H), 7.23 (d, *J* = 3.6 Hz, 1H), 7.18 (d, *J* = 3.6 Hz, 1H), 6.88 – 6.82 (m, 3H), 4.80 – 4.71 (m, 4H), 4.48 – 4.41 (m, 2H), 2.64 – 2.58 (m, 1H), 1.96 – 1.90 (m, 2H).

^{13}C NMR (101 MHz, DMSO-d$_6$) δ 173.7, 160.42 (d, *J* = 246.3 Hz), 158.9, 154.6, 150.1, 147.1, 143.06, 134.8, 130.4, 129.9, 129.7, 129.5, 129.0, 124.5, 123.7, 119.2, 118.3, 115.4, 114.5, 114.3, 107.6, 63.4, 60.3, 38.5, 29.5, 17.1.

Methyl 4-((8-(ethylcarbamoyl)-4-oxo-1-phenyl-1,3,8-triazaspiro[4.5]decan-3-yl)methyl)-3-fluorobenzoate (36). Compound **36** was synthesized following the general procedure for the synthesis of urea derivatives starting from ethyl isocyanate (0.132 mmol, 0.011 mL) providing compound **36** as yellow oil with quantitative yield (59.03 mg).

^{1}H NMR (700 MHz, $CDCl_3$) δ 7.77 (d, *J* = 1.6 Hz, 1H), 7.69 (d, *J* = 1.6 Hz, 1H), 7.34 (t, *J* = 7.6 Hz, 1H), 7.19 – 7.14 (m, 2H), 6.78 (t, *J* = 1.4 Hz, 1H), 6.64 (d, 2H), 4.65 (s, 2H), 4.56 (s, 2H), 3.86 (s, 3H), 3.84 – 3.78 (m, 2H), 3.64 – 3.59 (m, 2H), 3.29 – 3.22 (m, 2H), 2.54 – 2.43 (m, 2H), 1.65 – 1.59 (m, 2H), 1.11 (t, *J* = 7.2 Hz, 3H).

Methyl 4-((8-((cyclopentylmethyl)carbamoyl)-4-oxo-1-phenyl-1,3,8-triazaspiro[4.5]decan-3-yl)methyl)benzoate (37). Compound **37** was synthesized following the general procedure for the synthesis of urea derivatives starting from cyclopentyl isocyanate (0.138 mmol, 0.040 mL). Compound **37** was used in the next step without further purification.

^{1}H NMR (700 MHz, $CDCl_3$) δ 7.97 (d, 2H), 7.28 (d, *J* = 7.9 Hz, 2H), 7.15 (t, *J* = 7.8 Hz, 2H), 6.77 (t, *J* = 7.3 Hz, 1H), 6.61 (d, *J* = 8.1 Hz, 2H), 4.59 (s, 2H), 4.51 (s, 2H), 4.43 – 4.37 (m, 1H), 4.16 – 4.10 (m, 2H), 3.92 – 3.87 (m, 2H), 3.85 (s, 3H), 3.84 – 3.78 (m, 2H), 3.65 – 3.58 (m, 2H), 2.56 – 2.50 (m, 2H), 2.02 – 1.97 (m, 2H), 1.93 – 1.86 (m, 4H).

Methyl 4-((4-oxo-8-(phenethylcarbamoyl)-1-phenyl-1,3,8-triazaspiro[4.5]decan-3-yl)methyl)benzoate (38). Compound **38** was synthesized following the general procedure for the synthesis of urea derivatives starting from phenethyl isocyanate (0.139 mmol, 0.019 mL). Crude material was dissolved in EtOAc and extracted with 2 N HCl giving compound **38** with 36% yield (68 mg).

^{1}H NMR (700 MHz, $CDCl_3$) δ 7.97 (d, *J* = 1.7 Hz, 2H), 7.28 (d, *J* = 1.8 Hz, 2H), 7.25 – 7.21 (m, 3H), 7.18 – 7.13 (m, 5H), 6.78 (t, *J* = 7.3 Hz, 1H), 6.63 (d, *J* =

8.1 Hz, 2H), 4.59 (s, 2H), 4.50 (d, *J* = 1.6 Hz, 2H), 3.85 (d, *J* = 1.6 Hz, 3H), 3.79 – 3.74 (m, 2H), 3.65 – 3.57 (m, 2H), 3.50 – 3.45 (m, 2H), 2.80 (t, *J* = 6.9 Hz, 2H), 2.51 – 2.43 (m, 2H), 1.65 – 1.60 (m, 2H).

Methyl 4-((8-(benzylcarbamoyl)-4-oxo-1-phenyl-1,3,8-triazaspiro[4.5]decan-3-yl)methyl)benzoate (39). Compound **39** was synthesized following the general procedure for the synthesis of urea derivatives starting from benzyl isocyanate (0.277 mmol, 0.034 mL). Crude material was purified by silica gel column chromatography (DCM, DCM/MeOH 99:1 v/v) providing compound **39** as white solid with 28% yield (38 mg).

Methyl 3-fluoro-4-((8-((furan-2-ylmethyl)carbamoyl)-4-oxo-1-phenyl-1,3,8-triazaspiro[4.5]decan-3-yl)methyl)benzoate (40). Compound **40** was synthesized following the general procedure for the synthesis of urea derivatives starting from furfuryl isocyanate 0.158 mmol, 0.017 mL). Crude material was purified by liquid chromatography (DCM/MeOH 99:1 v/v) giving compound **40** as a colorless oil (30% yield, 24 mg).

^{1}H NMR (400 MHz, $CDCl_3$) δ 7.77 (d, *J* = 1.6 Hz, 1H), 7.69 (d, *J* = 1.6 Hz, 1H), 7.37 – 7.26 (m, 2H), 7.16 (t, 2H), 6.79 (t, *J* = 7.3 Hz, 1H), 6.64 (d, *J* = 8.2 Hz, 2H), 6.28 – 6.25 (m, 1H), 6.19 – 6.17 (m, 1H), 4.79 – 4.74 (m, 1H), 4.65 (s, 2H), 4.56 (s, 2H), 4.40 (d, *J* = 5.3 Hz, 2H), 3.86 (s, 3H), 3.85 – 3.80 (m, 1H), 3.70 – 3.57 (m, 2H), 2.54 – 2.40 (m, 2H), 1.69 – 1.60 (m, 2H).

***N*-Ethyl-3-(2-fluoro-4-(hydroxycarbamoyl)benzyl)-4-oxo-1-phenyl-1,3,8-triazaspiro[4.5]decane-8-carboxamide (41).** Compound **41** was prepared starting from compound **36** (0.125 mmol, 59 mg) following the general procedure for the preparation of hydroxamic acids with 18% yield (10 mg).

^{1}H NMR (700 MHz, DMSO) δ 10.33 (bs, 1H), 8.66 (bs, 1H), 7.63 (d, *J* = 1.7 Hz, 1H), 7.59 (d, *J* = 1.7 Hz, 1H), 7.44 (t, *J* = 7.7 Hz, 1H), 7.19 (t, *J* = 7.2 Hz, 2H), 6.77 (t, *J* = 7.3 Hz, 1H), 6.69 – 6.66 (m, 2H), 4.67 (s, 2H), 4.65 (s, 2H), 3.95 –

3.86 (m, 2H), 3.42 – 3.37 (m, 2H), 3.15 – 3.09 (m, 2H), 2.46 – 2.37 (m, 2H), 1.60 – 1.55 (m, 2H), 1.07 (t, *J* = 7.1 Hz, 3H).

^{13}C NMR (176 MHz, DMSO) δ 173.4, 166.0, 162.4, 160.5, 159.1, 157.4, 142.4, 134.2, 129.8, 129.0, 123.2, 118.0, 114.0, 62.6, 59.5, 48.5, 40.5, 37.8, 34.7, 27.6, 19.3, 15.7.

***N*-Cyclopentyl-3-(4-(hydroxycarbamoyl)benzyl)-4-oxo-1-phenyl-1,3,8-triazaspiro[4.5]decane-8-carboxamide (42).** Compound **42** was prepared starting from compound **37** (0.132 mmol, 65 mg) following the general procedure for the preparation of hydroxamic acids with 15% yield (10 mg).

(ESI) *m/z* calc. $[M+H]^+$ for $C_{27}H_{34}N_5O_4^+$: 492.60; found: $[M+Na]^+$ 514.48.

^{1}H NMR (700 MHz, DMSO-d$_6$) δ 7.76 (d, *J* = 7.8 Hz, 2H), 7.38 (d, *J* = 7.8 Hz, 2H), 7.18 (t, *J* = 7.8 Hz, 2H), 6.76 (d, *J* = 7.4 Hz, 1H), 6.65 (d, *J* = 8.1 Hz, 2H), 6.45 – 6.42 (m, 1H), 4.62 (d, *J* = 8.4 Hz, 4H), 4.03 – 3.98 (m, 1H), 3.97 – 3.93 (m, 2H), 3.43 – 3.36 (m, 3H), 2.48 – 2.39 (m, 3H), 1.87 – 1.81 (m, 2H), 1.53 – 1.44 (m, 5H).

^{13}C NMR (176 MHz, DMSO-d$_6$) δ 174.1, 158.0, 143.0, 139.8, 132.5, 129.5, 127.9, 118.4, 114.2, 63.1, 60.0, 52.5, 43.9, 41.4, 33.0, 28.2, 23.9.

3-(4-(Hydroxycarbamoyl)benzyl)-4-oxo-*N*-phenethyl-1-phenyl-1,3,8-triazaspiro[4.5]decane-8-carboxamide (43). Compound **43** was prepared starting from compound **38** (0.047 mmol, 25 mg) following the general procedure for the preparation of hydroxamic acids with 20% yield (5 mg).

(ESI) *m/z* calc. $[M+H]^+$ for $C_{30}H_{33}N_5O_4^+$: 527.25; found: 528.20; $[M+Na]^+$ 550.1

^{1}H NMR (700 MHz, DMSO-d$_6$) δ 7.76 (d, *J* = 8.8 Hz, 2H), 7.38 (d, *J* = 11.7 Hz, 2H), 7.32 – 7.27 (m, 2H), 7.25 – 7.22 (m, 2H), 7.22 – 7.16 (m, 3H), 6.83 – 6.80 (m, 1H), 6.76 (t, *J* = 7.3 Hz, 1H), 6.68 (d, *J* = 8.1 Hz, 2H), 4.62 (d, *J* = 9.7 Hz, 4H), 3.95 – 3.90 (m, 2H), 3.46 – 3.41 (m, 2H), 3.30 – 3.28 (m, 2H), 2.79 – 2.76 (m, 2H), 2.45 – 2.40 (m, 2H), 1.63 – 1.58 (m, 2H).

^{13}C NMR (176 MHz, DMSO-d_6) δ 174.0, 164.4, 158.0, 143.0, 140.3, 139.7, 132.6, 129.6, 129.1, 128.8, 127.9, 127.8, 126.5, 118.6, 114.6, 63.2, 60. 2, 43.9, 42.5, 41.0, 36. 8, 28.4.

***N*-Benzyl-3-(4-(hydroxycarbamoyl)benzyl)-4-oxo-1-phenyl-1,3,8-triazaspiro[4.5]decane-8-carboxamide (44).** Compound **44** was prepared starting from compound **39** (0.074 mmol, 38 mg) following the general procedure for the preparation of hydroxamic acids with 20% yield (7 mg).

^{1}H NMR (700 MHz, DMSO-d_6) δ 7.48 (d, *J* = 7.7 Hz, 2H), 7.38 (t, *J* = 7.6 Hz, 2H), 7.32 – 7.26 (m, 3H), 7.22 (t, *J* = 8.6 Hz, 2H), 6.81 (d, *J* = 8.3 Hz, 2H), 6.77 (t, *J* = 7.3 Hz, 1H), 4.56 (s, 2H), 4.52 (s, 2H), 3.72 (s, 2H), 2.87 – 2.81 (m, 2H), 2.79 – 2.74 (m, 2H), 2.54 – 2.52 (m, 1H), 1.64 – 1.57 (m, 2H).

^{13}C NMR (176 MHz, DMSO-d_6) δ 174.0, 158.0, 141.7, 129.6, 128.6, 127.9, 127.4, 126.9, 118.6, 114.6, 63.1, 60.2, 49.1, 43.9, 41.0, 28.6.

3-(2-Fluoro-4-(hydroxycarbamoyl)benzyl)-*N*-(furan-2-ylmethyl)-4-oxo-1-phenyl-1,3,8-triazaspiro[4.5]decane-8-carboxamide (45). Compound **45** was prepared starting from compound **40** (0.045 mmol, 24 mg) following the general procedure for the preparation of hydroxamic acids with 93% yield (21 mg).

(ESI) *m/z* calc. $[M+H]^+$ for $C_{27}H_{29}FN_5O_4^+$: 522.22; found: 522.20; $[M+Na]^+$ 545.10.

^{1}H NMR (700 MHz, DMSO-d_6) δ 9.18 (bs, 1H), 7.62 (d, *J* = 8.5 Hz, 1H), 7.58 (td, *J* = 10.7, 1.6 Hz, 1H), 7.55 (s, 1H), 7.44 (t, *J* = 7.7 Hz, 1H), 7.20 – 7.16 (m, 3H), 6.78 (t, *J* = 7.3 Hz, 1H), 6.67 (d, *J* = 8.4 Hz, 2H), 6.42 – 6.40 (m, 1H), 6.20 – 6.18 (m, 1H), 4.66 (d, *J* = 14.8 Hz, 4H), 4.28 (d, *J* = 5.6 Hz, 2H), 3.98 – 3.93 (m, 2H), 3.46 – 3.41 (m, 2H), 2.42 – 2.35 (m, 2H), 1.63 – 1.58 (m, 2H).

^{13}C NMR (101 MHz, DMSO-d_6) δ 173.9, 160.4 (d, *J* = 245.8 Hz), 157.7, 154.6, 143.0, 142.1, 134.8, 130.4, 123.8, 118. 8, 114.8, 110.9, 106.5, 63.2, 60.2, 38.4, 37.6, 28.5.

Methyl 3-fluoro-4-((4-oxo-8-(2-oxo-2-(pyrrolidin-1-yl)acetyl)-1-phenyl-1,3,8-triazaspiro[4.5]decan-3-yl)methyl)benzoate (46). To a cooled solution of compound **6b** (0.250 mmol, 100 mg) in dry DCM (1 mL), a solution of oxalyl chloride (1 mmol, 0.086 mL) in dry DCM (1 mL) was added dropwise. After 5 min, TEA (1 mmol, 0.140 mL) was added and the reaction mixture allowed under stirring. After 1 h, pyrrolidine (2.50 mmol, 0.210 mL) was added followed by TEA (2.50 mmol, 0.350 mL) and the reaction mixture left under stirring for 30 min. Reaction mixture was neutralized by the addition of 2 N HCl (5 mL) and aqueous layer extracted with DCM (5 mL). Organic layer was dried over Na_2SO_4 and evaporated under vacuum. Crude material was purified by silica gel column chromatography (PE/EtOAc 25:75 v/v) providing compound **46** as pale yellow oil with 41% yield (53 mg).

^{1}H NMR (700 MHz, $CDCl_3$) δ 7.82 – 7.74 (m, 1H), 7.73 – 7.66 (m, 1H), 7.37 – 7.31 (m, 1H), 7.19 – 7.10 (m, 2H), 6.85 – 6.77 (m, 1H), 6.74 – 6.63 (m, 2H), 4.66 (s, 2H), 4.57 (s, 2H), 3.87 (s, 3H), 3.70 – 3.35 (m, 4H), 2.70 – 2.57 (m, 1H), 2.58 – 2.41 (m, 1H), 1.97 – 1.83 (m, 2H), 1.75 – 1.58 (m, 3H), 1.33 – 1.18 (m, 4H), 0.89 – 0.79 (m, 3H).

Methyl 4-((8-(2-(dimethylamino)-2-oxoacetyl)-4-oxo-1-phenyl-1,3,8-triazaspiro[4.5]decan-3-yl)methyl)-3-fluorobenzoate (47). To a cooled solution of compound **6b** (0.186 mmol, 76 mg) in dry DCM (2mL), a solution of oxalyl chloride (0.744 mmol, 0.064 mL) in dry DCM (1 mL) was added dropwise. After 5 min, TEA (0.744 mmol, 0.103 mL) was added, and the reaction mixture allowed under stirring. After 1 h, dimethylamine hydrobromide (1.86 mmol, 234 mg) was added followed by TEA (1.86 mmol, 0.259 mL) and the reaction mixture left under stirring for 30 min. Reaction mixture was neutralized by the addition of 1 N HCl (5 mL) and extracted with DCM (5 mL). Organic layer was dried over Na_2SO_4 and evaporated under vacuum to give compound **47** with 47% yield (44 mg).

^{1}H NMR (400 MHz, DMSO-d_6) δ 7.78 (d, *J* = 8.0 Hz, 1H), 7.69 (d, *J* = 10.3 Hz, 1H), 7.34 (t, *J* = 7.5 Hz, 1H), 7.23 – 7.13 (m, 2H), 6.81 (t, *J* = 7.3 Hz, 1H), 6.70 (d, *J* = 8.1 Hz, 2H), 4.65 (s, 2H), 4.57 (s, 2H), 4.49 – 4.39 (m, 1H), 3.98 – 3.90 (m, 1H), 3.86 (s, 3H), 3.60 – 3.50 (m, 2H), 2.94 – 2.92 (m, 6H), 2.66 – 2.55 (m, 1H), 2.52 – 2.41 (m, 1H), 1.68 (t, *J* = 13.4 Hz, 2H).

3-Fluoro-*N*-hydroxy-4-((4-oxo-8-(2-oxo-2-(pyrrolidin-1-yl)acetyl)-1-phenyl-1,3,8-triazaspiro[4.5]decan-3-yl)methyl)benzamide (48). Compound **48** was prepared starting from compound **46** (0.033 mmol, 18 mg) following the general procedure for the preparation of hydroxamic acids with 50% yield (8.5 mg).

MS (ESI) m/z calc. $[M+H]^+$ for $C_{27}H_{30}FN_5O_5^+$: 523.2; found: 524.5.

^{1}H NMR (400 MHz, DMSO-d_6) δ 11.13 (bs, 1H), 9.17 (bs, 1H), 7.65 – 7.55 (m, 2H), 7.45 (t, *J* = 7.8 Hz, 1H), 7.23 (t, *J* = 7.8 Hz, 2H), 6.84 – 6.76 (m, 3H), 4.74 – 4.62 (m, 4H), 4.34 – 4.27 (m, 1H), 3.82 – 3.73 (m, 1H), 3.53 – 3.39 (m, 2H), 2.95 (s, 3H), 2.88 (d, *J* = 8.6 Hz, 3H), 2.47 – 2.31 (m, 2H), 1.85 – 1.72 (m, 2H).

^{13}C NMR (101 MHz, DMSO-d_6) δ 173.5, 165.0, 163.8, 143.0, 130.4, 129.7, 123.7, 119.3, 115.5, 63.4, 60.3, 42.5, 38.5, 37.5, 36.9, 33.3.

4-((8-(2-(Dimethylamino)-2-oxoacetyl)-4-oxo-1-phenyl-1,3,8-triazaspiro[4.5]decan-3-yl)methyl)-3-fluoro-*N*-hydroxybenzamide (49). Compound **49** was prepared starting from compound **47** (0.088 mmol, 45 mg) following the general procedure for the preparation of hydroxamic acids with 19% yield (9 mg).

(ESI) m/z calc. $[M+H]^+$ for $C_{25}H_{28}FN_5O5^+$:497.2; found: 498.5.

^{1}H NMR (400 MHz, DMSO-d_6) δ 11.13 (bs, 1H), 9.17 (bs, 1H), 7.65 – 7.55 (m, 2H), 7.45 (t, *J* = 7.8 Hz, 1H), 7.23 (t, *J* = 7.8 Hz, 2H), 6.85 – 6.74 (m, 3H), 4.74 – 4.59 (m, 4H), 4.35 – 4.27 (m, 1H), 3.82 – 3.73 (m, 1H), 3.54 – 3.39 (m, 2H), 2.95 (s, 3H), 2.88 (d, *J* = 8.6 Hz, 3H), 2.48 – 2.32 (m, 2H), 1.83 – 1.72 (m, 2H).

^{13}C NMR (101 MHz, DMSO-d_6) δ 173.5, 165.0, 163.8, 143.0, 130.4, 129.7, 123.7, 119.3, 115.5, 63.4, 60.3, 55.4, 42.5, 37.5, 36.9, 33.3, 29.5, 28.0.

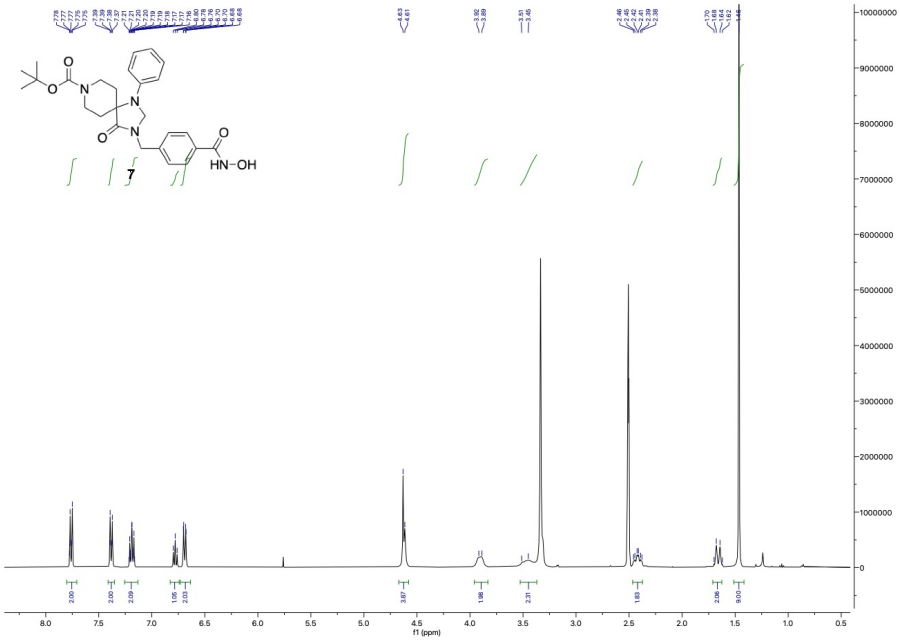
3.3.2 Solubility determination

Each compound was dissolved in dimethyl sulfoxide (DMSO) at a concentration of 10 mM. Then, 10 µL of the obtained solution was diluted either in 490 µL of water pH 7 or MeOH and maintained under agitation at 250 rpm for 24 h at room temperature. Tubes were subsequently centrifuged for 5 min at 4000 rpm and 10 µL of each sample were further diluted in 490 µL of MeOH and analyzed by LC−MS/MS. The ratio of mass signal area obtained in water and in organic solvent was then calculated and used to determine the solubility of each compound.

3.3.2 Supporting figures

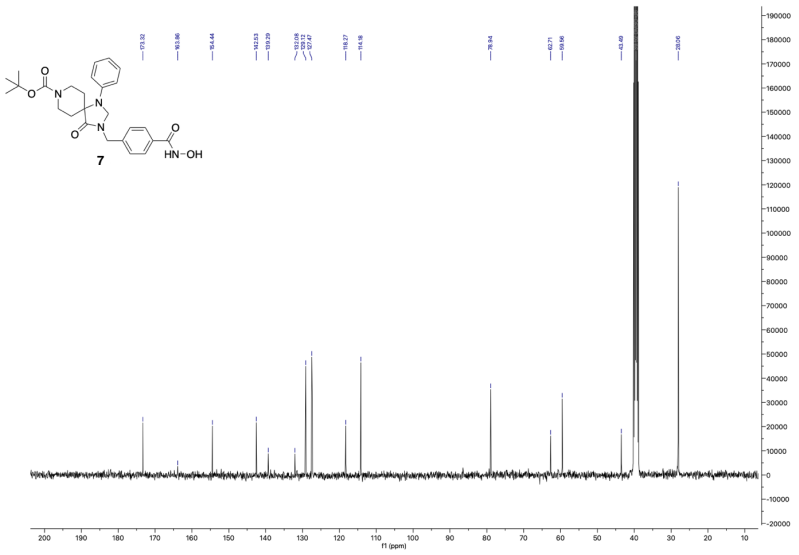
Supporting Figure 1

^{1}H NMR of 7



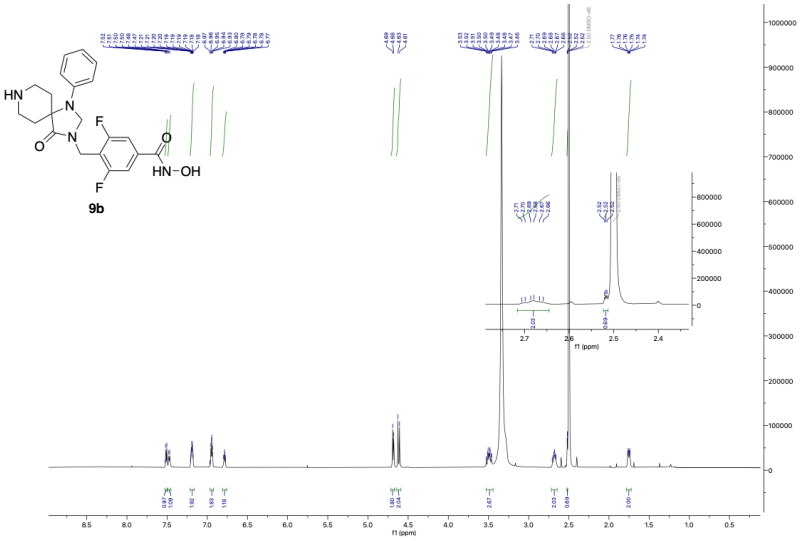
Supporting Figure 2

^{13}C NMR of 7



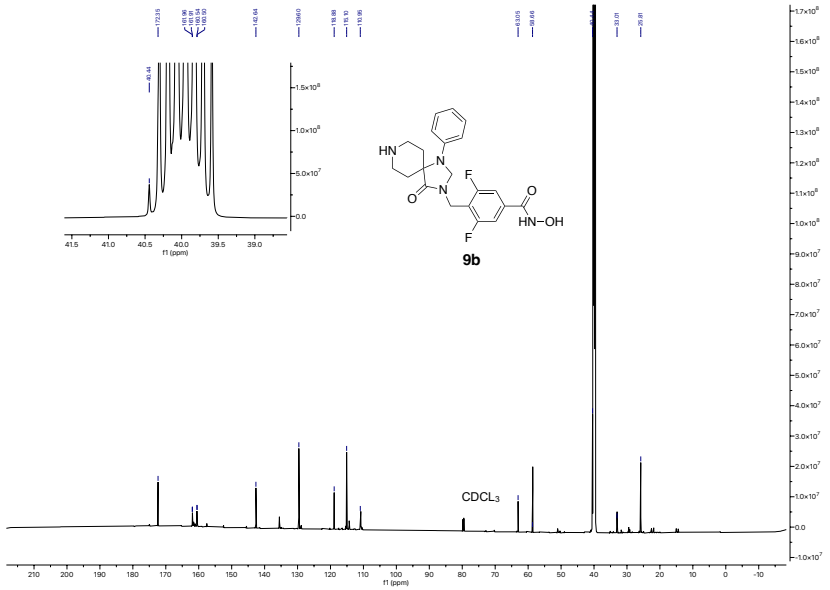
Supporting Figure 3

^{1}H NMR of 9b



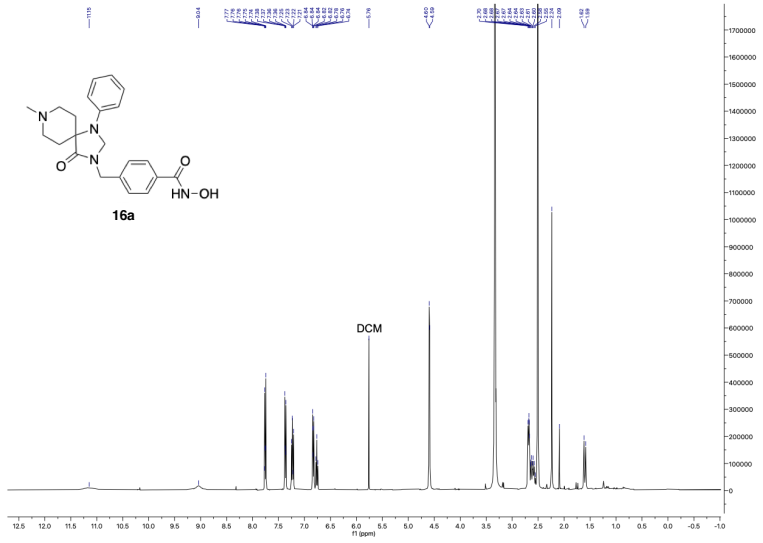
Supporting Figure 4

^{13}C NMR of 9b



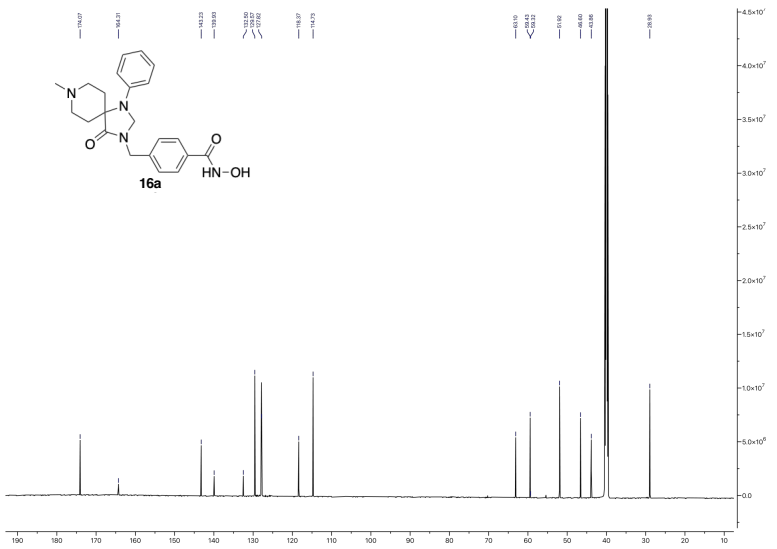
Supporting Figure 5

^{1}H NMR of 16a



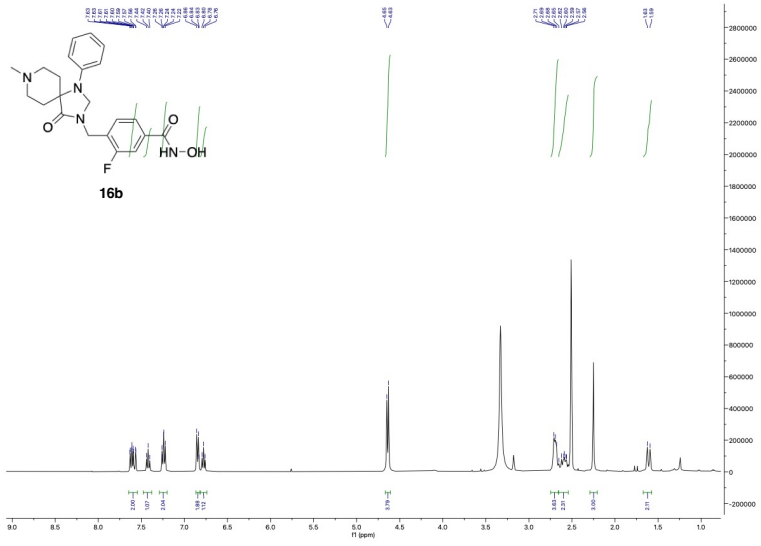
Supporting Figure 6

^{13}C NMR of 16a



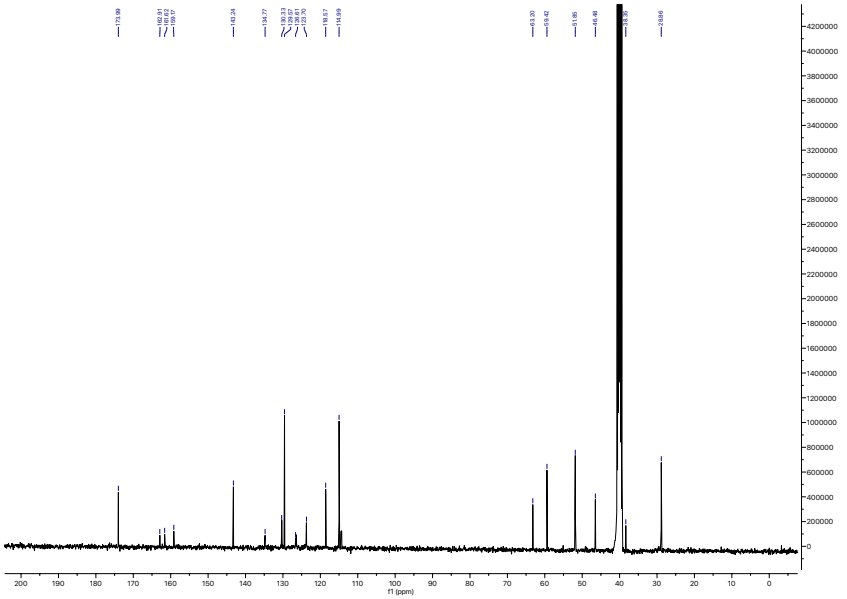
Supporting Figure 7

^{1}H NMR of 16b



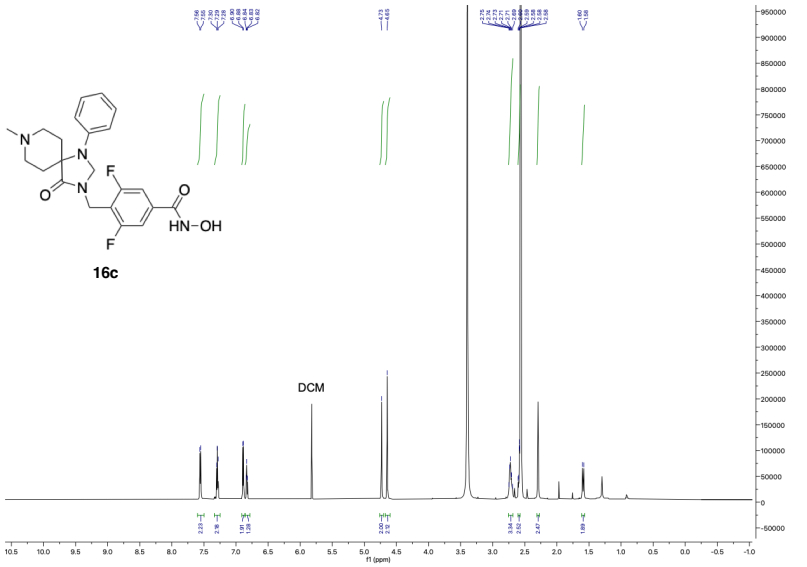
Supporting Figure 8

^{13}C NMR of 16b



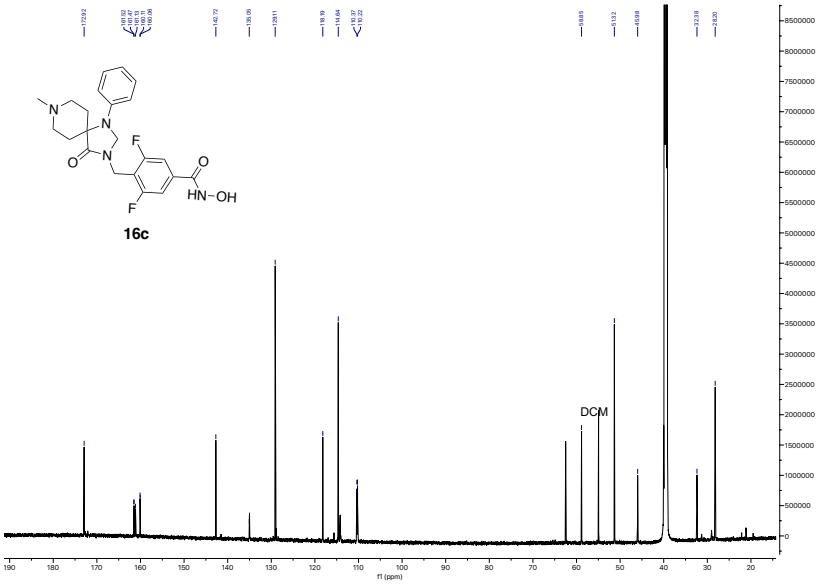
Supporting Figure 9

^{1}H NMR of 16c



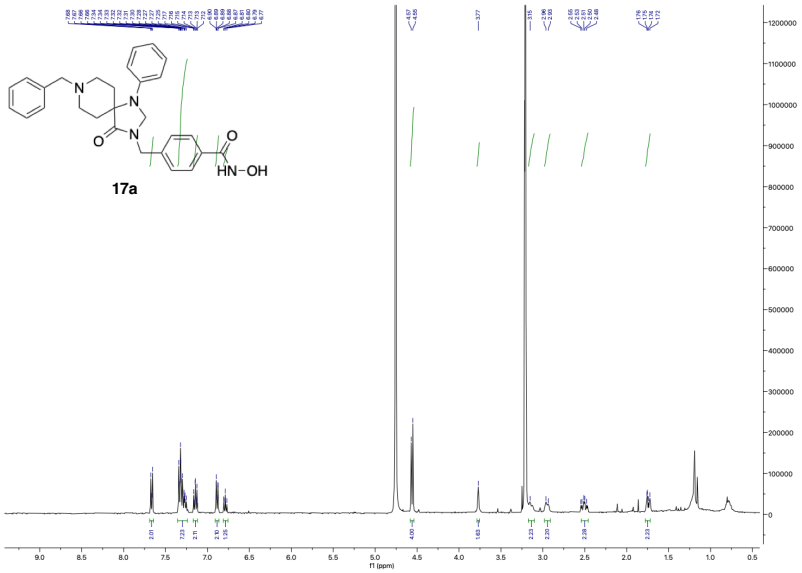
Supporting Figure 10

^{13}C NMR of 16c



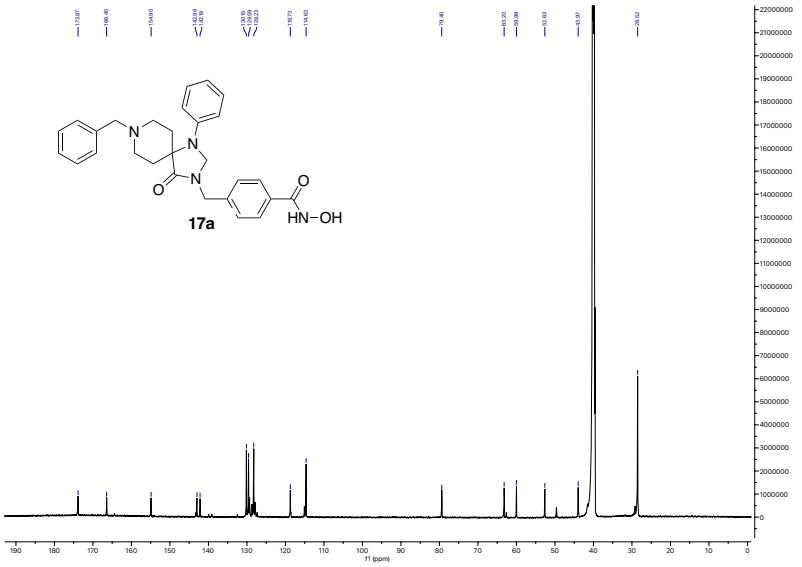
Supporting Figure 11

^{1}H NMR of 17a



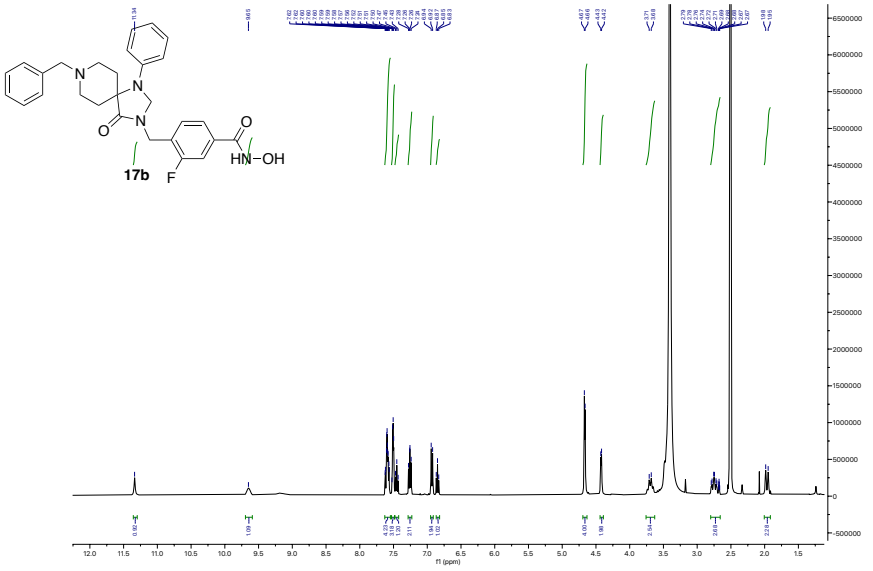
Supporting Figure 12

^{13}C NMR of 17a



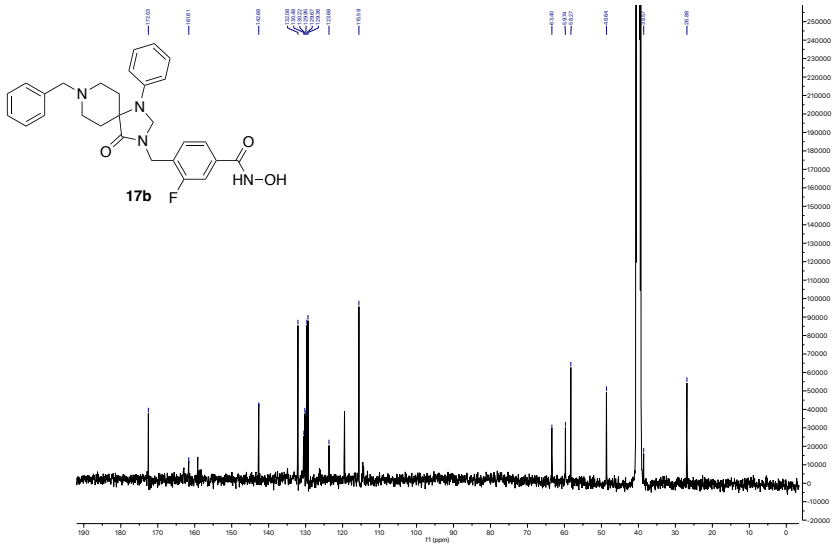
Supporting Figure 13

^{1}H NMR of 17b



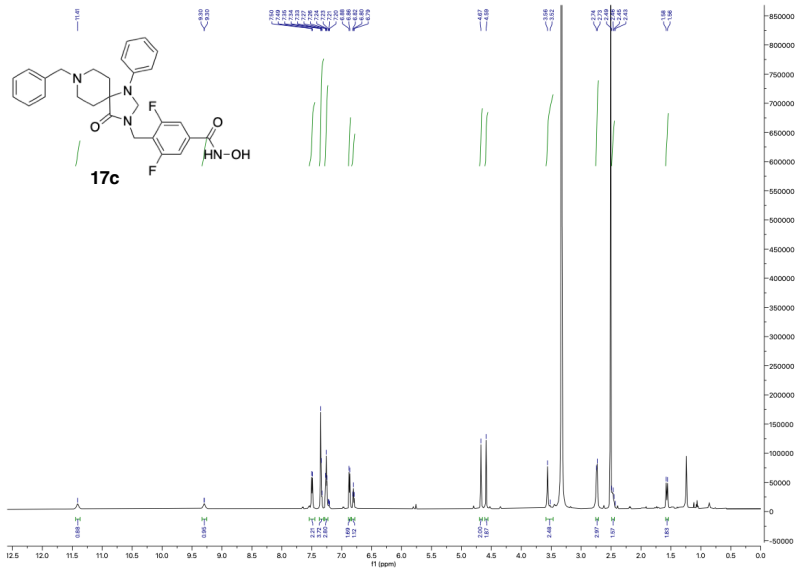
Supporting Figure 14

^{13}C NMR of 17b



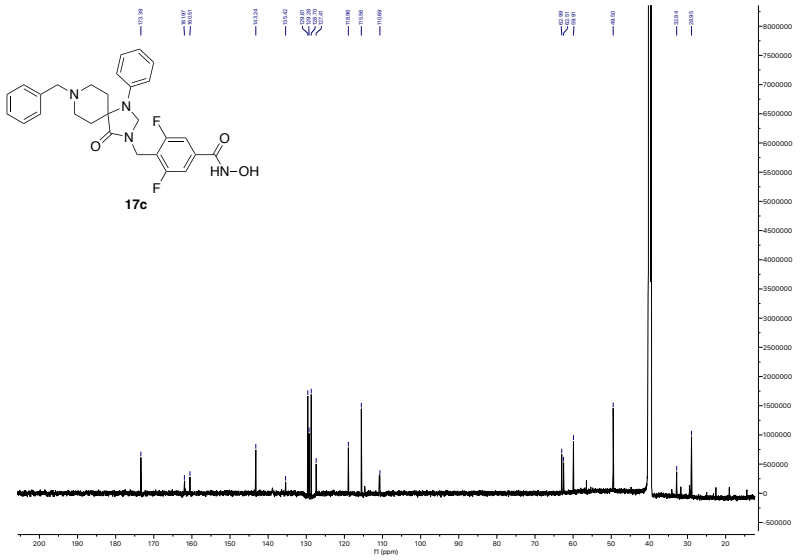
Supporting Figure 15

^{1}H NMR of 17c



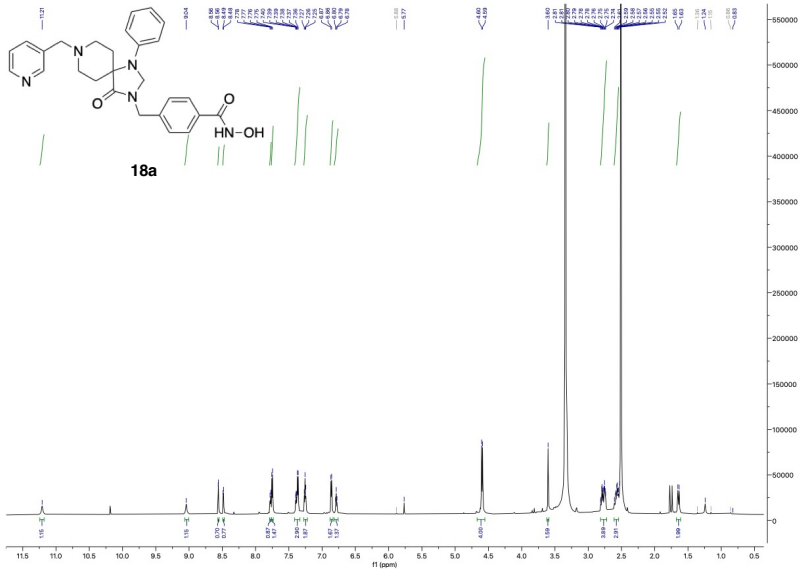
Supporting Figure 16

^{13}C NMR of 17c



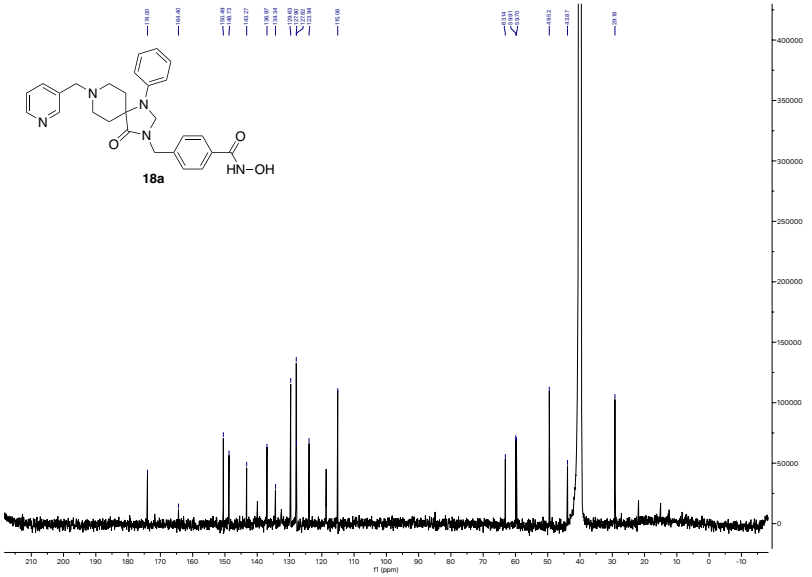
Supporting Figure 17

^{1}H NMR of 18a



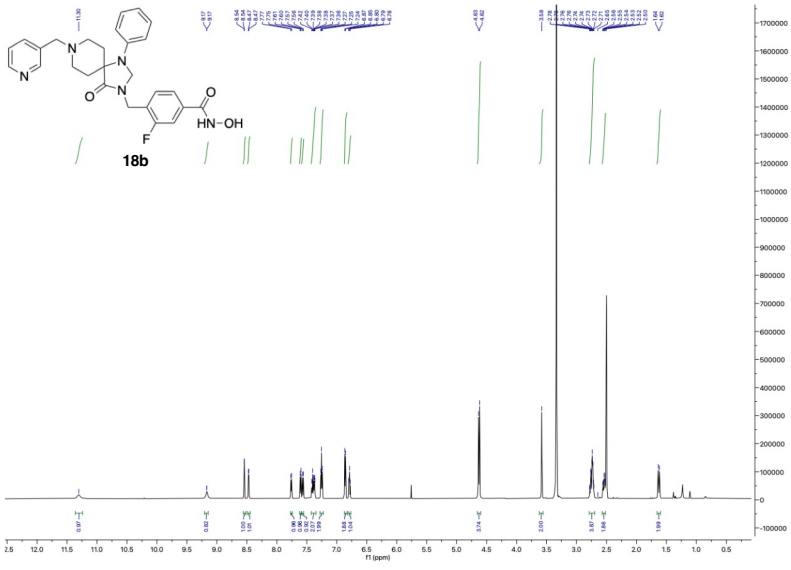
Supporting Figure 18

^{13}C NMR of 18a



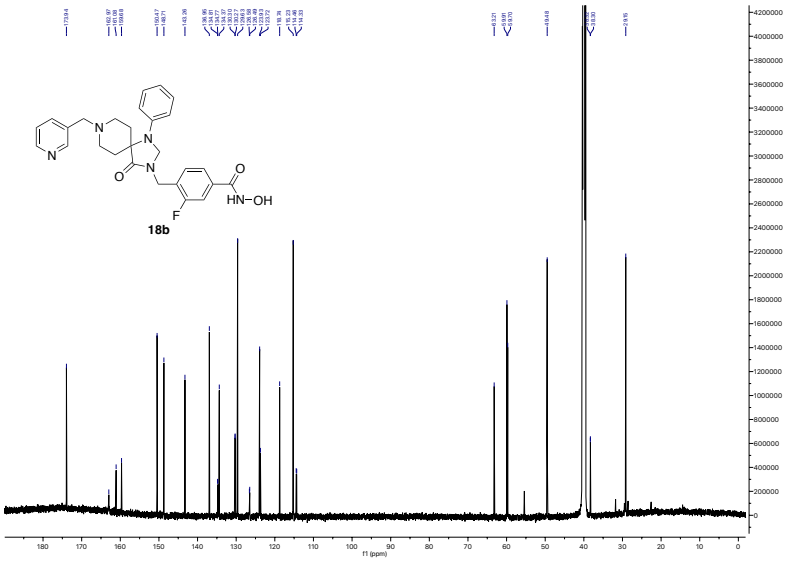
Supporting Figure 19

^{1}H NMR of 18b



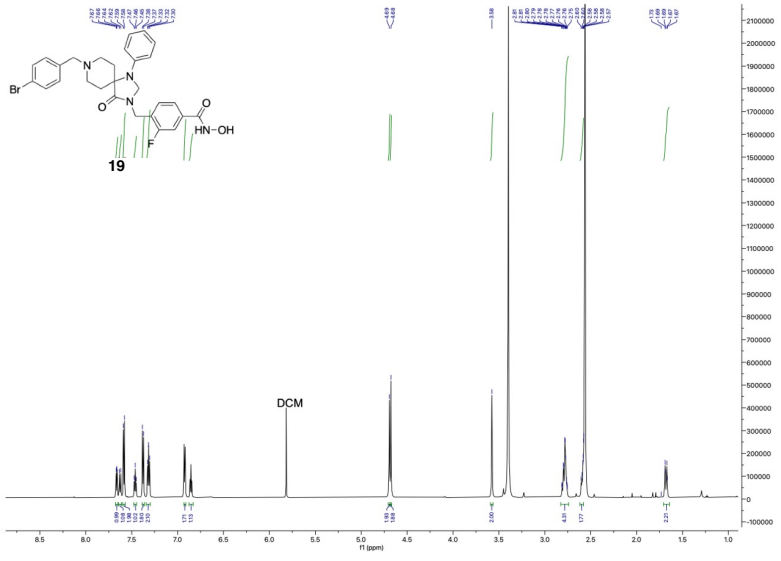
Supporting Figure 20

^{13}C NMR of 18b



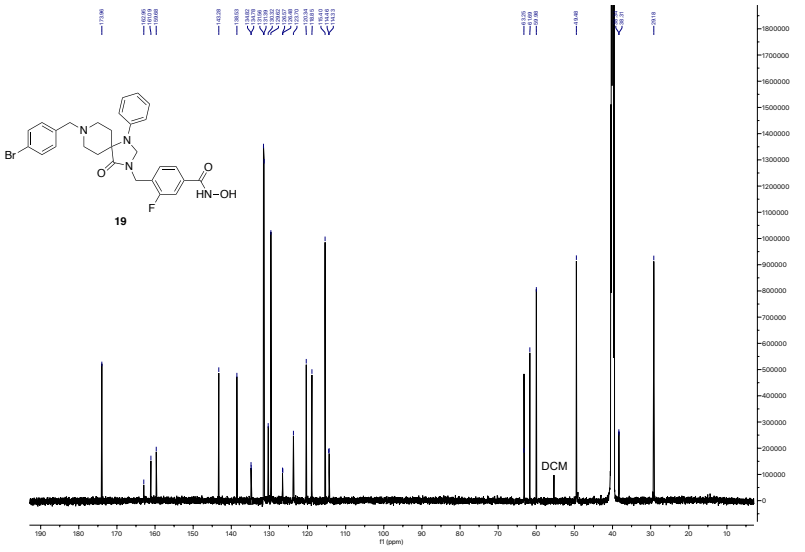
Supporting Figure 21

^{1}H NMR of 19



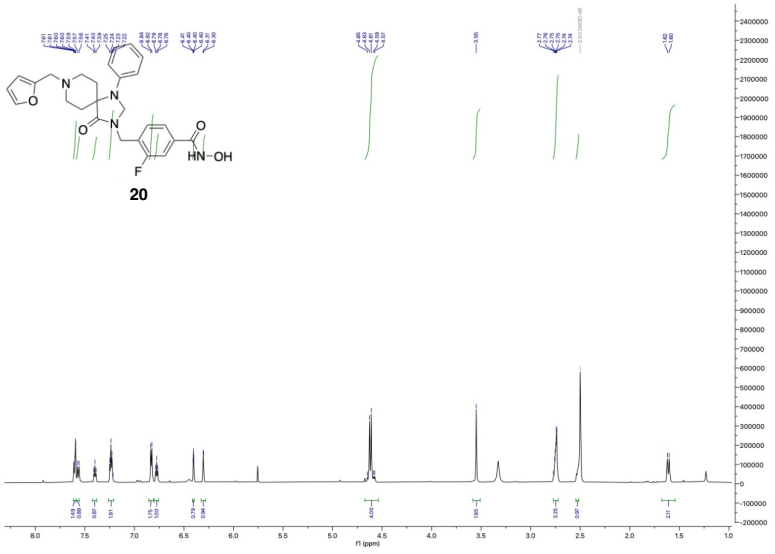
Supporting Figure 22

^{13}C NMR of 19



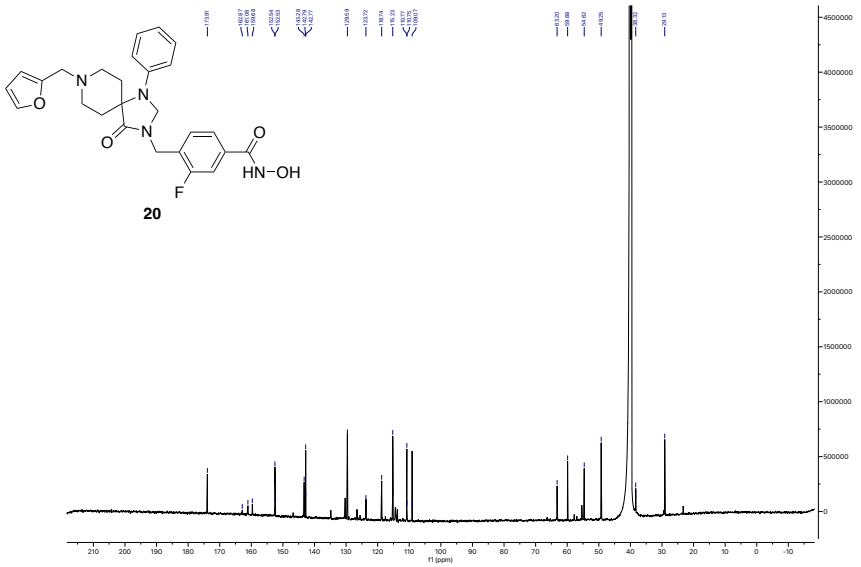
Supporting Figure 23

^{1}H NMR of 20



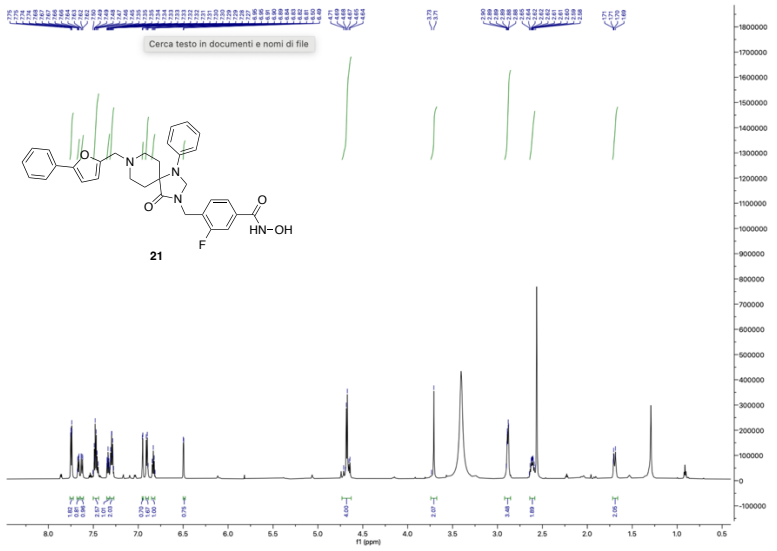
Supporting Figure 24

^{13}C NMR of 20



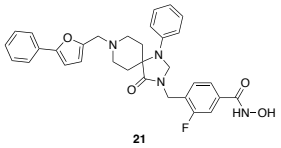
Supporting Figure 25

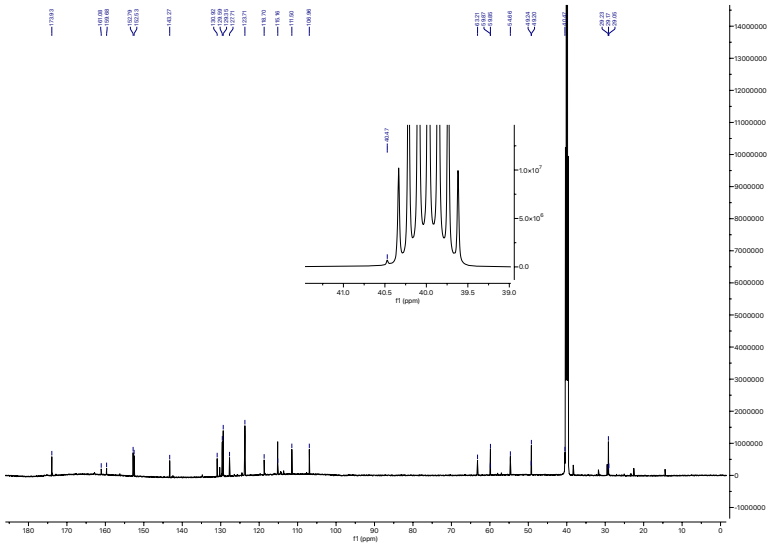
^{1}H NMR of 21



Supporting Figure 26

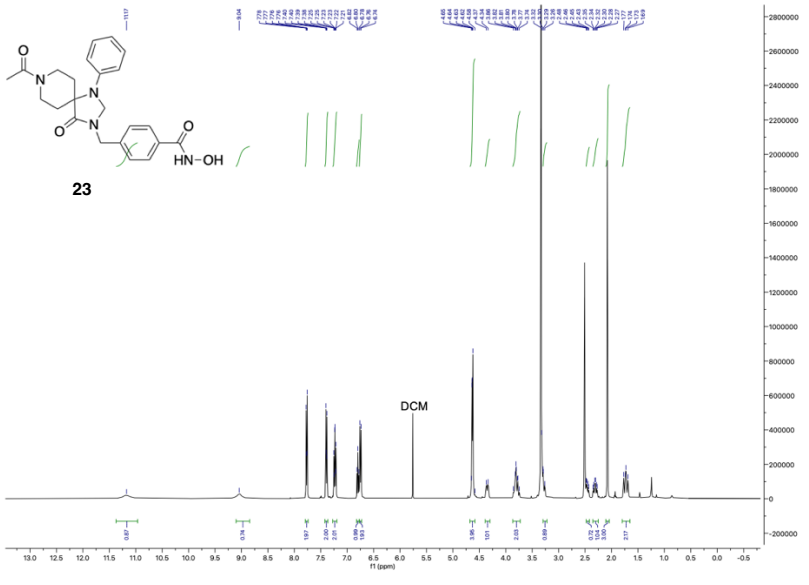
^{13}C NMR of 21





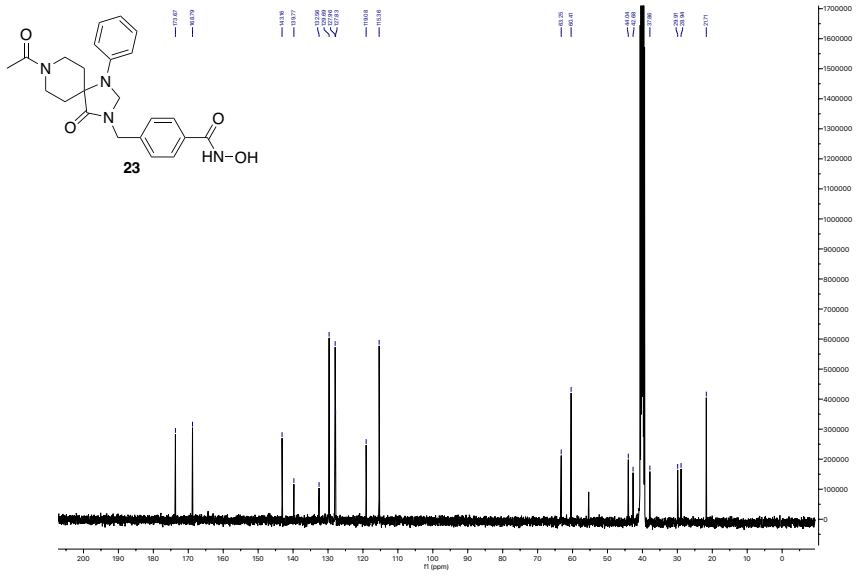
Supporting Figure 27

^{1}H NMR of 23



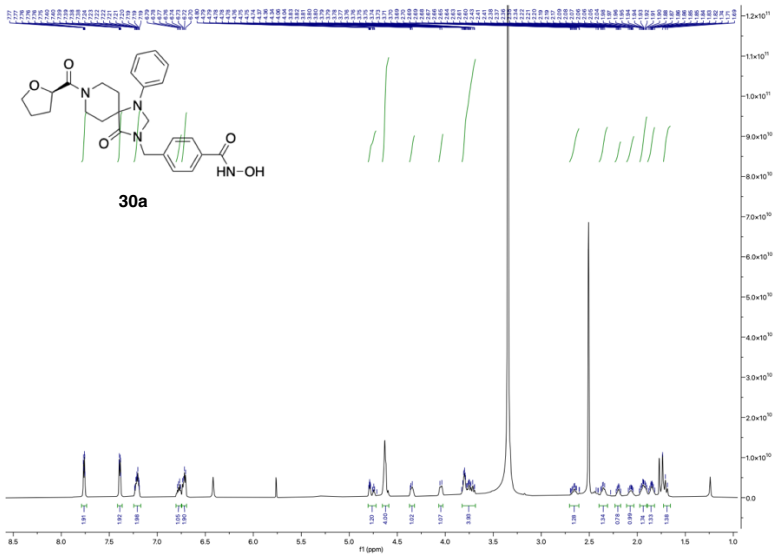
Supporting Figure 27

^{13}C NMR of 23



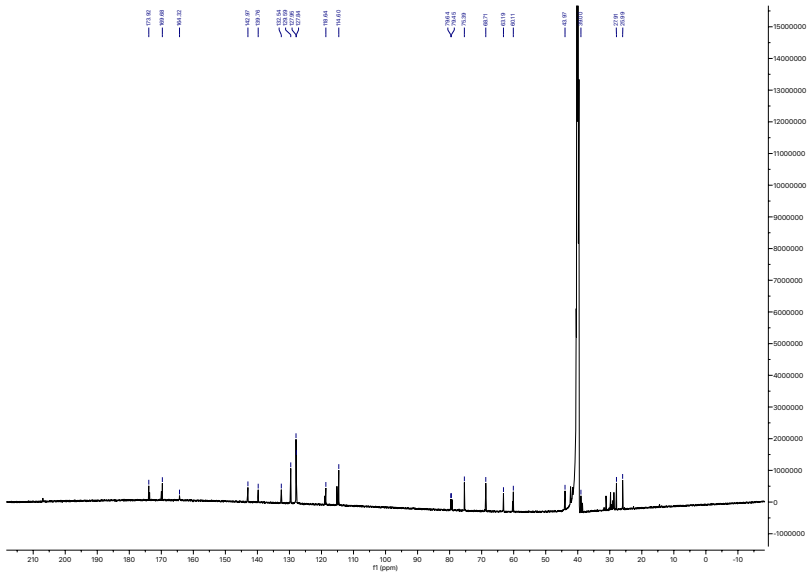
Supporting Figure 28

^{1}H NMR of 30a



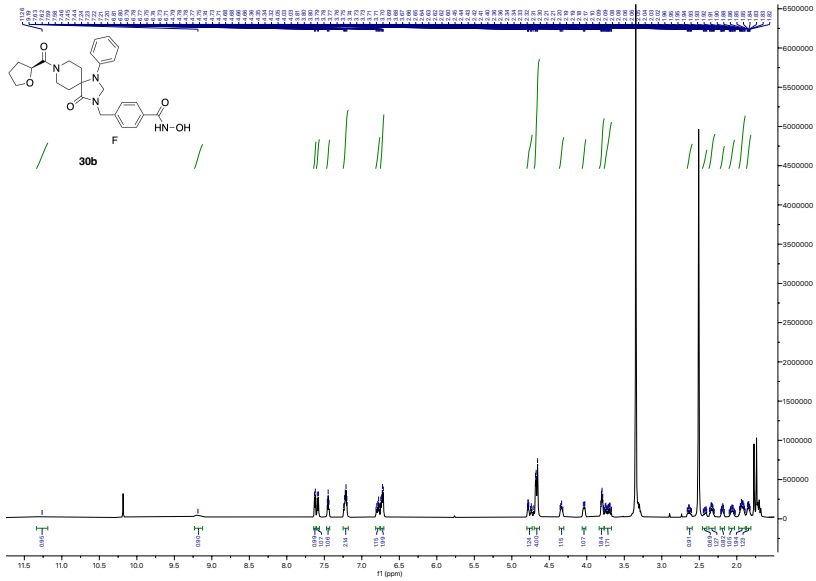
Supporting Figure 29

^{13}C NMR of 30a



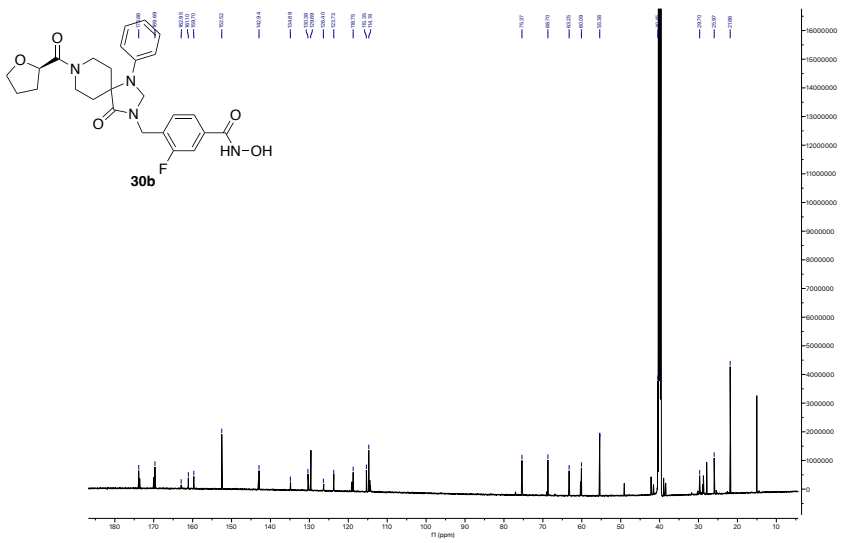
Supporting Figure 30

^{1}H NMR of 30b



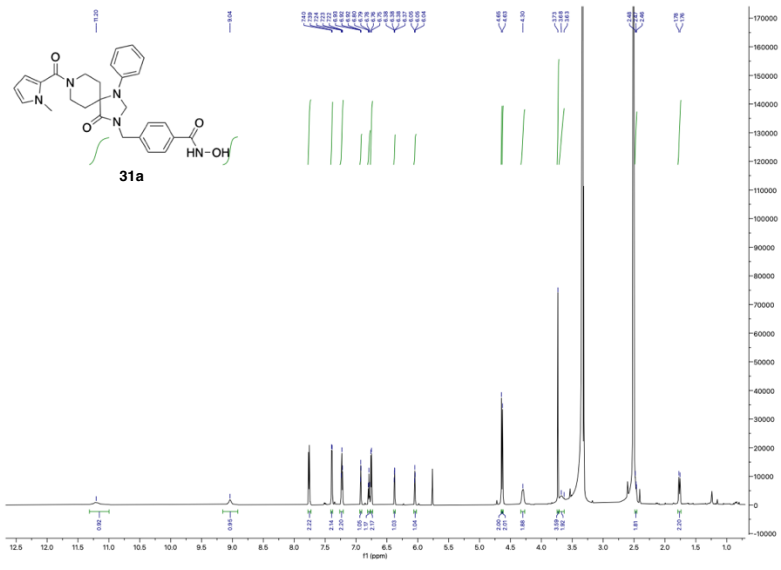
Supporting Figure 31

^{13}C NMR of 30b



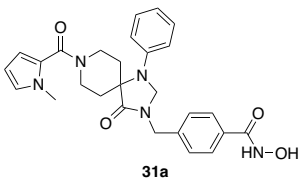
Supporting Figure 32

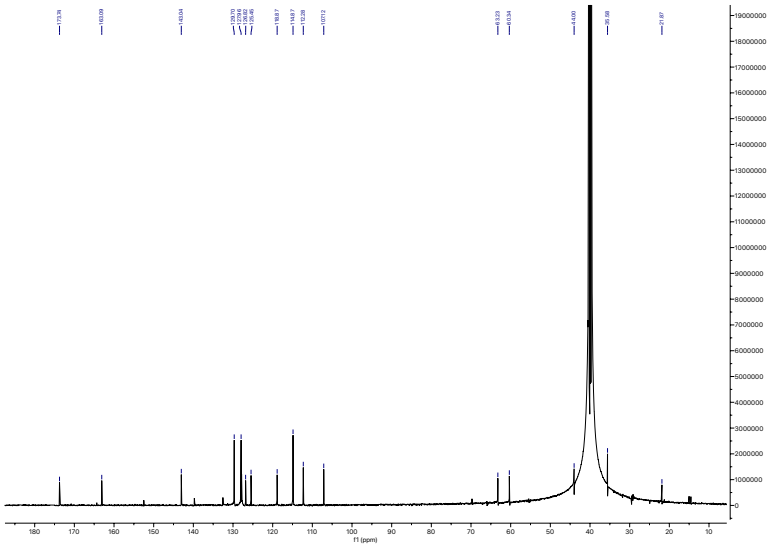
^{1}H NMR of 31a



Supporting Figure 33

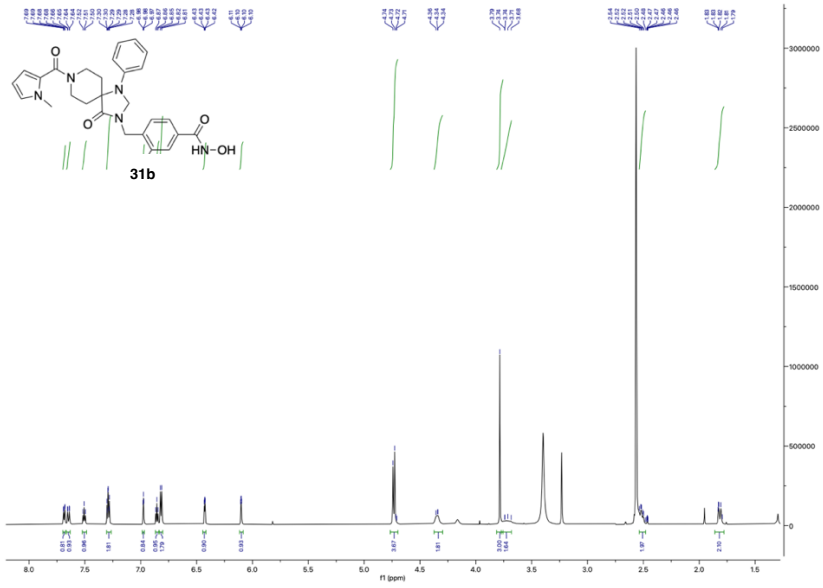
^{13}C NMR of 31a





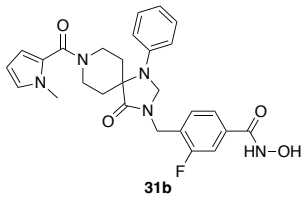
Supporting Figure 34

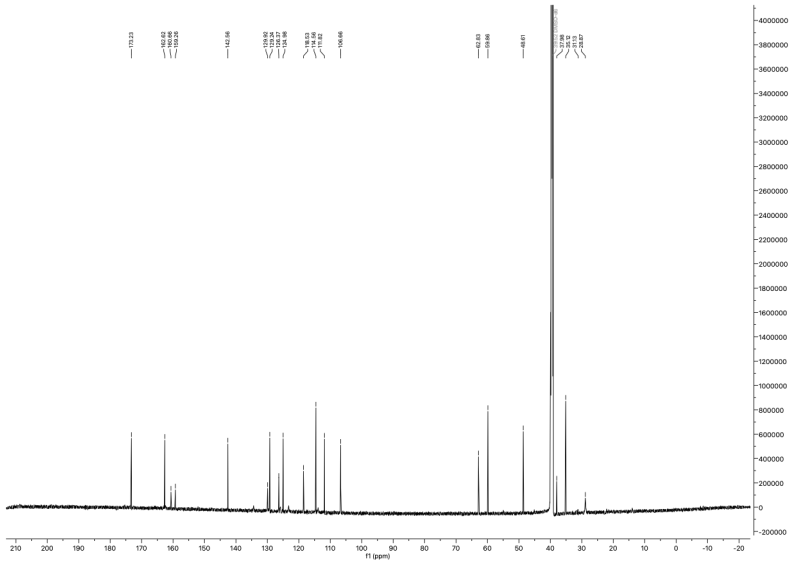
^{1}H NMR of 31b



Supporting Figure 35

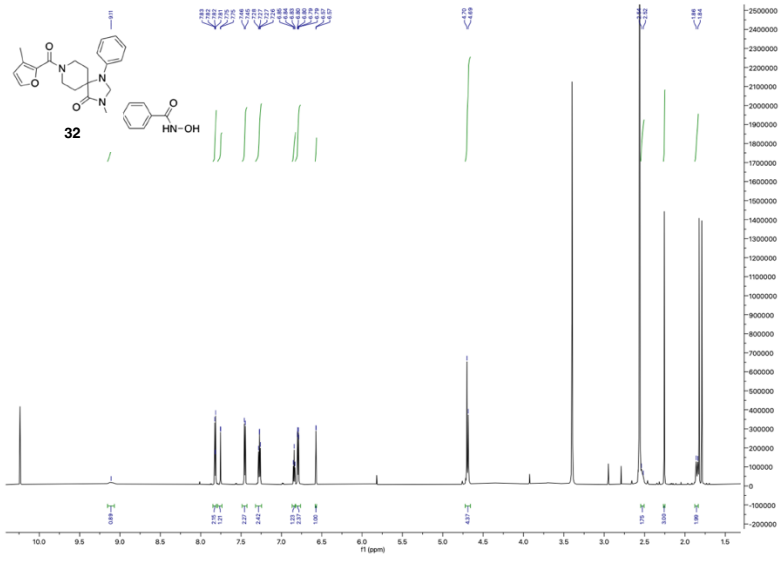
^{13}C NMR of 31b





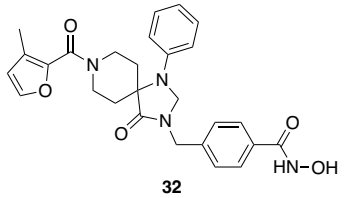
Supporting Figure 36

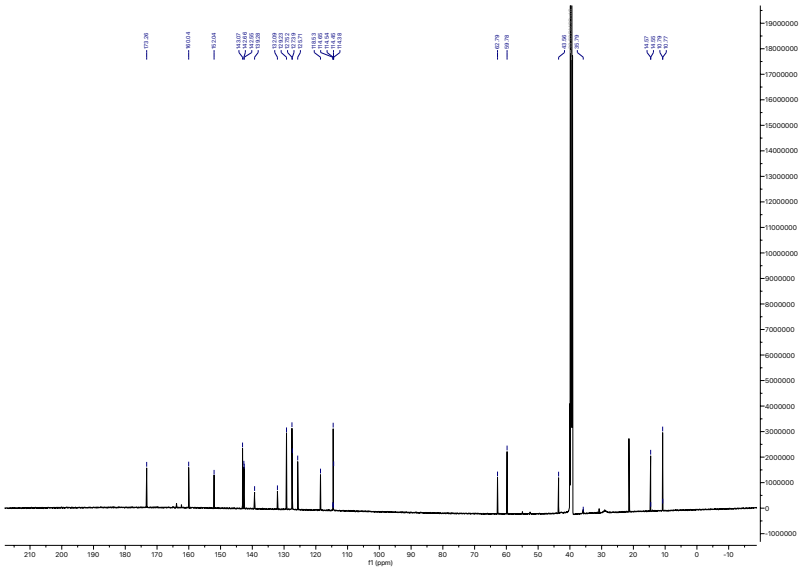
^{1}H NMR of 32



Supporting Figure 37

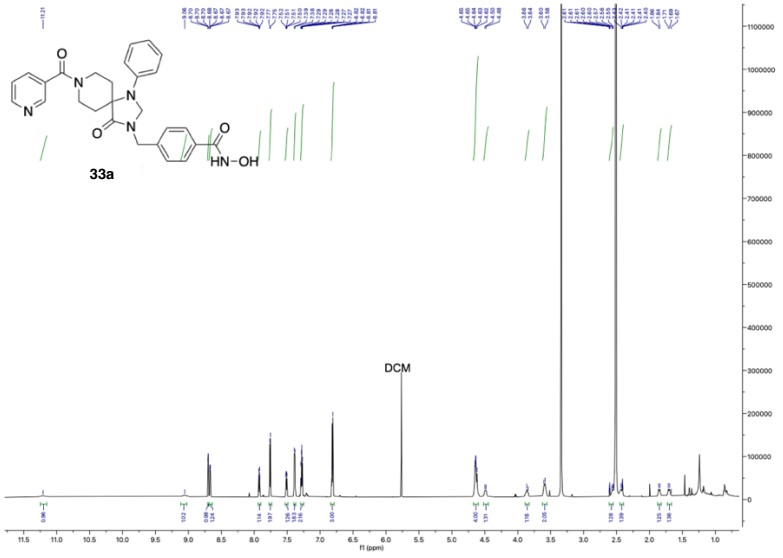
^{13}C NMR of 32





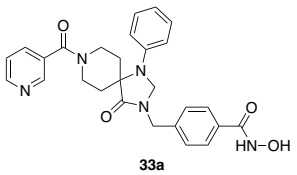
Supporting Figure 38

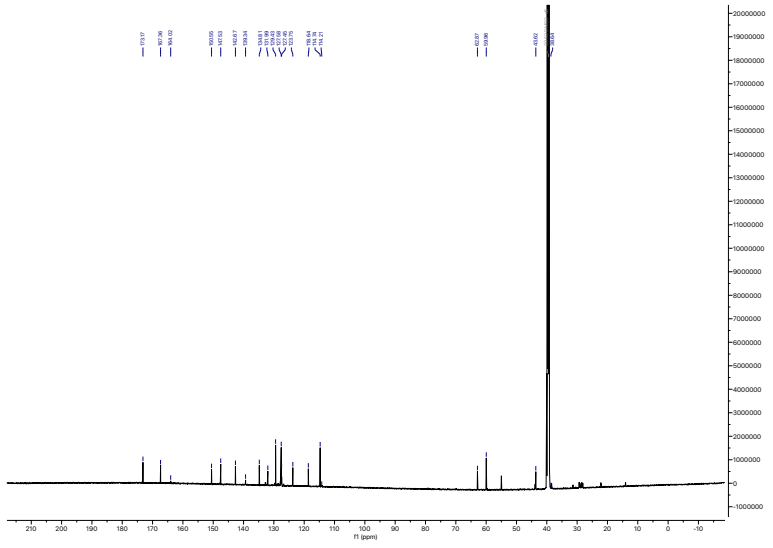
^{1}H NMR of 33a



Supporting Figure 39

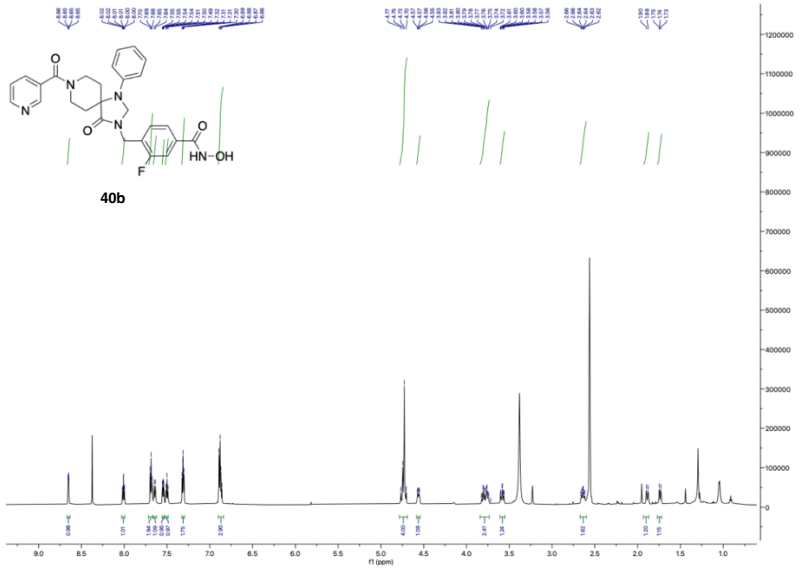
^{13}C NMR of 33a





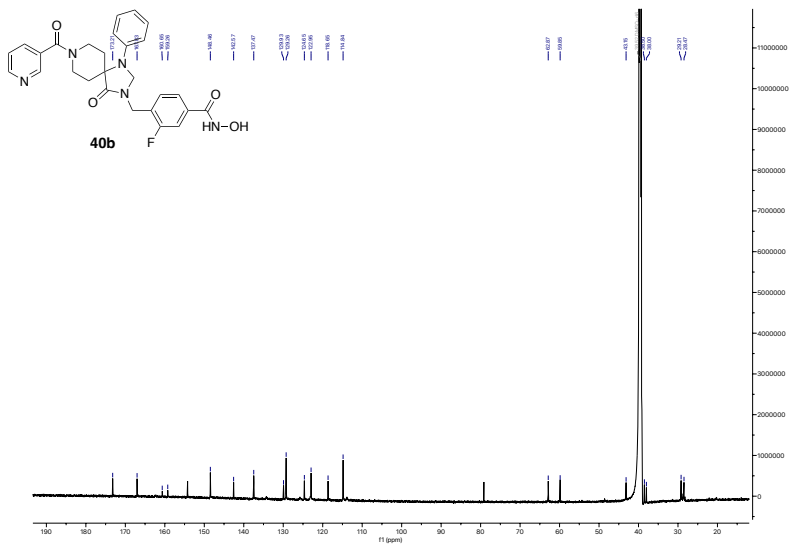
Supporting Figure 40

^{1}H NMR of 33b



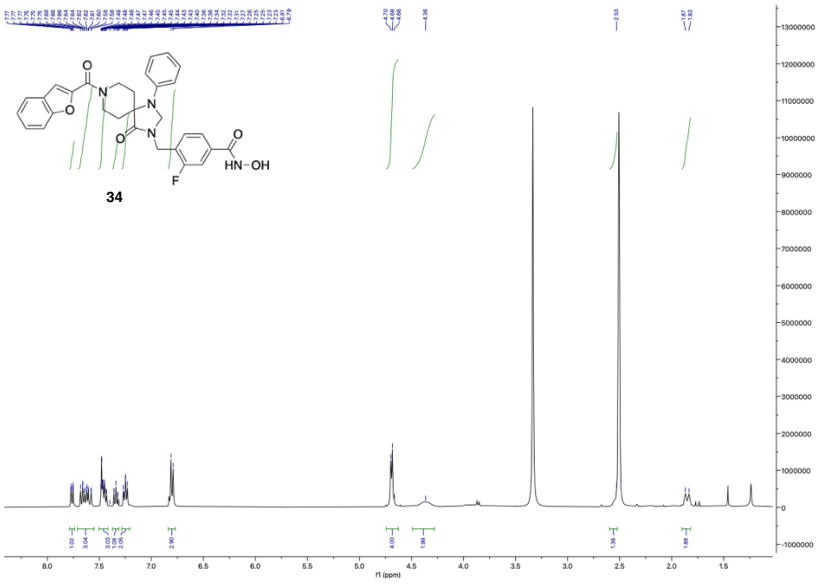
Supporting Figure 41

^{13}C NMR of 33b



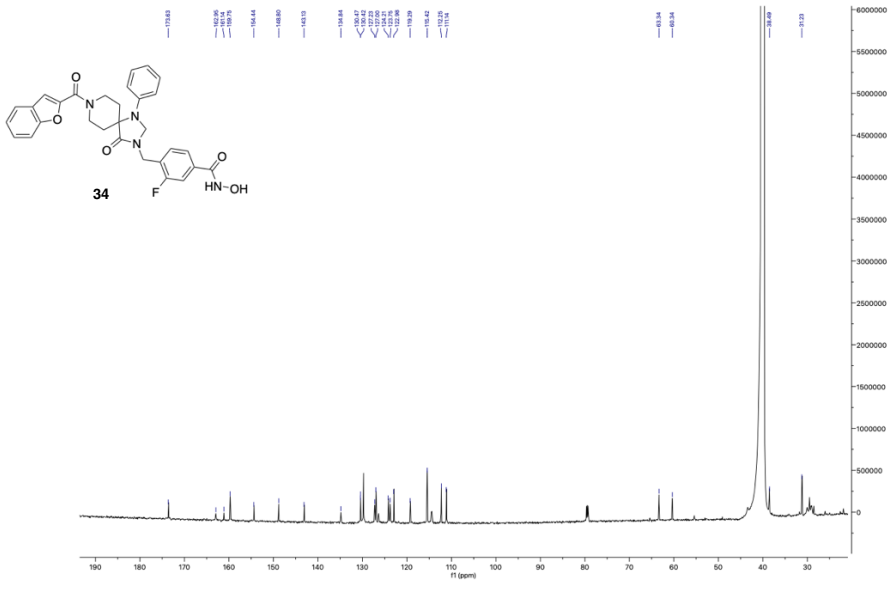
Supporting Figure 42

^{1}H NMR of 34



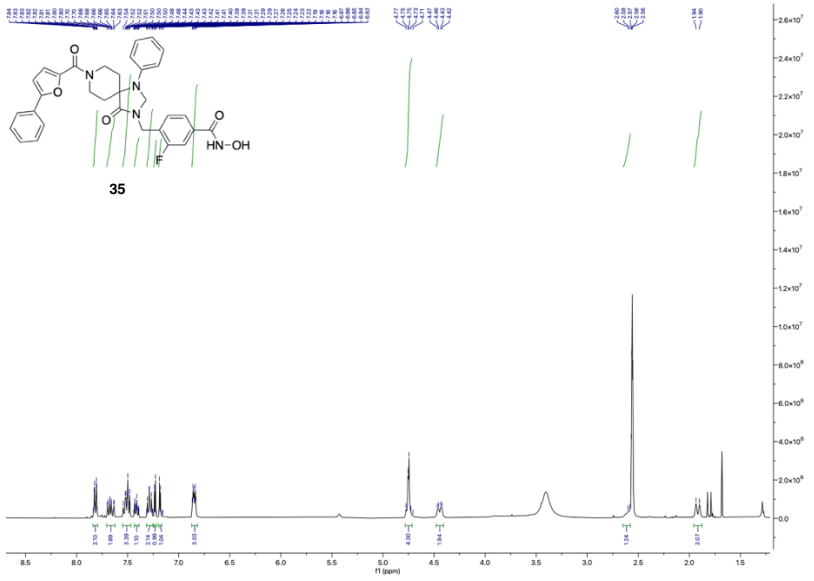
Supporting Figure 43

^{13}C NMR of 34



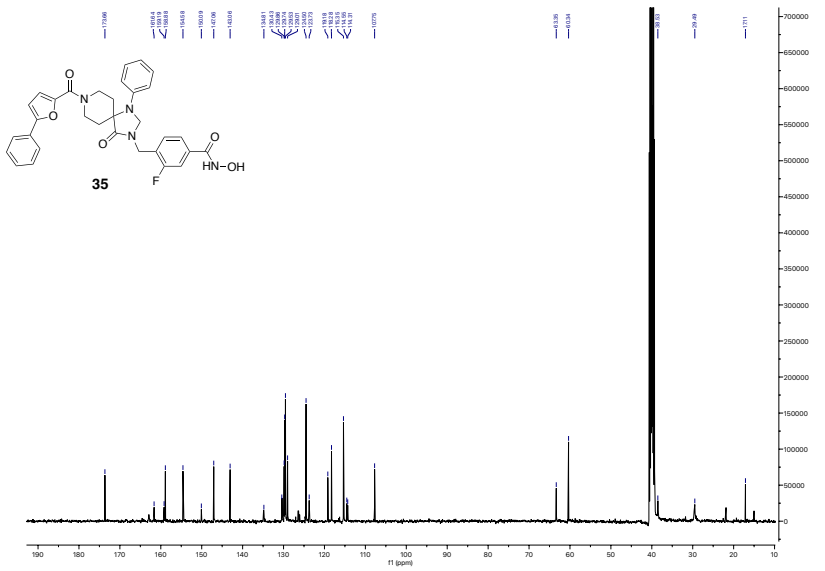
Supporting Figure 44

^{1}H NMR of 35



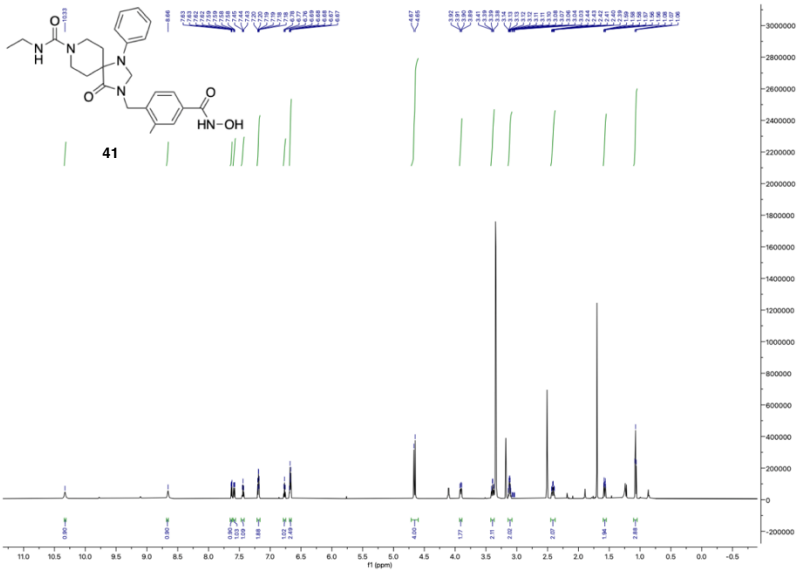
Supporting Figure 45

^{13}C NMR of 35



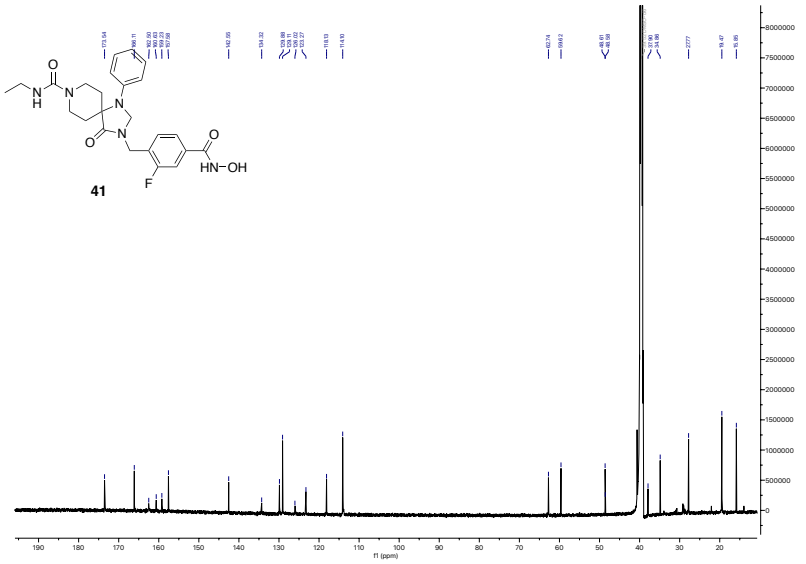
Supporting Figure 46

^{1}H NMR of 41



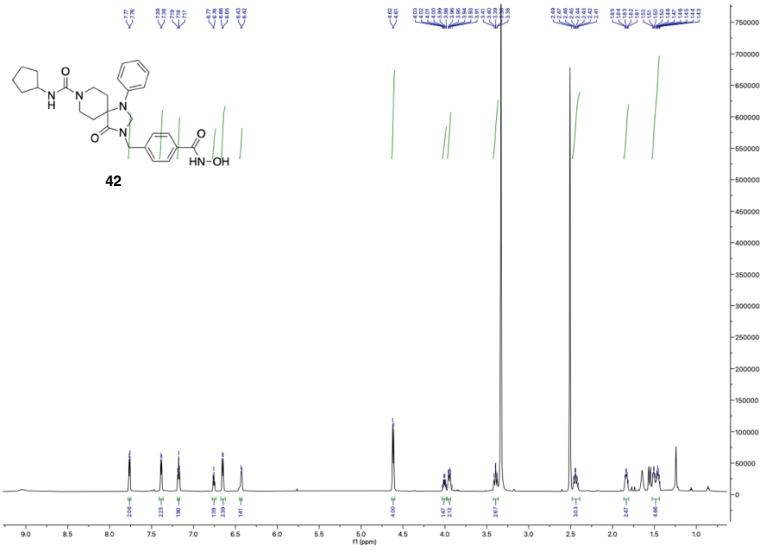
Supporting Figure 47

^{13}C NMR of 41



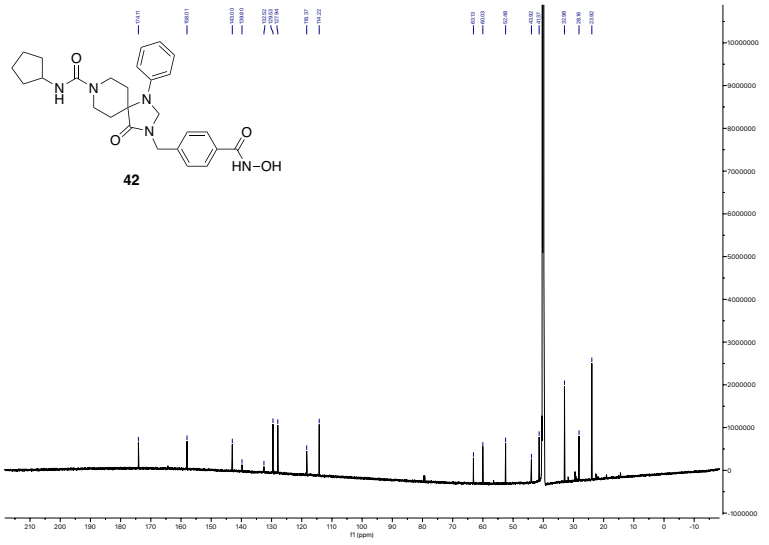
Supporting Figure 48

^{1}H NMR of 42



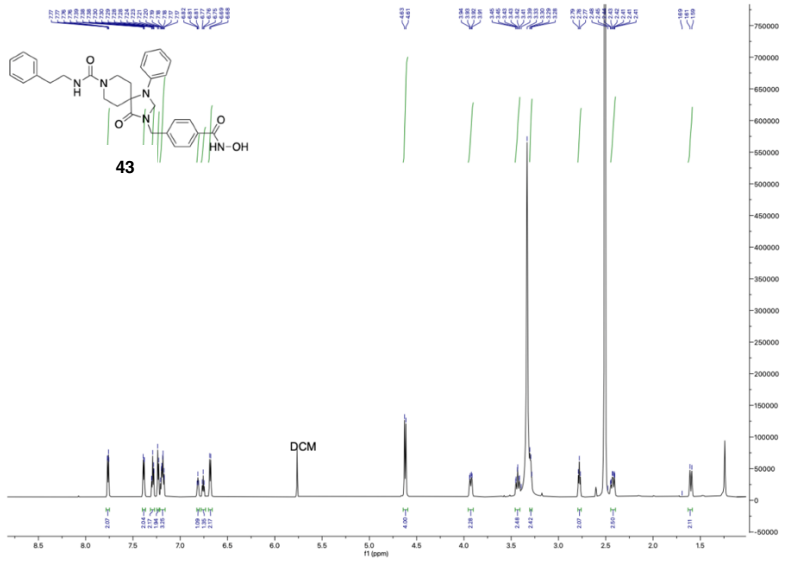
Supporting Figure 49

^{13}C NMR of 42



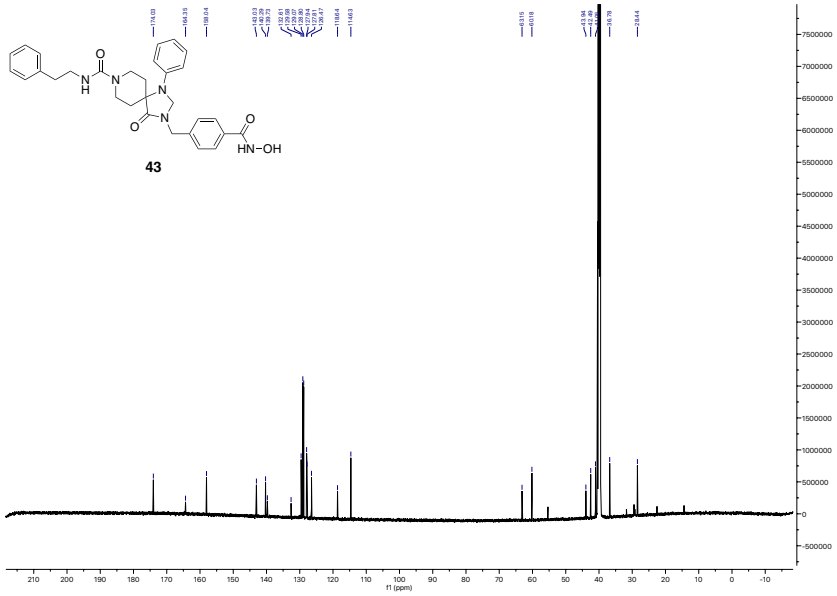
Supporting Figure 50

^{1}H NMR of 43



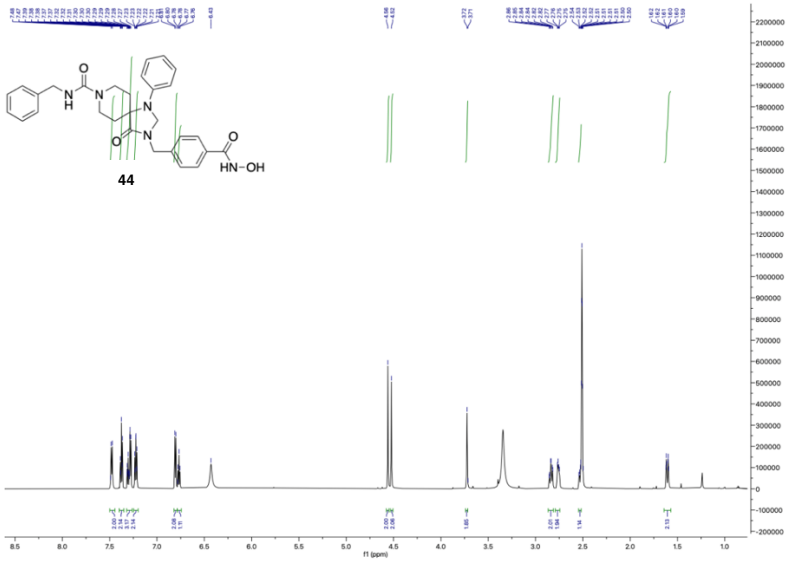
Supporting Figure 51

^{13}C NMR of 43



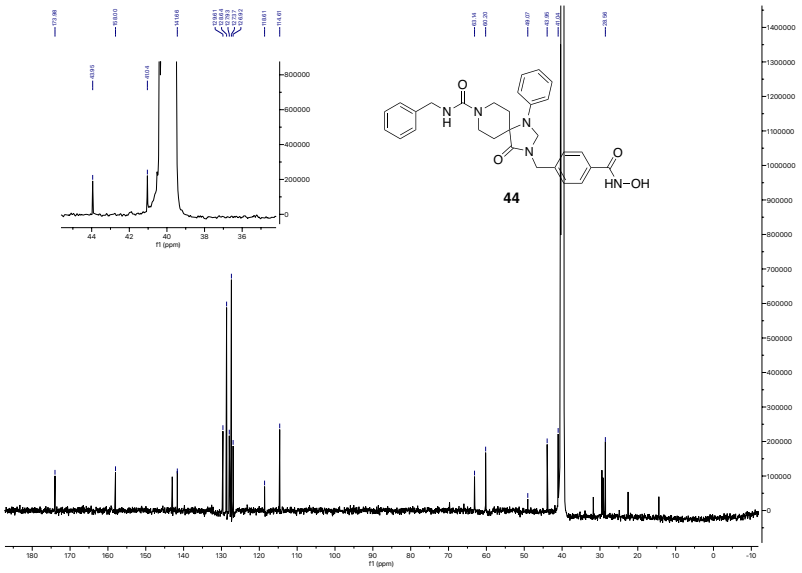
Supporting Figure 52

^{1}H NMR of 44



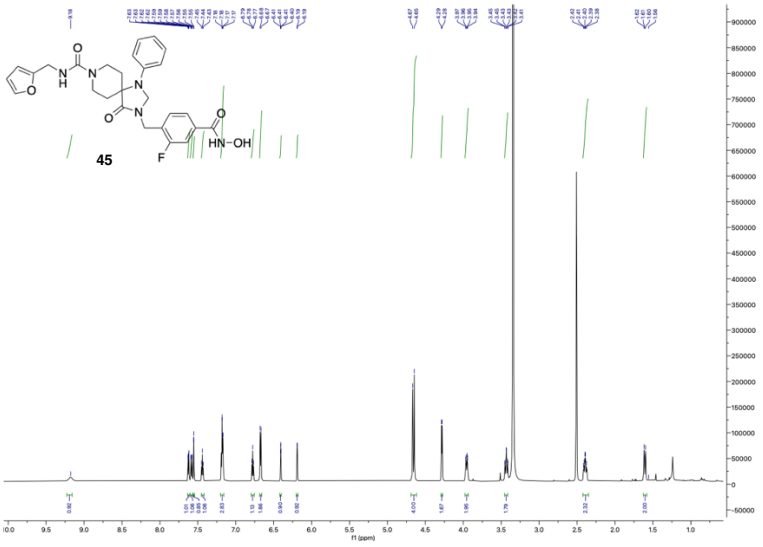
Supporting Figure 53

^{13}C NMR of 44



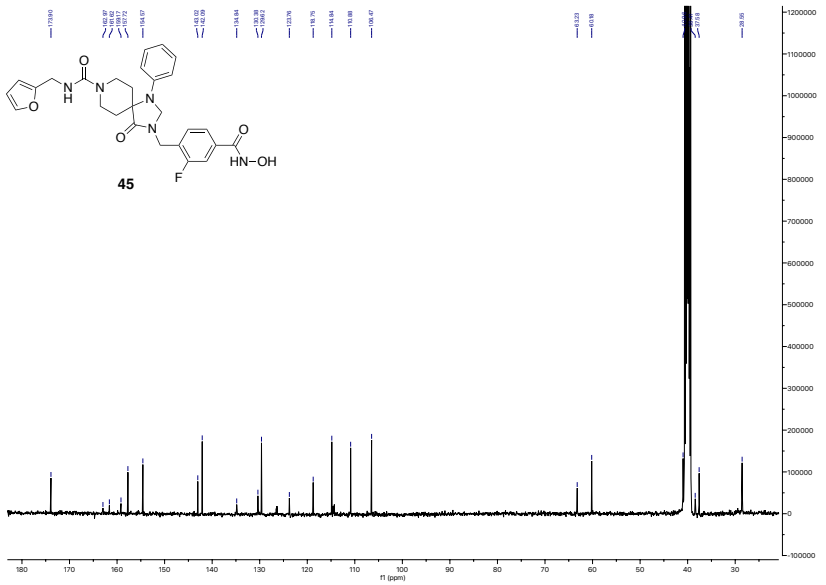
Supporting Figure 54

^{1}H NMR of 45



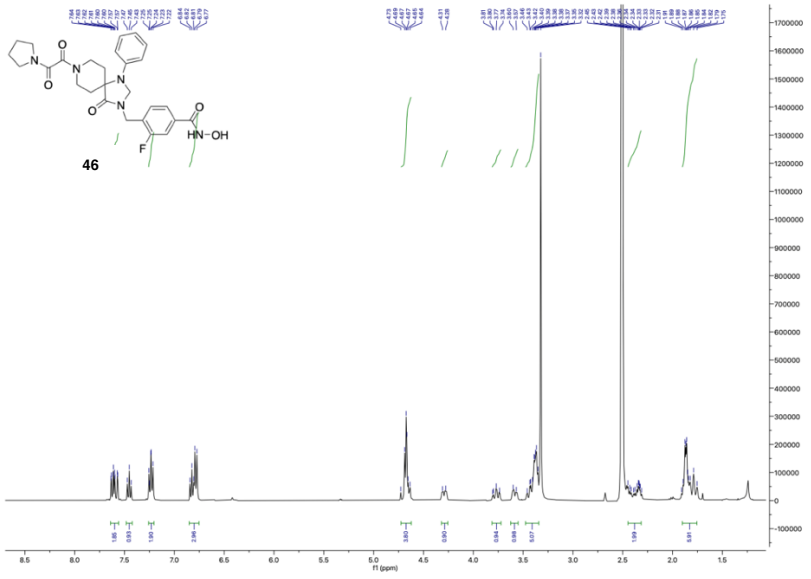
Supporting Figure 55

^{13}C NMR of 45



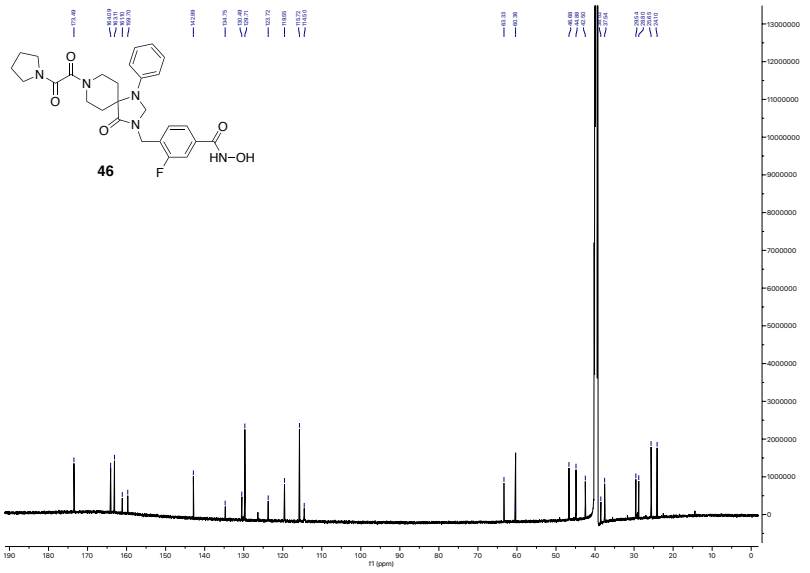
Supporting Figure 56

^{1}H NMR of 46



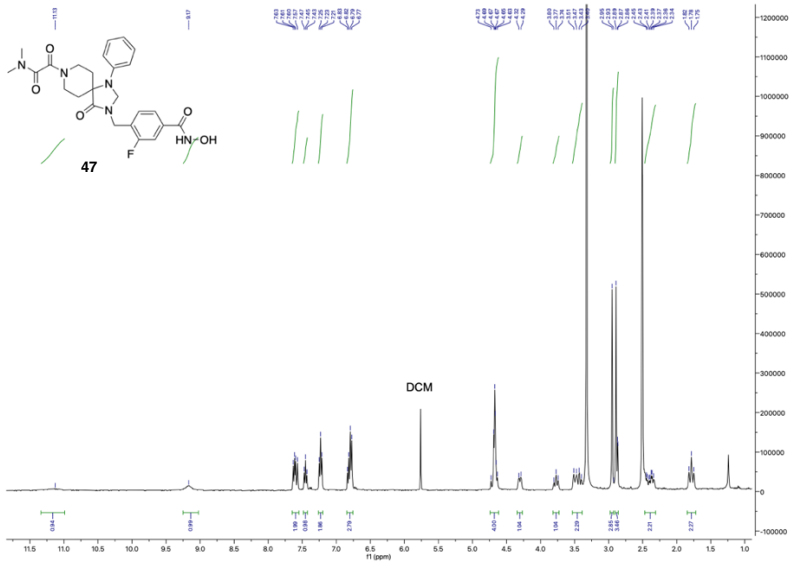
Supporting Figure 57

^{13}C NMR of 46



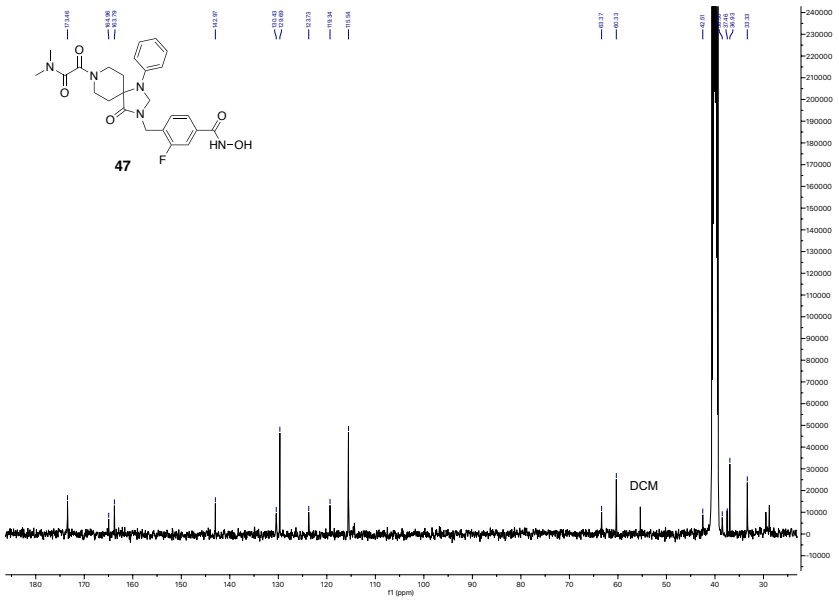
Supporting Figure 58

^{1}H NMR of 47



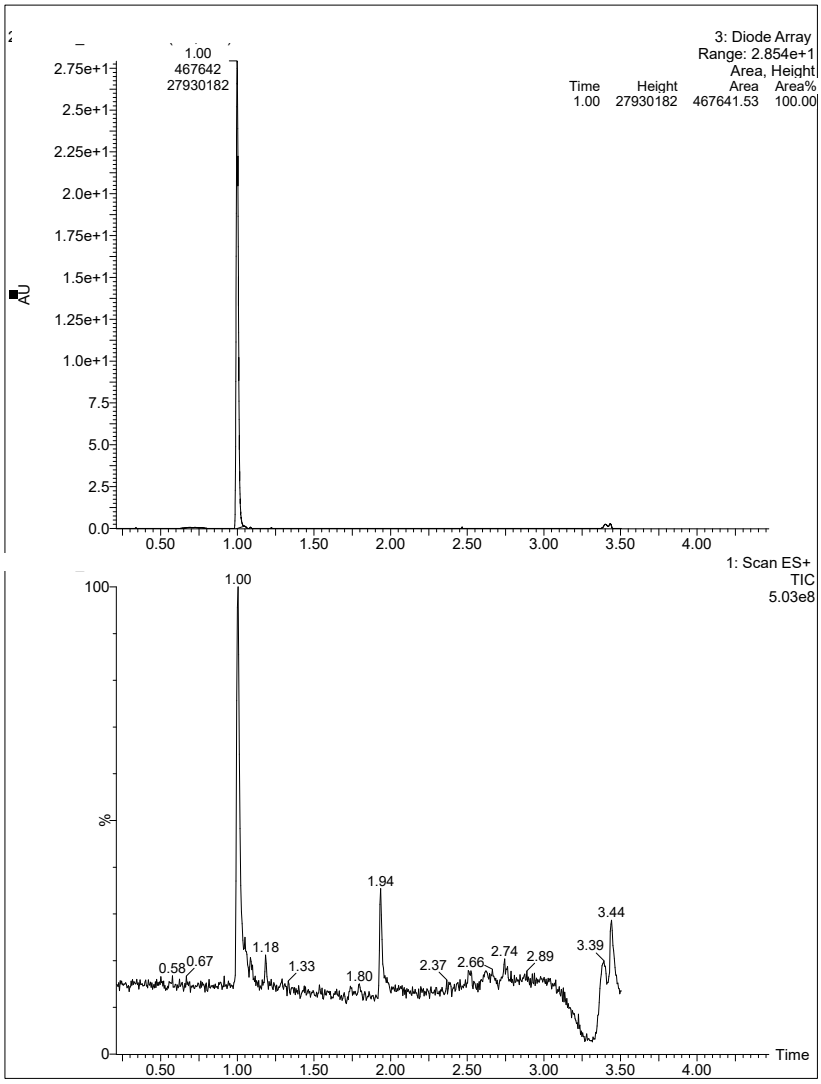
Supporting Figure 59

^{13}C NMR of 47



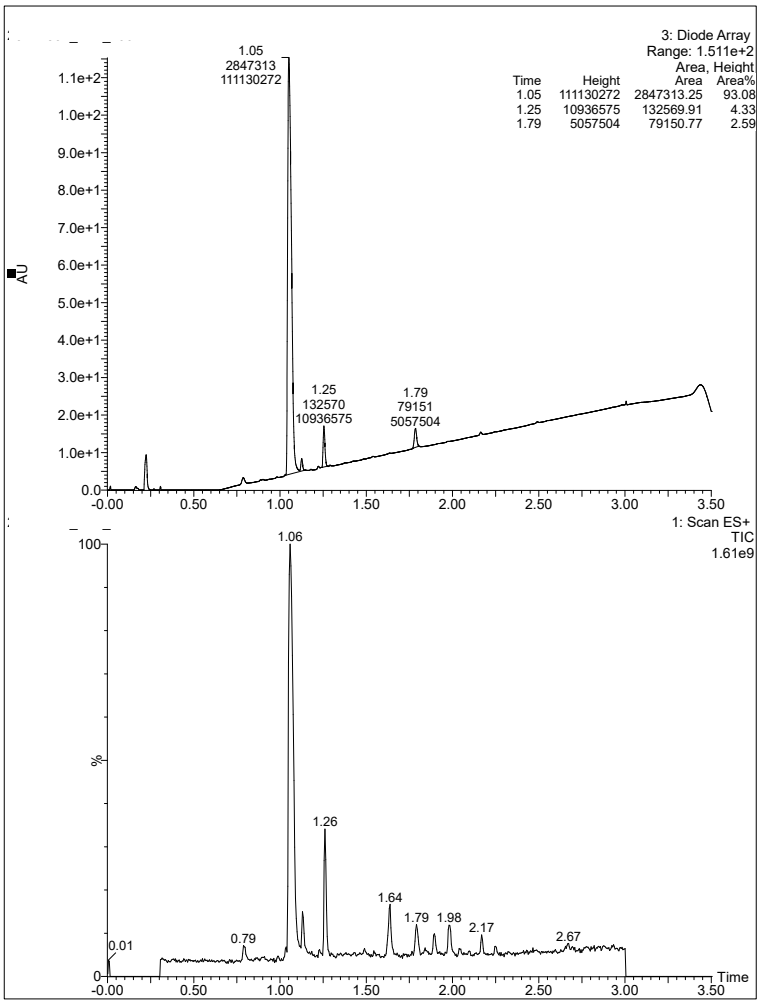
Supporting Figure 60

UPLC-MS spectra of compound 7



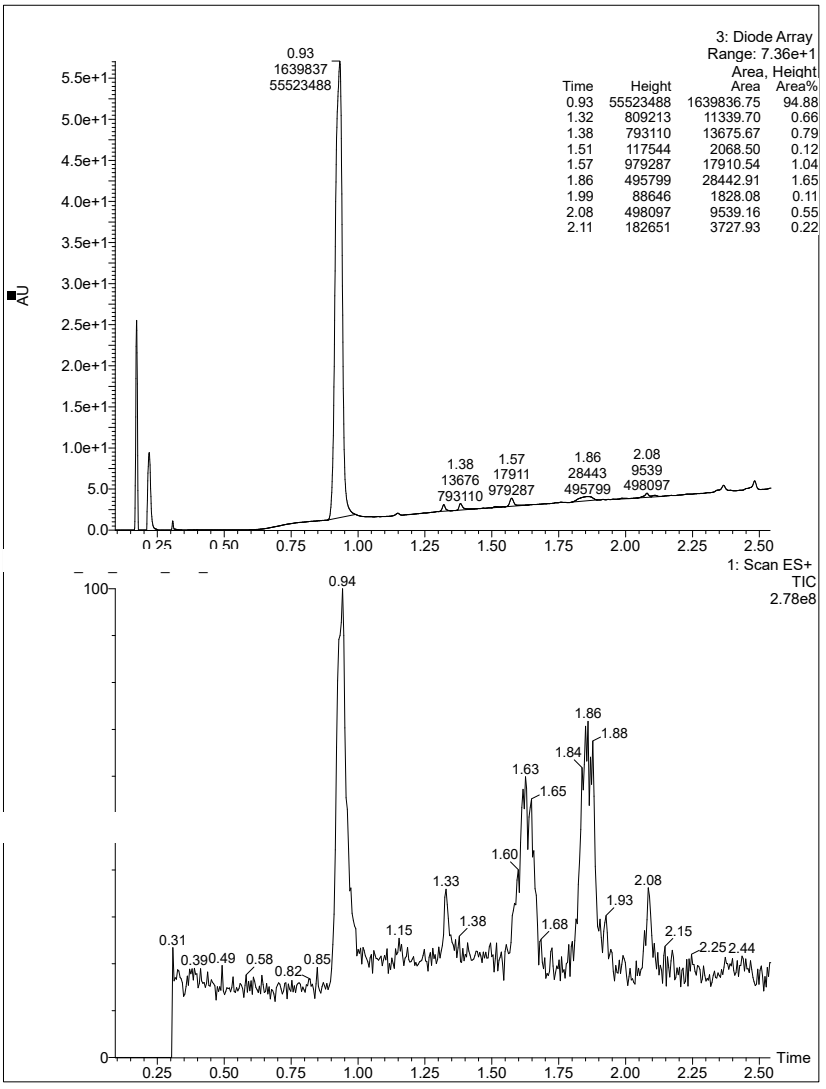
Supporting Figure 61

UPLC-MS spectra of compound 9a



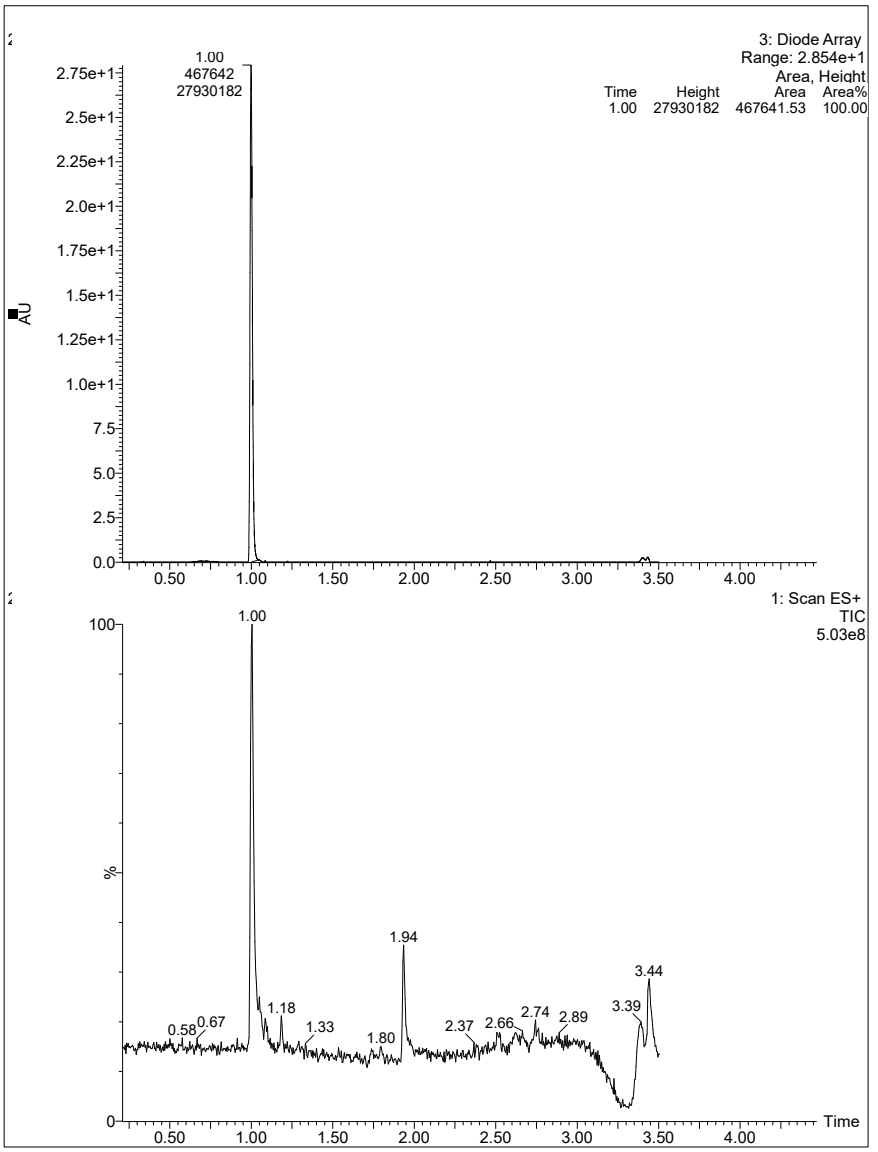
Supporting Figure 62

UPLC-MS spectra of compound 9b



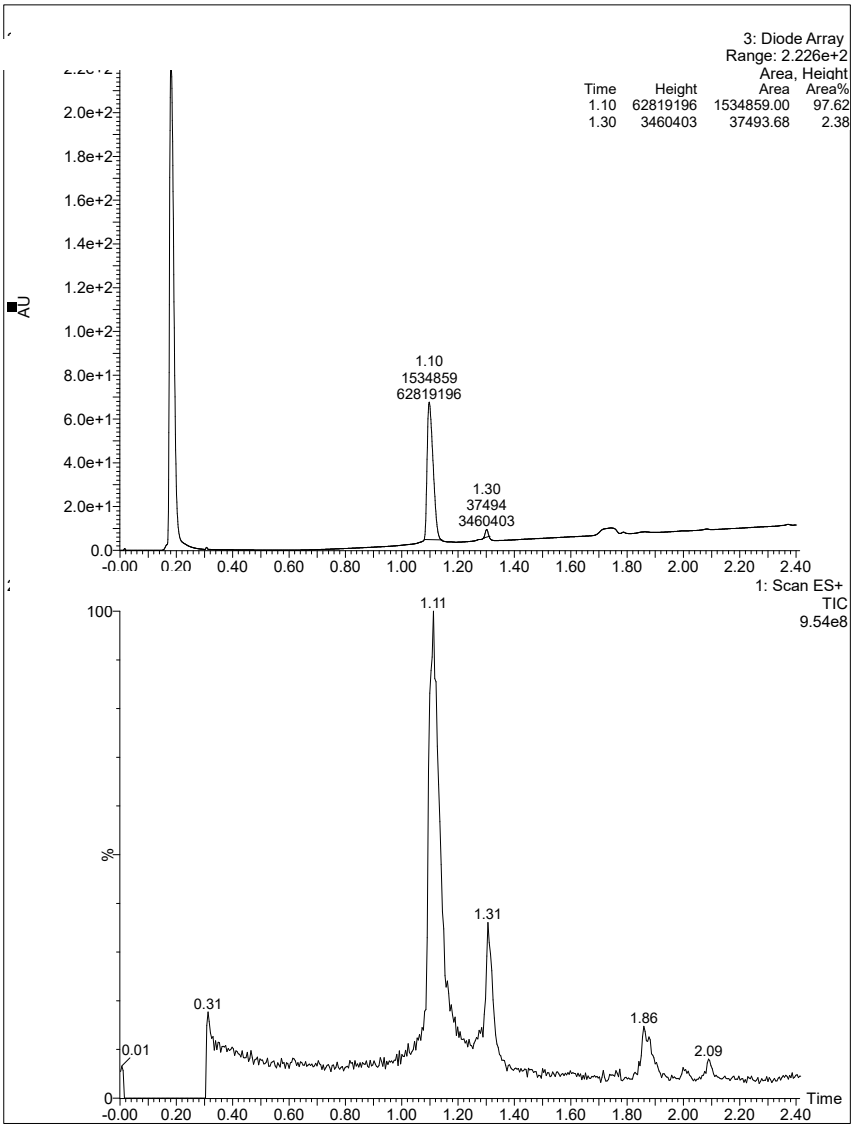
Supporting Figure 63

UPLC-MS spectra of compound 16a



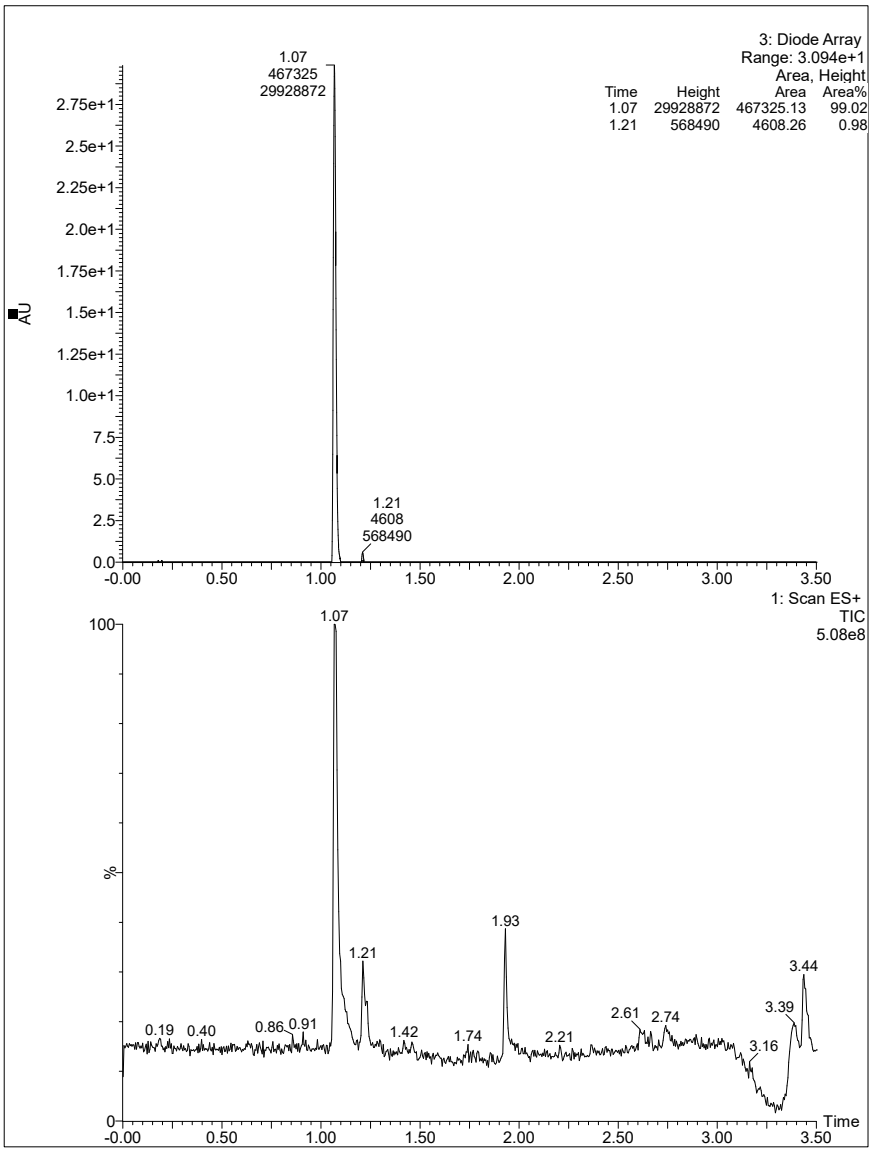
Supporting Figure 64

UPLC-MS spectra of compound 16b



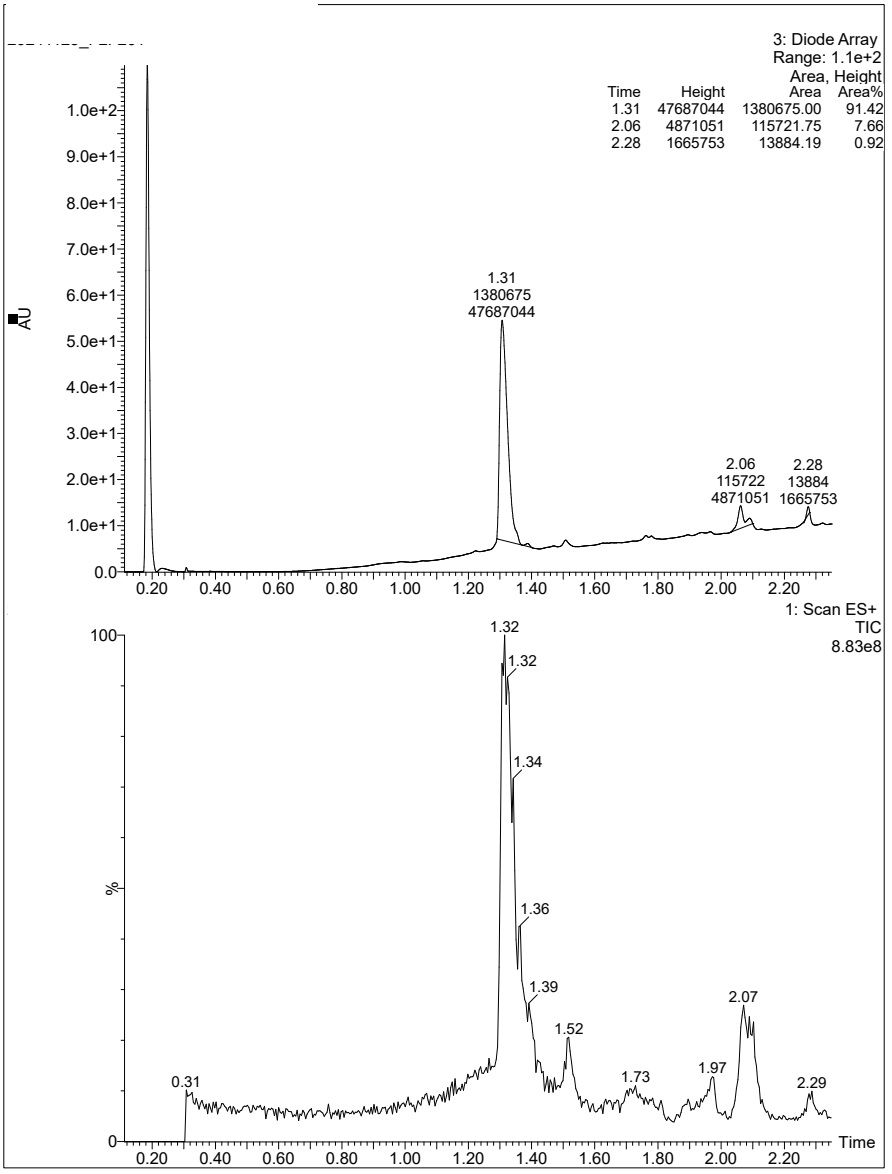
Supporting Figure 65

UPLC-MS spectra of compound 16c

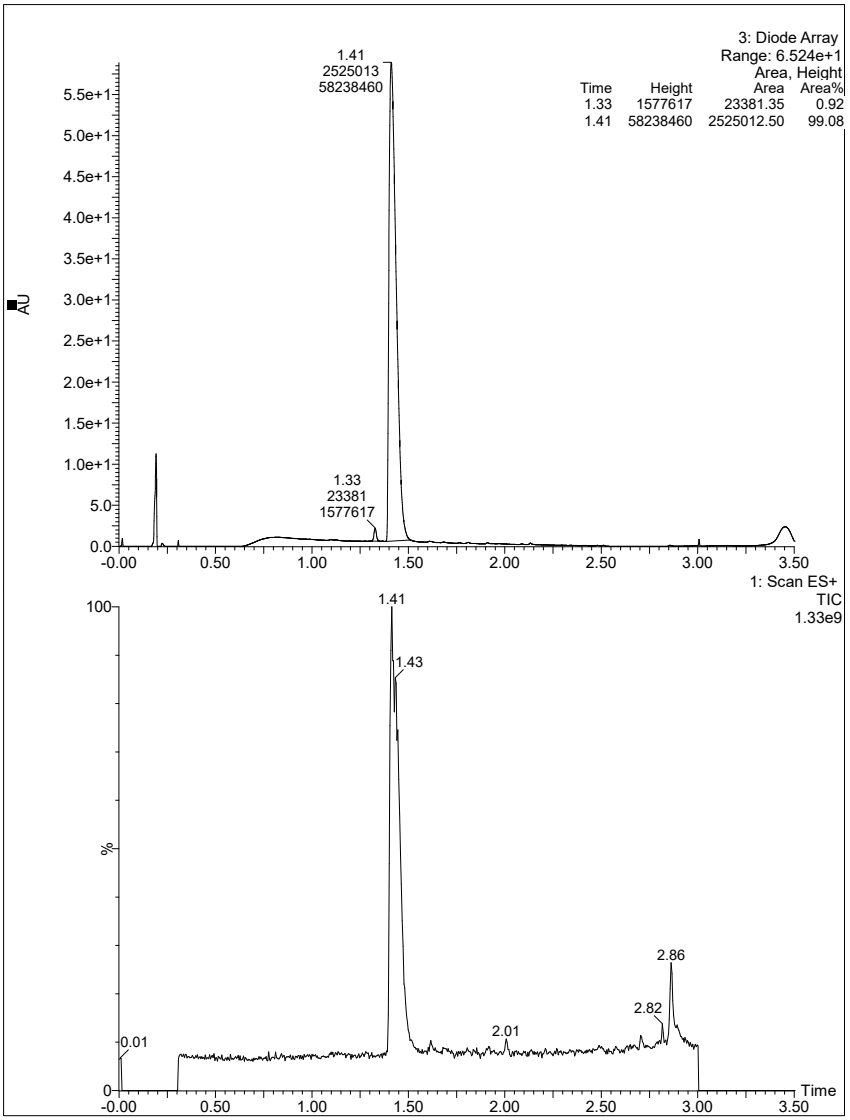


Supporting Figure 66

UPLC-MS spectra of compound 17a

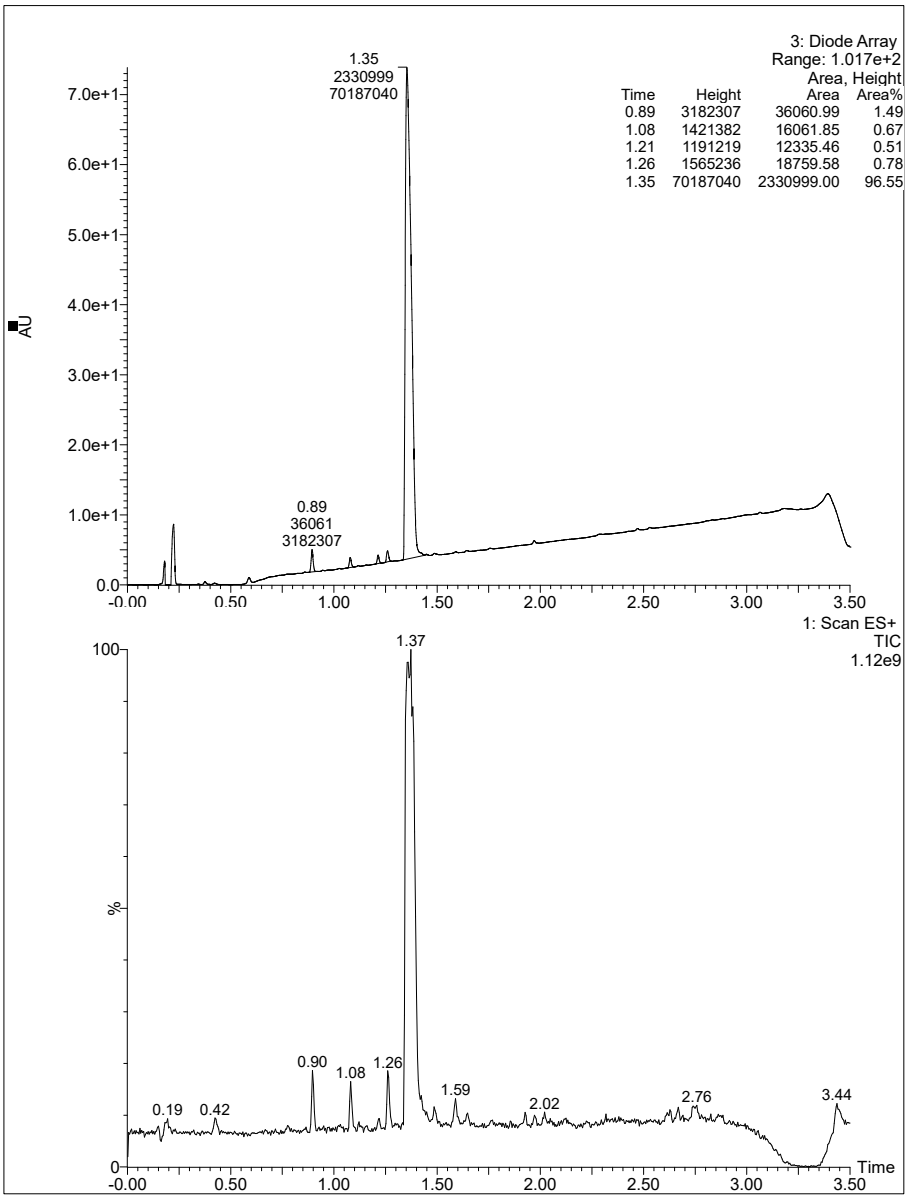


Supporting Figure 67
UPLC-MS spectra of compound 17b

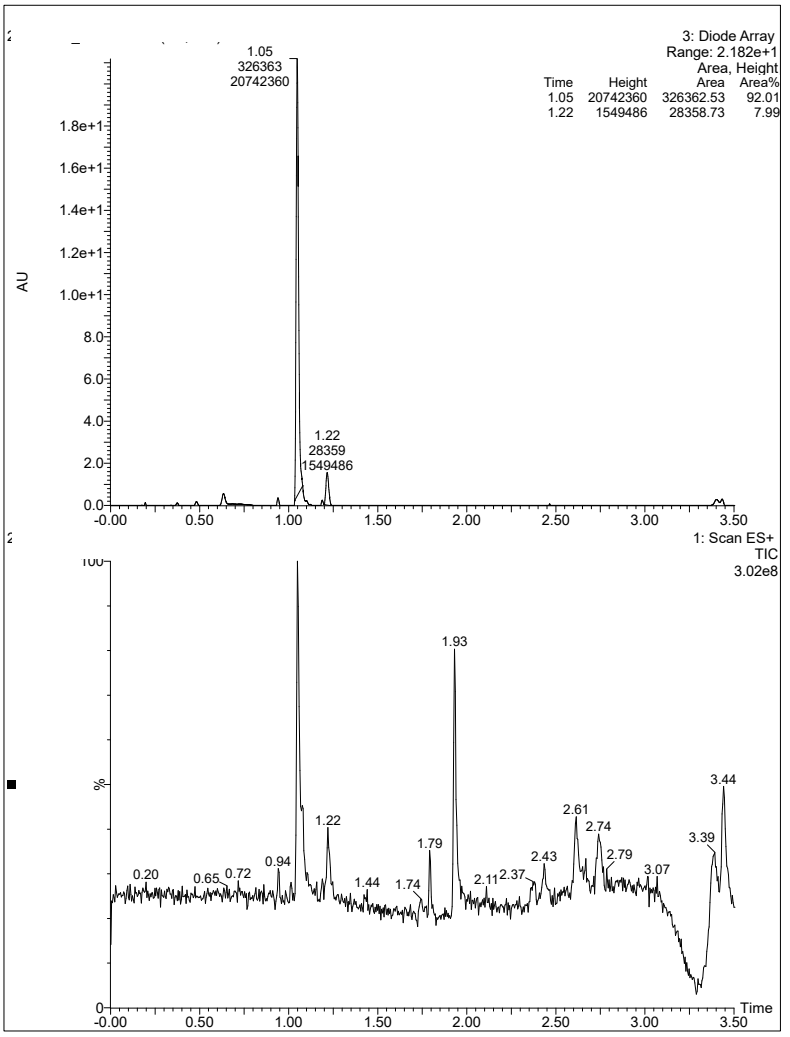


Supporting Figure 6°

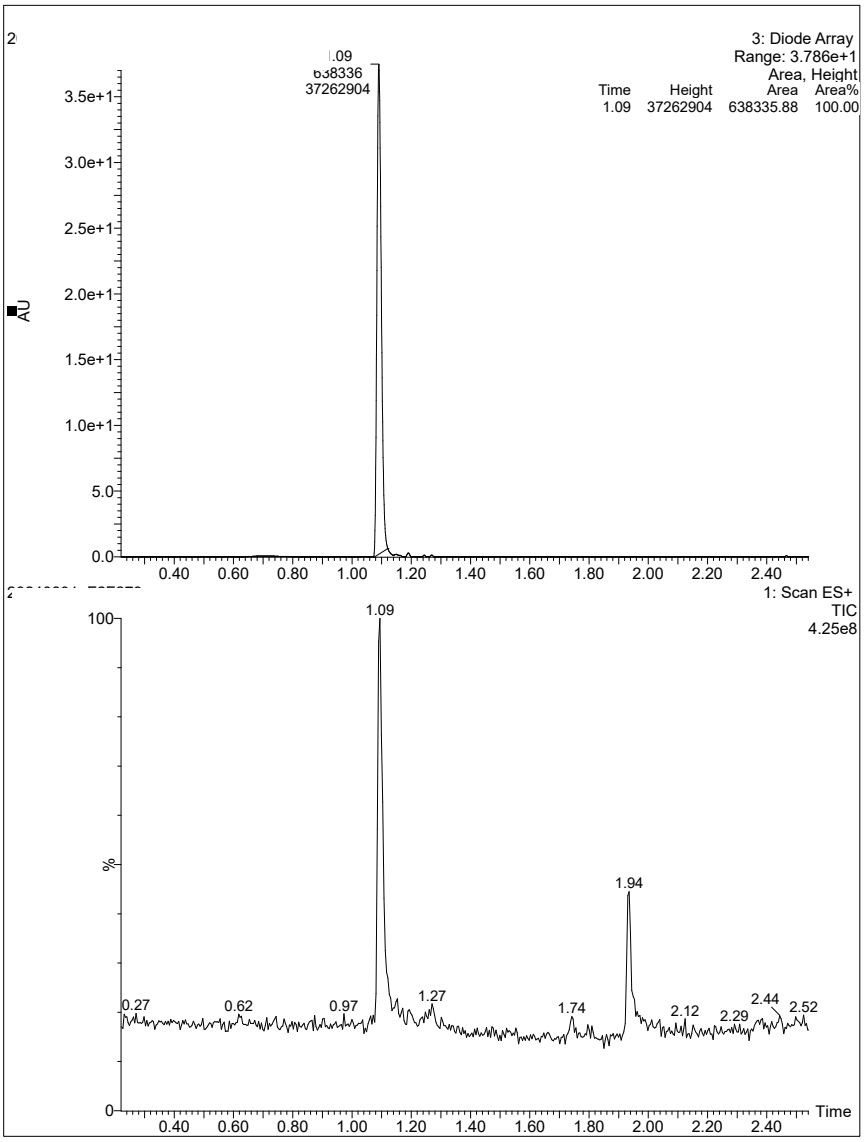
UPLC-MS spectra of compound 17c



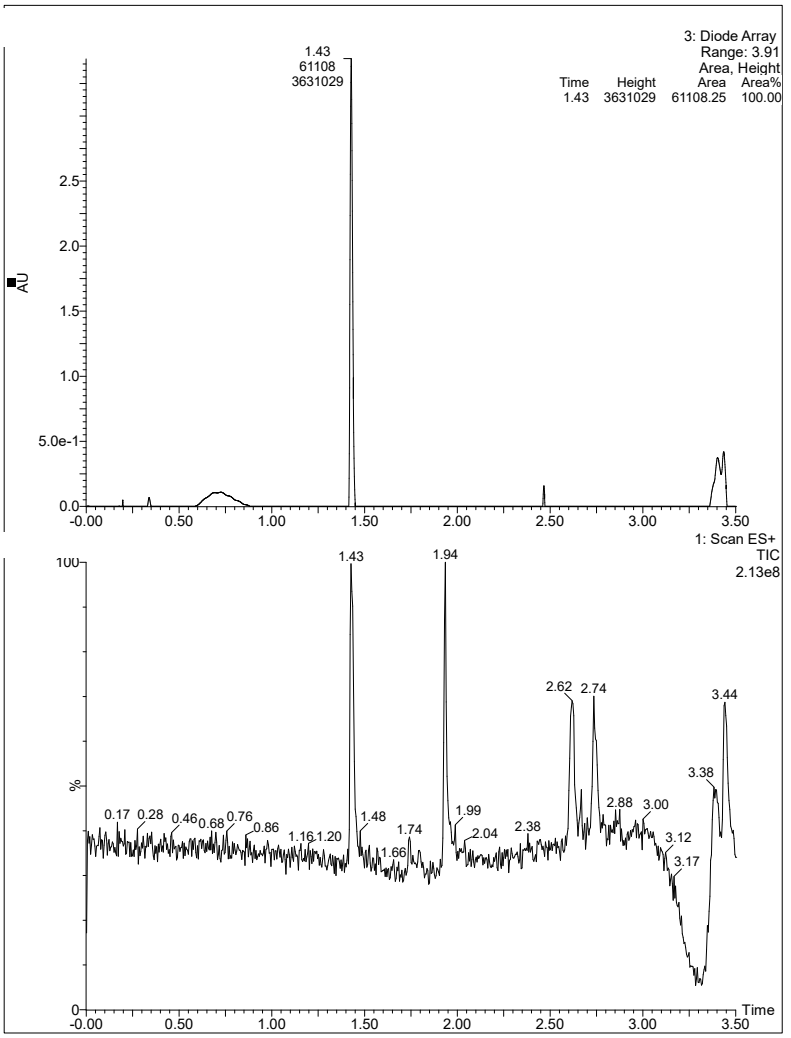
Supporting Figure 69
UPLC-MS spectra of compound 18a



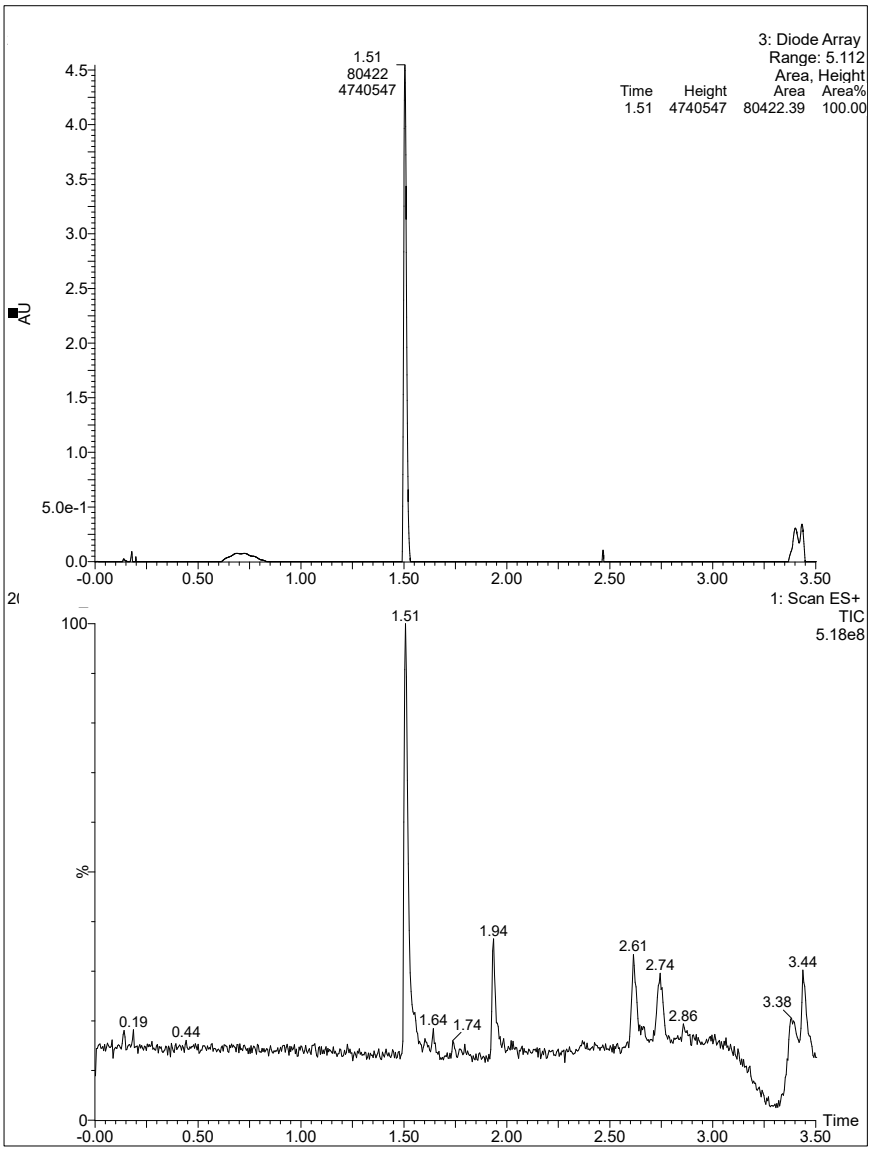
Supporting Figure 70
UPLC-MS spectra of compound 18b



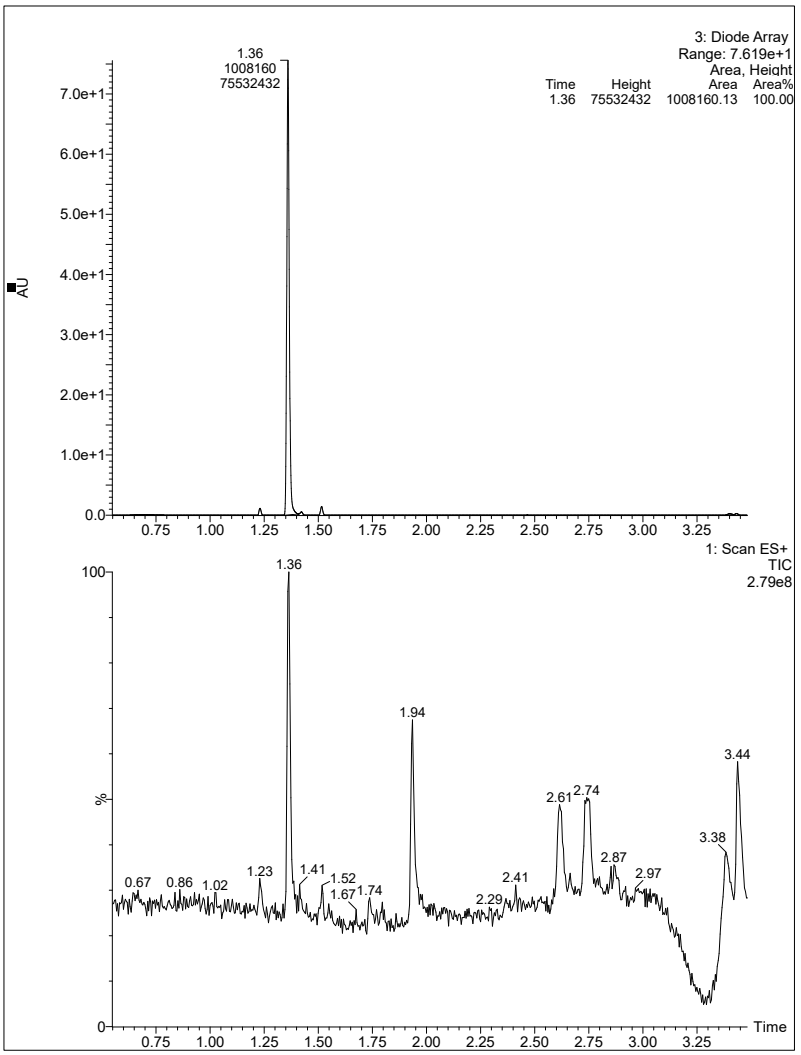
Supporting Figure 71
UPLC-MS spectra of compound 19



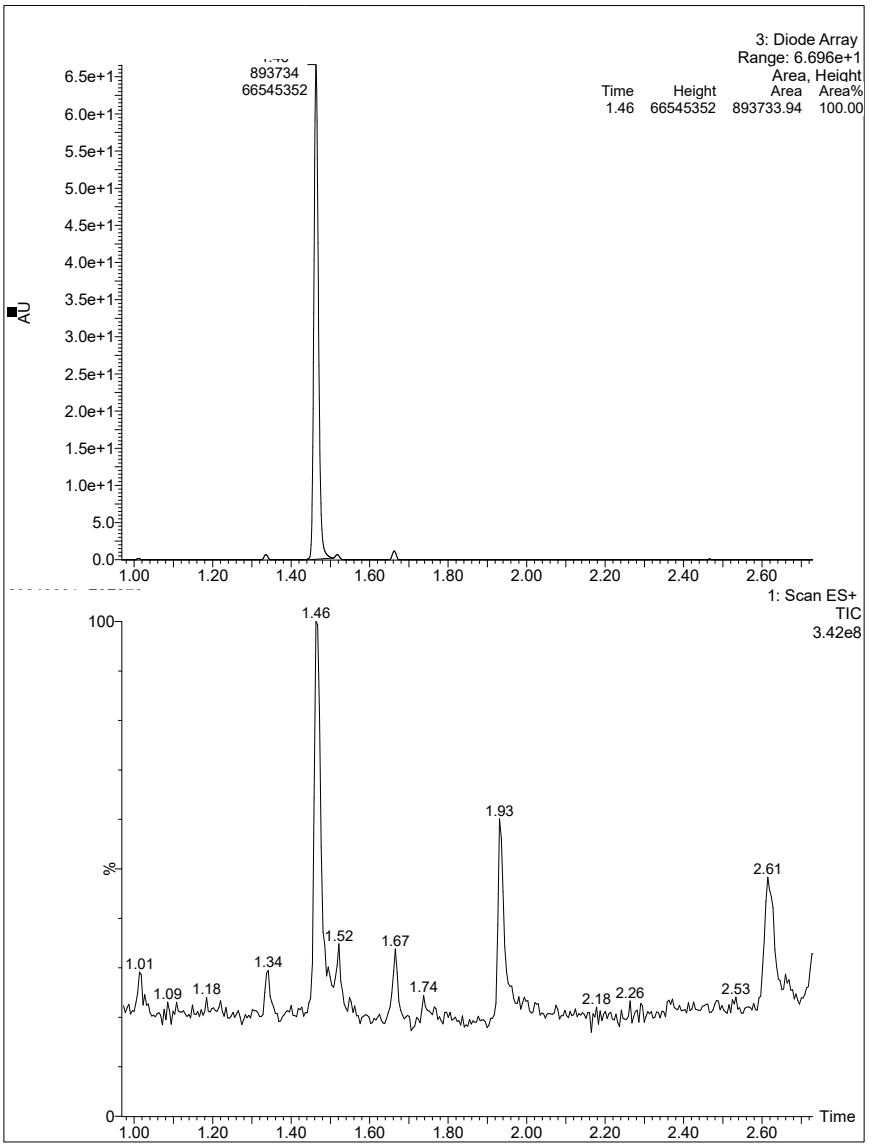
Supporting Figure 72
UPLC-MS spectra of compound 20



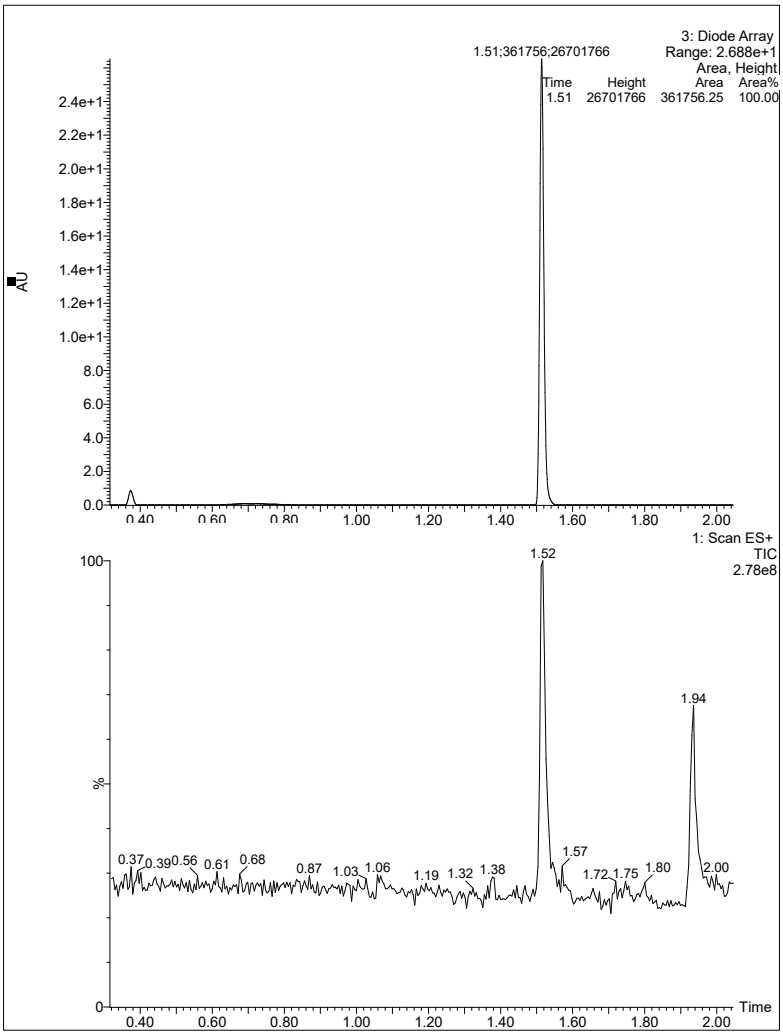
Supporting Figure 73
UPLC-MS spectra of compound 21



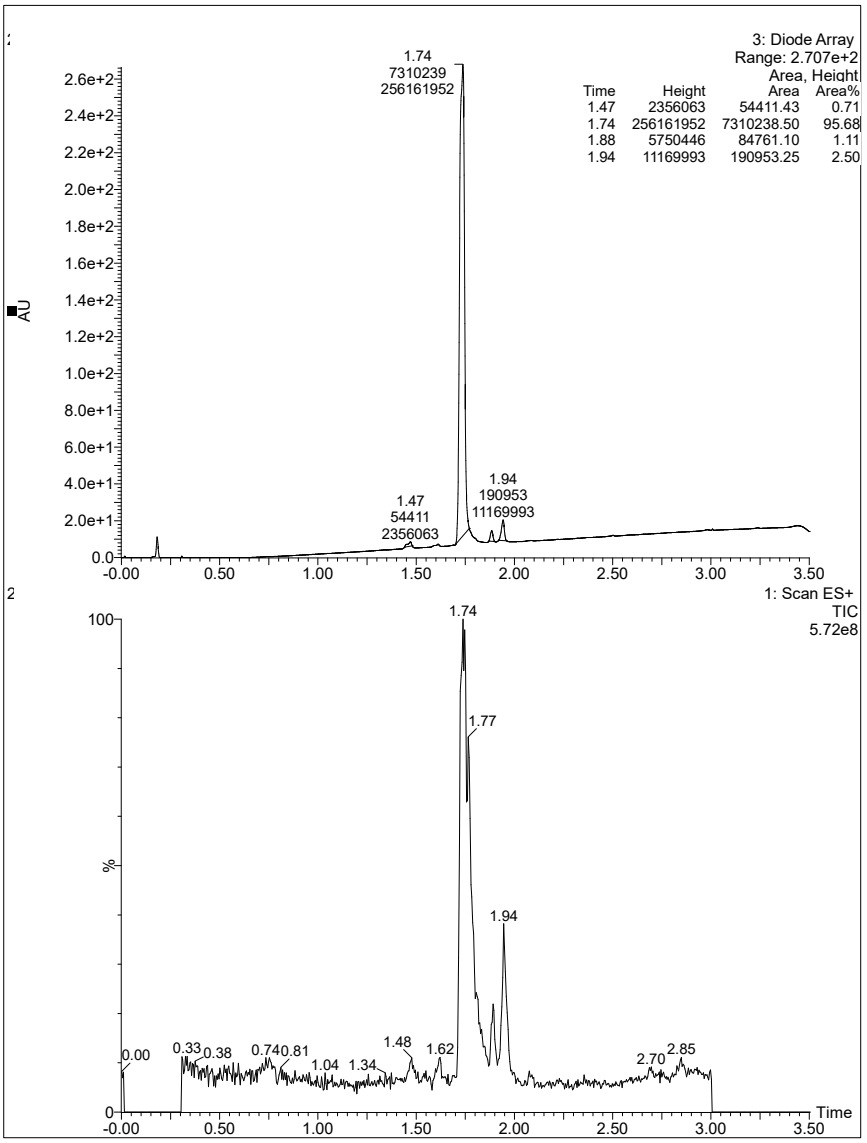
Supporting Figure 74
UPLC-MS spectra of compound 30a



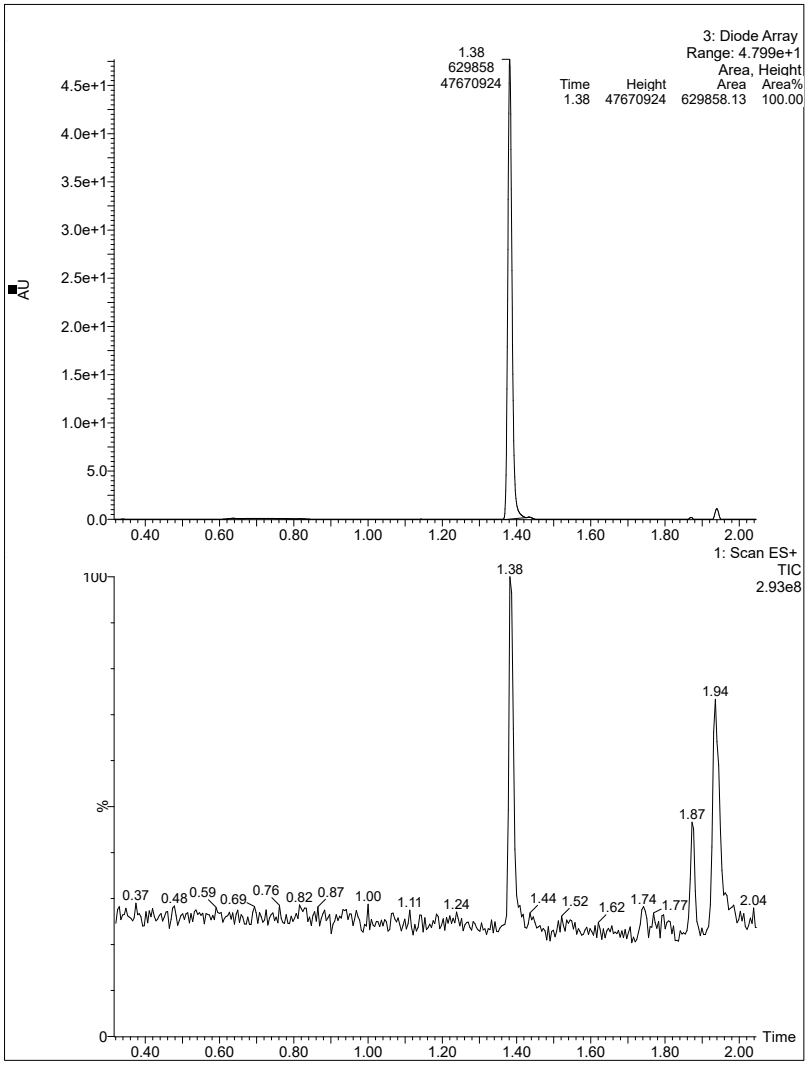
Supporting Figure 75
UPLC-MS spectra of compound 30b



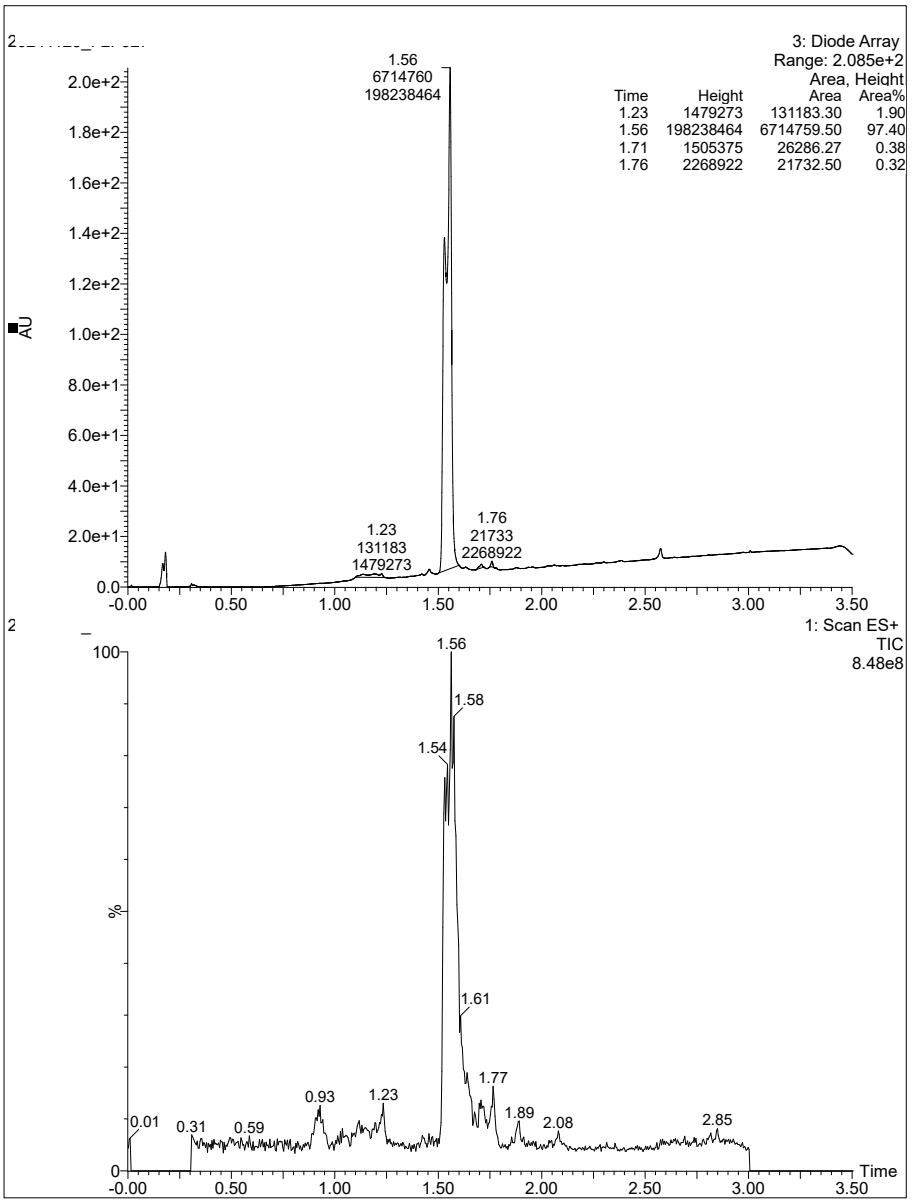
Supporting Figure 76
UPLC-MS spectra of compound 31b



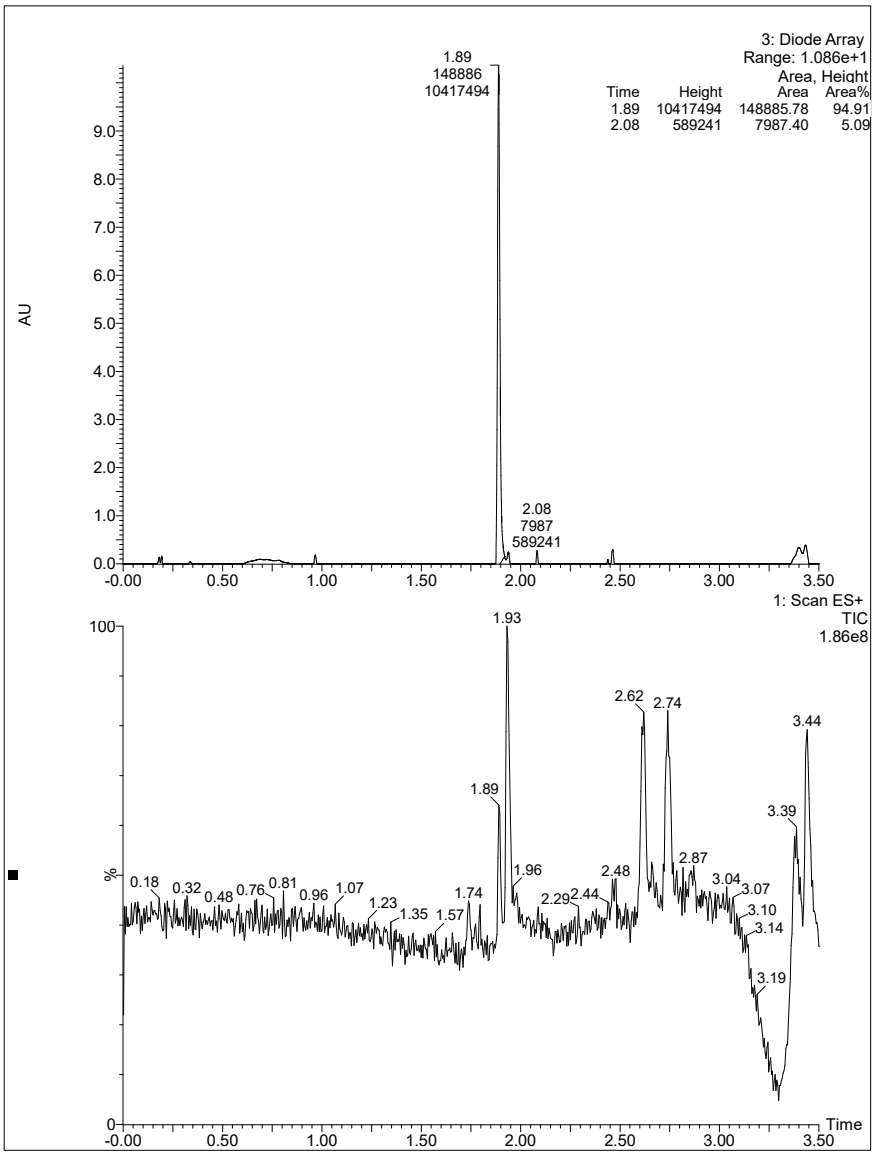
Supporting Figure 77
UPLC-MS spectra of compound 33a



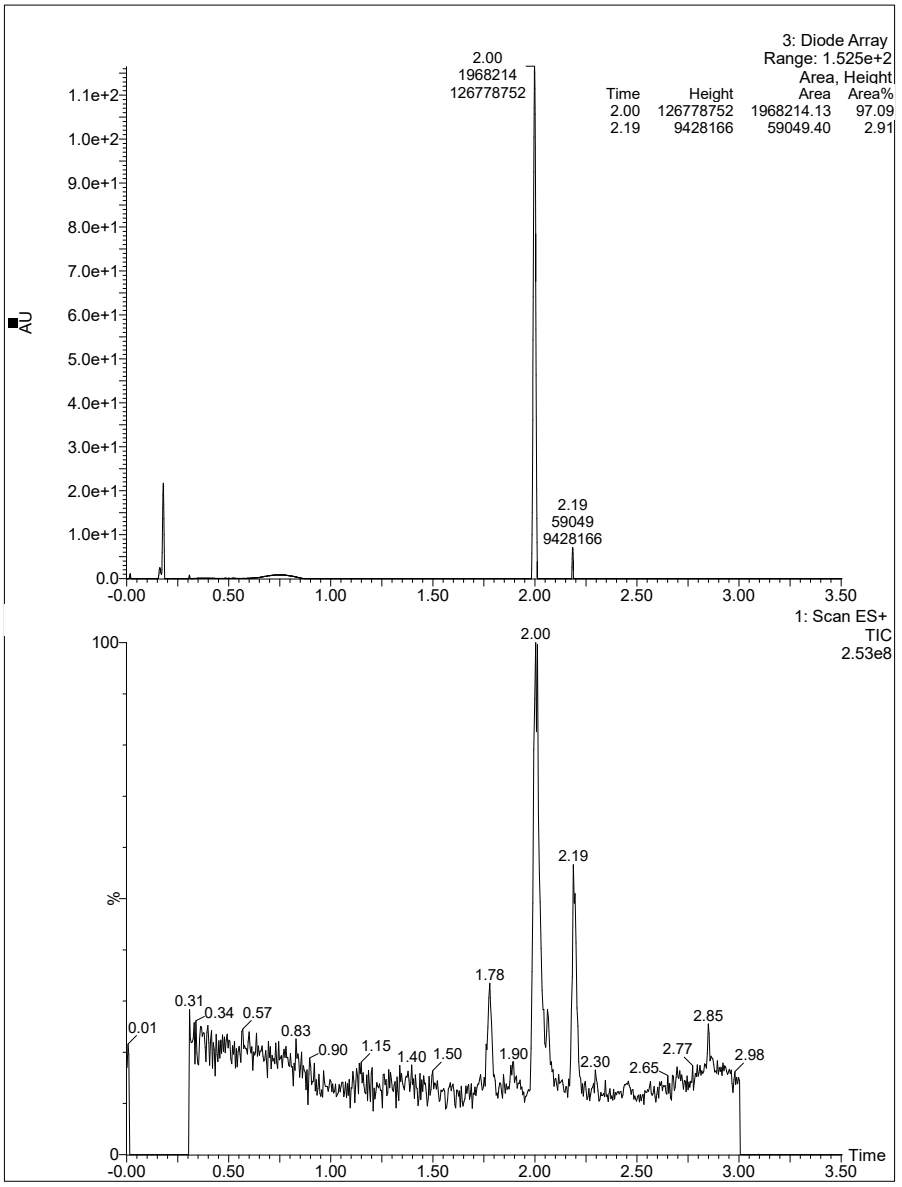
Supporting Figure 78
UPLC-MS spectra of compound 33b



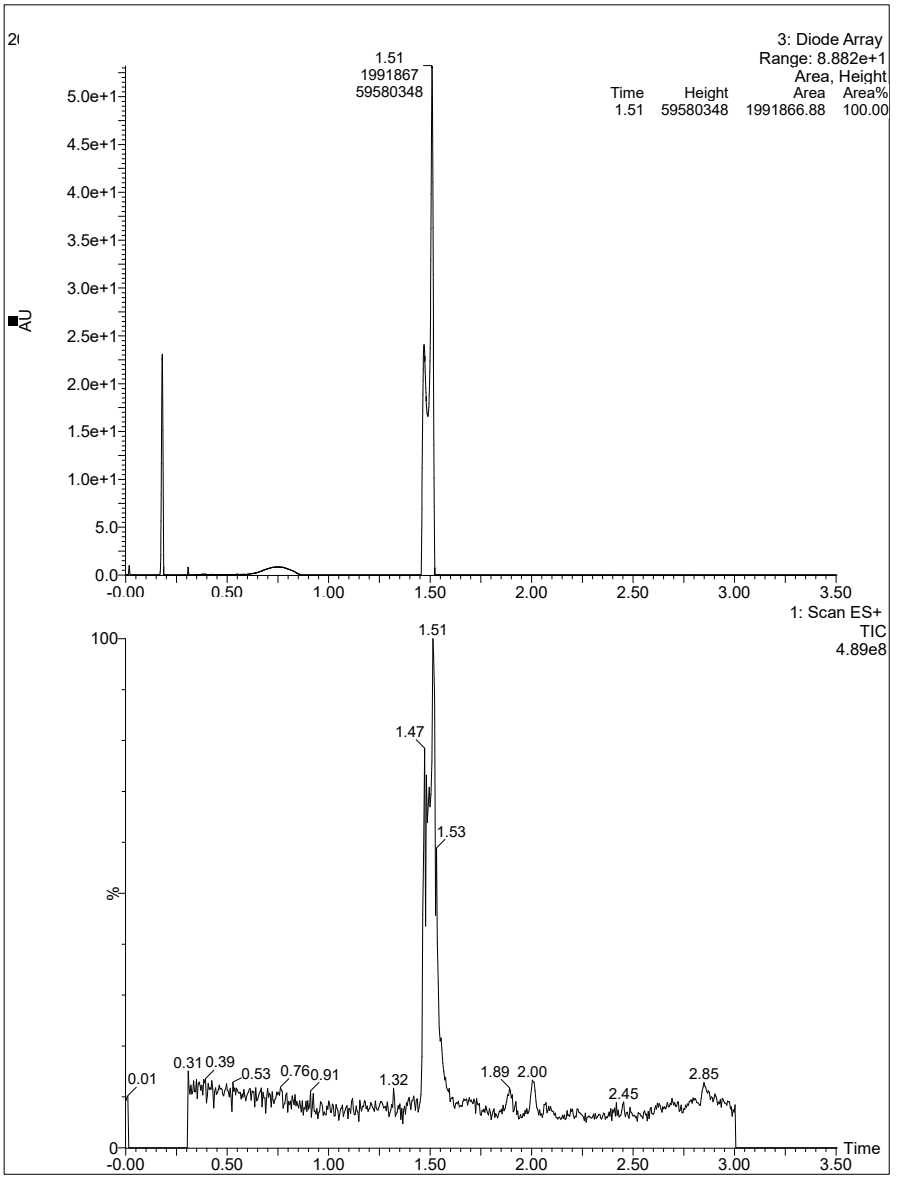
Supporting Figure 79
UPLC-MS spectra of compound 34



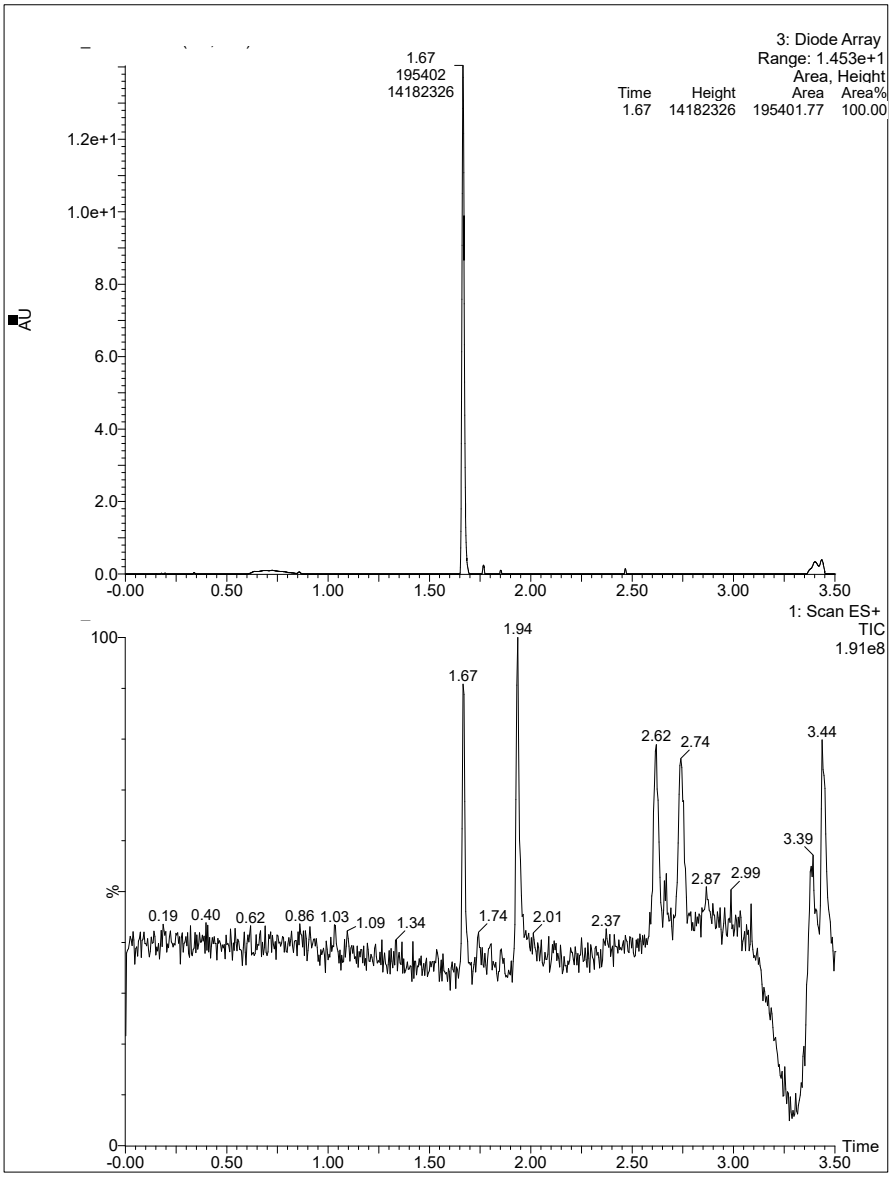
Supporting Figure 80
UPLC-MS spectra of compound 35



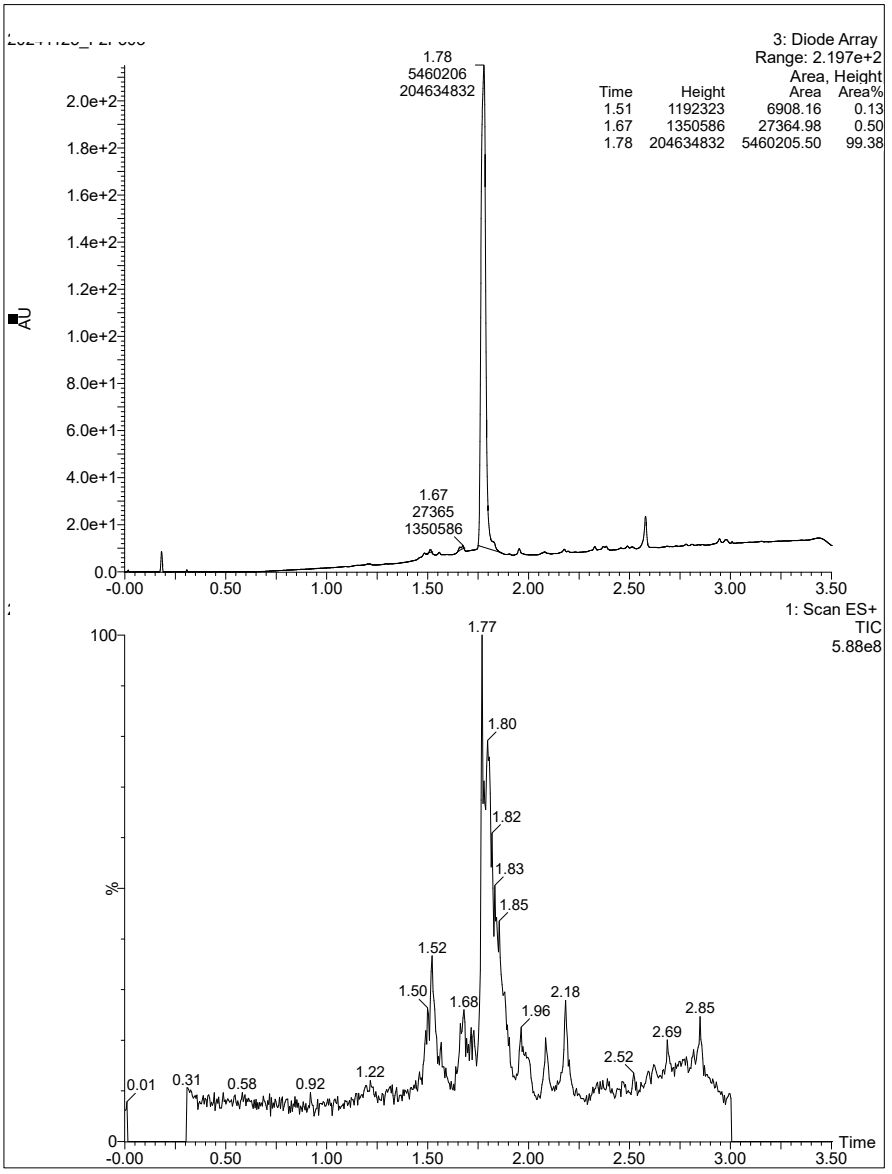
Supporting Figure 81
UPLC-MS spectra of compound 41



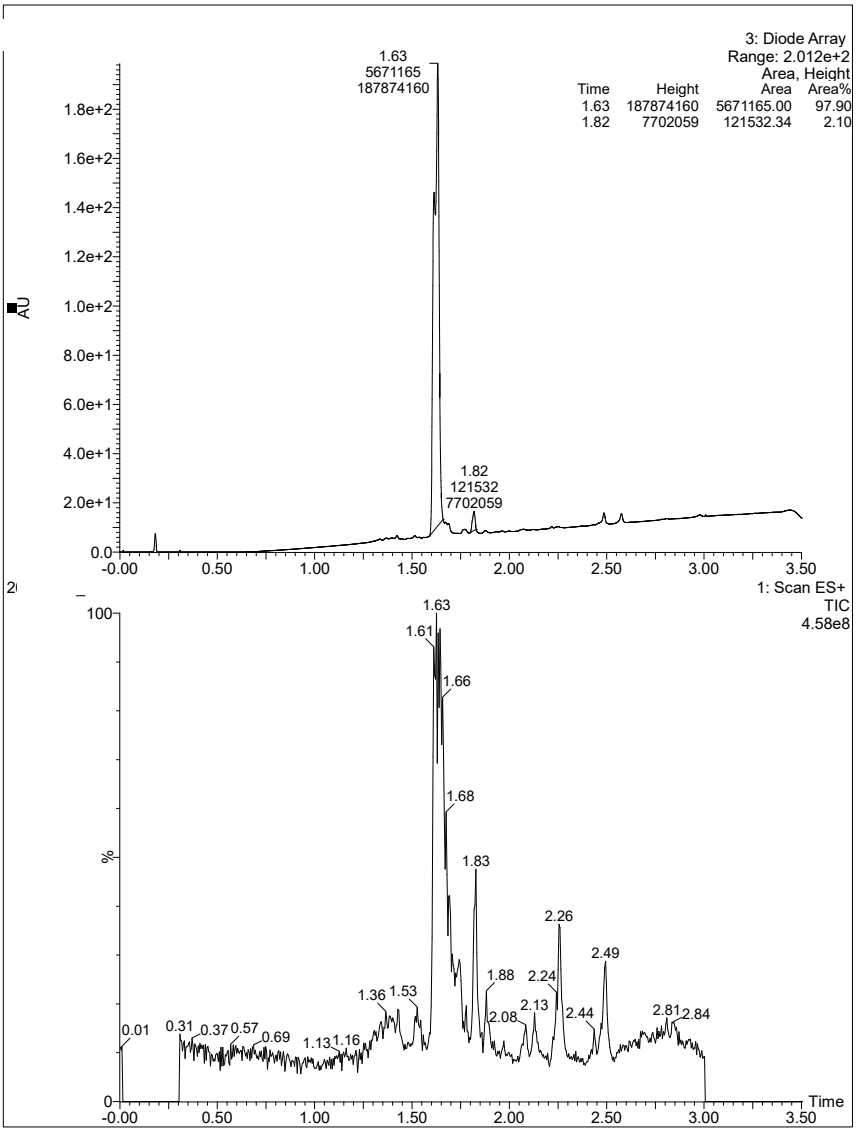
Supporting Figure 82
UPLC-MS spectra of compound 42



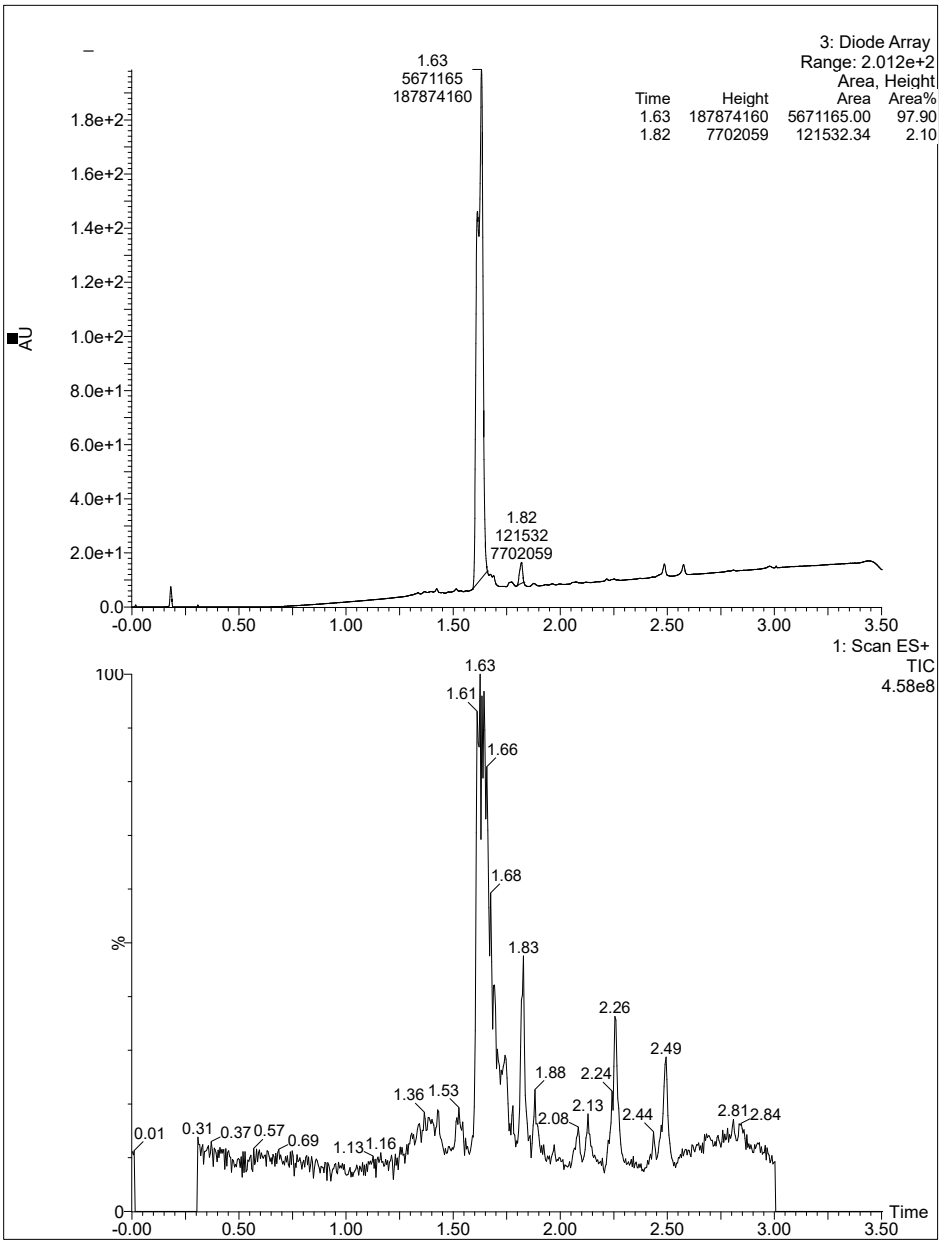
Supporting Figure 83
UPLC-MS spectra of compound 43



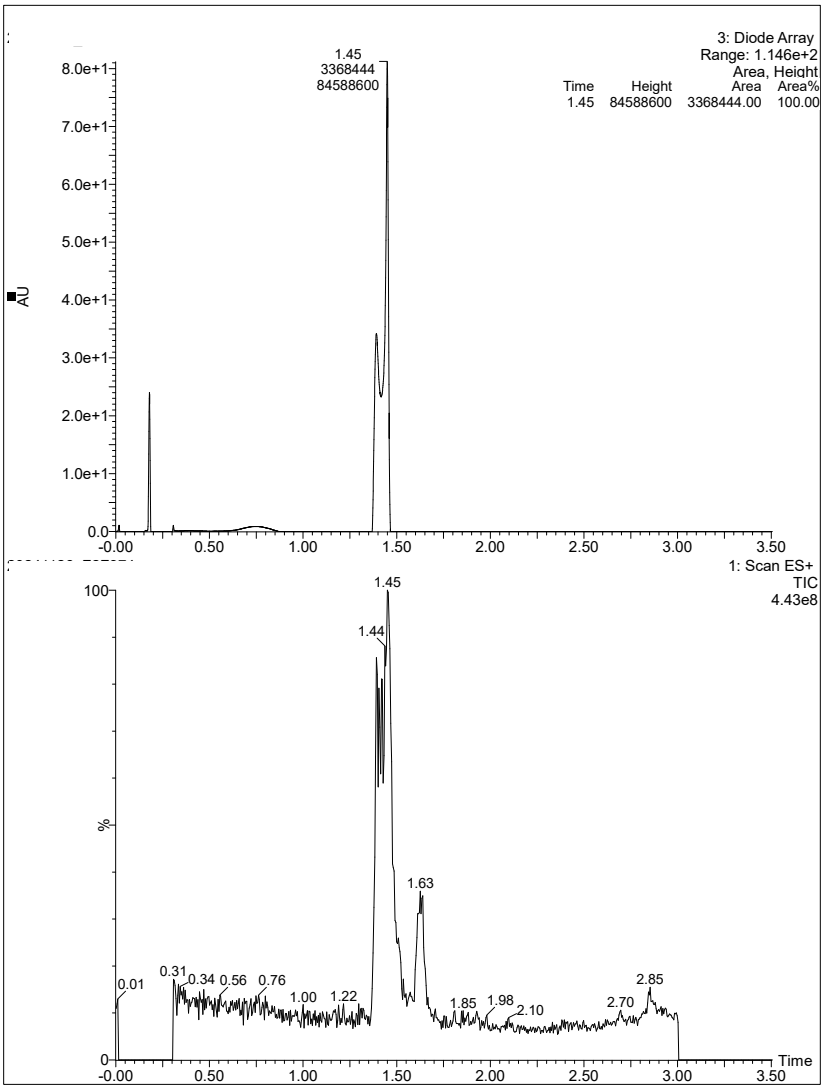
Supporting Figure 84
UPLC-MS spectra of compound 44



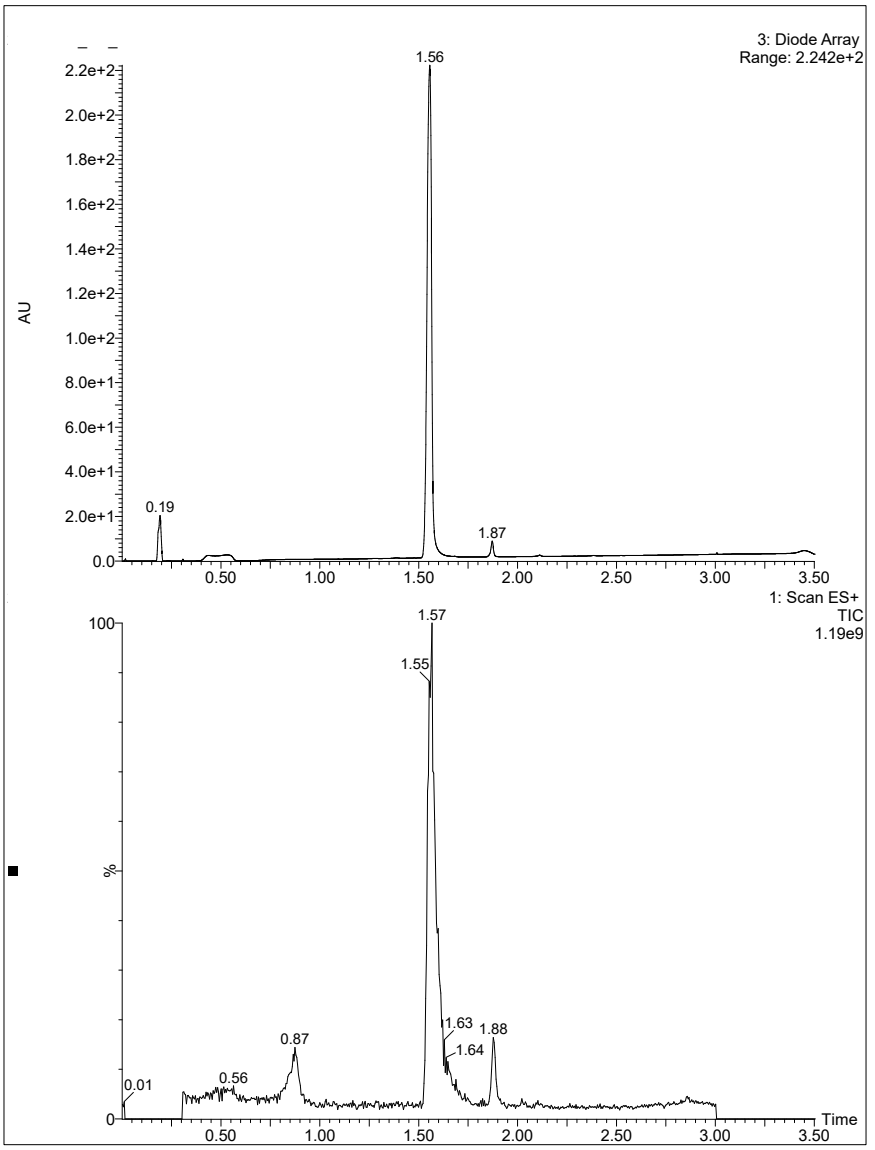
Supporting Figure 85
UPLC-MS spectra of compound 45



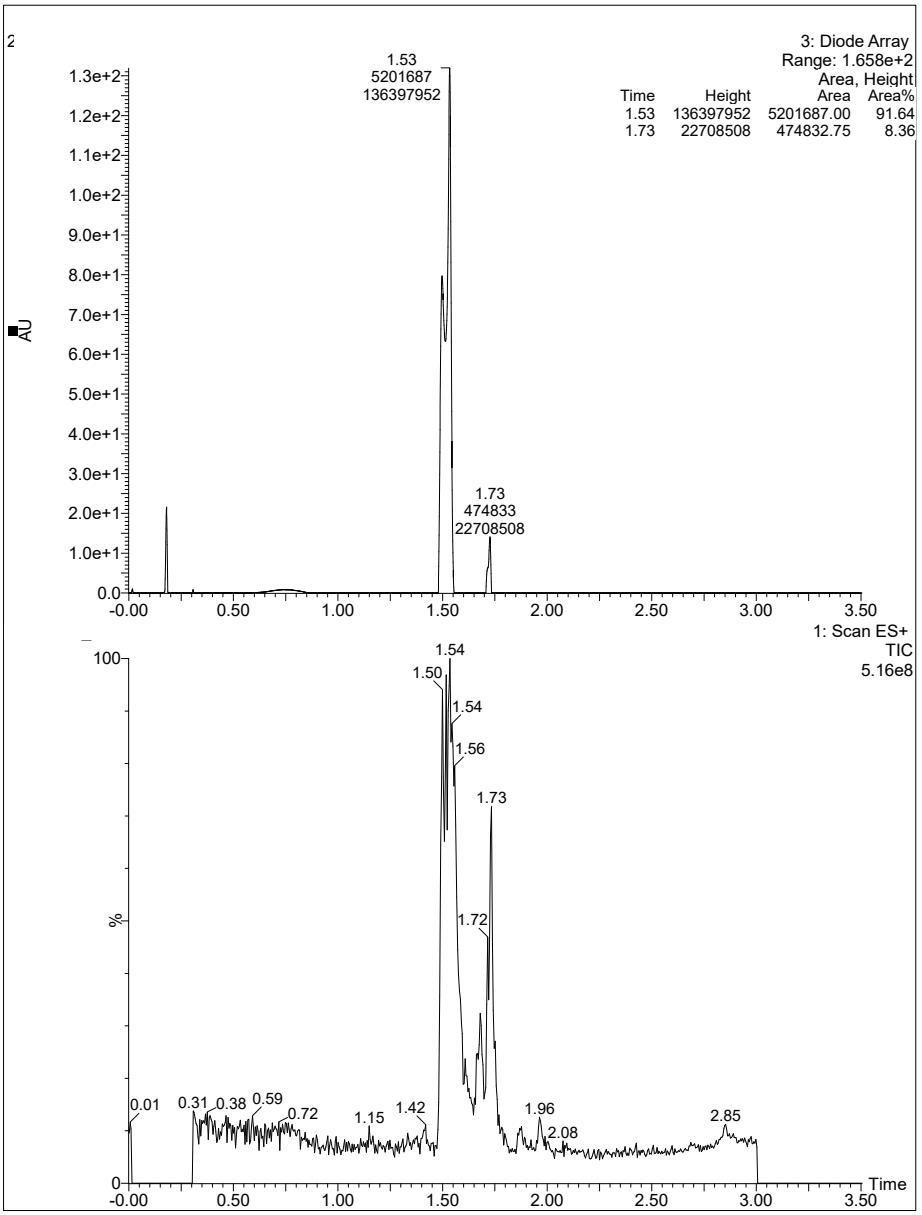
Supporting Figure 86
UPLC-MS spectra of compound 46



Supporting Figure 87
UPLC-MS spectra of compound 48



Supporting Figure 88
UPLC-MS spectra of compound 49



References

[1] A. Guadagni, S. Barone, A.I. Alfano, S. Pelliccia, I. Bello, E. Panza, V. Summa, M. Brindisi, Eur J Med Chem 279 (2024) 116884.

[2] S. Barone, I. Bello, A. Guadagni, C. Cerchia, G. Filocamo, E. Cassese, A.I. Alfano, C. Esposito, Á.J. Feliz Morel, M. Brunetti, A. Lavecchia, V. Summa, E. Panza, M. Brindisi, Eur J Med Chem 292 (2025) 117634.

[3] Y. Hai, D.W. Christianson, Nat Chem Biol 12 (2016) 741–747.

[4] K. V. Butler, J. Kalin, C. Brochier, G. Vistoli, B. Langley, A.P. Kozikowski, J Am Chem Soc 132 (2010) 10842–10846.

Chapter 4

Selective HDAC6 Inhibition by Mesinostat Impairs Tumor Growth and Stemness in Triple-Negative Breast Cancer

In the previous *Chapter*, a novel class of spiro-capped selective HDAC6is has been disclosed, showing efficacy in activating both pro- autophagic and apoptotic pathways, while inhibiting the migration process, in TNBC MDA-MB-231 cells. Building upon these promising results, we sought to further characterize the biological activity of proprietary HDAC6is in TNBC 3D-spheroids and patient-derived organoids (PDOs), more relevant models, mimicking the *in vivo* tumor environment. Accordingly, two-dimensional (2D) cell cultures play a crucial role in drug testing and understanding cell biology. However, they fail to replicate accurately the physiological environment, lacking not only cell-cell interactions, but also biochemical signals that constitute the tumor microenvironment, such as hypoxia, limited access to nutrients, or acidosis. In contrast, three-dimensional (3D) cultures offer significant advantages in drug research. They mimic the complex tissue structure of tumors, showing greater resistance to certain drugs compared to 2D cultures [1-3]. Additionally, 3D cultures can be maintained for up to 4 weeks, unlike the 1-week lifespan of 2D cultures, making them ideal for studying long-term drug effects with slower proliferation and increased resistance. Compound **16b** (Mesinostat, Figure 1, HDAC6 IC_{50} = 7.7 nM, HDAC6 IC_{50} = 2118, SI = 275, *Chapter 3*) was selected tacking into account its selectivity and potency profiles, coupled with favorable pharmacokinetic

properties (e.g. water solubility), making it a suitable preclinical candidate for further *in vivo* assessment. Mesinostat showed efficacy in inhibiting cell proliferation by inducing apoptosis, cell cycle arrest, and autophagy, as determined by transcriptomic and western blot analysis. Moreover, Mesinostat inhibited EMT by limiting migration of TNBC cells and induced a loss of integrity of TNBC 3D-spheroid formation. Finally, Mesinostat treatment of PDOs led to a dose-dependent reduction in cell viability and clonogenic capacity, resulting in a significant suppression of stemness and proliferation markers revealed through gene expression profiling.

4.1 Results and discussion

4.1.1 Mesinostat exerts antitumoral activity on MDA-MB-231 TNBC cells

- Mesinostat inhibits the proliferation of TNBC cells and induces α-tubulin acetylation.

Similarly to experimental flow showed in *Chapter 3* for **16c** and **17c**, we first investigated the potential effect of Mesinostat in human TNBC cells. We measured the proliferation capacity of MDA-MB-231 cells exposed to a crescent concentration of Mesinostat using the MTT assay. Mesinostat in a time-(24-48h) and concentration-(1–30 μM) dependent manner inhibited the growth of MDA-MB-231 cells, with an IC50 at 48 h of about 11 μM (Figure1C).

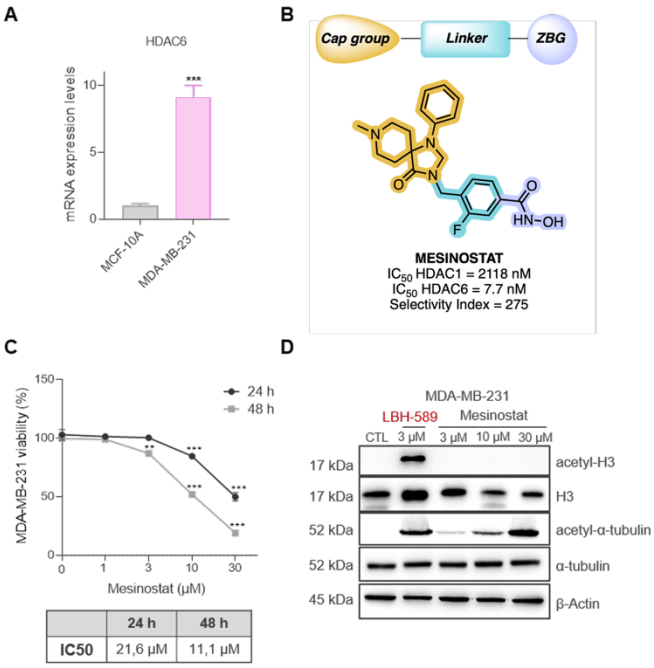


Figure 1. (A) mRNA expression levels of HDAC6 in MCF-10A and MDA-MB-231 cells were evaluated by qPCR analysis. The housekeeping gene (ribosomal protein S16) was used as an internal control to normalize the Ct values. ***p < 0.001 MDA-MB-231 versus MCF-10A. (B) General structure of HDACis and structure of selective HDAC6i Mesinostat. (C) MTT proliferation assay performed in MDA-MB-231 cells exposed or not to Mesinostat at the concentration of 1, 3, 10 and 30 μM for 24 and 48 h. Each point is the mean ± SEM of three independent experiments (n=3) with similar results. **p < 0.01, ***p < 0.001 versus CTL. (D) Representative blots of acetyl-H3, H3, acetyl-α-tubulin, α-tubulin and β-Actin in MDA-MB-231 whole-cell lysates following the treatment with the PAN-Inhibitor LBH-589 (3 μM) and Mesinostat (3, 10 and 30 μM) for 24 h. To investigate whether Mesinostat exhibited a specific inhibitory effect on HDAC6 also in cellular enviornment, the levels of acetylated *α*-tubulin (HDAC6 substrate) were measured in comparison to acetylated H3 (substrate for nuclear HDACs). Gratigyngly, while both Mesinostat and LBH-589 (pan-

HDACi used as a positive control) induced the upregulation of acetylated-α-tubulin expression, only the pan-HDACi LBH-589 was capable of inducing hyperacetylation of histone H3 (Figure 1D).

- *Mesinostat induces apoptosis and proautophagyc events in MDA-MB-231 cells*

On the next stage, to investigate the mechanism through which Mesinostat was able to induce TNBC cells death, we performed a cytofluorimetric assay with Annexin V/PI dual staining. Treatment of MDA-MB-23 cells for 48 h with Mesinostat (10- 30 µM) resulted in a significant and concentration-dependent induction of apoptosis (Figure 2A,B). This effect was confirmed by western blot analysis, revealing the time-dependent cleavage (hence activation) of Caspase-3 and its substrate poly (adenosine diphosphate ribose) polymerase (PARP) by Mesinostat (Figure 2C).

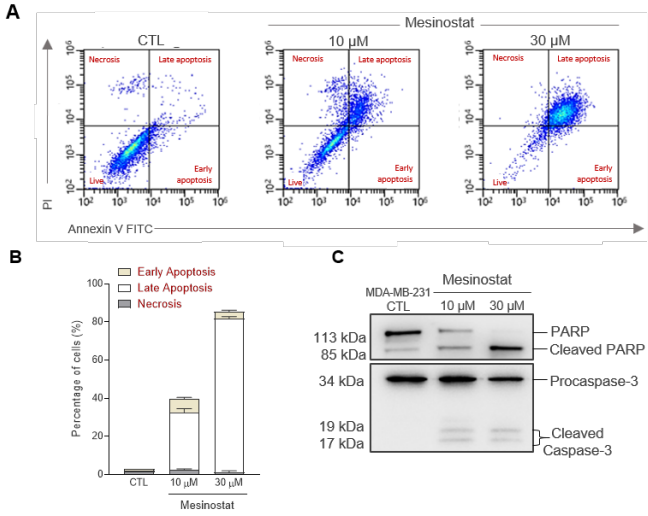


Figure 2. (A) Flow cytometric analysis of apoptosis detected by Annexin V/PI staining in MDA-MB-231 cells treated with Mesinostat (10 and 30 µM) for 48 h. (B) Quantitative analysis of apoptosis showing that approximately 40% and 80% of MDA-MB-231 cells treated respectively with Mesinostat 10 and 30 µM for 48 h exhibit markers of apoptosis. (C) Western blot analysis of PARP and Caspase-3 on MDA-MB-231 whole-cell lysates after treatment with Mesinostat (10 and

30 μM) for 48 h. The data shown are representative of three independent experiments (n = 3) with similar results.

As known, depending on tissue type and stage of tumor progression, autophagy functions a dual role, having pro-survival or pro-death effects. Therefore, we examined the ability of Mesinostat to modulate autophagy by assessing the levels of several key autophagy-related genes and proteins. Satisfyingly, we found Mesinostat promoted autophagy in MDA-MB-231 cells in a time-dependent manner, reflected by the increased expression of Beclin-1 and BNIP3 (Figure 3A,B). Additionally, Mesinostat significantly increased the expression of LC3II protein, which is a key positive regulator of autophagosome formation and activity (Figure 3D,E).

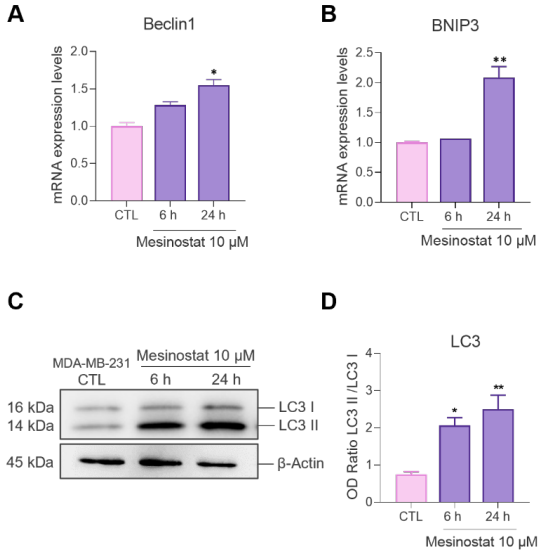


Figure 3. (A-B) mRNA expression levels of Beclin1 and BNIP3 in MDA-MB-231 cells following the treatment with Mesinostat (10 μM) for 6 and 24 h. The housekeeping gene (ribosomal protein S16) was used as an internal control to normalize the Ct values. (C-D) Representative blots and quantitative analysis of LC3 protein measured in MDA-MB-231 cells following the treatment with Mesinostat (10 μM) for 6 and 24 h. β-actin was detected as a loading control.

Each data point was obtained from at least three independent determinations (n=3) for each experimental condition. *p < 0.05, **p < 0.01 versus CTL.

- *Mesinostat causes cell cycle arrest of human TNBC cells.*

To investigate the effect of Mesinostat on cell cycle arrest in MDA-MB-231 cells, we performed flow cytometry analysis to assess cell cycle distribution. As shown in Figure 4A,B, treatment with Mesinostat (10 µM) for 24 and 48 hours led to a significant and time-dependent decrease in the S phase population. This latter effect was further confirmed by transcriptomic analysis of cell cycle-related genes showing that treatment of MDA-MB-231 with Mesinostat (10 µM) for 6 and 24 h, resulting in inhibited expression of cyclin B1, cyclin D1, CDC25A and Cyclin-Dependent Kinase 1 (CDK1), all of which are factors known to promote cell proliferation (Figure 4C-F).

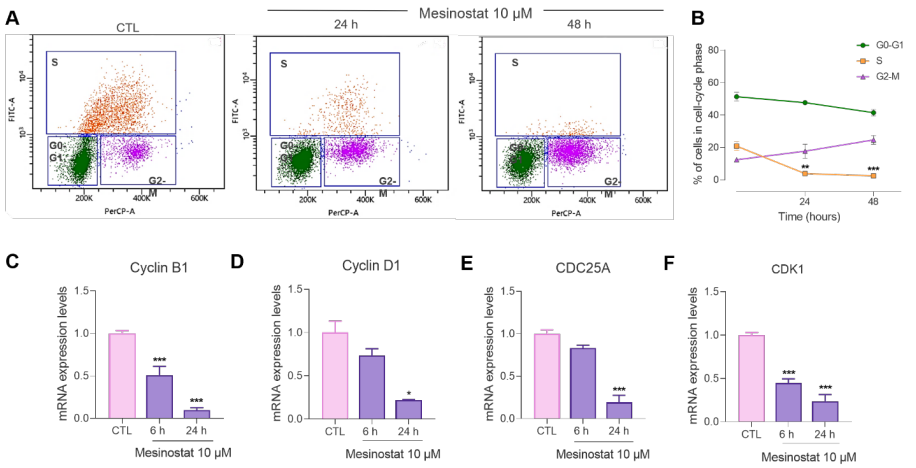


Figure 4. (A-B) Representative density plots and cell percentage, indicating the G0-G1, S and G2-M phase distribution of MDA-MB-231 cells treated or not with Mesinostat (10 µM) for 24 and 48 h. (C-F) mRNA expression levels of Cyclin B1, Cyclin D1, CDC25A and CDK1 proteins measured in MDA-MB-231 following the treatment with Mesinostat (10 µM) for 6 and 24 h. The housekeeping gene (ribosomal protein S16) was used as an internal control to normalize the Ct values. *p < 0.05, **p < 0.01, ***p < 0.001 versus CTL.

- *Mesinostat suppresses EMT in human TNBC cells.*

As previously discussed, EMT is a pivotal process in tumor cell metastasis characterized by the loss of typical epithelial traits and the acquisition of mesenchymal characteristics. In TNBC cells, this transition involves the remodeling of the cell cytoskeleton, reduced localization of junctional E-cadherin, heightened cell polarity, and degradation of the intercellular matrix. Consequently, this results in a weakening of cell-matrix connections and an increase in cellular motility [4]. Therefore, we employed real-time PCR and western blot analysis to quantify the expression levels of key epithelial and mesenchymal markers in MDA-MB-231 cells treated with Mesinostat. As shown in Figure 5, the treatment with Mesinostat (10 µM) for 6 and 24 h, resulted in a significant increase in the expression of E-Cadherin, a well-known marker of epithelial cells, accompanied by the inhibition of mesenchymal markers such as SLUG, N-Cadherin, Vimentin and Caveolin-1.

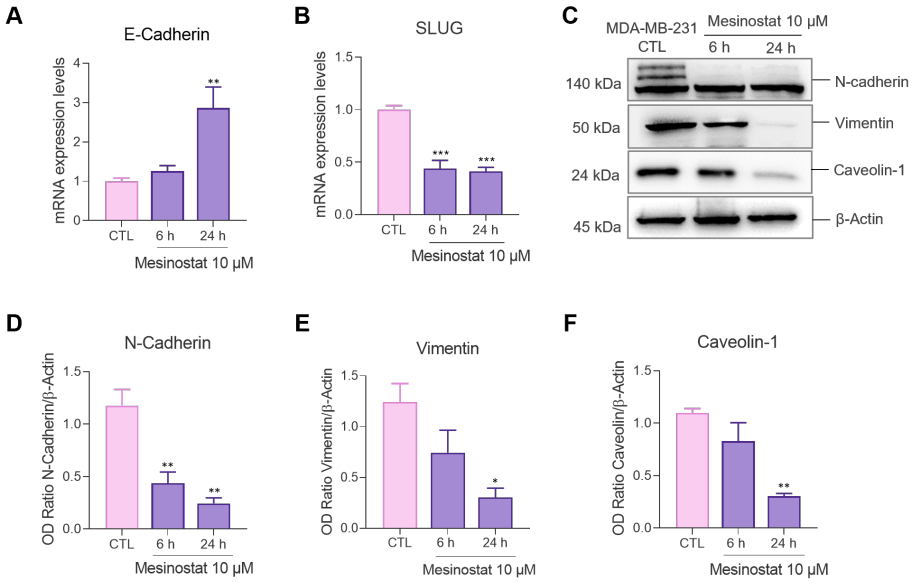


Figure 5. (A-B) mRNA expression levels of E-Cadherin and SLUG in MDA-MB-231 cells following the treatment with Mesinostat (10 µM) for 6 and 24 h. (C-F) representative western blot, and relative quantitative analysis of N-

Cadherin, Vimentin and Caveolin-1 carried out on MDA-MB-231 whole-cell lysates following the treatment with Mesinostat (10 μM) for 6 and 24 h. β-actin was detected as the loading control. The data shown are representative of three independent experiments (n = 3) with similar results. *p < 0.05; **p < 0.01, ***p < 0.001 versus CTL.

- *Mesinostat inhibits cell migration and colony formation of TNBC cells*

On the next stage, the antimetastatic activity of Mesinostat was investigated. Wound-healing assay was performed to determine whether Mesinostat would interfere with MDA-MB-231 cells motility, at concentrations which did not inhibit proliferation or cause apoptosis. Treatment with Mesinostat (1-3 μM) significantly and time-dependently reduced MDA-MB-231 cells migration as compared to untreated cells. Furthermore, Mesinostat significantly reduced the colony formation ability of MDA-MB-231 cells (Figure 6). This data correlates with the capacity of tumor cells to produce progeny and form metastasis *in vivo*.

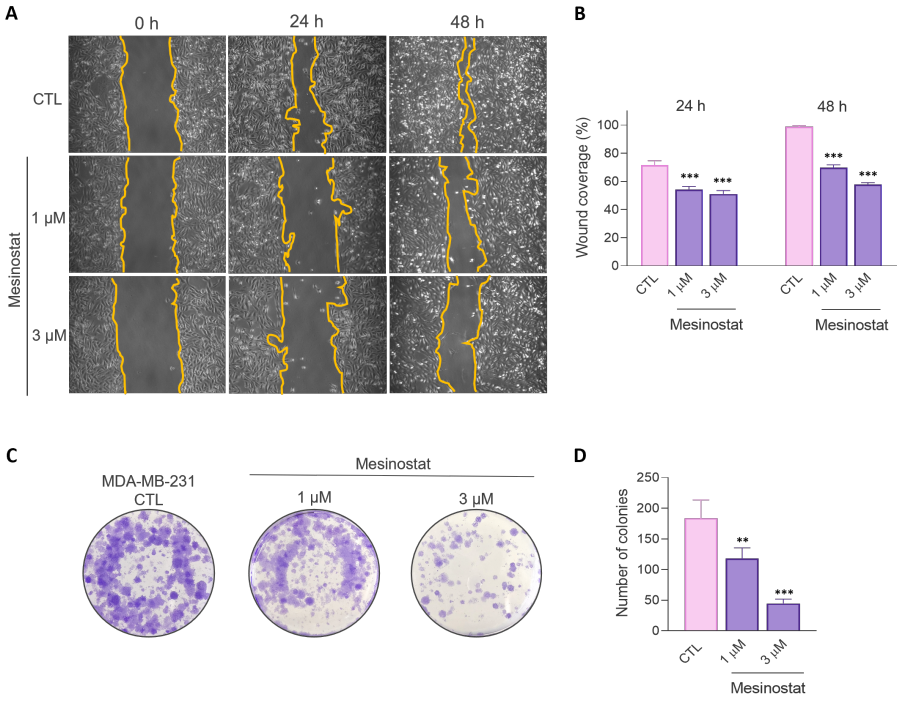


Figure 6. (A) Representative photographs of migratory MDA-MB-231 cells treated with Mesinostat (1–3 μM) at 0, 24 and 48 h. (B) The scratched areas were quantified in three random fields in each treatment. Data are shown as mean ± SEM of three independent experiments (n = 3). ***p < 0.001 versus CTL. (C-D) Representative photographs and the average number of MDA-MB-231 fixed and coloured colonies following the treatment with Mesinostat (1–3 μM). Data are shown as mean ± SEM of three independent experiments (n = 3). **p < 0.01, ***p < 0.001 versus CTL.

- *Mesinostat induces a loss of integrity in TNBC spheroids*

After screening the effect of Mesinostat in 2D cultures, it was assessed in TNBC spheroids, an established model that is more clinically predictive. To this end, MDA-MB-231 cells were cultured in 3D, and the resulting spheroids were treated with Mesinostat (1, 3 and 10 μM) for 12 days. Notably, exposure to Mesinostat induced a loss of integrity of MDA-MB-231 spheroids in a time- and concentration-dependent manner (Figure 7). Complete disaggregation was observed after 12 days of treatment with 10 μM. The integrity of spheroids is fundamental to processes such as adhesion, cell shape regulation, migration, and spreading, as it relies on cytoskeleton proteins, which are crucial for these mechanisms.

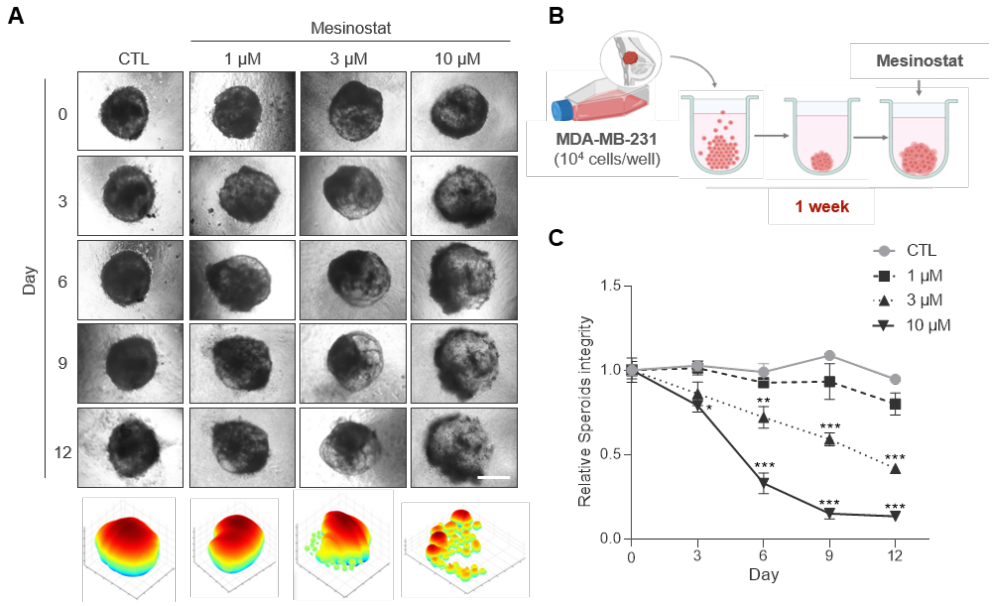


Figure 7. (A) Representative brightfield images showing alterations in spheroid integrity; the corresponding 3D reconstructions were obtained using ReViSP, http://sourceforge.net/p/revisp/. (B) Schematic representation of experimental design performed in MDA-MB-231 spheroids, created with BioRender.com. (C) Quantitative analysis of spheroids integrity calculated as quotient of manually versus automatically segmented spheroid areas. Values are expressed as Relative integrity. *p < 0.05, **p < 0.01, ***p < 0.001 versus relative condition at day 0. Scale bar = 200 µm. n = 5.

- *Mesinostat reduces viability and stem-like properties in lymph node metastasis-derived TNBC organoids*

To investigate the effects of HDAC6 inhibition in a model of metastatic TNBC, we treated patient-derived organoids established from axillary lymph node metastases (mTNBCOs) with Mesinostat. A 48-hour exposure to 1, 3, and 10 µM resulted in a significant, concentration-dependent reduction in cell viability, as revealed by the LIVE/DEAD assay (Figure 8). To assess the impact of treatment on long-term self-renewal capacity, a clonogenic assay was performed. Organoids were treated with Mesinostat for 48 h, then transferred into fresh,

inhibitor-free medium and maintained under growth conditions. The growth in term of diameter of organoids was evaluated after 7 days, revealing a marked reduction compared to controls. This finding indicates a loss of clonogenic potential following HDAC6 inhibition. In parallel, gene expression analysis by qPCR was performed on the organoids after 48 h of treatment. This analysis revealed a significant downregulation of genes associated with stemness and tumor proliferation, including Ki67, Bcl-2, c-Myc, CD44, SOX2, NANOG and OCT4 (Figure 9).

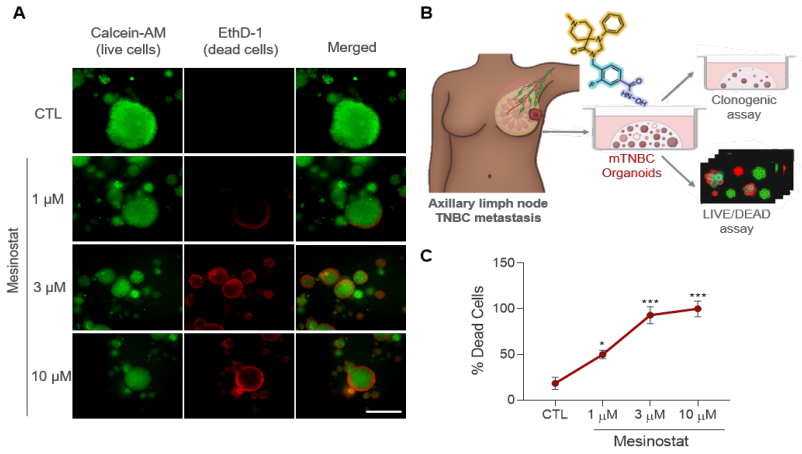


Figure 8. (A) Representative fluorescence images from a LIVE/DEAD assay performed on mTNBCOs treated with Mesinostat (1–10 µM) for 48 h. Live cells are stained with Calcein-AM (green), dead cells with EthD-1 (red), and merged images are shown for treatments with 1, 3, and 10 µM Mesinostat. (B) Schematic illustration of the experimental design, created with BioRender.com. (C) Quantification of cell death in organoids, expressed as the percentage of dead cells relative to the condition showing the highest level of cell death (set as 100%). *$p < 0.05$, **$p < 0.001$ versus CTL. Scale bar = 200 µm.

Collectively, these findings suggest that Mesinostat targets the cancer stem-like cell (CSC) subpopulation within lymph node metastasis-derived organoids, which is known to contribute to recurrence and therapeutic resistance.

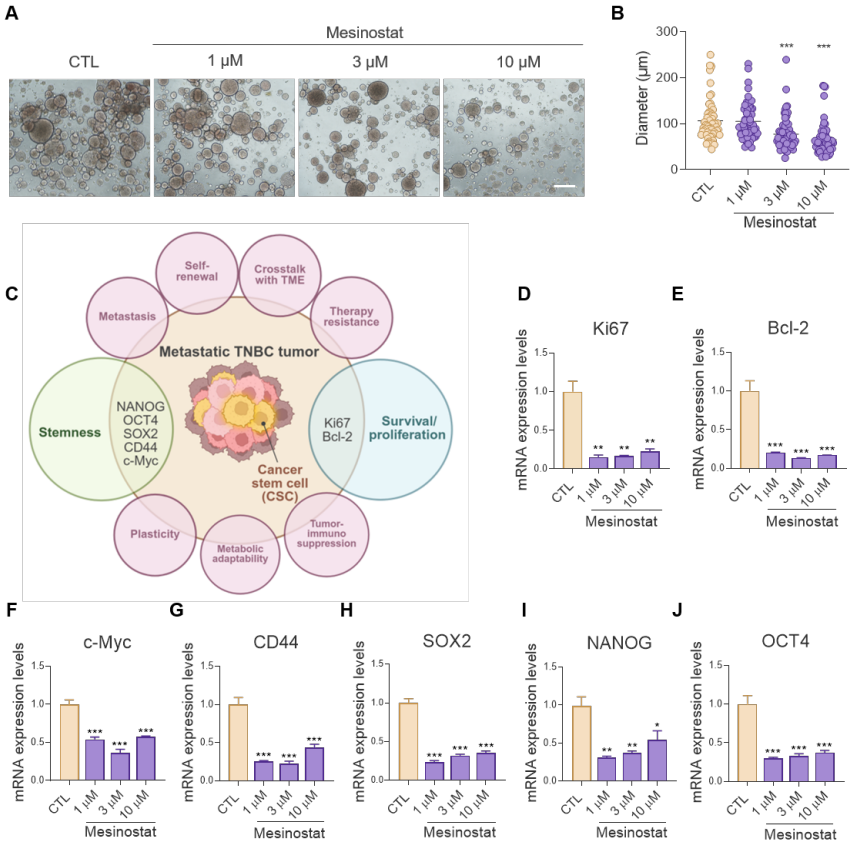


Figure 9. (A) Representative images from the clonogenic assay showing the colony-forming ability of organoids treated with Mesinostat (1–10 µM) for 48 h, then transferred and allowed to grow for 7 days in the absence of the inhibitor. (B) Quantification of organoid growth after 7 days, expressed as organoid diameter in micrometers. Scale bar = 200 µm. (C) Schematic representation of the role of CSCs and associated processes in TNBC metastasis, highlighting the factors analyzed in this study, created with BioRender.com. (D–J) mRNA expression levels of Ki67, Bcl-2, c-Myc, CD44, SOX2, NANOG, and OCT4 in mTNBCOs after treatment with Mesinostat (1–10 µM) for 48 h. *$p < 0.05$, **$p < 0.01$, **$p < 0.001$ versus CTL.

4.2 Conclusions

Selective HDAC6i Mesinostat effectively suppressed TNBC cell proliferation, accompanied by a marked increase in α-tubulin acetylation, a canonical non histone substrate of HDAC6. Beyond its antiproliferative effects, Mesinostat induced apoptotic cell death, as evidenced by activation of caspase-3 and cleavage of PARP. These molecular events suggest engagement of the intrinsic apoptotic pathway, potentially linked to cytoskeletal destabilization and impaired survival signaling. In parallel, Mesinostat promoted autophagic flux, indicated by the upregulation of key autophagy regulators such as Beclin-1, BNIP3, and LC3-II. Mesinostat also exerted a profound impact on cell cycle dynamics, leading to a reduction in proliferative markers and downregulation of cyclins and cyclin-dependent kinases. This suggests a blockade of cell cycle progression, which may synergize with apoptotic and autophagic mechanisms to reinforce growth inhibition. Given the central role of metastasis in TNBC progression, we assessed the effect of Mesinostat on EMT, a critical mechanism underlying tumor invasiveness and dissemination. The restoration of epithelial markers and repression of mesenchymal traits was observed upon treatment with Mesinistat, indicating a reversal of the EMT phenotype. These effects were functionally corroborated by reduced cell motility and clonogenic potential, highlighting Mesinostat ability to suppress metastatic potential. To better approximate *in vivo* tumor architecture and functional heterogeneity, we extended our investigation to 3D culture systems. Upon treatment with Mesinostat, we observed marked disintegration of spheroid architecture, suggesting disruption of cytoskeletal integrity and cell-cell adhesion, consistent with the EMT-inhibitory properties of the compound. In parallel, we employed PDOs derived from lymph node metastases. Mesinostat treatment in TNBC organoids resulted in increased cell death and a significant reduction in clonogenic potential, indicating functional impairment of survival and self-renewal capacity in metastatic tumor cells. These effects suggest that Mesinostat not only targets proliferative compartments but

may also affect therapy-resistant CSC populations. To further investigate this hypothesis, we performed transcriptomic analysis of organoids treated with Mesinostat, which revealed a significant downregulation of proliferation and stemness-associated genes, suggesting a depletion of CSC-like populations. These findings are in line with previous studies demonstrating a pivotal role for HDAC6 in CSC maintenance. Specifically, HDAC6 inhibition has been shown to suppress the expression of pluripotency regulators such as POU5F1, SOX2, and NANOG, while promoting differentiation and reducing tumorigenicity in CSC-enriched populations. Taken together, these findings position Mesinostat as a promising therapeutic candidate for TNBC, capable of orchestrating a multi-pronged attack on tumor growth, survival, plasticity, and stemness. Its selective inhibition of HDAC6 offers a mechanistic advantage by sparing nuclear histone acetylation, potentially reducing off-target effects associated with pan-HDAC inhibition. Accordingly, I am currently performing a scale-up synthesis of Mesinostat to assess its efficacy in an *in vivo* model of TNBC.

4.1.1 Cell culture and reagents

The human triple-negative breast cancer cell line MDA-MB-231 (cat. no. HTB-26) and the non-tumorigenic epithelial cell line MCF-10A (cat.no. CRL-10317) were acquired from the American Type Culture Collection (ATCC, Manassas, VA, USA). Cells were cultured in DMEM (cat. no. D6546, Sigma-Aldrich, Milan, Italy) supplemented with 10% fetal bovine serum (FBS) (Gibco, Milan, Italy; cat. no. A4736301), penicillin (100 U/mL), streptomycin (100 μg/mL) (cat. no. 30-002-CI), 2 mM L-glutamine (cat. no. 25-005-CI), and 10 mM HEPES (cat. no. 25-060-CI) (all from Corning, Manassas, VA, USA). MFC10-A were cultured in DMEM/F12 (Invitrogen cat.no. 11330-032) supplemented with 5% of Horse serum (Invitrogen cat.no. 16050-122), EGF (20 ng/ml) (Peprotech cat.no. AF-100-15), Hydrocortisone (0.5 mg/ml) (Sigma #H-0888, 1g), Cholera Toxin (100 ng/ml) (Sigma #C-8052, 2 mg Insulin (10 μg/ml) (Sigma #I-1882,

100 mg), and penicillin (100 U/mL)/ streptomycin (100 µg/mL). Cells were maintained in a humified incubator at 37 °C with 5% CO_2.

4.1.2 Organoid Culture

Human breast cancer organoids HCM-CSHL-0655-C50 (Cat. PDM-411) were obtained from ATCC. According to the data provided in the Human Cancer Models Initiative Searchable Catalog, this model is a primary tumor that is ERα-negative, PR-negative and HER2-negative as assessed by IHC. The organoids were maintained in polymerized droplets of Matrigel (Corning® Matrigel® Basement Membrane Matrix Phenol Red-Free, LDEV-Free, cat. n. CLS356237-1EA) in advanced DMEM/F12 (Thermo Fisher Scientific, Waltham, MA, cat. no. 12634028) supplemented with Organoid Growth Kit 1F (ATCC, cat. no ACS-7105), B-27 supplement (Thermo Fisher Scientific, cat. No. 17504-044), L-glutamine, ROCK inhibitor Y27632 (ATCC, cat. no ACS-3030) for cell recovery (final concentration of 10 µM). Organoids were grown under a humidified atmosphere of 5% CO2 at 37°C. For passage, Organoids were collected and dissociated into single cells by incubation in pre-warmed TrypLE Express Enzyme (Thermo Fisher Scientific, cat. No. 12604013) for 10 min at 37° C in agitation (1000 rpm). After addition of 5-ml Advanced DMEM/F12 with 2 mM L-glutamine, 10 mM HEPES and 10% FBS and centrifugation (400 rpm, 5 min, 4°C), dissociated cells were resuspended in ice-cold Matrigel. Matrigel-cell suspension in the form of 25 µL droplets were allowed to solidify as domes on a prewarmed 48-well culture plate at 37°C before adding complete medium. Change of complete culture medium was performed every other day until cells reached confluence. To perform RT-qPCR analysis, organoids were harvested by scraping them in ice-cold PBS containing 0,5 mM EDTA. The suspension was incubated on ice for 30 minutes to facilitate Matrigel dissolution. Organoids were then collected by centrifugation at 400 × g for 5 minutes at 4 °C, and the resulting pellets were used for subsequent RNA extraction.

4.1.3 LIVE/DEAD Viability assay on organoids

A total of 10,000 viable cells derived from dissociated organoids plated in 96-well plates (10 µL of Matrigel/well). The Matrigel domes were allowed to solidify, and organoids were then cultured for 7 days in complete medium. Then, cells were treated for 48 hours with Mesinostat at concentrations of 1 µM, 3 µM, and 10 µM. Samples were subsequently washed three times with PBS and fixed for 20 minutes in Paraformaldehyde Solution 4% (Cat. No. J19943.K2, Thermo Scientific). After fixation, three additional PBS washes were performed, and 100 µL per well of the LIVE/DEAD working solution (1×) was added. The solution was prepared according to the manufacturer's instructions (LIVE/DEAD Viability/Cytotoxicity Kit, Cat. No. L32250, Invitrogen). The working solution contains:

- Calcein-AM, a live cell indicator (excitation/emission: 494/517 nm; GFP/FITC filter set),
- Ethidium homodimer-1 (EthD-1), a dead cell indicator (excitation/emission: 528/617 nm; TRITC/RFP or Cy5 filter set).

The assay protocol was carried out as follows: i) 100 µL of the working solution was added to each well and incubated for 30 minutes at room temperature; ii) Wells were washed with PBS; iii) Fluorescence was measured and cell viability was assessed by imaging and quantification. Fluorescent images were acquired using a ZEISS Axio Observer 7 microscope with Colibri 5 (Carl Zeiss AG, Oberkochen, Germany), and plate fluorescence intensity was measured using a microplate reader (GloMax® Multi Detection System, Promega). To determine the relative percentage of dead cells relative to the well exhibiting the highest level of cell death (= 100 %), the following calculation was performed:

1. For each well:

$$R_i = \frac{EthD-1_i}{EthD-1_i + Calcein_i}$$

Where:

- R_i represents the ratio of dead cells to total cells (dead + live),
- *i* indicates the well index.

2. The maximum value across all wells was defined as, and the normalized relative cell death percentage for each well was calculated as:

$$\%\ Relative\ Cell\ Death_i = \left(\frac{R_i}{R_{max}}\right) x\ 100$$

4.1.4 Western blot analysis

Total cell proteins were extracted using the lysis RIPA buffer (50 mM Tris-HCl (pH 7.4), 1 mM EDTA, 150 mM NaCl, 1% Triton X-100, and 0.25% (v/v) sodium deoxycholate, 0.1% SDS) supplemented with Protease Inhibitor Cocktail (cat. no. P8340-1 mL, Merk, Milan, Italy). The protein content in the lysates was determined using the Bradford method (cat. no. 5000006, Bio-Rad, Italy). Equal amounts of proteins (40 μg) from each cell extract were loaded and separated on a sodium dodecyl sulfate polyacrylamide (SDS-PAGE) gel, followed by transfer onto a PVDF membrane using the Trans-Blot Turbo Transfer Starter System (Bio-Rad, Italy). Then, the membranes were blocked in 5% low-fat milk in PBS with 0.1% Tween 20 (PBST) for 1 h at room temperature before being incubated overnight at 4 °C with the following primary antibodies: (i) acetyl-Histone H3 (Lys27) (D5E4) XP (cat. no. 8173; Cell Signaling, MA, USA; diluted 1:1000); (ii) Histone H3 (D1H2) XP (cat. no. 4499; Cell Signaling; diluted 1:2000); (iii) Acetyl-α-Tubulin (Lys40) (D20G3) XP (cat. no. 5335; Cell Signaling; diluted 1:1000); (iv) α-tubulin (cat. no. 3873; Cell Signaling; diluted 1:1000); (v) Caspase 3 (cat. no. 9662, Cell Signaling, MA, USA; diluted 1:1000); (vi) PARP (cat. 9542, Cell Signaling, MA, USA; diluted 1:1000); (vii) LC3 (cat. 2775, Cell Signaling, MA, USA; diluted 1:1000); (viii) N-cadherin (cat. no. E-AB-70061; Elabscience Biotechnology Inc, Houston, Texas; diluted 1:1000); (ix) Vimentin (cat. no. E-AB-70061; Elabscience Biotechnology Inc, Houston, Texas; diluted

1:1000); (x) Caveolin-1 (cat. 3238, Cell Signaling; diluted 1:1000); (xi) β-actin (cat. sc-47,778; Santa Cruz Biotechnology, Santa Cruz, CA; diluted 1:1000). β-actin served as the control for normalization of protein levels. After three washes with PBST, the membranes were incubated with anti-mouse (cat. no. 115-035-003) or anti-rabbit (cat. no. 111-035-144) IgG secondary antibodies (Jackson ImmunoResearch, Cambridge, UK, dilution 1:3000) for 1.30 h at room temperature. Then, the membranes underwent again three washes with PBST. Protein bands were visualized using the ECL chemiluminescence method (Clarity TM Western ECL Substrate, cat. no. 1705061, Bio-Rad Laboratories, CA, USA) and Chemidoc XRS (Biorad, Milan, Italy). Quantification of results was conducted using ImageJ Software (version 1.52a, U.S. National Institutes of Health).

4.1.5 RNA purification and quantitative real-time PCR

Cellular total RNA was extracted utilizing the QIAzol Lysis Reagent following the manufacturer's instructions (cat. no. 79306, Qiagen, Hilden, Germany). Each purified RNA sample was spectrophotometrically quantified using a Nanodrop apparatus (Thermo Fisher Scientific, MA, USA). Purified RNA samples were considered free from DNA and protein contamination if the ratio of absorbance readings at 260/280 nm was ≥1.8. Then, isolated mRNA underwent reverse transcription using the iScript Reverse Transcription Supermix for RT-qPCR (cat. no. 1708841, Bio-Rad, Italy). The quantitative PCR (qPCR) analysis was conducted using a CFX96 real-time PCR detection system (Bio-Rad). The cycling protocol for real-time PCR was as follows: (i) polymerase activation and DNA denaturation 95 °C for 30 s; (ii) amplification for 40 cycles; (iii) denaturation at 95 °C for 15 s; (iv) annealing and extension at 60 °C for 30 s; (v) plate read at 60 °C; and (vi) melt-curve analysis conducted at 65–95 °C in 0.5 °C increments with 5 s/step. The housekeeping gene ribosomal protein S16 was used as an internal control to normalize the Ct values, using the $2^{-\Delta\Delta Ct}$ formula.

4.1.6 Proliferation assay

Cell proliferation was assessed via the MTT (3-(4,5-dimethylthiazol-2-yl) 2,5-diphenyltetrazolium bromide) assay. MDA-MB-231 cells were plated onto 96-well plates (3 × 103 cells/well). After 24 h, cells were exposed to Mesinostat at the concentration of 1, 3, 10 and 30 μM for 24 and 48 h. Then the culture medium was replaced with 100 μL/well of DMEM containing 0.25 mg/mL of MTT (cat. no. M5655, Merk, Italy). The plate was incubated for 3 h at 37 °C. The medium was then aspirated and 100 μL/well of DMSO (cat. no. 20-139, Sigma-Aldrich, Milan, Italy) was added and agitated for 15 min; the absorbance at 540 nm was measured using a microplate spectrophotometer (Thermo Scientific Multiskan GO, Thermo Fisher Scientific, MA, USA).

4.1.7 Flow Cytometry Analysis

MDA-MB-231 cells were seeded (2.5×10^5 cells/well) in 35 mm culture dishes. The day next, to assess apoptosis the cells were treated with or without Mesinostat 10 μM and 30 μM for 48 h, to assess the cell cycle progression the cells were treated with or without Mesinostat 10 μM for 24 h and 48 h. Then MDA-MB-231 cells were collected: apoptosis was detected staining cells with 5 μM of Annexin V-FITC and Propidium Iodide (PI) supplied by the Annexin V-FITC/PI Apoptosis Kit (cat. no. E-CK-A211, Elabscience Biotechnology Inc, Houston, Texas); cell cycle progression was measured using BD Pharmingen™ FITC BrdU Flow Kit (cat. no. 559619, BD Biosciences, Franklin Lakes, NJ, USA) according to the manufacturing instructions. Cell population was analysed using BriCyte flow cytometer (Mindray, Trezzano sul Naviglio Italy). A minimum of 50,000 events for each sample were collected.

4.1.8 Wound healing assay

MDA-MB-231 cells were seeded in 6-well plates (5×10^5 cells/well). Once the cells reached 90% of confluence, Mesinostat 1 and 3 μM were added, and a wound area was created by scraping the cell monolayer with a sterile 200 μL

pipette tip. Then, the cells were incubated at 37 °C in 5% CO_2. The scratched area was photographed using an inverted microscope at the time zero point, after 24 h and 48 h of treatment. The wounded area was measured using Image J software (version 1.52a, U.S. National Institutes of Health).

4.1.9 Clonogenic assay

MDA-MB-231 cells were plated in 6-well plates (1×10^3 cells/well) after 24 h, treated with Mesinostat (1 and 3 μM), and allowed to form colonies for 14 days. After washing with PBS, MDA-MB-231 colonies were fixed with 4% paraformaldehyde and coloured with 0.5% crystal violet. Colonies were manually counted and captured by a digital camera.

4.1.10 3D culture

MDA-MB-231 spheroids were generated by seeding 10^4 cells per well on 96-well plates coated with 1% agarose in complete DMEM. After centrifugation (5 min at 500 rcf) cells were allowed to clump for 24 h and medium containing 2.5% matrigel (cat. no. 354234, Corning) was added to a final volume of 100 μL/well. After 1 week, when spheroids were completely formed, Mesinostat 1, 3 and 10 μM were added. Brightfield pictures for spheroid analysis were captured with the inverted Leica DFC3000 microscope every three days. For further processing, the images were exported in TIFF format, and the area was analyzed with ImageJ. The integrity is calculated as quotient of manually versus automatically segmented spheroid areas. The final integrity value is relative to the same condition at day 0. Then the 3D reconstruction was obtained using the ReViSP software. Depicted are mean values ± SD. For each data point, 5 replicates were made.

4.1.11 Organoid clonogenic assay

Organoids were seeded as dissociated cells into 48-well plates and cultured for 3 days. Subsequently, they were treated with Mesinostat at concentrations of 1, 3, and 10 μM for 48 hours. To evaluate clonogenic potential, the entire content of

each well was transferred to a new well containing fresh, inhibitor-free medium, without prior dissociation of the organoids. The transfer was carried out using a 1:10 dilution of the original suspension. Organoids were then maintained under standard culture conditions, in the absence of Mesinostat, for an additional 7 days. Clonogenic capacity was assessed microscopically and compared to untreated controls. The measured organoid diameter served as an indicator of the ability to recover and proliferate following drug exposure. Brightfield images were acquired using a ZEISS Axio Observer 7 microscope (Carl Zeiss AG, Oberkochen, Germany), and image analysis, including diameter quantification, was performed using ZEISS ZEN software, version 3.1.

4.3 Experimental section

4.3.1 Cell culture and reagents

The human triple-negative breast cancer cell line MDA-MB-231 (cat. no. HTB-26) and the non-tumorigenic epithelial cell line MCF-10A (cat.no. CRL-10317) were acquired from the American Type Culture Collection (ATCC, Manassas, VA, USA). Cells were cultured in DMEM (cat. no. D6546, Sigma-Aldrich, Milan, Italy) supplemented with 10% fetal bovine serum (FBS) (Gibco, Milan, Italy; cat. no. A4736301), penicillin (100 U/mL), streptomycin (100 µg/mL) (cat. no. 30-002-CI), 2 mM L-glutamine (cat. no. 25-005-CI), and 10 mM HEPES (cat. no. 25-060-CI) (all from Corning, Manassas, VA, USA). MFC10-A were cultured in DMEM/F12 (Invitrogen cat.no. 11330-032) supplemented with 5% of Horse serum (Invitrogen cat.no. 16050-122), EGF (20 ng/ml) (Peprotech cat.no. AF-100-15), Hydrocortisone (0.5 mg/ml) (Sigma #H-0888, 1g), Cholera Toxin (100 ng/ml) (Sigma #C-8052, 2 mg Insulin (10 µg/ml) (Sigma #I-1882, 100 mg), and penicillin (100 U/mL)/ streptomycin (100 µg/mL). Cells were maintained in a humified incubator at 37 °C with 5% CO_2.

4.3.2 Organoid Culture

Human breast cancer organoids HCM-CSHL-0655-C50 (Cat. PDM-411) were obtained from ATCC. According to the data provided in the Human Cancer Models Initiative Searchable Catalog, this model is a primary tumor that is ERα-negative, PR-negative and HER2-negative as assessed by IHC. The organoids were maintained in polymerized droplets of Matrigel (Corning® Matrigel® Basement Membrane Matrix Phenol Red-Free, LDEV-Free, cat. n. CLS356237-1EA) in advanced DMEM/F12 (Thermo Fisher Scientific, Waltham, MA, cat. no. 12634028) supplemented with Organoid Growth Kit 1F (ATCC, cat. no ACS-7105), B-27 supplement (Thermo Fisher Scientific, cat. No. 17504-044), L-glutamine, ROCK inhibitor Y27632 (ATCC, cat. no ACS-3030) for cell recovery (final concentration of 10 μM). Organoids were grown under a humidified atmosphere of 5% CO_2 at 37 °C. For passage, Organoids were collected and dissociated into single cells by incubation in pre-warmed TrypLE Express Enzyme (Thermo Fisher Scientific, cat. No. 12604013) for 10 min at 37 °C in agitation (1000 rpm). After addition of 5-mL Advanced DMEM/F12 with 2 mM L-glutamine, 10 mM HEPES and 10% FBS and centrifugation (400 rpm, 5 min, 4 °C), dissociated cells were resuspended in ice-cold Matrigel. Matrigel-cell suspension in the form of 25 μL droplets were allowed to solidify as domes on a prewarmed 48-well culture plate at 37 °C before adding complete medium. Change of complete culture medium was performed every other day until cells reached confluence. To perform RT-qPCR analysis, organoids were harvested by scraping them in ice-cold PBS containing 0,5 mM EDTA. The suspension was incubated on ice for 30 minutes to facilitate Matrigel dissolution. Organoids were then collected by centrifugation at 400 × g for 5 minutes at 4 °C, and the resulting pellets were used for subsequent RNA extraction.

4.3.3 LIVE/DEAD Viability assay on organoids

A total of 10,000 viable cells derived from dissociated organoids plated in 96-well plates (10 μL of Matrigel/well). The Matrigel domes were allowed to

solidify, and organoids were then cultured for 7 days in complete medium. Then, cells were treated for 48 hours with Mesinostat at concentrations of 1 µM, 3 µM, and 10 µM. Samples were subsequently washed three times with PBS and fixed for 20 minutes in Paraformaldehyde Solution 4% (Cat. No. J19943.K2, Thermo Scientific). After fixation, three additional PBS washes were performed, and 100 µL per well of the LIVE/DEAD working solution (1×) was added. The solution was prepared according to the manufacturer's instructions (LIVE/DEAD Viability/Cytotoxicity Kit, Cat. No. L32250, Invitrogen). The working solution contains:

- Calcein-AM, a live cell indicator (excitation/emission: 494/517 nm; GFP/FITC filter set),
- Ethidium homodimer-1 (EthD-1), a dead cell indicator (excitation/emission: 528/617 nm; TRITC/RFP or Cy5 filter set).

The assay protocol was carried out as follows: i) 100 µL of the working solution was added to each well and incubated for 30 minutes at room temperature; ii) Wells were washed with PBS; iii) Fluorescence was measured and cell viability was assessed by imaging and quantification. Fluorescent images were acquired using a ZEISS Axio Observer 7 microscope with Colibri 5 (Carl Zeiss AG, Oberkochen, Germany), and plate fluorescence intensity was measured using a microplate reader (GloMax® Multi Detection System, Promega). To determine the relative percentage of dead cells relative to the well exhibiting the highest level of cell death (= 100 %), the following calculation was performed:

2. For each well:

$$R_i = \frac{EthD-1_i}{EthD-1_i + Calcein_i}$$

Where:

- R_i represents the ratio of dead cells to total cells (dead + live),
- i indicates the well index.

3. The maximum value across all wells was defined as, and the normalized relative cell death percentage for each well was calculated as:

$$\%\ Relative\ Cell\ Death_i = \left(\frac{R_i}{R_{max}}\right) x\ 100$$

4.3.4 Western blot analysis

Total cell proteins were extracted using the lysis RIPA buffer (50 mM Tris-HCl (pH 7.4), 1 mM EDTA, 150 mM NaCl, 1% Triton X-100, and 0.25% (v/v) sodium deoxycholate, 0.1% SDS) supplemented with Protease Inhibitor Cocktail (cat. no. P8340-1 mL, Merk, Milan, Italy). The protein content in the lysates was determined using the Bradford method (cat. no. 5000006, Bio-Rad, Italy). Equal amounts of proteins (40 μg) from each cell extract were loaded and separated on a sodium dodecyl sulfate polyacrylamide (SDS-PAGE) gel, followed by transfer onto a PVDF membrane using the Trans-Blot Turbo Transfer Starter System (Bio-Rad, Italy). Then, the membranes were blocked in 5% low-fat milk in PBS with 0.1% Tween 20 (PBST) for 1 h at room temperature before being incubated overnight at 4 °C with the following primary antibodies: (i) acetyl-Histone H3 (Lys27) (D5E4) XP (cat. no. 8173; Cell Signaling, MA, USA; diluted 1:1000); (ii) Histone H3 (D1H2) XP (cat. no. 4499; Cell Signaling; diluted 1:2000); (iii) Acetyl-α-Tubulin (Lys40) (D20G3) XP (cat. no. 5335; Cell Signaling; diluted 1:1000); (iv) α-tubulin (cat. no. 3873; Cell Signaling; diluted 1:1000); (v) Caspase 3 (cat. no. 9662, Cell Signaling, MA, USA; diluted 1:1000); (vi) PARP (cat. 9542, Cell Signaling, MA, USA; diluted 1:1000); (vii) LC3 (cat. 2775, Cell Signaling, MA, USA; diluted 1:1000); (viii) N-cadherin (cat. no. E-AB-70061; Elabscience Biotechnology Inc, Houston, Texas; diluted 1:1000); (ix) Vimentin (cat. no. E-AB-70061; Elabscience Biotechnology Inc, Houston, Texas; diluted 1:1000); (x) Caveolin-1 (cat. 3238, Cell Signaling; diluted 1:1000); (xi) β-actin (cat. sc-47,778; Santa Cruz Biotechnology, Santa Cruz, CA; diluted 1:1000). β-actin served as the control for normalization of protein levels. After three washes

with PBST, the membranes were incubated with anti-mouse (cat. no. 115-035-003) or anti-rabbit (cat. no. 111-035-144) IgG secondary antibodies (Jackson ImmunoResearch, Cambridge, UK, dilution 1:3000) for 1.30 h at room temperature. Then, the membranes underwent again three washes with PBST. Protein bands were visualized using the ECL chemiluminescence method (Clarity TM Western ECL Substrate, cat. no. 1705061, Bio-Rad Laboratories, CA, USA) and Chemidoc XRS (Biorad, Milan, Italy). Quantification of results was conducted using ImageJ Software (version 1.52a, U.S. National Institutes of Health).

4.3.5 RNA purification and quantitative real-time PCR

Cellular total RNA was extracted utilizing the QIAzol Lysis Reagent following the manufacturer's instructions (cat. no. 79306, Qiagen, Hilden, Germany). Each purified RNA sample was spectrophotometrically quantified using a Nanodrop apparatus (Thermo Fisher Scientific, MA, USA). Purified RNA samples were considered free from DNA and protein contamination if the ratio of absorbance readings at 260/280 nm was ≥1.8. Then, isolated mRNA underwent reverse transcription using the iScript Reverse Transcription Supermix for RT-qPCR (cat. no. 1708841, Bio-Rad, Italy). The quantitative PCR (qPCR) analysis was conducted using a CFX96 real-time PCR detection system (Bio-Rad). The cycling protocol for real-time PCR was as follows: (i) polymerase activation and DNA denaturation 95 °C for 30 s; (ii) amplification for 40 cycles; (iii) denaturation at 95 °C for 15 s; (iv) annealing and extension at 60 °C for 30 s; (v) plate read at 60 °C; and (vi) melt-curve analysis conducted at 65–95 °C in 0.5 °C increments with 5 s/step. The housekeeping gene ribosomal protein S16 was used as an internal control to normalize the Ct values, using the $2^{-\Delta\Delta Ct}$ formula.

4.3.6 Proliferation assay

Cell proliferation was assessed via the MTT (3-(4,5-dimethylthiazol-2-yl) 2,5-diphenyltetrazolium bromide) assay. MDA-MB-231 cells were plated onto 96-

well plates (3 × 103 cells/well). After 24 h, cells were exposed to Mesinostat at the concentration of 1, 3, 10 and 30 μM for 24 and 48 h. Then the culture medium was replaced with 100 μL/well of DMEM containing 0.25 mg/mL of MTT (cat. no. M5655, Merk, Italy). The plate was incubated for 3 h at 37 °C. The medium was then aspirated and 100 μL/well of DMSO (cat. no. 20-139, Sigma-Aldrich, Milan, Italy) was added and agitated for 15 min; the absorbance at 540 nm was measured using a microplate spectrophotometer (Thermo Scientific Multiskan GO, Thermo Fisher Scientific, MA, USA).

4.3.7 Flow Cytometry Analysis

MDA-MB-231 cells were seeded (2.5×10^5 cells/well) in 35 mm culture dishes. The day next, to assess apoptosis the cells were treated with or without Mesinostat 10 μM and 30 μM for 48 h, to assess the cell cycle progression the cells were treated with or without Mesinostat 10 μM for 24 h and 48 h. Then MDA-MB-231 cells were collected: apoptosis was detected staining cells with 5 μM of Annexin V-FITC and Propidium Iodide (PI) supplied by the Annexin V-FITC/PI Apoptosis Kit (cat. no. E-CK-A211, Elabscience Biotechnology Inc, Houston, Texas); cell cycle progression was measured using BD Pharmingen™ FITC BrdU Flow Kit (cat. no. 559619, BD Biosciences, Franklin Lakes, NJ, USA) according to the manufacturing instructions. Cell population was analysed using BriCyte flow cytometer (Mindray, Trezzano sul Naviglio Italy). A minimum of 50,000 events for each sample were collected.

4.3.8 Wound healing assay

MDA-MB-231 cells were seeded in 6-well plates (5×10^5 cells/well). Once the cells reached 90% of confluence, Mesinostat 1 and 3 μM were added, and a wound area was created by scraping the cell monolayer with a sterile 200 μL pipette tip. Then, the cells were incubated at 37 °C in 5% CO_2. The scratched area was photographed using an inverted microscope at the time zero point, after

24 h and 48 h of treatment. The wounded area was measured using Image J software (version 1.52a, U.S. National Institutes of Health).

4.3.9 Clonogenic assay

MDA-MB-231 cells were plated in 6-well plates (1×10^3 cells/well) after 24 h, treated with Mesinostat (1 and 3 μM), and allowed to form colonies for 14 days. After washing with PBS, MDA-MB-231 colonies were fixed with 4% paraformaldehyde and coloured with 0.5% crystal violet. Colonies were manually counted and captured by a digital camera.

4.3.10 3D culture

MDA-MB-231 spheroids were generated by seeding 10^4 cells per well on 96-well plates coated with 1% agarose in complete DMEM. After centrifugation (5 min at 500 rcf) cells were allowed to clump for 24 h and medium containing 2.5% matrigel (cat. no. 354234, Corning) was added to a final volume of 100 μL/well. After 1 week, when spheroids were completely formed, Mesinostat 1, 3 and 10 μM were added. Brightfield pictures for spheroid analysis were captured with the inverted Leica DFC3000 microscope every three days. For further processing, the images were exported in TIFF format, and the area was analyzed with ImageJ. The integrity is calculated as quotient of manually versus automatically segmented spheroid areas. The final integrity value is relative to the same condition at day 0. Then the 3D reconstruction was obtained using the ReViSP software. Depicted are mean values ± SD. For each data point, 5 replicates were made.

4.3.11 Organoid clonogenic assay

Organoids were seeded as dissociated cells into 48-well plates and cultured for 3 days. Subsequently, they were treated with Mesinostat at concentrations of 1, 3, and 10 μM for 48 hours. To evaluate clonogenic potential, the entire content of each well was transferred to a new well containing fresh, inhibitor-free medium, without prior dissociation of the organoids. The transfer was carried out using a

1:10 dilution of the original suspension. Organoids were then maintained under standard culture conditions, in the absence of Mesinostat, for an additional 7 days. Clonogenic capacity was assessed microscopically and compared to untreated controls. The measured organoid diameter served as an indicator of the ability to recover and proliferate following drug exposure. Brightfield images were acquired using a ZEISS Axio Observer 7 microscope (Carl Zeiss AG, Oberkochen, Germany), and image analysis, including diameter quantification, was performed using ZEISS ZEN software, version 3.1.

4.3.12 Statistical analysis

Data were expressed as mean ± SEM of $n = 3$ experiments. Data were analysed and presented using GraphPad Prism 10.2.2 software (San Diego, CA, USA). Significance was determined using Student's 2-tailed t-test. Results were considered significant at p values less than 0.05 and are labelled with a single asterisk. In addition, p-values lower than 0.01 and 0.001 are indicated with double and triple asterisks, respectively.

References

[1] A.S. Nunes, A.S. Barros, E.C. Costa, A.F. Moreira, I.J. Correia, Biotechnol Bioeng 116 (2019) 206–226.

[2] S. Lagies, M. Schlimpert, S. Neumann, A. Wäldin, B. Kammerer, C. Borner, L. Peintner, Commun Biol 3 (2020) 246.

[3] I. Giusti, G. Poppa, S. D'Ascenzo, L. Esposito, A.R. Vitale, G. Calvisi, V. Dolo, Int J Mol Sci 23 (2022) 11782.

[4] S. Lamouille, J. Xu, R. Derynck, Nat Rev Mol Cell Biol 15 (2014) 178–196.

Chapter 5

Unlocking L2 Pocket Interactions: Linker Inversion Enables the Design of Next-Generation Selective HDAC6 Inhibitors.

As discussed in *Chapter 1 (Part 2, Rational Design of HDACis)*, HDAC6 exhibits unique structural features, which can be strategically exploited for the design of molecular entities able to selectively interact with aminoacidic residues located in the HDAC6 catalytic cleft, thereby unlocking isoform selectivity while reducing side effects due to pan-HDAC inhibition [1,2]. Within the frame of this PhD thesis work, a novel class of highly potent and selective HDAC6is bearing 1,3,8-triazaspiro[4,5]decan-4-one cap group has been developed and disclosed (see *Chapter 3*) [3]. The design of this novel class of inhibitors has been guided by *in silico* studies, which revealed key interactions of the selected spirofused core within HDAC6 catalytic cleft. Accordingly, the size of the catalytic channel rim (defined by L1 and L2 pockets) in HDAC6 is notably wider and shallower compared to nuclear HDACs, allowing the interaction with large and rigid *cap group*s [1,4]. Most of the available HDAC6is interact with residues located in the L1 pocket, which shares key structural similarities across HDAC isoenzymes. This may explain their somehow limited isoform selectivity and thus represent a risk factor for potential off-target effects. In this context targeting L2 pocket would represent a viable strategy for selective interaction within HDAC6, due to L2 pocket unique structural features among HDACs, notably the presence of a S531 residue in *z*HDAC6 (corresponding to S568 in *h*DCA6) [2,5]. Indeed, in all other HDAC isoforms, S568 is replaced by an aspartate residue, which may establish a completely different pattern of interaction (*i.e.* electrostatic repulsion) with respect to those possible for the neutral and polar hydroxyl group present in the serine residues [6]. Accordingly, in this *Chapter*, I discuss the design and synthesis of a small subset of HDAC6is specifically tailored for interaction within L2 pocket. We planned a strategic linker overturning on the 1,3,8-

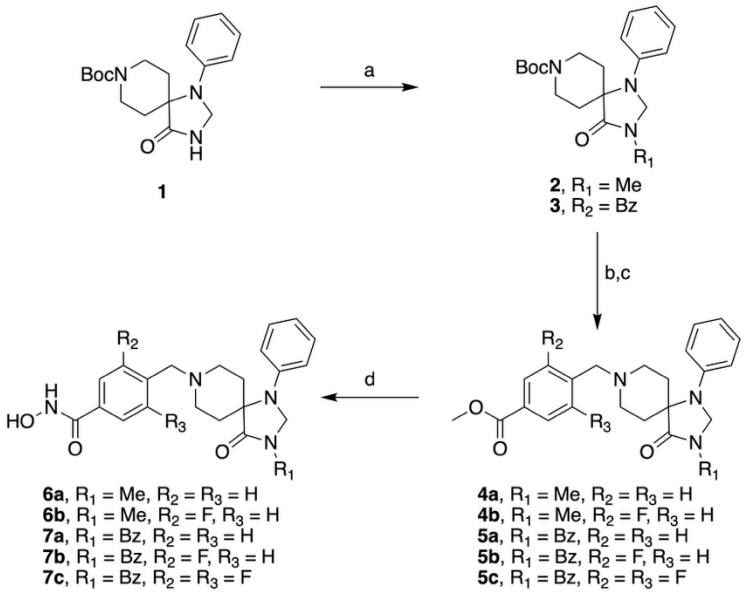
triazaspiro[4,5]decan-4-one cap group identified by our research group as discussed in *Chapter 3* [3]. Among the newly developed chemical entities, compound **7b** (*Table 1*) displayed the higher potency on HDAC6 and high selectivity towards the nuclear isoform HDAC1. X-ray crystal structure of compound **7b** in complex within *z*HDAC6, obtained in collaboration with Professor David Christianson at the University of Pennsylvania, confirmed its high selectivity profile is ascribable to the ability of fluorine atom to specifically interact within the residue S531 in the L2 loop of HDAC6 active site, thus fostering further investigation of structure-activity relationship studies and optimization studies for the newly conceived compounds.

4.1 Results and discussion

4.1.1 Chemistry

For the synthesis of derivatives **6a,b** and **7a-c**, the spirofused core **1** was first subjected to an alkylation reaction in the presence of iodomethane or benzyl bromide, employing NaH as the base, in dry THF, to obtain intermediates **2** and **3**, respectively. Boc deprotection in acidic environment afforded the corresponding amino derivatives, which were subsequently subjected to an alkylation with methyl-4-bromomethyl-benzoate (**4a**, **5a**), methyl-4-(bromomethyl)-3-fluorobenzoate (**4b**, **5b**), or 4-(bromomethyl)benzonitrile (**5c**), using anydrous K_2CO_3 as base, in anhydrous DMF at 25 °C. Subsequent treatment with 50% aqueous hydroxylamine in presence of 4 N methanolic KOH, using DCM/MeOH (2:1) as solvent, led to the desired final products **6a,b** and **7a-c** (Scheme 1).

Scheme 1. Synthesis of final compounds **6a,b** and **7a-c**.[a]



[a]Reagents and conditions: (a) iodomethane or benzyl bromide, NaH 60 % oil dispersion, dry THF, 24 h, 25 °C, 76% (**2**), 52% (**3**); (b) 4 N HCl in dioxane, DCM, 1 h, 25 °C, quant.; (c) methyl-4-bromomethyl-benzoate, methyl-4-(bromomethyl)-3-fluorobenzoate, or 4-(bromomethyl)benzonitrile, anhydrous K_2CO_3, dry DMF, 18 h, 25 °C, 90-31%; (d) 50% aq. NH_2OH, 4 M KOH in MeOH, DCM/MeOH (2:1), 1 h, 25 °C, 90-35%.

4.1.2 Linker overturning of 1,3,8-triazaspiro[4,5]decan-4-one cap group enabled the interaction within L2 on HDAC6 catalytic rim

Starting from structural and potency insights obtained for our previously developed spirofused HDAC6is, and with the aim of targeting binding interaction within L2 subsite, driven by computational hints, we sought to investigate the effect of a strategic overturning of the linker and the ZBG moieties from the piperidine nitrogen to the imidazolidone one, in order to evaluate whether this modification – resulting in a different molecule geometry and orientation - could also affect binding mode within HDAC6, thereby modulating compounds binding affinity, selectivity, and overall efficacy (Figure 1).

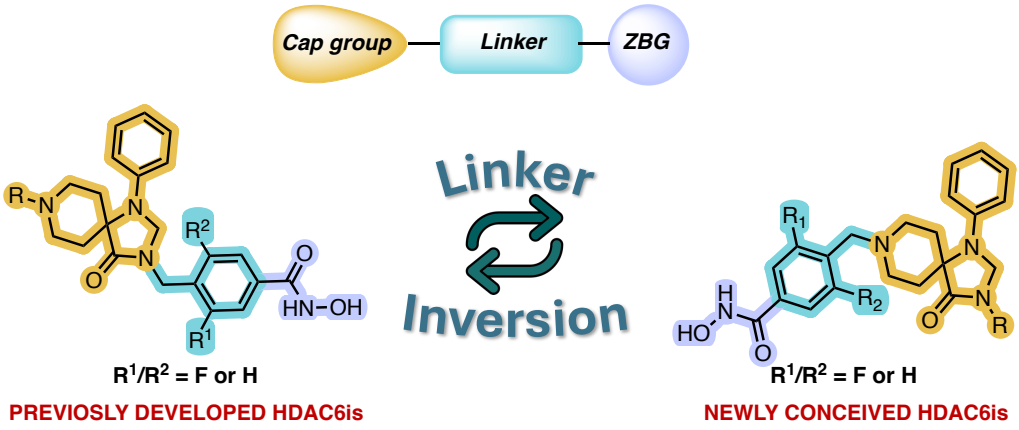


Figure 1. Strategic linker overturing performed on HDAC6is bearing 1,3,8-triazaspiro[4,5]decan-4-one cap group.

In silico studies were performed on compound **7a** in complex within *h*HDAC6 active site (PDB: 5EDU). Molecular modelling studies were undertaken by means of Glide (Glide, Schrödinger, LLC, New York, NY, 2021)[402,403]. Docking studies revealed compound **7a** is able to coordinate the catalytic Zn^{2+} ion in a bidentate fashion (Figure 2B) – similarly to analogues bearing the linker on the amide moiety). However, while the benzyl-capped *cap group* in compound **17a** (see *Chapter 3*) is engaged in further hydrophobic interactions with H499 in L1 loop, this portion of the molecule is more solved exposed in compound **6a**, thereby reducing its contribution to binding within HDAC6 L1 loop, and instead projecting towards HDAC6 L2 (Figure 2A). Moreover, the aromatic linker is involved in π-π stacking interactions with F680 and H651. Accordingly, this data supported our driving hypothesis for linker inversion as a winning strategy to target the L2 loop in HDAC6. Therefore, a focused set of compounds was designed to provide preliminary hints in structure-activity relationships for this class of inhibitors.

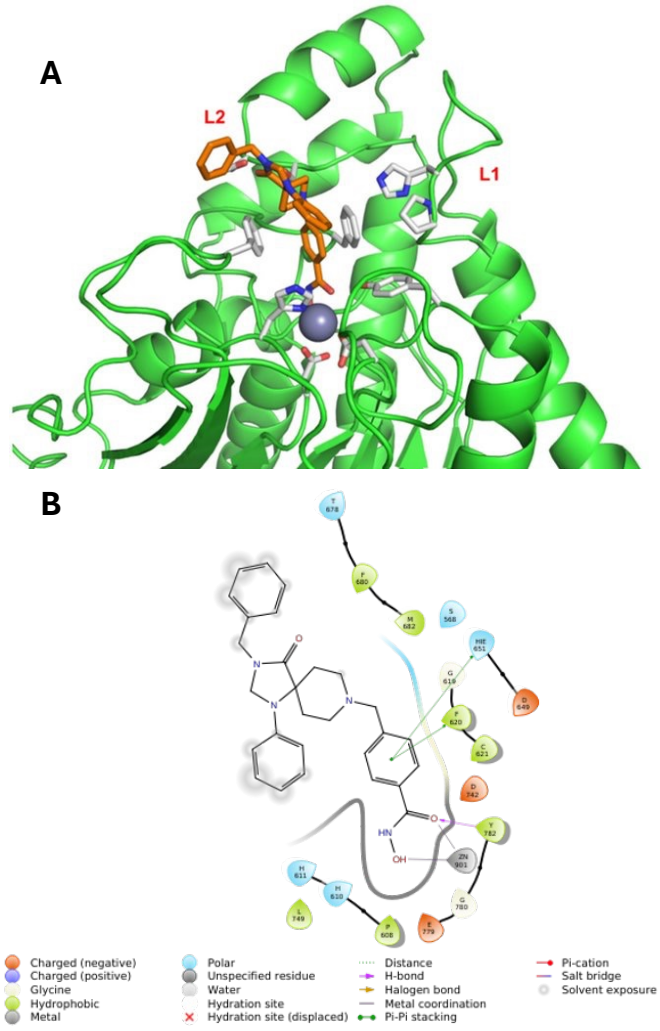


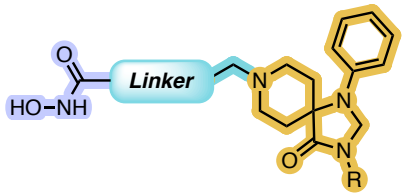
Figure 2. (A) Docking pose of compound **7a** within *h*HDAC6 active site (PDB: 5EDU) represented as green ribbon model. (B) Binding mode of **7a** within L1 loop in HDAC6 catalytic rim.

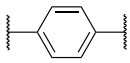
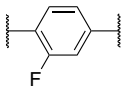
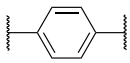
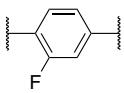
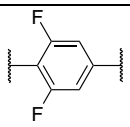
Similar to the design strategy pursuit for the previous set of compounds (*Chapter 3*), first, a simple *p*-phenyl hydroxamic acid moiety was explored as linker-ZBG combination, while amide nitrogen in spirofused cap group was decorated with a methyl or a benzyl group, in order to evaluate whether such linker inversion could affect molecules efficacy, in comparison to analogues **16a** and **17a** reported in the previous *Chapter* (*Table 1*). Despite both compounds **6a (**HDAC6 IC_{50} =

103.6 nM, HDAC1 IC_{50} = 8108 nM, SI = 78) and **7a (**HDAC6 IC_{50} = 134.8 nM, HDAC1 IC_{50} = 9279 nM, SI = 69) displayed nM activity on HDAC6, their selectivity indexes over the nuclear isoform HDAC1 were not satisfying in order to consider these new designed inhibitors as selective. This data perfectly aligned with *in silico* studies conducted on **7a**, in which the *cap group* moiety is mainly solved-exposed, thereby potentially limiting isoform-specific interactions. Moreover, it is worth noting that linker fluorination promotes π-π interactions in HDAC6 aromatic crevice, as well as halogen bonds with S531in *z*HDAC6 L2 (corresponding to S568 in *h*DCA6). This observation encouraged us to pursue linker inversion strategy through the introduction of fluorinated linkers, while maintaining methyl and benzyl substituents on amide portion, to evaluate the effect of point modifications in designed inhibitors. Accordingly, the introduction of a *m*-fluorobenzyl linker in compounds **6b** and **7b** resulted in a significant loss of potency on HDAC1 with a slight increased potency on HDAC6, thereby enhancing HDAC6 isoform selectivity and validating the hypothesis of linker fluorination to target L2 loop in such series of inhibitors, with **7b** resulting as the most potent and selective of this focused set of compounds **(**HDAC6 IC_{50} = 48.6 nM, HDAC1 IC_{50} = 39133 nM, SI = 568, *Table 1*). The introduction of a difluorinated linker in compound **7c**, while not influencing inhibitory activity on HDAC6, led to a complete loss of activity on HDAC1 at assessed concentrations **(**HDAC6 IC_{50} = 94.2 nM, not active on HDAC1, *Table 1*).

The observed *in vitro* potency and selectivity data, while confirming our initial design strategy, prompt further structure-activity relationship studies for this novel series of HDAC6 inhibitors.

Table 1. Structure and inhibitory activities of compounds **6a,b** and **7a-c**.



Cpd	R	Linker	IC_{50} HDAC6 (nM)	IC_{50} HDAC1 (nM)	SI
6a	Me		103.6	8108	78
6b	Me		66.8	14935	224
7a	Bn		134.8	9279	69
7b	Bn		48.5	39133	568
7c	Bn		94.2	NA	ND
16a* [3]	-	-	13.3	832	63
17a* [3]	-	-	12.9	1370	106

SI = selectivity index; NA = not active; ND = not determined; *For structures see *Chapter 3*

Gratifyingly, compound **7b** was co-crystalized within *z*HDAC6 active site, unveiling key structural determinants (Figure 3, PDB not deposited yet) for this

novel class of compounds. The hydroxamate moiety of compound **7b** engages in bidentate coordination with the zinc ion, through the hydroxamate carbonyl and N–O$^-$ groups, which displace the zinc-bound water molecule from the active site. The hydroxamate carbonyl group forms low-barrier hydrogen bonds with Y745. H573 and H574 form hydrogen bonds with the hydroxamate N–O$^-$ and NH groups, respectively. The piperidine ring adopts a chair conformation, allowing π-π stacking interactions of the fluoroaromatic ring in the F583-F643 aromatic crevice (Figure 3). No other enzyme-inhibitor contacts are observed for the capping group, much of which is characterized by weak or missing electron density (Figure 2), suggestive of conformational flexibility and disorder.

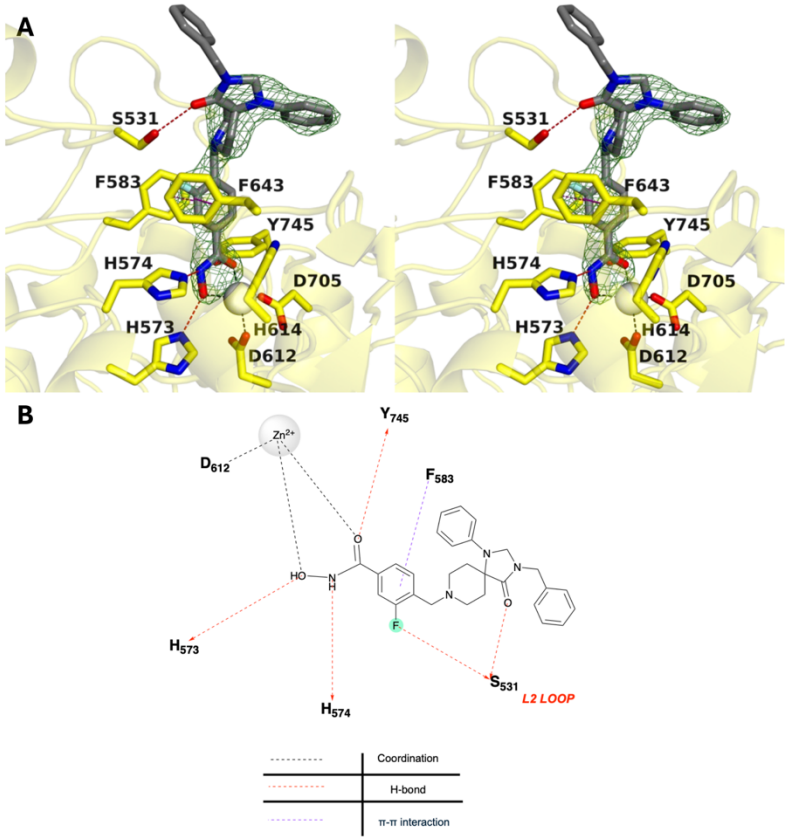


Figure 3. (A) Stereoscopic view of polder omit map contoured at 4σ showing the binding of **7b** in the active site of *z*HDAC6 CD2 (PDB non deposited yet). (B) Binding mode of **7b** within HDAC6 active site.

4.2 Conclusions

We performed a strategic linker overturning on 1,3,8-triazaspiro[4,5]decan-4-one core, previously identified by our research group as a suitable cap group for preferential interaction with HDAC6, thereby driving isoform selectivity. A small subset of inhibitors has been designed, bearing a methyl or benzyl substitution on imidazolidone nitrogen, while the linker-ZBG portion has been introduced on the nitrogen of the piperidine ring. All compounds have been assessed on both HDAC6 and HDAC1, showing nM potency towards HDAC6, thus confirming the suitability of this approach for HDAC inhibition. While compounds **6a** and **7a**, bearing a simple phenyl linker were also able to inhibit HDAC1 in nM range, the introduction of a *m*-fluorine or difluorine substitution resulted in a high drop in HDAC1 inhibition, thereby enhancing HDAC6 isoform selectivity. Furthermore, compound **7b** was co-crystalized within zHDAC6, revealing the m-fluorine atom in the linker portion is involved in hydrogen bond interaction with the key residue S531 in L2 loop – which is instead replaced to an aspartate in other HDAC isoforms - probably responsible for the high selectivity profile observed for this compound toward nuclear HDAC1. Starting from this data, further structure-activity relationship studies will be engaged in order to assess the effect of diverse structural modifications on the activity and selectivity profiles for this novel class of HDAC6 inhibitors.

4.3 Experimental section

4.3.1 Chemistry

General procedure for the synthesis of hydroxamic acids. To a stirring solution of the corresponding methyl ester in a mixture of DCM/MeOH (1:1), 50% aqueous hydroxylamine (100 eq) was added followed by methanolic 4 M

potassium hydroxide (50 eq). After 1 h, the reaction mixture was quenched by the addition of 6 N HCl and concentrated under vacuum. Crude material was purified by silica gel column chromatography (DCM/MeOH/NH_4OH 20:1:0.05 v/v to 20:1:1 v/v) giving desired hydroxamic acids **6a,b** and **7a-c**.

***tert*-butyl 3-methyl-4-oxo-1-phenyl-1,3,8-triazaspiro[4.5]decane-8-carboxylate (2).** To a solution of **1** (0.650 mmol, 216 mg) in dry THF (8mL) NaH (60% mineral oil dispersion, 0.716 mmol, 28.6 mg) was added. After 15 minutes, iodomethane (0.729 mmol, 45μL) was added and the reaction mixture was allowed to stir for 12 h at 25 °C. After completion, the solvent was removed under reduced pressure and the residue was washed with a saturated aqueous $NaHCO_3$ solution (5 mL) and extracted with DCM (3 x 5 mL). The combined organic layers were dried over Na_2SO_4, filtered and concentrated under reduced pressure. The reaction crude was purified by silica gel liquid chromatography (DCM/acetone 80:20 v/v), giving the desired product **2** with 76% yield (166mg). ^1H NMR (400 MHz, CDCl3) δ 7.25-7.21 (m, 2H), 6.84 (t, J = 7.3 Hz, 1H), 6.79-6.69 (m, 2H),4.68 (s, 2H), 4.13-3.92 (m, 2H), 3.69-3.30 (m, 2H), 3.01 (s, 3H), 1.51 (s, 9H), 1.31-1.13 (m, 2H).

***tert*-butyl 3-benzyl-4-oxo-1-phenyl-1,3,8-triazaspiro[4.5]decane-8-carboxylate (3).** To a solution of **1** (0.650 mmol, 216 mg) in dry THF (8mL) NaH (60% mineral oil dispersion, 0.716 mmol, 28.6 mg) was added. After 15 minutes, benzyl bromide (1.51 mmol, 258 mg) was added, and the reaction mixture was allowed to stir for 12 h at 25 °C. After completion, the solvent was removed under reduced pressure and the residue was washed with a saturated aqueous $NaHCO_3$ solution (5 mL) and extracted with DCM (3 x 5 mL). The combined organic layers were dried over Na_2SO_4, filtered and concentrated under reduced pressure. The reaction crude was purified by silica gel liquid chromatography (EP/EtOAc 30:10 v/v), giving the desired product **3** with 62% yield (393 mg).

^{1}H NMR (400 MHz, CDCl3) δ 7.40-7.26 (m, 5H), 7.20 (d, 2H), 6.81 (t, *J* = 7.3, 1.1 Hz, 1H), 6.68 (d, 2H), 4.61 (s, 2H), 4.56 (s, 2H), 4.31-3.86 (m, 2H), 3.80-3.39 (m, 2H), 1.66 (d, *J* = 13.5 Hz, 2H), 1.52 (s, 9H).

methyl 4-((3-benzyl-4-oxo-1-phenyl-1,3,8-triazaspiro[4.5]decan-8-yl)methyl)benzoate (**4a**). *Step 1:* To a solution of intermediate **2** (0.479 mmol, 166 mg) in DCM (5 mL), 4 M HCl in dioxane was added (4.79 mmol, 1.2 mL) and the resulting solution allowed to stir at 25 °C. was added. After 1 h, the solvent was evaporated under reduced pressure and the residue washed with EtOAc (7 mL) and partitioned with a saturated aqueous $NaHCO_3$ solution (3x7 mL) and extracted with. The combined organic layers were dried over Na_2SO_4, filtered and concentrated under reduced pressure. Desired *3-methyl-1-phenyl-1,3,8-triazaspiro[4.5]decan-4-one* was obtained with quantitative yield and employed in the next reaction step without further purification. *Step 2:* To a solution of *3-methyl-1-phenyl-1,3,8-triazaspiro[4.5]decan-4-*one (0.245 mmol, 60 mg) and anhydrous K_2CO_3 (0.49 mmol, 67.7 mg) in dry DMF (2 mL), methyl-4-(bromomethyl)-benzoate (0.245 mmol, 56 mg) was added and the reaction mixture was allowed under stirring for 18 h at 80 °C. After completion, reaction was quenched by adding distilled H_2O (10 mL) and extracted with EtOAc (10 mL). Organic layer was collected, then washed with distilled H_2O (3x 5mL) and brine (3x 5 mL). Organic layer was collected, dried over Na_2SO_4, filtered and concentrated under reduced pressure. The reaction crude was purified by silica gel liquid chromatography (DCM/MeOH 99:1 v/v), giving the desired product **4a** with 91% yield (140 mg).

^{1}H NMR (400 MHz, CDCl3) δ 7.93 (d, J = 8.3 Hz, 1H), 7.39 (d, J = 8.3 Hz, 1H), 7.28 – 7.18 (m, 2H), 6.89 – 6.77 (m, 2H), 4.59 (s, 1H), 3.84 (s, 2H), 3.57 (s, 1H), 2.92 (s, 2H), 2.82 – 2.57(m, 2H), 1.60 – 1.50 (m, 2H).

methyl 3-fluoro-4-((3-methyl-4-oxo-1-phenyl-1,3,8-triazaspiro[4.5]decan-8-yl)methyl)benzoate (**4b**). To a solution of compound *3-methyl-1-phenyl-1,3,8-*

triazaspiro[4.5]decan-4-one (0.245 mmol, 60 mg) and anhydrous K_2CO_3 (0.49 mmol, 68 mg) in dry DMF (2 mL), methyl-4-(bromomethyl)-3-fluorobenzoate (0.245 mmol, 61 mg) was added and the reaction mixture allowed under stirring for 18 h at 80 °C. After completion, reaction was quenched by adding distilled H_2O (10 mL) and extracted with EtOAc (10 mL). Organic layer was collected, then washed with distilled H_2O (3x 5mL) and brine (3x 5 mL). Organic layer was collected, dried over Na_2SO_4, filtered and concentrated under reduced pressure. The reaction crude was purified by liquid chromatography (DCM/MeOH 99:1 v/v), giving the desired product **4b** with 31% yield (31mg).

^{1}H NMR (400 MHz, CDCl3) δ 7.74 (d, *J* = 7.9 Hz, 1H), 7.61 (d, *J* = 10.3 Hz, 1H), 7.49 (t, *J* =7.6 Hz, 1H), 7.26 – 7.17 (m, 2H), 6.86 – 6.75 (m, 3H), 4.58 (s, 2H), 3.84 (s, 3H), 3.64 (s, 2H),2.90 (s, 3H), 2.88 – 2.57 (m, 6H), 1.58 (d, *J* = 14.0 Hz, 2H).

methyl 4-((3-benzyl-4-oxo-1-phenyl-1,3,8-triazaspiro[4.5]decan-8-yl)methyl)benzoate (5a). *Step 1:* To a solution of intermediate **3** (0.245 mmol, 100 mg) in DCM (3 mL), 4 M HCl in dioxane was added (2.45 mmol, 0.600 mL) and the resulting solution allowed to stir at 25 °C. After 1 h, the solvent was evaporated under reduced pressure and the residue washed with EtOAc (5 mL) and partitioned with a saturated aqueous $NaHCO_3$ solution (3x5 mL). The combined organic layers were dried over Na_2SO_4, filtered and concentrated under reduced pressure. Desired *3-benzyl-1-phenyl-1,3,8-triazaspiro[4.5]decan-4-one* was obtained with quantitative yield and employed in the next reaction step without further purification. *Step 2*: To a solution of *3-benzyl-1-phenyl-1,3,8-triazaspiro[4.5]decan-4-one* (0.245 mmol, 79 mg) in MeOH (8 mL), a catalytic amount of AcOH was added at 25 °C, followed by 4-methyl-4formyl benzoate (0.490 mmol, 81 mg). After 1 h, $NaBH_3CN$ (0.392 mmol, 25 mg) was added and the resulting mixture allowed under stirring at 25 °C for 18 h. After completion, the reaction was quenched by adding distilled H_2O (5 mL) and extracted with

EtOAc (3x5 mL). Organic layer was collected, dried over Na_2SO_4, filtered and concentrated under reduced pressure. The crude residue was purified by silica gel column chromatography (PE/EtOAc 50:10 v/v) affording desired product **5a** with 33% yield (37 mg).

^{1}H NMR (400 MHz, CDCl3) δ 8.01 (d, *J* = 8.0 Hz, 2H), 7,47 (d, *J* = 8.0 Hz, 2H), 7.39-7.27 (m, 7H), 6.89-6.80 (m, 4H), 4.60 (s, 2H), 3,91 (s, 3H), 3.66 (s, 2H), 2.94 (td, 2H), 2.84-2.76 (m, 2H), 2.71 (td, *J* = 13.1, 5.2 Hz, 2H), 1.69 (d, *J* = 13.6 Hz, 2H).

methyl 4-((3-benzyl-4-oxo-1-phenyl-1,3,8-triazaspiro[4.5]decan-8-yl)methyl)-3-fluorobenzoate (5b). To a solution of compound *3-benzyl-1-phenyl-1,3,8-triazaspiro[4.5]decan-4-one* (0.320 mmol, 120 mg) and anhydrous K_2CO_3 (0.640 mmol, 88 mg) in dry DMF (2 mL), methyl-4-(bromomethyl)-3-fluorobenzoate (0.320 mmol, 79 mg) was added and the reaction mixture allowed allowed under stirring for 18 h at 80 °C. After completion, reaction was quenched by adding distilled H_2O (10 mL) and extracted with EtOAc (10 mL). Organic layer was collected, then washed with distilled H_2O (3x 5mL) and brine (3x 5 mL). Organic layer was collected, dried over Na_2SO_4, filtered and concentrated under reduced pressure. The reaction crude was purified by liquid chromatography (DCM/MeOH 99:1 v/v) affording desired compound **5b** with 90% yield (140 mg).

^{1}H NMR (400 MHz, CDCl3) δ 7.83 (d, *J* = 7.8 Hz, 1H), 7.70 (d, *J* = 10.3 Hz, 1H), 7.58 (t, *J* = 8.2 Hz, 1H), 7.37-7.27 (m, 7H), 6.85 (d, *J* = 8.3 Hz, 3H), 4.59 (s, 2H), 4.54 (d, J = 3.3 Hz, 2H), 3.92 (d, J= 3.4 Hz, 3H), 3.73 (s, 2H), 3.04-2.63 (m, 6H), 1.70 ((d, *J* = 13.6 Hz, 2H).

methyl 4-((3-benzyl-4-oxo-1-phenyl-1,3,8-triazaspiro[4.5]decan-8-yl)methyl)-3,5-difluorobenzoate (5c). To a solution of compound *3-benzyl-1-phenyl-1,3,8-triazaspiro[4.5]decan-4-one* (0.345 mmol, 111 mg) and anhydrous K_2CO_3 (0.690 mmol, 66 mg) in dry DMF (2 mL), methyl 4-(bromomethyl)-3,5-

difluorobenzoate (0.345 mmol, 92 mg) was added and the reaction mixture allowed allowed under stirring for 18 h at 80 °C. After completion, reaction was quenched by adding distilled H_2O (10 mL) and extracted with EtOAc (10 mL). Organic layer was collected, then washed with distilled H_2O (3x 5mL) and brine (3x 5 mL). Organic layer was collected, dried over Na_2SO_4, filtered and concentrated under reduced pressure. The reaction crude was purified by liquid chromatography (DCM/MeOH 99:1 v/v) affording desired compound **5c** with 38% yield (66 mg).

^{1}H NMR (700 MHz, $CDCl_3$) δ 7.58 – 7.54 (m, 2H), 7.36 – 7.32 (m, 2H), 7.31 – 7.28 (m, 2H), 7.26 – 7.20 (m, 4H), 6.83 – 6.78 (m, 3H), 4.56 (d, *J* = 3.7 Hz, 2H), 4.52 (d, *J* = 3.7 Hz, 2H), 3.83 (s, 2H), 3.01 (ddqd, *J* = 939.6, 23.3, 11.9, 3.3 Hz, 2H), 2.87 – 2.83 (m, 2H), 2.70 – 2.63 (m, 2H), 1.67 (d, *J* = 13.8 Hz, 2H).

N-hydroxy-4-((3-methyl-4-oxo-1-phenyl-1,3,8-triazaspiro[4.5]decan-8-yl)methyl)benzamide (6a). Compound **6a** was prepared starting from intermediate **4a** (0.080 mmol, 32 mg) following the general procedure for the preparation of hydroxamic acids with 90% yield (29 mg).

MS (ESI) m/z calc. $[M+H]^+$ for $C_{22}H_{27}N_4O_3^+$: 395.21; found: 395.4

^{1}H NMR (400 MHz, DMSO) δ 11.10 (bs, 1H), 8.99 (bs, 1H), 7.72 (d, *J* = 8.0 Hz, 2H), 7.42 (d, *J* = 8.1 Hz, 2H), 7.28 (t, *J* = 8.2 Hz, 2H), 6.88 (d, *J* = 8.2 Hz, 2H), 6.79 (t, *J* = 7.3 Hz, 1H), 4.63 (s, 2H), 3.57 (s, 2H), 2.86 (d, *J* = 527.6 Hz, 3H), 2.79 – 2.65 (m, 4H), 1.56 (d, *J* = 13.3 Hz, 2H).

^{13}C NMR (176 MHz, DMSO) δ 129.16, 128.56, 126.84, 117.85, 114.33, 64.31, 61.68, 59.17, 54.93, 49.15, 40.08, 39.88, 28.63.

3-fluoro-*N*-hydroxy-4-((3-methyl-4-oxo-1-phenyl-1,3,8-triazaspiro[4.5]decan-8-yl)methyl)benzamide (6b). Compound **6b** was prepared starting from intermediate **4b** (0.076 mmol, 31 mg) following the general procedure for the preparation of hydroxamic acids with with with 64% yield (20 mg).

MS (ESI) m/z calc. $[M+H]^+$ for $C_{22}H_{26}FN_4O_3^+$: 413.20; found: 413.2

^{1}H NMR (400 MHz, DMSO) δ 11.23 (bs, 1H), 9.14 (bs, 1H), 7.63 – 7.50 (m, 3H), 7.27 (t, *J* = 7.6 Hz, 2H), 6.87 (d, *J* = 7.9 Hz, 2H), 6.79 (t, *J* = 7.4 Hz, 1H), 4.64 (s, 2H), 3.64 (s, 2H), 2.87 (s, 3H), 2.84 – 2.70 (m, 4H), 1.57 (d, *J* = 13.6 Hz, 2H).

^{13}C NMR (176 MHz, DMSO) δ 173.32, 162.92, 159.78, 143.07, 131.58, 129.26, 122.84, 118.02, 114.51, 64.43, 59.21, 54.48, 49.08, 28.74, 27.17.

4-((3-benzyl-4-oxo-1-phenyl-1,3,8-triazaspiro[4.5]decan-8-yl)methyl)-*N*-hydroxybenzamide (7a). Compound **7a** was prepared starting from intermediate **5a** (0.080 mmol, 37 mg) following the general procedure for the preparation of hydroxamic acids with 66% yield (25mg).

MS (ESI) *m/z* calc. $[M+H]^+$ for $C_{28}H_{31}N_4O_3^+$: 471.24; found: 471.3

^{1}H NMR (400 MHz, DMSO-*d6*) δ 11.20 (s, 2H), 10.23 (s, 1H), 9.06 (s, 2H), 7.79 (d, *J* = 8.3 Hz, 2H), 7.52 – 7.42 (m, 3H), 7.35 (dd, *J* = 8.9, 2.4 Hz, 3H), 6.92 (d, *J* = 8.0 Hz, 2H), 6.85 (t, *J* = 7.3 Hz, 1H), 4.62 (d, *J* = 12.6 Hz, 4H), 3.66 (s, 2H), 2.90 – 2.78 (m, 2H), 1.81 (d, *J* = 13.6 Hz, 7H).

^{13}C NMR (176 MHz, DMSO-*d6*) δ 206.9, 143.2, 136.6, 129.5, 129.2, 129.0, 127.8, 127.2, 118.5, 115.0, 62.9, 62.1, 59.9, 49.5, 44.0, 29.1.

4-((3-benzyl-4-oxo-1-phenyl-1,3,8-triazaspiro[4.5]decan-8-yl)methyl)-3-fluoro-*N*-hydroxybenzamide (7b). Compound **7b** was prepared starting from intermediate **5b** (0.144 mmol, 70 mg) following the general procedure for the preparation of hydroxamic acids with 55% (39 mg).

MS (ESI) *m/z* calc. $[M+H]^+$ for $C_{28}H_{30}FN_4O_3^+$: 489.23; found: 489.3

^{1}H NMR (700 MHz, DMSO-*d6*) δ 11.27 (s, 1H), 7.65-7.51 (m, 4H), 7.38 (t, *J* = 7.6 Hz, 3H), 7.33-7.28 (m, 5H), 7.26-7.23 (m, 3H), 6.86-6.77 (m, 5H), 4.57 (s, 3H), 4.54 (s, 3H), 3.66 (s, 3H), 2.87-2.74 (m, 5H), 2.62-2.53 (m, 4H), 1.62 (d, *J* = 13.8 Hz, 4H).

^{13}C NMR (176 MHz, DMSO- *d6*) δ 173.0, 160.7, 159.3, 142.5, 135.9, 131.2, 128.8, 128.4, 127.1, 122.4, 117.8, 114.3, 62.2, 59.0, 54.0, 48.6, 43.3, 28.4.

4-((3-benzyl-4-oxo-1-phenyl-1,3,8-triazaspiro[4.5]decan-8-yl)methyl)-3,5-difluoro-*N*-hydroxybenzamide (7c). Compound **7c** was prepared starting from intermediate **5c** (0.130 mmol, 66 mg) following the general procedure for the preparation of hydroxamic acids with 35% (23 mg).

MS (ESI) *m/z* calc. $[M+H]^+$ for $C_{28}H_{29}F_2N_4O_3^+$: 507.56; found: 507.2

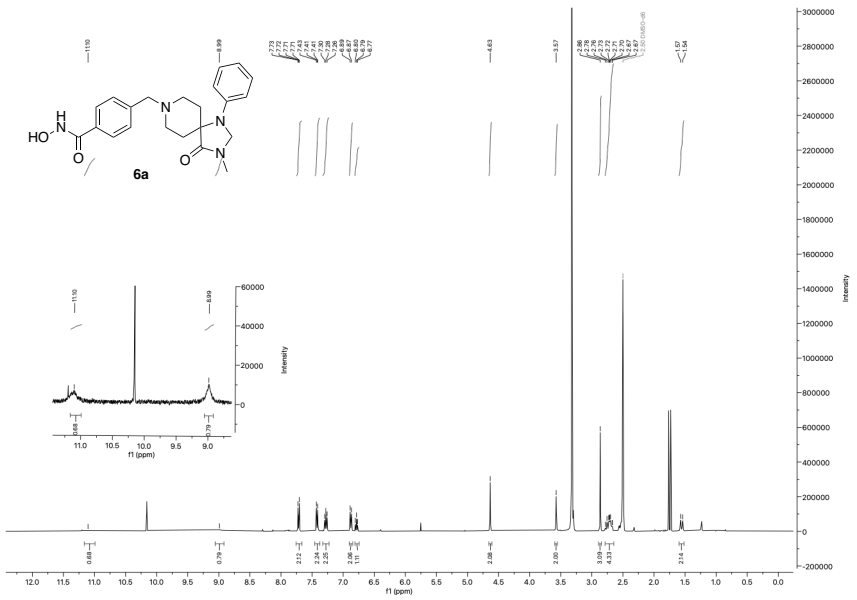
^{1}H NMR (400 MHz, DMSO) δ 7.47 (d, *J* = 8.0 Hz, 2H), 7.40 – 7.34 (m, 2H), 7.32 – 7.25 (m, 3H), 7.25 – 7.19 (m, 2H), 6.82 – 6.73 (m, 3H), 4.55 (s, 2H), 4.51 (s, 2H), 3.71 (s, 2H), 2.89 – 2.80 (m, 2H), 2.80 – 2.71 (m, 2H), 2.56 – 2.52 (m, 1H), 2.49 – 2.46 (m, 1H), 1.60 (d, *J* = 13.5 Hz, 2H).

^{13}C NMR (176 MHz, DMSO) δ 173.29, 161.36 (d, *J* = 243.1 Hz), 161.36, 160.39 (d, *J* = 249.2 Hz), 142.80, 129.09, 128.76, 127.52, 127.46, 118.23, 114.71, 109.87 (d, *J* = 25.8 Hz), 62.78, 48.36, 43.60, 40.02, 28.72.

4.3.2 Supporting Figures

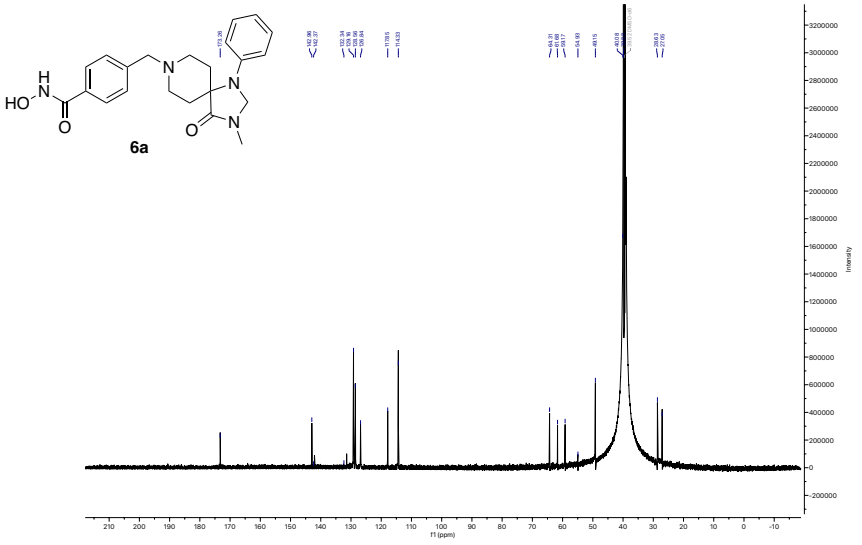
Supporting Figure 1

^{1}H NMR of 6a



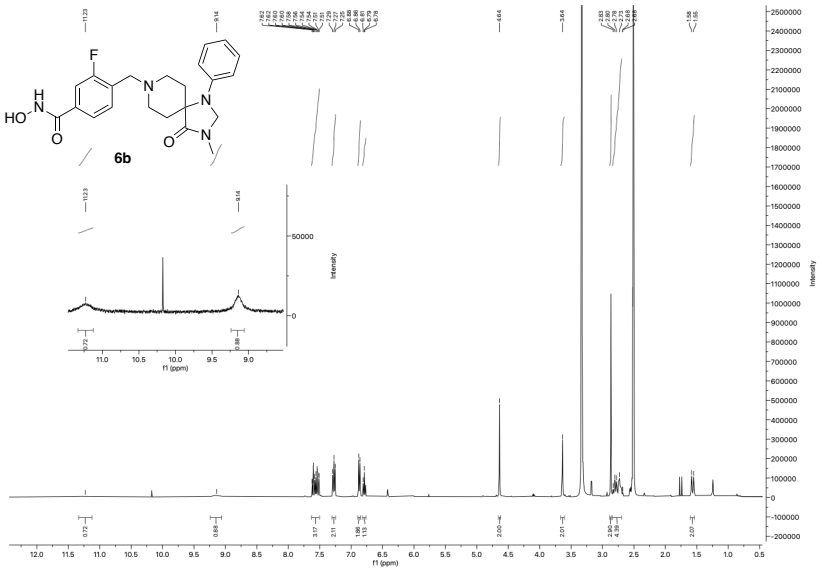
Supporting Figure 2

^{13}C NMR of 6a



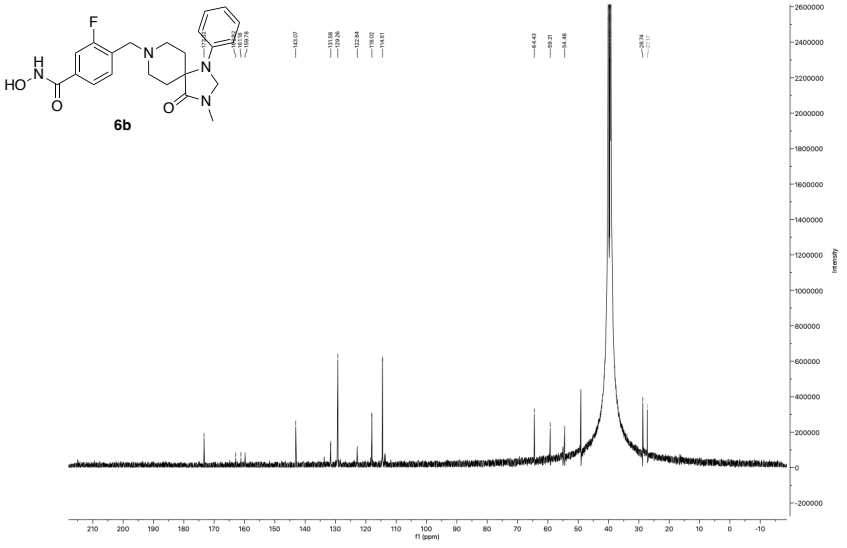
Supporting Figure 3

^{1}H NMR of 6b



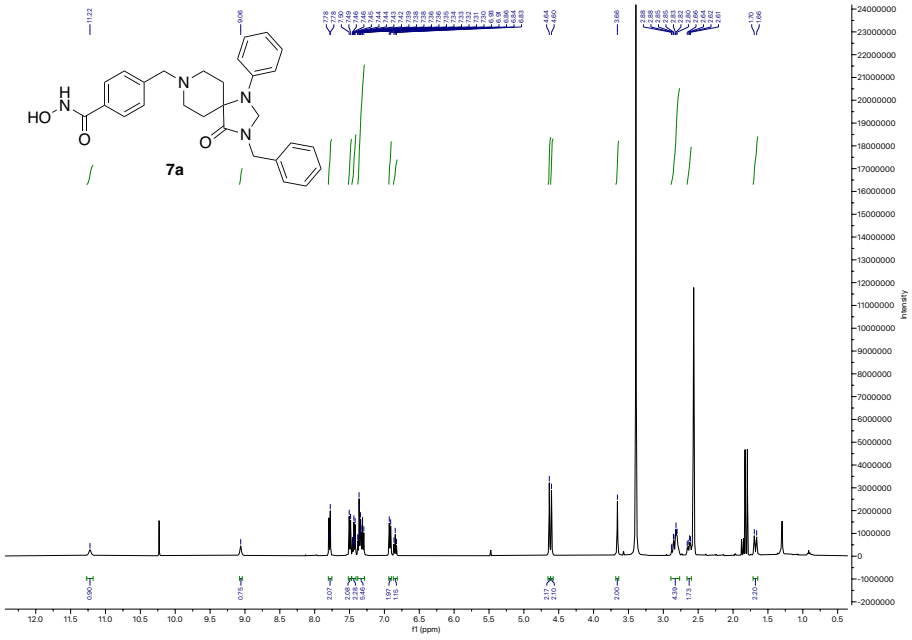
Supporting Figure 4

^{13}C NMR of 6b



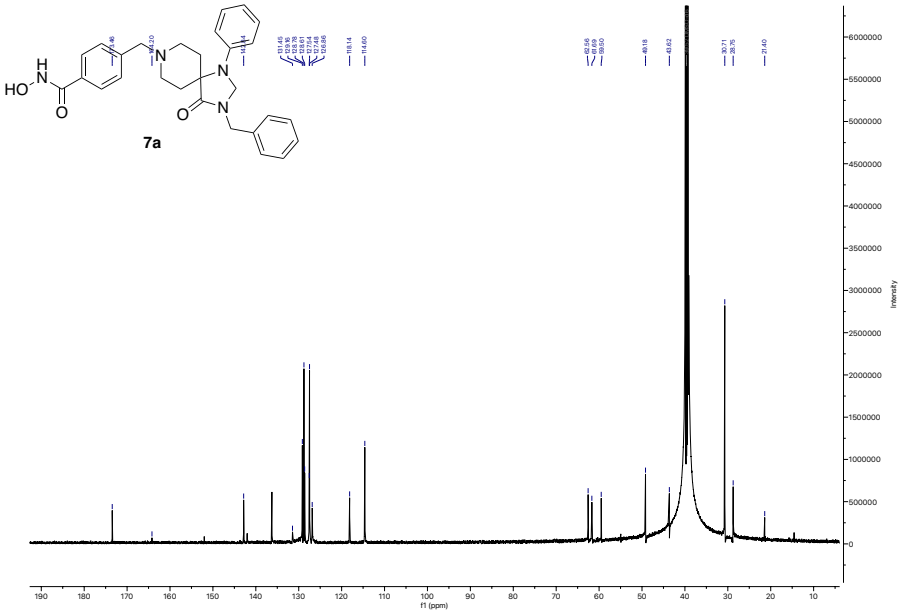
Supporting Figure 5

^{1}H NMR of 7a



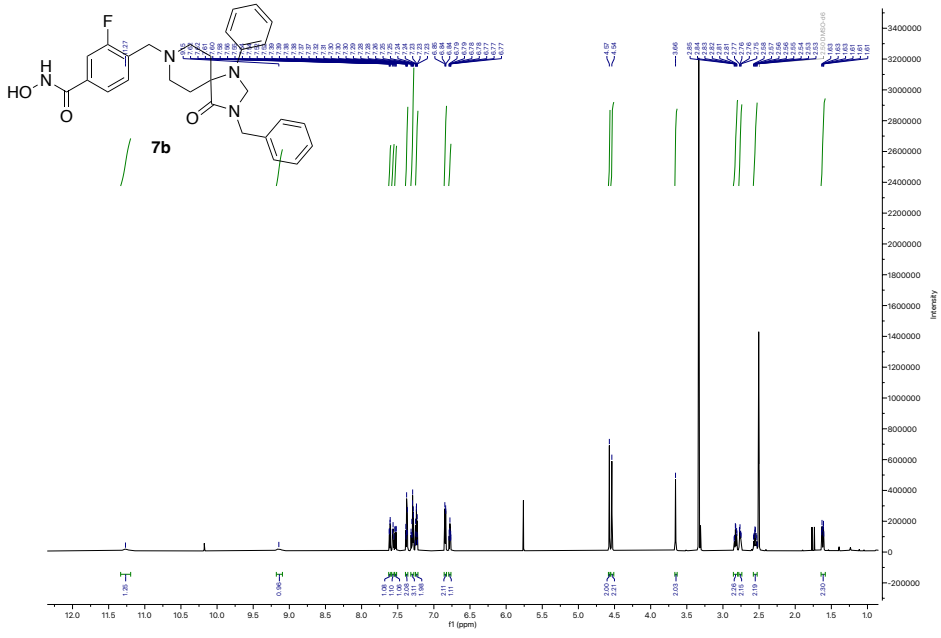
Supporting Figure 6

^{13}C NMR of 7a



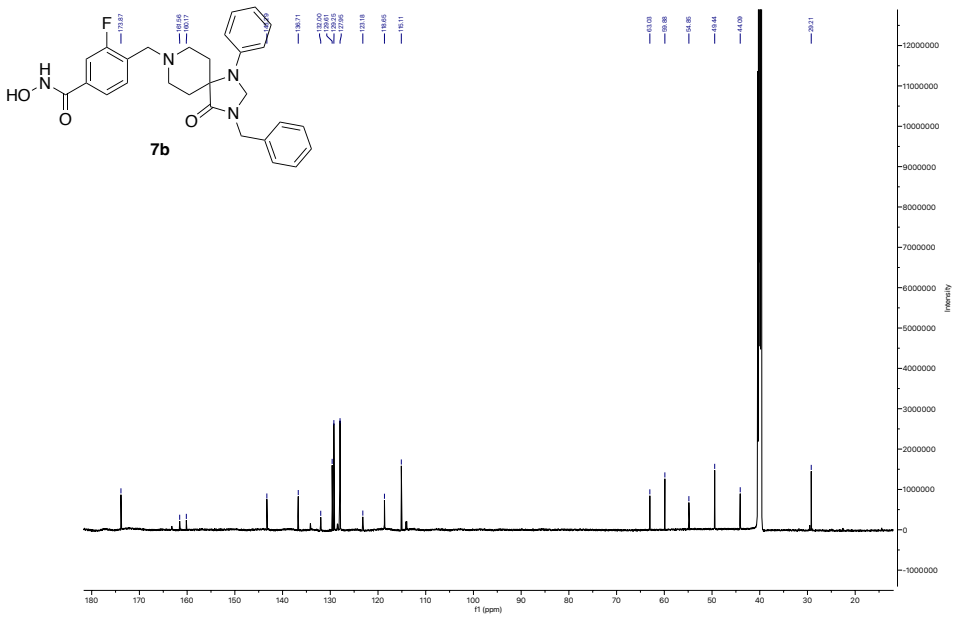
Supporting Figure 7

^{1}H NMR of 7b



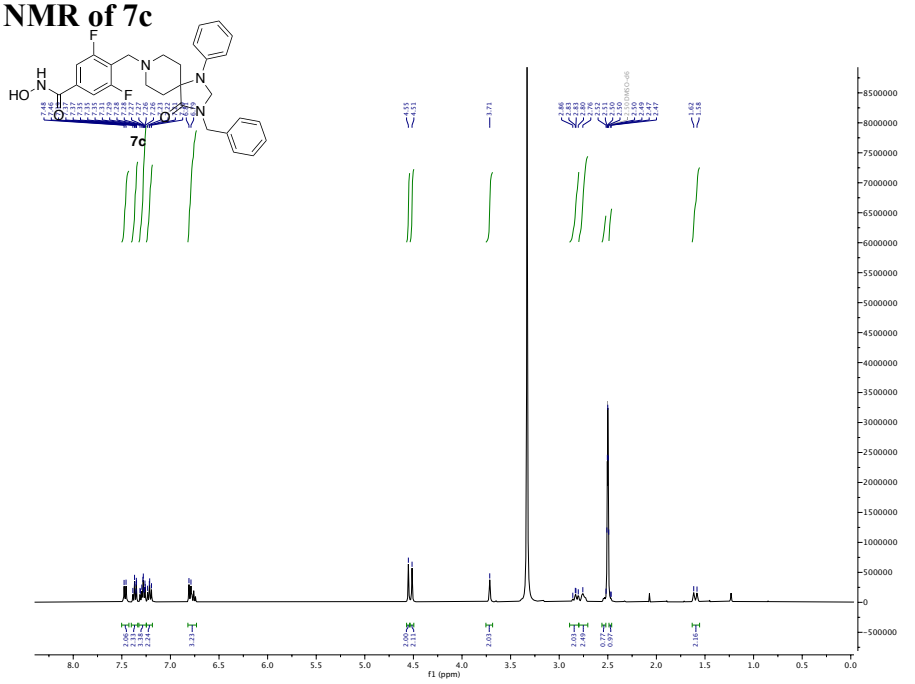
Supporting Figure 8

^{13}C NMR of 7b



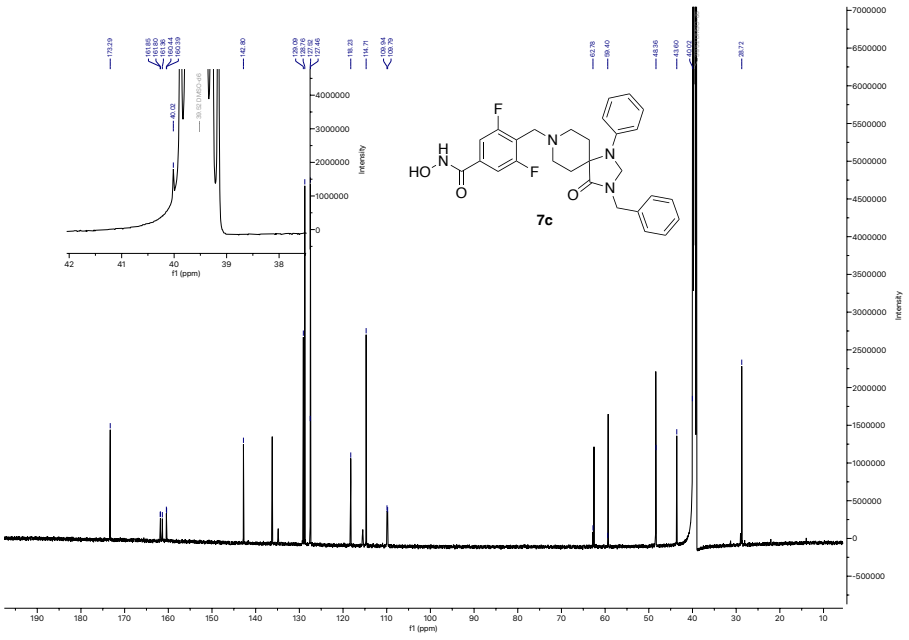
Supporting Figure 9

^{1}H NMR of 7c



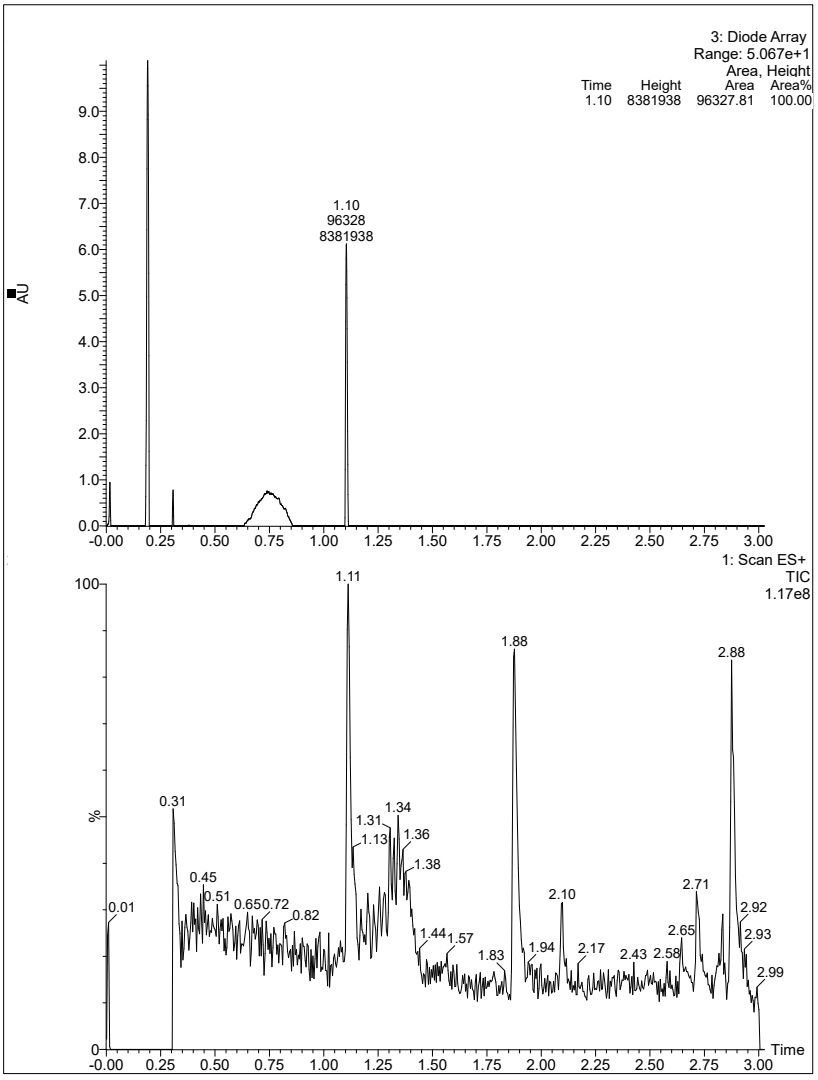
Supporting Figure 10

^{13}C NMR of 7c



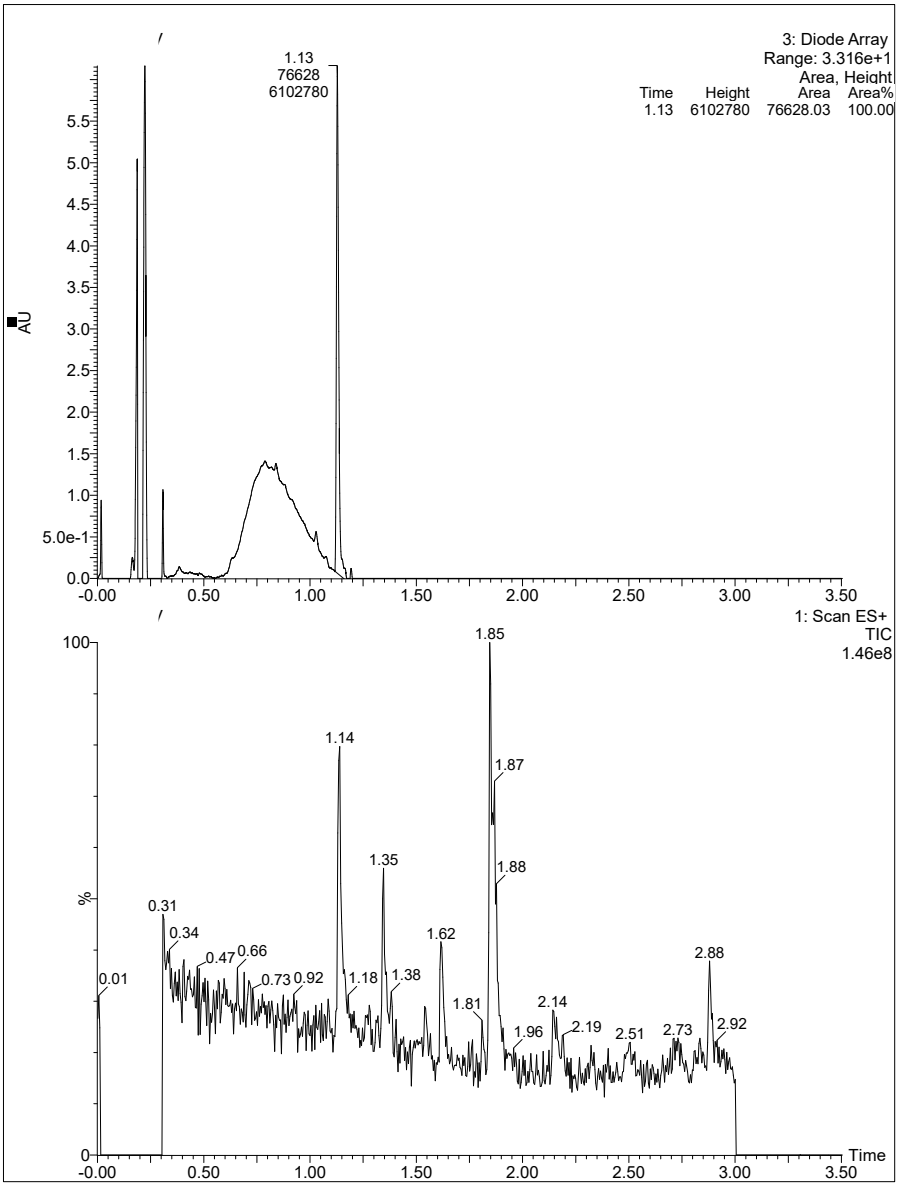
Supporting Figure 11

UPLC-MS spectrum of 6a



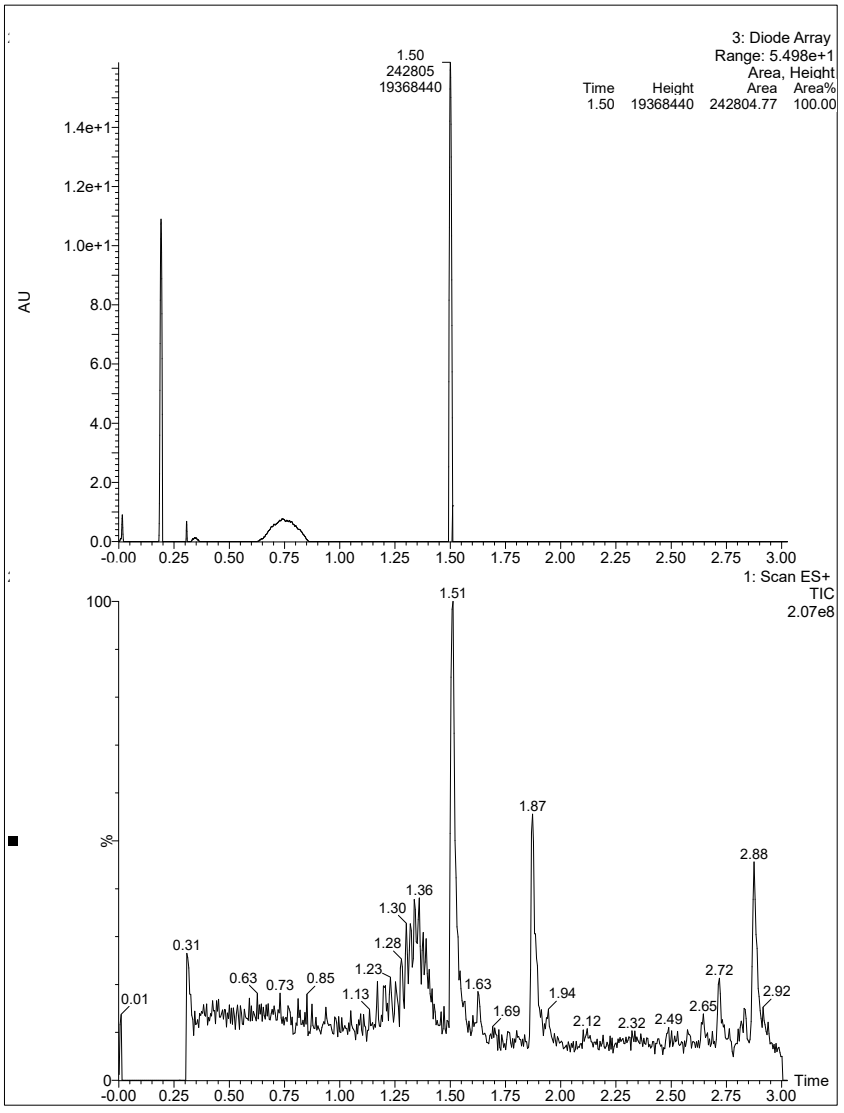
Supporting Figure 12

UPLC-MS spectrum of 6b



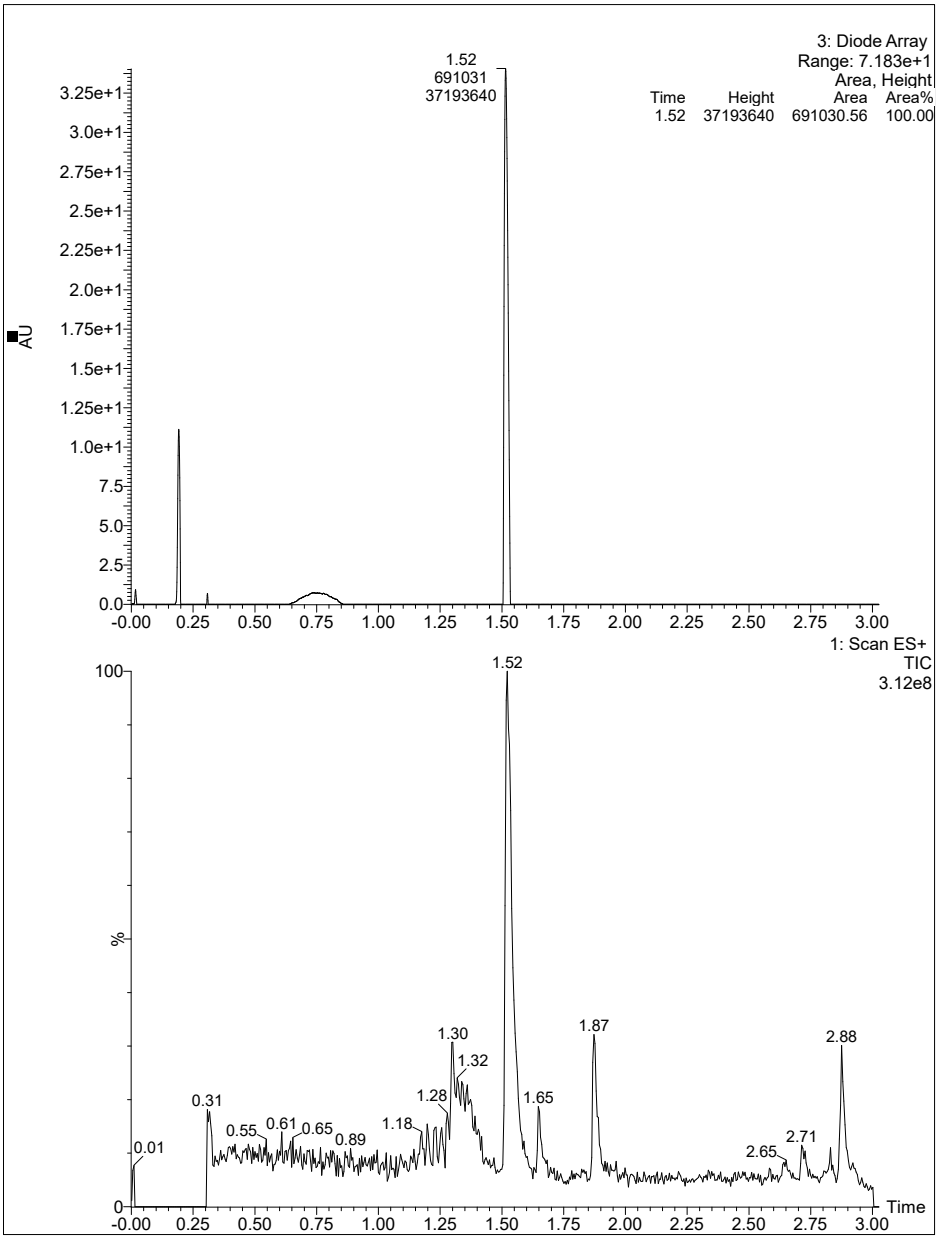
Supporting Figure 13

UPLC-MS spectrum of 7a


3: Diode Array
Range: 5.498e+1
Area, Height
Time Height Area Area%
1.50 19368440 242804.77 100.00
1.50
242805
19368440
AU
1.4e+1
1.2e+1
1.0e+1
8.0
6.0
4.0
2.0
0.0
-0.00 0.25 0.50 0.75 1.00 1.25 1.50 1.75 2.00 2.25 2.50 2.75 3.00
1: Scan ES+
TIC
2.07e8
100
%
0
1.51
1.87
2.88
1.36
1.30
1.28
0.31
1.23
0.63
0.73
0.85
1.13
1.63
1.94
0.01
1.69
2.12
2.32
2.49
2.65
2.72
2.92
Time

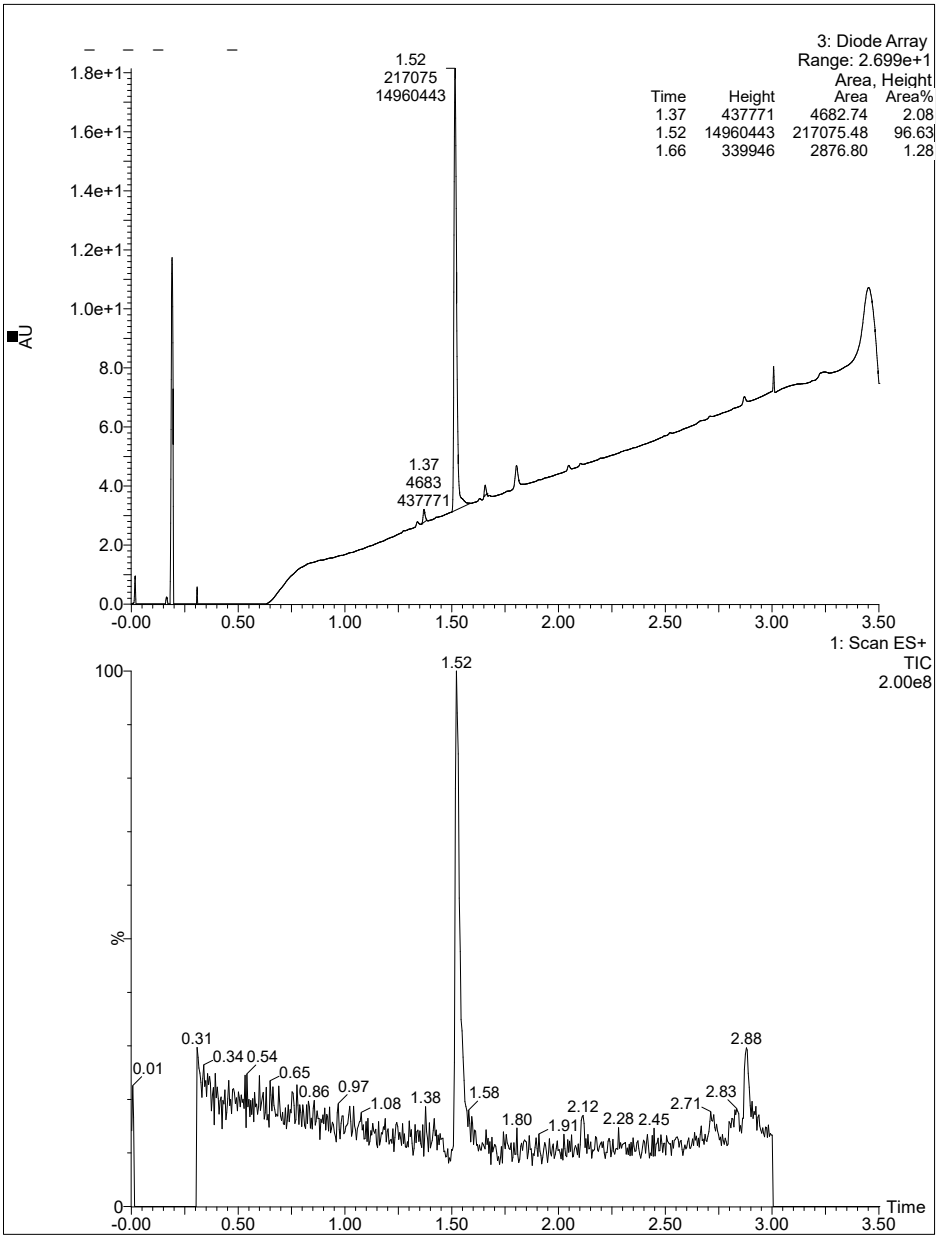
Supporting Figure 14

UPLC-MS spectrum of 7b



Supporting Figure 15

UPLC-MS spectrum of 7c



References

[1] Y. Hai, D.W. Christianson, Nat Chem Biol 12 (2016) 741–747.

[2] N.J. Porter, A. Mahendran, R. Breslow, D.W. Christianson, Proceedings of the National Academy of Sciences 114 (2017) 13459–13464.

[3] S. Barone, I. Bello, A. Guadagni, C. Cerchia, G. Filocamo, E. Cassese, A.I. Alfano, C. Esposito, Á.J. Feliz Morel, M. Brunetti, A. Lavecchia, V. Summa, E. Panza, M. Brindisi, Eur J Med Chem 292 (2025) 117634.

[4] K. V. Butler, J. Kalin, C. Brochier, G. Vistoli, B. Langley, A.P. Kozikowski, J Am Chem Soc 132 (2010) 10842–10846.

[5] N.J. Porter, J.D. Osko, D. Diedrich, T. Kurz, J.M. Hooker, F.K. Hansen, D.W. Christianson, J Med Chem 61 (2018) 8054–8060.

[6] N.J. Porter, D.W. Christianson, Curr Opin Struct Biol 59 (2019) 9–18.

[7] T.A. Halgren, R.B. Murphy, R.A. Friesner, H.S. Beard, L.L. Frye, W.T. Pollard, J.L. Banks, J Med Chem 47 (2004) 1750–1759.

[8] R.A. Friesner, J.L. Banks, R.B. Murphy, T.A. Halgren, J.J. Klicic, D.T. Mainz, M.P. Repasky, E.H. Knoll, M. Shelley, J.K. Perry, D.E. Shaw, P. Francis, P.S. Shenkin, J Med Chem 47 (2004) 1739–1749.

Chapter 6

Isoform-Selective HDAC6 Inhibition via Spirocyclic Capping and Heterocyclic Zinc-Binding Group Modulation (Finn K. Hansen Research Group)

As discussed in *Chapter 1*, the structural architecture of HDACis is tipically defined by a cap group, a linker and a ZBG moieites, whereas fine-tuning all these structural moieties is essential to achieve isoform selectivity. While bulky cap groups are required to avoid off target interaction with nuclear HDACs, as well as aromatic linkers are preferred to establish hydrophobic interactions within HDAC6 catalytic crevice, the choice of the ZBG is crucial in order to both influence the strength and geometry of interaction with the catalytic Zn^{2+}.

Furthermore, the nature of the ZBG has also been demonstrated to strongly influence isoform selectivity and pharmacokinetic profiles of designed Over years, the quest for alternative and safer ZBGs led to the identification of novel structural templates able to interact with catalytic zinc ions while driving potency and selectivity of the designed inhibitors. Accordingly, benzamide-based ZBG have been found to display inhibition preference for Class I HDACs [1], while DFMOs have recently emerged as high selective, irreversible and mechanism-based HDAC6is [2]. Also, structural optimization of TFMOs through variations on the cap group moiety may be useful in the modulation of isoform selectivity [3].

During the second year of my PhD, I had the opportunity to spend six months in Finn K. Hansen research group (Bonn University), pioneering the development of HDAC6is incorporating DFMOs as ZBGs [4,5]. During this time, we sought to explore the effect on HDAC6 inhibition of the combination of spirofused cap groups with non-hydroxamic ZBGs, namely DFMOs and TFMOs. This structural exploration not only provided clear hints for further design, but also allowed to clarify the importance of ZBG in driving the biological activity of the compounds. Also, kinetics and target engagements studies allowed to further depict a clear-cut profile for the newly disclosed series of compounds, thus paving the way to the development of HDAC6is endowed with tuneable potency, selectivity and biological activity profiles.

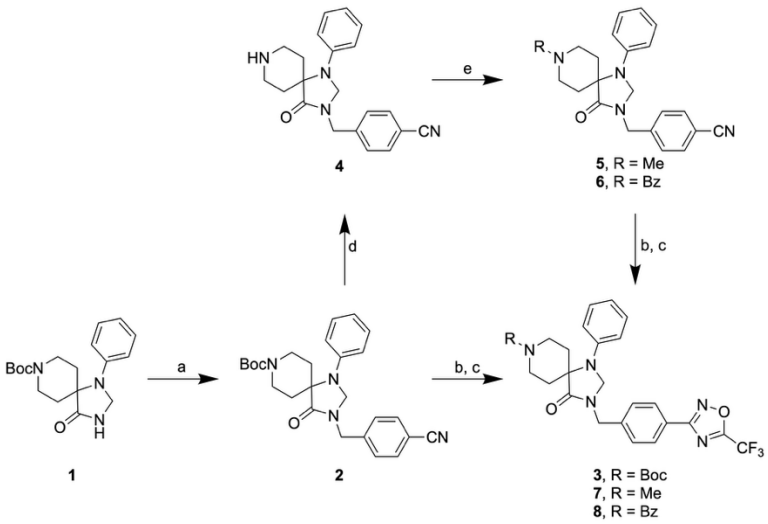
6.1 Results and discussion

6.1.1 Chemistry

Scheme 1 describes the alkylation of 1-phenyl-1,3,8-triazaspiro[4.5]decane-8-carboxylate (**1**) with 4-bromomethyl benzonitrile, in presence of NaH (60% oil dispersion) as base, to provide intermediate **3** (278 mg, 42% yield). Boc protecting group removal and subsequent reductive amination in presence of paraformaldehyde or benzaldehyde provided key synthetic intermediates **5** and

6, respectively, which were first quantitatively converted into the corresponding amidoximes, in presence of 50% aqueous hydrazine, and then subjected to a dehydration-cyclization reaction in presence of trifluoroacetic anhydride (TFAA) to provide the corresponding TFMOs **7** and **8** with 25% and 13% yields, respectively. For the synthesis of *tert*-butoxycarbonyl derivative **3**, intermediate **2** was directly converted into the corresponding amidoxime, then treated with TFAA in presence of DIPEA to provide compound **3** in 38% yield.

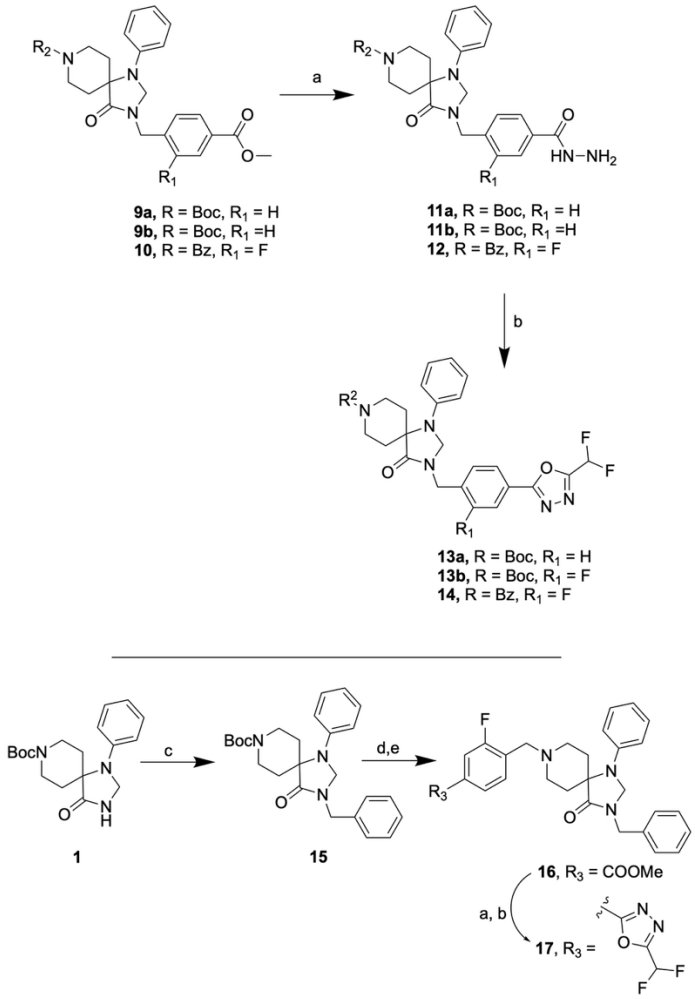
Scheme 1. Synthetic route for the synthesis of TFMO derivatives bearing the *tert*-butyl 4-oxo-1-phenyl-1,3,8-triazaspiro[4.5]decane-8-carboxylate cap-group **3**, **7** and **8**.[a]



[a]Reagents and conditions: (a) 4-bromomethyl benzonitrile, NaH 60 % oil dispersion, dry THF, 12 h, 25 °C, 42%; (b) NH_2OH (50% solution in water) EtOH, 12 h, 80 °C, quant.; (c) TFAA, DIPEA, dry DCM, 0 °C to 25 °C, 12 h,13%-38%; (d) 4 N HCl in dioxane, DCM, 1 h, 25 °C, quant.; (e) paraformaldehyde or benzaldehyde, AcOH, 25 °C, 1 h, $NaBH_3CN$, 18 h, 25 °C, 68% and 77% respectively .

Scheme 2 describes the synthesis of DFMOs derivatives **13a,b**, **14** and **18**. Methyl esters **9a,b** and **10** [6] were treated with hydrazine monohydrate and converted into the corresponding hydrazides **11a,b** and **12**, subsequently subjected to dehydration-cyclization reaction to provide the corresponding DFMOs **13a,b** and **14** in the presence of difluoroacetic anhydride (DFAA) and Burgess reagent with 23%, 24% and 7% yield respectively. For the synthesis of DFMO **17**, the methyl ester **16** (synthesised as described in *Chapter 4, Paragraph 4.1.1*) was treated with hydrazine monohydrate as previously described and then converted into the corresponding DFMO derivative **17** with 20% yield.

Scheme 2. Synthetic route for the synthesis of DFMOs bearing the *tert*-butyl 4-oxo-1-phenyl-1,3,8-triazaspiro[4.5]decane-8-carboxylate cap-group **13a,b**, **14** and **17**.[a]



9a, R = Boc, R_1 = H
9b, R = Boc, R_1 =H
10, R = Bz, R_1 = F

11a, R = Boc, R_1 = H
11b, R = Boc, R_1 =H
12, R = Bz, R_1 = F

13a, R = Boc, R_1 = H
13b, R = Boc, R_1 = F
14, R = Bz, R_1 = F

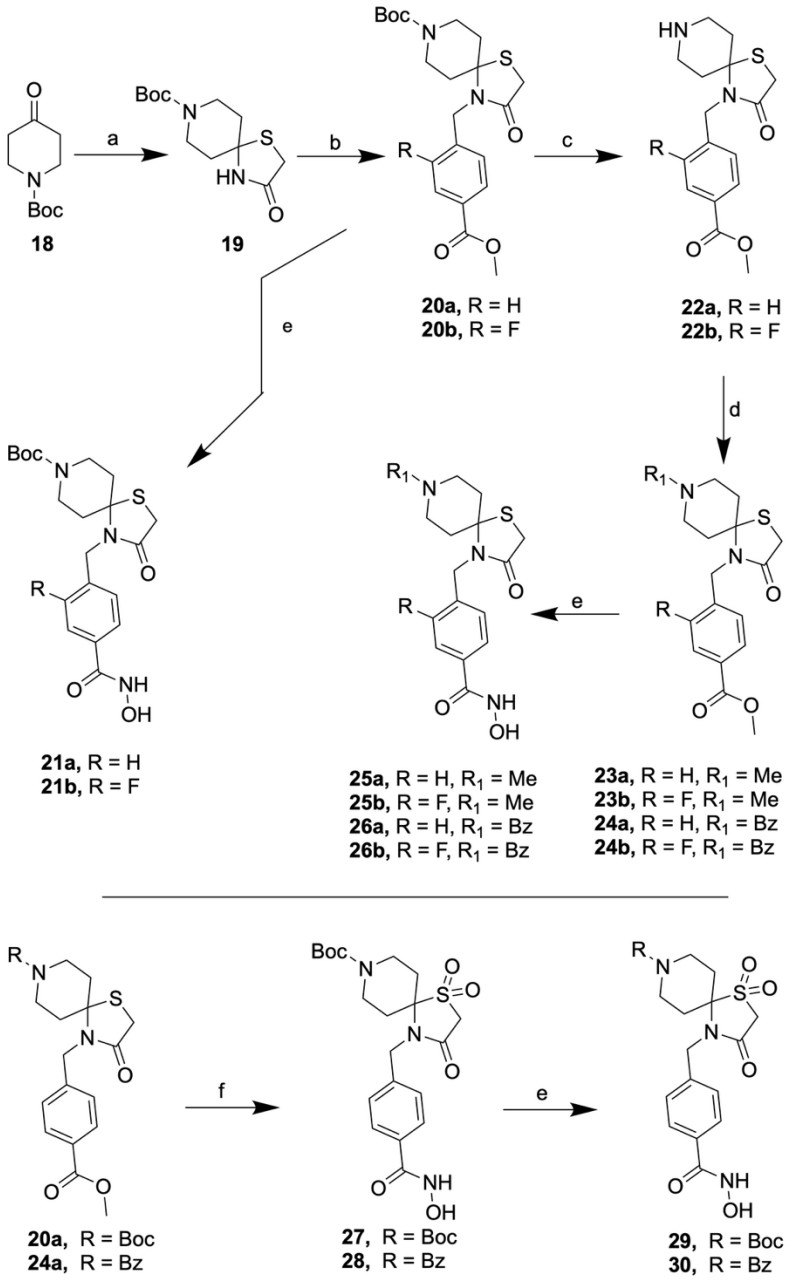
[a]Reagents and conditions: (a) $NH_2NH_2 \cdot H_2O$, EtOH, 12 h, 80 °C, quant. ; (b) (i) DFAA, TEA, dry DCM, 0 °C to 25 °C, 12 h, (ii) Burgess reagent, dry DCM, 12 h, 25 °C, 7-24%; (c) benzyl bromide, NaH 60% oil dispersion, dry THF, 12 h, 25 °C, 62%; (d) 4 N HCl in dioxane, DCM, 1 h, 25 °C, quant.; (e) methyl 4-(bromomethyl)-3-fluorobenzoate, anhydrous K_2CO_3, dry DMF, 12 h, 80 °C, 90%.

According to in Scheme 3, commercially available *N*-Boc-piperidone **18** was treated with 2-thioglycolic acid in presence of ammonium carbonate as nitrogen donor, to provide the key spirofused core **19**. The latter was then subjected to an alkylation reaction with methyl-4-bromomethyl-benzoate or methyl-4-

(bromomethyl)-3-fluorobenzoate, as previously described, to provide the corresponding methyl esters **20a,b** with 70% and 83% yields, respectively. The Boc protected intermediates **20a,b** were then converted into the corresponding hydroxamic acids **21a,b** upon treatment with 4 N methanolic KOH using DCM/MeOH (2:1) as solvent mixture. Boc protecting group removal in acidic conditions provided the corresponding free amines **22a,b** in quantitative yield. The latter amines were subjected to reductive amination with paraformaldehyde or benzaldehyde in presence of acetic acid as catalyst and sodium cyanoborohydride ($NaBH_3CN$) as reductant, then treated with 50% aqueous hydroxylamine and 4 M methanolic KOH to provide the final hydroxamic acid derivatives **25a,b** and **26a,b.**

Intermediates **20a** and **24a** were converted into the corresponding sulfone derivatives employing *m*-chloroperbenzoic acid as the oxidant in dry DCM. Corresponding sulfones **27** and **29** were converted into the corresponding hydroxamic acids **29** and **30** as previously described in 15% and 30% yields, respectively.

Scheme 3. Synthetic route for the synthesis of *tert-butyl 3-oxo-1-thia-4,8-diazaspiro[4.5]decane-8-carboxylate* cap-group **19** and final compounds **21a,b**, **25a,b**, **26a,b**, **29** and **30**.[a]



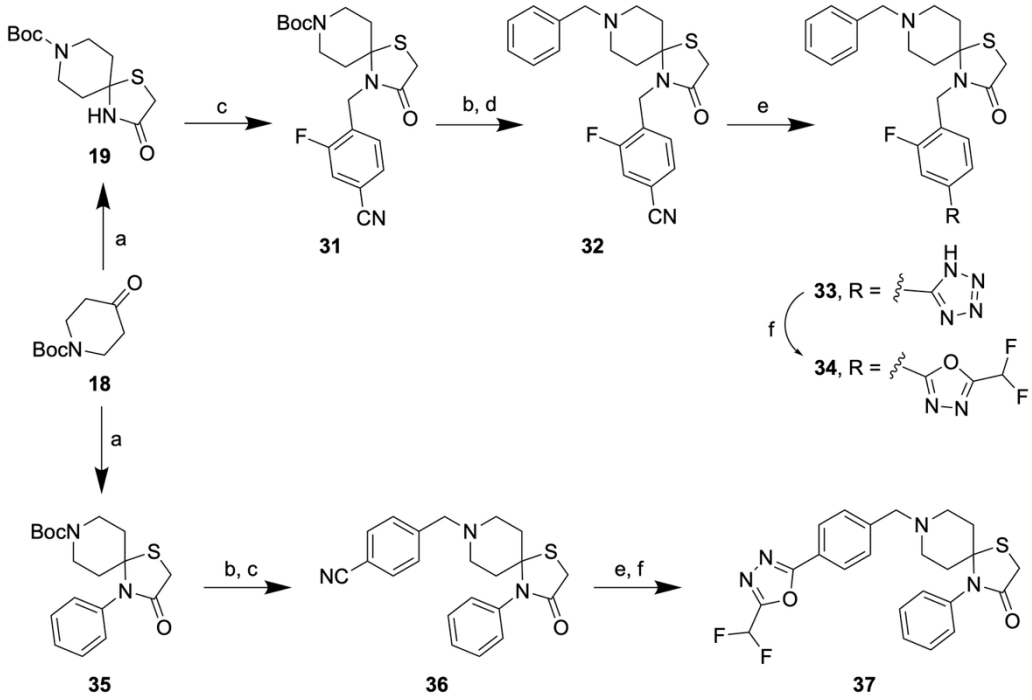
[a]Reagents and conditions: (a) $(NH_4)_2CO_3$, toluene, 18 h, 110 °C, 88%; (b) methyl 4-(bromomethyl)benzoate or methyl 4-(bromomethyl)-3-fluorobenzoate, NaH 60 % oil dispersion, dry THF, 12 h, 25 °C, 70% and 83% respectivelt; (c) 4 N HCl in dioxane, DCM, 1 h, 25 °C, quant.; (d) paraformaldehyde or benzaldehyde,

AcOH, 25 °C, 1 h, $NaBH_3CN$, 18 h, 25 °C, 50-85%; (e) 50% aq. NH_2OH, 4 M KOH in MeOH, DCM/MeOH (2:1), 1 h, 25 °C, 15-73%; (f) *m*CPBA, dry DCM, 2 h, 25 °C, 15-81% .

The synthesis of DFMOs **34** and **37** is described in Scheme 4. The spiro core **19** was first subjected to an alkylation reaction with 4-(bromomethyl)-3-fluorobenzonitrile using sodium hydride as base, in anhydrous THF at 25 °C, to provide the corresponding intermediate **31** with 52% yield. The latter intermediate **31** was subjected to Boc group deprotection in presence of 4 N HCl in dioxane. The corresponding amine was then subjected to reductive amination with benzaldehyde, in the presence of acetic acid as catalyst and $NaBH_3CN$ as reductant, providing the key synthetic intermediate **32** with 48% yield.

For the synthesis of the spiro-core **35**, aniline, Boc-piperidone and thioglycolic acid were employed. Intermediate **35** was submitted to Boc removal followed by alkylation at the N^1 position in the presence of 4-bromomethyl benzonitrile and sodium hydride as the base, affording intermediate **36** with 51% yield. Nitriles **32** and **36** were then converted into the corresponding tetrazoles within quantitative yields using a dipolar cycloaddition reaction employing sodium azide, in the presence of ammonium chloride, and LiCl as catalyst. Following treatment with DFAA in dry toluene provided final compounds **34** and **37** in 34% and 25% yield, respectively.

Scheme 4. Synthetic route for the synthesis of final compounds **34** and **37**.[a]

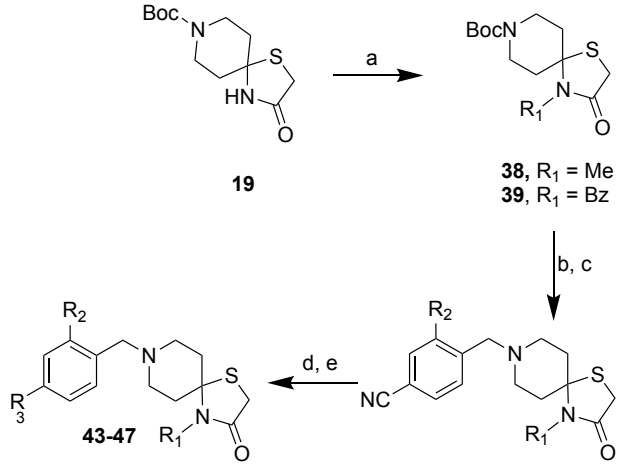


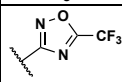
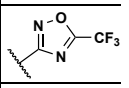
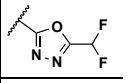
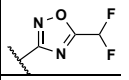
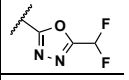
[a]**Reagents and reaction conditions:** (a) $(NH_4)_2CO_3$ (or aniline for **35**) toluene, 18 h, 110 °C, 88% (for **19**), 49% (for **35**); (b) 4 N HCl in dioxane, DCM, 1 h, 25 °C, 88% and 55% respectively; (c) 4-(bromomethyl)-3-fluorobenzonitrile, NaH 60 % oil dispersion, dry THF, 12 h, 25 °C, 52%; (d) benzaldehyde, AcOH, 25 °C, 1 h, $NaBH_3CN$, 18 h, 25 °C, 46%; (e) NaN_3, LiCl, NH_4Cl, dry DMF, 24 h, 100 °C, quant.; (f) DFAA, dry toluene, 70 °C, 2 h, 25-35% .

The synthesis of final compounds **43-47** is reported in Scheme 5. The amide group of spiro-core **19** was subjected to an alkylation reaction employing iodomethane or benzyl chloride as alkylating agents, and sodium hydride as base, respectively affording intermediates **38** (76%) and **39** (78%). Boc deprotection was performed under acidic conditions, then the benzonitrile linker (or 3-fluoro benzonitrile) was introduced on N^1 position employing potassium carbonate as base in dry DMF. Resulting nitriles **40-42** were converted into the corresponding tetrazoles or amidoximes, subsequently treated with TFAA or DFAA to

respectively provide the corresponding DFMOs **45**, **47** (24% and 31%) and TFMOs **43**, **44** and 46 (19%-30%).

Scheme 5. Synthetic route for the synthesis of final compounds **43-47**.[a]



Cpd	R_1	R_2	R_3
43	Me	H	
44	Me	F	
45	Me	F	
46	Me	H	
47	Bz	H	

[a]**Reagents and reaction conditions:** (a) iodomethane or benzyl chloride, NaH 60 % oil dispersion, dry THF, 12 h, 25 °C, 76% and 78% respectively; (b) 4 N HCl in dioxane, DCM, 1 h, 25 °C, quant.; (c) 4-bromomethyl benzonitrile or 4-(bromomethyl)-3-fluorobenzonitrile, anhydrous K_2CO_3, dry DMF, 12 h, 80 °C, 50%-70% ; (d) for **43**, **44** and **46**: NH_2NH_2, EtOH, 12 h, 80 °C, quant.; for **45** and **47**: NaN_3, LiCl, NH_4Cl, dry DMF, 24 h, 100 °C, quant.; (e) for **43**, **44**: dry

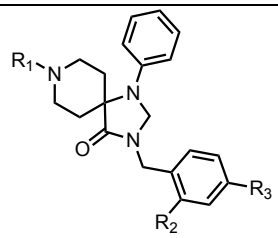
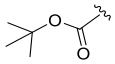
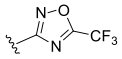
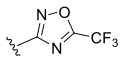
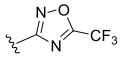
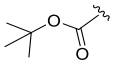
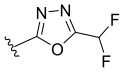
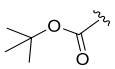
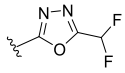
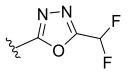
pyridine, TFAA or DFAA (for **46**), 2 h, 75 °C, 19%-30%; for **45** and **47** : DFAA, dry toluene, 2 h, 70 °C, 24% and 31% respectively.

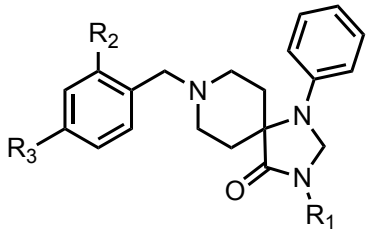
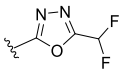
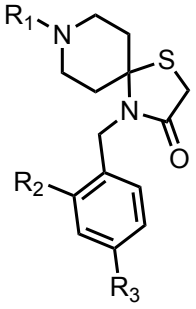
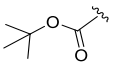
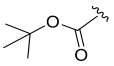
6.1.2 Investigation of novel TFMO and DFMO ZBGs on 1,3,8-triazaspiro[4,5]decan-4-one cap group

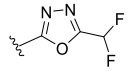
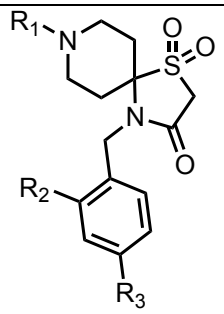
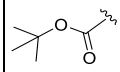
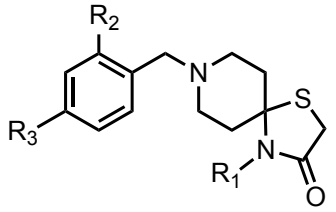
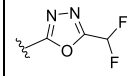
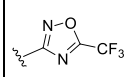
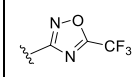
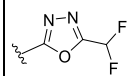
Prompted by emerging literature about the potential of DFMOs and TFMOs as alternative ZBGs to address limitations related to hydroxamate HDAC6i, while improving selectivity towards HDAC6 isoform, we sought to evaluate the impact of replacing the hydroxamic acid ZBG with DFMO or TFMO for the most active and selective compounds belonging to hydroxamate-based series bearing 1,3,8-triazaspiro[4,5]decan-4-one cap group (*Chapter 3*). As a general trend, the replacement of the hydroxamic acid with either the TFMO (**3**, **7**, **8**) or the DFMO (**13a,b**, **14**) ZBGs resulted in a significant loss of potency on HDAC6 (Table 1) in comparison to hydroxamate counterparts **48** and **49** (*Chapter 3*), while derivatives **8**, **13a,b**, **14** did not showed any activity on HDAC1 (selected as representative of nuclear HDACs) in enzymatic assays at assessed concentrations. Beyond the relevant potency drop, the replacement of the hydroxamic acid with TFMO ZBG in compounds **3** ($IC_{50\ HDAC6}$ = 2996 nM, $IC_{50\ HDAC1}$ = 2483 nM; Selectivity Index = 1.21) and **7** ($IC_{50\ HDAC6}$ = 158.7 nM, $IC_{50\ HDAC1}$ = 410.8 nM; Selectivity Index = 2.5) also led to loss of selectivity over HDAC1. These data are perfectly aligned with literature, since most of published TFMOs are recognized as selective Class IIa or, at least, Class II inhibitors with no isoform specificity. Notably, the replacement of the carbamate group (**3**) with a tertiary amine (**7**) increased of about 20-fold HDAC6 inhibitory potency, likely suggesting a better accommodation of the cap group within HDAC6 catalytic surface and improved positioning of the ZBG for Zn coordination. Accordingly, the introduction of a benzyl group on N^1 position in compound **8** ($IC_{50\ HDAC6}$ = 1163 nM), while less effective in enhancing the inhibitory potency on HDAC6 compared to methyl substitution in compound **7**, resulted in greater inhibitory

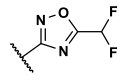
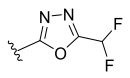
profile than the corresponding carbamate derivative **3**. These data support the hypothesis that amine derivatives adopt a more favorable conformation within HDAC6 catalytic surface. Also, compound **8** is the only selective inhibitor of TFMO series towards HDAC1, likely to unfavorable steric hindrace effects to allow the accommodation of the linker bearing the ZBG in HDAC1 active site.

Table 1. Structures, inhibitory activities (HDAC6 and HDAC1) and selectivity indexes of inhibitors **3**, **7**, **8**, **13a,b**, **14**, **17**, **21a,b, 25-26**, **29**, **30**, **34**, **37**, **43-47**.

Subseries I						
						
Cpd	R_1	R_2	R_3	IC_{50} HDAC6 (nM)	IC_{50} HDAC1 (nM)	SI
3		H		2996	2483	1.21
7	Me	H		158.7	410.8	2.5
8	Bn	H		1163	N.A.[b]	N.D.[c]
13a		H		751.9	N.A.[b]	N.D.[c]
13b		F		576.4	N.A.[b]	N.D.[c]
14	Bn	F		384.3	N.A.[b]	N.D.[c]
Subseries II						

						
17	Bn	F		40% [d]	N.A.[b]	N.D.[c]
Subseries III						
						
21a		H	CONHOH	190	3273	17
21b		F	CONHOH	118.8	2205	19
25a	**Me**	H	CONHOH	198.8	2022	10
25b	**Me**	F	CONHOH	91.94	2603	28
26a	**Bn**	H	CONHOH	98.40	639	7
26b	**Bn**	F	CONHOH	85.69	702	8

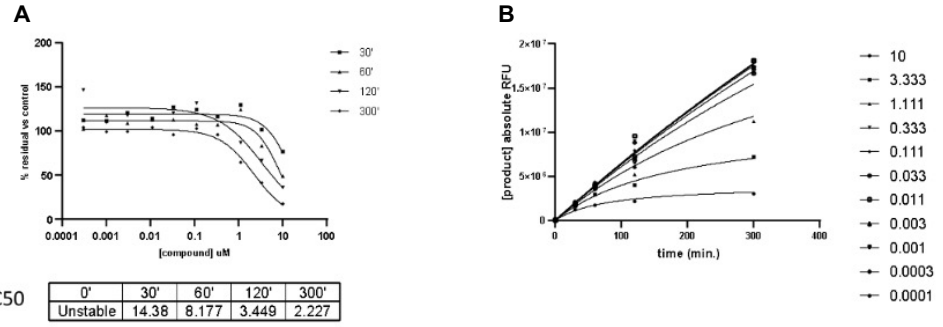
34	**Bn**	F		2189	N.A.	N.D.
Subseries IV						
						
29		H	CONHOH	17.65	53%[d]	N.D.[c]
30	Bn	H	CONHOH	36.3	N.A.[b]	N.D.[c]
Subseries V						
						
37	Ph	H		N.A.[b]	N.A.[b]	N.D.[c]
43	Me	H		1727	N.A.[b]	N.D.[c]
44	Me	F		2068	N.A.[b]	N.D.[c]
45	Me	H		1165	N.A.[b]	N.D.[c]

46	Me	F		53%[d]	N.A.[b]	N.D.[c]
47	Bn	H		N.A.[b]	N.A.[b]	N.D.[c]
48 [6]*	-	-	-	17.6	7373	419
49 [6]*	-	-	-	7.7	2118	275

a = Selectivity Index; b = not active at 100 μM; c = not determined; d = at 100 μM; *See *Chapter 3* for compounds structure.

These data are further corroborated by results obtained for hydroxamate inhibitor **48**, which exhibits higher selectivity profile compared to the N^1-methyl capped inhibitor **49** (*Table 1*) accountable to cap group steric hindrance. Thus, the TFMO ZBG in compounds **7** and **8** was replaced with the DFMO counterpart, in order to explore the impact of different ZBG in driving isoform selectivity. Gratifyingly, the DFMO-based analogues **13a,b** and **14** resulted completely inactive on HDAC1 in enzymatic assays (*Table 1*) while retaining nM potency on HDAC6, thereby confirming high isoform selectivity towards HDAC6. Compound **14** (N^1-benzyl capped) resulted the most potent inhibitor of DFMO series ($IC_{50\ HDAC6}$ = 384.5 nM), underscoring both the favorable impact of DFMO ZBG to drive isoform selectivity and the positive outcome for the steric and electronical contribution of the benzyl cap group to enhance both HDAC6 potency and selectivity profiles. As a general trend, all DFMOs and TFMOs displayed a weaker in vitro inhibitory profile in comparison to their hydroxamate counterparts, probably suggesting a lower ability to coordinate the catalytic Zn ion as such for the designed compounds and to their slow-binding mechanism of inhibition [5,7]. Accordingly, the weaker HDAC6 inhibition observed for DFMO-based inhibitors is largely ascribable the short incubation time (1 h)

employed in the classical enzymatic assay. Given that DFMOs are characterized by a slow-binding mechanism of action insufficient pre-incubation time may lead to underestimate *in vitro* inhibitory activity. Thus, time-course studies on compound **13b** were performed. Preincubation of compound **13b** with HDAC6 showed a progressive decrease of the IC_{50} of the inhibitor over time (Figure 1A), from 14.38 nM at 30 min to 2.227 at 300 min, confirming the time-dependent behaviour of such class of inhibitors. This pattern is consistent with a slow-binding mechanism of action, wherein the inhibitor requires extended incubation time to reach the equilibrium binding with the enzyme to properly inhibiting its activity. Additionally, kinetic analysis of enzymatic reaction product at varying concentration of compound **13b** (Figure 1B) revealed a dose-dependent reduction in enzymatic activity, as showed by shallower reaction slopes over time, further supporting the hypothesis for the time-dependent inhibitory mechanism.



IC50

0'	30'	60'	120'	300'
Unstable	14.38	8.177	3.449	2.227

Figure 1. (A) Enzymatic activity of HDAC6 upon treatment with compound **13b** at different concentrations. (B) Enzymatic activity of HDAC6 upon treatment with compound **13b** at different time points. Increased curve slopes over time suggest a time-dependent inhibitory profile in which the affinity of compound **13b** for the target enzyme increases with time.

Also, the introduction of *m*-fluoro or benzyl linkers did not affect the overall potency of DMFOs derivatives **13b** and **14**, likely due to the more rigid conformation of these ZBGs in comparison to hydroxamate analogues, where

such modifications markedly influence metal coordination, as further corroborated by literature evidence.

To further evaluate whether the geometry of the cap group could influence the proper orientation and binding of the ZBG within HDAC6 active site, we performed a linker inversion of compound **14**, introducing the linker bearing the DFMO ZBG on the N^1 position of the piperidine ring. This structural modification led to compound **17**, which resulted completely inactive in enzymatic assays on HDAC1 at tested concentration (*Table 1*). Notably, while complete loss of activity was not observed on target enzyme HDAC6, compound **17** exhibited approximately 40% of inhibition at the highest assessed concentration. This data, along with a dose-dependent inhibitory profile, suggests a potential slow-binding mechanism toward HDAC6, possibly requiring extended incubation to reach maximal inhibition.

6.1.3 Exploration of a thia-diazaspiro[4.5]decane cap group

Based on these data, we considered it valuable to explore further structural simplifications of the cap group portion, with the aim of identifying new variants capable of maintaining or even improving the selectivity and potency toward HDAC6, while ensuring favourable PK properties. Therefore, our approach was to elaborate a novel versatile and chemically tractable spirofused cap group to be introduced in the structure of designed inhibitors, preserving key interactions within the enzyme active site, ultimately aiming to develop HDAC6is potent, selective and synthetically accessible. For this purpose, the privileged scaffold 1-thia-4,8-diazaspiro[4.5]decan-3-one (**19**) [8,9] (Figure 2) was selected as cap group, in order to: (i) increase the fraction of sp^3 hybridized carbon (Fsp^3), an important parameter which reflects the three-dimensionality of a molecule and is often associated with lower toxicity and an improved pharmacological profile.

Accordingly, very recently, Olaoye et al. reported a novel class of sulphonamide-capped inhibitors which displayed high selectivity towards HDAC6, while

modification on the sulphonamide moiety allowed to improve PK properties, as demonstrated to 120-fold increase in plasma concentration for 2-chlorobenzene sulfonamide capped inhibitor in comparison to other compounds belonging to a progenitor subseries [10]. These data further corroborated our approach for the introduction of sulfur or sulphone group in novel conceived class of inhibitors. Notably, the 1,3,8-triazaspiro[4,5]decan-4-one cap group identified in our previous work already exhibited highest Fsp^3 (0.71) in comparison to other cap groups reported in literature. In this context, we further increased the Fsp^3 of designed HDAC6is through the introduction of the novel identified 1-thia-4,8-diazaspiro[4.5]decan-3-one cap group (Fsp^3 = 0.80), highlighting a substantial enhancement in molecular saturation and three-dimensional character; (ii) enable a more accessible synthetic route, since the 1-thia-4,8-diazaspiro[4.5]decan-3-one cap group was synthesized through a one-pot reaction, making the synthetic process simpler and efficient in enabling the easy generation of various derivatives. To evaluate the effectiveness of this novel cap group, in a first design we kept the canonical benzyl or *m*-fluorobenzyl linker, while the hydroxamic acid ZBG was an attractive choice for both its synthetic feasibility and its high capability to coordinate zinc ions, with respect to other classes of ZBGs.

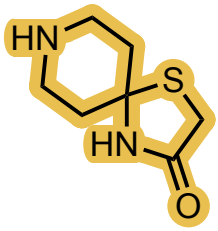


Figure 2. Structure of 1-thia-4,8-diazaspiro[4.5]decan-3-one cap group.

Therefore, the primary objective of this work was to evaluate whether the novel cap group **19** conformed to the structural requirements necessary for the interaction with the catalytic surface of HDAC6, thereby conferring selectivity over nuclear isoforms. All hydroxamic-acid based inhibitors bearing the 1-thia-

4,8-diazaspiro[4.5]decan-3-one core linked to the ZBG through the canonical *p*-benzyl linker (**21a**, **25a** and **26a**) displayed nM IC_{50} towards HDAC6. Despite the optimal potency profile on the target enzyme, as reported in *Table 1*, the selectivity indexes of designed compounds were not satisfying in order to consider newly designed inhibitors as selective. This data is probably accountable to inadequate steric bulk or spatial orientation of this newly conceived cap group to prevent the interaction of designed molecules with other HDAC isoenzymes, thereby limiting the overall selectivity profile. The introduction of a *m*-fluorobenzyl linker in compounds **21b**, **25b** and **26b** – a strategy often employed into the design of HDAC6is and able to enable selective interaction with HDAC6 hydrophobic surface channel – did not lead to a significant improvement the inhibitory potency on HDAC6, thus suggesting that the cap group does not optimally engage the catalytic surface of HDAC6 likely resulting in suboptimal positioning of the linker bearing the ZBG in HDAC6 catalytic channel.

To further investigate the role of steric hindrance, spatial orientation and the possibility for further polar interaction for the cap group **19**, compounds **29** and **30** were synthesised, in which the sulphur group was converted into the correspondent sulfone. Gratifyingly, compounds **29** and **30** exhibited complete lack of activity on HDAC1 at the tested concentration, while retaining the inhibitory profile in the nanomolar range on HDAC6.

Once confirmed the suitability of the spiro cap group **19** to efficiently occupy HDAC6 catalytic site allowing the proper linker orientation to allow the hydroxamate ZBG to reach HDAC6 catalytic channel, we next investigated whether the replacement of the hydroxamic ZBG with DFMO or TFMO moieties could further influence isoform selectivity towards this enzymatic class.

In a first design, compound **26b** was selected for the replacement of the hydroxamate ZBG with DMFO since it showed (i) superior inhibitory potency on HDAC6 among sulfur-containing derivatives, (ii) pan-HDAC inhibition

across evaluated isoenzymes, making it an ideal candidate to evaluate the impact of site-specific modifications for isoform selectivity. Although compound **34** exhibited a marked reduction in potency compared to its hydroxamate counterpart **26b** (*Table 1*), it resulted completely inactive against HDAC1 (*Table 1*), consistently with literature supporting the preferential selectivity of DFMO-based inhibitors for HDAC6 over Class I HDACs. Also, as showed for DFMOs **13a,b** and **14**, the loss of potency of DFMO **34** in comparison to its hydroxamate counterpart **26b** may be attributable to the time-depending mechanism of action of DMFOs, potentially compounded by insufficient incubation time (1 h or 2 h) in enzymatic assays.

On the next stage, to further explore the structural requirements for HDAC6 selectivity and to assess the spatial tolerance of the linker region, we performed a linker inversion on compound **34** (likely to the strategy applied into the design of compound **17** as "inverted" analogue of compound **14**). As expected, the corresponding compound **47** was found to be completely inactive both across HDAC6 and HDAC1. To simplify the molecular framework, we subsequently replaced the benzyl moiety linked to the amide group with a phenyl group (**37**) to reduce the flexibility of the cap group substituent. Similar to all analogues of this subset (**34**, **47**), compound **37** resulted completely inactive across assessed HDACs (*Table 1*). This lack of activity may be attributed to impaired positioning of ZBG within the catalytic channel, plausibly due to both increased cap group rigidity and steric hindrance of the phenyl group. Indeed, given the established slow-binding inhibition mechanism of DMFOs, increased steric bulk (benzyl group for compound **34** and **47**; phenyl group for compound **37**) of the cap may further slowdown the catalysed DFMO ring-opening, thus underestimating the inhibitory potency in enzymatic assays due to the limited incubation times. Thus, a second subseries of optimized compounds was designed, in which the amide moiety was substituted with a less bulky methyl group (**43-46**). This modification

aimed to reduce steric hindrance around the linker moiety, potentially facilitating a more favorable orientation of the DFMO within the HDAC6 catalytic pocket. By minimizing spatial constraints, this design sought to improve binding kinetics and restore inhibitory potency while maintaining isoform selectivity. The introduction of the methyl group in DFMO-based inhibitor **45** successfully restored the inhibitory activity on HDAC6 in enzymatic assay (*Table 1*), yielding a potency profile comparable to other active compounds of the two previous subseries, while retaining high selectivity towards HDAC6, supporting the hypothesis that reducing steric bulk near the amide linkage may favourably influence both binding efficiency and isoform selectivity. Building from promising results obtained for compound **45**, TFMO analogues **43** and **44** were synthesised, in order to determine whether the observed gain in activity for compound **45** was directly attributable to the incorporation of the DFMO ZBG, and to evaluate the influence of the introduction of the *m*-fluorobenzyl linker in the structure of such designed inhibitor. As expected, the presence of a *m*-fluorine linker in compounds **44** and **45** did not affect the overall activity of designed inhibitors. Notably, TFMO analogues **43** and **44** exhibited an inhibitory activity comparable to compound **45** on HDAC6, while do not showing significant activity on HDAC1. Surprisingly, compound **46** - designed as control - bearing the difluoro 1,2,4-oxadiazole exhibited dose-dependent inhibitory activity on HDAC6, even though its potency was weaker in comparison to its DFMO and TFMO analogues. This result suggested that, despite the diverse electronic and steric properties of this scaffold, it can still engage HDAC6 catalytic site, albeit less efficiently, thus highlighting the sensitivity of DFMO and TFMO based inhibitors to subtle structural modifications.

6.1.4 Target engagement by Western Blot analysis

Once structure-activity relationships for designed inhibitors were delineated, their behaviour was further assessed in cell-based settings, by assessing their

activity in the acetylation of α-tubulin (HDAC6 target) compared to the acetylation of H3 (target of nuclear HDACs). HeLa cells were treated for 16 h with serial dilutions of the five selected compounds, cell lysates were collected and the acetylation levels of both tubulin and H3 were evaluated by western blot analysis as markers for selective inhibition of HDAC6. As The potent pan-HDACi LAQ824 was ass in parallel as reference. For normalization both GAPDH and Vinculin proteins were immunodetected. Acetyl-tubulin and acetyl-H3 signals detected in western blot were quantified and normalized to signals of vinculin, to obtain an acetyl-tubulin to acetyl-H3 ratio in each sample.

As shown in Figure 3, all compounds belonging to the first subseries (TFMOs **3**, **7** and **8**) and DFMOs (**13a,b** and **17**) showed a dose dependent increase in acetylated tubulin (indicating the inhibition of HDAC6). According, except for **7**, H3 acetylation appeared much lower, indicating higher specificity versus HDAC6 in comparison to the pan HDACi LAQ824. These data perfectly aligned with the results obtained in enzymatic assays, showing that the introduction of TFMO ZBG in compounds **3** and **7** led to lack of selectivity towards HDAC1, while the introduction of the most hindered benzyl-cap restored the preferential inhibition on the target enzyme HDAC6, whit TFMOs resulting more potent compared to the DFMOs counterparts as a general trend also in cell-based experiments.

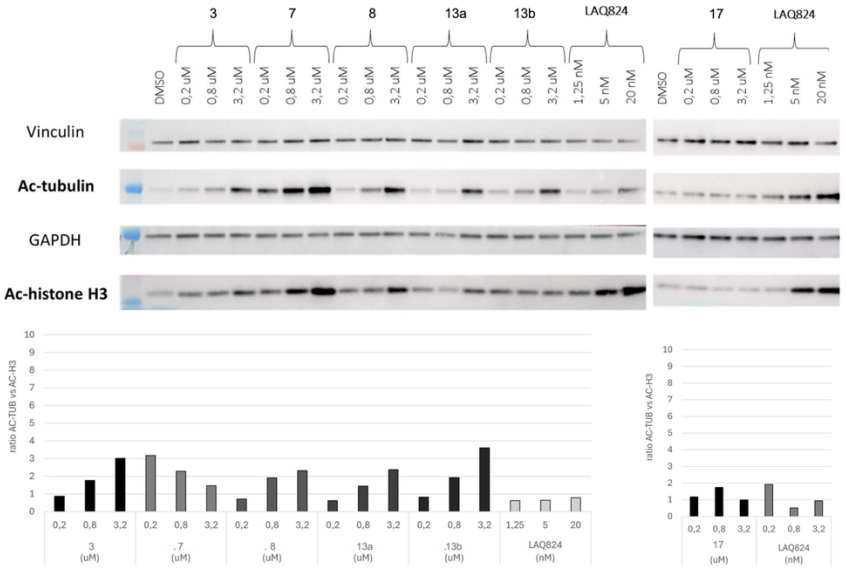


Figure 3. Western blot analysis of acetylated α-tubulin and acetylated histone H3 (AC H3) levels in HeLa Cells treated with 0.2, 0.8, 3.2 μM of the indicated compounds for 16 h at 37 °C (upper). Vinculin served as a loading control. Bands detected with anti-acetyl-tubulin and anti-acetyl-H3 antibodies were quantified and normalized to signals of vinculin, and the ratio of AC α-TUB: AC H3 was calculated and shown (lower).

According to the their activity in enzymatic assays, among hydroxamate based compounds bearing the 1-thia-4,8-diazaspiro[4.5]decan-3-one cap group, compounds **29** and **30** displayed the best ratio of tubulin to H3 ascetylation, thereby confirming their selective inhibitory activity on HDAC6 (Figure 4).

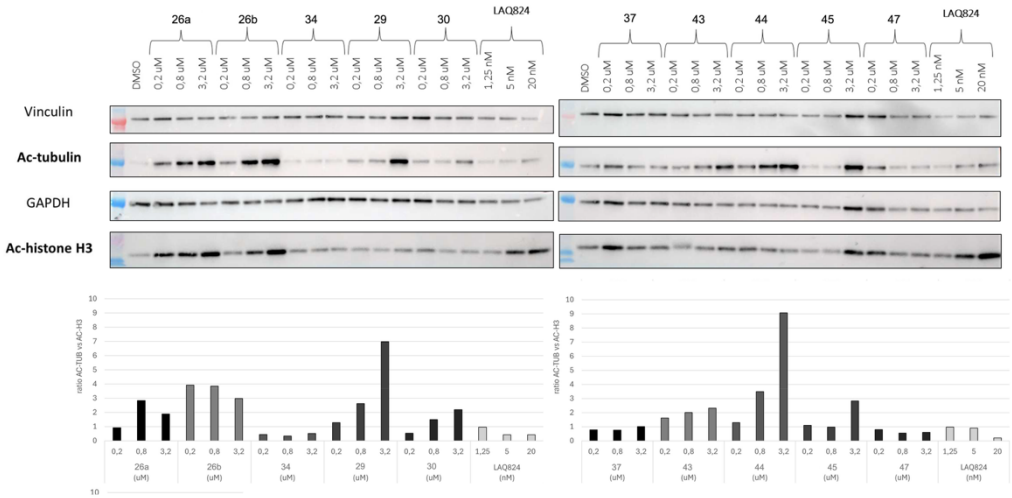


Figure 4. Western blot analysis of acetylated α-tubulin and acetylated histone H3 (AC H3) levels in HeLa Cells treated with 0.2, 0.8, 3.2 μM of the indicated compounds for 16 h at 37 °C (upper). Vinculin served as a loading control. Bands detected with anti-acetyl-tubulin and anti-acetyl-H3 antibodies were quantified and normalized to signals of vinculin, and the ratio of AC α-TUB: AC H3 was calculated and shown (lower).

Moreover, DFMOs **37**, **45** and **47** resulted in a weaker effect on acetylated tubulin – and consequently on their target enzyme HDAC6 - compared to TFMOs 44, 45, probably accountable to their inhibitory slow kinetics and insufficient incubation time. Among this subseries, compound **44** proved to be the most potent and selective, as confirmed by the ratio of tubulin versus H3 ascetylation shown in Figure 4.

6.1.5 Target engagement by NanoBRET assay on HDAC6

The cellular target engagement of derivatives **43-45** bearing heterocyclic ZBGs was also assessed in cell-based NanoBRET assay [11-14]. As shown in *Table 2*, the compounds displayed low nM IC_{50} in NanoBRET assay, despite the micromolar inhibitory profile registered upon their standard in vitro inhibitory assessment. These data strongly confirmed both the target engagement of this set

of compounds as HDAC6is, and also the hypothesis for the slow-binding mechanism of action. Interestingly, compound **46 -** bearing the difluoro 1,2,4-oxadiazole - exhibited 2.5 nM IC_{50}, thereby resulting the most active compound of the series, and suggesting the difluoro 1,2,4-oxadiazole may act with a distinct inhibitor mode to the corresponding difluoro 1,3,4-oxadiazoles reported in the present work.

Table 2. IC_{50} values of compounds **26b, 43-46** in NanoBRET cell-based assay

Cpd	IC_{50} HDAC6 (nM) NanoBRET	IC_{50} HDAC6 (nM) Enzymatic assay
26b	4.2	2068
43	45% @ 6 μM	85.69
44	13	2068
45	83% @ 6 μM	1165
46	2.5	53% @ 100 μM
Vorinostat	160	39

6.1.6 Kinetic studies

Prompted by NanoBRET assays results, we sought to deeper investigate the hypothesis for the slow binding inhibition investigating the dissociation behaviour of compounds **7**, **13a** and **34** by 100-fold jump dilution experiments using vorinostat as control. As reported in literature, 100-fold dilution of vorinostat completely restored HDAC6 deacetylase activity in comparison to blank (DMSO 1%) [15]. This data is perfectly aligned with the fast on/off kinetic of hydroxamate based inhibitors such as vorinostat. In contrast, DFMO based inhibitors **7**, **13a** and **34** were confirmed to act as tight-bind inhibitors retaining

significant HDAC6 inhibition even after a 100-fold dilution, thereby supporting an essentially irreversible inhibitory mechanism (Figure 3). Surprisingly, TFMO **7** displayed a kinetic profile similar to compounds **13a** and **34**, irreversibly inhibiting HDAC6 activity under the same dilution conditions. This behaviour indicates a unique mechanism of action compared to TFMOs already reported in literature, which typically inhibit HDACs *via* reversible coordination of the catalytic Zn^{2+} ion through the trifluoromethyl group - mimicking the binding mode of hydroxamate-based inhibitors.

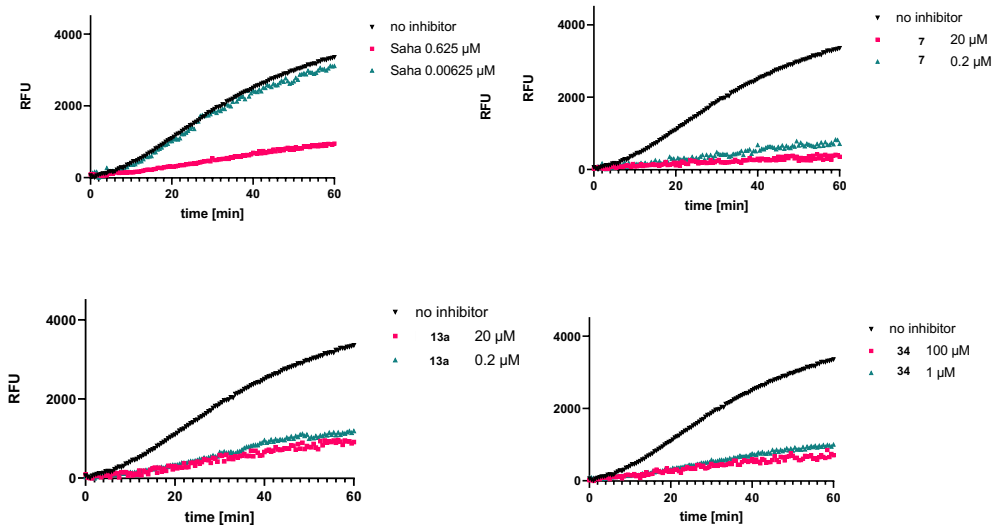


Figure 3. Analysis of the association and dissociation behavior of **7**, **13a** and **34** at HDAC6.

6.1.7 Biological assessment in human bladder carcinoma T24 cell lines

Since many evidence have been provided for the role of HDACs in bladder cancer (See *Chapter 1, 1.5.2 HDAC6 in oncological diseases*), we sought to investigate both hydroxamate HDACis **25a** and **26a,b** – which did not display strict selectivity between HDAC6 and the nuclear isoform HDAC1, thereby they can be considered pan-HDACis - and selective HDAC6is **29** and **30** in human urothelial carcinoma cell line T24, in order to confirm pan-HDACis efficacy to

inhibit BC cell survival. Since most of HDAC6is in the present work display non-hydroxamate ZBG, DFMO or TFMO based compounds **34**, **37**, **43** and **47** were assessed in order to evaluate whether different inhibitory mechanism on HDAC6 could influence the modulation of downstream signalling pathways. Thus, we performed an MTT assay, exposing the cells to two concentrations of each compound (10 μM and 30 μM). Among them, the compound **26a** exhibited the highest activity (*Table 3*).

Table 3. Effect of **25-26**, **29**, **30**, **34**, **37**, **43** and **47** on T24 cell proliferation.

Cpd	10 μM	30 μM
25a	93.292 ± 1.054	74.079 ± 3.114
26a	70.392 ± 2.963	42.650 ± 1.684
26b	74.079 ± 2.230	46.928 ± 1.637
29	89.875 ± 1.859	86.897 ± 2.025
30	86.807 ± 2.025	81.156 ± 2.393
34	88.368 ± 1.030	84.197 ± 1.995
37	79.595 ± 2.088	76.815 ± 9.325
43	79.784 ± 1.564	74.133 ± 0.914
47	90.412 ± 0.235	88.287 ± 2.149

Cell viability is expressed as a percentage relative to control (CTL, 100 ± 2.135 %) ± SEM following treatment with various compounds at concentrations of 10 and 30 μM. Among the compounds tested, only compound 42a showed a notable effect, with cell viability of 70.39 ± 2.96 % at 10 μM and 42.65 ± 1.68 % at 30

μM. Experiments were performed in triplicate, each in quadruplicate. Statistical significance is indicated as *p < 0.05, **p < 0.01, and ***p < 0.001 vs. CTL.

Consequently, we assessed cell viability following the exposure with compound **26a** to a range of concentrations (0.3, 1, 3, 10, and 30 μM) for 48 and 72 hours. Cell viability was determined using the colorimetric MTT assay (Figure 4). Compound **26a** reduced T24 cell viability in a concentration-dependent manner, with IC_{50} values of 7,60 μM at 48 hours (Figure 4) and 8,13 μM at 72 hours (Figure 4).

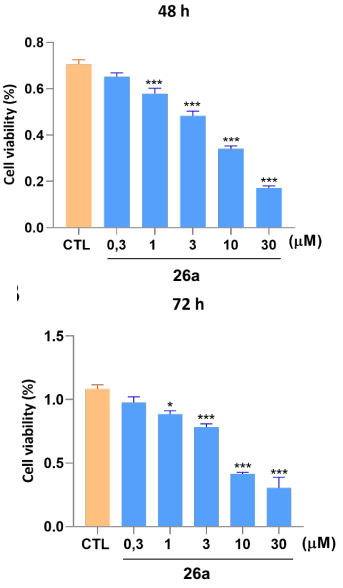


Figure 4. Effect of compound **26a** on T24 cell proliferation. Cell viability was assessed by MTT assay at 48 and 72 h following treatment with compound **26a** (0,3 - 1 – 3 – 10 – 30 μM). Each experiment (n = 3) was performed in quadruplicate. Data are expressed as percentage of cell viability relative to control (CTL). *$p < 0.05$, ***$p < 0.001$ *vs* CTL.

Based on these results, we further evaluated whether compound **26a** induces apoptosis in T24 cells. Flow cytometry analysis using Annexin V/ propidium

iodide (PI) dual staining showed that treatment with **26a** (10 µM) for 48 h led to apoptosis (both early and late) in approximately 20% of cells (Figure 6A and B). Given the known interplay between apoptosis and autophagy, we then investigated whether autophagic processes were also involved in the cellular response to **26a**. T24 cells treated with **26a** (10 µM) for 24 hours were analyzed by quantitative PCR (qPCR) to assess the expression of key autophagy-related genes. The results showed a significant upregulation of BECLIN1, BNIP3, LAMP1, and VPS34 (Figure 5C-F), indicating activation of autophagy.

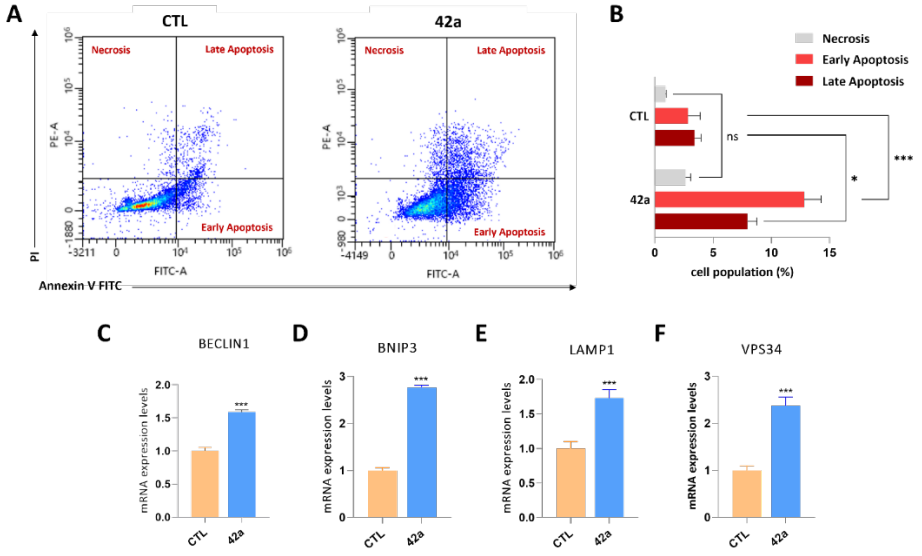


Figure 5. Induction of apoptosis and modulation of autophagy-related gene expression by compound **26a** in T24 cells. (A) Representative flow cytometry dot plots of T24 cells treated with compound **26a** (10 µM) for 48 h, showing apoptotic populations detected by dual Annexin V-FITC and propidium iodide (PI) staining, compared to untreated control cells. (B) Quantification of apoptotic cells based on Annexin V/PI staining. Data are expressed as percentage of total cells. *$p \leq 0.05$; ***$p < 0.001$ *vs* CTL. (C–F) mRNA expression levels of BECLIN1, BNIP3, LAMP1, and VPS34 in T24 cells treated with compound **26a** (10 µM) for 24 h. Gene expression was normalized to RPS16 and calculated

using the $2^{-\Delta\Delta Ct}$ method. Bars represent the mean ± SEM of three independent biological replicates. ***$p < 0.001$ vs. CTL.

6.2 Conclusions

We herein disclose a novel cap group, namely 1-thia-4,8-diazaspiro[4.5]decan-3-one for HDAC6 selective inhibition coupled by non-hydroxamate ZBGs. Design, synthesis, and biological studies are reported for this new series of compounds. Building on our recent disclosure of high selective HDAC6is bearing 1,3,8-triazaspiro[4,5]decan-4-one cap-group, we first explored the replacement of the hydroxamate ZBG with DFMOs and TFMOs, in order to address pharmacological limitations related to hydroxamic acid group, while interrogating whether these ZBGs could enhance isoform selectivity rather than their hydroxamic acid counterparts. While DFMOs **13a,b** and **14** exhibited lower potency compared to their hydroxamate analogues, they resulted completely inactive on HDAC1 thus confirming high isoform selectivity for this class of inhibitors. As expected, TFMOs **3** and **7** resulted in pan-HDAC inhibition towards HDAC6 and 1, while the introduction of a benzyl group in the structure of TFMO **8** restored selectivity, highlighting the crucial interplay between the cap group and ZBG to achieve isoform selectivity. As second objective, we aimed to structurally simplify the cap group portion in order to increase the Fsp^3 fraction, linked to improved PK properties, while retaining optimal geometry for preferential HDAC6 inhibition. While inhibitors **21a,b**, **25a,b** and **26a,b**, bearing the hydroxamate ZBG lost selectivity towards HDAC1, the introduction of the bulkier sulfone in the cap group in compounds **29** and **30** led to completely loss of activity on nuclear HDAC1, while retaining nM inhibitory profile towards HDAC6. After validating the suitability of this novel cap group for HDAC modulation, it was combined with DFMO and TFMO ZBGs. Compounds in both subseries displayed tight-binding and time-dependent inhibition. Indeed, despite their modest potency in enzymatic assays (μM range), compounds **34**, **44**,

and **46** exhibited strong activity in cell-based assays, with IC_{50} values of 4.2 nM, 2.5 nM, and 13 nM, respectively. The discrepancy in potency profiles between enzymatic and *in vitro* assays strongly supports the hypothesis of a slow-binding inhibition mechanism, with longer incubation times in cellular assays allowing improved inhibition kinetics, while remaining completely inactive on HDAC1. Jump dilution assays performed on compounds **7**, **13a** and **34 -** as representative of this series – further corroborated the hypothesis of thigh-binding inhibitory mechanism, confirming the ability of new designed DFMOs and TFMOs to irreversibly inhibit HDAC6 catalytic activity. Thereby, our findings strongly support the importance of fine-tuning both the cap group and the ZBG in order to achieve isoform selectivity in HDAC6 modulation. Indeed, while selectivity indexes of hydroxamate inhibitors bearing the 1-thia-3,8-diazaspiro[4.5]decan-4-one were not satisfying in order to define designed compounds as selective HDAC6is – thereby suggesting the steric hindrance of the cap group moiety is not adequate to ensure isoform selectivity - the replacement of the hydroxamate ZBG with both DFMO and TFMO moiety led to complete loss of activity of nuclear representative isoform HDAC1, resulting in selective HDAC6 inhibition both in enzymatic assays and *in vitro* settings. Furthermore, we analysed the effect of pan-HDAC and selective HDAC6is on the viability of the T24 human urothelial carcinoma cell line. As expected, the pan-HDACi **26a** was the most active one in inhibiting the proliferative capacity of T24 cells, with IC_{50} values of 7.60 μM and 8.13 μM at 48 and 72 hours, respectively. To elucidate the potential mechanisms underlying this effect, we analyzed two cell death pathways: apoptosis and autophagy. Treatment with 10 μM of compound **26a** for 48 hours induced apoptosis in approximately 20% of the cell population, as evidenced by FACS analysis. In addition, after 24 hours of treatment, the compound significantly upregulated the expression of four key autophagy-related genes (BECN1, LAMP1, BNIP3, and VPS34) suggesting

activation of the autophagic process. These findings suggest that compound **26a** inhibits T24 cell proliferation by sequentially activating autophagy and apoptosis, two interconnected cell death pathways that may cooperate in mediating its anticancer effects. These data are consistent with literature evidence for the importance of modulating the expression of oncogenic genes in BC through the regulation of nuclear HDACs. Further studies are warranted on designed selective HDAC6is in combination with commonly used chemotherapeutics in BC. This approach may not only enhance therapeutic outcome of selective HDAC6is but also provide deeper insights into the still poorly explored landscape of HDAC6 role in Bc phenotype.

6.3 Experimental section

6.3.1 Chemistry

General procedure for the synthesis of hydroxamic acids. To a stirring solution of the corresponding methyl ester in a mixture of DCM/MeOH (1:1), 50% aqueous hydroxylamine (100 eq) was added followed by methanolic 4 M potassium hydroxide (50 eq). After 1 h, the reaction mixture was quenched by the addition of 6 N HCl and concentrated under vacuum. Crude material was purified by silica gel column chromatography (DCM/MeOH/NH_4OH 20:1:0.05 v/v to 20:1:1 v/v) giving desired hydroxamic acids.

tert-butyl 3-(4-cyanobenzyl)-4-oxo-1-phenyl-1,3,8-triazaspiro[4.5]decane-8-carboxylate (2). NaH (60% mineral oil dispersion, 27 mg, 1.65 mmol) was added to a solution of **1** (500 mg, 1.50 mmol) in dry THF (2.5 mL). After 20 minutes, 4-(bromomethyl)benzonitrile (324 mg, 1.65 mmol) was added, and the resulting mixture allowed to stir at 25 °C for 18 h. After completion, THF was evaporated under vacuum, the crude residue dissolved in EtOAc (10 mL) and partitioned with a saturated solution of $NaHCO_3$ (10 mL x 3). Organic layer was collected, dried over Na_2SO_4 and evaporated under reduced pressure. The crude material

was purified with silica gel Biotage® flash chromatography (PE/EtOAc 1:1 v/v) affording desired compound **2** with 50% yield (335 mg).

^{1}H NMR (700 MHz, CDCl3) δ 7.67 (d, J = 8.2 Hz, 2H), 7.40 (d, J = 8.0 Hz, 2H), 7.22 (t, J = 7.2 Hz, 2H), 6.85 (t, J = 7.3 Hz, 1H), 6.70 (d, J = 8.2 Hz, 2H), 4.66 (s, 2H), 4.59 (s, 2H), 4.16 – 4.09 (m, 1H), 4.03 – 3.94 (m, 1H), 3.66 – 3.50 (m, 2H), 2.64 – 2.49 (m, 2H), 1.71 – 1.63 (m, 2H), 1.51 (s, 9H).

tert-butyl 4-oxo-1-phenyl-3-(4-(5-(trifluoromethyl)-1,2,4-oxadiazol-3-yl)benzyl)-1,3,8-triazaspiro[4.5]decane-8-carboxylate (3). *Step 1:* To a solution of compound **2** (0.223 mmol, 100 mg) in EtOH at 25 °C, 50% aqueous hydroxylamine solution (0.892 mmol, 0.027 mL) was added dropwise, and the reaction mixture was heated at reflux and left under stirring for 3 h. After the time reaction had elapsed, the reaction mixture was concentrated under reduced pressure to obtain the desired product tert-butyl 3-(4-(N-hydroxycarbamimidoyl)benzyl)-4-oxo-1-phenyl-1,3,8-triazaspiro[4.5]decane-8-carboxylate with quantitative yield (106 mg).

^{1}H NMR (400 MHz, CDCl3) δ 7.62 (d, 2H), 7.32 (d, J = 8.2 Hz, 2H), 7.21 (dt, J = 2298.5, 8.0 Hz, 2H), 6.83 (t, J = 7.3 Hz, 1H), 6.68 (d, J = 8.2 Hz, 2H), 4.85 (s, 2H), 4.63 (s, 2H), 4.19 – 3.90 (m, 2H), 3.68 – 3.54 (m, 2H), 2.63 – 2.49 (m, 2H), 1.71 – 1.61 (m, 2H), 1.49 (s, 9H).

Step 2: to a cooled solution of tert-butyl 3-(4-(N-hydroxycarbamimidoyl)benzyl)-4-oxo-1-phenyl-1,3,8-triazaspiro[4.5]decane-8-carboxylate (0.223 mmol, 106 mg) and DIPEA (0.077 mL) in dry DCM (3 mL), TFAA was added and the resulting mixture stirred for 1 h at 0 °C. After completion, the reaction mixture was diluted with DCM (5 mL) and partitioned with a saturated solution of $NaHCO_3$ (3 x 5 mL). Organic layer was dried over Na_2SO_4 and evaporated under reduced pressure and the crude material purified by neutral alumina liquid chromatography eluting with PE/EtOAc (4:1 v/v) to afford compound **3** with 38 % yield (48 mg).

MS (ESI) m/z calc. $[M+H]^+$ for $C_{28}H_{31}F_3N_5O_4^+$: 558.23; found: 458.2.

^{1}H NMR (400 MHz, CDCl3) δ 8.06 (d, J = 9.8 Hz, 2H), 7.38 (d, J = 8.2 Hz, 2H), 7.14 (t, J = 7.9 Hz, 2H), 6.77 (t, J = 7.3 Hz, 1H), 6.63 (d, J = 8.2 Hz, 2H), 4.62 (s, 2H), 4.54 (s, 2H), 4.11 – 3.94 (m, 2H), 3.65 – 3.47 (m, 2H), 2.59 – 2.42 (m, 2H), 1.67 – 1.52 (m, 3H), 1.44 (s, 9H).

^{13}C NMR (176 MHz, CDCl3) δ 174.50, 168.84, 166.07 (q, J = 132.1 Hz), 155.28, 142.60, 140.19, 129.48, 128.69, 128.57, 124.93, 119.40, 115.15, 79.84, 63.15, 44.62, 31.10, 29.85, 28.60.

4-((4-oxo-1-phenyl-1,3,8-triazaspiro[4.5]decan-3-yl)methyl)benzonitrile (4). To a stirred solution of the corresponding Boc protected amine **18** (1.12 mmol, 500 mg) in DCM (5 mL), 4 M HCl in dioxane was added (10 eq) and the resulting solution allowed to stir at 25 °C. After 1 h, the reaction mixture was concentrated under vacuum, the residue was dissolved in EtOAc and washed with $NaHCO_3$ saturated solution for three times. Organic layer was dried over Na_2SO_4 and evaporated under reduced pressure. The obtained deprotected amine was used in the next synthetic step without further purification.

4-((8-methyl-4-oxo-1-phenyl-1,3,8-triazaspiro[4.5]decan-3-yl)methyl)benzonitrile (5). To a stirred solution of the corresponding amine **4**(0.288 mmol, 100 mg) in MeOH, a catalytic amount of acetic acid was added followed by paraformaldehyde (143 mg, 10 eq) and the reaction mixture allowed under stirring at 25 °C. After 1 h, $NaBH_3CN$ (0.460 mmol, 29 mg) was added and the resulting mixture allowed under stirring for 18 h at 25 °C. MeOH was evaporated under vacuum, the residue dissolved in EtOAc (5 mL) and washed with distilled H_2O (5 mL x 3). Organic layer was dried over Na_2SO_4 and evaporated under reduced pressure. Crude material was purified by silica gel liquid chromatography eluting with DCM/MeOH (98:2 v/v), providing desired compound **5** with 68% yield (71 mg).

^{1}H NMR (400 MHz, CDCl3) δ 7.67 (d, J = 8.2 Hz, 2H), 7.40 (d, J = 8.0 Hz, 2H), 7.29 – 7.23 (m, 3H), 6.87 (d, J = 8.7 Hz, 2H), 4.65 (s, 2H), 4.59 (s, 2H), 2.99 – 2.90 (m, 2H), 2.90 – 2.71 (m, 4H), 2.41 (s, 3H), 1.74 – 1.68 (m, 2H).

4-((8-benzoyl-4-oxo-1-phenyl-1,3,8-triazaspiro[4.5]decan-3-yl)methyl)benzonitrile (6). To a stirred solution of the corresponding amine **4** (0.288 mmol, 100 mg) in MeOH, a catalytic amount of acetic acid was added followed by benzaldehyde (0.577 mmol, 0.060 mL) and the reaction mixture allowed under stirring at 25 °C. After 1 h, $NaBH_3CN$ (0.577 mmol, 36 mg) was added and the resulting mixture allowed under stirring for 18 h at 25 °C. MeOH was evaporated under vacuum, the residue dissolved in EtOAc (5 mL) and washed with distilled H_2O (5 mL x 3). Organic layer was dried over Na_2SO_4 and evaporated under reduced pressure. Crude material was purified by silica gel liquid chromatography eluting with DCM/MeOH (98:2 v/v), providing desired compound **6** with 77% yield (98 mg).

^{1}H NMR (700 MHz, $CDCl_3$) δ 7.66 (d, J = 7.9 Hz, 2H), 7.39 (t, J = 8.4 Hz, 4H), 7.33 (t, J = 7.4 Hz, 2H), 7.30 – 7.24 (m, 3H), 6.87 (d, J = 3636.8 Hz, 3H), 4.65 (s, 2H), 4.57 (s, 2H), 3.61 (s, 2H), 2.91 – 2.81 (m, 4H), 2.74 – 2.65 (m, 2H), 1.70 – 1.65 (m, 2H).

8-methyl-1-phenyl-3-(4-(5-(trifluoromethyl)-1,2,4-oxadiazol-3-yl)benzyl)-1,3,8-triazaspiro[4.5]decan-4-one (7). *Step 1:* To a solution of compound **5**(0.197 mmol, 71 mg) in EtOH at 25 °C, 50% aqueous hydroxylamine solution (0.788 mmol, 0.027 mL) was added dropwise, and the reaction mixture was heated at reflux and left under stirring for 3 h. After the time reaction had elapsed, the reaction mixture was concentrated under reduced pressure to obtain the desired product N-hydroxy-4-((8-methyl-4-oxo-1-phenyl-1,3,8-triazaspiro[4.5]decan-3-yl)methyl)benzimidamide with a quantitative yield (77 mg).

Step 2: to a cooled solution of tert-butyl 3-(4-(N-hydroxycarbamimidoyl)benzyl)-4-oxo-1-phenyl-1,3,8-triazaspiro[4.5]decane-8-carboxylate (0.197 mmol, 77 mg) and DIPEA (0.394 mmol, 0.069 mL) in dry DCM (3 mL), trifluoroacetic anhydride (0.256 mmol, 0.036 mL) was added and the resulting mixture stirred for 1 h at 0 °C. After completion, the reaction mixture was diluted with DCM (5 mL) and partitioned with a saturated solution of $NaHCO_3$ (3 x 5 mL). Organic layer was dried over Na_2SO_4 and evaporated under reduced pressure and the crude material purified by neutral alumina liquid chromatography eluting with PE/EtOAc (1:1 v/v) affording compound **7** with 18% yield (17 mg).

MS (ESI) m/z calc. $[M+H]^+$ for $C_{24}H_{25}F_3N_5O_2^+$: 472.20; found: 472.3

^{1}H NMR (400 MHz, MeOD) δ 8.11 (d, J = 8.4 Hz, 1H), 7.71 (d, J = 7.9 Hz, 1H), 7.54 – 7.46 (m, 2H), 7.23 – 7.18 (m, 2H), 6.95 (d, J = 9.1 Hz, 2H), 6.86 – 6.80 (m, 1H), 4.69 – 4.63 (m, 4H), 3.03 – 2.92 (m, 2H), 2.86 – 2.78 (m, 2H), 2.67 – 2.55 (m, 2H), 2.35 (d, J = 4.6 Hz, 3H), 1.81 – 1.70 (m, 2H).

^{13}C NMR (101 MHz, MeOD) δ 176.08, 170.23, 167.09 (d, J = 44.2 Hz), 144.27, 143.12, 142.07, 133.87, 129.74 (d, J = 86.4 Hz), 125.96, 121.14, 118.20, 64.67, 61.29, 52.60, 46.07, 45.19, 30.00.

8-benzyl-1-phenyl-3-(4-(5-(trifluoromethyl)-1,2,4-oxadiazol-3-yl)benzyl)-1,3,8-triazaspiro[4.5]decan-4-one (8). *Step 1:* To a solution of compound **6** (0.272 mmol, 119 mg) in EtOH at 25 °C, 50% aqueous hydroxylamine solution (1.09 mmol, 0.067 mL) was added dropwise, and the reaction mixture was heated at reflux and left under stirring for 18 h. After the time reaction had elapsed, the reaction mixture was concentrated under reduced pressure to obtain the desired product *4-((8-benzyl-4-oxo-1-phenyl-1,3,8-triazaspiro[4.5]decan-3-yl)methyl)-N-hydroxybenzimidamide* with a quantitative yield (128 mg).

Step 2: to a cooled solution of tert-butyl 4-((8-benzyl-4-oxo-1-phenyl-1,3,8-triazaspiro[4.5]decan-3-yl)methyl)-N-hydroxybenzimidamide (0.224 mmol, 105

mg) and DIPEA (0.448 mmol, 0.078 mL) in dry DMF (1 mL), trifluoroacetic anhydride (0.291 mmol, 0.041 mL) was added and the resulting mixture stirred for 18 h at 0 °C. After completion, the reaction mixture was diluted with distilled water (5 mL) and extracted with DCM (5 ML). Organic layer was partitioned with a distilled water (3 x 5 mL), dried over Na_2SO_4 and evaporated under reduced pressure. Crude material purified by neutral alumina liquid chromatography eluting with PE/EtOAc (3:1 v/v), affording desired compound **8** with 13% yield (17 mg).

MS (ESI) m/z calc. $[M+H]^+$ for $C_{30}H_{29}F_3N_5O_2^+$: 548.23; found: 548.2

^{1}H NMR (400 MHz, MeOD) δ 8.14 (d, J = 7.9 Hz, 2H), 7.55 (d, J = 8.2 Hz, 2H), 7.42 – 7.29 (m, 5H), 7.27 – 7.21 (m, 2H), 7.00 (d, J = 7.9 Hz, 2H), 6.86 (t, J = 7.4 Hz, 1H), 4.71 (s, 2H), 4.68 (s, 2H), 3.71 (s, 2H), 3.13 – 3.01 (m, 2H), 2.97 – 2.89 (m, 2H), 2.69 – 2.56 (m, 2H), 1.84 – 1.76 (m, 2H).

^{13}C NMR (101 MHz, MeOD) δ 174.73, 168.83, 165.68 (q, J_{C-F} = 134.4 Hz), 142.91, 140.66, 129.66, 128.34 (d, J = 90.4 Hz), 128.09, 127.46, 124.55, 119.83, 116.90, 63.30, 62.37, 60.48, 49.08, 43.88, 28.56.

tert-butyl 3-(4-(hydrazinecarbonyl)benzyl)-4-oxo-1-phenyl-1,3,8-triazaspiro[4.5]decane-8-carboxylate (11a). To a solution of intermediate **9a** (0.42 mmol, 200 mg) in MeOH (8 mL), hydrazine monohydrate (21 mmol, 1 mL) was added and the resulting mixture allowed under stirring at 80 °C. After 18 h,, the reaction mixture was cooled down to 25 °C and concentrated under reduced pressure to afford compound **11a** with 90% yield (180 mg).

^{1}H NMR (400 MHz, $CDCl_3$) δ 7.75 (d, J = 8.1 Hz, 2H), 7.37 (d, J = 8.0 Hz, 2H), 7.21 (t, J = 7.8 Hz, 2H), 6.84 (t, J = 7.3 Hz, 1H), 6.69 (d, J = 8.5 Hz, 2H), 4.66 (s, 2H), 4.57 (s, 2H), 4.10 (br, 2H), 3.92 (br, 1H), 3.61 (br, 2H), 2.56 (br, 2H), 1.66 (d, J = 12.4 Hz, 2H), 1.52 (s, 9H).

tert-butyl 3-(2-fluoro-4-(hydrazinecarbonyl)benzyl)-4-oxo-1-phenyl-1,3,8-triazaspiro[4.5]decane-8-carboxylate (11b). To a solution of intermediate **9b**

(0.42 mmol, 200 mg) in MeOH (8 mL), hydrazine monohydrate (21 mmol, 1 mL) was added and the resulting mixture allowed under stirring at 80 °C. After 18 h, the reaction mixture was cooled down to 25 °C and concentrated under reduced pressure to afford compound **11b** with 90% yield (180 mg).

^{1}H NMR (400 MHz, $CDCl_3$) δ 7.75 (d, J = 8.1 Hz, 2H), 7.37 (d, J = 8.0 Hz, 2H), 7.21 (t, J = 7.8 Hz, 2H), 6.84 (t, J = 7.3 Hz, 1H), 6.69 (d, J = 8.5 Hz, 2H), 4.66 (s, 2H), 4.57 (s, 2H), 4.10 (br, 2H), 3.92 (br, 1H), 3.61 (br, 2H), 2.56 (br, 2H), 1.66 (d, J = 12.4 Hz, 2H), 1.52 (s, 9H).

4-((8-benzyl-4-oxo-1-phenyl-1,3,8-triazaspiro[4.5]decan-3-yl)methyl)-3-fluorobenzohydrazide (12). To a solution of intermediate **10** (0.218 mmol, 100 mg) in MeOH (3 mL), hydrazine monohydrate (4.36 mmol, 0 211 mL) was added and the resulting mixture allowed under stirring at 80 °C. After 18 h, the reaction mixture was cooled down to 25 °C and concentrated under reduced pressure to afford compound **12** with quantitative yield (106 mg).

^{1}H NMR (400 MHz, $CDCl_3$) δ 7.56 – 7.27 (m, 20H), 6.92 – 6.83 (m, J = 14.9, 7.6 Hz, 6H), 4.69 (s, 4H), 4.62 (s, 4H), 4.20 – 3.99 (m, 3H), 2.92 – 2.73 (m, J = 11.9 Hz, 8H), 2.76 – 2.59 (m, J = 16.4, 8.5 Hz, 4H), 1.72 – 1.59 (m, J = 13.6 Hz, 7H).

tert-butyl 3-(4-(5-(difluoromethyl)-1,3,4-oxadiazol-2-yl)benzyl)-4-oxo-1-phenyl-1,3,8-triazaspiro[4.5]decane-8-carboxylate (13a). *Step 1:* To a cooled solution of **11a** (0.36mmol, 175 mg) and TEA (0.43 mmol, 0.06 mL) in dry DCM (8 mL) DFFA (0.40 mmol, 0.05 mL) was added and the mixture was stirred at 25 °C. After 12 h, saturated aqueous NH4Cl solution was added to the reaction mixture (8 mL), followed by extraction with DCM. The organic layer was washed with brine, dried over Na_2SO_4, filtered and concentrated under reduce pressure. The reaction crude was purified by silica gel liquid chromatography (PE/EtOAc 7:3 v/v), affording tert-butyl 3-(4-(2-(2,2-difluoroacetyl)hydrazine-

1-carbonyl)benzyl)-4-oxo-1-phenyl-1,3,8-triazaspiro[4.5]decane-8-carboxylate, as a colorless oil, with 70% yield (140 mg).

MS (ESI) m/z calc. $[M+H]^+$ for $C_{28}H_{33}F_2N_5O_5^+$: 557.2; found: 558.5.

^{1}H NMR (400 MHz, CDCl3) δ 9.27 (br, 1H), 8.83 (br, 1H), 7.85 (d, J = 8.3 Hz, 2H), 7.40 (d, J = 8.2 Hz, 2H), 7.21 (dd, J = 8.6, 7.4 Hz, 2H), 6.84 (t, J = 7.3 Hz, 1H), 6.70 (d, J = 8.0 Hz, 2H), 6.08 (t, J = 53.5 Hz, 1H), 4.67 (s, 2H), 4.58 (s, 2H), 4.12 (br, 2H), 3.59 (br, 2H), 2.56 (br, 2H), 1.66 (d, J = 12.7 Hz, 2H), 1.53 (s, 9H).

Step 2: title compound *tert-butyl 3-(4-(2-(2,2-difluoroacetyl)hydrazine-1-carbonyl)benzyl)-4-oxo-1-phenyl-1,3,8-triazaspiro[4.5]decane-8-carboxylate* (140 mg) was dissolved in dry DMF (3 mL) and treated with Burgess reagent (0.753 mmol, 180 mg). After 2 h, reaction was stopped by adding distilled water (10 mL) and extracted with DCM (10 mL). Organic layer partitioned with distilled water (3 x 10 mL), dried over Na_2SO_4, filtered and concentrated under reduce pressure. Crude material was purified by silica gel liquid chromatography eluting with PE/EtOAc (2:1 v/v) affording title compound **29a** with 23% yield (45 mg).

MS (ESI) m/z calc. $[M+H]^+$ for $C_{28}H_{32}F_2N_5O_4^+$: 540.24; found: 540.5.

^{1}H NMR (400 MHz, CDCl3) δ 8.13 (d, J = 8.2 Hz, 2H), 7.49 (d, J = 10.7 Hz, 2H), 7.25 – 7.18 (m, 2H), 7.09 – 6.76 (t, 1H), 6.85 (t, J = 7.3 Hz, 1H), 6.71 (d, J = 8.3 Hz, 2H), 4.70 (s, 2H), 4.61 (s, 2H), 4.10 (br, 2H), 3.61 (br, 2H), 2.58 (br, 2H), 1.68 (d, J = 13.6 Hz, 2H), 1.52 (s, 9H).

^{13}C NMR (101 MHz, MeOD) δ 176.18, 167.24, 160.19 (t, J = 29.6 Hz), 156.88, 144.08, 142.62, 130.32, 130.05, 129.01, 123.59, 120.89, 117.31, 107.92 (t, J = 239.1 Hz), 81.32, 64.61, 62.02, 45.25, 30.76, 28.71.

tert-butyl 3-(4-(5-(difluoromethyl)-1,3,4-oxadiazol-2-yl)-2-fluorobenzyl)-4-oxo-1-phenyl-1,3,8-triazaspiro[4.5]decane-8-carboxylate (13b). To a cooled solution of **11b** (0.200 mmol, 100 mg) in dry DCM (2 mL), TEA (1 mmol, 0.140 mL) and DFAA (1 mmol, 0.125 mL) were added and the reaction mixture

allowed under stirring at 25 °C. After 1 h, a saturated solution of NH4Cl was added to the reaction mixture and extracted with DCM. Organic layer was extracted with brine, dried over dried over Na_2SO_4 and evaporated under reduced pressure. Crude material purified by neutral alumina liquid chromatography eluting with DCM, DCM/MeOH (99.5/0.5 – 9:1 v/v), affording desired compound **13b** with 30% yield (27 mg).

MS (ESI) m/z calc. $[M+H]^+$ for $C_{28}H_{31}F_3N_5O_4^+$: 558.23; found:. $[M\text{-}Boc+H]^+$ 458.2

^1H NMR (400 MHz, $CDCl_3$) δ 7.86 (dd, J = 7.9, 1.7 Hz, 1H), 7.80 (dd, J = 9.8, 1.7 Hz, 1H), 7.47 (t, J = 7.6 Hz, 1H), 7.19 – 7.13 (m, 2H), 6.87 (t, J = 51.7 Hz, 1H), 6.79 (t, J = 6.8 Hz, 1H), 6.68 – 6.63 (m, 2H), 4.68 (s, 2H), 4.60 (s, 2H), 4.09 – 3.84 (m, 2H), 3.62 – 3.44 (m, 2H), 2.54 – 2.34 (m, 2H), 1.64 – 1.53 (m, 10H), 1.44 (s, 9H).

^{13}C NMR (101 MHz, $CDCl_3$) δ 174.57, 162.33, 159.86, 158.62 (t, J = 29.4 Hz), 155.27, 142.58, 131.51, 131.47, 129.51, 127.99, 127.84, 124.50, 124.41, 124.01, 123.97, 115.49, 115.10, 114.86, 105.82 (t, J = 241.3 Hz), 79.86, 63.38, 60.72, 38.44, 29.85, 29.19, 28.60.

8-benzyl-3-(4-(5-(difluoromethyl)-1,3,4-oxadiazol-2-yl)-2-fluorobenzyl)-1-phenyl-1,3,8-triazaspiro[4.5]decan-4-one (14). *Step 1:* To a cooled solution of **12** (0.088 mmol, 43 mg) and TEA (0.43 mmol, 0.06 mL) in dry DCM (2 mL) DFFA (0.40 mmol, 0.05 mL) was added and the mixture was stirred at 25 °C. After 12 h, sutured aqueous NH_4Cl solution was added to the reaction mixture (4 mL), followed by extraction with DCM. The organic layer was washed with brine, dried over Na_2SO_4, filtered and concentrated under reduce pressure affording *4-((8-benzyl-4-oxo-1-phenyl-1,3,8-triazaspiro[4.5]decan-3-yl)methyl)-N'-(2,2-difluoroacetyl)-3-fluorobenzohydrazide* in quantitative yield. *Step 2:* title compound *4-((8-benzyl-4-oxo-1-phenyl-1,3,8-triazaspiro[4.5]decan-3-yl)methyl)-N'-(2,2-difluoroacetyl)-3-*

fluorobenzohydrazide (0.360 mmol, 200 mg) was dissolved in dry DCM (3 mL) and treated with Burgess reagent (1.08 mmol, 149 mg). After 12 h, reaction was stopped by adding distilled water (10 mL) and extracted with DCM (10 mL). The organic layer was washed with brine, dried over Na_2SO_4, filtered and concentrated under reduce pressure. The reaction crude was purified by neutral alumina liquid chromatography eluting with PE/EtOAc (3:1 v/v), affording the title compound **14** with 23% yield (45 mg).

MS (ESI) m/z calc. $[M+H]^+$ for $C_{30}H_{29}F_3N_5O_2^+$: 548.23; found: 548.3

^{1}H NMR (400 MHz, CDCl3) δ 7.92 (dd, *J* = 7.9, 1.7 Hz, 1H), 7.86 (dd, *J* = 9.8, 1.7 Hz, 1H), 7.54 (t, *J* = 7.6 Hz, 1H), 7.42 – 7.27 (m, 7H), 6.91 (t, *J* = 103.3 Hz, 1H), 6.93 – 6.83 (m, 3H), 4.73 (s, 2H), 4.66 (s, 2H), 3.63 (s, 2H), 2.86 (s, 4H), 2.69 (s, 2H).

tert-butyl 3-benzyl-4-oxo-1-phenyl-1,3,8-triazaspiro[4.5]decane-8-carboxylate (15). To a stirring solution of **1** (1.51 mmol, 500 mg) in dry THF (10 mL) NaH (60% mineral oil dispersion, 1.51 mmol, 54 mg) was added and the reaction mixture allowed under stirring for 30 min. Benzyl bromide (1.51 mmol, 0.180 mmol). After completion, THF was evaporated under vacuum, the crude residue dissolved in EtOAc (10 mL) and partitioned with a saturated solution of $NaHCO_3$ (10 mL x 3). Organic layer was collected, dried over Na_2SO_4 and evaporated under reduced pressure. The crude material was purified with silica gel liquid chromatography (PE/EtOAc 3:1 to 1:1 v/v) affording desired compound **15** with 56% yield (360 mg).

^{1}H NMR (400 MHz, CDCl3) δ 7.40-7.26 (m, 5H), 7.20 (d, 2H), 6.81 (t, J = 7.3, 1.1 Hz, 1H), 6.68 (d, 2H), 4.61 (s, 2H), 4.56 (s, 2H), 4.31-3.86 (m, 2H), 3.80-3.39 (m, 2H), 1.66 (d, J =13.5 Hz, 2H), 1.52 (s, 9H).

methyl 4-((3-benzyl-4-oxo-1-phenyl-1,3,8-triazaspiro[4.5]decan-8-yl)methyl)-3-fluorobenzoate (16). *Step 1:* To a stirred solution of the corresponding Boc protected amine **15** (0.854 mmol, 360 mg) in DCM (5 mL), 4

M HCl in dioxane was added (4 mL) and the resulting solution allowed to stir at 25 °C. After 1 h, the reaction mixture was concentrated under vacuum, the residue was dissolved in EtOAc and washed with $NaHCO_3$ saturated solution for three times. Organic layer was dried over Na_2SO_4 and evaporated under reduced pressure. The obtained deprotected amine was used in the next synthetic step without further purification. *Step 2:* a solution of *3-benzyl-1-phenyl-1,3,8-triazaspiro[4.5]decan-4-one* (0.854 mmol) in dry DMF (1 mL) was treated with anhydrous potassium carbonate (1.66 mmol, 229 mg). After 15 min, methyl 4-(bromomethyl)-3-fluorobenzoate (0.854 mmol, 205 mg) was added and the resulting mixture stirred at 80 °C for 18 h. Reaction was stopped by adding distilled water (5 mL) and extracted with EtOAc (10 mL). Organic layer was collected, partitioned wit distilled water (3 x 10 mL), dried over Na_2SO_4 and evaporated under reduced pressure. Crude material was purified by silica gel liquid chromatography eluting with (PE/EtOAc 3:2 v/v), affording compound **32** with 90% yield (375 mg).

^{1}H NMR (400 MHz, CDCl3) δ 7.83 (d, J = 7.8 Hz, 1H), 7.70 (d, J = 10.3 Hz, 1H), 7.58 (t, J = 8.2 Hz, 1H), 7.37-7.27 (m, 7H), 6.85 (d, J = 8.3 Hz, 3H), 4.59 (s, 2H), 4.54 (d, J = 3.3 Hz, 2H), 3.92 (d, J= 3.4 Hz, 3H), 3.73 (s, 2H), 3.04-2.63 (m, 6H), 1.70 ((d, J = 13.6 Hz, 2H).

3-benzyl-8-(4-(5-(difluoromethyl)-1,3,4-oxadiazol-2-yl)-2-fluorobenzyl)-1-phenyl-1,3,8-triazaspiro[4.5]decan-4-one (17). *Step 1:* To a solution of intermediate **32** (0.172 mmol, 84 mg) in MeOH (2 mL), hydrazine monohydrate (8.61 mmol, 0.418 mL) was added and the resulting mixture allowed under stirring at 80 °C. After 18 h, the reaction mixture was cooled down to 25 °C and concentrated under reduced pressure to afford title compound 4-((3-benzyl-4-oxo-1-phenyl-1,3,8-triazaspiro[4.5]decan-8-yl)methyl)-3-fluorobenzohydrazide with quantitative yield (83 mg).

^{1}H NMR (400 MHz, $CDCl_3$) δ 7.45 – 7.40 (m, 1H), 7.32 – 7.23 (m, 5H), 7.22 – 7.15 (m, 5H), 6.81 – 6.74 (m, 2H), 4.52 (s, 2H), 4.48 (s, 2H), 3.66 (s, 2H), 2.99 – 2.87 (m, 2H), 2.81 – 2.71 (m, 2H), 2.69 – 2.60 (m, 2H), 1.63 (d, J = 13.9 Hz, 2H).

Step 2: To a cooled solution of 4-((3-benzyl-4-oxo-1-phenyl-1,3,8-triazaspiro[4.5]decan-8-yl)methyl)-3-fluorobenzohydrazide (0.170 mmol, 83 mg) and TEA (0.851 mmol, 0.118 mL) in dry DCM (4 mL) DFFA (0.765 mmol, 0.097 mL) was added and the mixture was stirred at 25 °C. After 3 h, Burgess reagent was added (0.510 mmol, 122 mg) and the resulting mixture allowed under stirring for 12 h. Sutured aqueous NH_4Cl solution was added to the reaction mixture (4 mL), followed by extraction with DCM. The organic layer was washed with brine, dried over Na_2SO_4, filtered and concentrated under reduce pressure. Crude material was purified by neutral alumina liquid chromatography (PE/EtOAc 3:1 – 1:1 v/v) affording desired compound 33 with 20% yield (19 mg).

MS (ESI) m/z calc. $[M+H]^+$ for $C_{30}H_{29}F_3N_5O_2^+$: 548.23; found: 548.3

^{1}H NMR (400 MHz, $CDCl_3$) δ 7.45 – 7.40 (m, 1H), 7.32 – 7.23 (m, 5H), 7.22 – 7.15 (m, 5H), 6.81 – 6.74 (m, 2H), 4.52 (s, 2H), 4.48 (s, 2H), 3.66 (s, 2H), 2.99 – 2.87 (m, 2H), 2.81 – 2.71 (m, 2H), 2.69 – 2.60 (m, 2H), 1.63 (d, J = 13.9 Hz, 2H).

^{13}C NMR (176 MHz, $CDCl_3$) δ 173.39, 164.28, 160.97, 159.56, 157.23 (t, J = 29.0 Hz), 141.85, 134.58, 131.00 (d, J = 5.0 Hz), 130.21 (d, J = 14.6 Hz), 128.23, 127.95, 127.00, 126.87, 122.07 (d, J = 3.8 Hz), 121.74 (d, J = 8.9 Hz), 117.87, 114.13, 113.44, 113.29, 104.73 (t, J = 241.0 Hz), 61.92, 59.33, 53.94, 48.70, 43.69, 29.94, 28.43.

tert-butyl 3-oxo-1-thia-4,8-diazaspiro[4.5]decane-8-carboxylate (19). To a suspension of $(NH_4)_2CO_3$ (1.45 g, 15.05 mmol) in a solution of Boc-piperidone (**18**, 2.00 g, 10.04 mmol) in toluene, thioglycolic acid (1 mL, 15.06 mmol) was

added. The reaction mixture was stirred at reflux. After 48 h, toluene was evaporated under vacuum and the reaction crude purified by Agilent® flash chromatography (Hex/EtOAc 1:1 v/v), providing compound **19** with 88% yield (1.2 g).

MS (ESI) m/z calc. $[M+H]^+$ for $C_{12}H_{21}N_2O_3S^+$: 273.13; found: 272.9

^{1}H NMR (400 MHz, CDCl3) δ 7.75 (bs, 1H), 3.95 – 3.81 (m, 2H), 3.58 (s, 2H), 3.22 – 3.10 (m, 2H), 1.98 – 1.84 (m, 4H), 1.45 (s, 9H).

tert-butyl 4-(4-(methoxycarbonyl)benzyl)-3-oxo-1-thia-4,8-diazaspiro[4.5]decane-8-carboxylate (20a). Compound **19** (500 mg, 1.83 mmol) was dissolved in dry THF (3 mL) and NaH (65.76 mg, 2.74 mmol, 60% dispersion oil) was added. The reaction mixture was stirred at 25 °C for 30 minutes. Methyl 4-(bromomethyl) benzoate was added, and the reaction mixture stirred at 25 °C. After 48 h, solvent was evaporated under vacuum, the residue dissolved in EtOAc (15 mL) and extracted three times with $NaHCO_3$ (15 mL). The organic phase was dried over Na_2SO_4, filtered, and concentrated under vacuum. The crude reaction mixture was purified by silica gel liquid chromatography (PE/EtOAc 3:1 to 1:1 v/v), affording the product **20a** in 41% yield (317 mg).

^{1}H NMR (400 MHz, $CDCl_3$) δ 7.96 – 7.87 (m, 2H), 7.25 (d, J = 8.0 Hz, 2H), 4.53 (s, 2H), 3.84 (s, 3H), 3.61 (s, 2H), 2.86 (t, J = 13.1 Hz, 2H), 1.85 (s, 2H), 1.57 (d, J = 12.7 Hz, 2H), 1.37 (s, 9H).

tert-butyl 4-(2-fluoro-4-(methoxycarbonyl)benzyl)-3-oxo-1-thia-4,8-diazaspiro[4.5]decane-8-carboxylate (20b). Compound **19** (600 mg, 2.20 mmol) was dissolved in dry THF (2 mL) and NaH (120 mg, 5 mmol, 60% dispersion oil) was added. The reaction mixture was stirred at 25 °C for 30 minutes. Methyl 4-(bromomethyl)-3-fluorobenzoate (600 mg, 2.42 mmol) was added, and the reaction mixture stirred at 25 °C. After 48 h, solvent was evaporated under vacuum, the residue dissolved in EtOAc (15 mL) and extracted

three times with NaHCO3 (15 mL). The organic phase was dried over Na2SO4, filtered, and concentrated under vacuum. The crude reaction mixture was purified by silica gel liquid chromatography (PE/EtOAc 2:1 v/v), affording the product **20b** in 42% yield (411 mg).

^{1}H NMR (600 MHz, $CDCl_3$) δ 7.76 (d, J = 1.6 Hz, 1H), 7.68 (d, J = 1.6 Hz, 1H), 7.34 (t, J = 7.7 Hz, 1H), 4.61 (s, 2H), 3.90 (s, 3H), 3.66 (s, 2H), 2.97 – 2.87 (m, 2H), 1.95 – 1.84 (m, 2H), 1.42 (s, 9H).

tert-butyl 4-(4-(hydroxycarbamoyl)benzyl)-3-oxo-1-thia-4,8-diazaspiro[4.5]decane-8-carboxylate (21a). Compound 21a was prepared following the genral procedure for the synthesis of hydroxamic acids starting from **20a** (90 mg, 0.214 mmol) with 33% yield (30 mg).

MS (ESI) m/z calc. $[M+H]^+$ for $C_{20}H_{28}N_3O_5S^+$: 422.17; found: $[M – Boc + H]^+$ 322.1

^{1}H NMR (400 MHz, DMSO) δ 7.69 (d, J = 8.1 Hz, 2H), 7.30 (d, J = 8.1 Hz, 2H), 4.59 (s, 2H), 4.03 – 3.89 (m, 2H), 3.71 (s, 2H), 2.90 – 2.73 (m, 2H), 1.96 (td, J = 12.8, 4.6 Hz, 2H), 1.61 (d, J = 12.5 Hz, 2H), 1.37 (s, 9H).

^{13}C NMR (101 MHz, DMSO) δ 171.67, 164.31, 154.04, 141.84, 132.23, 127.33, 127.14, 79.65, 79.55, 72.26, 44.30, 36.93, 31.17, 30.65, 29.49, 28.50.

tert-butyl 4-(2-fluoro-4-(hydroxycarbamoyl)benzyl)-3-oxo-1-thia-4,8-diazaspiro[4.5]decane-8-carboxylate (21b). Compound **21b** was prepared following the general procedure for the synthesis of hydroxamic acids starting from intermediate **20b** (70 mg, 0.160 mmol) with 36% yield (25 mg).

MS (ESI) m/z calc. $[M+H]^+$ for $C_{20}H_{27}FN_3O_5S^+$: 440.17; found: $[M – Boc + H]^+$ 340.2

^{1}H NMR (600 MHz, DMSO) δ 11.26 (bs, 1H), 9.12 (bs, 1H), 7.56 (d, J = 8.1 Hz, 1H), 7.52 (d, J = 10.9 Hz, 1H), 7.28 (t, J = 7.8 Hz, 1H), 4.58 (s, 2H), 4.05 – 3.93 (m, 2H), 3.71 (s, 2H), 2.94 – 2.74 (m, 2H), 1.96 (td, J = 12.7, 4.7 Hz, 2H), 1.69 (d, J = 12.7 Hz, 2H), 1.38 (s, 9H).

^{13}C NMR (151 MHz, DMSO) δ 171.26, 162.50, 159.15 (d, J = 245.3 Hz), 153.54, 151.97, 133.60, 128.61, 127.97, 122.86, 113.69, 113.54, 71.57, 40.06, 38.19, 36.20, 30.06, 27.98, 21.34, 14.50.

methyl 4-((3-oxo-1-thia-4,8-diazaspiro[4.5]decan-4-yl)methyl)benzoate (22a). To a solution of compound **20a** (0.426 mmol, 180 mg) in DCM, a solution of 4 N HCl in dioxane (1 mL) was added and the reaction mixture was stirred at 25 °C for 1 h. Upon completion, the reaction mixture was quenched with saturated aqueous $NaHCO_3$ and extracted with DCM (3 x 5 mL). Combined organic phases were washed with brine (10 mL), dried over Na_2SO_4, filtered, and concentrated under vacuum, affording compound **22a** in quantitative yield.

MS (ESI) m/z calc. $[M+H]^+$ for $C_{16}H_{21}N_2O_3S^+$: 321.13; found: 321.2

^{1}H NMR (400 MHz, $CDCl_3$) δ 7.97 (d, 2H), 7.33 (d, J = 8.3 Hz, 2H), 4.63 (s, 2H), 3.90 (s, 3H), 3.65 (s, 2H), 3.06 – 2.99 (m, 2H), 2.89 – 2.80 (m, 2H), 2.02 – 1.92 (m, 2H), 1.69 – 1.61 (m, 2H).

tert-butyl 4-(2-fluoro-4-(methoxycarbonyl)benzyl)-3-oxo-1-thia-4,8-diazaspiro[4.5]decane-8-carboxylate (22b). To a solution of compound **20b** (311 mg, 0.709 mmol) in DCM (3 mL), a solution of 4 N HCl in dioxane (2.65 mL) was added and the reaction mixture was stirred at 25 °C for 1 h. Upon completion, the reaction mixture was quenched with saturated aqueous $NaHCO_3$ and extracted with DCM (3 x 5 mL). Combined organic phases were washed with brine (10 mL), dried over Na_2SO_4, filtered, and concentrated under vacuum, affording compound **38b** in quantitative yield.

methyl 4-((8-methyl-3-oxo-1-thia-4,8-diazaspiro[4.5]decan-4-yl)methyl)benzoate (23a). To a solution of compound **22a** (100 mg, 0.312 mmol) in MeOH, a catalytic amount of acetic acid was added followed by paraformaldehyde (310 mg), and the resulting mixture allowed to stir at 25 °C. After 1 h, $NaBH_3CN$ (31 mg, 0.498 mmol) was added and the reaction mixture was stirred for 18 h at 25 °C. MeOH was evaporated under vacuum, the obtained

residue was dissolved in EtOAc (5 mL) and washed three times with $NaHCO_3$ (5 mL). The organic phase was dried over Na_2SO_4, filtered, and concentrated under vacuum. The crude reaction mixture was purified by silica gel liquid chromatography (DCM/MeOH 98:2 to 97:3 v/v), affording product **23a** in 50% yield (52 mg).

^{1}H NMR (400 MHz, $CDCl_3$) δ 7.91 (d, 1H), 7.26 (d, 1H), 4.55 (s, 1H), 3.83 (s, 2H), 3.59 (s, 1H), 2.72 (d, J = 1.8 Hz, 1H), 2.21 – 2.01 (m, 4H), 1.57 (d, 1H).

methyl 3-fluoro-4-((8-methyl-3-oxo-1-thia-4,8-diazaspiro[4.5]decan-4-yl)methyl)benzoate (23b). To a solution of compound **22b** (80 mg, 0.236 mmol) in MeOH, a catalytic amount of acetic acid was added followed by paraformaldehyde (142 mg), and the resulting mixture allowed to stir at 25 °C. After 1 h, $NaBH_3CN$ (24 mg, 0.378 mmol) was added and the reaction mixture was stirred for 18 h at 25 °C. MeOH was evaporated under vacuum, the obtained residue was dissolved in EtOAc (5 mL) and washed three times with $NaHCO_3$ (5 mL). The organic phase was dried over Na_2SO_4, filtered, and concentrated under vacuum. The crude reaction mixture was purified by silica gel liquid chromatography (DCM/MeOH 98:2 v/v), affording product **23b** in 84% yield (70 mg).

^{1}H NMR (500 MHz, $CDCl_3$) δ 7.76 (d, J = 1.6 Hz, 1H), 7.67 (d, J = 1.6 Hz, 1H), 7.32 (t, J = 7.7 Hz, 1H), 4.66 (s, 2H), 3.89 (s, 3H), 3.65 (s, 2H), 3.04 – 2.93 (m, 2H), 2.54 – 2.29 (m, 7H), 1.75 – 1.66 (m, 2H).

methyl 4-((8-benzyl-3-oxo-1-thia-4,8-diazaspiro[4.5]decan-4-yl)methyl)benzoate (24a). To a solution of compound **22a** (120 mg, 0.375 mmol) in MeOH, a catalytic amount of acetic acid was added followed by benzaldehyde (0.056 mL, 0.562 mmol), and the resulting mixture allowed to stir at 25 °C. After 1 h, $NaBH_3CN$ (37.70 mg, 0.6 mmol) was added and the reaction mixture was stirred 18 h at 25 °C. MeOH was evaporated under vacuum, the obtained residue dissolved in ethyl acetate (10 mL) and washed three times with

$NaHCO_3$ (10 mL). The organic phase was dried over Na_2SO_4, filtered, and concentrated under vacuum. The crude reaction mixture was purified by silica gel liquid chromatography (DCM/MeOH 98:2 v/v), affording product **24a** in 85% yield (110 mg).

^1H NMR (400 MHz, $CDCl_3$) δ 7.90 (d, 2H), 7.32 – 7.10 (m, 7H), 4.55 (s, 2H), 3.82 (s, 3H), 3.40 (s, 2H), 2.75 (d, J = 2.0 Hz, 2H), 2.23 – 2.10 (m, 2H), 2.08 – 1.94 (m, 2H), 1.55 (d, J = 2.8 Hz, 2H).

methyl 4-((8-benzyl-3-oxo-1-thia-4,8-diazaspiro[4.5]decan-4-yl)methyl)-3-fluorobenzoate (24b). To a stirring solution of compound **22b** (80 mg, 0.236 mmol) in MeOH, a catalytic amount of acetic acid was added followed by benzaldehyde (0.036 mL, 0.354 mmol) and the resulting mixture allowed to stir at 25 °C. After 1 h, $NaBH_3CN$ (24 mg, 0.378 mmol) was added and the reaction mixture was stirred 18 h at 25 °C. MeOH was evaporated under vacuum, the obtained residue was dissolved in ethyl acetate (5 mL) and washed three times with $NaHCO_3$ (5 mL). The organic phase was dried over Na_2SO_4, filtered, and concentrated under vacuum. The crude reaction mixture was purified by silica gel liquid chromatography (DCM/MeOH 98:2 v/v) affording product **24b** in 69% yield (70 mg).

^1H NMR (500 MHz, CDCl3) δ 7.74 (dd, J = 8.0, 1.6 Hz, 1H), 7.67 (dd, J = 10.5, 1.6 Hz, 1H), 7.46 – 7.39 (m, 1H), 7.37 – 7.26 (m, 5H), 4.66 (s, 2H), 3.88 (s, 3H), 3.63 (s, 2H), 3.59 – 3.42 (m, 1H), 2.99 – 2.75 (m, 2H), 2.41 – 1.99 (m, 3H), 1.71 – 1.64 (m, 2H).

N-hydroxy-4-((8-methyl-3-oxo-1-thia-4,8-diazaspiro[4.5]decan-4-yl)methyl)benzamide (25a). Compound **25a** was prepared following the general procedure for the synthesis of hydroxamic acids starting from intermediate **23a** (0.102 mmol, 43 mg) with 40% yield (14 mg).

MS (ESI) m/z calc. $[M+H]^+$ for $C_{16}H_{22}N_3O_3S^+$: 336.14; found: 336.2

^{1}H NMR (400 MHz, DMSO) δ 11.16 (bs, 1H), 9.00 (bs, 1H), 7.68 (d, J = 8.5 Hz, 2H), 7.35 – 7.29 (m, 2H), 4.57 (s, 2H), 3.67 (s, 2H), 2.75 – 2.69 (m, 2H), 2.13 (s, 3H), 2.10 – 2.00 (m, 4H), 1.59 – 1.50 (m, 2H).

^{13}C NMR (101 MHz, DMSO) δ 171.27, 163.87, 141.65, 131.61, 126.92, 126.75, 71.57, 52.23, 45.41, 43.89, 36.77, 30.69, 30.26.

3-fluoro-N-hydroxy-4-((8-methyl-3-oxo-1-thia-4,8-diazaspiro[4.5]decan-4-yl)methyl)benzamide (25b). Compound **25b** was prepared following the general procedure for the synthesis of hydroxamic acids starting from intermediate **23b** (0.199 mmol, 70 mg) with 53% yield (37 mg).

^{1}H NMR (500 MHz, DMSO) δ 11.26 (bs, 1H), 9.11 (bs, 1H), 7.61 – 7.45 (m, 2H), 7.29 (t, J = 7.8 Hz, 1H), 4.55 (s, 2H), 3.66 (s, 2H), 2.78 – 2.69 (m, 2H), 2.14 (s, 3H), 2.10 – 2.02 (m, 4H), 1.68 – 1.60 (m, 2H).

^{13}C NMR (126 MHz, DMSO) δ 171.53, 162.66, 159.28 (d, J = 245.4 Hz), 128.90, 123.05, 113.91, 71.44, 52.31, 45.47, 38.19, 36.62, 30.31, 21.51, 14.66.

4-((8-benzyl-3-oxo-1-thia-4,8-diazaspiro[4.5]decan-4-yl)methyl)-N-hydroxybenzamide (26a). Compound **26a** was prepared following the general procedure for the synthesis of hydroxamic acids starting from intermediate **24a** (0.267 mmol, 110 mg) with 60% yield (66 mg).

MS (ESI) m/z calc. $[M+H]^+$ for $C_{22}H_{26}N_3O_3S^+$: 412.17; found: 412.2

^{1}H NMR (400 MHz, DMSO) δ 11.16 (bs, 1H), 9.00 (bs, 1H), 7.70 (d, J = 8.4 Hz, 2H), 7.39 – 7.15 (m, 7H), 4.60 (s, 2H), 3.67 (s, 2H), 3.45 (s, 2H), 2.78 (d, J = 10.6 Hz, 2H), 2.22 – 2.02 (m, 4H), 1.59 (d, J = 11.4 Hz, 2H).

^{13}C NMR (101 MHz, DMSO) δ 171.72, 164.50, 152.48, 142.19, 138.53, 131.92, 72.44, 62.02, 50.45, 44.33, 37.35, 30.71, 21.86.

4-((8-benzyl-3-oxo-1-thia-4,8-diazaspiro[4.5]decan-4-yl)methyl)-3-fluoro-N-hydroxybenzamide (26b). Compound **26b** was prepared following the general

procedure for the synthesis of hydroxamic acids starting from intermediate **24b** (0.163 mmol, 70 mg) with 73% yield (51 mg).

MS (ESI) m/z calc. $[M+H]^+$ for $C_{22}H_{25}FN_3O_3S^+$: 430.16; found: 412.2

^{1}H NMR (500 MHz, DMSO) δ 11.25 (bs, 1H), 9.10 (bs, 1H), 7.53 (t, J = 9.2 Hz, 2H), 7.33 – 7.19 (m, 6H), 4.56 (s, 2H), 3.65 (s, 2H), 3.45 (s, 2H), 2.83 – 2.75 (m, 2H), 2.18 – 2.11 (m, 2H), 2.11 – 2.02 (m, 2H), 1.69 – 1.61 (m, 2H).

^{13}C NMR (126 MHz, DMSO) δ 171.51, 162.74, 159.29 (d, J = 242.9 Hz), 138.24, 133.75, 128.78, 127.08, 123.02, 113.90, 71.90, 61.61, 50.06, 38.32, 36.77, 30.30.

tert-butyl 4-(4-(methoxycarbonyl)benzyl)-3-oxo-1-thia-4,8-diazaspiro[4.5]decane-8-carboxylate 1,1-dioxide (27). To a stirring solution of **20a** (0.754 mmol, 317 mg) in dry DCM (4mL), *m*-CPBA was added (1.66 mmol, 287 mg) and the resulting mixture allowed under stirring at 25 °C. After 2 h, DCM was evaporated under vacuum and the crude material purified by silica gel liquid chromatography (DMC/MeOH 98:2 v/v) affording desired compound **27** with 15% yield (50 mg).

^{1}H NMR (400 MHz, $CDCl_3$) δ 7.98 – 7.87 (m, 2H), 7.22 (d, J = 8.1 Hz, 2H), 4.60 (s, 2H), 4.03 (s, 2H), 3.89 (s, 2H), 3.85 (s, 3H), 3.15 (s, 2H), 2.12 (d, 2H), 1.38 (s, 9H).

methyl 4-((8-benzyl-1,1-dioxido-3-oxo-1-thia-4,8-diazaspiro[4.5]decan-4-yl)methyl)benzoate (28). To a stirring solution of **24a** (0.168 mmol, 69 mg) in dry DCM (2 mL), *m*-CPBA was added (0.672 mmol, 116 mg) and the resulting mixture allowed under stirring at 25 °C. After 2 h, DCM was evaporated under vacuum and the crude material purified by silica gel liquid chromatography (DMC/MeOH 98:2 – 90:10 v/v) affording desired compound **28** with 81% yield (60 mg).

^{1}H NMR (400 MHz, $CDCl_3$) δ 7.93 – 7.89 (m, 2H), 7.46 – 7.40 (m, 2H), 7.39 – 7.30 (m, 3H), 7.25 (d, J = 8.0 Hz, 2H), 4.71 (s, 2H), 4.30 (s, 2H), 3.88 (s, 2H), 3.83 (s, 3H), 3.58 – 3.48 (m, 2H), 3.14 – 2.95 (m, 4H), 2.07 – 1.97 (m, 2H).

tert-butyl 4-(4-(hydroxycarbamoyl)benzyl)-3-oxo-1-thia-4,8-diazaspiro[4.5]decane-8-carboxylate 1,1-dioxide (29). Compound **29** was prepared following the general procedure for the synthesis of hydroxamic acids starting from intermediate **20a** (0.110 mmol 50 mg) with 15% yield (8 mg).

MS (ESI) m/z calc. $[M+H]^+$ for $C_{20}H_{28}N_3O_7S^+$: 454.16; found: $[M - Boc + H]^+$ 354.2

^{1}H NMR (700 MHz, DMSO) δ 11.19 (bs, 1H), 9.03 (bs, 1H), 7.71 (d, J = 8.0 Hz, 2H), 7.26 (d, J = 8.0 Hz, 2H), 4.70 (s, 3H), 4.60 (s, 2H), 4.00 – 3.93 (m, 2H), 2.61 – 2.58 (m, 1H), 2.42 – 2.38 (m, 1H), 2.23 – 2.18 (m, 2H), 1.97 – 1.90 (m, 2H), 1.38 (s, 9H).

^{13}C NMR (176 MHz, DMSO) δ 164.3, 163.8, 154.1, 141.0, 132.1, 127.5, 126.9, 79.7, 79.1, 55.4, 49.5, 42.7, 31.1, 28.4, 21.8, 21.2, 15.0, 14.5.

4-((8-benzyl-1,1-dioxido-3-oxo-1-thia-4,8-diazaspiro[4.5]decan-4-yl)methyl)-N-hydroxybenzamide (30). Compound **30** was prepared following the general procedure for the synthesis of hydroxamic acids starting from intermediate **24a** (0.090 mmol, 40 mg) with 30% yield (12 mg).

MS (ESI) m/z calc. $[M+H]^+$ for $C_{22}H_{26}N_3O_5S^+$: 444.16; found: 444.1

^{1}H NMR (400 MHz, DMSO) δ 7.68 (d, J = 8.3 Hz, 2H), 7.58 (d, J = 8.0 Hz, 2H), 7.43 – 7.34 (m, 3H), 7.24 (d, J = 8.0 Hz, 2H), 4.64 (s, 4H), 4.50 (s, 2H), 3.51 (t, J = 12.5 Hz, 2H), 3.18 – 3.12 (m, 2H), 2.81 – 2.64 (m, 2H), 2.19 (d, J = 14.5 Hz, 2H).

^{13}C NMR (101 MHz, DMSO) δ 164.21, 163.67, 140.49, 133.37, 132.37, 130.09, 129.83, 128.54, 127.61, 126.87, 76.96, 73.28, 59.48, 49.37, 43.24, 24.10.

tert-butyl 4-(4-cyano-2-fluorobenzyl)-3-oxo-1-thia-4,8-diazaspiro[4.5]decane-8-carboxylate (31). Compound **19** (0.443 mmol, 500 mg) was dissolved in dry THF (12 mL) and NaH (2.76 mmol, 90 mg, 60% dispersion oil) was added. The reaction mixture was stirred at 25 °C for 30 minutes. 4-(bromomethyl)-3-fluorobenzonitrile (2.01 mmol, 430 mg) was

added, and the reaction mixture stirred at 25 °C. After 48 h, solvent was evaporated under vacuum, the residue dissolved in EtOAc (15 mL) and extracted three times with NaHCO3 (15 mL). The organic phase was dried over Na2SO4, filtered, and concentrated under vacuum. The crude reaction mixture was purified by silica gel liquid chromatography (PE/EtOAc 3:1 to 2:1 v/v), affording the product **31** in 52% yield (344 mg).

^{1}H NMR (500 MHz, $CDCl_3$) δ 7.43 – 7.37 (m, 2H), 7.36 – 7.33 (m, 1H), 4.58 (s, 2H), 4.20 – 4.02 (m, 2H), 3.65 (s, 2H), 2.98 – 2.91 (m, 2H), 1.96 – 1.85 (m, 2H), 1.69 – 1.61 (m, 2H), 1.43 (s, 9H).

4-((8-benzyl-3-oxo-1-thia-4,8-diazaspiro[4.5]decan-4-yl)methyl)-3-fluorobenzonitrile (32*).* *Step 1:* To a solution of compound **31** (0.320 mmol, 200 mg) in DCM (3 mL), a solution of 4 N HCl in dioxane (4.3 mL) was added and the reaction mixture was stirred at 25 °C for 1 h. Upon completion, the reaction mixture was quenched with saturated aqueous $NaHCO_3$ and extracted with DCM (3 x 5 mL). Combined organic phases were washed with brine (10 mL), dried over Na2SO4, filtered, and concentrated under vacuum, affording *3-fluoro-4-((3-oxo-1-thia-4,8-diazaspiro[4.5]decan-4-yl)methyl)benzonitrile* in quantitative yield. *Step 2:* To a solution of *3-fluoro-4-((3-oxo-1-thia-4,8-diazaspiro[4.5]decan-4-yl)methyl)benzonitrile* (0.317 mmol, 97 mg) in MeOH (3 mL), a catalytic amount of acetic acid was added followed by benzaldehyde (0.317 mmol, 0.049 mL), and the resulting mixture allowed to stir at 25 °C. After 1 h, $NaBH_3CN$ (0.508 mmol, 32 mg) was added and the reaction mixture was stirred for 18 h at 25 °C. MeOH was evaporated under vacuum, the obtained residue was dissolved in EtOAc (5 mL) and washed three times with NaHCO3 (5 mL). The organic phase was dried over Na2SO4, filtered, and concentrated under vacuum. The crude reaction mixture was purified by silica gel liquid chromatography (DCM/MeOH 99:1 v/v), affording product **32** in 48% yield (60 mg).

^{1}H NMR (500 MHz, $CDCl_3$) δ 7.45 – 7.27 (m, 8H), 4.67 (s, 2H), 3.64 (s, 2H), 3.50 (s, 2H), 2.91 – 2.82 (m, 2H), 2.35 – 2.19 (m, 2H), 2.15 – 2.02 (m, 2H), 1.73 – 1.62 (m, 2H).

8-benzyl-4-(2-fluoro-4-(1H-tetrazol-5-yl)benzyl)-1-thia-4,8-diazaspiro[4.5]decan-3-one (33). To a stirring solution of **32** (0.152 mmol, 0.060 mg) in dry DMF (0.6 mL) catalytic LiCl was added, followed by NaN_3 (0.303 mmol, 20 mg), and NH_4Cl (0.197 mmol, 11 mg). The resulting mixture allowed to stir at 100 °C for 24 h, then the solvent was evaporated under vacuum and the crude residue purified by silica gel liquid chromatography (DCM/MeOH/AcOH 97:3:0.100 to 95:5:0.150 v/v) affording desired compound **33** with 99% yield (66 mg).

^{1}H NMR (500 MHz, DMSO) δ 7.85 – 7.78 (m, 2H), 7.39 (t, J = 8.0 Hz, 1H), 7.36 (d, J = 4.3 Hz, 4H), 7.33 – 7.27 (m, 1H), 4.60 (s, 2H), 3.77 (s, 2H), 3.72 (s, 2H), 3.00 (d, J = 13.7 Hz, 2H), 2.22 (td, J = 13.0, 4.1 Hz, 2H), 1.78 (d, J = 13.9 Hz, 2H).

^{13}C NMR (126 MHz, DMSO) δ 171.90, 171.35, 160.50, 158.56, 135.32, 129.55, 129.48, 129.44, 128.36, 127.80, 126.89, 126.77, 122.75, 113.42, 113.23, 70.75, 60.43, 49.56, 38.18, 35.62, 30.24, 20.99.

8-benzyl-4-(4-(5-(difluoromethyl)-1,3,4-oxadiazol-2-yl)-2-fluorobenzyl)-1-thia-4,8-diazaspiro[4.5]decan-3-one (34). To a cooled solution of tetrazole **33** (0.160 mmol, 80 mg) in dry toluene (3.2 mL) DFAA (0.482 mmol, 0.060 mL) was added. The resulting mixture was heated to 70 °C and left under stirring for 2 h. After completion, the solvent was evaporated under reduced pressure and the crude residue purified by silica gel liquid chromatography (DCM/MeOH/AcOH 99:1:0.100 to 98:2:0.100 v/v) to afford compound **34** with 35% yield (30 mg).

MS (ESI) m/z calc. $[M+H]^+$ for $C_{24}H_{24}F_3N_4O_2S^+$: 489.16; found: 489.1

^{1}H NMR (600 MHz, DMSO) δ 7.87 (s, 1H), 7.86 (d, *J* = 4.3 Hz, 1H), 7.53 (t, *J* = 50.1 Hz, 1H), 7.48 – 7.44 (m, 2H), 7.42 – 7.30 (m, 4H), 4.63 (s, 2H), 3.85 (s,

2H), 3.74 (s, 2H), 3.11 – 3.03 (m, 2H), 2.65 – 2.56 (m, 1H), 2.35 – 2.22 (m, 2H), 1.81 (d, *J* = 13.0 Hz, 2H).

^{13}C NMR (151 MHz, DMSO) δ 171.88, 165.11 – 164.45 (m), 160.77, 159.75 – 158.61 (m), 130.25, 128.90, 128.52, 123.46, 123.40, 114.40 (d, *J* = 24.8 Hz), 107.00 (t, *J* = 238.7 Hz), 70.92, 60.52, 49.85, 38.83, 35.69, 30.74.

tert-butyl 3-oxo-4-phenyl-1-thia-4,8-diazaspiro[4.5]decane-8-carboxylate (35). To a solution of aniline (3.76 mmol, 0.344 mL) and Boc piperidone (2.51 mmol, 500 mg) in toluene (13 mL) thioglycolic acid (3.76 mmol, 0.262 mL) was added and the resulting reaction mixture heated at 110 °C for 12 h. Toluene was evaporated under vacuum and the crude residue purified by silica gel liquid chromatography (PE/EtOAc 3:1 v/v) to afford compound **35** with 49% yield (420 mg).

^{1}H NMR (600 MHz, $CDCl_3$) δ 7.47 – 7.39 (m, 3H), 7.12 – 7.09 (m, 2H), 4.16 – 4.01 (m, 2H), 3.71 (s, 2H), 3.03 – 2.90 (m, 2H), 1.91 – 1.78 (m, 4H), 1.36 (s, 9H).

4-((3-oxo-4-phenyl-1-thia-4,8-diazaspiro[4.5]decan-8-yl)methyl)benzonitrile (36). *Step1:* To a solution of compound **35** (1.20 mmol, 420 mg,) in DCM (3 mL), a solution of 4 N HCl in dioxane (4.5 mL) was added and the reaction mixture was stirred at 25 °C for 1 h. Upon completion, the reaction mixture was quenched with saturated aqueous $NaHCO_3$ and extracted with DCM (3 x 5 mL). Combined organic phases were washed with brine (10 mL), dried over Na2SO4, filtered, and concentrated under vacuum, affording *4-phenyl-1-thia-4,8-diazaspiro[4.5]decan-3-one* in quantitative yield. *Step 2:* To a solution of *4-phenyl-1-thia-4,8-diazaspiro[4.5]decan-3-one* (300 mg, 1.21 mmol) in dry DMF (3 mL), anhydrous K_2CO_3 (331 mg, 2.4 mmol) was added and the resulting mixture allowed under stirring at 25 °C. After 30 min, 4-(bromomethyl)benzonitrile (355 mg, 1.81 mmol) was added and the reaction mixture heated at 80 °C for 18 h. Reaction was stopped by adding distilled water (10 mL) and washed with EtOAc (10 mL). Organic layer was partitioned with

distilled water (3 x 10 mL) and brine (5 mL), dried over Na_2SO_4, filtered, and concentrated under vacuum. The crude reaction mixture was purified by silica gel liquid chromatography (DCM, DCM/MeOH 99:1 v/v) to afford desired compound **36** with 51% yield (223 mg).

^{1}H NMR (600 MHz, $CDCl_3$) δ 7.57 – 7.52 (m, 2H), 7.48 – 7.40 (m, 4H), 7.35 – 7.31 (m, 1H), 7.12 (d, J = 7.6 Hz, 2H), 3.68 (s, 2H), 3.49 (s, 2H), 2.82 – 2.74 (m, 2H), 2.38 – 2.29 (m, 2H), 2.06 – 1.95 (m, 2H), 1.93 – 1.85 (m, 2H).

8-(4-(5-(difluoromethyl)-1,3,4-oxadiazol-2-yl)benzyl)-4-phenyl-1-thia-4,8-diazaspiro[4.5]decan-3-one (37). *Step 1:* To a stirring solution of **36** (0.550 mmol, 200 mg) in dry DMF (2.2 mL) catalytic LiCl was added, followed by NaN3 (1.10 mmol, 72 mg), and NH_4Cl (0.715 mmol, 38 mg). The resulting mixture allowed to stir at 100 °C for 24 h, then the solvent was evaporated under vacuum and the crude residue purified by silica gel liquid chromatography (DCM/MeOH/AcOH 97:3:0.100 to 95:5:0.100 v/v) affording *8-(4-(1H-tetrazol-5-yl)benzyl)-4-phenyl-1-thia-4,8-diazaspiro[4.5]decan-3-one* with 46% yield (104 mg).

^{1}H NMR (600 MHz, DMSO) δ 10.11 (bs, 1H), 8.12 (d, J = 7.0 Hz, 2H), 7.73 (d, J = 8.0 Hz, 2H), 7.51 – 7.42 (m, 3H), 7.19 (d, J = 7.3 Hz, 2H), 4.39 (s, 2H), 3.79 (s, 2H), 3.43 – 3.40 (m, 2H), 3.24 – 3.12 (m, 3H), 2.22 – 2.18 (m, 3H).

Step 2: To a cooled solution of *8-(4-(1H-tetrazol-5-yl)benzyl)-4-phenyl-1-thia-4,8-diazaspiro[4.5]decan-3-one* (0.148 mmol, 60 mg) in dry toluene (2 mL) DFAA (0.443 mmol, 0.055 mL,) was added. The resulting mixture was heated to 70 °C and left under stirring for 2 h. After completion, the solvent was evaporated under reduced pressure and the crude residue purified by reverse phase HPLC (ACN/H_2O + 0.1% TFA) to afford compound **53** with 25% yield (17 mg).

MS (ESI) m/z calc. $[M+H]^+$ for $C_{23}H_{23}F_2N_4O_2S^+$: 457.15; found: 457.4

^{1}H NMR (600 MHz, DMSO) δ 8.12 (d, J = 7.8 Hz, 1H), 7.71 – 7.65 (m, 2H), 7.59 (t, J = 51.8 Hz, 1H), 7.52 – 7.48 (m, 2H), 7.48 – 7.44 (m, 1H), 7.22 – 7.18

(m, 2H), 4.43 (s, 2H), 3.79 (s, 2H), 3.22 (s, 2H), 2.28 – 2.20 (m, 2H), 2.12 – 2.03 (m, 2H).

^{13}C NMR (151 MHz, DMSO) δ 171.07, 164.83, 158.51 (t, J = 29.4 Hz), 157.94, 157.73, 135.80, 130.75, 129.40, 128.82, 127.49, 106.58 (t, J = 238.7 Hz), 49.29, 30.70.

tert-butyl 4-methyl-3-oxo-1-thia-4,8-diazaspiro[4.5]decane-8-carboxylate (38). To a stirring solution of **19** (0.844 mmol, 230 mg) in dry DMF (1 mL), NaH (60% mineral oil dispersion, 1.25 mmol, 30 mg) was added and the reaction mixture allowed under stirring for 30 min. Iodomethane (1.27 mmol, 0.079 mL) was added and the resulting mixture allowed under stirring for 18 h at 25 °C. Reaction was stopped by adding distilled water (5 mL) and partitioned with EtOAc (5 mL). Organic layer was collected and washed with distilled water (3 x 5 mL) and brine (10 mL), dried over Na_2SO_4, filtered, and concentrated under vacuum. The crude reaction mixture was purified by silica gel liquid chromatography (DCM, DCM/MeOH 97:3 v/v) to afford desired compound **38** with 74% yield (180 mg).

^{1}H NMR (500 MHz, $CDCl_3$) δ 4.22 – 4.16 (m, 2H), 3.55 (s, 2H), 3.00 – 2.93 (m, 2H), 2.85 (s, 3H), 2.07 (td, J = 12.7, 4.7 Hz, 2H), 1.70 – 1.63 (m, 3H), 1.44 (s, 9H).

tert-butyl 4-benzyl-3-oxo-1-thia-4,8-diazaspiro[4.5]decane-8-carboxylate (39). To a stirring solution of **19** (0.734 mmol, 200 mg) in dry DMF (2 mL), NaH (60% mineral oil dispersion, 1.67 mmol, 40 mg) was added and the reaction mixture allowed under stirring for 30 min. Benzyl chloride (0.808 mmol, 0.093 mL) was added and the resulting mixture allowed under stirring for 18 h at 25 °C. Reaction was stopped by adding distilled water (5 mL) and partitioned with EtOAc (5 mL). Organic layer was collected and washed with distilled water (3 x 5 mL) and brine (10 mL), dried over Na_2SO_4, filtered, and concentrated under vacuum. The crude reaction mixture was purified by silica gel liquid

chromatography (PE/EtOAc 3:1 v/v) to afford desired compound **39** with 78% yield (209 mg).

^{1}H NMR (500 MHz, $CDCl_3$) δ 7.31 – 7.27 (m, 2H), 7.26 – 7.20 (m, 3H), 4.54 (s, 2H), 4.17 – 4.00 (m, 2H), 3.65 (s, 2H), 2.92 (t, J = 13.4 Hz, 1H), 1.93 (t, J = 10.3 Hz, 2H), 1.61 (d, J = 13.1 Hz, 2H), 1.42 (s, 9H).

4-((4-methyl-3-oxo-1-thia-4,8-diazaspiro[4.5]decan-8-yl)methyl)benzonitrile (40). *Step 1:* To a solution of compound **38** (1.20 mmol, 420 mg) in DCM (3 mL), a solution of 4 N HCl in dioxane (4.5 mL) was added and the reaction mixture was stirred at 25 °C for 1 h. Upon completion, volatile components were evaporated under reduced pressure, affording *4-phenyl-1-thia-4,8-diazaspiro[4.5]decan-3-one hydrochloride* in quantitative yield. To a solution of *4-methyl-1-thia-4,8-diazaspiro[4.5]decan-3-one hydrochloride* (230 mg, 1.03 mmol) in dry DMF (1 mL), anhydrous K_2CO_3 (285 mg, 2.07 mmol) was added and the resulting mixture allowed under stirring at 25 °C. After 30 min, 4-(bromomethyl)benzonitrile (243 mg, 1.24 mmol) was added and the reaction mixture heated at 80 °C for 18 h. Reaction was stopped by adding distilled water (5 mL) and washed with EtOAc (5 mL). Organic layer was partitioned with distilled water (3 x 5 mL) and brine (5 mL), dried over Na_2SO_4, filtered, and concentrated under vacuum. The crude reaction mixture was purified by silica gel liquid chromatography (PE/EtOAc 3:1 – 1:1 v/v) to afford desired compound **40** with 64% yield (250 mg).

^{1}H NMR (500 MHz, $CDCl_3$) δ 7.62 (d, *J* = 7.8 Hz, 2H), 7.46 (d, *J* = 7.5 Hz, 2H), 3.56 (d, *J* = 13.7 Hz, 4H), 2.91 (s, 3H), 2.88 – 2.82 (m, 2H), 2.42 – 2.17 (m, 4H), 1.73 – 1.66 (m, 2H).

3-fluoro-4-((4-methyl-3-oxo-1-thia-4,8-diazaspiro[4.5]decan-8-yl)methyl)benzonitrile (41). To a solution of *4-methyl-1-thia-4,8-diazaspiro[4.5]decan-3-one hydrochloride* (230 mg, 1.03 mmol) in dry DMF (1 mL), anhydrous K_2CO_3 (285 mg, 2.07 mmol) was added and the resulting mixture

allowed under stirring at 25 °C. After 30 min, 4-(bromomethyl)-3-fluorobenzonitrile (265 mg, 1.24 mmol) was added and the reaction mixture heated at 80 °C for 18 h. Reaction was stopped by adding distilled water (5 mL) and washed with EtOAc (5 mL). Organic layer was partitioned with distilled water (3 x 5 mL) and brine (5 mL), dried over Na_2SO_4, filtered, and concentrated under vacuum. The crude reaction mixture was purified by silica gel liquid chromatography (PE/EtOAc 3:1 – 1:1 v/v) to afford desired compound **41** with 46% yield (180 mg).

^{1}H NMR (500 MHz, $CDCl_3$) δ 7.64 (d, J = 7.8 Hz, 2H), 7.48 (d, J = 7.7 Hz, 2H), 3.60 (s, 2H), 3.57 (s, 2H), 2.93 (s, 3H), 2.91 – 2.85 (m, 2H), 2.39 – 2.22 (m, 4H), 1.72 (d, J = 11.9 Hz, 2H).

4-((4-benzyl-3-oxo-1-thia-4,8-diazaspiro[4.5]decan-8-yl)methyl)-3-fluorobenzonitrile (42). *Step 1:* To a solution of compound **39** (0.964 mmol, 350 mg) in DCM (3 mL), a solution of 4 N HCl in dioxane (3.6 mL) was added and the reaction mixture was stirred at 25 °C for 1 h. Upon completion, volatile components were evaporated under reduced pressure, affording *4-benzyl-1-thia-4,8-diazaspiro[4.5]decan-3-one hydrochloride* in quantitative yield. *Step 2:* To a solution of *4-benzyl-1-thia-4,8-diazaspiro[4.5]decan-3-one hydrochloride* (0.965 mmol, 288 mg) in dry DMF (1 mL), anhydrous K_2CO_3 (1.93 mmol, 266 mg) was added and the resulting mixture allowed under stirring at 25 °C. After 30 min, 4-(bromomethyl) 3-fluoro benzonitrile (1.16 mmol, 227 mg) was added and the reaction mixture heated at 80 °C for 18 h. Reaction was stopped by adding distilled water (5 mL) and washed with EtOAc (5 mL). Organic layer was partitioned with distilled water (3 x 5 mL) and brine (5 mL), dried over Na_2SO_4, filtered, and concentrated under vacuum. The crude reaction mixture was purified by silica gel liquid chromatography (PE/EtOAc 3:1 – 2:1 v/v) to afford desired compound **42** with 50% yield (200 mg).

4-methyl-8-(4-(5-(trifluoromethyl)-1,2,4-oxadiazol-3-yl)benzyl)-1-thia-4,8-diazaspiro[4.5]decan-3-one (43). *Step 1:* To a solution of compound **40** (0.398 mmol, 120 mg) in EtOH (2 mL) at 25 °C, 50% aqueous hydroxylamine solution (1.60 mmol, 0.060 mL) was added dropwise, and the reaction mixture was heated at 80 °C for 18 h. After the time reaction had elapsed, the reaction mixture was concentrated under reduced pressure to obtain the desired product *N-hydroxy-4-((4-methyl-3-oxo-1-thia-4,8-diazaspiro[4.5]decan-8-yl)methyl)benzimidamide* with a quantitative yield (133 mg).

^{1}H NMR (600 MHz, DMSO) δ 8.02 (d, J = 7.7 Hz, 2H), 7.56 (d, J = 8.0 Hz, 2H), 3.60 (s, 2H), 3.51 (s, 2H), 2.88 – 2.85 (m, 2H), 2.79 (s, 3H), 2.26 – 2.22 (m, 4H), 1.62 (d, J = 12.7 Hz, 2H).

^{13}C NMR (151 MHz, DMSO) δ 170.36, 168.81, 143.85, 130.19, 127.79, 123.54, 71.63, 61.51, 50.44, 36.44, 30.88, 27.53.

Step 2: to a cooled solution of *N-hydroxy-4-((4-methyl-3-oxo-1-thia-4,8-diazaspiro[4.5]decan-8-yl)methyl)benzimidamide* (0.200 mmol, 67 mg) in dry pyridine (1.20 mmol, 0.097 mL) DFAA (0.601 mmol, 0.085 mL) was added. The resulting mixture was heated at 75 °C and stirred for 2 h. After completion, DCM (5 mL) was added and partitioned with distilled water (3 x 5 mL). Organic layer was dried over Na_2SO_4, filtered, and concentrated under vacuum. The crude reaction mixture was purified by silica gel liquid chromatography (DCM/MeOH 98:2 - 97:3 v/v) to afford desired compound **43** with 48% yield (0.040 mg).

MS (ESI) m/z calc. $[M+H]^+$ for $C_{19}H_{20}F_3N_4O_2S^+$: 413.13; found: 413.2

^{1}H NMR (600 MHz, DMSO) δ 8.02 (d, J = 8.5 Hz, 2H), 7.56 (d, J = 8.0 Hz, 2H), 3.60 (s, 2H), 3.51 (s, 2H), 2.88 – 2.85 (m, 2H), 2.79 (s, 3H), 2.27 – 2.20 (m, 4H), 1.64 – 1.60 (m, 2H).

^{13}C NMR (151 MHz, DMSO) δ 169.89, 168.35, 164.94 (q, J = 43.5 Hz), 143.38, 129.72, 127.32, 123.07, 116.67 (q, J = 270.5 Hz), 71.16, 61.04, 49.97, 35.97, 30.41, 27.06.

8-(2-fluoro-4-(5-(trifluoromethyl)-1,2,4-oxadiazol-3-yl)benzyl)-4-methyl-1-thia-4,8-diazaspiro[4.5]decan-3-one (44). Step 1: To a solution of compound **41** (0.282 mmol, 89 mg) in EtOH (2 mL) at 25 °C, 50% aqueous hydroxylamine solution (1.13 mmol, 0.050 mL) was added dropwise, and the reaction mixture was heated at reflux and left under stirring for 18 h. After the time reaction had elapsed, the reaction mixture was concentrated under reduced pressure to obtain the desired product *3-fluoro-N-hydroxy-4-((4-methyl-3-oxo-1-thia-4,8-diazaspiro[4.5]decan-8-yl)methyl)benzimidamide* (99 mg). *Step 2:* to a cooled solution of *3-fluoro-N-hydroxy-4-((4-methyl-3-oxo-1-thia-4,8-diazaspiro[4.5]decan-8-yl)methyl)benzimidamide* (0.200 mmol, 99 mg) in dry pyridine (1.69 mmol, 136 mL) DFAA (0.842 mmol, 119 mL) was added. The resulting mixture was heated at 75 °C and stirred for 2 h. After completion, DCM (5 mL) was added and partitioned with distilled water (3 x 5 mL). Organic layer was dried over Na_2SO_4, filtered, and concentrated under vacuum. The crude reaction mixture was purified by silica gel liquid chromatography (DCM, DCM/MeOH 99:1 - 98:2 v/v) to afford desired compound **60** with 33% yield (40 mg).

MS (ESI) m/z calc. $[M+H]^+$ for $C_{19}H_{19}F_4N_4O_2S^+$: 431.12; found: 431.4

^{1}H NMR (600 MHz, DMSO) δ 7.90 (d, J = 6.3 Hz, 1H), 7.80 (d, J = 8.5 Hz, 1H), 7.70 (t, J = 7.6 Hz, 1H), 3.65 (s, 2H), 3.50 (s, 2H), 2.89 (d, J = 9.7 Hz, 2H), 2.78 (s, 3H), 2.31 – 2.20 (m, 4H), 1.65 – 1.59 (m, 2H).

^{13}C NMR (151 MHz, DMSO) δ 170.36, 168.00, 165.63 (q, J = 43.7 Hz), 162.03, 160.40, 133.16 (d, J = 4.9 Hz), 125.60 (d, J = 8.8 Hz), 123.81 (d, J = 3.6 Hz), 116.16 (q, J = 273.0 Hz), 114.49 (d, J = 24.8 Hz), 71.51, 54.40, 50.35, 36.40, 30.87, 27.52.

8-(4-(5-(difluoromethyl)-1,3,4-oxadiazol-2-yl)-2-fluorobenzyl)-4-methyl-1-thia-4,8-diazaspiro[4.5]decan-3-one (45). *Step 1:* To a stirring solution of **41** (0.278 mmol, 89 mg) in dry DMF (1 mL) catalytic LiCl was added, followed by

NaN_3 (0.557 mmol, 36 mg), and NH_4Cl (0.362 mmol, 19 mg). The resulting mixture allowed to stir at 100 °C for 24 h, then the solvent was evaporated under vacuum and the crude residue purified by silica gel liquid chromatography (DCM/MeOH/ 95:5 v/v) affording *8-(2-fluoro-4-(1H-tetrazol-5-yl)benzyl)-4-methyl-1-thia-4,8-diazaspiro[4.5]decan-3-one* with 98% yield (100 mg). *Step 2:* To a cooled solution of *8-(2-fluoro-4-(1H-tetrazol-5-yl)benzyl)-4-methyl-1-thia-4,8-diazaspiro[4.5]decan-3-one* (0.276 mmol, 100 mg) and TEA (1.38 mmol, 0.187 mL) in dry toluene (2 mL) DFAA (0.828 mmol, 103 mL) was added. The resulting mixture was heated to 70 °C and left under stirring for 2 h. After completion, the solvent was evaporated under reduced pressure and the crude residue purified by reverse phase HPLC (ACN/H_2O + 0.1% TFA) to afford compound **45** with 23% yield (27 mg).

MS (ESI) m/z calc. $[M+H]^+$ for $C_{18}H_{20}F_3N_4O_2S^+$: 413.13; found: 413.4

^1H NMR (600 MHz, DMSO) δ 7.89 (d, J = 1.6 Hz, 1H), 7.83 (d, J = 1.7 Hz, 1H), 7.70 (t, J = 7.6 Hz, 1H), 7.54 (t, J = 51.3 Hz, 2H), 3.65 (s, 2H), 3.50 (s, 2H), 2.89 (d, J = 10.0 Hz, 2H), 2.78 (s, 3H), 2.31 – 2.21 (m, 4H), 1.65 – 1.59 (m, 2H).

^{13}C NMR (151 MHz, DMSO) δ 170.36, 164.76, 161.93, 160.30, 158.93 (t, ^2J C-F = 29.6 Hz), 133.17 (d, ^3J C-F = 4.8 Hz), 130.40 (d, ^2J C-F = 14.8 Hz), 123.55 (d, J = 3.3 Hz), 123.47 (d, J = 9.1 Hz), 114.40, 114.23, 107.01 (t, J = 238.7 Hz), 71.49, 54.37, 50.34, 36.40, 30.87, 27.52.

8-(4-(5-(difluoromethyl)-1,2,4-oxadiazol-3-yl)benzyl)-4-methyl-1-thia-4,8-diazaspiro[4.5]decan-3-one **(46).** To a cooled solution *N-hydroxy-4-((4-methyl-3-oxo-1-thia-4,8-diazaspiro[4.5]decan-8-yl)methyl)benzimidamide* (0.200 mmol, 67 mg) in dry pyridine (1.20 mmol, 0.097 mL) DFAA (0.601 mmol, 0.085 mL) was added. The resulting mixture was heated at 75 °C and stirred for 2 h. After completion, DCM (5 mL) was added and partitioned with distilled water (3 x 5 mL). Organic layer was dried over Na_2SO_4, filtered, and concentrated under vacuum. The crude reaction mixture was purified by silica gel liquid

chromatography (DCM/MeOH 98:2 - 97:3 v/v) to afford desired compound **46** with 19% yield (15 mg).

MS (ESI) m/z calc. $[M+H]^+$ for $C_{18}H_{21}F_2N_4O_2S^+$: 395.14; found: 395.3

^{1}H NMR (600 MHz, DMSO) δ 8.15 (d, J = 7.9 Hz, 2H), 7.74 (d, J = 7.8 Hz, 2H), 7.56 (t, J = 51.6 Hz, 2H), 4.47 (s, 2H), 3.62 (s, 2H), 3.28 – 3.09 (m, 3H), 2.77 (s, 3H), 2.48 – 2.44 (m, 1H), 1.93 – 1.85 (m, 2H).

^{13}C NMR (151 MHz, DMSO) δ 170.91 (t = 29.7 Hz), 170.37, 168.13, 158.46 (q, J = 31.9 Hz), 132.64, 128.20, 126.46, 107.22 (t, J = 241.0 Hz), 68.86, 58.75, 49.70, 33.88, 31.11, 27.51.

4-benzyl-8-(4-(5-(difluoromethyl)-1,3,4-oxadiazol-2-yl)benzyl)-1-thia-4,8-diazaspiro[4.5]decan-3-one (47). *Step 1:* To a stirring solution of **42** (0.225 mmol, 85 mg) in dry DMF (2.2 mL) catalytic LiCl was added, followed by NaN_3 (0.450 mmol, 29 mg), and NH_4Cl (0.293 mmol, 15 mg). The resulting mixture allowed to stir at 100 °C for 24 h. Distilled water was added (7 mL) and partitioned with EtOAc (7 mL). Organic layer was collected, partitioned with brine (3 x 5 mL), then dried over Na_2SO_4, filtered, and concentrated under vacuum. The obtained compound *8-(4-(1H-tetrazol-5-yl)benzyl)-4-benzyl-1-thia-4,8-diazaspiro[4.5]decan-3-one* (68% yield, 64%) was employed in the next synthetic step without further purification. *Step 2:* To a cooled solution of *8-(4-(1H-tetrazol-5-yl)benzyl)-4-benzyl-1-thia-4,8-diazaspiro[4.5]decan-3-one* (0.166 mmol, 70 mg) in dry toluene (6 mL) DFAA (0.062 mL, 0.499 mmol) was added. The resulting mixture was heated to 70 °C and left under stirring for 2 h. After completion, the solvent was evaporated under reduced pressure and the crude residue purified by reverse phase HPLC (ACN/H_2O + 0.1% TFA) to afford compound **47** with 30% yield (24 mg).

MS (ESI) m/z calc. $[M+H]^+$ for $C_{24}H_{25}F_2N_4O_2S^+$: 471.17; found: 471.4

^{1}H NMR (600 MHz, DMSO) δ 8.14 (d, J = 7.8 Hz, 2H), 7.73 (d, J = 7.9 Hz, 2H), 7.55 (t, J = 51.4 Hz, 1H), 7.31 (t, J = 7.4 Hz, 2H), 7.23 (t, J = 7.8 Hz, 3H), 4.49

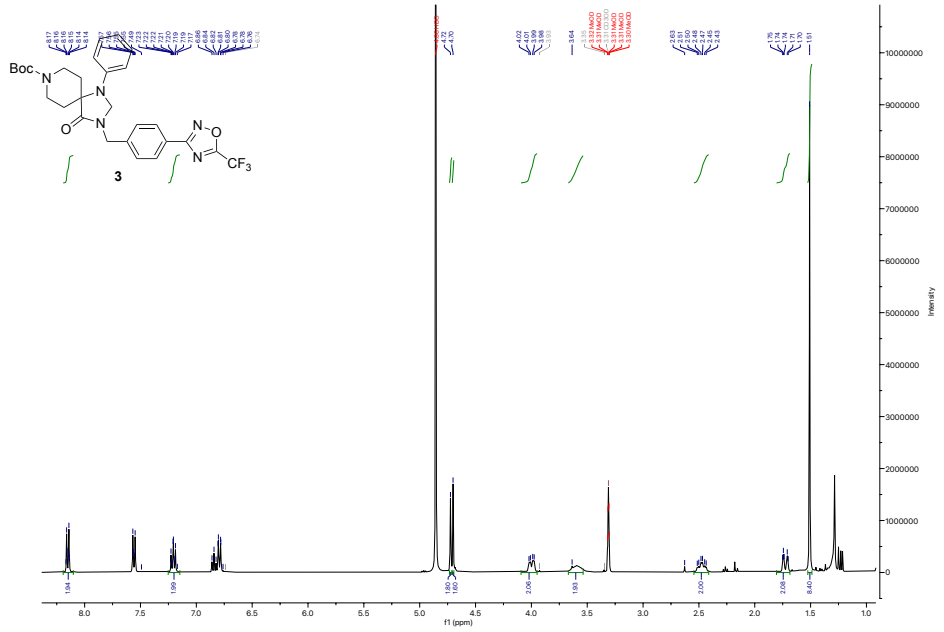
(s, 2H), 3.78 (s, 2H), 3.17 – 3.04 (m, 2H), 2.41 – 2.29 (m, 2H), 1.84 (d, J = 14.0 Hz, 2H).

^{13}C NMR (151 MHz, DMSO) δ 171.55, 165.30, 158.99 (t, J = 29.5 Hz), 158.61, 158.39, 138.27, 132.66, 128.91, 128.03, 127.57, 127.07, 107.05 (t, J = 238.6 Hz), 69.47, 58.62, 49.80, 44.75, 34.73, 30.94.

5.3.2 Supporting Figures

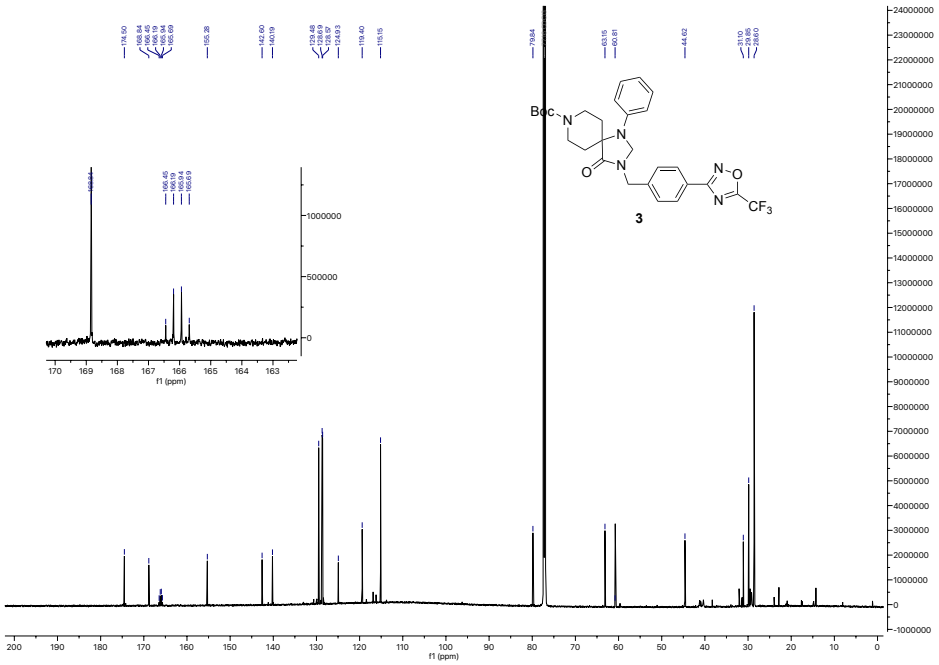
Supporting Figure 1

^{1}H NMR of 3



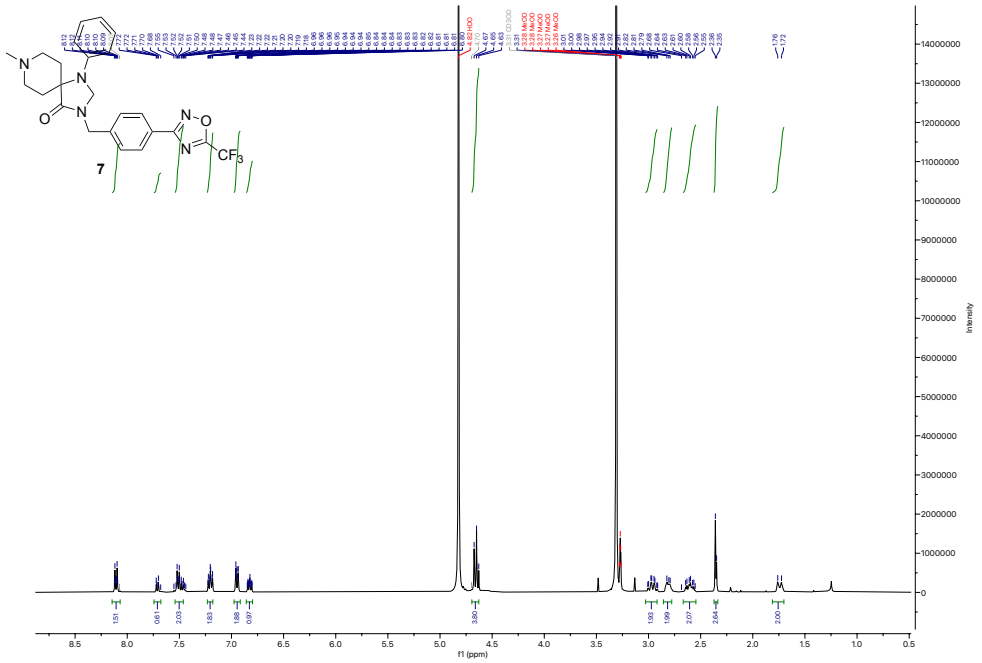
Supporting Figure 2

^{13}C NMR of compound 3



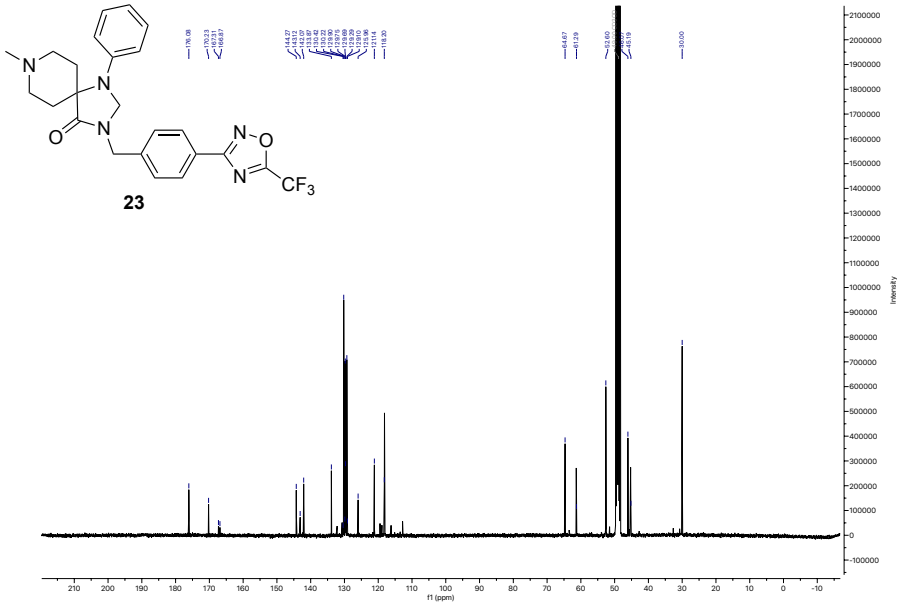
Supporting Figure 3

^{1}H NMR of compound 7



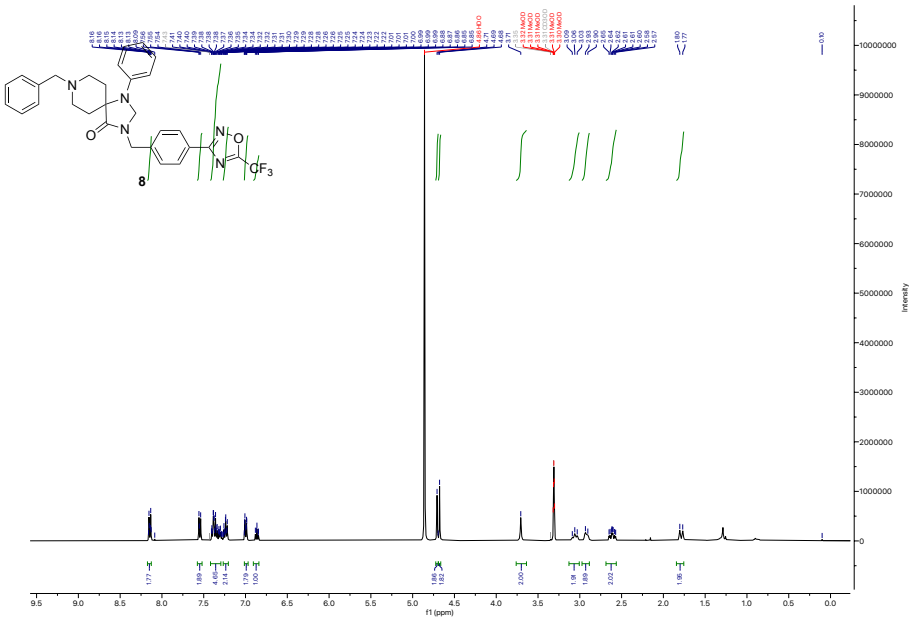
Supporting Figure 4

^{13}C NMR of compound 7



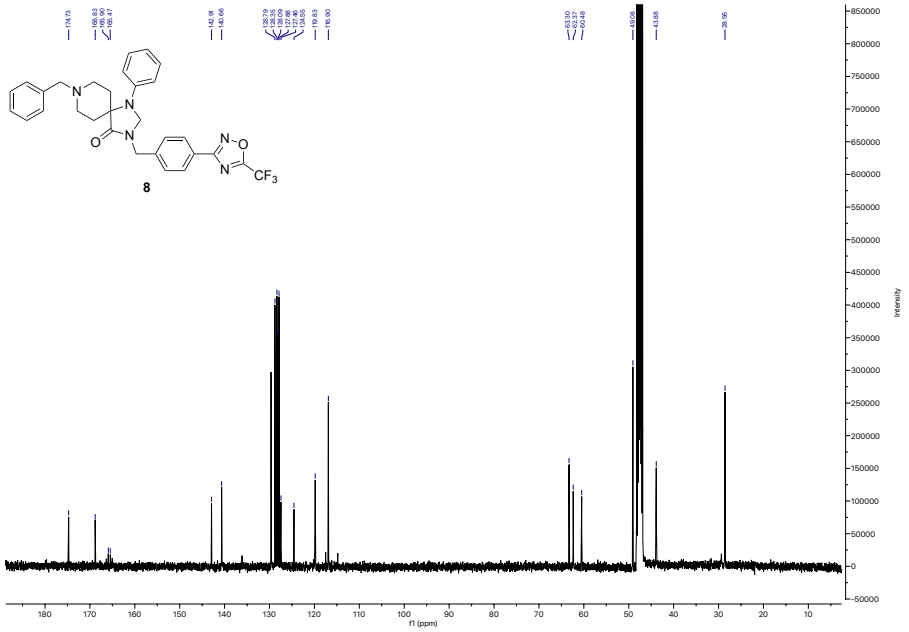
Supporting Figure 5

^{1}H NMR of compound 8



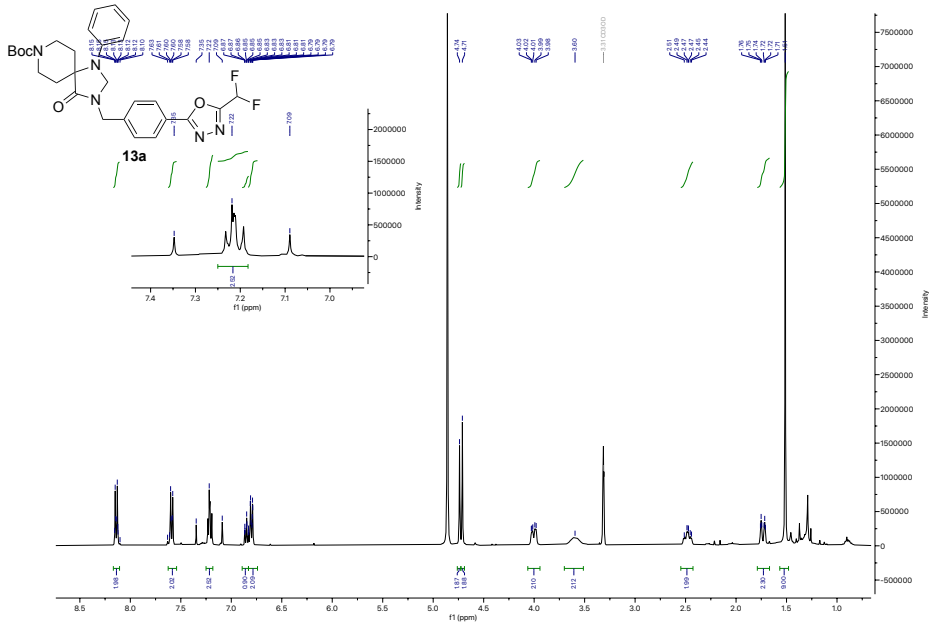
Supporting Figure 6

^{13}C NMR of compound 8



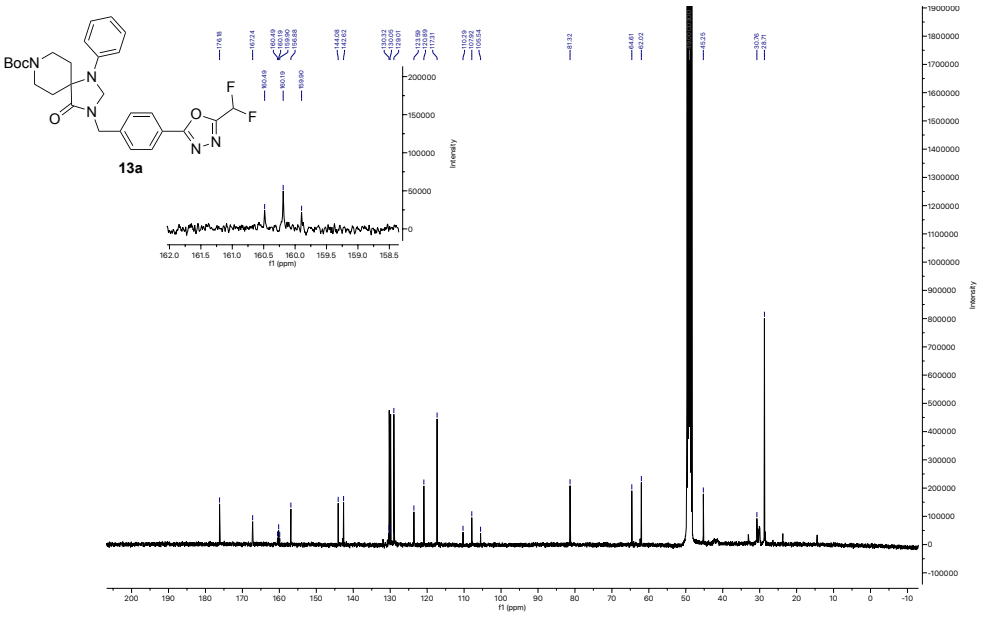
Supporting Figure 7

^{1}H NMR of compound 13a



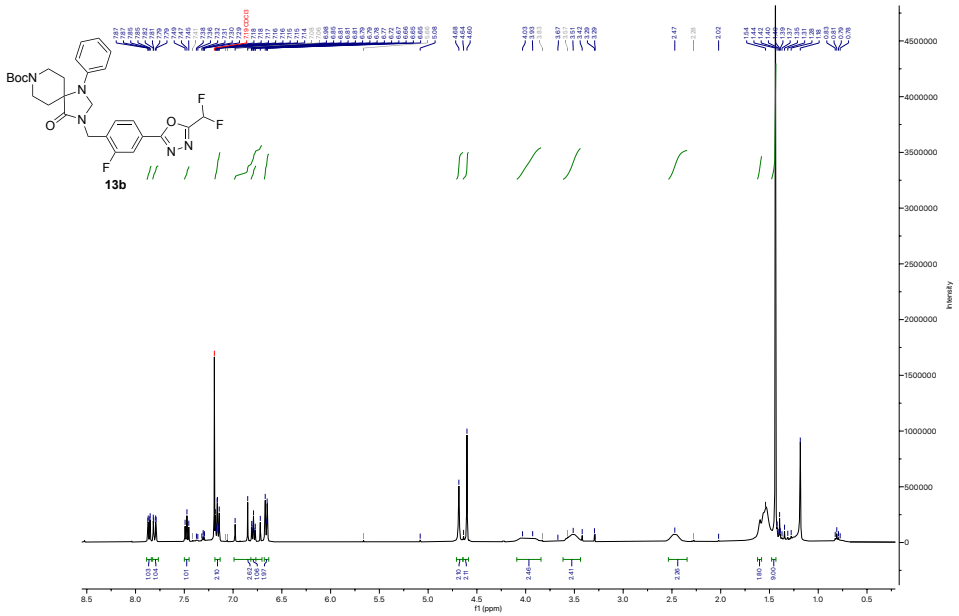
Supporting Figure 8

^{13}C NMR of compound 13a



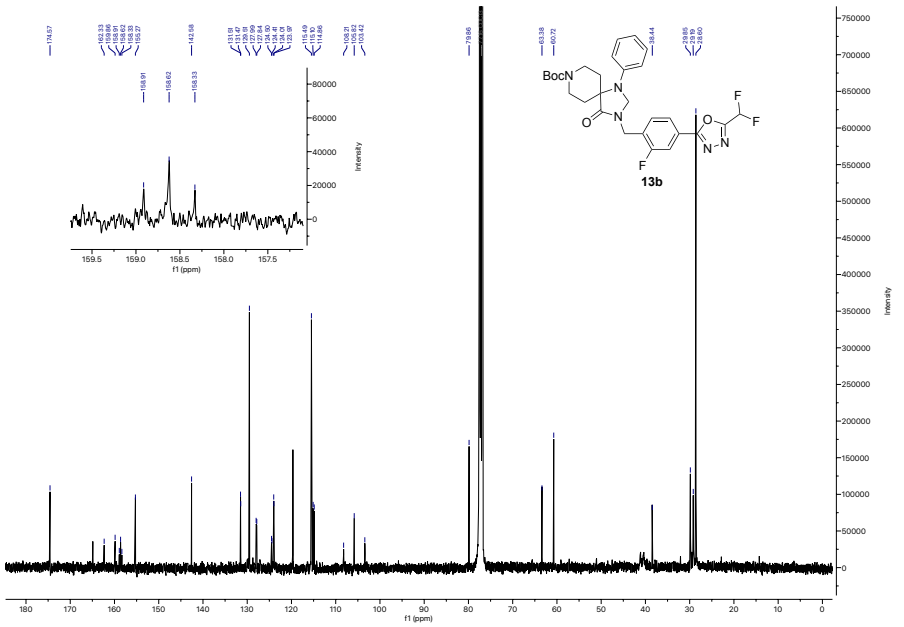
Supporting Figure 9

^{1}H NMR of compound 13b



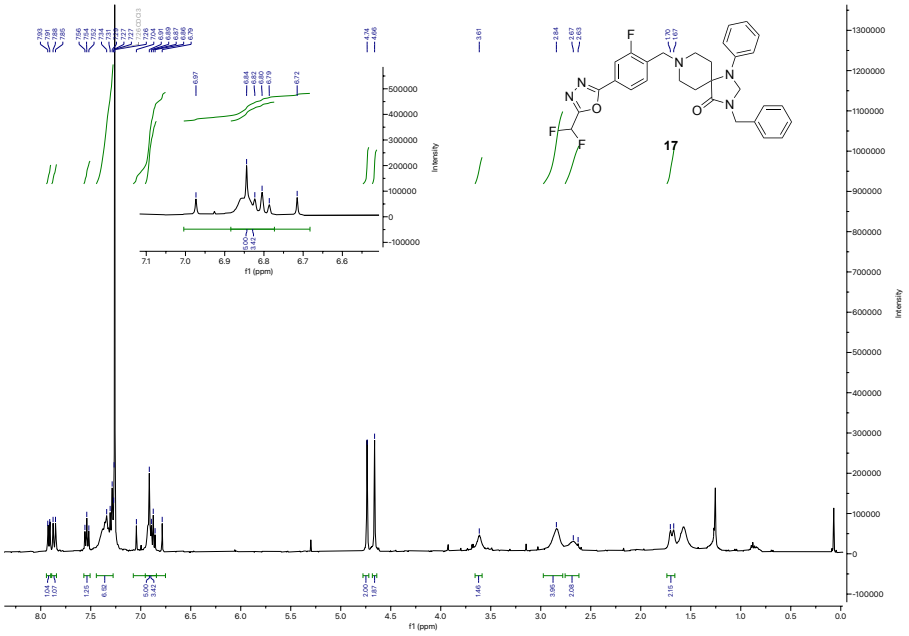
Supporting Figure 10

^{13}C NMR of compound 13b



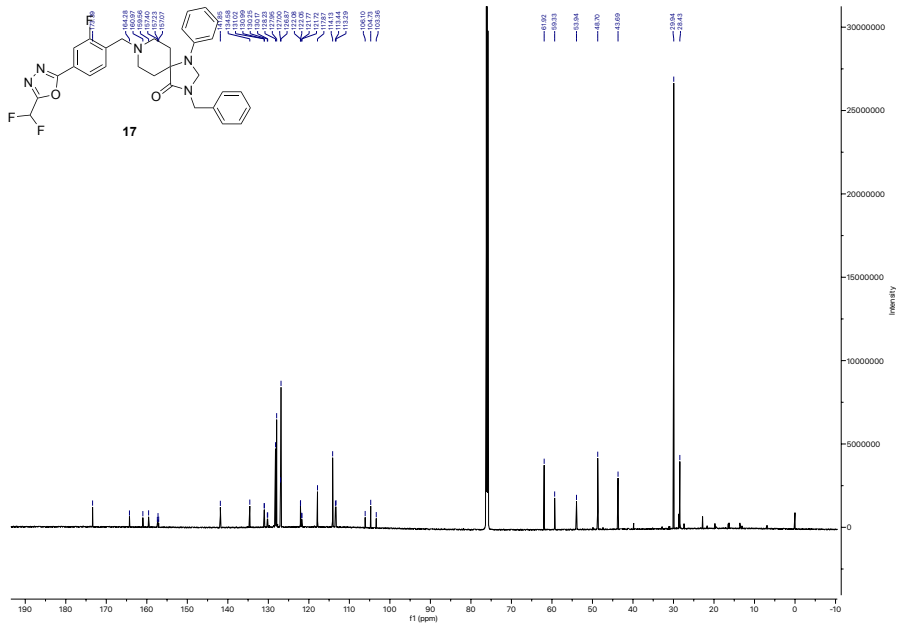
Supporting Figure 11

^{1}H NMR of compound 17



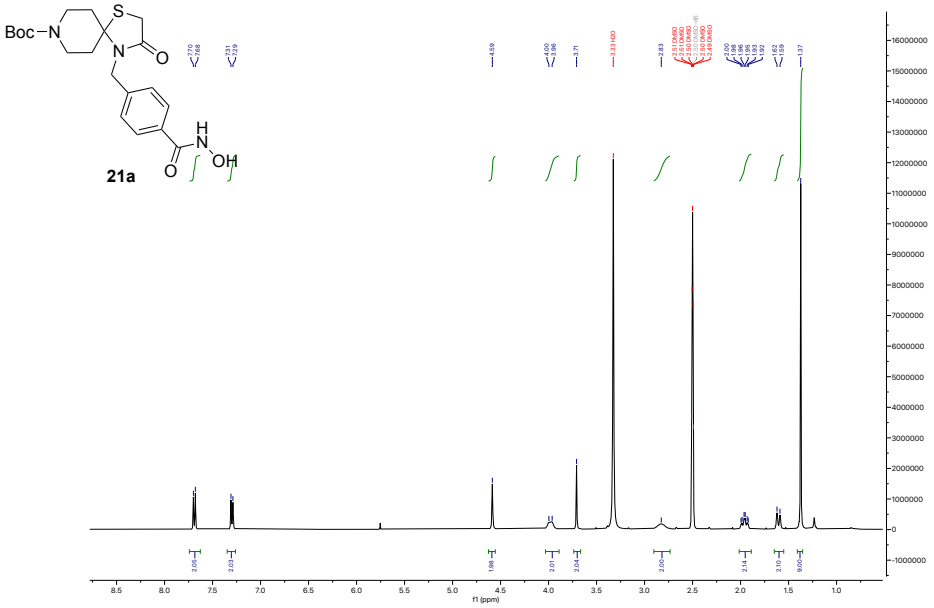
Supporting Figure 12

^{13}C NMR of compound 17



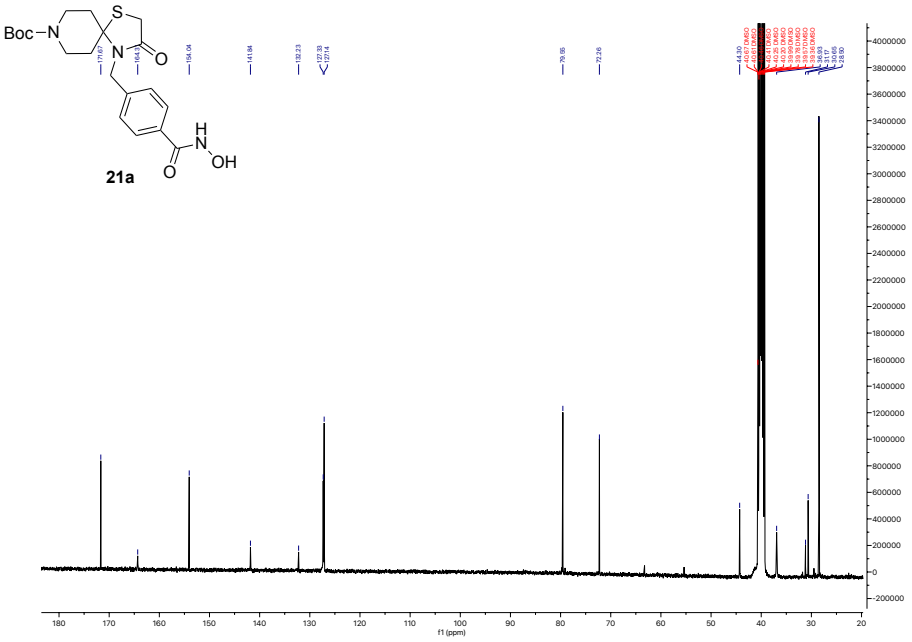
Supporting Figure 13

^{1}H NMR of compound 21a



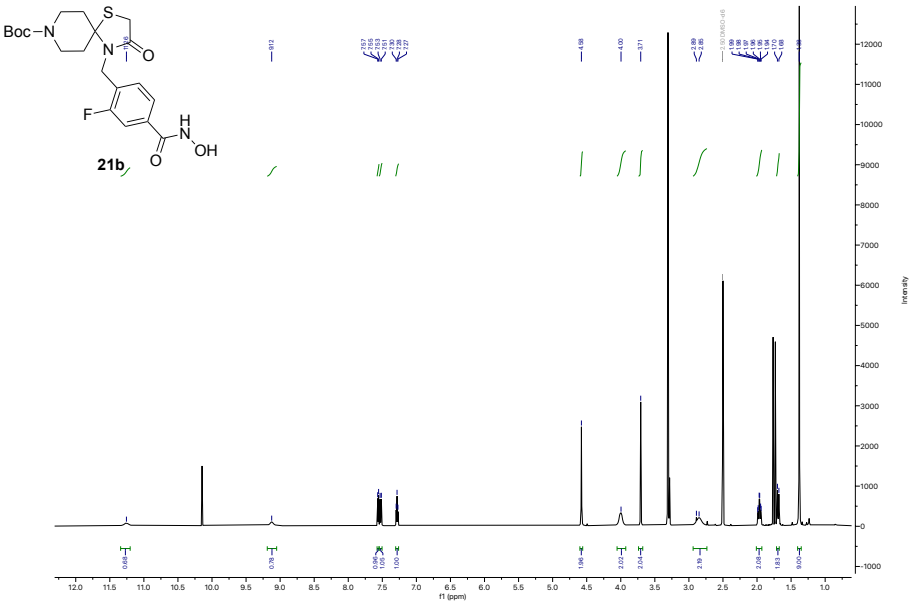
Supporting Figure 14

^{13}C NMR of compound 21a



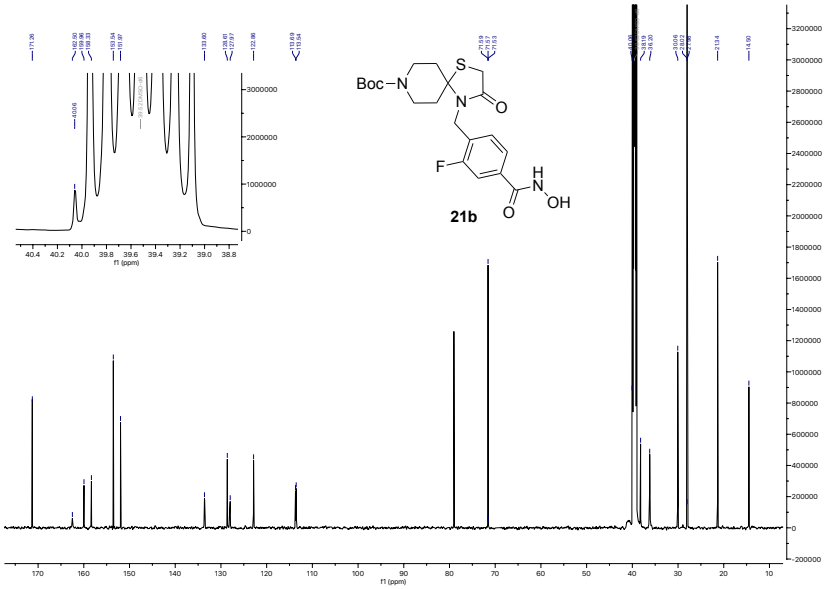
Supporting Figure 15

^{1}H NMR of compound 21b



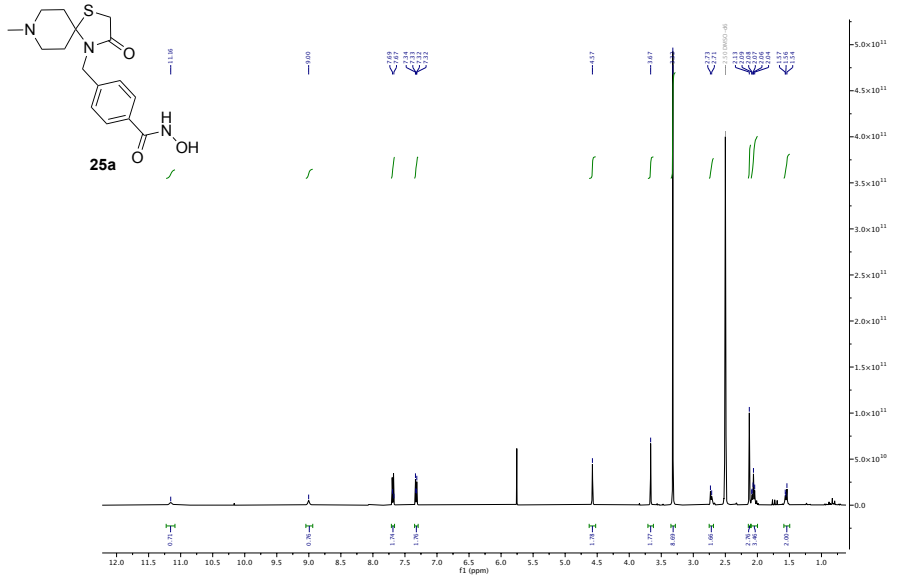
Supporting Figure 16

^{13}C NMR of compound 21b



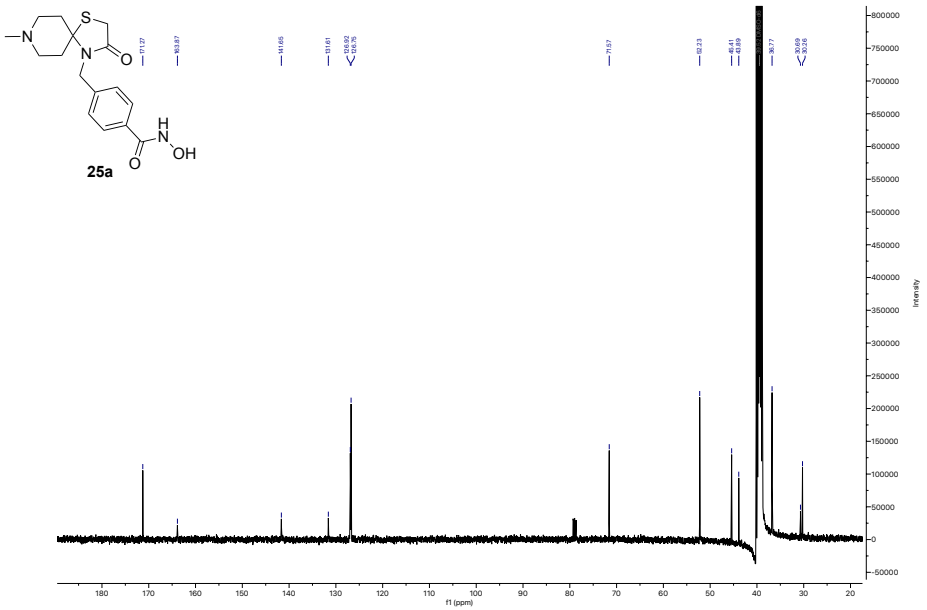
Supporting Figure 17

^{1}H NMR of compound 25a



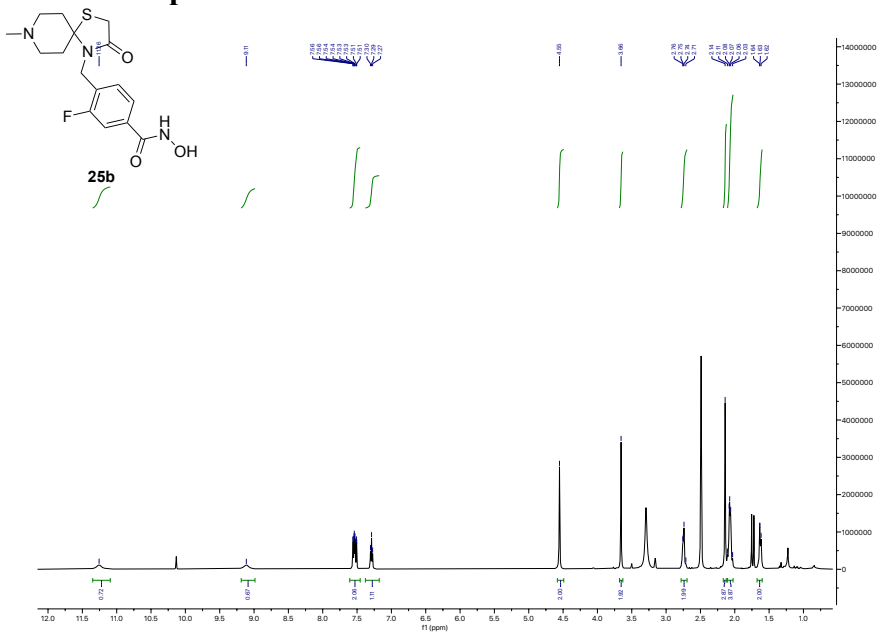
Supporting Figure 18

^{13}C NMR of compound 25a



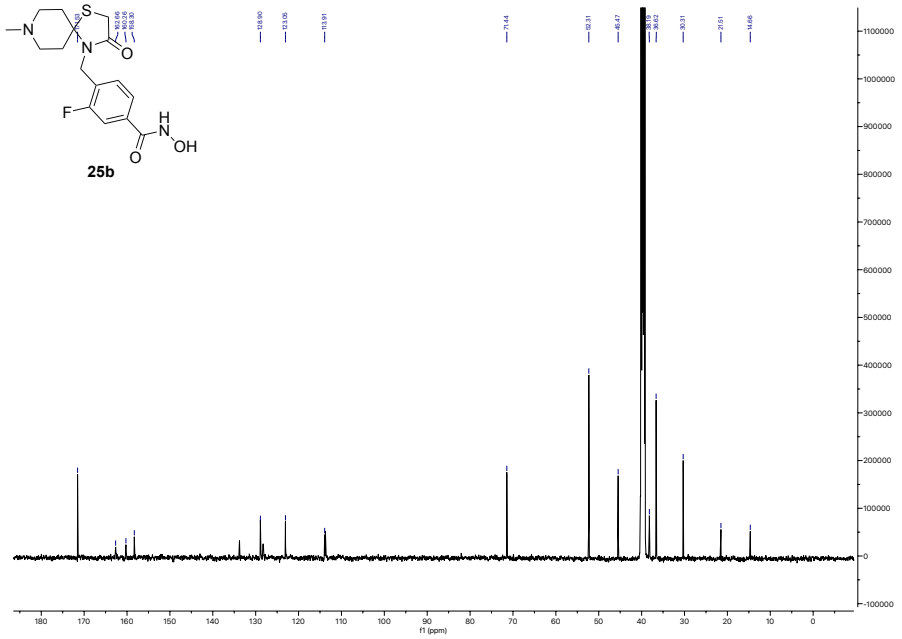
Supporting Figure 19

^{1}H NMR of compound 25b



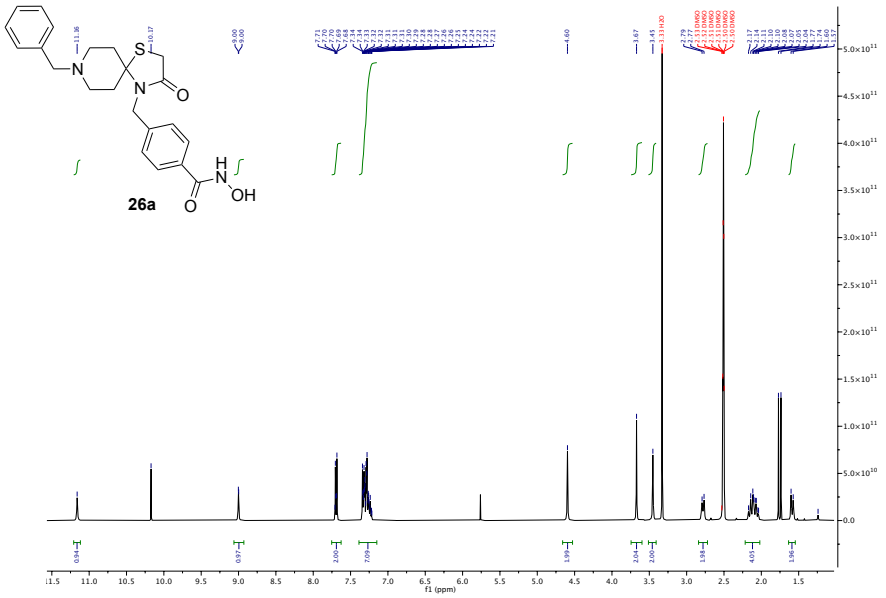
Supporting Figure 20

^{13}C NMR of compound 25b



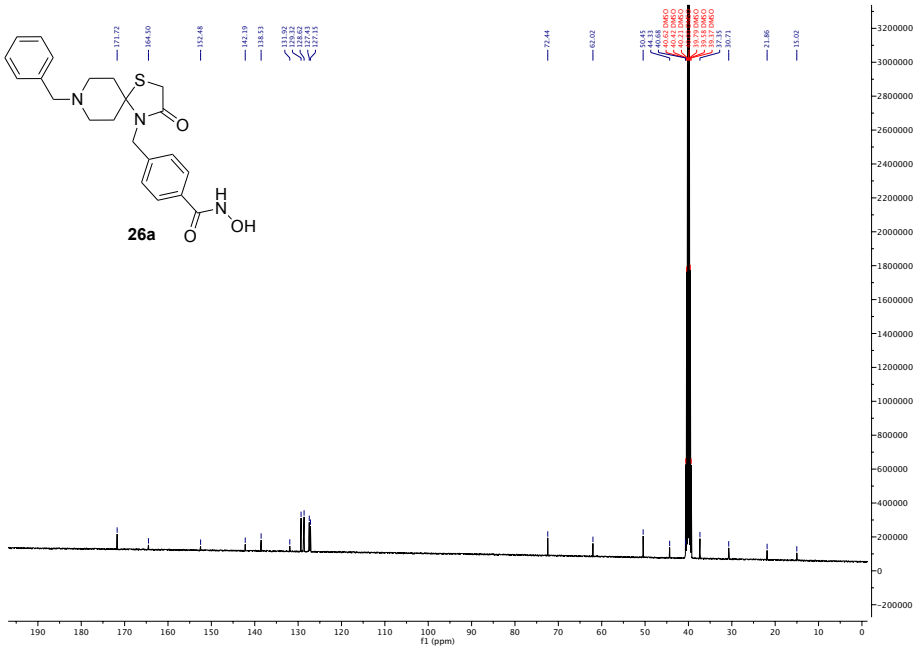
Supporting Figure 21

^{1}H NMR of compound 26a



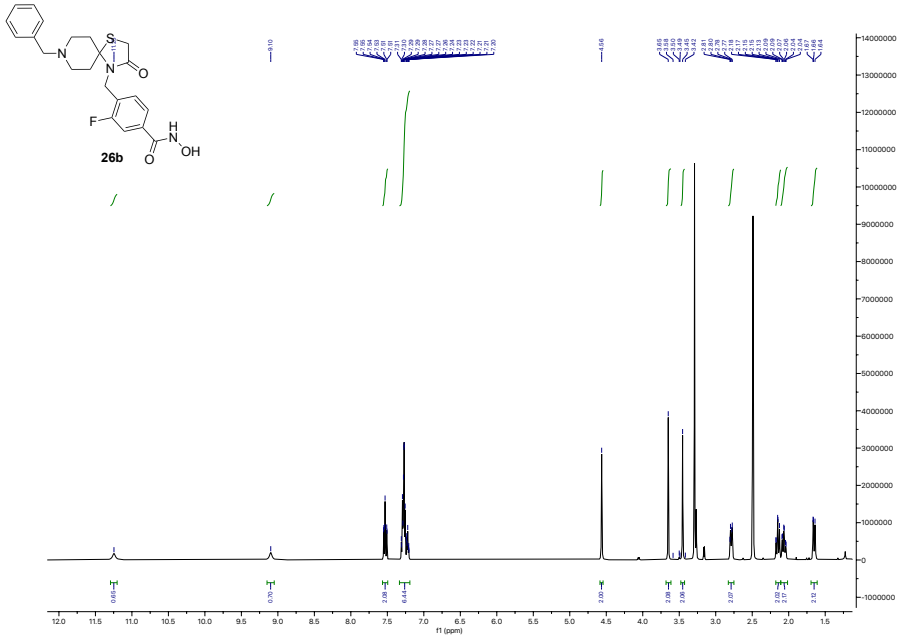
Supporting Figure 22

^{13}C NMR of compound 26a



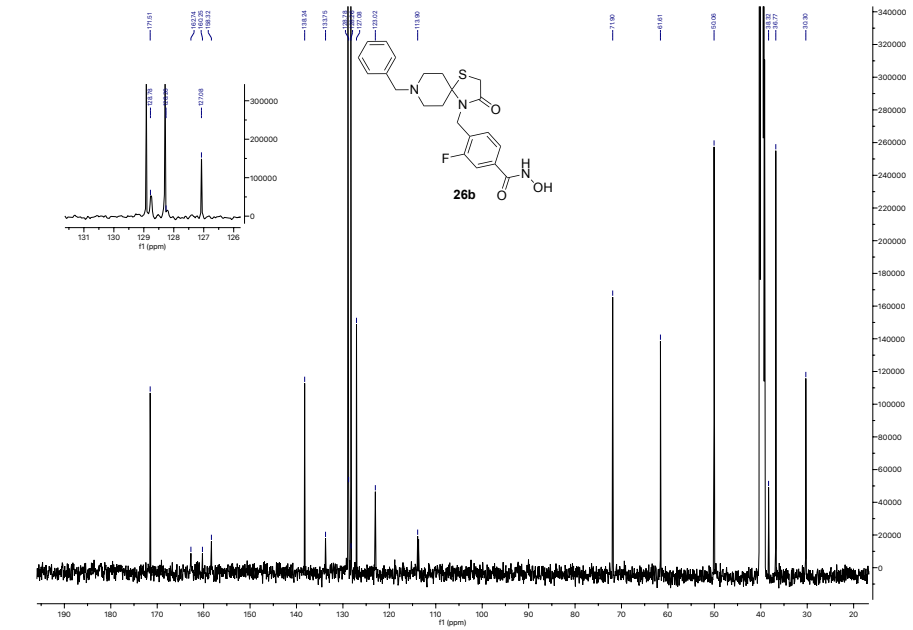
Supporting Figure 23

^{1}H NMR of compound 26b



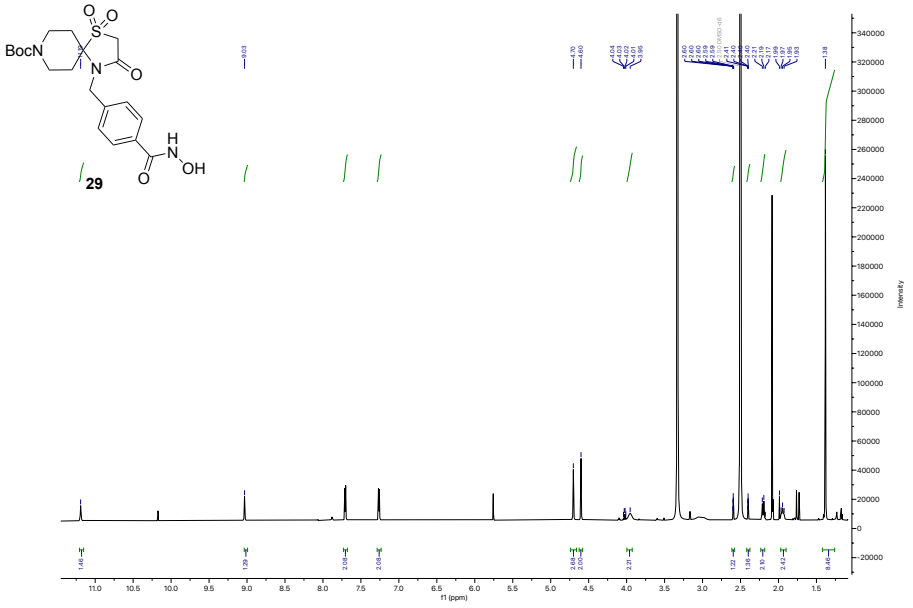
Supporting Figure 24

^{13}C NMR of compound 26b



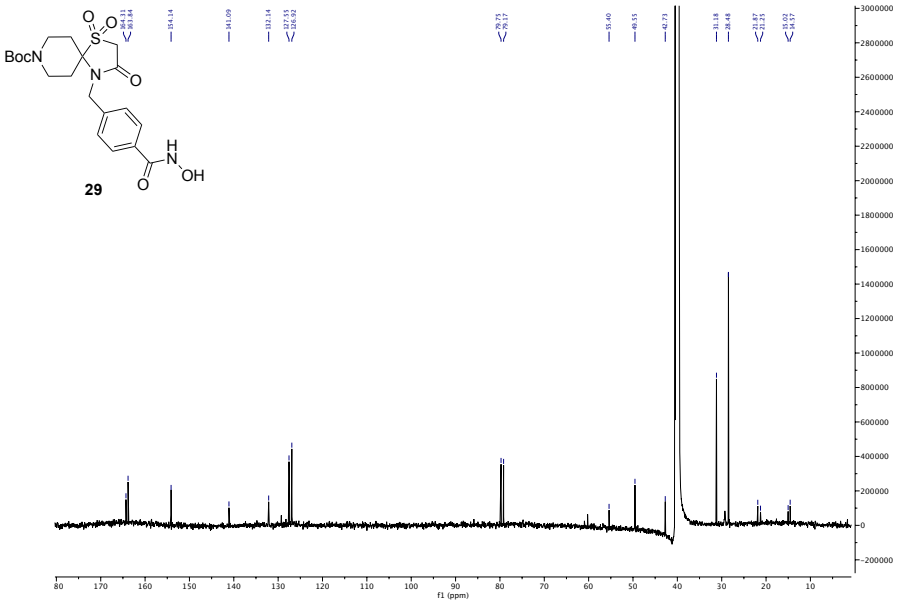
Supporting Figure 25

^{1}H NMR of compound 29



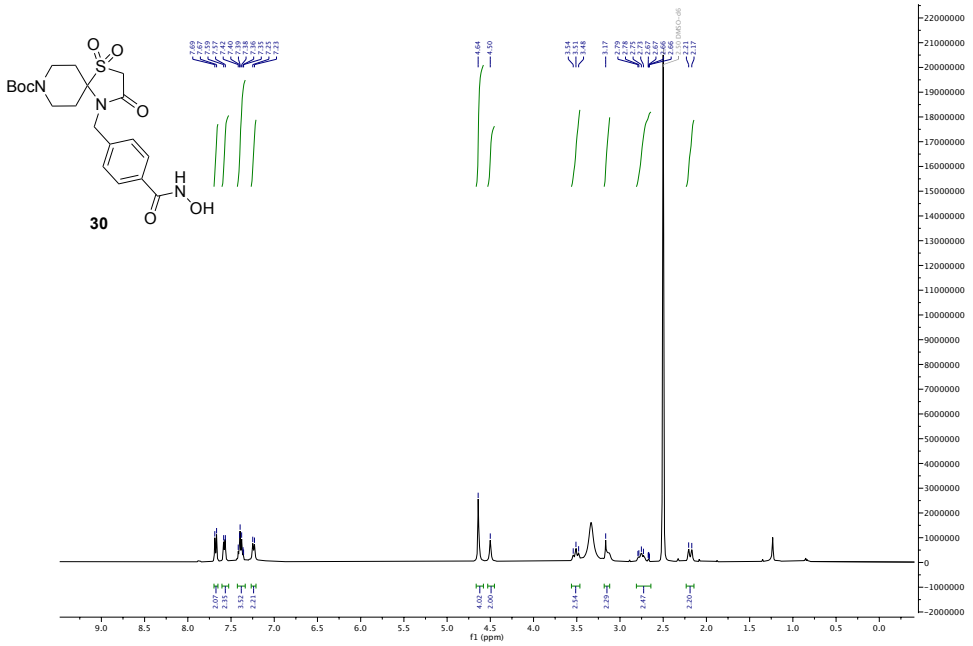
Supporting Figure 26

^{13}C NMR of compound 29



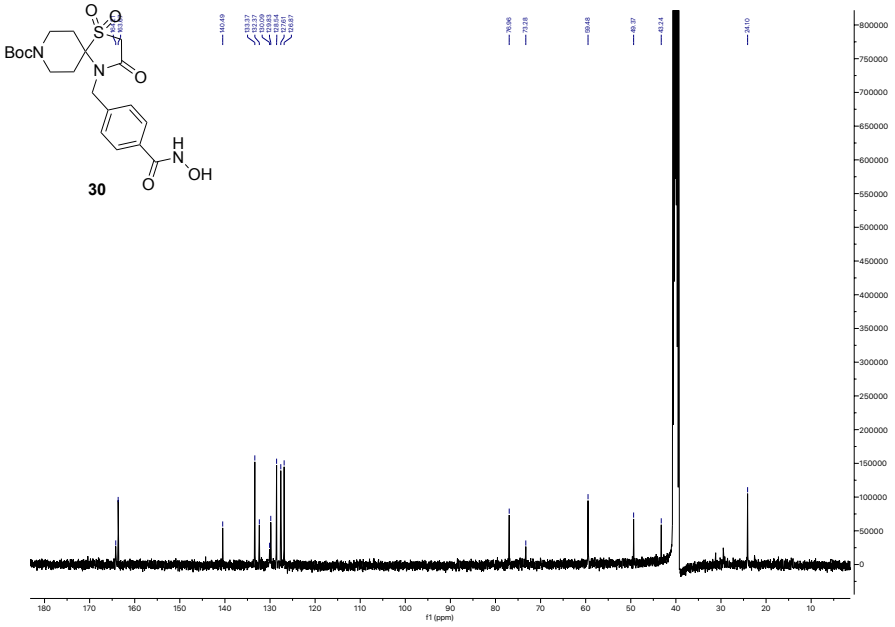
Supporting Figure 27

^{1}H NMR of compound 30



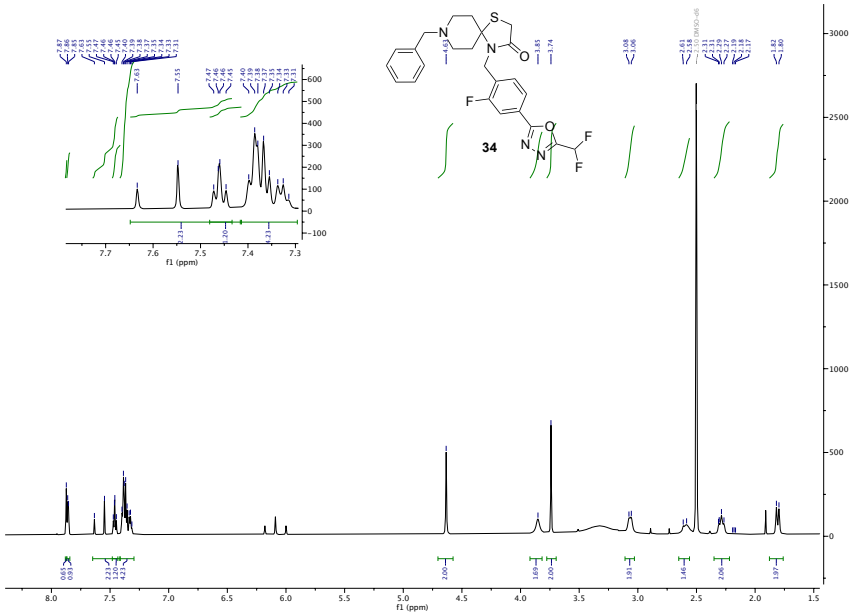
Supporting Figure 28

^{13}C NMR of compound 30



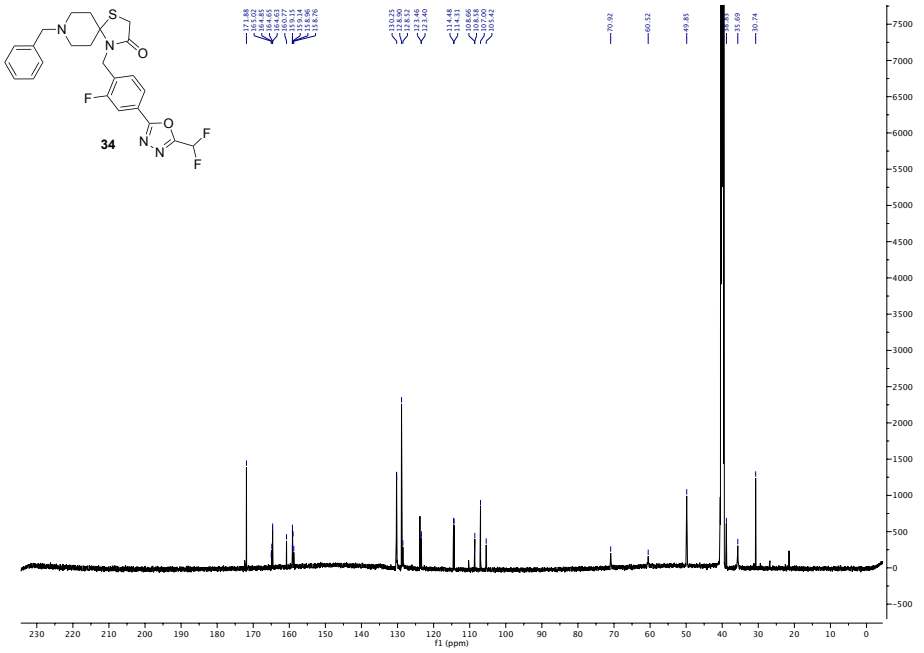
Supporting Figure 29

^{1}H NMR of compound 34



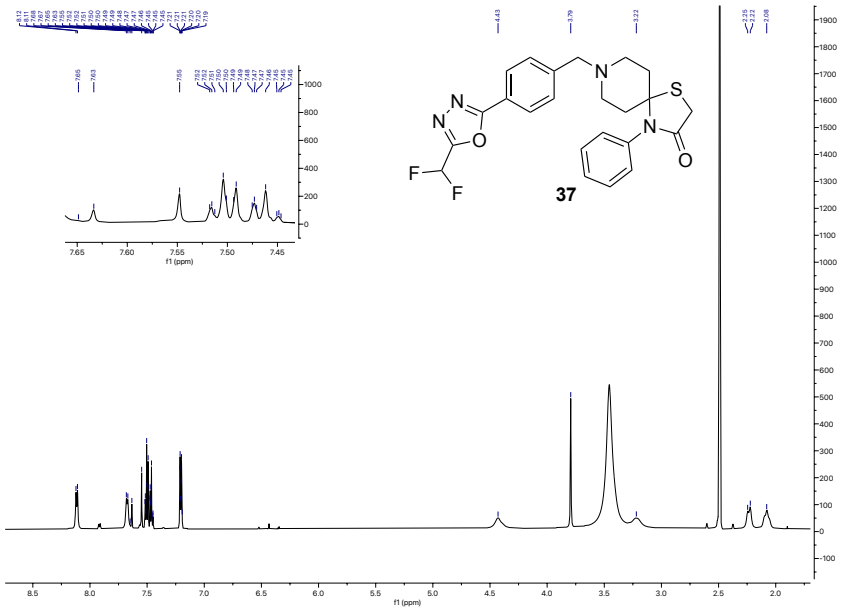
Supporting Figure 30

^{13}C NMR of compound 34



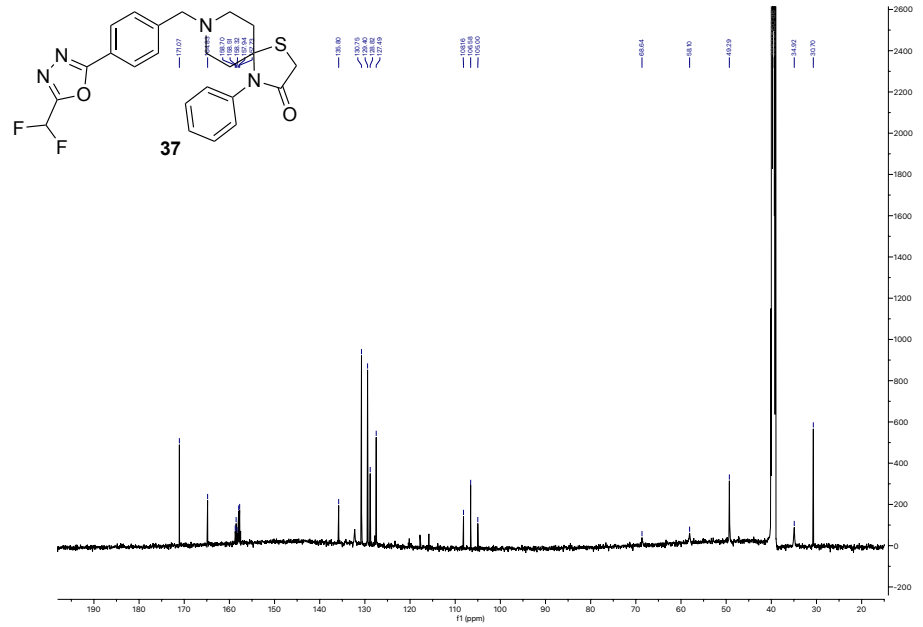
Supporting Figure 31

^{1}H NMR of compound 37



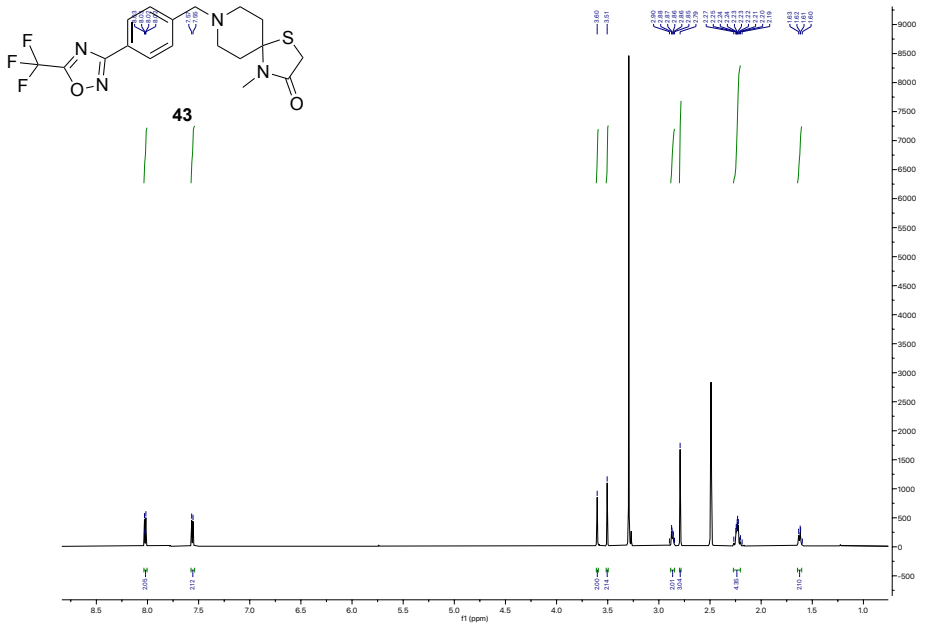
Supporting Figure 32

^{13}C NMR of compound 37



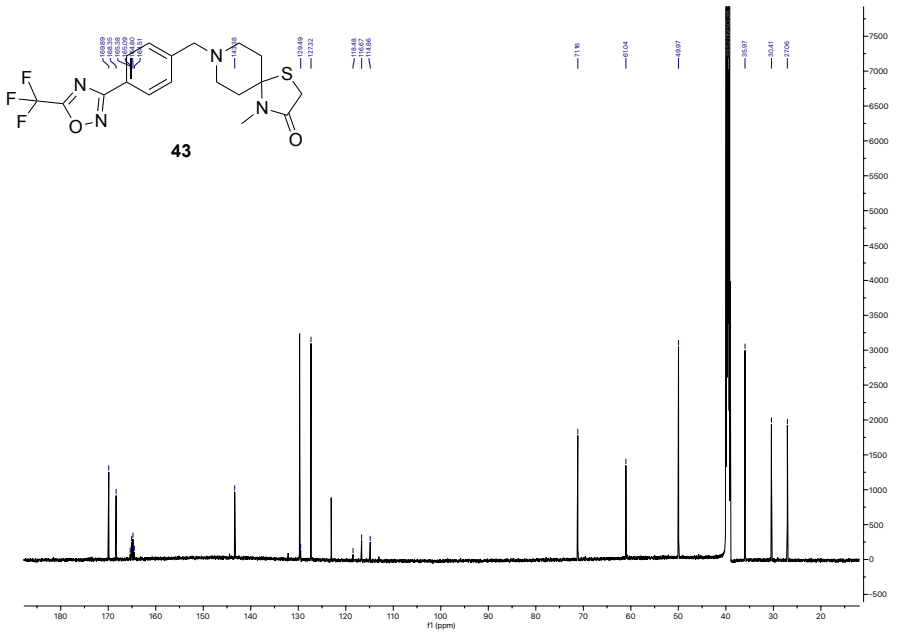
Supporting Figure 33

^{1}H NMR of compound 43



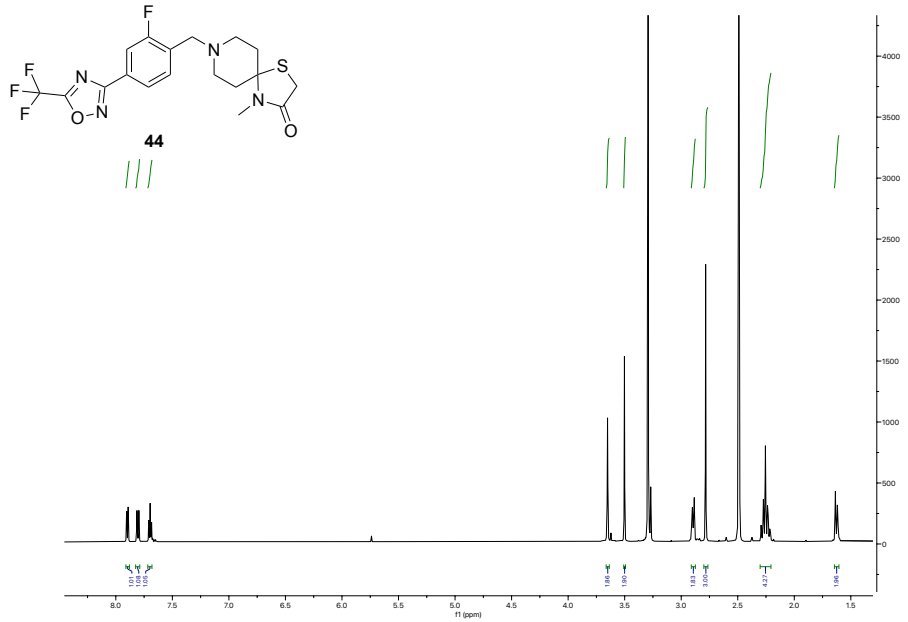
Supporting Figure 34

^{13}C NMR of compound 43



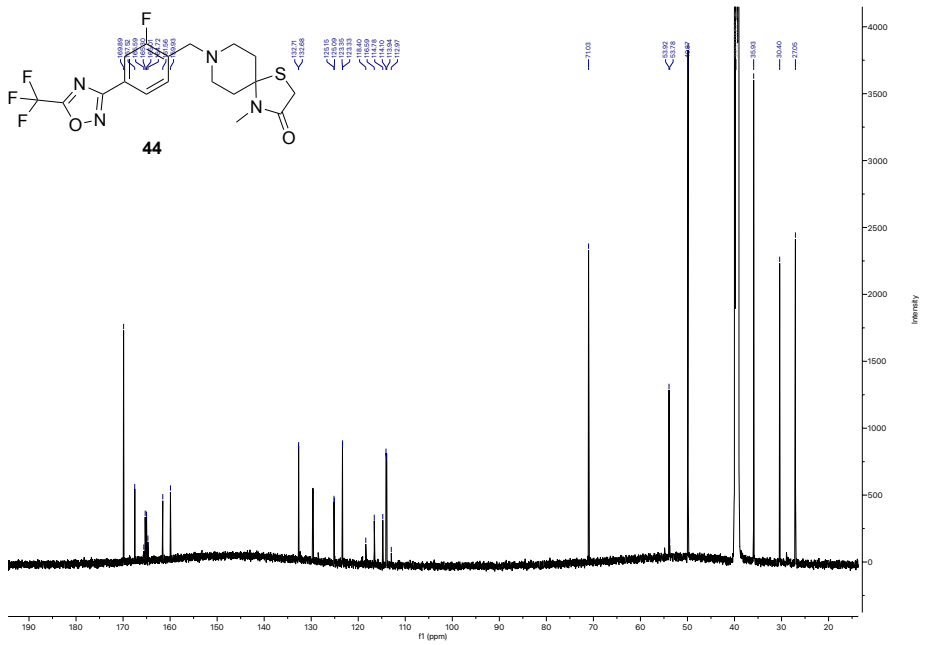
Supporting Figure 35

^{1}H NMR of compound 44



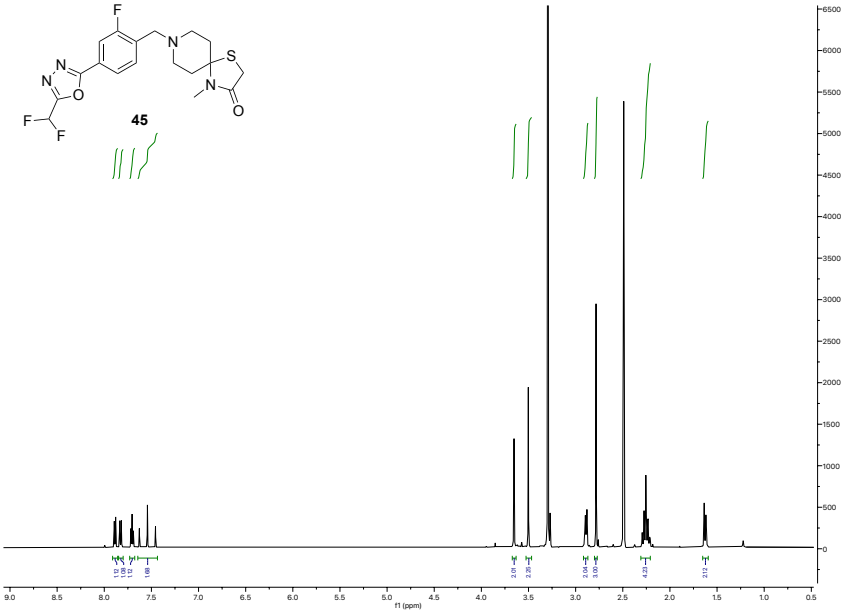
Supporting Figure 36

^{13}C NMR of compound 44



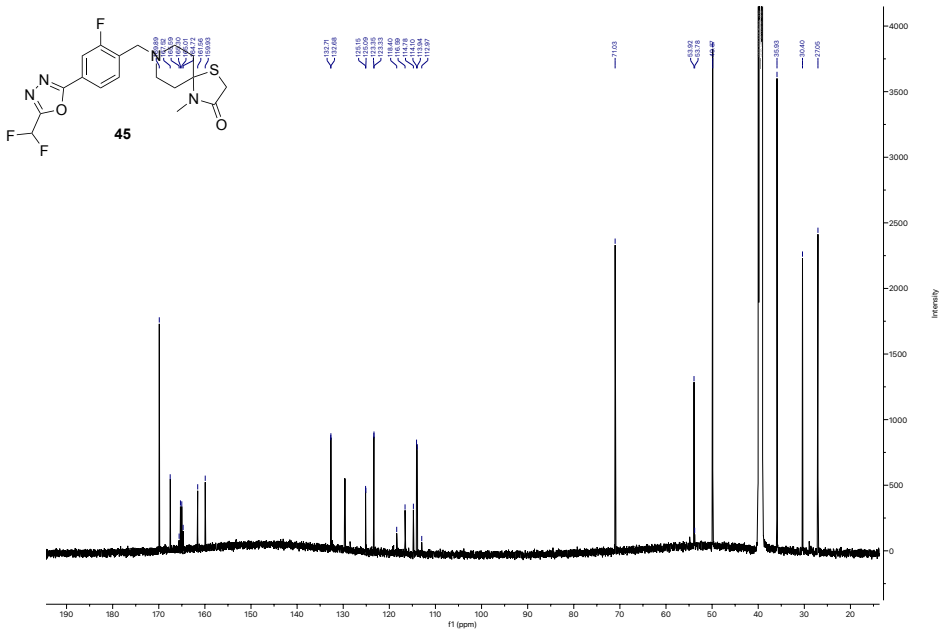
Supporting Figure 37

^{1}H NMR of compound 45



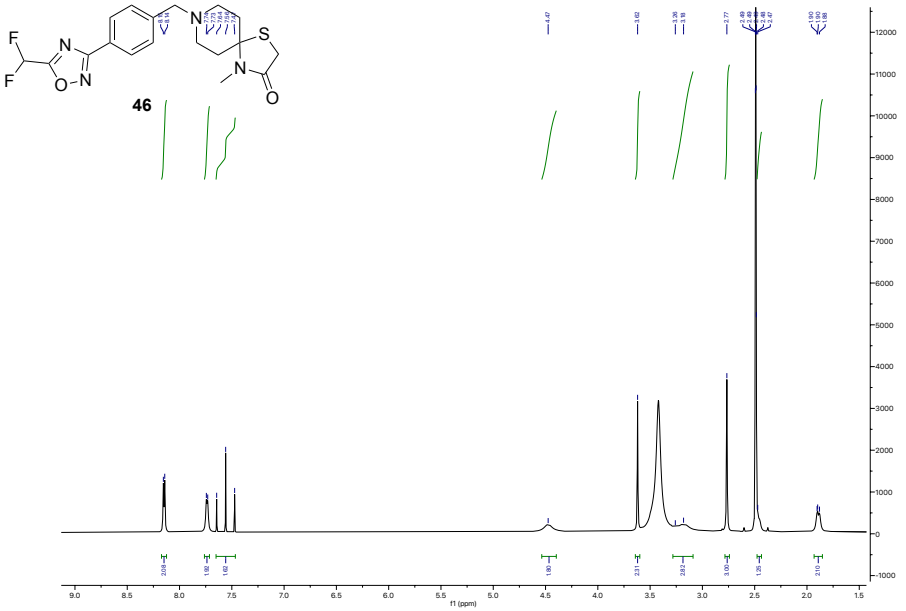
Supporting Figure 38

^{13}C NMR of compound 45



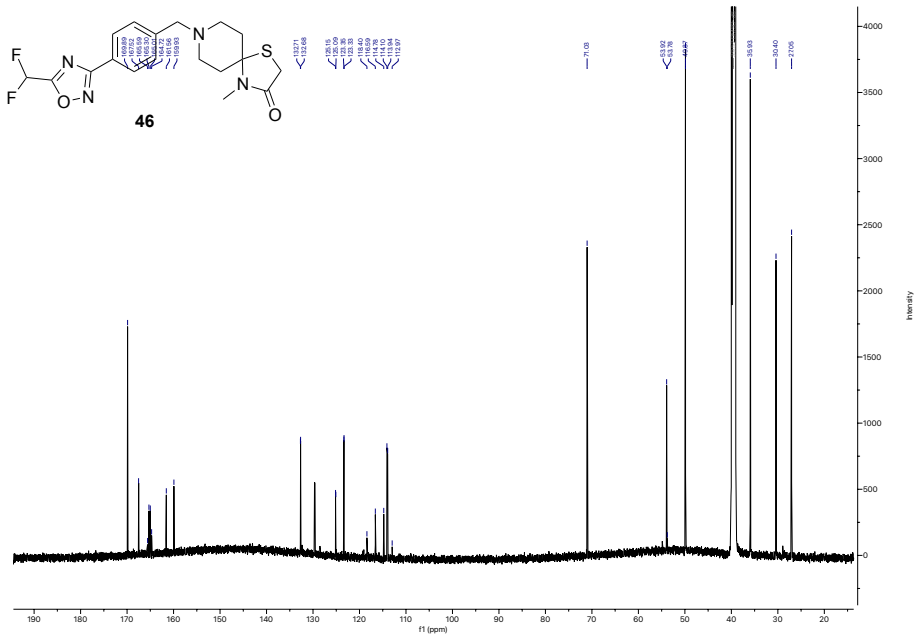
Supporting Figure 39

^{1}H NMR of compound 46



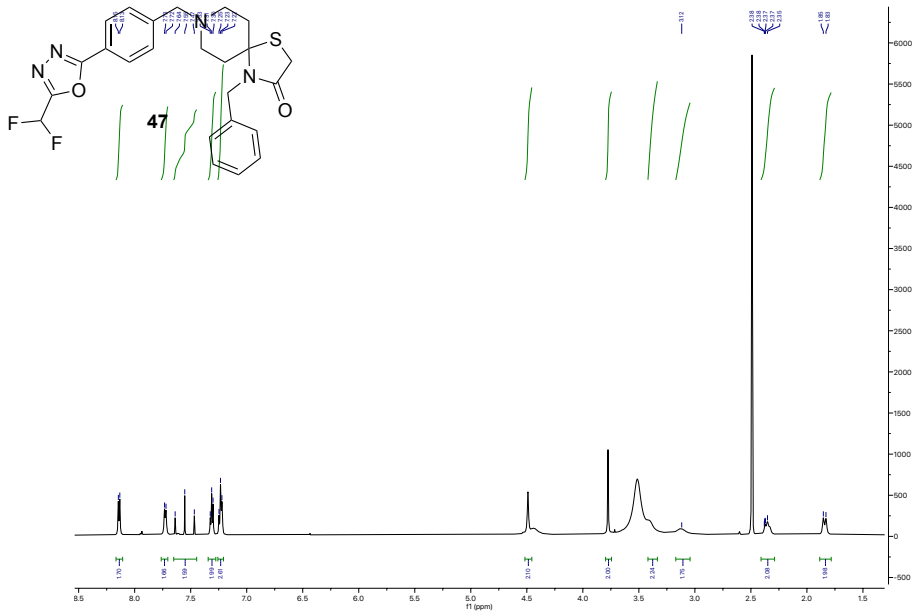
Supporting Figure 40

^{13}C NMR of compound 46



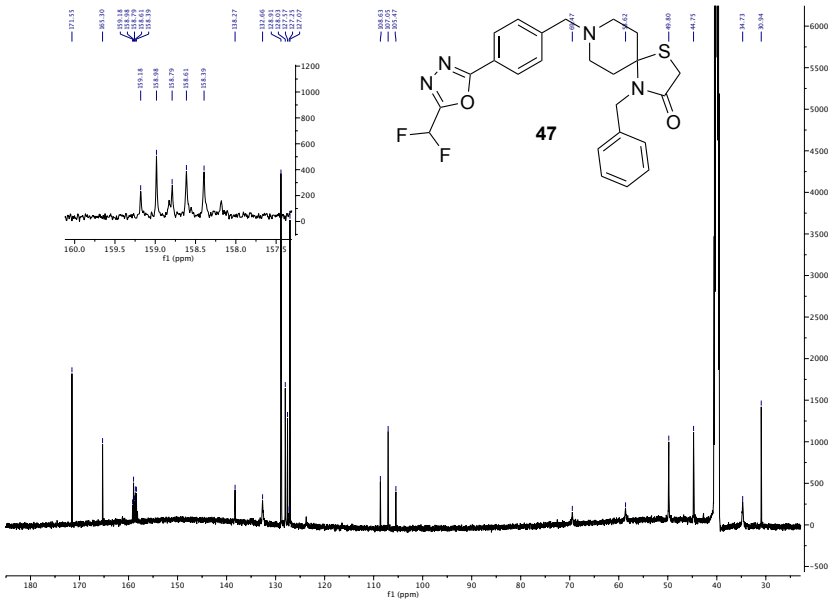
Supporting Figure 31

^{1}H NMR of compound 47



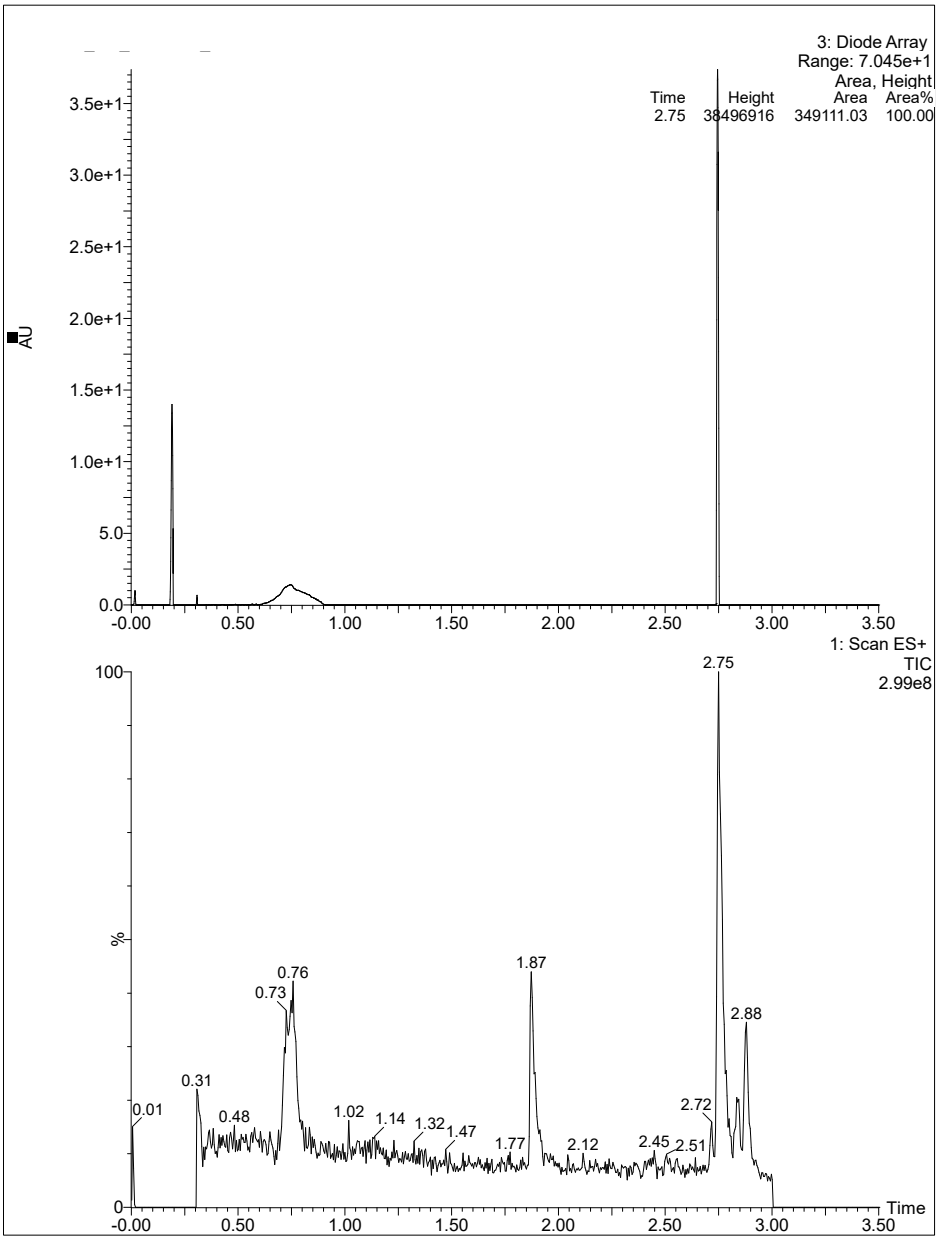
Supporting Figure 42

^{13}C NMR of compound 47



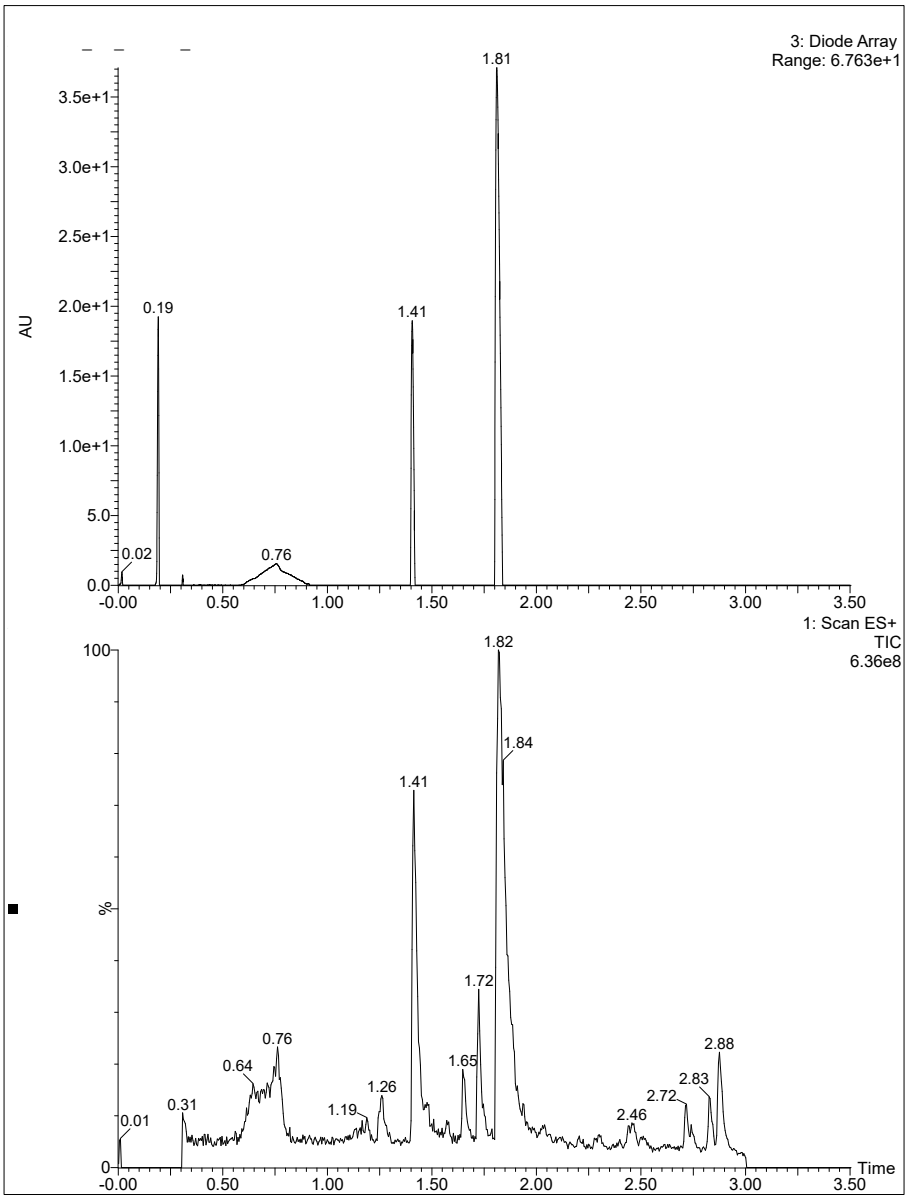
Supporting Figure 44

UPLC-MS spectrum of 3



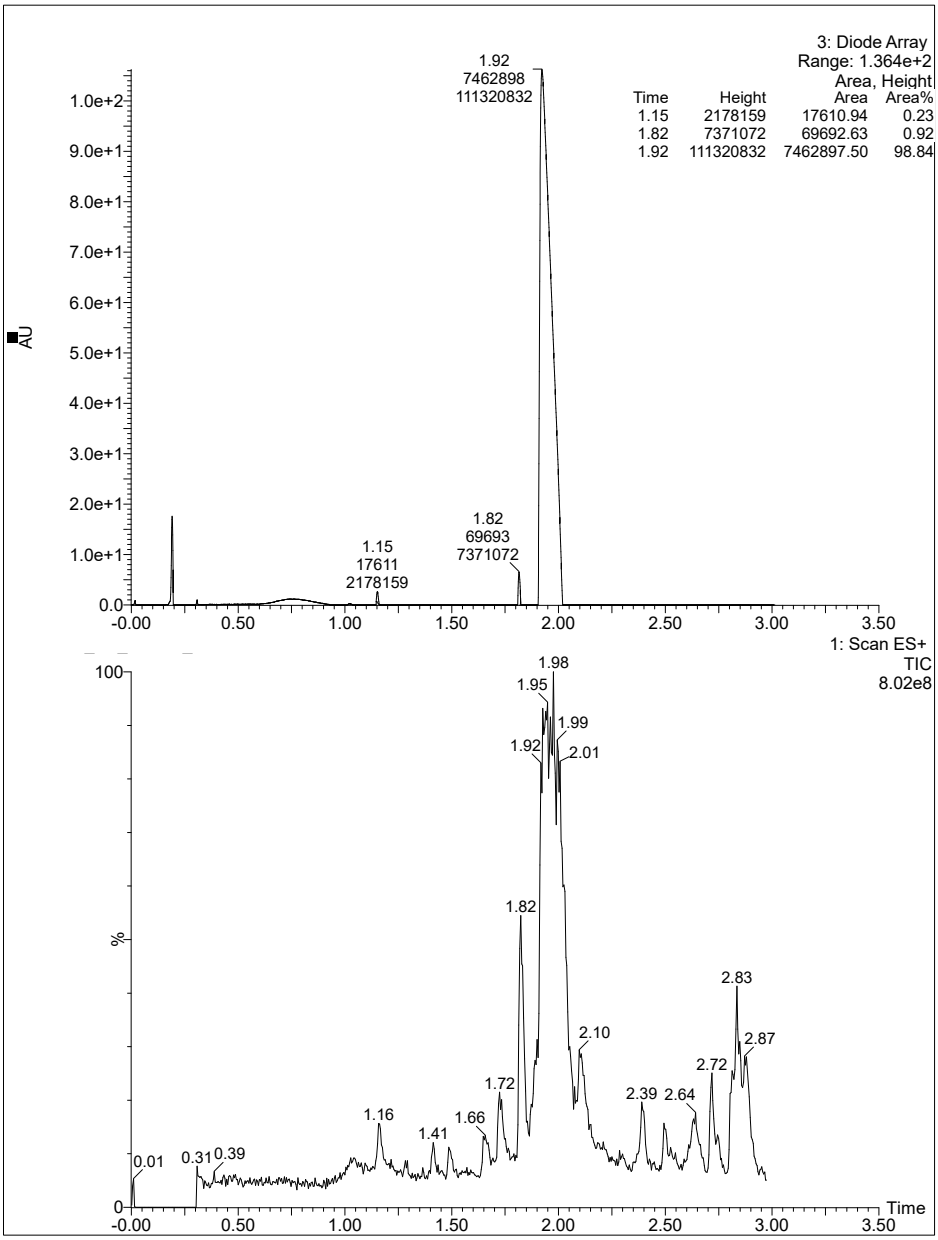
Supporting Figure 45

UPLC-MS spectrum of 7



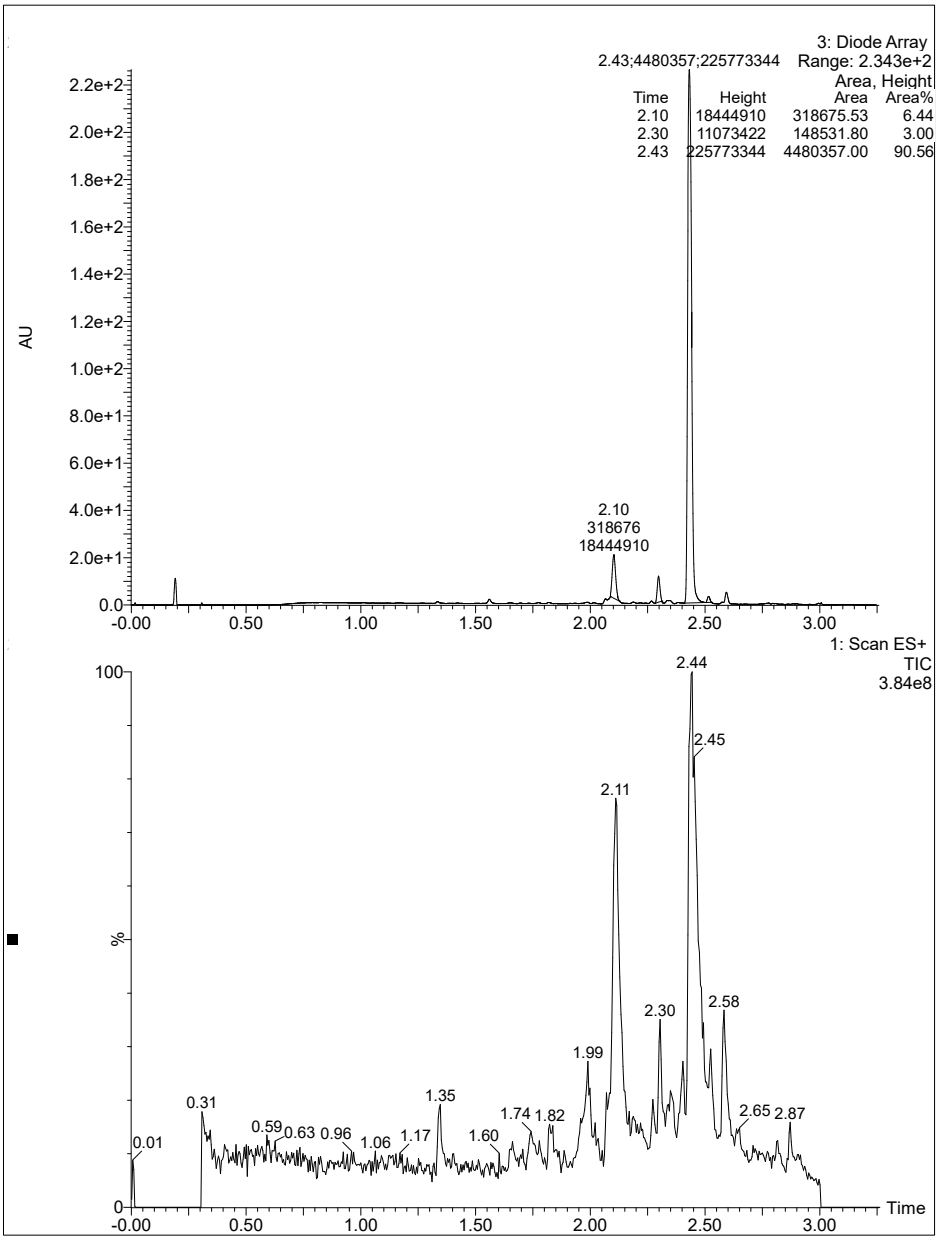
Supporting Figure 46

UPLC-MS spectrum of 8



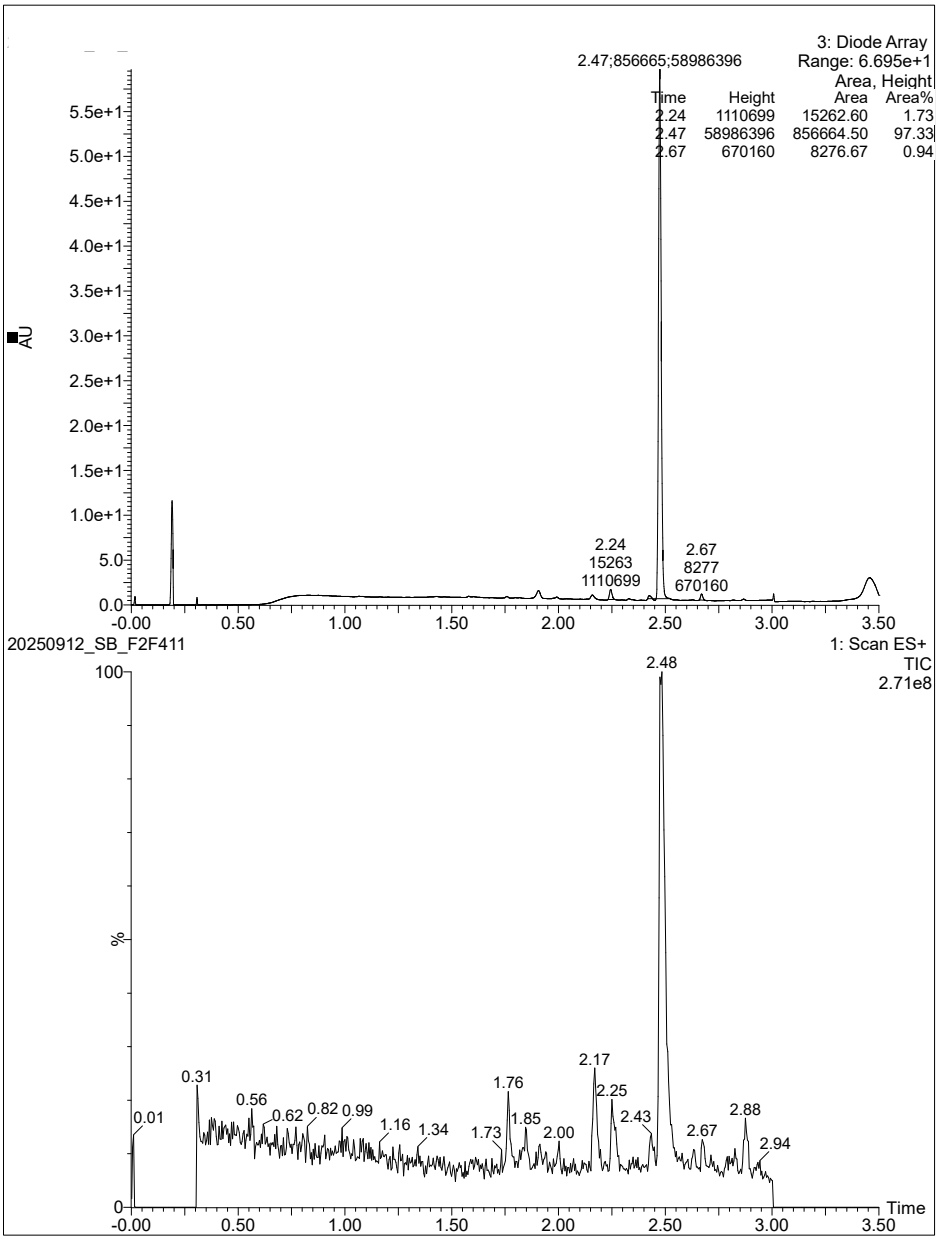
Supporting Figure 47

UPLC-MS spectrum of 13a



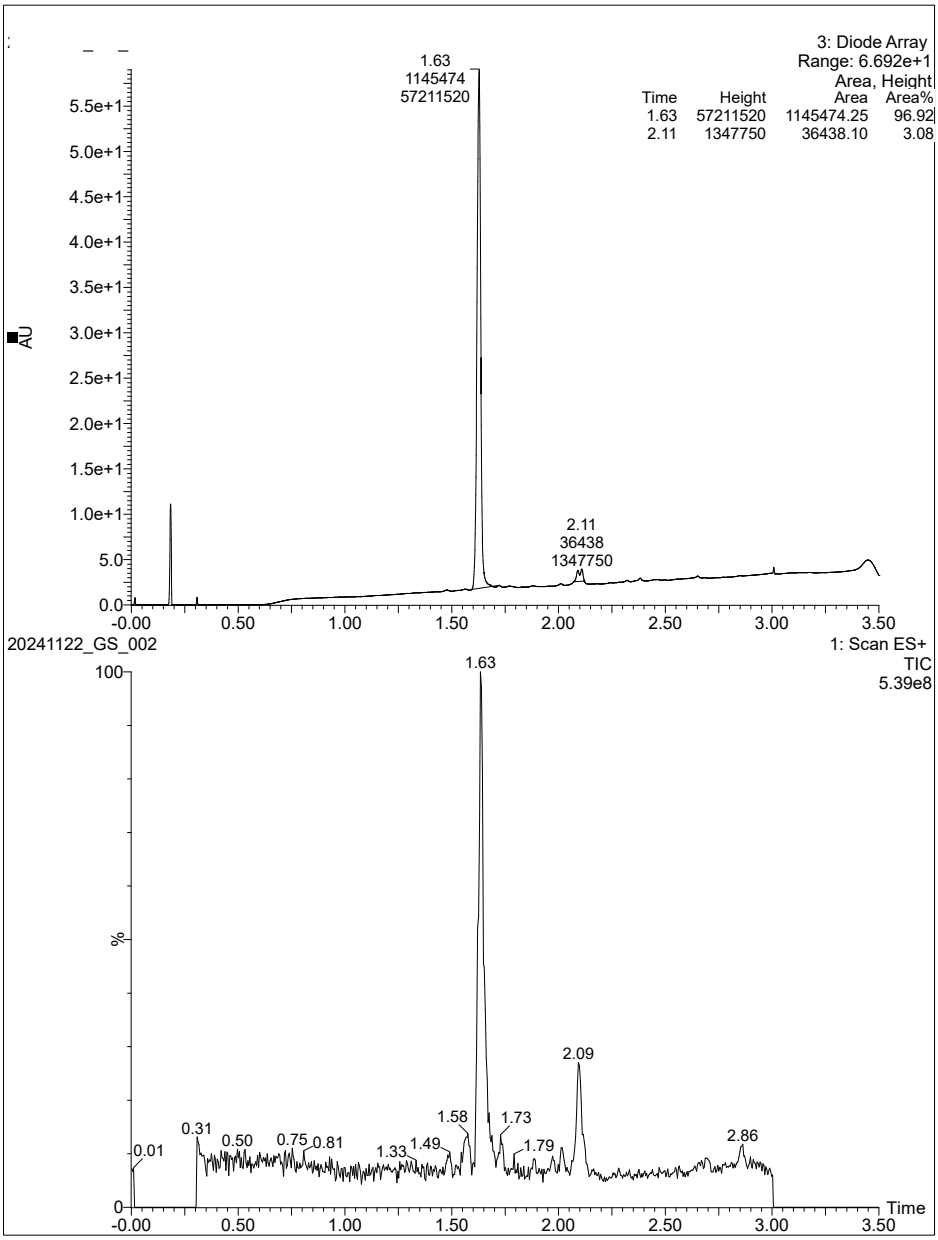
Supporting Figure 47

UPLC-MS spectrum of 13b



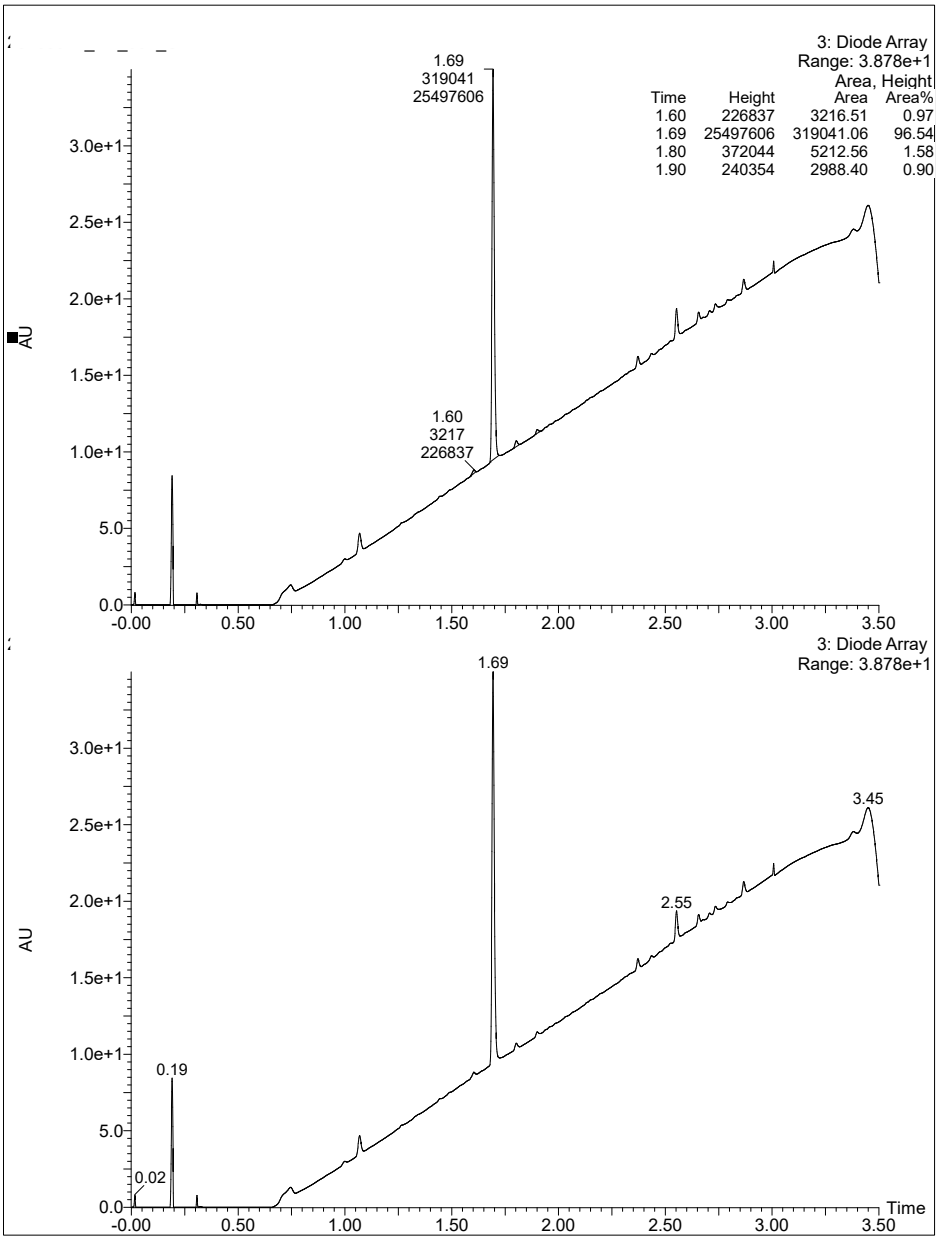
Supporting Figure 48

UPLC-MS spectrum of 21a



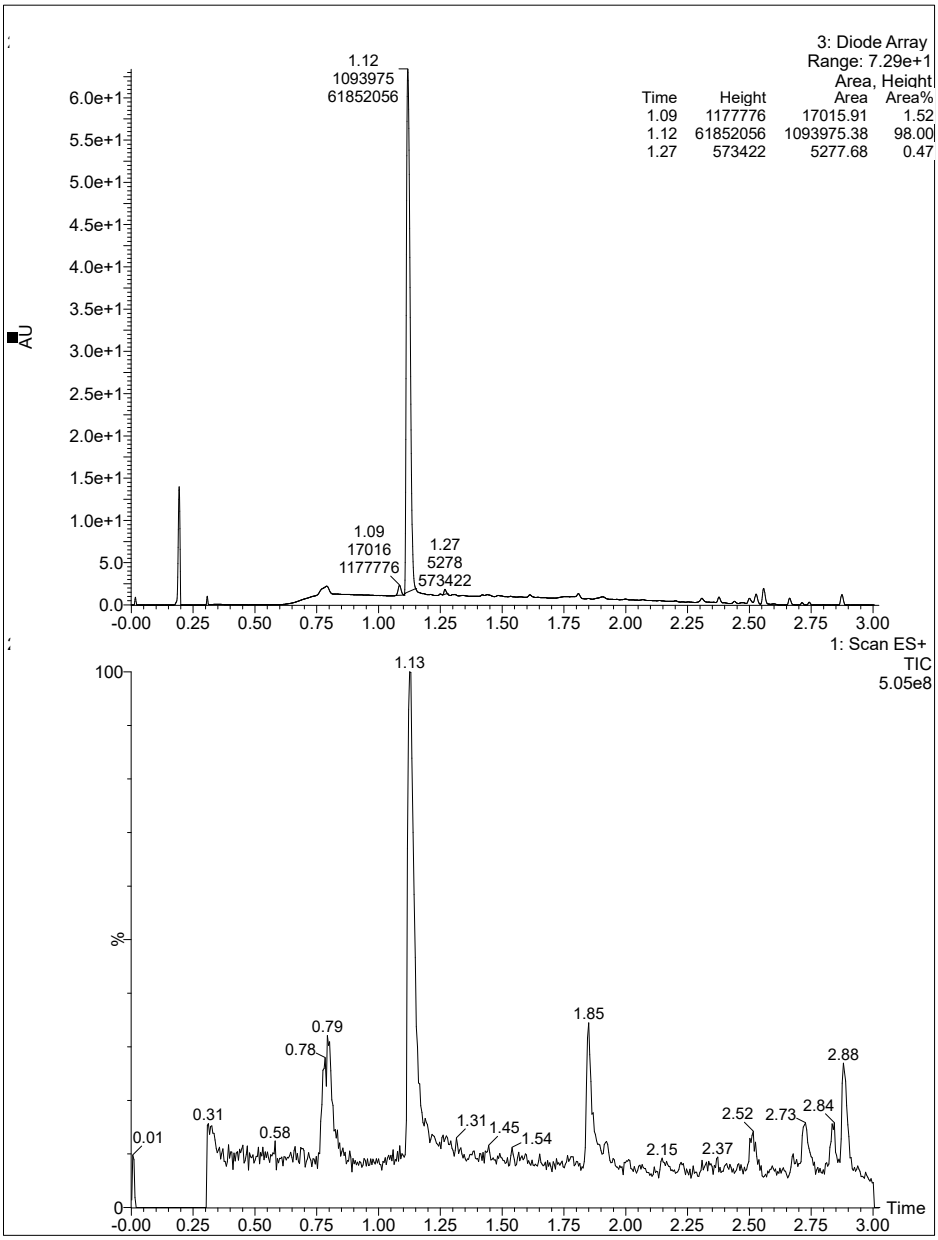
Supporting Figure 49

UPLC-MS spectrum of 21b



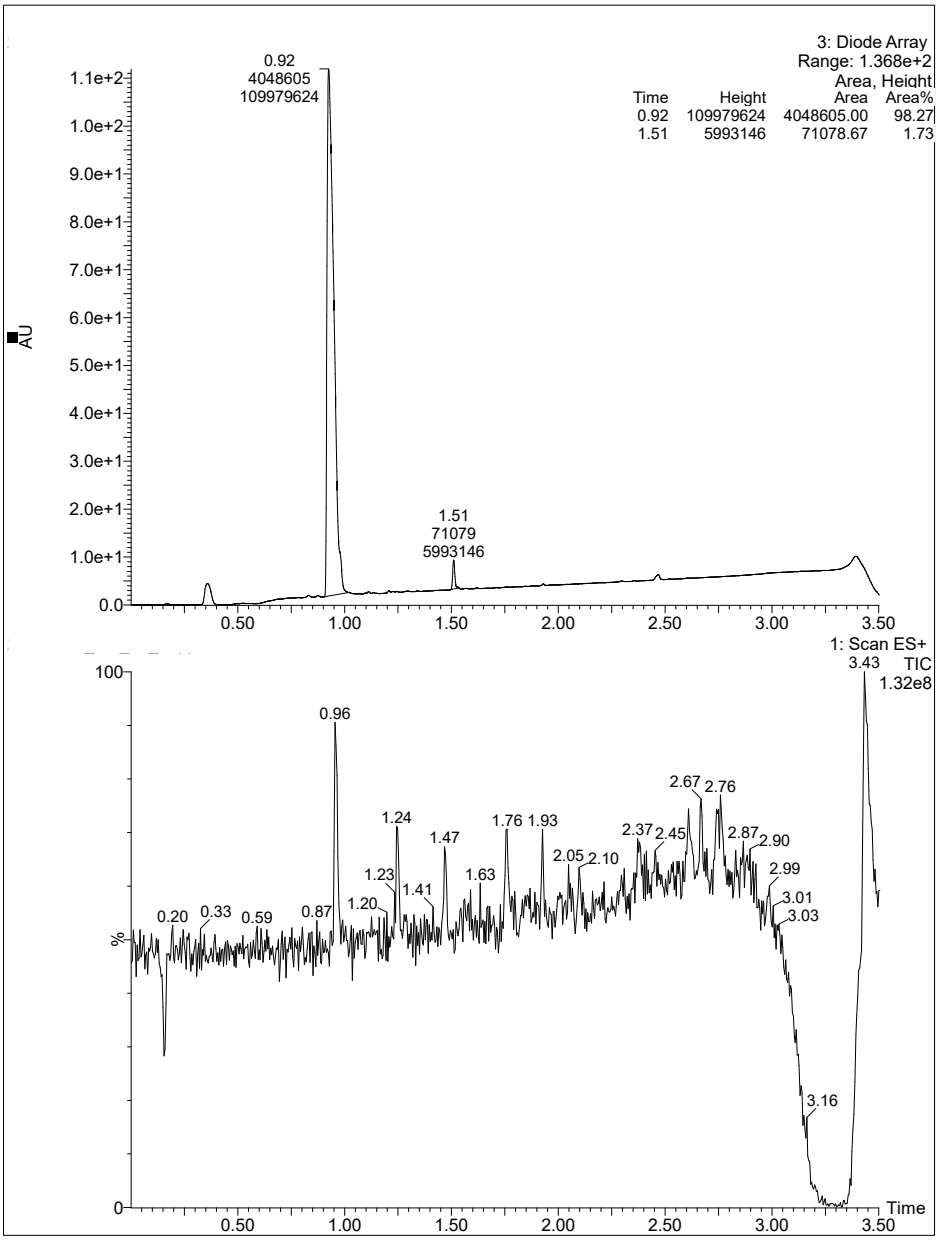
Supporting Figure 50

UPLC-MS spectrum of 25a



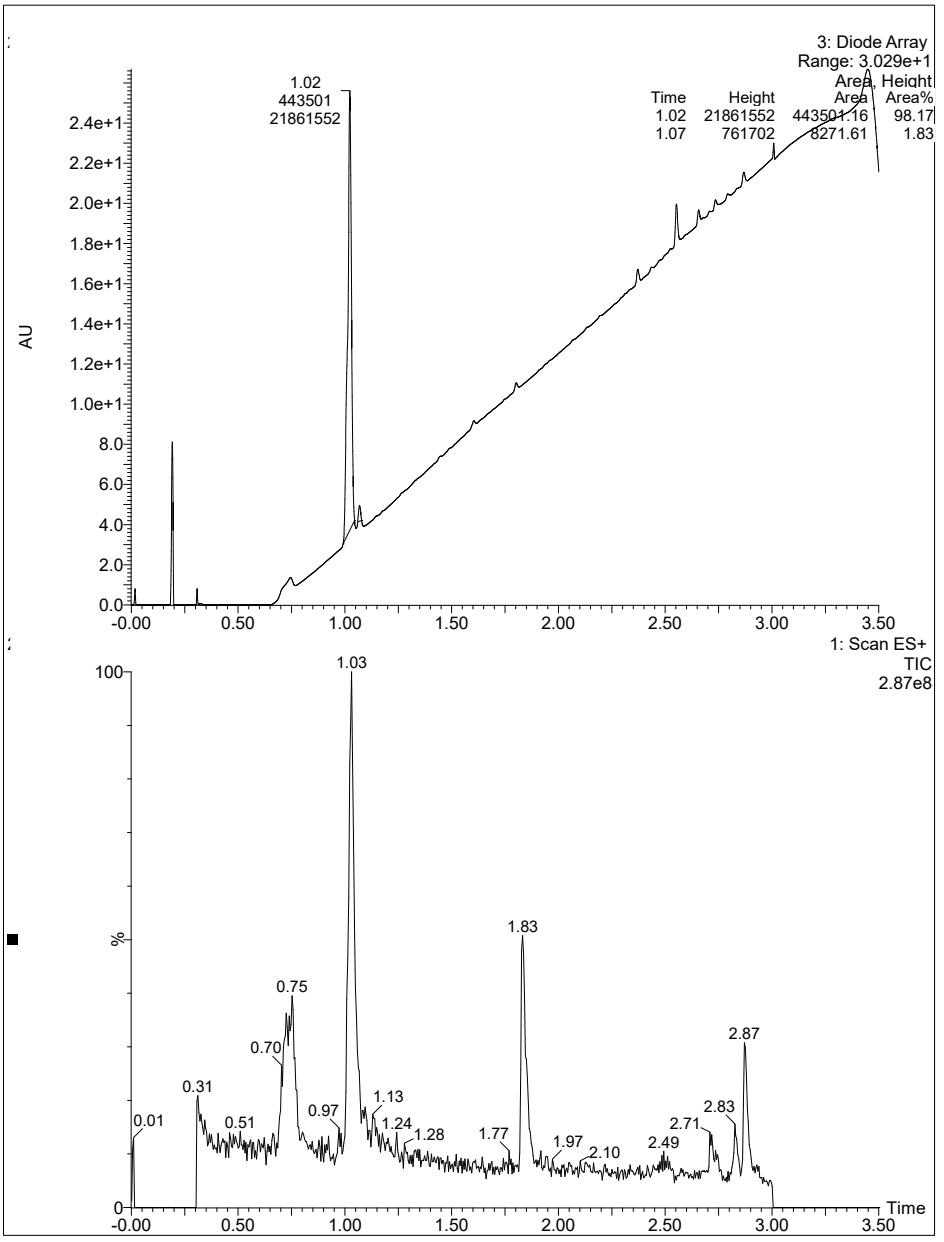
Supporting Figure 51

UPLC-MS spectrum of 26a



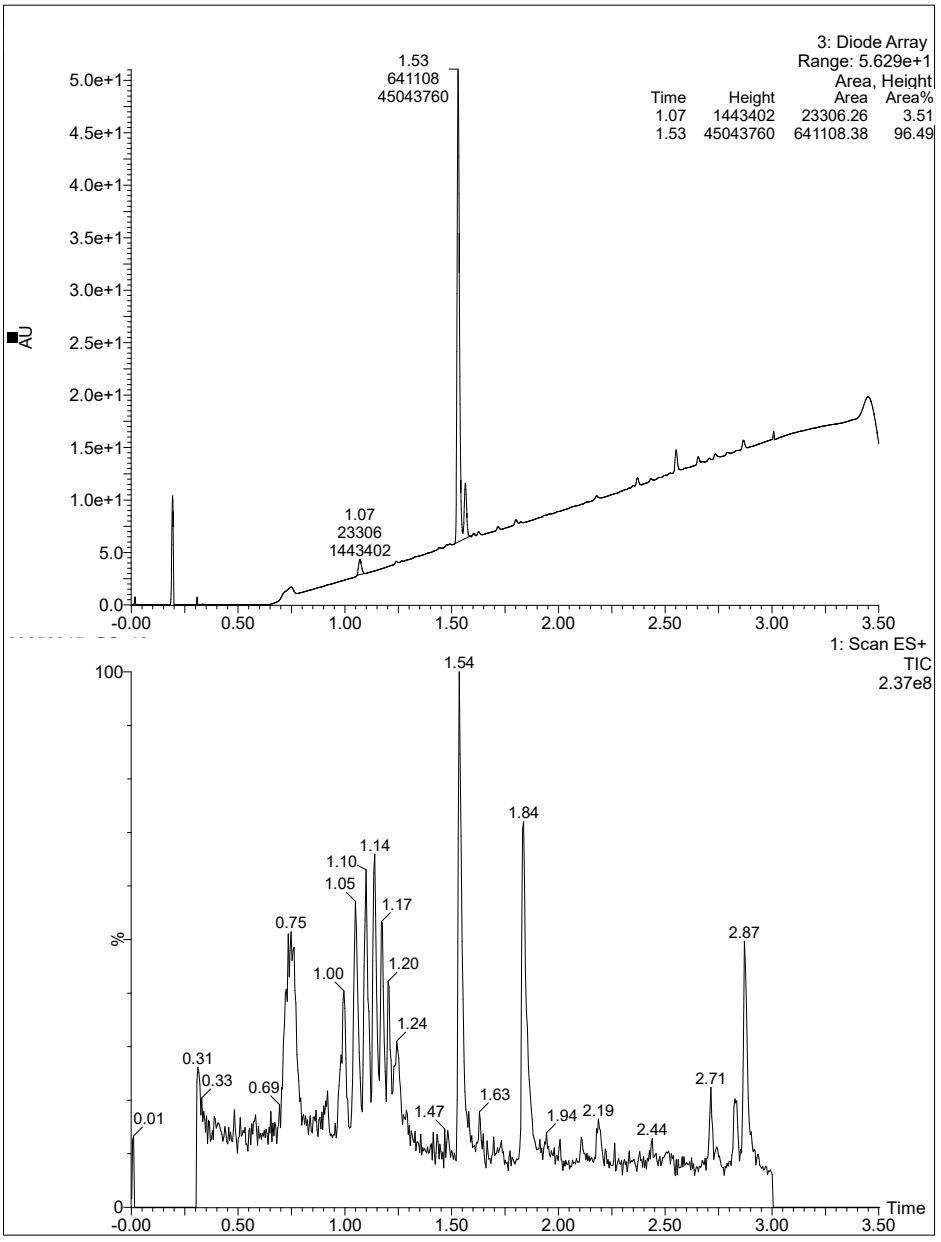
Supporting Figure 52

UPLC-MS spectrum of 26b



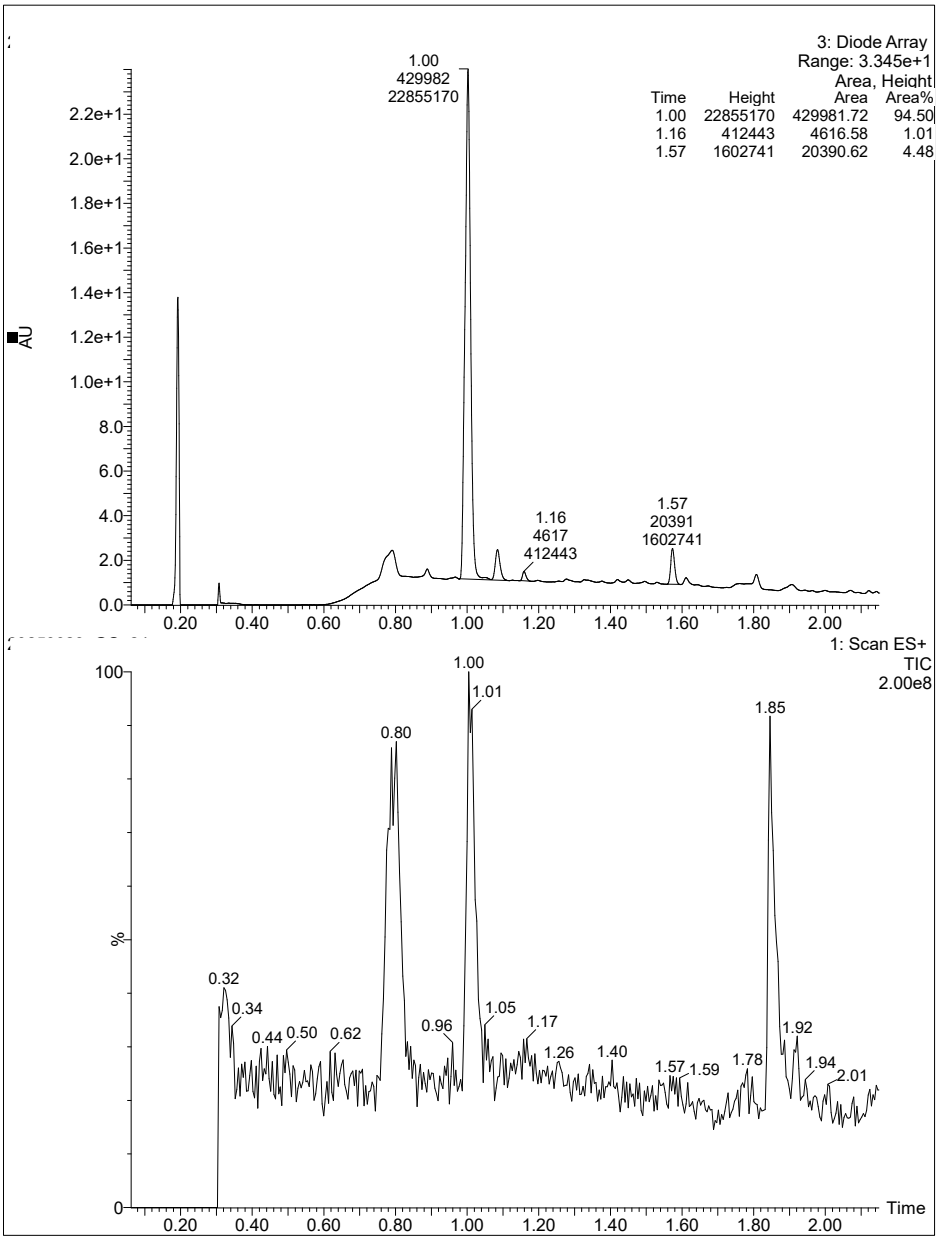
Supporting Figure 53

UPLC-MS spectrum of 29



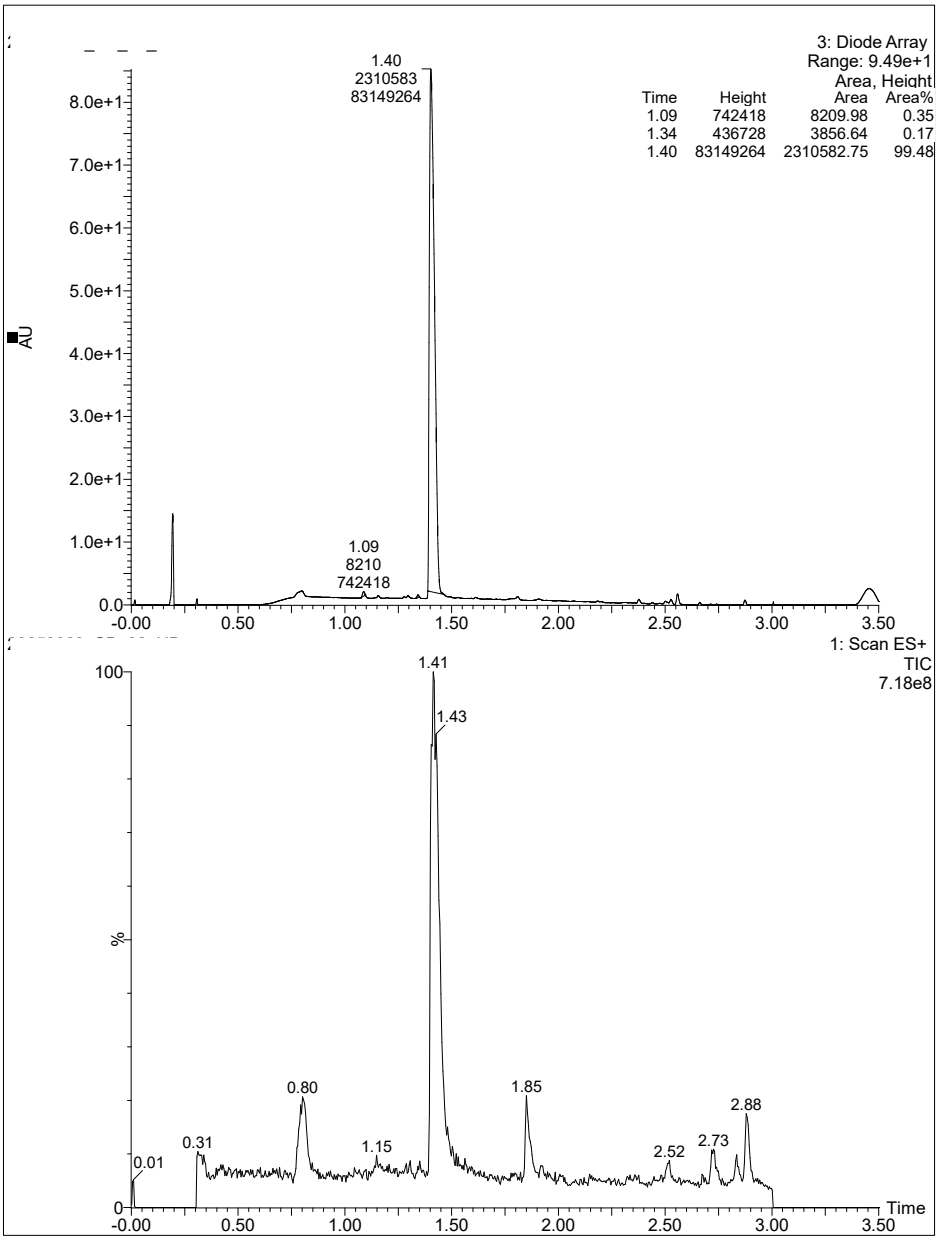
Supporting Figure 54

UPLC-MS spectrum of 30



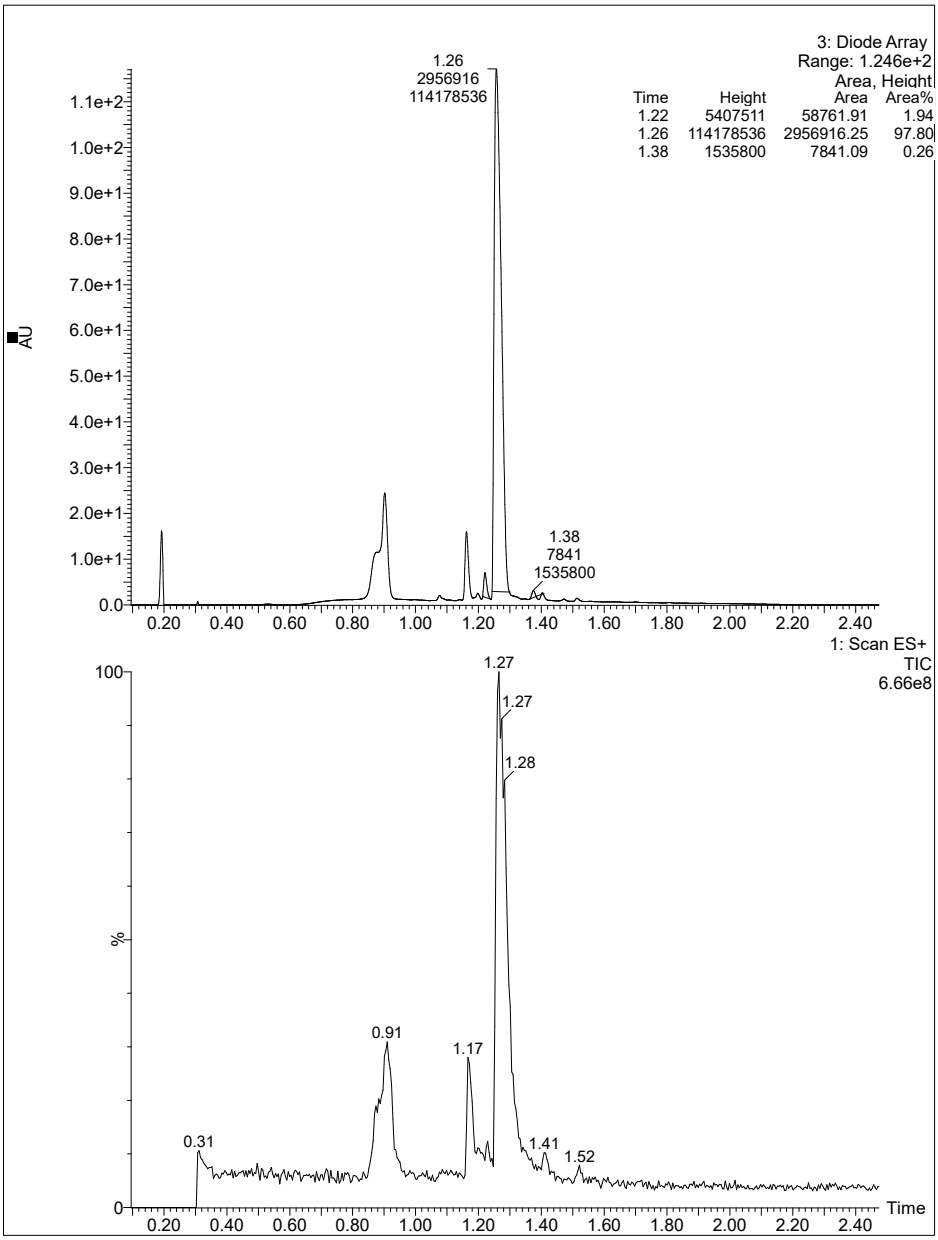
Supporting Figure 55

UPLC-MS spectrum of 34



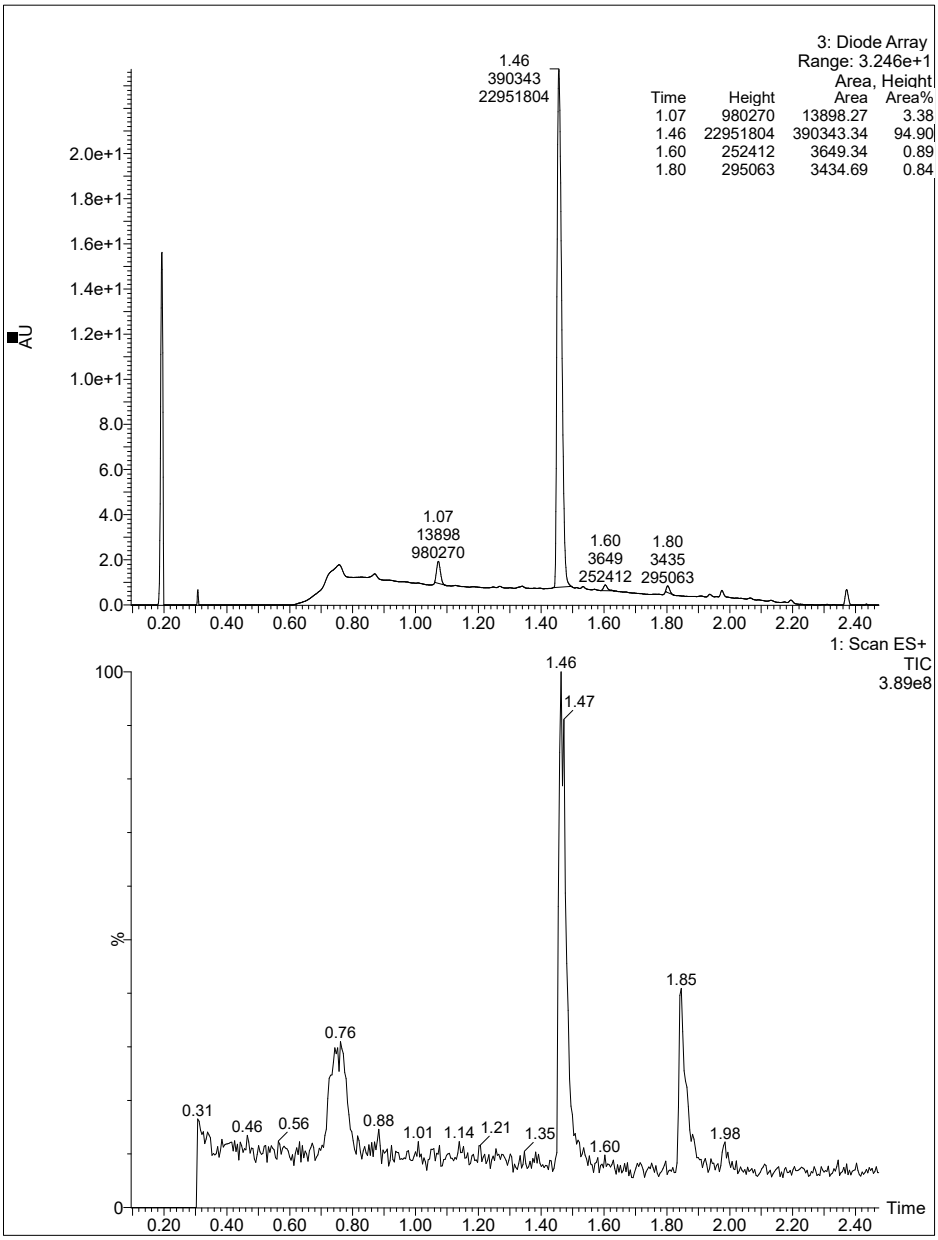
Supporting Figure 56

UPLC-MS spectrum of 37



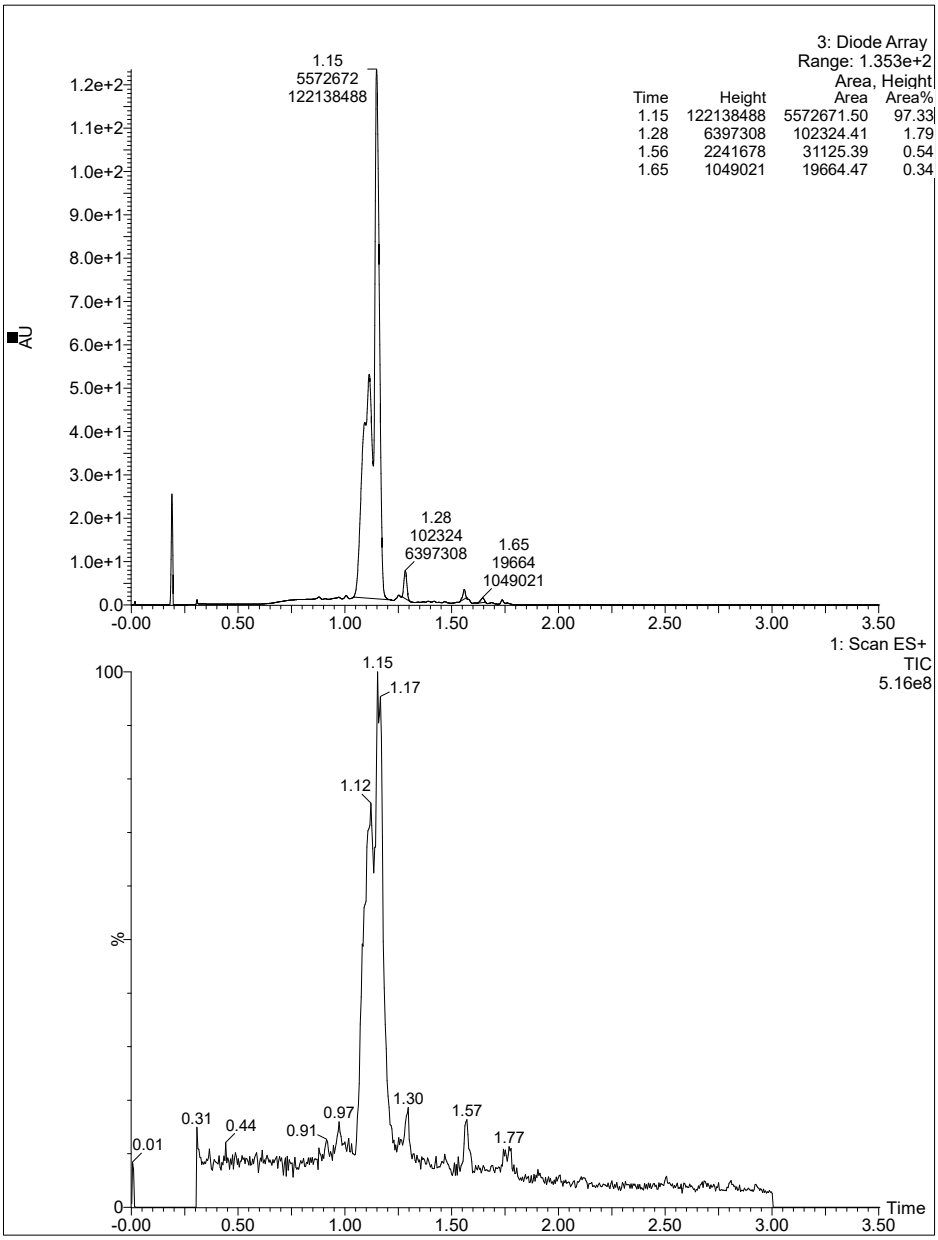
Supporting Figure 57

UPLC-MS spectrum of 43



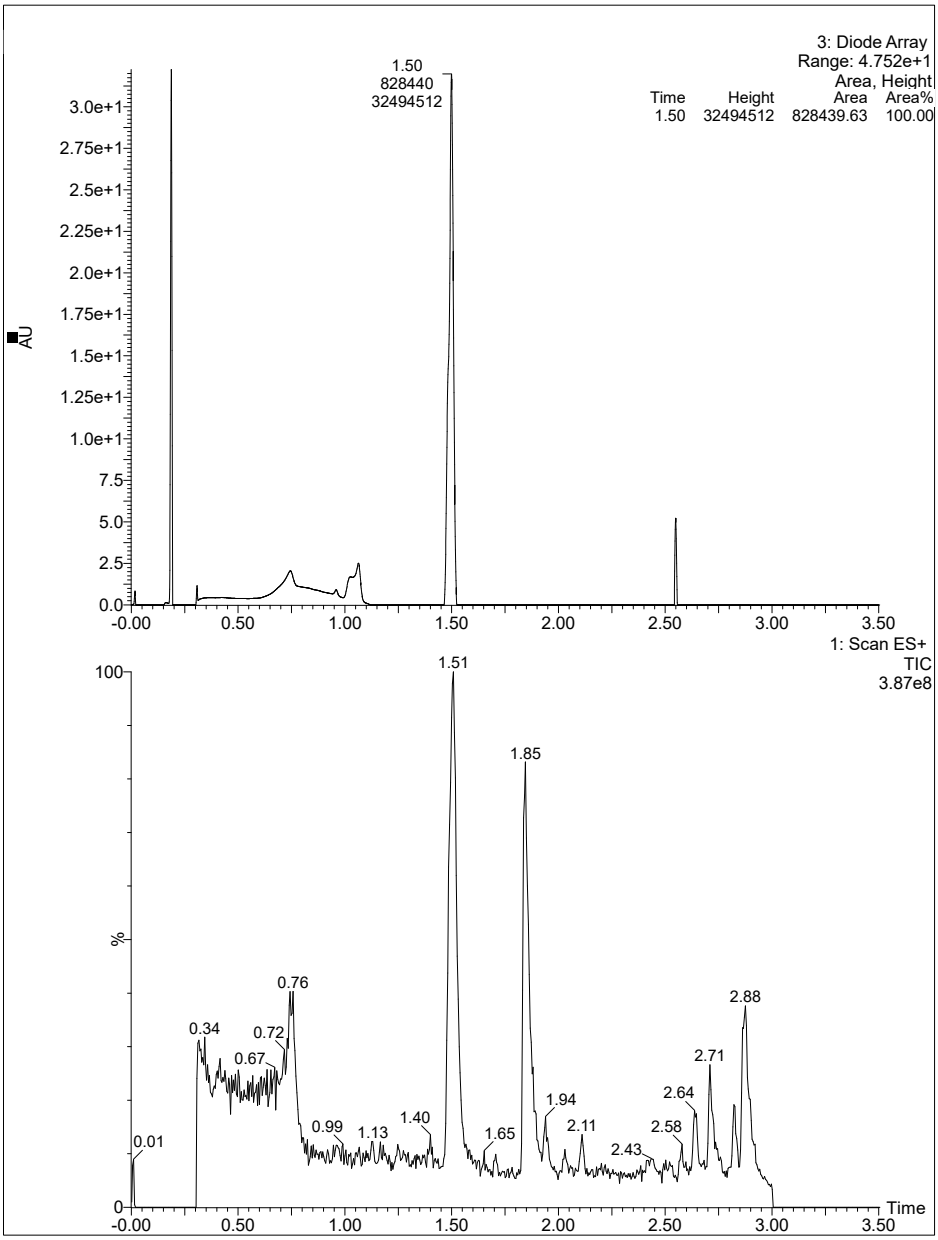
Supporting Figure 58

UPLC-MS spectrum of 44



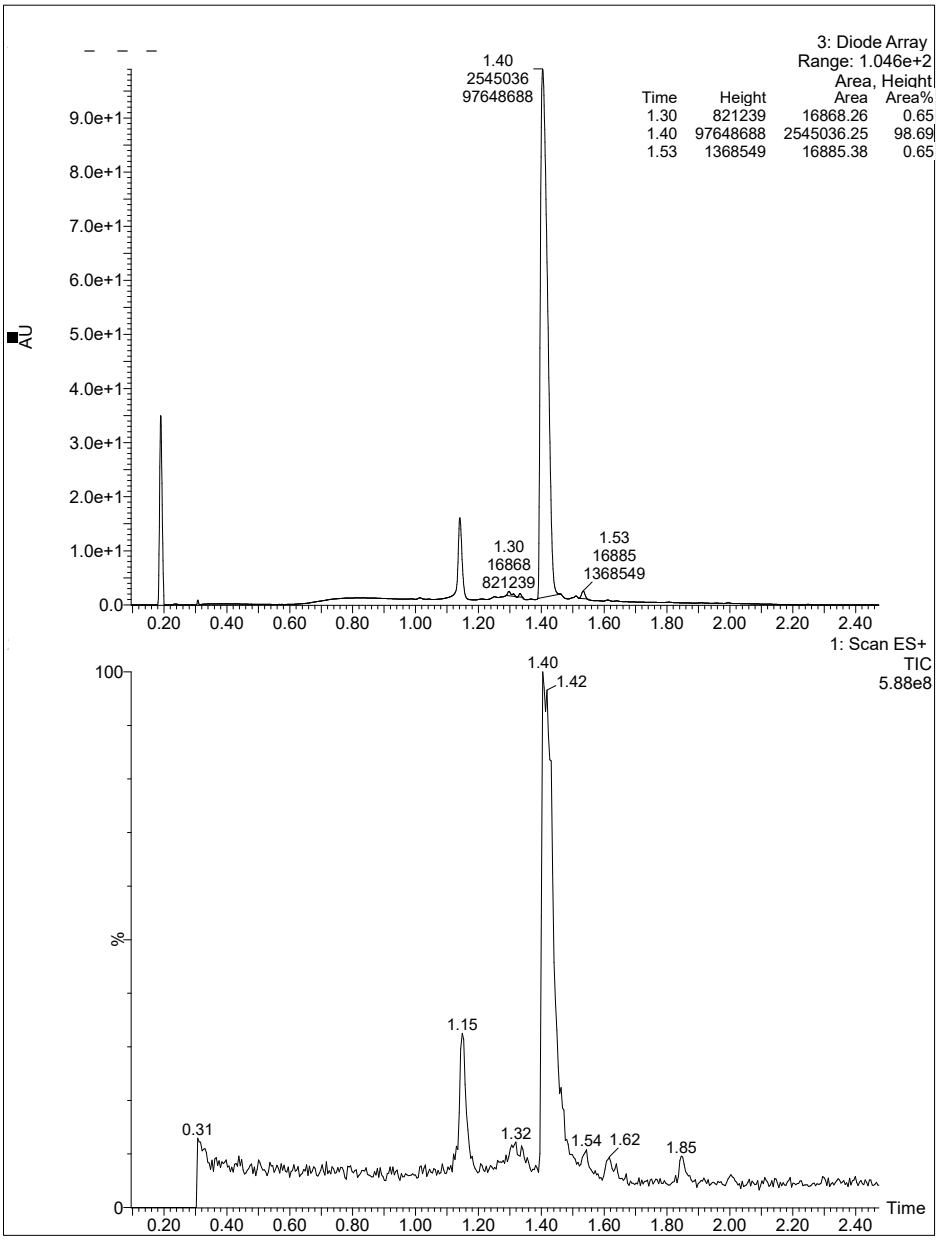
Supporting Figure 59

UPLC-MS spectrum of 45



Supporting Figure 60

UPLC-MS spectrum of 47



References

[1] J. Knipstein, L. Gore, Expert Opin Investig Drugs 20 (2011) 1455–1467.

[2] E. Cellupica, G. Caprini, P. Cordella, C. Cukier, G. Fossati, M. Marchini, I. Rocchio, G. Sandrone, M.A. Vanoni, B. Vergani, K. Źrubek, A. Stevenazzi, C. Steinkühler, Journal of Biological Chemistry 299 (2023) 102800.

[3] D. Moi, D. Bonanni, S. Belluti, P. Linciano, A. Citarella, S. Franchini, C. Sorbi, C. Imbriano, L. Pinzi, G. Rastelli, Eur J Med Chem 260 (2023) 115730.

[4] B. König, F.K. Hansen, ACS Pharmacol Transl Sci 7 (2024) 899–903.

[5] B. König, P.R. Watson, N. Reßing, A.D. Cragin, L. Schäker-Hübner, D.W. Christianson, F.K. Hansen, J Med Chem 66 (2023) 13821–13837.

[6] S. Barone, I. Bello, A. Guadagni, C. Cerchia, G. Filocamo, E. Cassese, A.I. Alfano, C. Esposito, Á.J. Feliz Morel, M. Brunetti, A. Lavecchia, V. Summa, E. Panza, M. Brindisi, Eur J Med Chem 292 (2025) 117634.

[7] E. Cellupica, G. Caprini, P. Cordella, C. Cukier, G. Fossati, M. Marchini, I. Rocchio, G. Sandrone, M.A. Vanoni, B. Vergani, K. Źrubek, A. Stevenazzi, C. Steinkühler, Journal of Biological Chemistry 299 (2023) 102800.

[8] A. Niu, L. Lin, D. Zhang, K. Jiang, D. Weng, W. Zhou, J. Wang, Bioorg Med Chem 59 (2022) 116686.

[9] D.I. Ivankin, M.S. Borisova, D.N. Sokolov, O.A. Luzina, T.G. Tolstikova, N.F. Salakhutdinov, Pharm Chem J 55 (2022) 1288–1292.

[10] O.O. Olaoye, F. Erdogan, M. Gracia-Hernandez, H.K. Garcha, A. Sedighi, Q.F. Ashraf, N. Nawar, M. Geletu, H.-S. Seo, D.I. Abdallah, A. Abdeldayem, M.M. Hassan, S. Dhe-Paganon, E.D. de Araujo, A. Villagra, P.T. Gunning, J Med Chem 68 (2025) 18216–18229.

[11] T. Machleidt, C.C. Woodroofe, M.K. Schwinn, J. Méndez, M.B. Robers, K. Zimmerman, P. Otto, D.L. Daniels, T.A. Kirkland, K. V. Wood, ACS Chem Biol 10 (2015) 1797–1804.

[12] M. Hanl, F. Feller, I. Honin, K. Tan, L. Schäker-Hübner, N. Bückreiß, M. Schiedel, M. Gütschow, G. Bendas, F.K. Hansen, (2025).

[13] A. Vogelmann, M. Jung, F.K. Hansen, M. Schiedel, ACS Pharmacol Transl Sci 5 (2022) 138–140.

[14] M.E. Huber, S.L. Wurnig, A.F.A. Moumbock, L. Toy, E. Kostenis, A. Alonso Bartolomé, M. Szpakowska, A. Chevigné, S. Günther, F.K. Hansen, M. Schiedel, ChemMedChem 19 (2024).

[15] L. Schäker-Hübner, R. Haschemi, T. Büch, F.B. Kraft, B. Brumme, A. Schöler, R. Jenke, J. Meiler, A. Aigner, G. Bendas, F.K. Hansen, ChemMedChem 17 (2022).

Chapter 7

Selective HDAC6 inhibitors disrupt P. aeruginosa virulence factor production and biofilm production.

Over years, bacterial infections have emerged as a public health burden due to the onset of multidrug resistant bacterial strains. Indeed, several gram-negative bacteria, named as "*ESKAPE*" (***E****nterococcus faecium,* ***S****taphylococcus aureus,* ***K****lebsellia pneumoniae,* ***A****cinetobacter baumannii,* ***P****seudomonas aeruginosa,* ***E****nterobacted* spp.), have become resistant to the majority of antibiotics under clinical use. This urgent medical need justifies the quest for novel therapies aimed to overcome drug resistance, to be used alone or in combination with available therapies [1]. Among ESKAPE pathogens, *P. aeruginosa* is implied in persistent lungs infections, and it is the most frequent bacterium isolated from the sputum of patients affected with CF, resulting in chronic and difficult-to-eradicate infections even at the initial stages, characterized by lower bacterial load (see *Chapter 1, Cystic Fibrosis*) [2-6]. In CF lungs, excessive mucus production impairs mucociliary clearance and compromises host immune response, overall contributing to chronic inflammation which, together with persistent colonization by pathogens as *P. auerigonosa* or *Staphylococcus aureus*, exacerbates lung damage. Although host immune system weakening is ascribable to CF phenotype, *P. aeruginosa* is able to adapt to airway environment by the

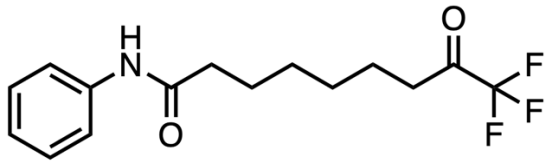
production of virulence factors which enable biofilm formation and multidrug resistance, overall contributing to the persistence of this pathogen in lungs and worsening disease progression [7]. Among virulence factors produced by *P. aeruginosa*, exopolysaccharide (EPS) alginate – a protection factor produced in response to stressed CF lung condition - is related by mucoid phenotypes, which is in turn related to CF lungs deterioration, tissue damage, and poor prognosis [8]. Similarly, in the context of CF, *P. aeruginosa* strains isolated by patients usually lack flagella – which limits bacteria motility. This phenotype is related to enhanced evasion of immune system surveillance and weak susceptibility to phagocytosis [9-11]. Beyond morphological adaptation, bacterial cells are often encased in biofilm matrices, which provide protection against stress conditions derived surrounding environment, including antibiotic treatment [12,13]. It is worth of note that biofilm formation and intercellular communication is regulated by cellular quorum sensing (QS) signals, which coordinates bacterial virulence behaviour [14]. In *P. aeruginosa strains,* the main QS systems are Las, Rhl, and Pqs [15]. Las system stands at the top of QS hierarchy, and it is activated by the N-3-oxododecanoyl-homoserine lactone autoinducer, which in turns activates the transcriptional factor LasR. This event results in the expression of genes encoding for extracellular proteases, elastases, and biofilm maturation factors [16]. Moreover, Las signalling downstream activates Rhl and Pqs QS systems. The former is strictly involved in biofilm development through the production of key virulence factors, namely pyocyanin and rhamnolipids. Pyocyanin is a phenazine secreted approximatively by 95% of *P. aeruginosa.* Pyocyanin can cross biological membranes, allowing *P. aeruginosa* to receive and transport electrons arising from the respiration process and to survive in oxygen-limited environments [17,18]. In biofilm matrix, pyocyanin creates a redox potential gradient that enhances iron bioavailability, a key factor for biofilm formation. Interestingly, pyocyanin secretion has been proved to be detrimental on host

immune function, including modulation of multidrug efflux pump expression in *P. aeruginosa* biofilm, and antibiotic resistance [19,20]. Rhamnolipids are biosurfactants, key virulence factors for bacterial swarming motility, thereby promoting bacteria dissemination [21]. Also, rhamnolipids can insert into epithelial tight junctions, disrupting host epithelial barrier integrity and facilitating bacterial spread and invasion [22]. Interestingly, rhamnolipids are often found in the sputa of CF patients and are responsible for inactivating mammalian tracheal cilial motility [23]. Pqs QS pathway regulates virulence and biofilm development, regulating 12% of *P. aeruginosa* genome approximatively [24]. As previously discussed, posttranscriptional epigenetic modifications mediated by HDAC enzymes have been unveiled as key regulators of immune response in infectious diseases (See *Chapter 1*, *Cystic Fibrosis section*) [25-34]. Beyond host immune system regulation mediated by HDACs, *P. aeruginosa* genome expresses enzymes which are structural analogues of human HDACs, namely PA0321, PA1409, and PA3774 [35]. Similar to mammalians, in bacteria, small molecules such as spermidine undergo acetylation on Ɛ-lysine residues, thereby regulating different cellular responses, such as cell cycle regulation, DNA packaging, biofilm formation, RNA stability, and so on [36-42]. Polyamine acetylation is thereby regulated by enzymes with opposite roles, namely acetylases and deacetylases, whereas *P. aeruginosa* deacetylases PA0321 and PA1409 – structurally analogues of human HDAC10 polyamine deacetylase - respectively target N^1-acetylputrescine and N^1-acetylcadaverine [36,37]. While human HDAC enzymes have been widely studied so far, nowadays only limited data are available describing bacterial Zn^{2+} dependent lysine deacetylases, and the main findings are briefly summarized below:

1. Histone deacetylase-like protein from *Aquifex aeolicus* (ApaH, Class I), which share structural homology with human HDACs, thus they are considered to derive from a common ancestor [43].

2. Acetoin-utilization protein C (AcuC) expressed by *Bacillus subtilis* and *Staphylococcus aureus* (Class I) and *Aeromonas hydrophila* (Class II) [44].
3. Kdac1, expressed by the multidrug-resistant pathogen *Acinetobacter baumannii* [45].
4. PA3774, expressed by *P. aeruginosa* [46].
5. Histone deacetylase like amidohydrolase (HDAH) FB188 [47].

Interestingly, while PA0321 and PA1409 are polyamine deacetylases, PA3774 is not catalytically active. On the contrary, PA3774 is structurally related to human HDACs and it has shown deacetylase activity artificial acetylated lysine substrate [48]. Crystal structure of PA3774 from *P. aeruginosa* PA01 strain revealed a tetrameric structure in which a L1 loop of each subunit promotes the tetramerization and stabilize three-dimensional structure of the protein. Importantly, PA3774 L1 loop is elongated with comparison to HDAC family L1 loop. As similarly observed for HDAC family, the active site of PA3774 protein consists in the catalytic Zn^{2+} ion, which is coordinated by D181, H183 and D269 residues, while residues H143, H144, and Y313 form hydrogen bonds with bound ligands (PDB: 5G0Y) [46]. One potassium ion is coordinated by D179, D181, H183, L203, S203 and D179, serving to keep in the correct position zinc-coordinating residues, as found in most Class II HDACs. Interestingly, the crystal structure of PA3774 in complex with HDAC8i SATFMK (Figure 1) - a close structural analogue of SAHA - revealed a remarkable binding affinity.



SATFMK
1

Figure 1. Structure of HDAC8i SATFMK **1**.

The trifluoro ketone moiety coordinates the catalytic Zn^{2+} ion in its gem-diol form in a bidentate fashion (Figure 2, PDB: 5G10). More in detail, one oxygen of the gem-diol accepts hydrogen bonds from H144 and H143 residues, while the other is involved in hydrogen bonding with Y313. The fluorine atoms form multipolar interactions with Y313, G311, C154 and P141. Interestingly, PA3774 catalytic center is highly conserved in Class II HDACs, as confirmed by co-crystal structures of SATFMK in complex with HDAH (PDB entry 2GH6) [49] and of analogue trifluoromethylketone inhibitors with HDAC4 (PDB: 2VQM) [50].

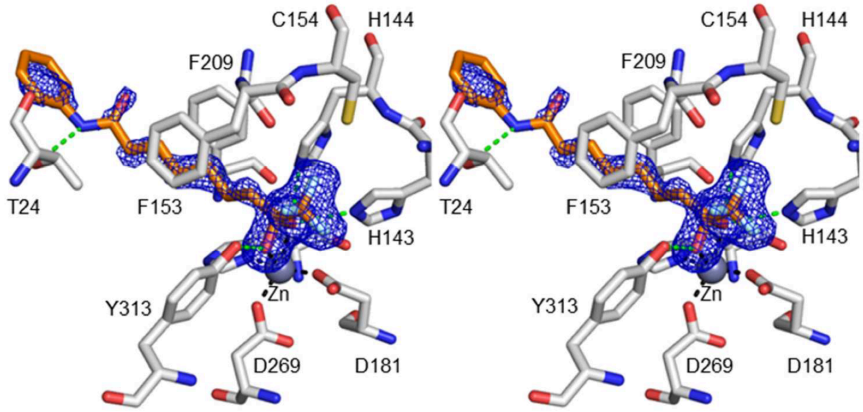


Figure 2. Stereo view of the inhibitor SATFMK **1** within PA3774 binding pocket [46].

Given the compelling new evidence demonstrating the potential for HDAC inhibition in counteracting inflammatory states in chronic infections reducing bacterial load in several *P. aeruginosa* infection models related to CF, we sought to assess the ability of proprietary HDAC6is in modulating biofilm formations and virulence process in *P. aeruginosa* in a PAO1 strain infection model.

Furthermore, in order to fully investigate the mechanism of action our HDAC6is we have engaged a small set of compounds in biochemical assays in the *P. aeruginosa* HDAC analogue PA3774.

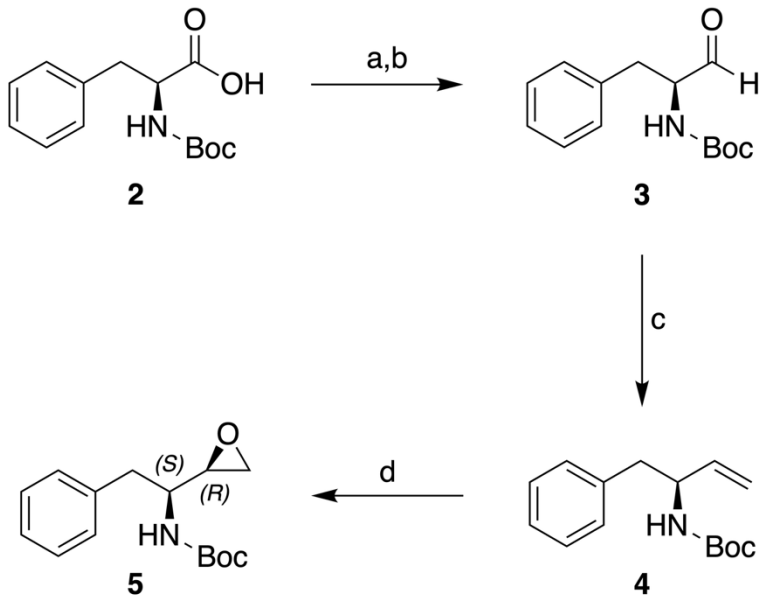
The data obtain within this activity led to a valuable advance in the knowledge on the mechanisms underlying HDAC modulation in bacterial infections and offer significant hints for the application of potent and selective HDAC6i to tackle resistant bacterial strains exploiting their multifaced mechanism of action modulating key infection pathways.

7.1 Results and discussion

7.1.1 Chemistry

Scheme 1 describes synthesis of the key synthetic intermediate tert-butyl ((S)-1-((R)-oxiran-2-yl)-2-phenylethyl)carbamate (**5**). The first reaction step involves a coupling reaction between Boc-L-phenylalanine and N,O-dimethylhydroxyamine hydrochloride, in the presence of NMM as base, and isobutylchloroformate (IBCF) as coupling agent. The obtained Weinreb' amide was subsequently reduced to the corresponding aldehyde **3** upon treatment with a suspension of $LiAlH_4$ in dry Et_2O at - 40 °C. Intermediate **3** was converted into the corresponding alkene **4** by Wittig reaction in the presence of triphenylmethylphosphonium bromide, and potassium bis(trimethylsilyl)amide (KHMDS, 0.5 M solution in toluene) as base in dry toluene as solvent for 1.5 h at 0 °C. The final reaction mixture was then allowed to react for 18 h at 25 °C, giving the corresponding alkene **4** with 20% yield. Finally, the latter was subjected to epoxidation reaction, in the presence of *m*CPBA in dry DCM, giving desired epoxide **5** in 53% yield.

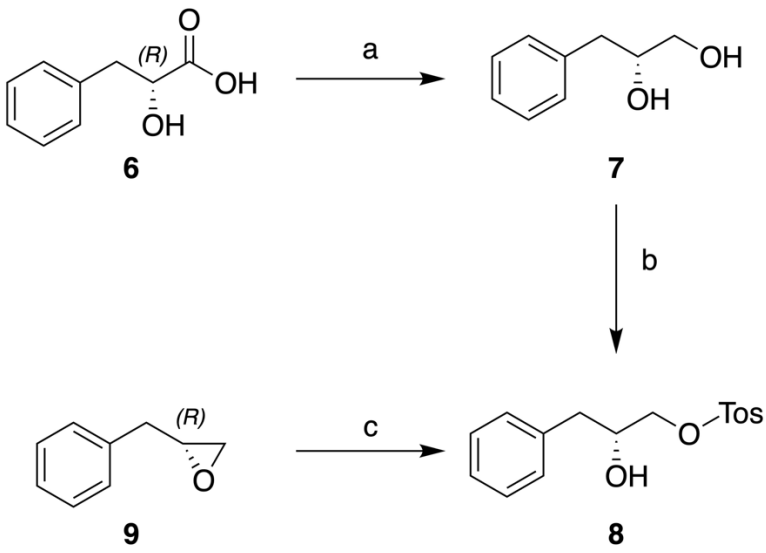
Scheme 1. Synthesis of the key intermediate **5**[a].



[a]Reagents and conditions: (a) N(Me)OMe HCl, NMM, IBCF, dry THF/dry DCM 1:4, 1 h, - 20 °C, 50%; (b) $LiAlH_4$, dry Et_2O, 45 min, - 40 °C, quant.; (c) $CH_3PPh_3^+$ Br^-, 0.5 M KHMDS in toluene, anhydrous toluene, 12 h, - 78 °C to 25 °C, 20%; (d) *m*-CPBA, dry DCM, 20 h, 25 °C, 53%.

Scheme 2 describes the synthesis of the key synthetic intermediate **9**. (R)-2-hydroxy-3-phenylpropanoic acid **6** was first treated with BH_3-THF complex in dry THF giving the corresponding diol **7**, whose primary alcoholic function was activated by reaction with TsCl in the presence of TEA as base. Following epoxidation reaction in the presence of sodium hydride, employing DMF as solvent, provided epoxide **9**.

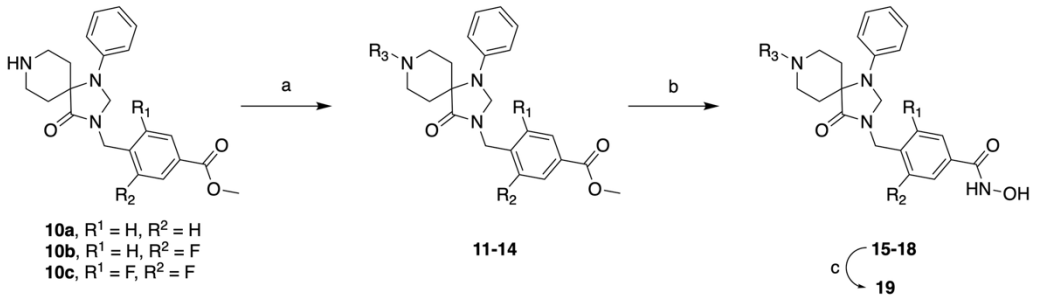
Scheme 2. Synthesis of the key intermediate **9**[a].

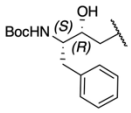
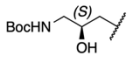
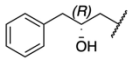
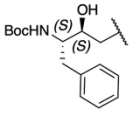


[a]Reagents and reaction conditions: (a) BH_3-THF, dry THF, 12 h, 25 °C, quant.; (b) TEA, dry DCM, 2 h, 0 °C to 25 °C, 40%; (c) NaH (60 % oil dispersion), dry DMF, 12 h, 0 °C, quant.

Scheme 3 describes the synthesis of N-amine capped final compounds **15-19**. For the synthesis of methyl esters **11-14**, intermediates **10a-c** (for the synthesis see *Chapter 3, 3.1.1 Chemistry*)[401] were exploited as nucleophiles for ring opening reaction, employing *i*PrOH as solvent, of commercially available epoxides (2S,3S)-N-t-Boc-3-amino-1,2-epoxy-4-phenylbutane and tert-butyl (*S*)-(oxiran-2-ylmethyl)carbamate, or **5** and **9**, respectively. Intermediates **11-14** were then converted into the corresponding hydroxamic acids **15-18** as previously described. Hydroxamic acid **15c** was then treated with 3 N HCl in MeOH to remove Boc protecting group, providing final compound **19** as hydrochloric salt.

Scheme 3. Synthesis of final compounds **15-19**[a].

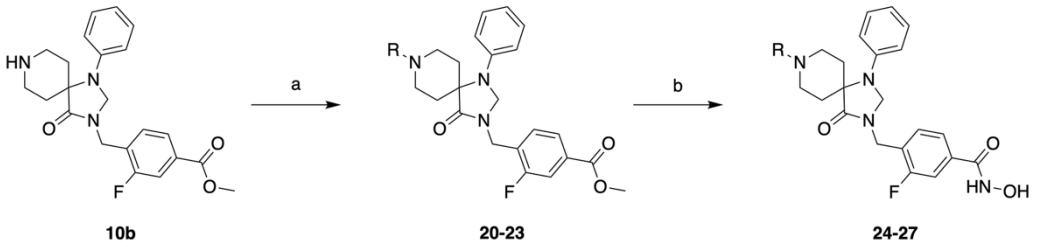


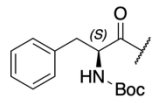
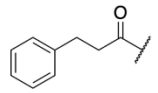
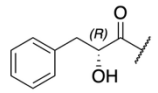
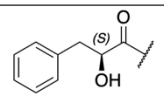
Cpd	R^1, R^2	R^3
11a/15a 11b/15b 11c/15c	R^1 = H, R^2 = H R^1 = H, R^2 = F R^1 = F, R^2 = F	
12/16	R^1 = H, R^2 = F	
13/17	R^1 = H, R^2 = F	
14a/18a 14b/18b	R^1 = H, R^2 = H R^1 = H, R^2 = F	

[a]Reagents and reaction conditions: (a) (2S,3S)-N-t-Boc-3-amino-1,2-epoxy-4-phenylbutane (66-48%), or tert-butyl (*S*)-(oxiran-2-ylmethyl)carbamate (67%), or 6 (51%), or **10** (54% for **14a**, 30% for **14b**), iPrOH, 18 h, 80 °C; (b) 50% aq. NH_2OH, 4 M KOH in MeOH, DCM/MeOH (2:1), 1 h, 25 °C, 26-52%; (c) 3 N HCl in MeOH, MeOH, 4 h, 25 °C, quant.

Scheme 4 describes the synthesis of N-amide capped inhibitors. Amine **10b** was subjected to a coupling reaction with commercially available (*tert*-butoxycarbonyl)-L-phenylalanine (**2**), 3-phenylpropanoic acid, (R)-2-hydroxy-3-phenylpropanoic acid (**6**) or (S)-2-hydroxy-3-phenylpropanoic acid, to provide intermediates **20-23**, respectively. The latter were then subjected to a reaction in the presence of 50% aqueous hydroxylamine to provide the corresponding hydroxamic acids **24-27** following the previously described procedure.

Scheme 4. Synthesis of final compounds **24-27**[a].



Cpd	R
20/24	
21/25	
22/26	
23/27	

[a]Reagents and reaction conditions: (a) carboxylic acid, NMM, HBTU, dry DCM, 12 h, 25 °C, 51-85%; (b) 50% aq. NH_2OH, 4 M KOH in MeOH, DCM/MeOH (2:1), 1 h, 25 °C, 45-75%.

7.1.2 Design and synthesis of novel HDAC6 inhibitors for the modulation of P. aeruginosa infection

We developed a small set of HDAC6is with the aim of investigating their ability in the modulation of *P. aeruginosa* infection and also with the final goal of assessing their effect on bacterial deacetylases enzyme. By pursuing this strategy, we sought to simultaneously exploit host system modulation – by HDAC6 inhibition - and interfere with *P. aeruginosa* virulence factor production by PA3774 inhibition, in order to identify innovative anti-infective agents for the treatment of persistent and multidrug resistant infections.

Our design strategy started from the previously identified 1,3,8-triazaspiro[4,5]decan-4-one cap group, and followed two main driving ideas

during the strategical scaffold morphing: (i) enhance potency and selectivity on HDAC6 towards nuclear Class I HDACs; (ii) enable the interaction of such class of spirofused inhibitors within the *P. aeruginosa* deacetylase PA3774 binding site.

Supported by literature data and in-house *in silico* studies, we sought to insert on the piperidine nitrogen of our spirofused cap-group a 'smart' structural moiety, which could allow the introduction through simple synthetic steps of multiple points for polar (hydrogen bonding donors and acceptors) and hydrophobic interactions within HDAC6 catalytic pocket. The progenitor of this new series is represented by compound **15a** (*Table 1*), bearing a tert-butyl ((2*S*,3*R*)-3-hydroxy-1-phenylbutan-2-yl)carbamate substituent on the nitrogen of the piperidine moiety.

Compound **15a** was assessed on both HDAC6 and the nuclear HDAC1isoform in order to confirm the suitability of this cap group decoration to guarantee potency and isoform selectivity. Gratifyingly, compound **15a** displayed IC_{50} = 7.1 nM on HDAC6 with high selectivity towards nuclear HDAC1 (IC_{50} HDAC1 = 2191 nM; SI = 422; *Table 1*), thus confirming the reliability of our initial design.

Docking studies were supportive of the experimentally registered data. The hydroxamate moiety coordinates the catalytic Zn^{2+} ion in a monodentate fashion – similarly to compounds bearing the simple phenyl-hydroxamate linker-ZBG reported in *Chapter 3* - while the hydroxamate nitrogen and the carbonyl group establish further hydrogen bonds with and the main chain carbonyl of G619 and OH group of Y782 respectively (Figure 3). Moreover, the hydroxyl group and Boc-protected amine of the cap group establish key hydrogen bonding interaction with D497 residue on the L1 loop of HDAC6.

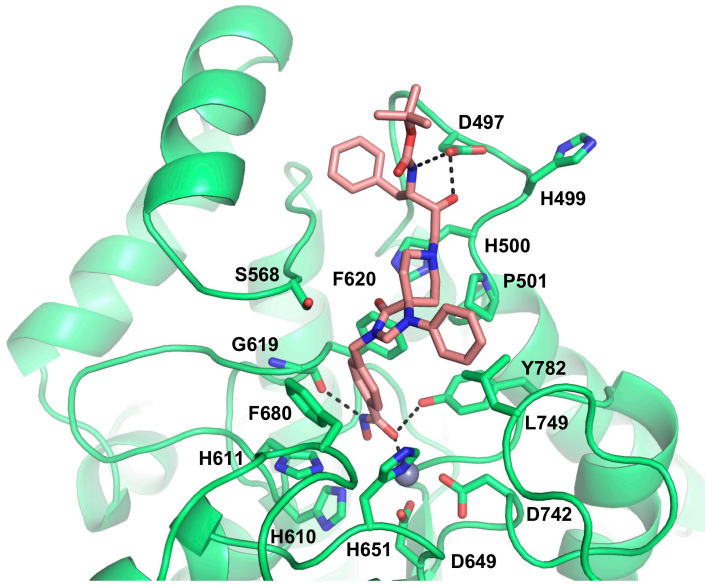
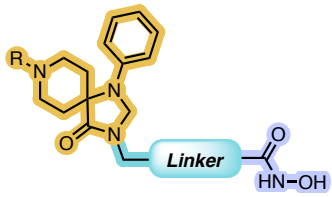


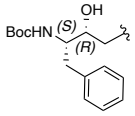
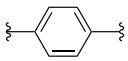
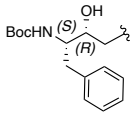
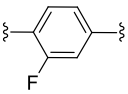
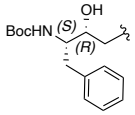
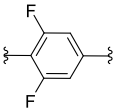
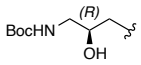
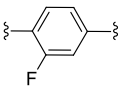
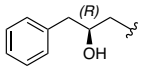
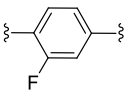
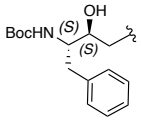
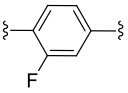
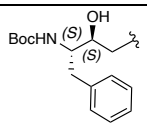
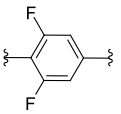
Figure 3. Docking pose of compound **15a** (slate sticks) within *h*HDAC6 active site (PDB 5EDU) represented as green transparent ribbon model. Residues in the active site are displayed as white sticks and labeled. H-bonds discussed in the text are depicted as dashed black lines. The catalytic Zn^{2+} ion is represented as a gray sphere; metal coordination is shown as dashed black lines.

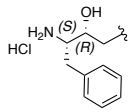
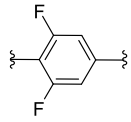
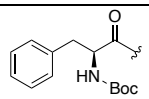
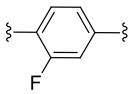
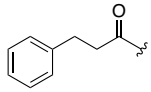
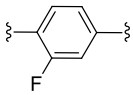
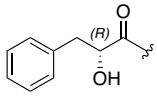
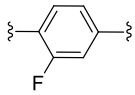
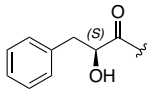
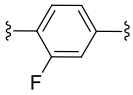
Taking into account the high potency and selectivity towards HDAC1 of compound **15a** – explained by the key hydrogen bond interaction established between the hydroxyl group and Boc-protected amine of the cap group with D497 residue on the L1 loop -, we carried out further structure-activity relationship studies, in order to identify structural determinants underlying potency and selectivity profiles for this class of compounds. As expected, the introduction of *m*-fluorobenzyl (**15b**, $IC_{50\ HDAC6}$ = 3.4 nM, $IC_{50\ HDAC1}$ = 4626.3 nM, SI = 1361) and *m*-difluorobenzyl linkers (**15c**, $IC_{50\ HDAC6}$ = 22.5) resulted in a significant loss of potency on nuclear HDAC1, with compound **15c** resulting completely inactive on HDAC1 at assessed concentration, thereby exhibiting the highest selectivity index for amine subseries of compounds.

First, the interrogated influence of stereochemistry of the OH group (compounds **18a,b**). In parallel, structural simplifications were investigated by removing either the phenyl ring (**16**) or the amino group (**17**).

Table 2. Structure and activities of compounds **15b,c**, **16**, **17**, **18a,b**, **23-27**.



Cpd	R	Linker	IC_{50} HDAC6 (nM)	IC_{50} HDAC1 (nM)	SI
15a			7.1	2191	422
15b			3.4	4626.3	1361
15c			22.5	29% @10uM	ND
16			21.7	3242	150
17			6.3	2035.5	323
18a			13.6	5657.0	415
18b			9.4	6517.0	693

19			31.8	5027.8	158
24			17.2	31% @10uM	ND
25			24.3	2782.0	114
26			4.2	1630.7	388
27			6.3	2035.5	323

SI = Selectivity Index; ND = Not Determined

Structural simplification of R substituent in compound **17** ($IC_{50\ HDAC6}$ = 21.7 nM, $IC_{50\ HDAC1}$ = 3242.0 nM; SI = 150) led to dropped potency and selectivity toward HDAC6. However, the removal of aromatic elements may be useful to achieve an increased solubility and increase Fsp3 fraction, thus potentially improving drug-like properties. Additionally, the removal of the amine functionality in compound **17** did not significantly affect HDAC6 binding affinity, while slightly worsening selectivity towards nuclear HDAC1 ($IC_{50\ HDAC6}$ = 6.3 nM, $IC_{50\ HDAC1}$ = 2035.5 nM; SI = 323). Also, the role of 3-hydroxyl group orientation to correctly establish hydrogen bonding with D497 residue was investigated by a stereocenter inversion approach. Compounds **18a** ($IC_{50\ HDAC6}$ = 13.6 nM, $IC_{50\ HDAC1}$ = 5657.0 nM; SI = 415) and **18b** ($IC_{50\ HDAC6}$ = 9.4 nM, $IC_{50\ HDAC1}$ = 6517.0 nM; SI = 693), while retaining high potency on HDAC6 displayed a significant drop in selectivity - compared to progenitor compounds **15b** and **15c** – probably suggesting the spatial orientation of 3-hydroxyl group influences binding affinity within HDAC1 L1 (*Table 2*). Interestingly, compound **19** containing a free amine, while displaying a comparable inhibitory profile on HDAC6 to its Boc-

protected analogue **15c**, gained some potency on HDAC1 isoform ($IC_{50\ HDAC6}$ = 31.8 nM, $IC_{50\ HDAC1}$ = 5027.8 nM; SI = 158).

A second subset of compounds was designed replacing the piperidine amine functionality with a piperidine amide moiety (compounds **24-27**), in order to both probe additional hydrogen-bonding interactions of the cap group within HDAC6 L1 and assessing the effect of a neutral functionality rather than a basic amine.

Amide derivative **24** (*Table 1*, $IC_{50\ HDAC6}$ = 17.2 nM) was designed as analogue of **15a**, by replacing the 3-hydroxyl group with an amide function. Satisfyingly, this substitution fully restored the high selectivity toward HDAC1, resulting in the lack of activity of compound **24** on HDAC1 at the tested concentration. Therefore, further structure-activity relationship studies were carried on for this amide subseries. Structural simplification on compound **25** – by replacing the N-Boc functionality with a simpler methylene – resulted in a significant drop in inhibitory potency toward HDAC6 (*Table 2*, $IC_{50\ HDAC6}$ = 24.3 nM, $IC_{50\ HDAC1}$ = 2782.0 nM; SI = 114). Therefore, we can assume that the presence of a functional group on the carbonyl α-carbon of the R substituent is of key importance, mainly ascribable to additional hydrogen or hydrophobic interactions with the enzyme surface. Accordingly, *in silico* studies performed on compound **28** confirmed 3-(*R*)-hydroxyl group is engaged in hydrogen bonding D497, consistently to the observed binding mode of compound **15a** (Figure 10). Enzymatic assays confirmed the 3-hydroxyl substitution in compounds **26** ($IC_{50\ HDAC6}$ = 4.2 nM, $IC_{50\ HDAC1}$ = 1630.7 nM; SI = 388) and **27** ($IC_{50\ HDAC6}$ = 6.3 nM, $IC_{50\ HDAC1}$ = 2035.5 nM; SI = 323) restored single-digit potency on HDAC6, while suggesting the stereochemistry at this position is not critical for HDAC6 inhibition.

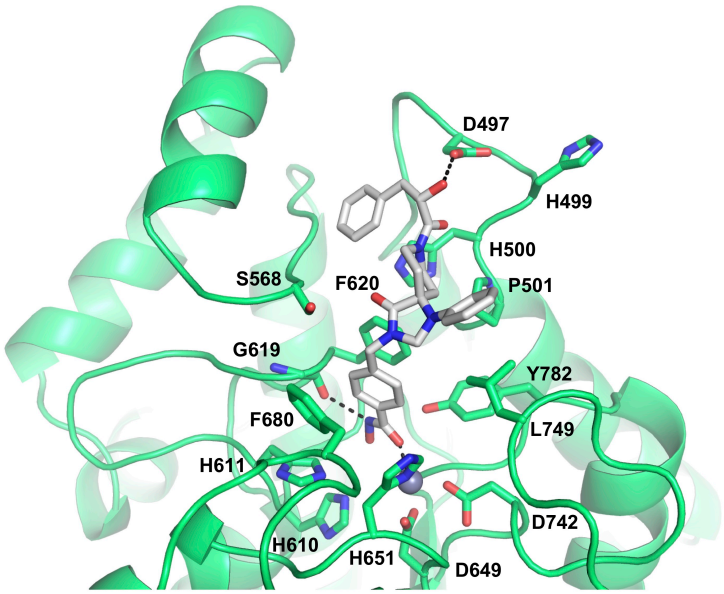


Figure 10. Docking pose of compound **26** (slate sticks) within *h*HDAC6 active site (PDB 5EDU) represented as green transparent ribbon model. Residues in the active site are displayed as white sticks and labeled. H-bonds discussed in the text are depicted as dashed black lines. The catalytic Zn^{2+} ion is represented as a gray sphere; metal coordination is shown as dashed black lines.

Target engagement was also confirmed by western blot analysis in A549 cells, revealing a dose dependent increase of acetylated tubulin upon treatment with compound **15a**, thus confirming its preferential HDAC6 inhibition also in cell-based settings (Figure 4).

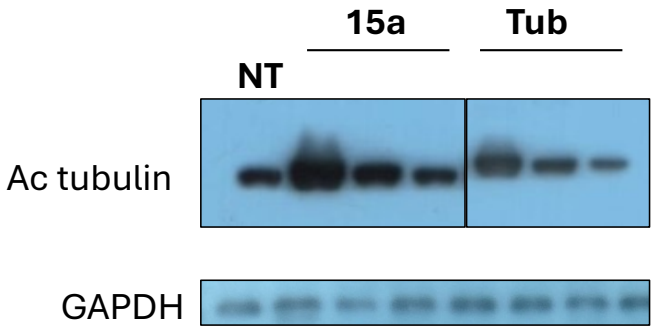


Figure 4. Western blot analysis of compound **15a** in comparison to TubA in A549 cells.

We therefore engaged compound **15a** for its ability in modulating biofilm and virulence in *P. aeruginosa*.

7.1.4 Compound 15a modulates Pseudomonas aeruginosa virulence and biofilm formation.

- *MIC determination*

Compound **15a** was first tested for its ability to affect bacterial cell growth on the *P. aeruginosa* PAO1 strain. As reported in Figure 5, the compound did not affect cell growth at 30 and 15 μM. Only at 60 μM, a slight reduction of cell growth was observed (growth reduction percentage = 18%), thereby confirming compound **15a** did not display an intrinsic antibacterial effect [52].

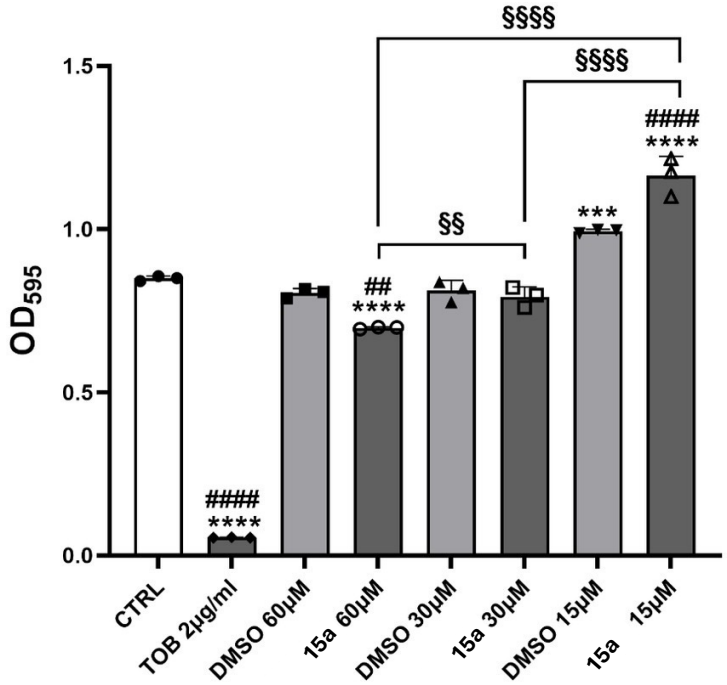


Figure 5. MIC determination of compound **15a** against P. aeruginosa PAO-1. The bacterial growth was determined at different concentrations of compound

15a (from here onward reported in figures as **15a**, 60, 30, and 15 μM) after 24 h incubation time at 37°C. CTRL represents the untreated bacteria. DMSO 60 μM and 30 μM (0.3 and 0.15%, respectively) served as the negative controls. TOB represents tobramycin at 2 μg/mL (4.27 μM). Three replicates were performed. The error bars indicate the mean ± standard deviation of the mean. Statistical differences were determined using ANOVA followed by Tukey's test (***$p < 0.001$ and ****$p < 0.0001$ vs. CTRL; ##$p < 0.01$; ####$p < 0.0001$ vs. DMSO; §$p < 0.01$ and §§§§$p < 0.0001$ for significant differences among the compound F2F-2020202 at different concentrations). Tobramycin showed a significant difference with DMSO at every concentration (####$p < 0.0001$) [52].

- *Compound **15a** affects the production of P. aeruginosa virulence factors*

While not significantly affecting cell growth, 30 μM treatment with **16a** resulted in a visible reduction in pyocyanin production (yellow staining of the medium) when compared to the control cells (green staining) (Figure 6).

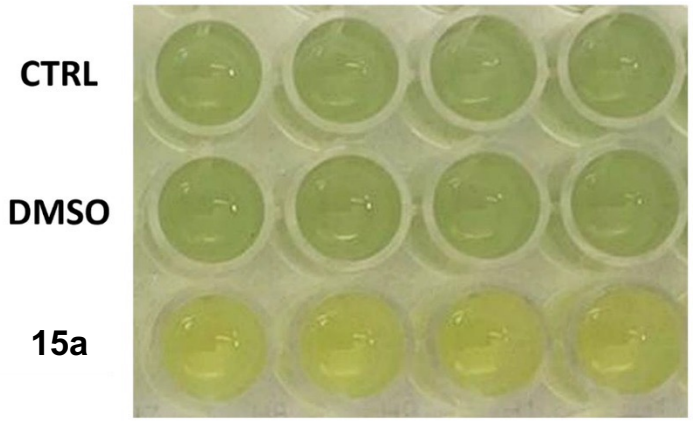


Figure 6. Pyocyanin reduction induced by compound **15a** at 30 μM. CTRL represents the untreated bacteria. DMSO 30 μM (0.15%) served as the negative control. The yellow staining of 30 μM **15a** -treated cell media reflects a reduction of pyocyanin production when compared to the control and DMSO-treated cells (green staining). The image is representative of nine different experiments [425].

This data was confirmed by biochemical quantification, which showed a 22% decrease in pyocyanin levels, as well as 44% decrease of rhamnolipids (Figure 7), thereby confirming compound **15a** efficacy in impairing the production of *P. aeruginosa* virulence factors [52].

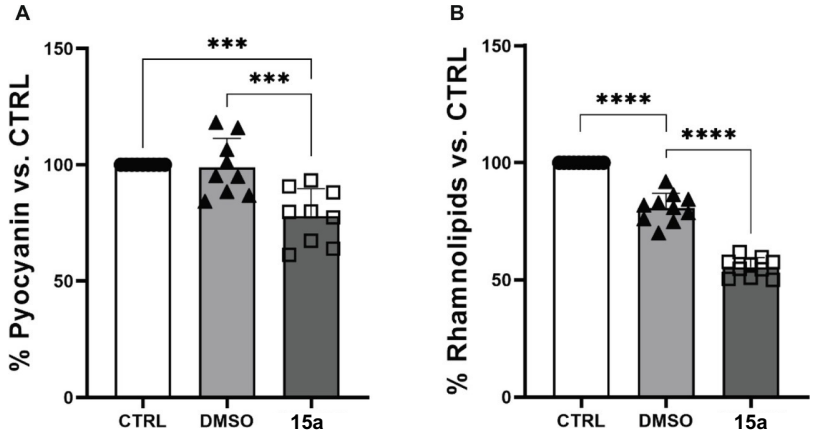


Figure 7. Effect of compound **15a** on virulence factors secreted by *P. aeruginosa* PAO1. CTRL represents the untreated bacteria. DMSO 30 μM (0.15%) served as the negative control. F2F-202 is the abbreviation for **15a**. The levels of pyocyanin (A) and rhamnolipids (B) at 30 μM concentration were evaluated. Bar errors showed the standard deviations of nine, nine, and ten replicates, respectively. Statistical differences were determined using ANOVA followed by Tukey's test (***$p < 0.001$ and ****$p < 0.0001$[52].

- *Compound **15a** impairs biofilm formation*

Given the key role of pyocyanin in biofilm formation, we analyzed the potential effect of **15a** on biofilm inhibition at 30 μM. The treatment with **15a** significantly affected *P. aeruginosa* biofilm formation (Figure 8A). Moreover, biofilm formation was estimated by crystal violet assay. Biofilm formation decreased of 38% upon treatment with **15a** compared to untreated and DMSO-treated cells (Figure 8B). We used also a second method to allow the microscopic visualization of *P. aeruginosa* biofilm on glass surfaces. More in detail, as shown in Figure 8C, biofilm was allowed to form on a 1 cm^2 glass piece. Upon treatment

with **15a**, the thickness of the biofilm was reduced, resulting in less organization and compactness compared to DMSO-treated and control cells [52].

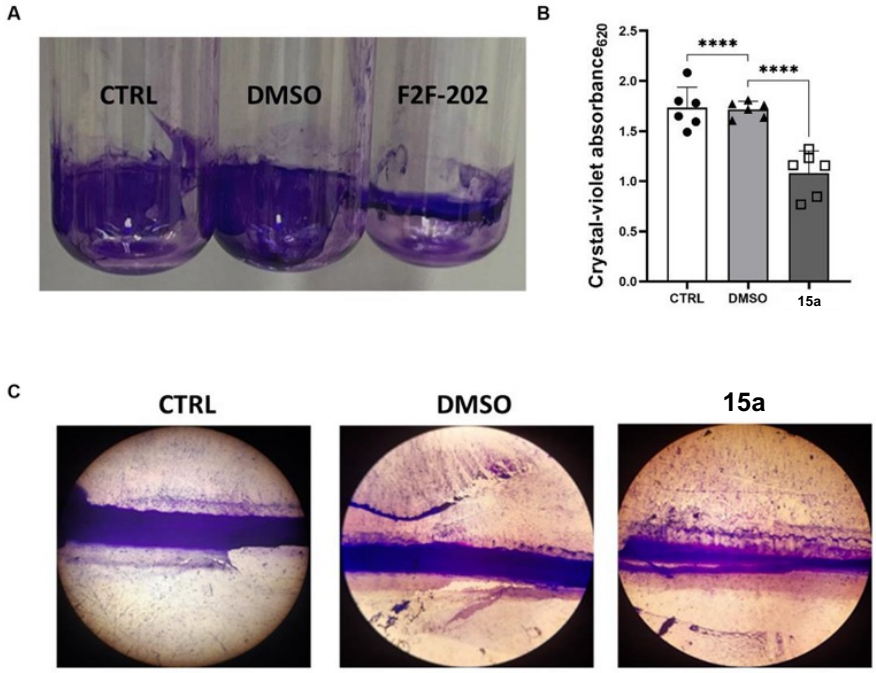


Figure 8. Effect of compound **15a** at 30 µM on biofilm formation. CTRL represents the untreated bacteria. DMSO 30 µM (0.15%) served as the negative control. (A) The biofilm assay in glass tubes at air–liquid interfaces showed a visible reduction of the biomass attached to the glass walls. (B) Crystal violet staining. The absorbance values obtained at 620 nm are presented as mean ± standard deviation. Statistical differences were determined using ANOVA followed by Tukey's test (****$p < 0.0001$). (C) Representative image of three independent experiments performed on *P. aeruginosa* PAO1 showing the reduction of the biofilm organization and compactness. Images were micrographed using the light microscope [52].

- *Compound **15a** impairs P. aeruginosa cells swarming motility*

Given the results obtained for compound **15a** in reducing rhamnolipids production (Figure 7B), its activity on swarming motility was evaluated. Indeed,

as described, rhamnolipids are surface-active molecule with haemolytic activity, which allow swarming motility, an organized form of surface translocation useful in the early stages of biofilm development. According to reduced rhamnolipid production, swarming motility was affected upon treatments with **15a** (Figure 9), thereby definitely confirming the efficacy of our proprietary HDAC6i in affecting *P. aeruginosa* biofilm formation and virulence factors production.

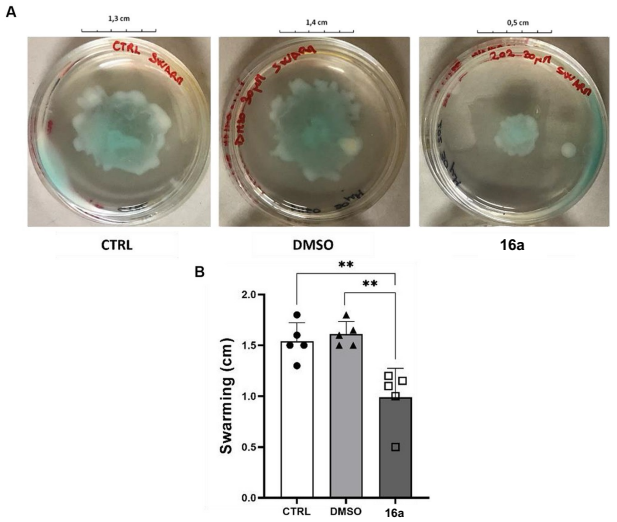


Figure 9. (A) CTRL represents the untreated bacteria. DMSO 30 μM (0.15%) served as the negative control. **15a** at 30 μM showed a visible reduction in the swarming mobility on plate agar. (B) The bar chart shows the effect of compound **15** at 30 μM on the swarming motility. Five replicates were done for the statistical comparisons. The measurements are presented as centimeters ± standard deviation. Statistical differences were determined using ANOVA followed by Tukey's test (**$p < 0.01$) [52].

7.1.5 Crystallographic studies of compund 15b in complex with zHDAC6 CD2

In collaboration with Professor David W. Christianson (University of Pennsylvania), we were able to solve the X-ray crystal structure of compound **15b** in complex with *z*HDAC6 CD2 (PDB not deposited yet). Interestingly, the hydroxamate carbonyl group coordinates to Zn^{2+} and does not displace the Zn^{2+}-

bound water molecule (Figure 10). This water molecule also forms hydrogen bonds with H573 and H574 and makes a van der Waals contact with the hydroxamate NH group. Y745 forms a hydrogen bond with the hydroxamate hydroxyl group. The fluoroaromatic ring of **15b** forms offset π-π stacking interactions in the F583-F643 aromatic crevice, and the C–F group is oriented exclusively into this crevice. The C–F group is also within hydrogen bonding distance to the hydroxyl group of S531 (Figure 10). Regarding the capping group of **16b, it** is well-defined in the electron density map (Figure 10), and a single molecule of ethylene glycol forms a pair of hydrogen bonds that bridge the carbonyl group of the triazospiro ring and Zn^{2+} ligand H614. The 6-membered piperidine ring adopts a favorable chair conformation. The phenyl ring adjacent to the *tert*-butyloxycarbonyl group in the capping group of **16b** makes an edge-to-face interaction with F642 in the outer active site cleft. No other enzyme-inhibitor hydrogen bonds or weakly polar interactions are observed for the inhibitor capping group.

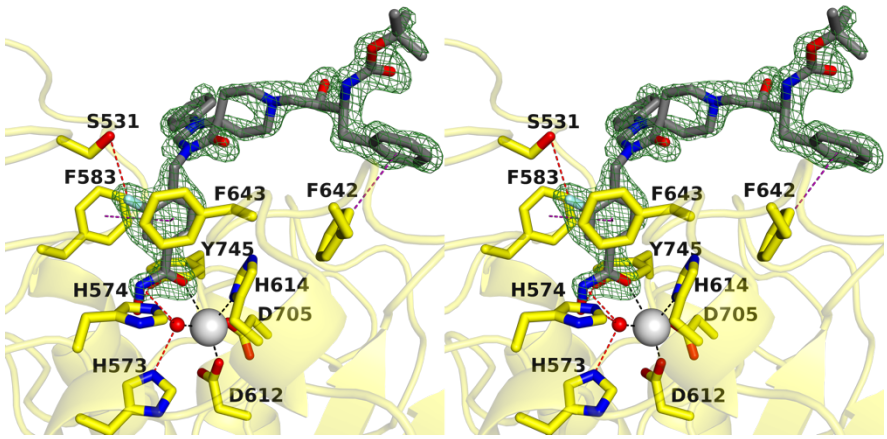


Figure 10. Stereoscopic view of polder omit map contoured at 4σ showing the binding of **15b** in the active site of *z*HDAC6 CD2 (PDB non deposited yet).

7.1.6 Enzymatic assays on PA3774

With the aim of further unveiling molecular determinants of the infection modulation by our HDAC6is, we interrogated the ability of most active

compounds of this series to directly inhibit *P. aeruginosa* HDAC homologue (*Table 2*).

First, since both Class II HDACs (HDAC4 and HDAC8) show high isoform selectivity within PA3774, selected compounds were assessed on both HDAC4 and HDAC8 isoforms in order to fully characterize their selectivity profile.

Table 2. Activities of compounds **15a,b**, **16**, **18b**, **24-27** on HDAC4, HDAC8 and PA3774.

Cpd	IC_{50} HDAC4 (nM)	IC_{50} HDAC8 (nM)	IC_{50} PA3774 (nM)	SI 4/6	SI 8/6
15a	345	2540	139	50	358
15b	410	2590	30	121	762
16	184	1740	12	9	80
18b	520	7220	190	56	776
24	566	6860	76	33	399
25	114	1920	22	5	80
26	42	1190	15	10	474
27	188	2330	15	30	370

SI = Selectivity Index

Interestingly, all assessed compounds displayed high HDAC6 selectivity towards Class I HDAC8 (*Table 2*), while a moderate selectivity was registered over HDAC4 isoform (*Table 2*), consistent with the higher protein homology between HDAC4 and PA3774 [162]. On the next stage, we investigated our compounds on PA3774 *P. aeruginonsa* HDAC homologue. As shown in *Table 4*, all compound also inhibited PA3774 with low nM potency, with compounds **15b** ($IC_{50\ PA3774}$ = 30 nM), **16** ($IC_{50\ PA3774}$ = 12 nM), **25** ($IC_{50\ PA3774}$ = 22 nM), **26** ($IC_{50\ PA3774}$ = 15 nM) and **27** ($IC_{50\ PA3774}$ = 15 nM) resulting the most active of the series.

Compound **15b** was found as the most selective inhibitor over human HDACs ($IC_{50\ HDAC6}$ = 3.4 nM, $IC_{50\ HDAC1}$ = 4626.3 nM, $IC_{50\ HDAC4}$ = 410 nM , $IC_{50\ HDAC8}$

= 2590 nM; SI 1/6 = 1361, SI 4/6 = 121, SI 8/6 = 762) retaining high potency on PA3774 ($IC_{50\ PA3774}$ = 30 nM). This data represents the first evidence of HDAC6 inhibitors also acting as potent inhibitors of a bacterial deacetylase and pave the way to more detailed structural studies in order to gain insight for targeting potency and selectivity over bacterial isoforms. . However, we cannot rule out the utility of a dual inhibition profile in order to simultaneously tackling host and bacterial deacetylases as a dual weapon against resistant bacterial infections.

7.2 Conclusions

Developing new therapeutic options for bacterial infections is closely linked to the urgent need for innovative therapeutic options, able to overcome multidrug resistance and infection persistence, especially in patients with complex clinical pictures, such as CF patients. Clear evidence has been provided in the last years that host protein acetylation status is correlated to the CF-immune response against pathogens and intracellular transport in CF-related inflammatory responses. In this context, HDAC6 stood out as a promising target for its ability to modulate host immune system in chronic bacterial infections. We designed and synthesized a new set of new potent and selective HDAC6is inhibitors unlocking a key hydrogen bonding interaction with the D497 residue within HDAC6 L1, accounting for the high potency and selectivity profiles registered for this class of inhibitors. We assessed compound **15a** in *P. aeruginosa* PAO1 strain, unveiling for the first time the efficacy of a selective HDAC6i in modulating *P. aeruginosa* virulence. Compound **15a** affected the production of pyocyanin and rhamnolipds and disrupted *P. aeruginosa* ability to form biofilm. Prompted by this data and to further deepen the knowledge on the mechanism of action of our newly developed compounds, we assessed a small set of analogues on PA3774 enzyme, a close HDAC homologue from *P. aeruginosa*. Most of the assessed compound displayed nanomolar inhibition potency toward this enzyme

and represent the first HDAC6is able to effectively inhibit a bacterial deacetylase. Further optimization studies are ongoing in our laboratories.

7.3 Experimental section

7.3.1 Chemistry

General procedure for epoxide ring opening. To a stirring solution of of the corresponding amine (**10a**, **10b**, or **10c**, 1 eq) in iPrOH, the appropriate oxirane (1 eq) was added and the resulting mixture allowed under stirring at 80 °C for 18 h. Upon completion, iPrOH was evaporated under reduced pressure and the crude material purified by silica gel column chromatography affording desired products.

General procedure for coupling reaction. To a solution of the corresponding amine **10b** (1 eq) and the opportune carboxylic acid (1.15 eq) in dry DCM, NMM (1.5 eq) was added followed by HBTU (1.5 eq) and the resulting mixture was allowed to stir at 25 °C for 24 h.

General procedure for the synthesis of hydroxamic acids. To a stirring solution of the corresponding methyl ester in a mixture of DCM/MeOH (1:1), 50% aqueous hydroxylamine (100 eq) was added followed by methanolic 4 M potassium hydroxide (50 eq). After 1 h, the reaction mixture was quenched by the addition of 6 N HCl and concentrated under vacuum. Crude material was purified by silica gel column chromatography (DCM/MeOH/NH_4OH 20:1:0.05 v/v to 20:1:1 v/v) giving desired hydroxamic acids **15-18** and **24-27.**

***tert*-butyl (*S*)-(1-oxo-3-phenylpropan-2-yl)carbamate (3).** *Step 1:* To a stirred solution of *N*,*O*-Dimethylhydroxylamine hydrochloride (4.15 mmol, 405 mg) in anhydrous DCM (2 mL) under N_2 atmosphere, NMM (4.15 mmol, 0.46 mL) was added dropwise at 0 °C. The resulting mixture was stirred at 0 °C for 30 minutes. In a separate flask, (*tert*-butoxycarbonyl)-L-phenylalanine (**2**, 3.77 mmol, 1 g) was dissolved in a mixture of anhydrous THF (3.3 mL) and anhydrous DCM (13.2 mL) under N_2 atmosphere. The resulting solution was

cooled to -20 °C and NMM (4.15 mmol, 0.46 mL) was added, followed by IBCF (4.15 mmol, 0.54 mL). The resulting mixture was stirred for 5 minutes at -20 °C and the above solution of *N*,*O*-Dimethylhydroxylamine was added to it. The reaction mixture was left under stirring at -20 °C for 1 hour and then warmed to 25 °C. The reaction was quenched with H_2O (10 mL) and the aqueous layer was extracted with DCM (3 x 8 mL) . The combined organic layers were washed with 10% aqueous citric acid solution, a satured aqueous $NaHCO_3$ solution and brine. The organic layer was dried over Na_2SO_4 and concentrated under reduced pressure. The residue was purified by liquid chromatography (EP/EtOAc 3:1 v/v) to give the desired *tert-butyl (S)-(1-(methoxy(methyl)amino)-1-oxo-3-phenylpropan-2-yl)carbamate*, as a pale yellow oil, with 50% yield (585 mg).
^{1}H NMR (400 MHz, $CDCl_3$) δ 7.21 (m, 5H), 5.13 (br, 1H), 4.94 (br, 1H), 3.64 (s, 3H), 3.15 (s, 3H), 3.03 (dd, *J* = 13.6, 6.0 Hz, 1H), 2.94 – 2.81 (m, 1H), 1.37 (s, 9H).

*Step 2: tert-butyl (S)-(1-(methoxy(methyl)amino)-1-oxo-3-phenylpropan-2-yl)carbamat*e (1.41 mmol, 436 mg) in anhydrous Et_2O (1.50 mL) was added to a stirred suspension of $LiAlH_4$ (1.55 mmol, 59 mg) in anhydrous Et_2O (5 mL) at -40 °C, under N_2 atmosphere. After 30 min, the reaction mixture was quenched by adding 10% aqueous $NaHSO_4$ solution (7 mL) at 0 °C. The resulting reaction mixture was then warmed to 25 °C and stirred for 30 min. The resulting mixture was filtered and the filter cake washed with of Et_2O (3 x 7 mL). The combined organic layers were washed with a sutured aqueous $NaHCO_3$ solution (3 x 7 mL), brine (3 x 7 mL) and dried over Na_2SO_4. Evaporation of the solvent under reduced pressure afforded the title aldehyde **3** (352 mg) as a pale yellow oil. The resulting aldehyde was used immediately without further purification.

***tert*-butyl (*S*)-(1-phenylbut-3-en-2-yl)carbamate (4).**

To a cooled suspension of triphenylmethylphosphonium bromide (2.12 mmol, 756 mg) in anhydrous toluene (15 mL), and a solution of KHMDS (0.5 M in

toluene, 2.12 mmol, 4.2 mL) was added dropwise under argon atmosphere. The mixture was stirred for 1.5 hours at 0 °C, then cooled to −78 °C. Intermediate **3** (1.41 mmol, 352 mg) was added and the resulting solution was stirred for 10 min at − 78 °, warmed up at 25 °C and left after stirring for 18 h. Upon completion, saturated aqueous NH_4Cl solution (10 mL) was added and the biphasic mixture washed with EtOAc (3 x 15 mL). The combined organic layers were collected, dried over Na_2SO_4 and the solvent removed under vacuum. Crude residue was purified by silica gel liquid chromatography (Ep/EtOAc 20:1 v/v), giving product **4**, as a colourless solid, with 20% yield (66 mg).

^{1}H NMR (400 MHz, $CDCl_3$) δ 7.33 – 7.15 (m, 5H), 5.79 (ddd, *J* = 17.1, 10.4, 5.1 Hz, 1H), 5.08 (dd, *J* = 13.8, 9.7 Hz, 2H), 4.42 (br, 2H), 2.83 (d, *J* = 6.0 Hz, 2H), 1.40 (s, 9H).

***tert*-butyl ((*S*)-1-((*R*)-oxiran-2-yl)-2-phenylethyl)carbamate (5).**

To a stirred solution of the corresponding alkene **4** (0.26 mmol, 61 mg) in anhydrous DCM (5 mL), *m*CPBA (1.04 mmol, 179.5 mg) and the resulting mixture allowed under stirring at 25 °C. Upon completion, reaction mixture was diluted with Et_2O (5 mL), nd washed with 10% aqueous Na_2S0_3 (10 mL) solution at 0 °C, saturated aqueous $NaHCO_3$ (3 x 10 mL), and brine (3 x 10 mL), dried over Na_2SO_4 and concentrated under vacuum. The residue was purified by silica gel liquid chromatography (PE/EtOAc 20:1 v/v), giving epoxide **5** with 53% yield (36 mg).

^{1}H NMR (400 MHz, $CDCl_3$) δ 7.36 – 7.13 (m, 5H), 4.48 (br, 1H), 4.09 (d, *J* = 33.5 Hz, 1H), 3.03 – 2.99 (m, 1H), 2.88 (dd, *J* = 13.4, 8.0 Hz, 1H), 2.69 (t, *J* = 4.4 Hz, 1H), 2.58 (br, 1H), 1.38 (s, *J* = 2.4 Hz, 9H).

(*R*)-3-phenylpropane-1,2-diol (7).

To a cooled solution of *(R)-2-hydroxy-3-phenylpropanoic acid* (**6**, 3.00 mmol, 500 mg) in anhydrous THF (10 mL), BH_3-THF complex (9.00 mmol, 9 mL) was slowly added under N_2 atmosphere, and the resulting reaction mixture was left

under stirring for 18 h at 25 °C. Upon completion, the reaction mixture was quenched by adding distilled H_2O (3 mL) and the solvent removed under reduced pressure. The crude residue was diluted with H_2O (10 mL) and washed with EtOAc (3 x 10 mL), the combined organic layers were dried over Na_2SO_4 and concentrated under reduced pressure, to afford desired product **7** in 86% yield (392 mg) without further purification step.

^{1}H NMR (400 MHz, $CDCl_3$) δ 7.38 – 7.23 (m, 5H), 3.89 (d, *J* = 70.6 Hz, 2H), 3.71 (d, *J* = 10.4 Hz, 1H), 3.61 – 3.50 (m, 1H), 2.99 – 2.68 (m, 2H), 2.48 – 2.03 (m, 1H).

(*R*)-2-hydroxy-3-phenylpropyl 4-methylbenzenesulfonate (8).

To a cooled solution of compound **7** (2.58 mmol, 392 mg) and TEA (2.58 mmol, 0.4 mL) in anhydrous DCM (5.5 mL), TsCl (2.58 mmol, 490 mg) was added in one portion and the reaction mixture left under stirring at 0 °C. After 1 h, reaction mixture was warmed up to 25 °C and left under stirring. After 1 h, the resulting mixture was quenched by adding distilled H_2O and the organic layer washed with satured aqueous $NaHCO_3$ solution (3 x 6 mL). Organic layer was collected, dried over Na_2SO_4, filtered and concentrated under vacuum. The reaction crude was purified by silica gel liquid chromatography (PE/EtOAc 20:10 v/v), giving the desired product **8,** as colorless oil, with 39% yield (332 mg).

^{1}H NMR (400 MHz, $CDCl_3$) δ 7.81 (d, *J* = 8.2 Hz, 2H), 7.36 (d, *J* = 8.1 Hz, 2H), 7.33 – 7.22 (m, 3H), 7.16 (d, *J* = 6.9 Hz, 2H), 4.12 – 4.02 (m, 2H), 3.96 (dd, *J* = 10.9, 7.2 Hz, 1H), 2.84 – 2.73 (m, 2H), 2.47 (s, 3H).

(*R*)-2-benzyloxirane (9).

To a cooled solution of intermediate **8** (0.52 mmol, 160 mg) in anhydrous DMF (2.3 mL) under N_2 atmosphere, NaH (60% oil dispersion, 0.35 mmol, 8.5 mg) was added and the resulting reaction mixture left under stirring at 0 °C. After 18 h, the reaction mixture was diluted with distilled H_2O (20 mL) and the aqueous layer washed with EtOAc (20 mL). Organic layer was collected, washed with

distilled water (3 x 20 mL) and brine (2 x 10 mL), then dried over Na_2SO_4, filtered and concentrated under vacuum, to effort desired product **9** without further purification (127 mg).

methyl 4-((8-((2*R*,3*S*)-3-((*tert*-butoxycarbonyl)amino)-2-hydroxy-4-phenylbutyl)-4-oxo-1-phenyl-1,3,8-triazaspiro[4.5]decan-3-yl)methyl)benzoate (11a). Compound **11a** was obtained following the general procedure for epoxide ring opening starting from (2S,3S)-N-t-Boc-3-amino-1,2-epoxy-4-phenylbutane (0.225 mmol, 59 mg). Crude material was purified by silica gel liquid chromatography (DCM, DCM/MeOH 99:1 v/v) affording desired product **11a** with 66% yield (88 mg).

MS (ESI) *m/z*calc. $[M+H]^+$ for $C_{37}H_{47}N_4O_6^+$: 643.35; found: 643.4

^{1}H NMR (700 MHz, CDCl3) δ 8.00 – 7.93 (m, 2H), 7.27 (m, 4H), 7.22– 7.13 (m, 6H), 7.12 6.76 (m, 1H), 6.74 (d, *J* = 8.1 Hz, 2H), 4.91 (br, 1H), 4.57 (s, 2H), 4.49 (m, 3H), 3.90 (m, 1H), 3.78 (s, 3H), 3.71 (dd, *J* = 12.5, 3.3 Hz, 1H), 3.55 (m, 1H), 3.48 (dd, *J* = 12.5, 4.4 Hz, 1H), 3.15 (m, 1H), 2.93 (m, 1H), 2.87 – 2.76 (m, 3H), 2.75 – 2.43 (m, 4H), 1.64 (m, 2H), 1.30 (s, 9H).

methyl 4-((8-((2*R*,3*S*)-3-((*tert*-butoxycarbonyl)amino)-2-hydroxy-4-phenylbutyl)-4-oxo-1-phenyl-1,3,8-triazaspiro[4.5]decan-3-yl)methyl)-3-fluorobenzoate (11b). Compound **11b** was obtained following the general procedure for epoxide ring opening starting from (2S,3S)-N-t-Boc-3-amino-1,2-epoxy-4-phenylbutane (0.251 mmol, 100 mg). Crude material was purified by silica gel liquid chromatography (PE/EtOAc 60:40 v/v) giving desired product **11b** with 40% yield (64 mg).

^{1}H NMR (700 MHz, $CDCl_3$) δ 7.76 (d, *J* = 7.9 Hz, 1H), 7.68 (d, *J* = 10.2 Hz, 1H), 7.33 (t, *J* = 7.5 Hz, 1H), 7.24 – 7.10 (m, 9H), 6.80 (t, *J* = 7.3 Hz, 1H), 4.63 (s,

2H), 4.55 (s, 2H), 4.50 – 4.44 (m, 1H), 3.18 – 3.08 (m, 1H), 2.97 – 2.90 (m, 2H), 2.85 – 2.78 (m, 3H), 2.72 – 2.41 (m, 6H), 1.63 – 1.59 (m, 1H), 1.28 (s, 9H).

methyl 4-((8-((2*R*,3*S*)-3-((*tert*-butoxycarbonyl)amino)-2-hydroxy-4-phenylbutyl)-4-oxo-1-phenyl-1,3,8-triazaspiro[4.5]decan-3-yl)methyl)-3,5-difluorobenzoate (11c). Compound **11c** was obtained following the general procedure for epoxide ring opening starting from (2S,3S)-N-t-Boc-3-amino-1,2-epoxy-4-phenylbutane (0.241 mmol, 54 mg). Crude material was purified by silica gel liquid chromatography (PE/EtOAc 60:40 v/v) giving desired product **11c** with 48% yield (78 mg).

^{1}H NMR (400 MHz, $CDCl_3$) δ 7.54 (d, *J* = 5.3 Hz, 2H), 7.26 – 7.11 (m, 8H), 6.83 – 6.72 (m, 3H), 4.69 (s, 2H), 4.52 (d, *J* = 2.4 Hz, 2H), 4.49 – 4.39 (m, 1H), 3.87 (s, 3H), 3.81 – 3.72 (m, 1H), 3.58 – 3.47 (m, 1H), 3.12 (t, *J* = 11.7 Hz, 1H), 2.96 – 2.87 (m, 1H), 2.84 – 2.75 (m, 3H), 2.67 – 2.36 (m, 5H), 1.60 (d, *J* = 13.7 Hz, 2H), 1.28 (s, 9H).

methyl (S)-4-((8-(3-((tert-butoxycarbonyl)amino)-2-hydroxypropyl)-4-oxo-1-phenyl-1,3,8-triazaspiro[4.5]decan-3-yl)methyl)-3-fluorobenzoate (12). Compound **12** was obtained following the general procedure for epoxide ring opening starting from (S)-N-Boc-2,3-epoxypropylamine (0.503 mmol, 87.12 mg). Crude material was purified by silica gel liquid chromatography (DCM/Acetone 3:1 to 2:1 v/v) affording desired product **12** with 67% yield (193 mg).

^{1}H NMR (400 MHz, $CDCl_3$) δ 7.67 (d, J = 7.9 Hz, 1H), 7.59 (d, J = 10.2 Hz, 1H), 7.24 (t, J = 7.6 Hz, 1H), 7.14 – 7.01 (m, 2H), 6.70 (dd, J = 15.9, 7.9 Hz, 3H), 4.90 (bs, 1H), 4.54 (s, 2H), 4.45 (s, 2H), 3.76 (s, 3H), 3.66 (d, J = 3.3 Hz, 1H), 3.20 (d, J = 11.7 Hz, 1H), 3.05 (t, J = 10.5 Hz, 1H), 2.96 – 2.85 (m, 1H), 2.76 (d, J = 7.4 Hz, 2H), 2.65 – 2.55 (m, 1H), 2.48 (ddd, J = 24.0, 13.5, 6.8 Hz, 1H), 2.37 – 2.21 (m, 2H), 1.54 (d, J = 13.7 Hz, 2H), 1.28 (s, 9H).

methyl (*R*)-3-fluoro-4-((8-(2-hydroxy-3-phenylpropyl)-4-oxo-1-phenyl-1,3,8-triazaspiro[4.5]decan-3-yl)methyl)benzoate (13). Compound **13** was obtained following the general procedure for epoxide ring opening starting from intermediate **9** (0.125 mmol, 42 mg). Crude material was purified by silica gel column chromatography (DCM/Acetone 3:1 v/v) affording desired product **13** with 51% yield (34 mg).

^{1}H NMR (400 MHz, $CDCl_3$) δ 7.85 – 7.72 (m, 2H), 7.42 – 7.19 (m, 9H), 7.15 (d, *J* = 6.7 Hz, 1H), 6.84 (dd, *J* = 13.6, 7.6 Hz, 2H), 4.69 (s, 2H), 4.61 (s, 2H), 4.09 – 4.01 (m, 1H), 3.92 (s, 3H), 3.22 (br, 1H), 3.02 – 2.62 (m, 7H), 2.56 – 2.30 (m, 2H), 1.68 (d, *J* = 13.6 Hz, 2H).

methyl 4-((8-((2*S*,3*S*)-3-((*tert*-butoxycarbonyl)amino)-2-hydroxy-4-phenylbutyl)-4-oxo-1-phenyl-1,3,8-triazaspiro[4.5]decan-3-yl)methyl)-3-fluorobenzoate (14a).

Compound **14a** was obtained following the general procedure for epoxide ring opening starting from intermediate **5** (0.14 mmol, 36 mg). Crude material was purified by silica gel liquid chromatography (PE/EtOAc 3:2 v/v) giving product **14a** with 54% yield (50 mg).

^{1}H NMR (400 MHz, $CDCl_3$) δ 7.82 (d, *J* = 8.2 Hz, 1H), 7.74 (d, *J* = 11.2 Hz, 1H), 7.39 (t, *J* = 7.6 Hz, 1H), 7.32 – 7.18 (m, 7H), 6.87 (t, *J* = 7.4 Hz, 1H), 6.82 (d, *J* = 8.1 Hz, 2H), 5.00 (d, *J* = 9.7 Hz, 1H), 4.69 (s, 2H), 4.60 (s, 2H), 3.92 (s, 3H), 3.69 (d, *J* = 8.8 Hz, 2H), 3.18 (d, *J* = 10.0 Hz, 1H), 2.92 (dd, *J* = 19.9, 11.5 Hz, 2H), 2.80 (t, 2H), 2.77 – 2.46 (m, 4H), 2.36 (d, *J* = 11.2 Hz, 1H), 1.56 – 1.48 (m, 1H), 1.40 (s, 9H).

methyl 4-((8-((2*S*,3*S*)-3-((*tert*-butoxycarbonyl)amino)-2-hydroxy-4-phenylbutyl)-4-oxo-1-phenyl-1,3,8-triazaspiro[4.5]decan-3-yl)methyl)-3,5-difluorobenzoate (14b). Compound **14b** was obtained following the general procedure for epoxide ring opening starting from intermediate **6** (0.17 mmol, 45

mg).vCrude material was purified by silica gel liquid chromatography (PE/EtOAc 3:2 v/v) giving product **14b** with 30% yield (35 mg).

^{1}H NMR (400 MHz, $CDCl_3$) δ 7.61 (d, *J* = 7.6 Hz, 2H), 7.31 – 7.23 (m, 7H), 7.20 (d, *J* = 3.9 Hz, 1H), 6.87 (t, *J* = 7.4 Hz, 2H), 5.05 (d, *J* = 9.9 Hz, 1H), 4.75 (s, 2H), 4.59 (s, 2H), 3.93 (s, 3H), 3.85 (d, *J* = 9.6 Hz, 1H), 3.70 (dd, *J* = 16.5, 8.5 Hz, 1H), 3.42 (br, 1H), 3.16 (d, *J* = 15.6 Hz, 2H), 3.03 (br, 1H), 2.79 (d, *J* = 13.7 Hz, 4H), 2.51 (d, *J* = 13.2 Hz, 2H), 1.67 (d, *J* = 14.1 Hz, 2H), 1.40 (s, 9H).

***tert*-butyl ((2*S*,3*R*)-3-hydroxy-4-(3-(4-(hydroxycarbamoyl)benzyl)-4-oxo-1-phenyl-1,3,8-triazaspiro[4.5]decan-8-yl)-1-phenylbutan-2-yl)carbamate (15a).** Compound **15a** was obtained following general procedure for hydroxamic acids synthesis starting from intermediate **15a** (0.137 mmol, 88 mg) and giving product **15a** with 25% yield (22 mg).

MS (ESI) *m/z* calc. $[M+H]^+$ for $C_{36}H_{46}N_5O_6^+$: 644.34; found: 644.4

^{1}H NMR (400 MHz, DMSO) δ 11.19 (bs, 1H), 9.03 (bs, 1H), 7.75 (d, *J* = 6.4 Hz, 2H), 7.36 (d, *J* = 8.4 Hz, 2H), 7.27 – 7.15 (m, 6H), 6.87 (d, *J* = 8.1 Hz, 2H), 6.77 (t, *J* = 7.4 Hz, 1H), 6.63 (d, *J* = 9.0 Hz, 1H), 4.59 (d, *J* = 4.2 Hz, 4H), 3.71 – 3.58 (m, 2H), 3.00 – 2.92 (m, 1H), 2.85 – 2.73 (m, 4H), 2.68 – 2.53 (m, 3H), 2.46 – 2.31 (m, 2H), 1.60 (d, *J* = 12.4 Hz, 2H), 1.26 (s, 9H).

^{13}C NMR (101 MHz, DMSO) δ 173.62, 155.24, 142.84, 139.93, 139.48, 132.03, 129.15, 129.06, 127.87, 127.41, 127.35, 125.60, 118.00, 114.52, 77.29, 69.97, 62.65, 59.47, 55.13, 49.99, 49.67, 43.40, 35.32, 28.70, 28.22.

***tert*-butyl ((2*S*,3*R*)-4-(3-(2-fluoro-4-(hydroxycarbamoyl)benzyl)-4-oxo-1-phenyl-1,3,8-triazaspiro[4.5]decan-8-yl)-3-hydroxy-1-phenylbutan-2-yl)carbamate (15b).** Compound **15b** was obtained following general procedure for hydroxamic acids synthesis starting from intermediate **15b** (0.097 mmol, 64 mg) and giving product **15b** with 40% yield (26 mg).

$[M+H]^+$ for $C_{36}H_{45}FN_5O_6^+$: 662.34; found: 662.8.

^{1}H NMR (400 MHz, DMSO) δ 8.31 (bs, 1H), 8.19 (bs, 1H), 7.64 – 7.55 (m, 2H), 7.42 (t, *J* = 7.8 Hz, 1H), 7.29 – 7.12 (m, 7H), 6.88 (d, *J* = 8.6 Hz, 2H), 6.79 (t, *J* = 7.3 Hz, 1H), 6.65 (bs, 1H), 4.64 (d, *J* = 6.7 Hz, 4H), 3.70 – 3.63 (m, 2H), 3.00 – 2.83 (m, 5H), 2.68 – 2.52 (m, 4H), 2.47 – 2.43 (m, 1H), 1.64 (d, *J* = 13.4 Hz, 2H), 1.27 (s, 9H).

^{13}C NMR (101 MHz, DMSO) δ 173.39, 163.61, 162.41, 161.14, 158.70, 155.26, 142.77, 139.78, 134.31 (d, *J* = 6.8 Hz), 129.84 (d, *J* = 4.2 Hz), 129.16, 129.08, 127.89, 125.64, 123.24, 118.21, 114.70, 113.94 (d, *J* = 23.0 Hz), 79.18, 77.36, 69.56, 67.02, 62.75, 61.05, 59.27, 55.14, 49.99, 49.40, 37.86, 35.37, 28.21, 27.84.

***tert*-butyl ((2*S*,3*R*)-4-(3-(2,6-difluoro-4-(hydroxycarbamoyl)benzyl)-4-oxo-1-phenyl-1,3,8-triazaspiro[4.5]decan-8-yl)-3-hydroxy-1-phenylbutan-2-yl)carbamate (15c).** Compound **15c** was obtained following general procedure for hydroxamic acids synthesis starting from intermediate **11c** (0.120 mmol, 78 mg) and giving product **15c** with 38% yield (28 mg).

MS (ESI) *m/z* calc. $[M+H]^+$ for $C_{36}H_{44}F_2N_5O_6^+$: 680.33; found: 680.5.
^{1}H NMR (400 MHz, DMSO) δ 11.41 (bs, 1H), 9.38 (bs, 1H), 7.49 (d, *J* = 8.3 Hz, 2H), 7.27 – 7.13 (m, 6H), 6.87 (d, *J* = 8.6 Hz, 2H), 6.79 (t, *J* = 7.2 Hz, 1H), 6.62 (d, *J* = 8.8 Hz, 1H), 4.67 (s, 2H), 4.58 (s, 2H), 3.70 – 3.52 (m, 2H), 2.95 (d, *J* = 14.1 Hz, 2H), 2.83 – 2.72 (m, 3H), 2.59 – 2.53 (m, 2H), 2.42 – 2.29 (m, 3H), 1.54 (d, *J* = 13.3 Hz, 2H), 1.26 (s, 9H).
^{13}C NMR (101 MHz, DMSO) δ 172.91, 161.21 (d, *J* = 248.8 Hz), 159.50 (d, *J* = 248.8 Hz), 155.24, 142.78, 139.86, 134.98, 129.14, 129.05, 127.86, 125.60, 118.32, 114.95, 110.29 (d, *J* = 27.7 Hz), 77.31, 69.76, 62.49, 61.18, 59.34, 55.13, 49.93, 35.33, 32.36, 28.21.

***tert*-butyl (*S*)-(3-(3-(2-fluoro-4-(hydroxycarbamoyl)benzyl)-4-oxo-1-phenyl-1,3,8-triazaspiro[4.5]decan-8-yl)-2-hydroxypropyl)carbamate (16).**

Compound **16** was obtained following general procedure for hydroxamic acids synthesis starting from intermediate **12** (0.170 mmol, 97 mg) and giving product **16** with 37% yield (36 mg).

MS (ESI) *m/z* calc. $[M+H]^+$ for $C_{29}H_{39}FN_5O_6^+$: 572.29; found $[M\text{-}Boc+H]^+$ 472.3

^{1}H NMR (400 MHz, DMSO) δ 11.31 (bs, 1H), 9.16 (bs, 1H), 7.63 – 7.54 (m, 2H), 7.41 (t, *J* = 7.8 Hz, 1H), 7.23 (t, *J* = 7.1 Hz, 2H), 6.87 (d, *J* = 8.2 Hz, 2H), 6.78 (t, *J* = 7.3 Hz, 1H), 4.63 (d, *J* = 8.9 Hz, 4H), 3.69 – 3.59 (m, 1H), 3.08 – 3.01 (m, 1H), 2.97 – 2.89 (m, 1H), 2.87 – 2.72 (m, 4H), 2.59 – 2.53 (m, 2H), 2.39 – 2.28 (m, 2H), 1.60 (d, *J* = 13.4 Hz, 2H), 1.37 (s, 9H).

^{13}C NMR (151 MHz, DMSO) δ 173.97, 161.20, 159.57, 156.25, 143.27, 134.73 (d, *J* = 7.3 Hz), 129.57, 126.57 (d, *J* = 15.1 Hz), 123.71, 118.80, 115.40, 114.40 (d, *J* = 22.9 Hz), 67.48, 63.21, 62.56, 50.16, 40.30, 28.97, 28.70.

$[a]_D^{20} = 0.0131$

***(S)-4-((8-(3-(benzylamino)-2-hydroxypropyl)-4-oxo-1-phenyl-1,3,8-triazaspiro[4.5]decan-3-yl)methyl)-3-fluoro-N-hydroxybenzamide* (17).**

Compound **17** was obtained following general procedure for hydroxamic acids synthesis starting from intermediate **13** (0.063 mmol, 34 mg) and giving product **17** with 30% yield (10 mg).

MS (ESI) *m/z*calc. $[M+H]^+$ for $C_{31}H_{37}FN_5O_4^+$: 562.28; found: 562.5

^{1}H NMR (400 MHz, DMSO) δ 7.64 – 7.54 (m, 2H), 7.40 (t, *J* = 7.8 Hz, 1H), 7.29 – 7.18 (m, 7H), 6.87 (d, *J* = 8.4 Hz, 2H), 6.78 (t, *J* = 7.3 Hz, 1H), 6.54 (bs, 1H), 4.62 (d, *J* = 8.2 Hz, 4H), 3.91 – 3.81 (m, 1H), 2.86 – 2.54 (m, 8H), 2.36 – 2.30 (m, 2H), 1.59 (d, *J* = 13.4 Hz, 2H).

^{13}C NMR (101 MHz, DMSO) δ 173.49, 162.40, 161.12, 142.82, 139.51, 129.83, 129.39, 129.07, 127.93, 125.70, 123.25, 118.21, 114.77, 113.93 (d, *J* = 22.4 Hz), 68.56, 63.60, 62.72, 59.45, 50.06, 49.43, 41.59, 28.98.

***tert*-butyl ((2*S*,3*S*)-4-(3-(2-fluoro-4-(hydroxycarbamoyl)benzyl)-4-oxo-1-phenyl-1,3,8-triazaspiro[4.5]decan-8-yl)-3-hydroxy-1-phenylbutan-2-yl)carbamate (18a).**
Compound **18a** was obtained following general procedure for hydroxamic acids synthesis starting from intermediate **14a** (0.076 mmol, 50 mg) and giving product **18a** with 52% yield (26 mg).

MS (ESI) *m/z* calc. $[M+H]^+$ for $C_{36}H_{44}FN_5O_6^+$: 661.3; found: 661.8.

^{1}H NMR (400 MHz, DMSO) δ 11.31 (bs, 1H), 9.15 (bs, 1H), 7.62 – 7.54 (m, 2H), 7.40 (t, *J* = 7.6 Hz, 1H), 7.30 – 7.14 (m, 7H), 6.88 (d, *J* = 7.8 Hz, 2H), 6.79 (t, *J* = 7.4 Hz, 1H), 4.63 (d, *J* = 7.3 Hz, 4H), 3.89 – 3.74 (m, 1H), 3.64 – 3.57 (m, 1H), 2.90 – 2.60 (m, 6H), 2.43 – 2.26 (m, 4H), 1.66 – 1.51 (m, 2H), 1.30 (s, 9H).

^{13}C NMR (176 MHz, DMSO) δ 169.61, 162.99, 161.08, 159.68, 155.82, 152.56, 143.19, 134.76, 130.28, 129.57, 129.50, 128.50, 126.29, 123.72, 115.11, 114.40 (d, *J* = 23.1 Hz), 78.04, 63.20, 61.22, 54.96, 45.72, 38.31, 29.46, 28.62.

$[a]_D^{20}$ = 0.0005

***tert*-butyl ((2*S*,3*S*)-4-(3-(2,6-difluoro-4-(hydroxycarbamoyl)benzyl)-4-oxo-1-phenyl-1,3,8-triazaspiro[4.5]decan-8-yl)-3-hydroxy-1-phenylbutan-2-yl)carbamate (18b).** Compound **18b** was obtained following general procedure for hydroxamic acids synthesis starting from intermediate **14b** (0.076 mmol, 35 mg) and giving product **18b** with 26% yield (7 mg).

MS (ESI) *m/z* calc. $[M+H]^+$ for $C_{36}H_{44}F_2N_5O_6^+$: 680.33; found: 680.5.

^{1}H NMR (400 MHz, DMSO) δ 7.49 (d, *J* = 8.1 Hz, 2H), 7.26 – 7.21 (m, 5H), 7.19 – 7.12 (m, 1H), 6.86 (d, *J* = 8.4 Hz, 2H), 6.79 (t, *J* = 7.3 Hz, 1H), 6.29 (d, *J* = 9.5 Hz, 1H), 4.66 (s, 2H), 4.57 (s, 2H), 3.88 – 3.77 (m, 1H), 3.62 – 3.53 (m, 1H), 2.86 – 2.79 (m, 1H), 2.72 – 2.61 (m, 4H), 2.47 – 2.24 (m, 5H), 1.47 (d, *J* = 13.0 Hz, 2H), 1.29 (s, 9H).

^{13}C NMR (151 MHz, DMSO) δ 172.97, 172.16, 162.29, 161.04 (d, *J* = 249.9 Hz), 159.91 (d, *J* = 249.9 Hz), 155.29, 142.76, 139.61, 129.04, 129.01, 127.98, 125.76, 118.24, 114.85, 110.25 (d, *J* = 25.9 Hz), 77.47, 68.11, 62.45, 60.59, 59.31, 54.43, 49.81, 49.70, 36.46, 35.77, 32.33, 30.76, 28.14, 21.16.

4-((8-((2R,3S)-3-amino-2-hydroxy-4-phenylbutyl)-4-oxo-1-phenyl-1,3,8-triazaspiro[4.5]decan-3-yl)methyl)-3,5-difluoro-N-hydroxybenzamide (19). To a stirring solution of **15c** (0.015 mmol, 10 mg) in MeOH (0.500 mL), 3 M HCl in MeOH (0.044 mmol, 0.150 mL) was added and the resulting mixture allowed under stirring for 4 h. Upon completion, volatile components were eliminated under reduced pressure affording desired compound **19** with quantitative yield (9 mg).

MS (ESI) *m/z* calc. $[M+H]^+$ for $C_{31}H_{35}F_2N_5O_4^+$: 579.3; found: 579.3.

^{1}H NMR (400 MHz, DMSO) δ 10.83 (bs, 1H), 10.29 (bs, 2H), 8.22 (bs, 2H), 7.65 (d, *J* = 7.5 Hz, 2H), 7.41 – 7.19 (m, 7H), 7.07 (d, *J* = 8.2 Hz, 2H), 6.81 (t, *J* = 7.2 Hz, 1H), 4.70 (d, *J* = 26.1 Hz, 4H), 4.43 – 4.39 (m, 1H), 3.74 – 3.64 (m, 2H), 3.62 – 3.51 (m, 3H), 3.50 – 3.44 (m, 1H), 3.05 – 2.94 (m, 3H), 2.92 – 2.82 (m, 2H), 1.87 (d, *J* = 14.5 Hz, 2H).

^{13}C NMR (101 MHz, DMSO) δ 175.47, 142.11, 136.31, 129.50, 129.13, 128.63, 126.95, 118.60, 114.72, 112.46 (d, *J* = 26.8 Hz), 64.78, 57.69, 55.26, 52.88, 48.57, 32.91.

$[a]_D^{20} = 0.0076$

methyl 4-((8-((*tert*-butoxycarbonyl)-L-phenylalanyl)-4-oxo-1-phenyl-1,3,8-triazaspiro[4.5]decan-3-yl)methyl)-3-fluorobenzoate (20). Compound **20** a was synthesized following the general coupling procedure starting from (*tert*-butoxycarbonyl)-L-phenylalanine (0.433 mmol, 115 mg). Crude material was purified by silica gel liquid chromatography (DCM, DCM/MeOH 99:1 v/v) giving compound **20** with 70% yield (170 mg).

^{1}H NMR (400 MHz, $CDCl_3$) δ 7.84 (dd, *J* = 7.9, 1.6 Hz, 1H), 7.75 (d, *J* = 8.8 Hz, 1H), 7.44 – 7.31 (m, 2H), 7.31 – 7.09 (m, 7H), 6.85 (t, *J* = 8.3 Hz, 1H), 6.69 (dd, *J* = 7.9, 4.1 Hz, 2H), 4.69 (d, *J* = 3.9 Hz, 2H), 4.61 – 4.51 (m, 3H), 3.93 (s, 3H), 3.75 – 3.34 (m, 4H), 3.06 – 2.92 (m, 2H), 2.53 – 2.13 (m, 3H), 1.39 (t, *J* = 7.4 Hz, 9H).

methyl 3-fluoro-4-((4-oxo-1-phenyl-8-(3-phenylpropanoyl)-1,3,8-triazaspiro[4.5]decan-3-yl)methyl)benzoate (21). Compound **21** a was synthesized following the general coupling procedure starting from 3-phenylpropanoic acid (0.289 mmol, 43 mg). Crude material was purified by silica gel liquid chromatography (DCM, DCM/MeOH 99:1 to 98:2 v/v) giving compound **21** with 75% yield (100 mg).

^{1}H NMR (400 MHz, $CDCl_3$) δ 7.86 (d, *J* = 7.8 Hz, 1H), 7.78 (d, *J* = 10.2 Hz, 1H), 7.42 (t, *J* = 7.6 Hz, 1H), 7.34 – 7.19 (m, 5H), 6.91 (t, *J* = 7.3 Hz, 1H), 6.72 (d, *J* = 8.1 Hz, 2H), 4.73 (s, 2H), 4.62 (d, *J* = 13.7 Hz, 3H), 3.94 (s, 3H), 3.90 (d, *J* = 12.6 Hz, 1H), 3.77 (d, *J* = 10.4 Hz, 1H), 3.49 (dd, *J* = 12.7, 10.2 Hz, 1H), 3.03 (t, *J* = 7.9 Hz, 2H), 2.75 – 2.66 (m, 2H), 2.41 (m, 2H), 1.74 (t, *J* = 13.2 Hz, 2H).

methyl (*R*)-3-fluoro-4-((8-(2-hydroxy-3-phenylpropanoyl)-4-oxo-1-phenyl-1,3,8-triazaspiro[4.5]decan-3-yl)methyl)benzoate (22). Compound **22** a was synthesized following the general coupling procedure starting from (*R*)-2-hydroxy-3-phenylpropanoic acid (0.289 mmol, 43 mg). Crude material was

purified by silica gel liquid chromatography (DCM, DCM/MeOH 99:1 to 98:2 v/v) giving compound **22** with 85% yield (134 mg).

methyl (*S*)-3-fluoro-4-((8-(2-hydroxy-3-phenylpropanoyl)-4-oxo-1-phenyl-1,3,8-triazaspiro[4.5]decan-3-yl)methyl)benzoate (23). Compound **23** a was synthesized following the general coupling procedure starting from (*S*)-2-hydroxy-3-phenylpropanoic acid (0.289 mmol, 43 mg). Crude material was purified by silica gel liquid chromatography (DCM, DCM/MeOH 99:1 to 98:2 v/v) giving compound **23** with 51% yield (80 mg).

^{1}H NMR (700 MHz, $CDCl_3$) δ 7.98 (d, *J* = 2.5 Hz, 2H), 7.29 (d, *J* = 8.0 Hz, 2H), 7.25 (t, *J* = 7.4 Hz, 2H), 7.21 – 7.15 (m, 5H), 6.67 (d, *J* = 8.2 Hz, 1H), 6.62 (dd, *J* = 1656.4, 8.2 Hz, 1H), 4.58 (dd, *J* = 55.4, 8.0 Hz, 2H), 4.53 – 4.48 (m, 2H), 3.85 (s, 3H), 3.77 – 3.68 (m, 2H), 3.59 – 3.49 (m, 2H), 2.93 – 2.78 (m, 3H), 2.37-2.33 (m, 2H), 1.79 – 1.67 (m, 2H).

***tert*-butyl (*S*)-(1-(3-(2-fluoro-4-(hydroxycarbamoyl)benzyl)-4-oxo-1-phenyl-1,3,8-triazaspiro[4.5]decan-8-yl)-1-oxo-3-phenylpropan-2-yl)carbamate (24).** Compound **24** was obtained following general procedure for hydroxamic acids synthesis starting from intermediate **20** (0.26 mmol, 170 mg) and giving product **24** with 75% yield (128 mg).

MS (ESI) *m/z* calc. $[M+H]^+$ for $C_{35}H_{41}FN_5O_6^+$: 646.30; found: 646.1.

^{1}H NMR (400 MHz, DMSO) δ 11.23 (bs, 1H), 9.17 (bs, 1H), 7.63 – 7.54 (m, 2H), 7.43 (t, *J* = 7.7 Hz, 1H), 7.37 (d, *J* = 8.4 Hz, 1H), 7.30 – 7.17 (m, 6H), 6.87 – 6.62 (m, 3H), 4.80 – 4.52 (m, 4H), 4.45 – 4.26 (m, 1H), 4.03 – 3.82 (m, 1H), 3.81 – 3.51 (m, 1H), 3.27 – 3.18 (m, 1H), 2.97 – 2.79 (m, 2H), 2.69 – 2.57 (m, 1H), 2.45 – 2.33 (m, 1H), 2.22 – 2.00 (m, 1H), 1.84 – 1.58 (m, 2H), 1.26 (s, 9H).

^{13}C NMR (101 MHz, DMSO) δ 173.72, 170.25, 161.62, 159.17, 155.78, 142.89, 138.40, 134.91, 130.35, 129.81, 129.69, 128.45, 126.70, 123.74, 118.18, 116.30, 114.21, 78.41, 63.19, 60.07, 51.68, 41.97, 38.85, 38.39, 37.68, 29.50, 28.52.

$[a]_D^{20}$ = 0.0224

3-fluoro-*N*-hydroxy-4-((4-oxo-1-phenyl-8-(3-phenylpropanoyl)-1,3,8-triazaspiro[4.5]decan-3-yl)methyl)benzamide (25). Compound **25** was obtained following general procedure for hydroxamic acids synthesis starting from intermediate **21** (0.188 mmol, 100 mg) and giving product **25** with 67% yield (61 mg).

MS (ESI) *m/z* calc. $[M+H]^+$ for $C_{30}H_{32}FN_4O_4^+$: 530.24; found: 531.5.

^{1}H NMR (400 MHz, DMSO) δ 7.65 – 7.55 (m, 2H), 7.44 (t, *J* = 7.8 Hz, 1H), 7.30 – 7.25 (m, 5H), 7.22 (t, *J* = 7.7 Hz, 3H), 6.81 (t, *J* = 7.4 Hz, 1H), 6.72 (d, *J* = 8.2 Hz, 2H), 4.66 (d, *J* = 9.5 Hz, 4H), 4.41 – 4.34 (m, 1H), 3.89 (d, *J* = 13.5 Hz, 1H), 3.70 (t, *J* = 12.9 Hz, 1H), 3.35 – 3.25 (m, 1H), 2.86 (t, *J* = 7.6 Hz, 2H), 2.77 – 2.63 (m, 2H), 2.43 – 2.21 (m, 2H), 1.71 (d, *J* = 13.6 Hz, 2H).

^{13}C NMR (101 MHz, DMSO) δ 173.62, 170.51, 159.18, 143.09, 141.92, 130.38, 129.68, 128.83, 128.70, 126.32, 123.71, 119.22, 115.52, 114.42 (d, *J* = 23.6 Hz), 63.29, 60.39, 41.82, 34.22, 31.25, 31.16, 29.88, 28.92.

(*R*)-3-fluoro-*N*-hydroxy-4-((8-(2-hydroxy-3-phenylpropanoyl)-4-oxo-1-phenyl-1,3,8-triazaspiro[4.5]decan-3-yl)methyl)benzamide (26). Compound **26** was obtained following general procedure for hydroxamic acids synthesis starting from intermediate **22** (0.151 mmol, 70 mg) and giving product 26 with 60% yield (48 mg).

MS (ESI) *m/z* calc. $[M+H]^+$ for $C_{30}H_{32}FN_4O_5^+$: 547.24; found: 547.2.

^{1}H NMR (400 MHz, DMSO) δ 7.65 – 7.56 (m, 2H), 7.44 (t, *J* = 7.8 Hz, 1H), 7.28 – 7.17 (m, 7H), 6.83 – 6.68 (m, 3H), 5.23 (bs, 1H), 4.69 – 4.61 (m, 4H), 4.61 – 4.56 (m, 1H), 4.42 – 4.30 (m, 1H), 4.01 (t, *J* = 14.5 Hz, 1H), 3.77 – 3.59 (m, 1H), 3.00 – 2.90 (m, 1H), 2.87 – 2.75 (m, 1H), 2.61 – 2.54 (m, 1H), 2.40 – 2.18 (m, 2H), 1.71 (t, *J* = 13.5 Hz, 2H).

^{13}C NMR (101 MHz, DMSO) δ 173.07, 171.05, 162.33, 159.93 (d, *J* = 246.0 Hz), 141.15, 139.14, 133.67, 129.89, 129.53, 129.44, 129.20, 126.47, 126.01, 123.22, 118.96, 118.45, 113.89 (d, *J* = 23.9 Hz), 69.44, 68.87, 63.73, 59.97, 59.82, 42.22, 40.97, 38.23, 37.99, 28.52.

(*S*)-3-fluoro-*N*-hydroxy-4-((8-(2-hydroxy-3-phenylpropanoyl)-4-oxo-1-phenyl-1,3,8-triazaspiro[4.5]decan-3-yl)methyl)benzamide (27). Compound **27** was obtained following general procedure for hydroxamic acids synthesis starting from intermediate **23** (0.123 mmol, 80 mg) and giving product **27** with 45% yield (30 mg).

MS (ESI) *m/z* calc. $[M+H]^+$ for $C_{30}H_{32}FN_4O_5^+$: 547.24; found: 547.2.

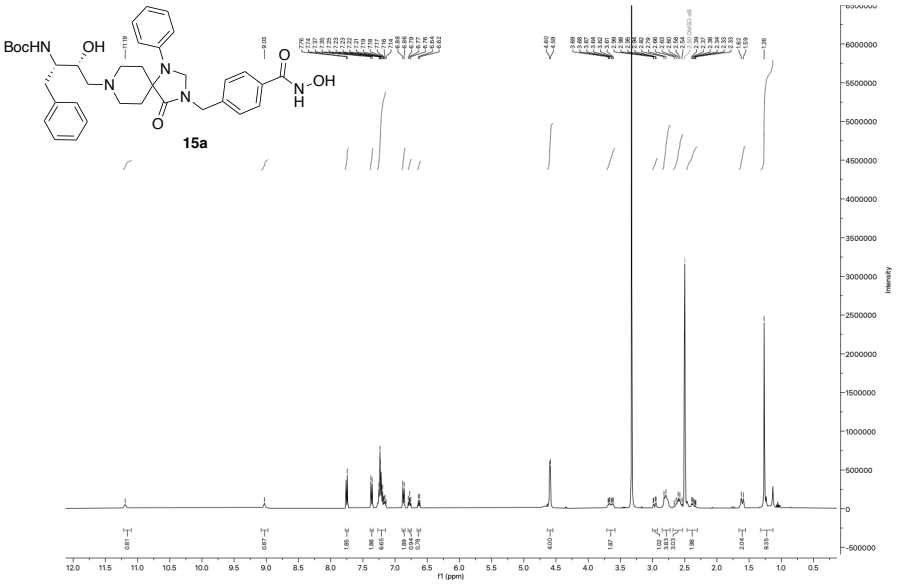
^{1}H NMR (700 MHz, DMSO) δ 7.75 (d, *J* = 8.3 Hz, 2H), 7.38 (d, *J* = 8.3 Hz, 2H), 7.26 (q, *J* = 2.3 Hz, 3H), 7.23 – 7.16 (m, 3H), 6.82 – 6.76 (m, 1H), 6.76 – 6.72 (m, 1H), 6.72 – 6.67 (m, 1H), 5.24 (dd, *J* = 25.8, 7.8 Hz, 1H), 4.65 – 4.56 (m, 4H), 4.41 – 4.32 (m, 1H), 4.08 – 3.97 (m, 1H), 3.76 – 3.65 (m, 1H), 3.00 – 2.91 (m, 1H), 2.84 – 2.76 (m, 1H), 2.61 – 2.55 (m, 1H), 2.40 – 2.32 (m, 1H), 2.31 – 2.21 (m, 1H), 1.75 – 1.66 (m, 2H).

^{13}C NMR (176 MHz, DMSO) δ 173.38, 173.25, 171.26, 171.18, 163.96, 142.77, 142.69, 139.42, 138.60, 138.35, 132.20, 129.67, 129.58, 129.33, 128.09, 127.62, 127.54, 126.15, 118.91, 118.44, 115.27, 114.62, 69.58, 69.00, 62.85, 60.09, 59.96, 43.69, 41.44, 40.33, 38.39, 38.27, 29.62, 28.53, 21.53, 14.68.

6.3.2 Supporting Figures

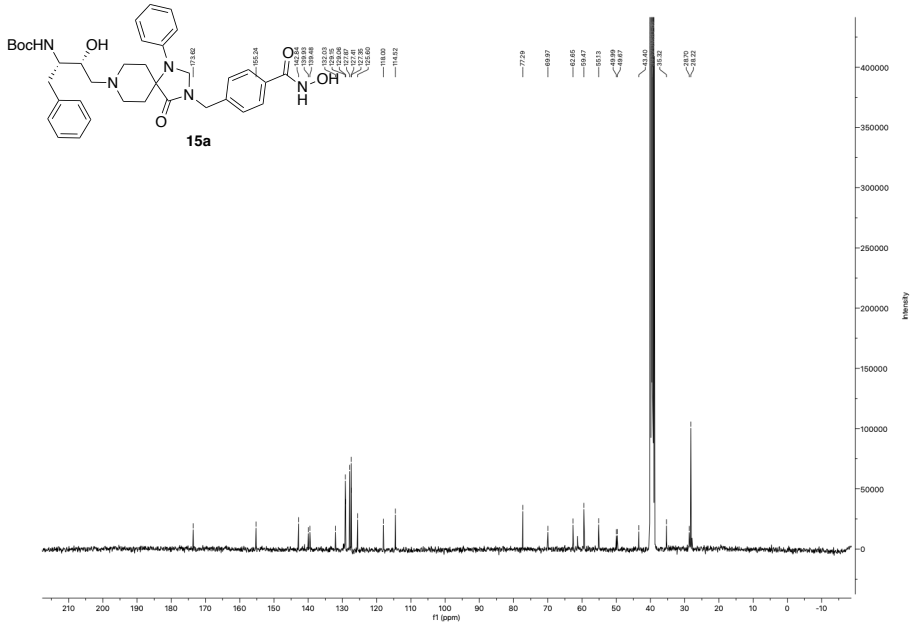
Supporting Figure 1

^{1}H NMR of 15a



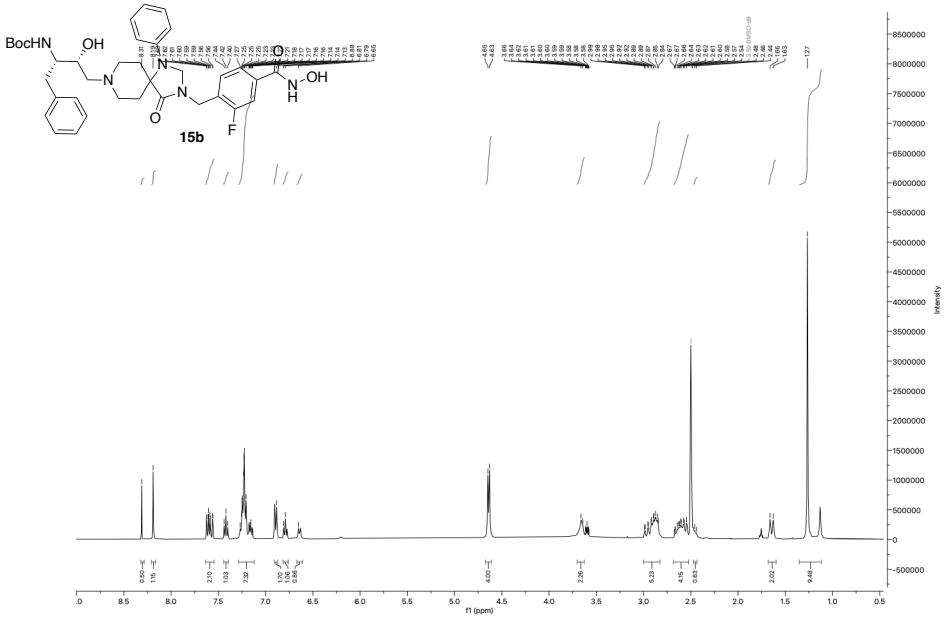
Supporting Figure 2

^{13}C NMR of 15a



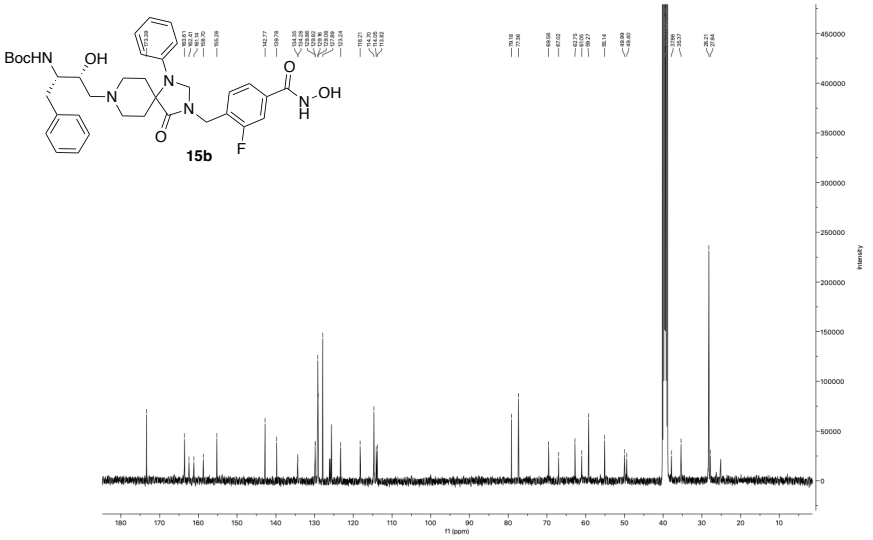
Supporting Figure 3

^{1}H NMR of 15b



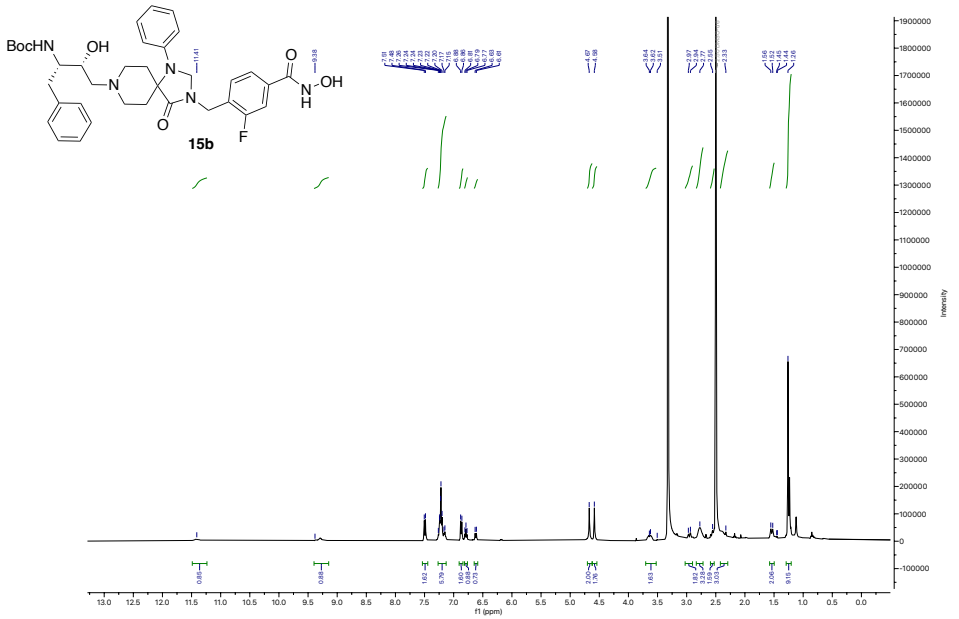
Supporting Figure 4

^{13}C NMR of 16b



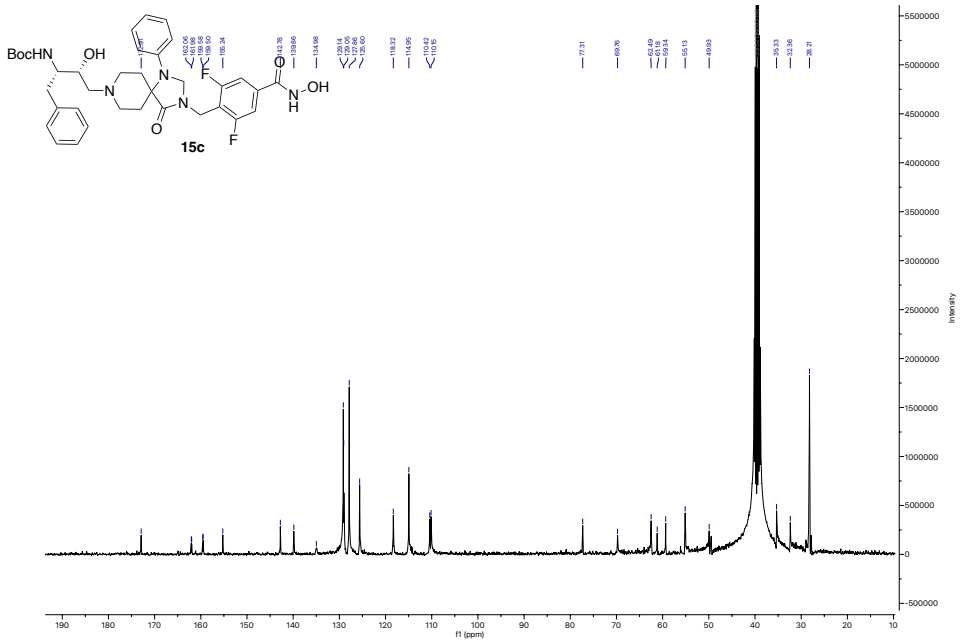
Supporting Figure 5

^{1}H NMR of 15c



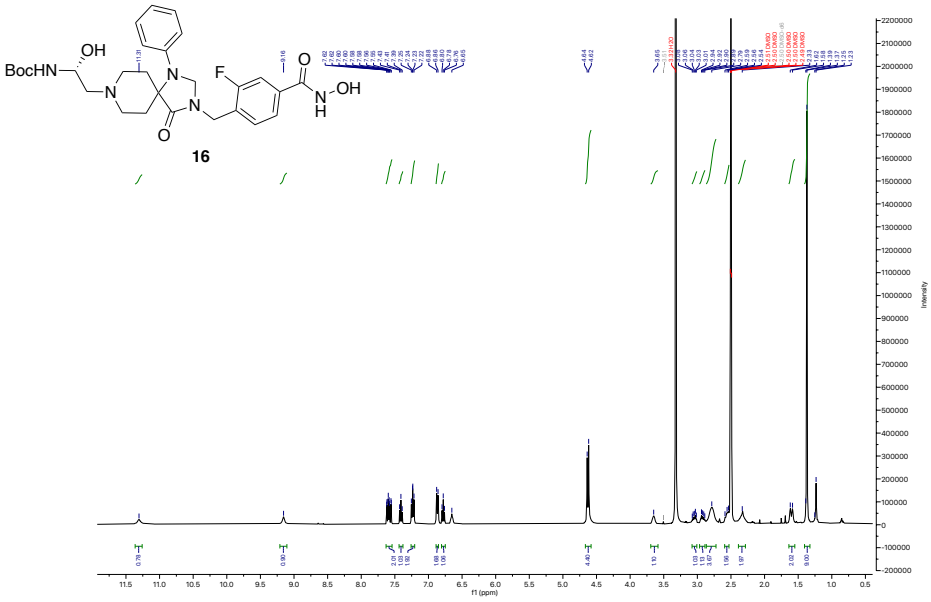
Supporting Figure 6

^{13}C NMR of 15c



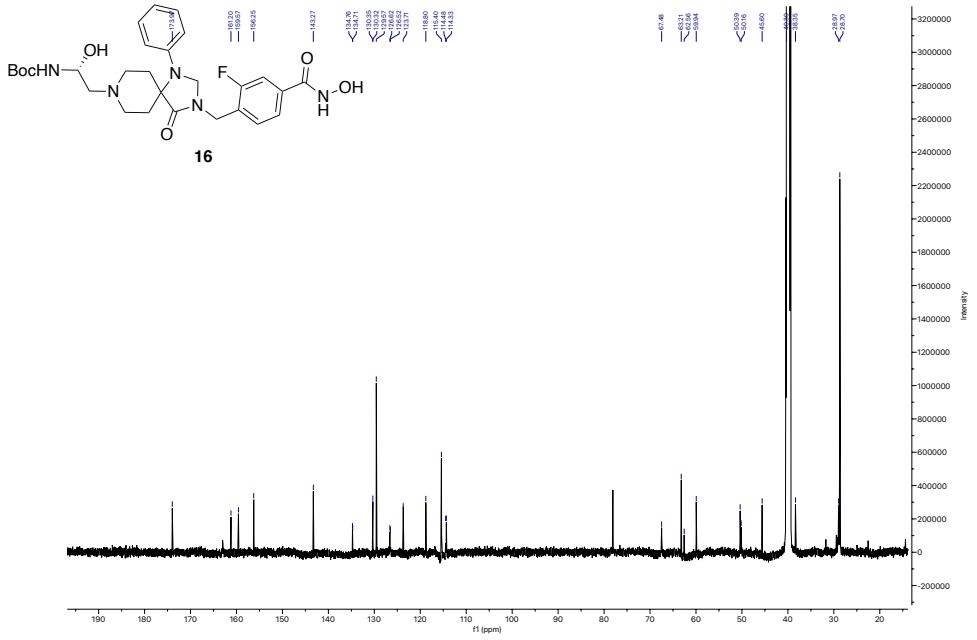
Supporting Figure 7

^{1}H NMR of 16



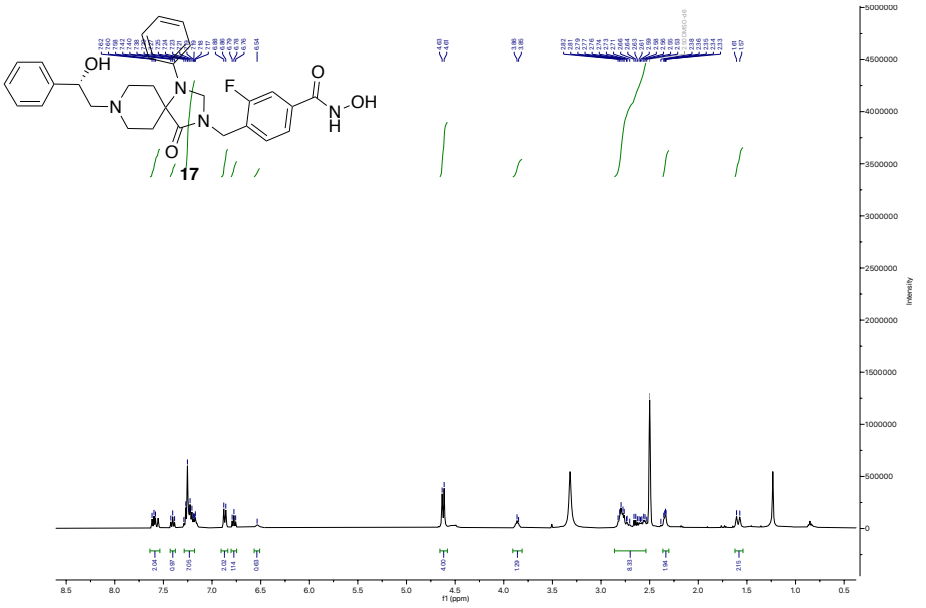
Supporting Figure 8

^{13}C NMR of 16



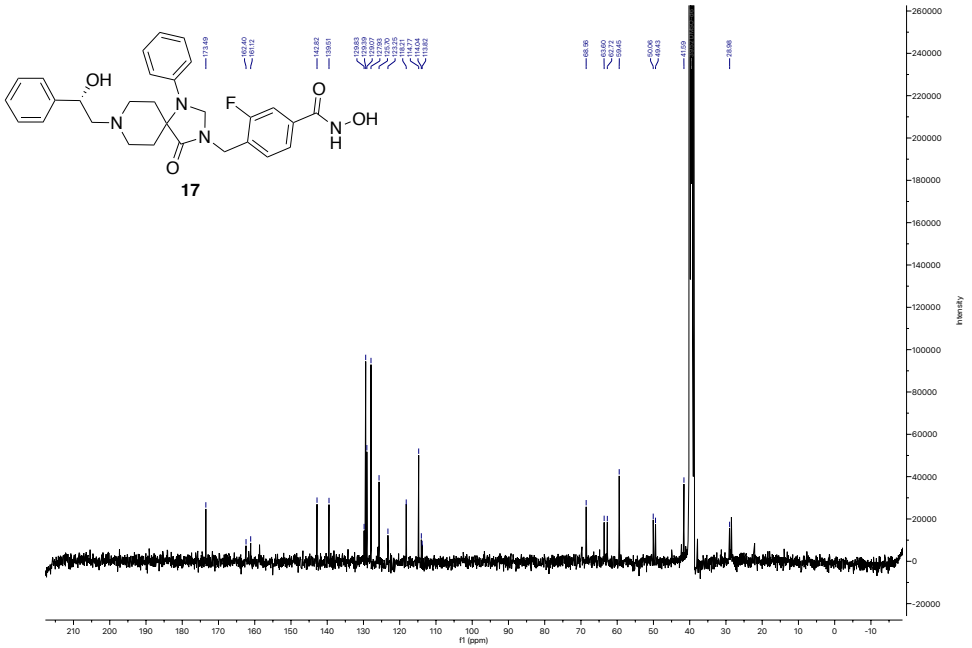
Supporting Figure 9

^{1}H NMR of 17



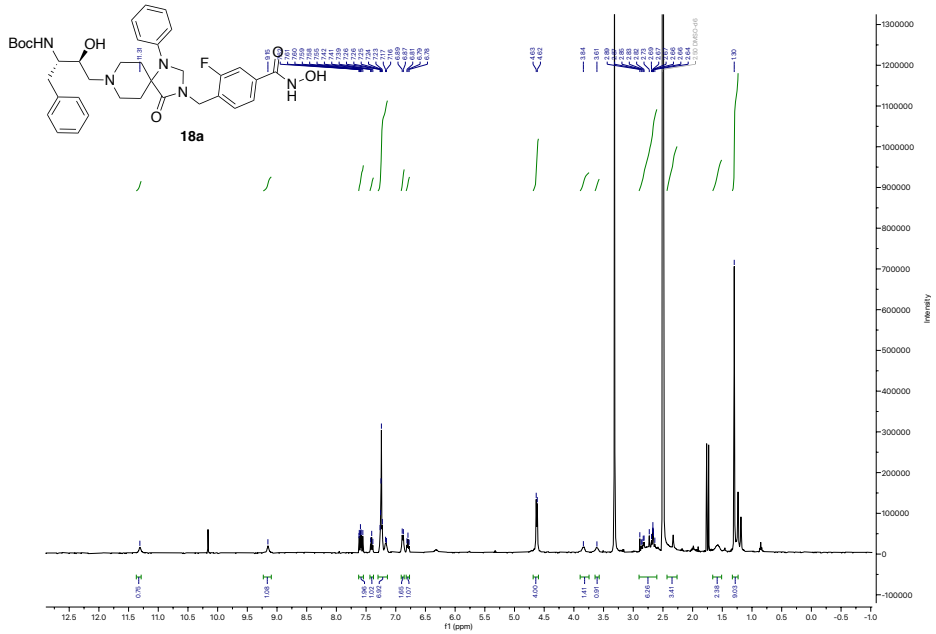
Supporting Figure 10

^{13}C NMR of 17



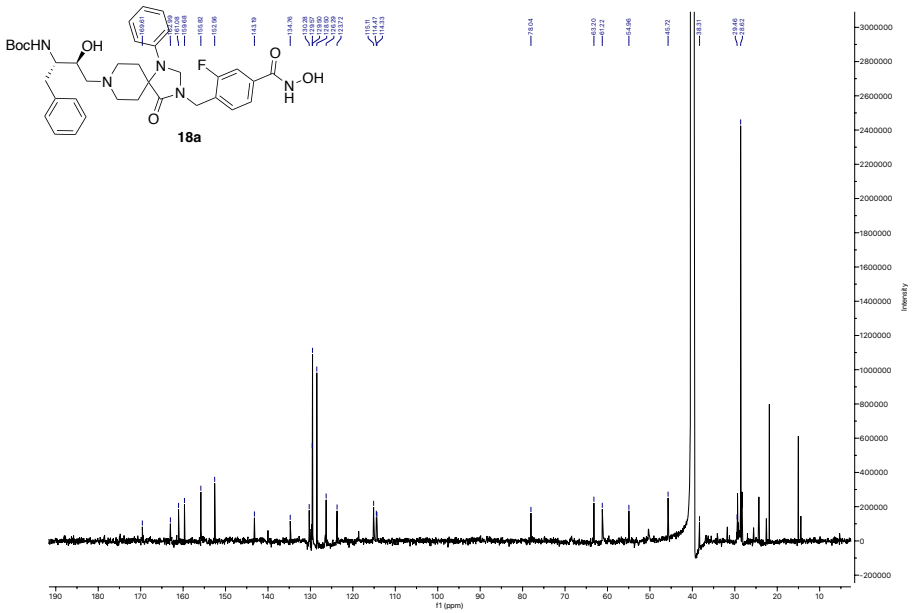
Supporting Figure 11

^{1}H NMR of 18a



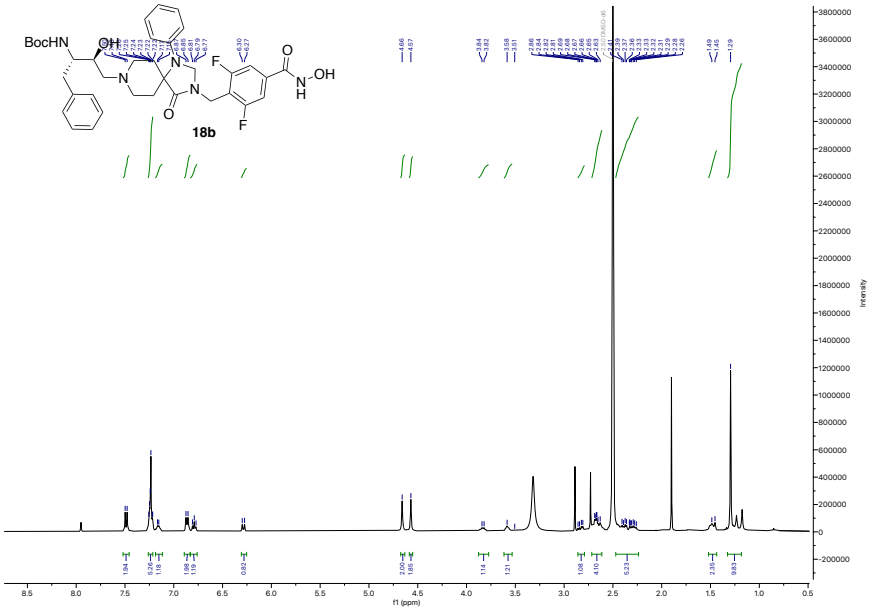
Supporting Figure 12

^{13}C NMR of 18a



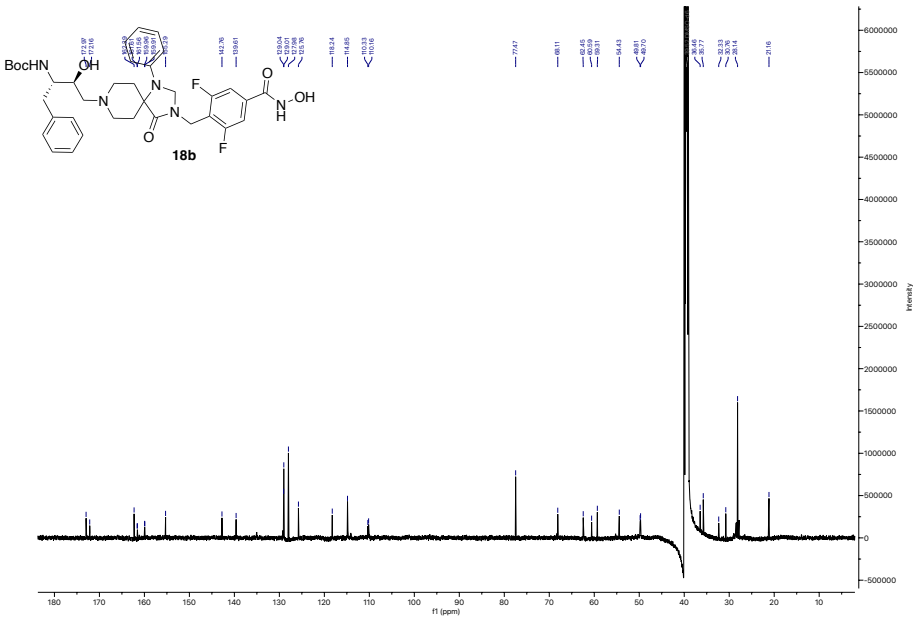
Supporting Figure 13

^{1}H NMR of 18b



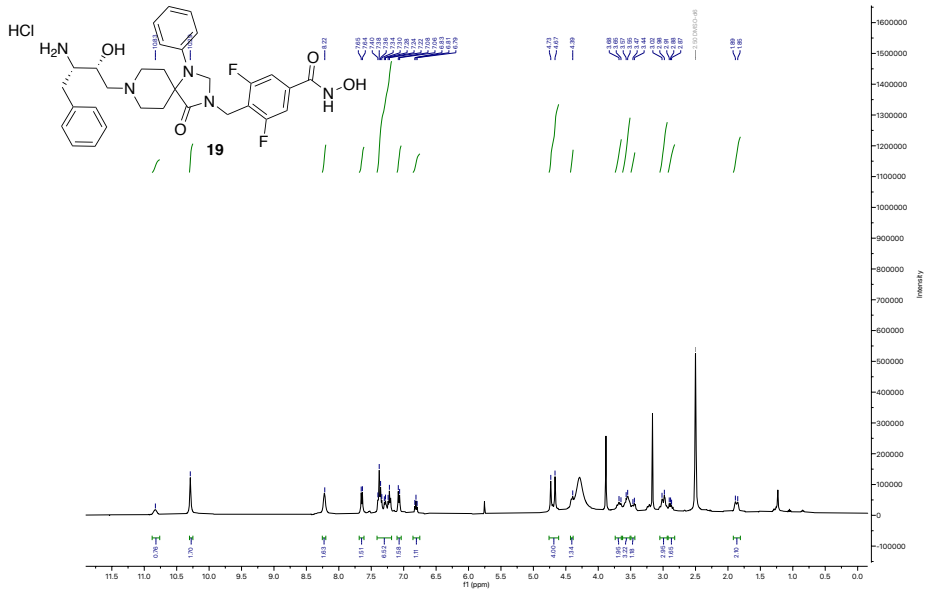
Supporting Figure 14

^{13}C NMR of 18b



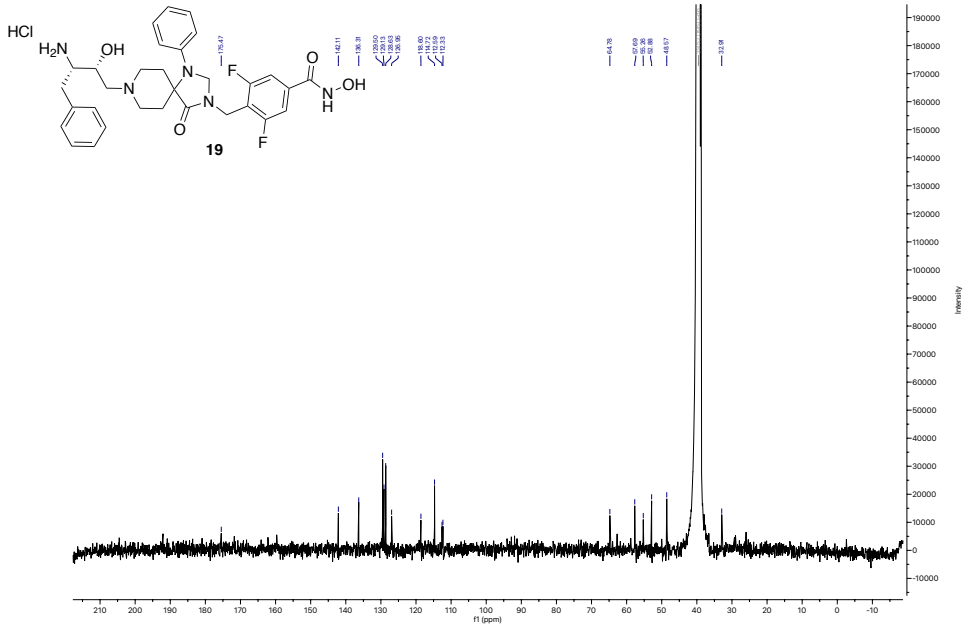
Supporting Figure 15

^{1}H NMR of 19



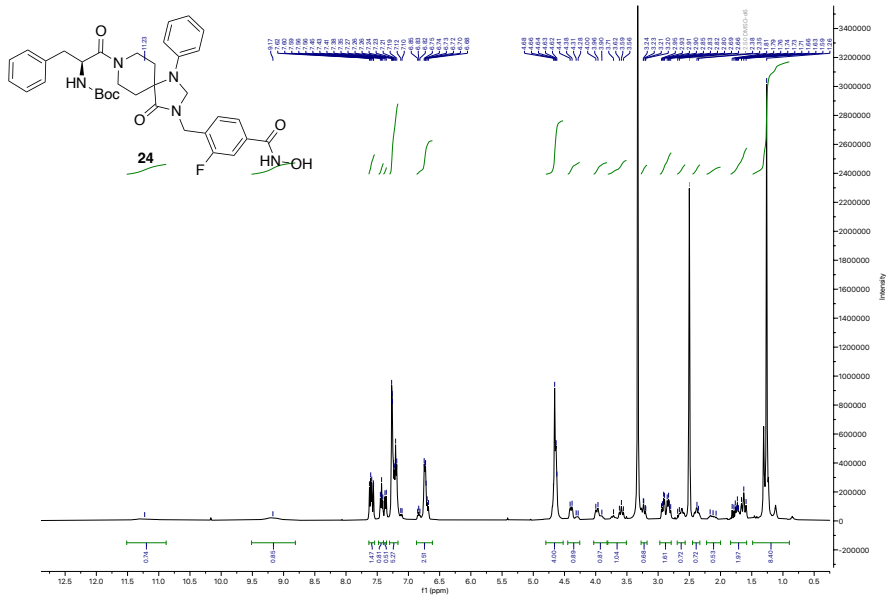
Supporting Figure 16

^{13}C NMR of 19



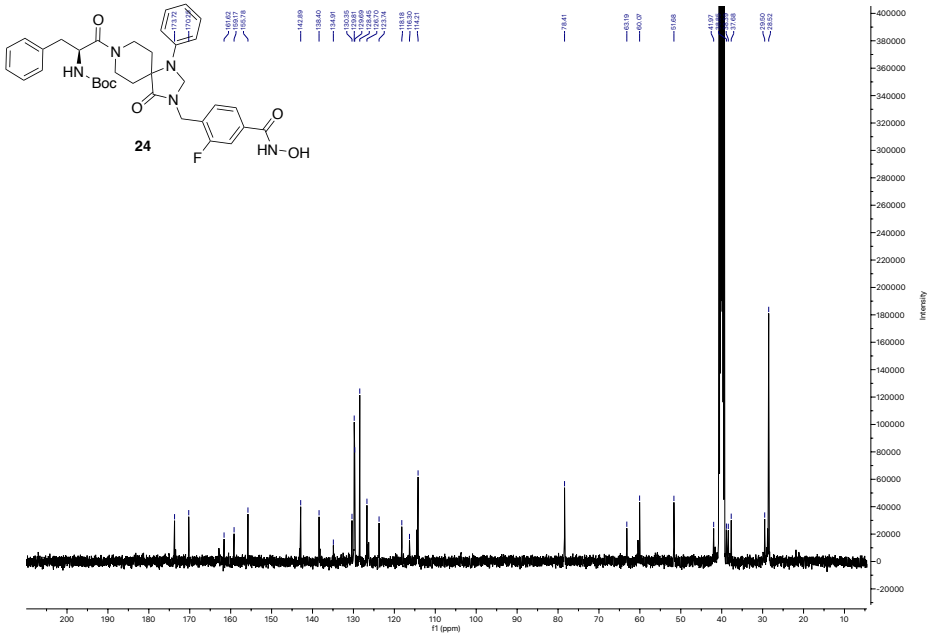
Supporting Figure 17

^{1}H NMR of 24



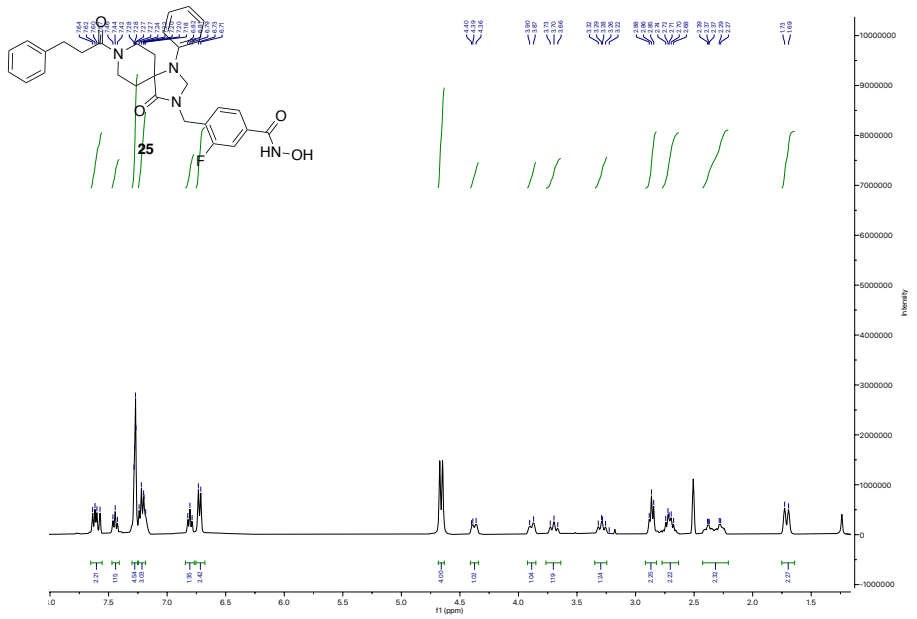
Supporting Figure 18

^{13}C NMR of 24



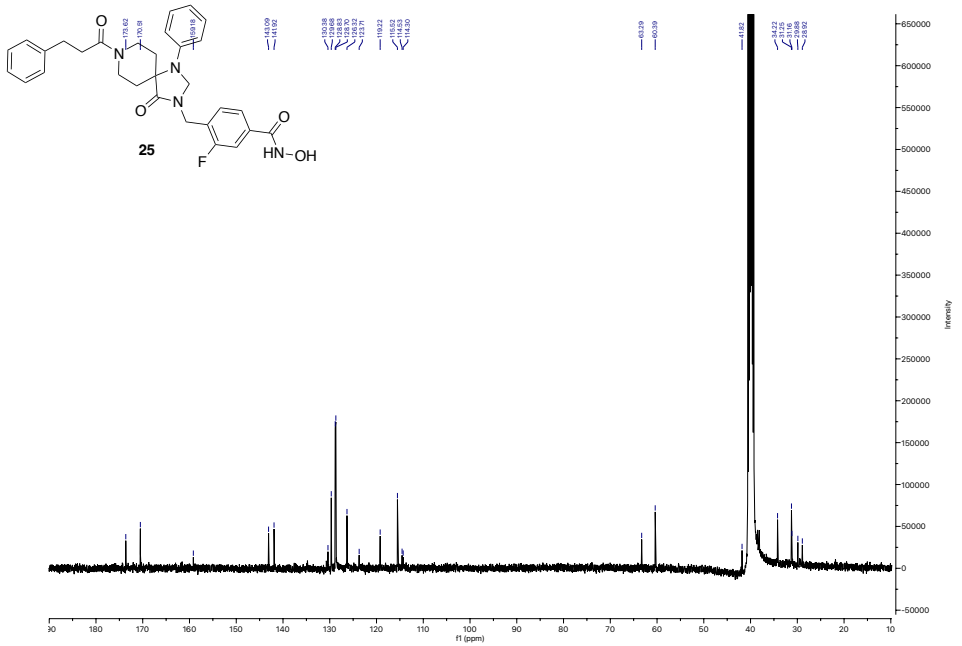
Supporting Figure 19

^{1}H NMR of 25



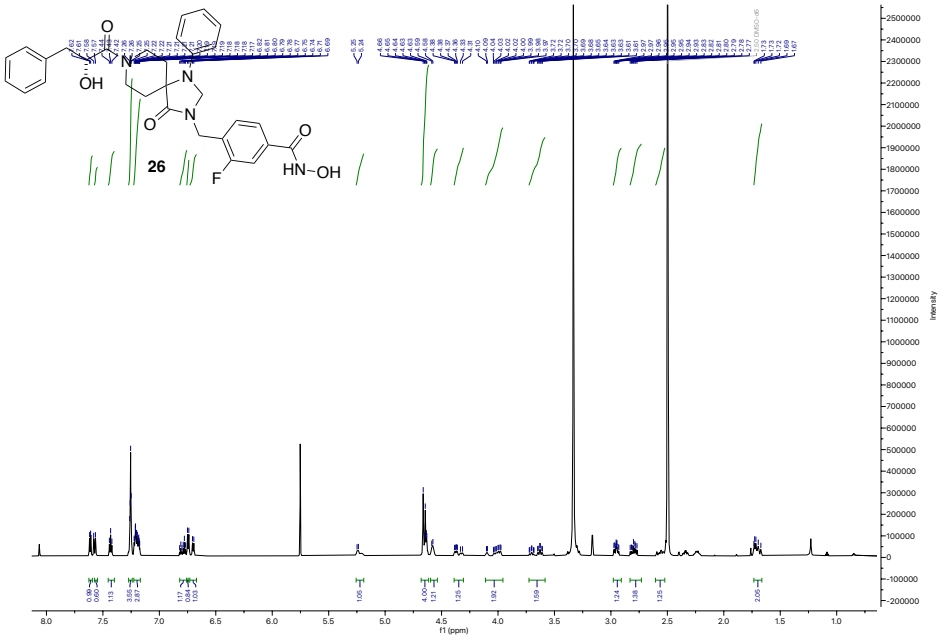
Supporting Figure 20

^{13}C NMR of 25



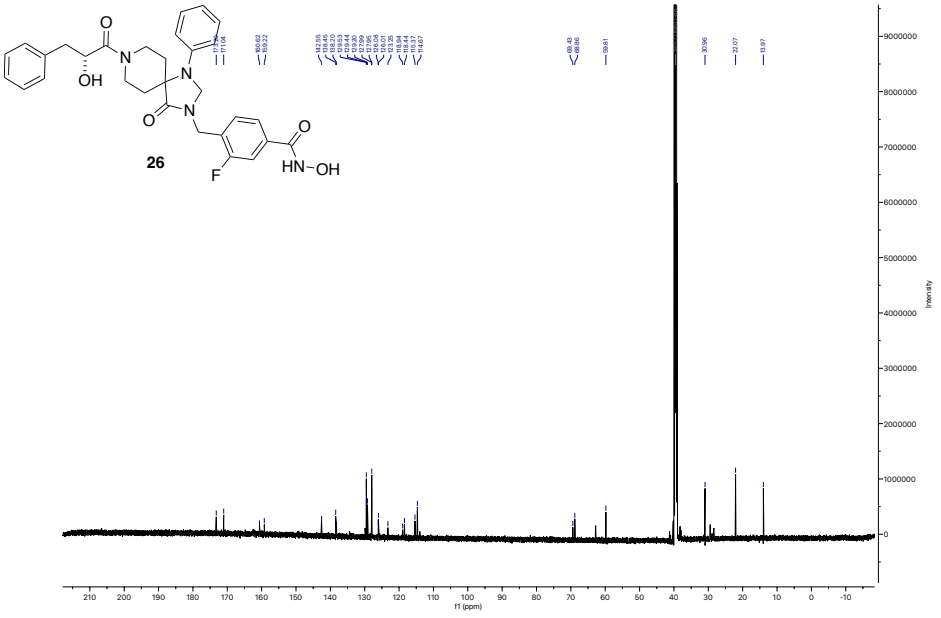
Supporting Figure 21

^{1}H NMR of 26



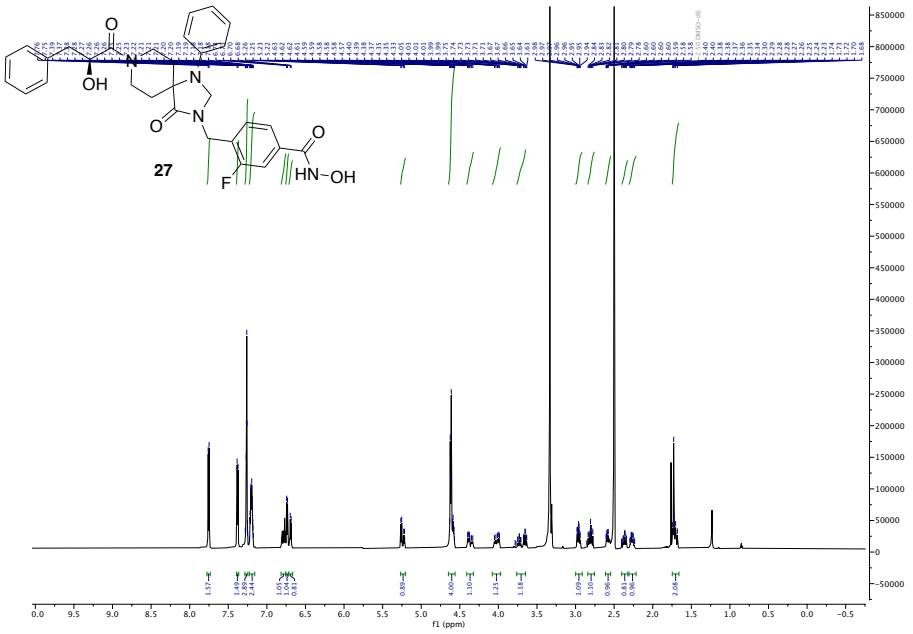
Supporting Figure 22

^{13}C NMR of 26



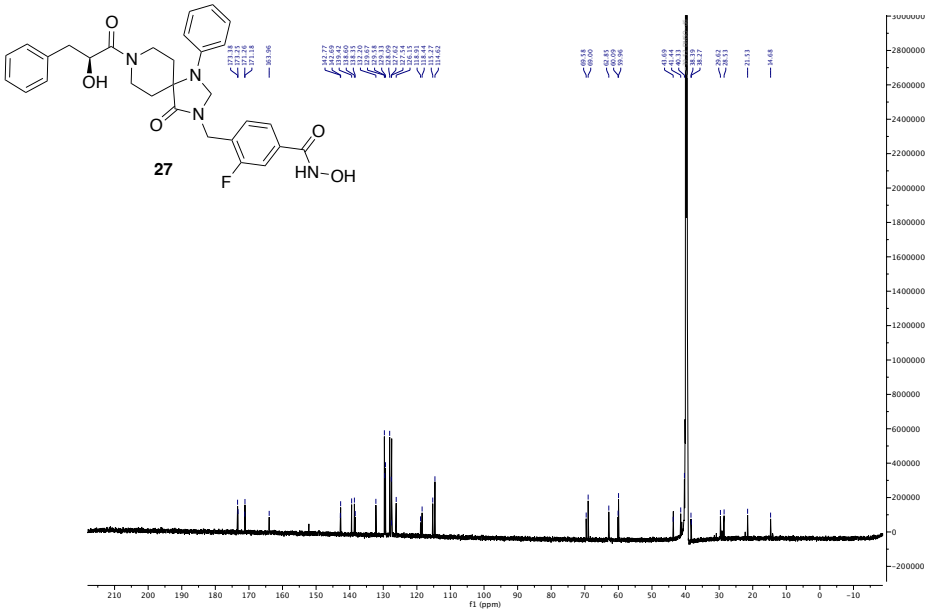
Supporting Figure 23

^{1}H NMR of 27



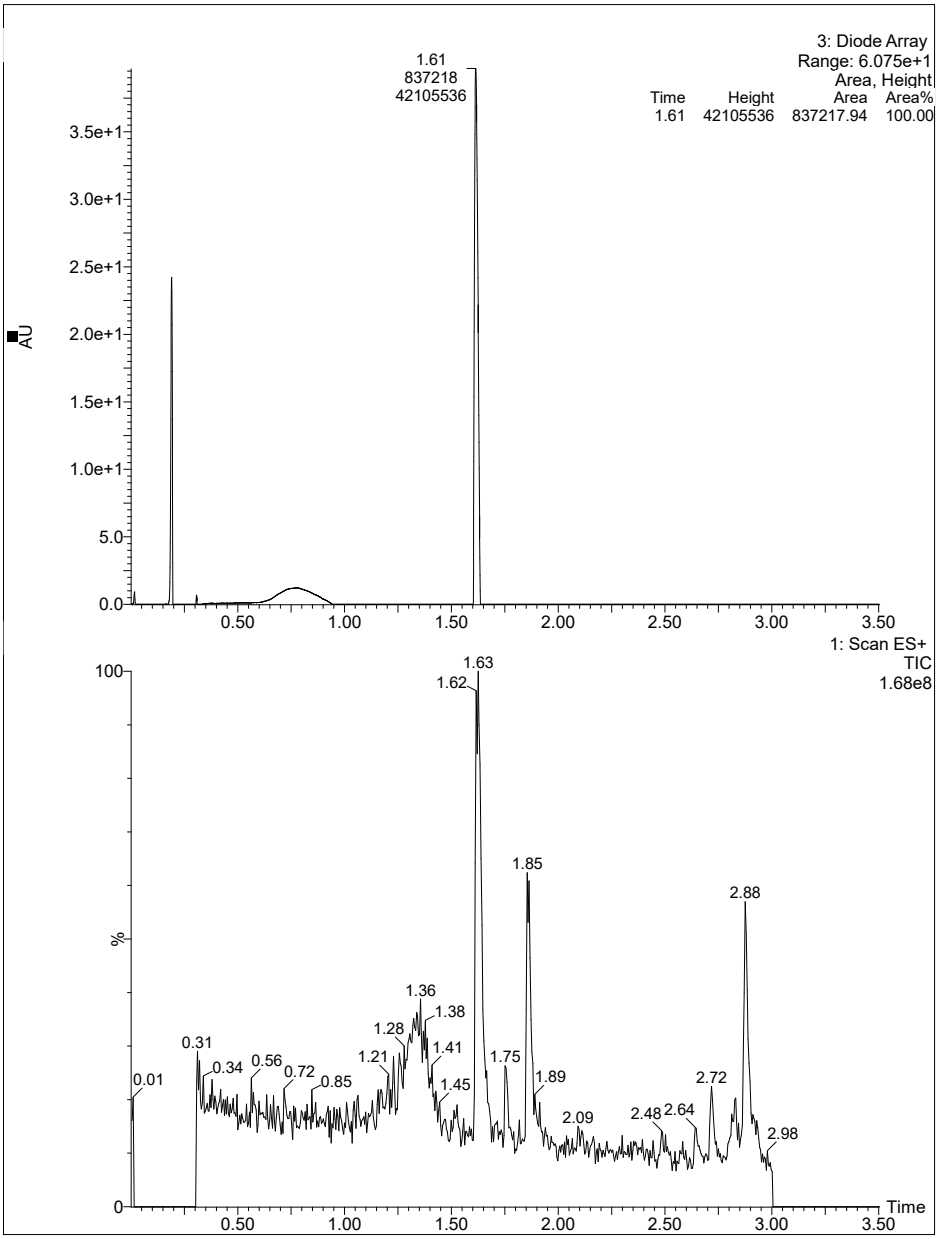
Supporting Figure 24

^{13}C NMR of 27



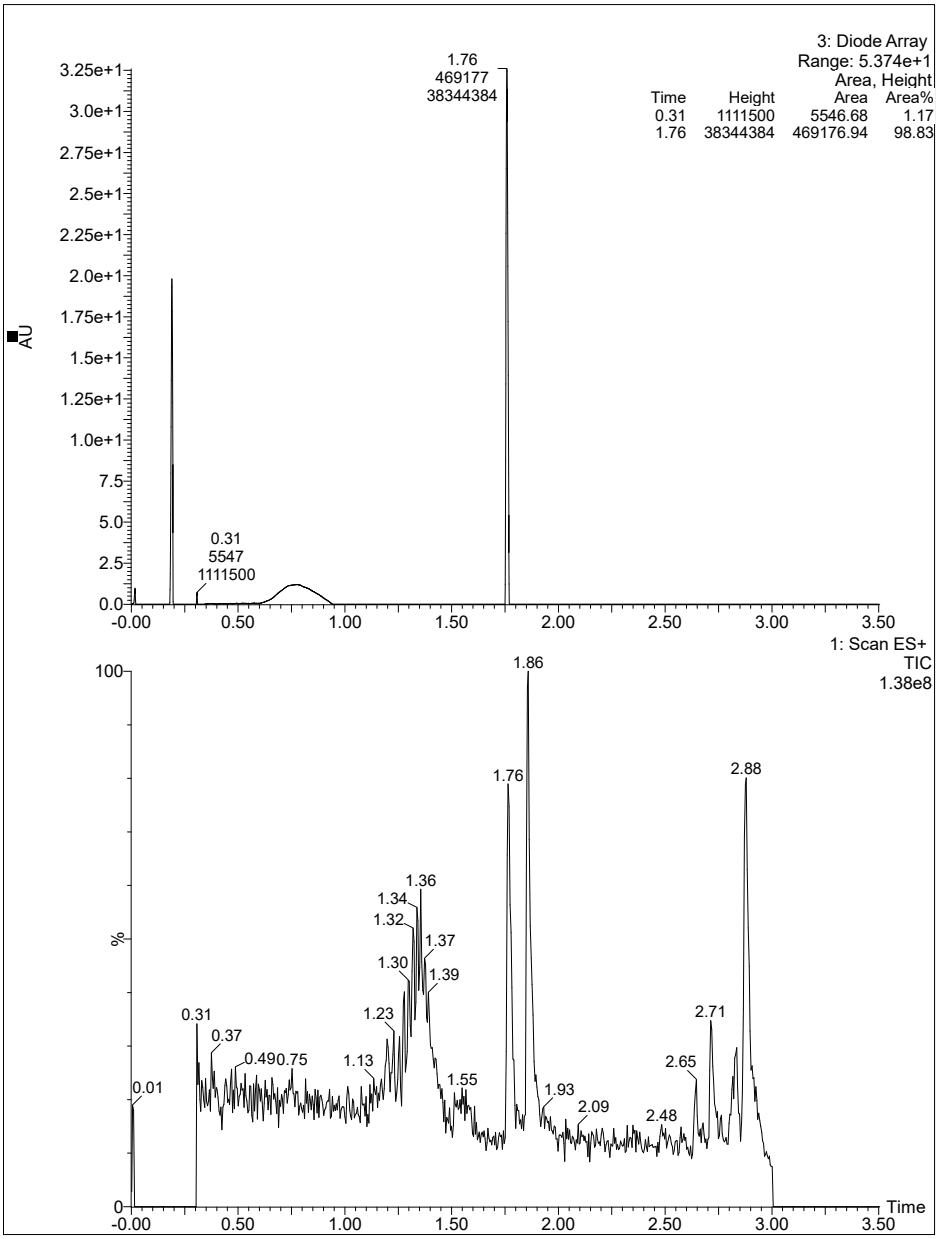
Supporting Figure 25

UPLC-MS spectra of compound 15a



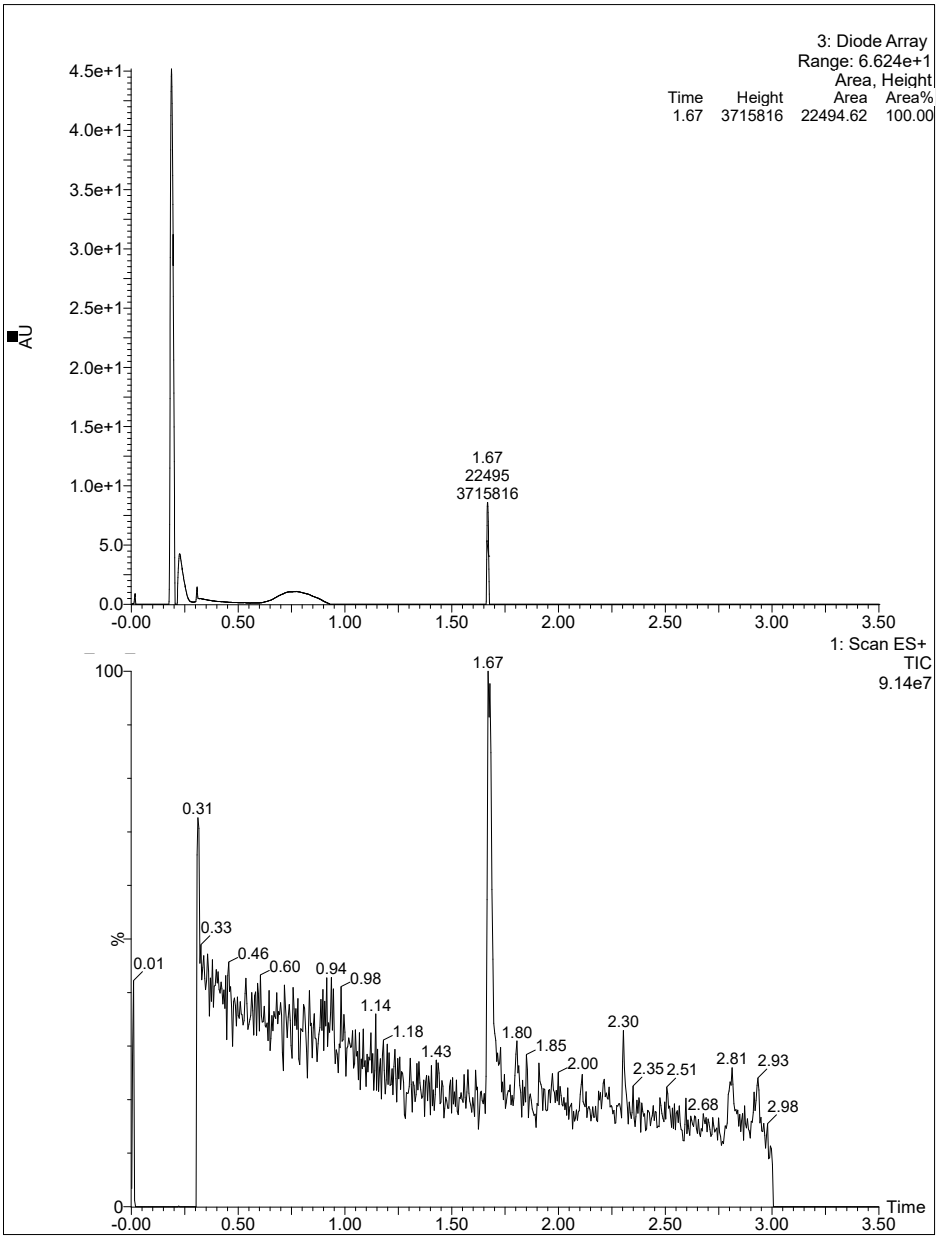
Supporting Figure 26

UPLC-MS spectra of compound 15b



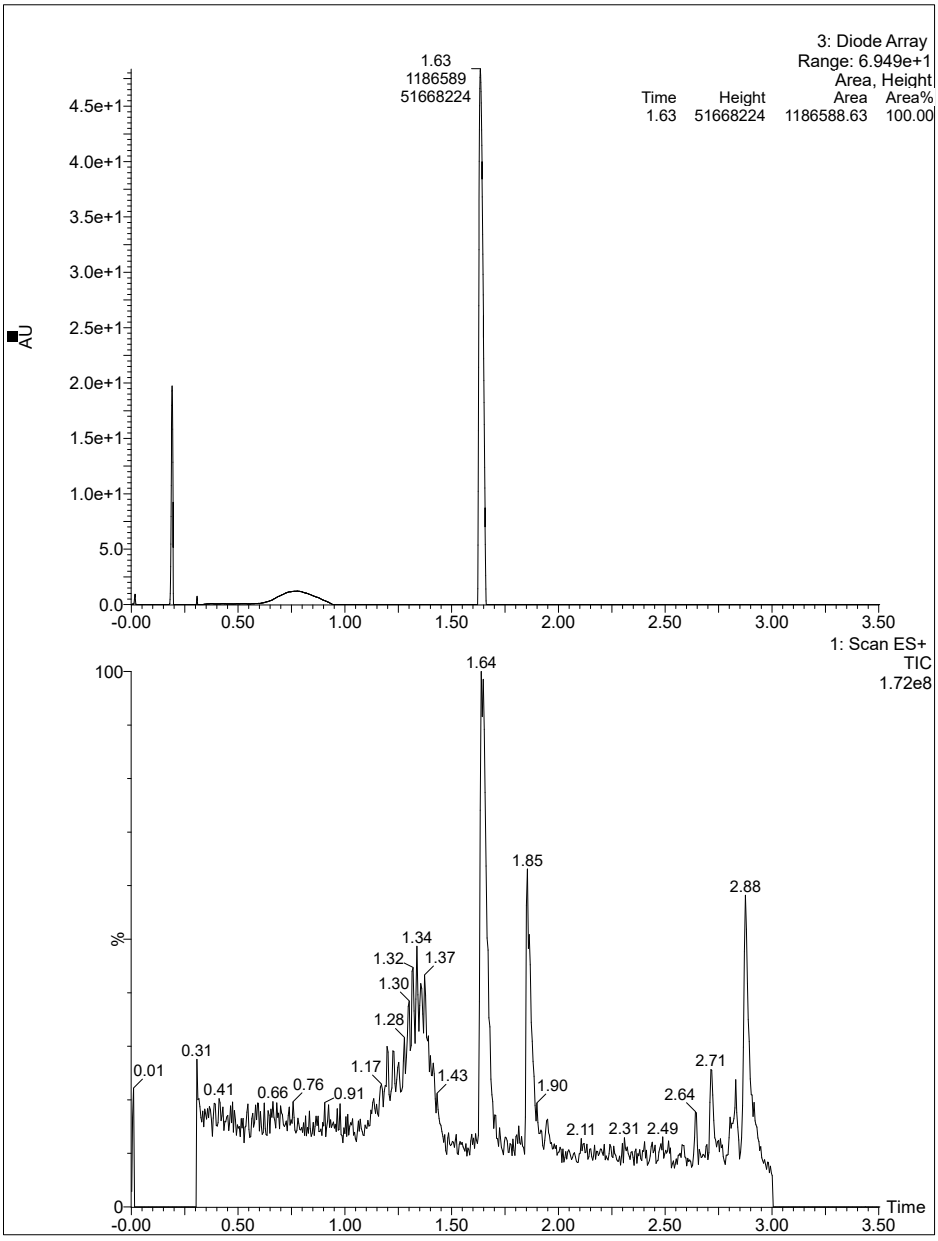
Supporting Figure 27

UPLC-MS spectra of compound 15c



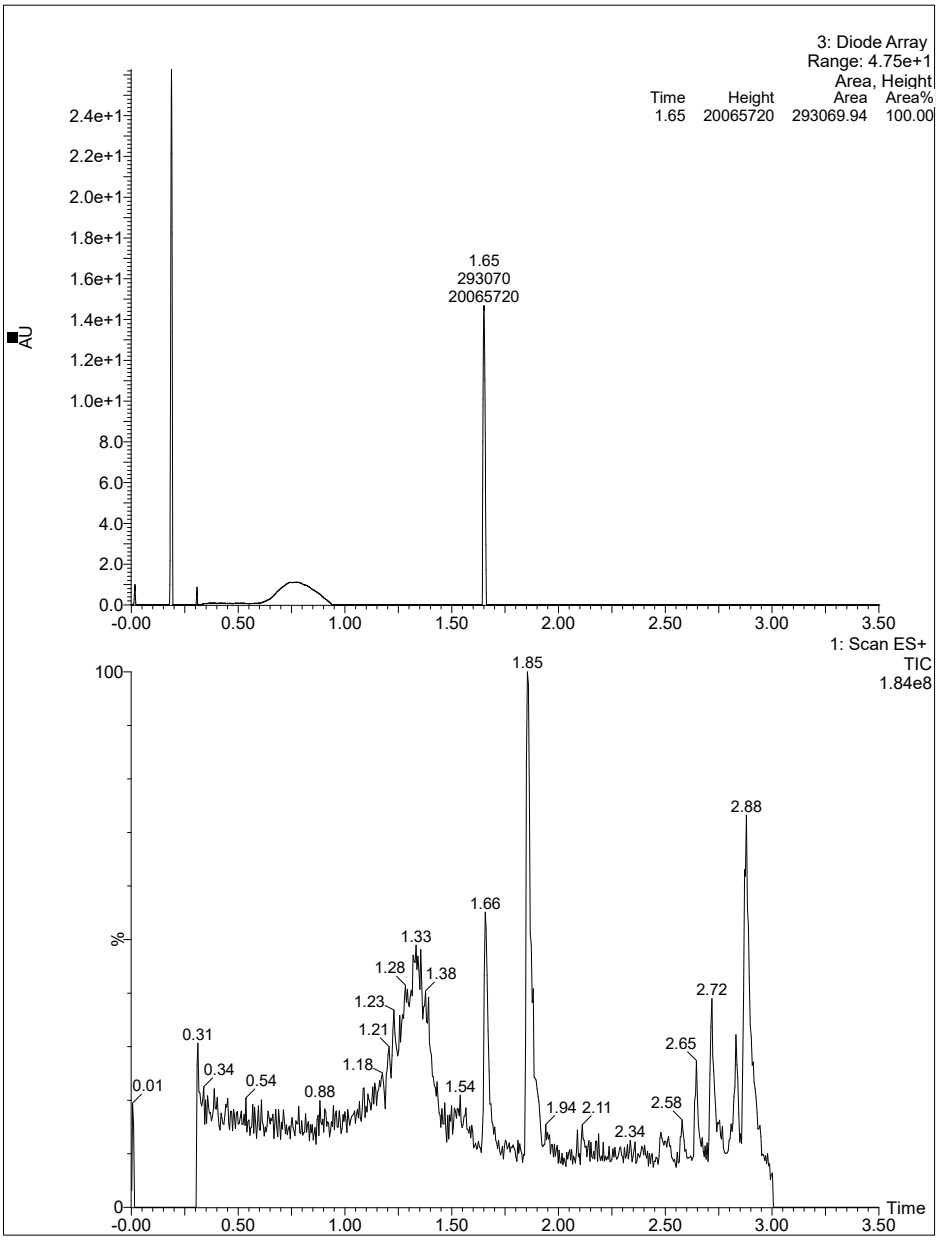
Supporting Figure 28

UPLC-MS spectra of compound 16



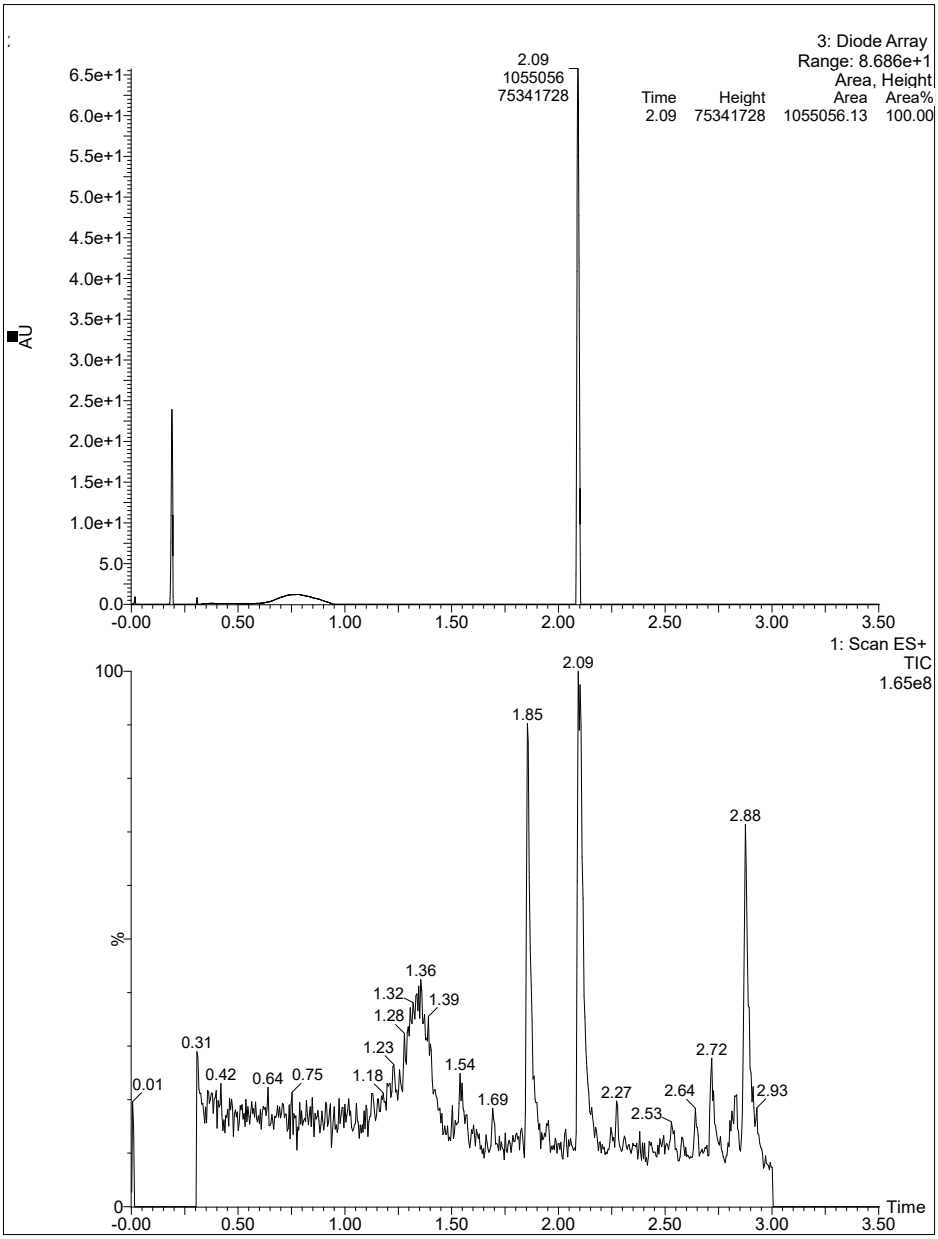
Supporting Figure 29

UPLC-MS spectra of compound 18a


3: Diode Array
Range: 4.75e+1
Area, Height
Time Height Area Area%
1.65 20065720 293069.94 100.00
AU
1.65
293070
20065720
1: Scan ES+
TIC
1.84e8
%
Time
0.01
0.31
0.34
0.54
0.88
1.18
1.21
1.23
1.28
1.33
1.38
1.54
1.66
1.85
1.94
2.11
2.34
2.58
2.65
2.72
2.88

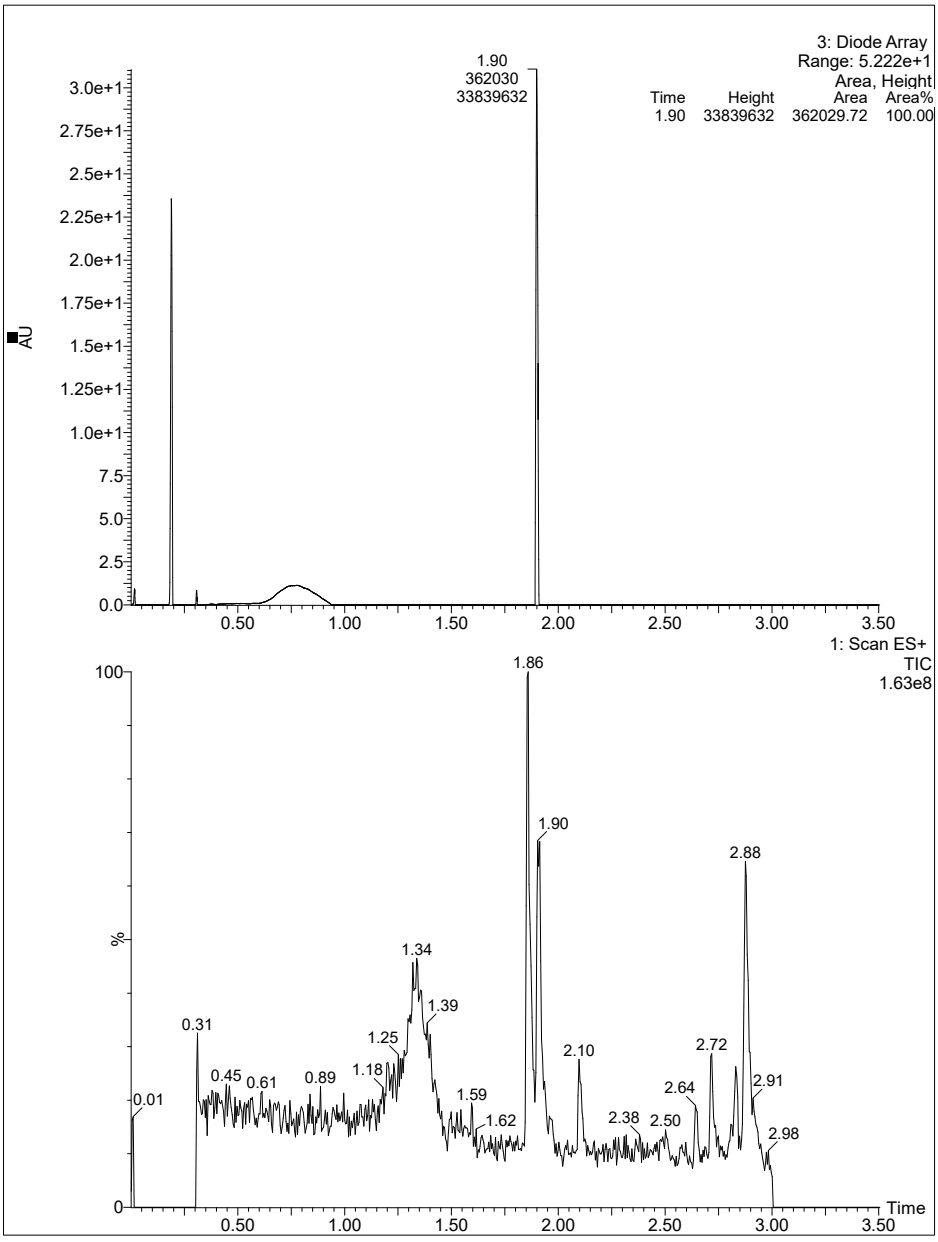
Supporting Figure 30

UPLC-MS spectra of compound 24



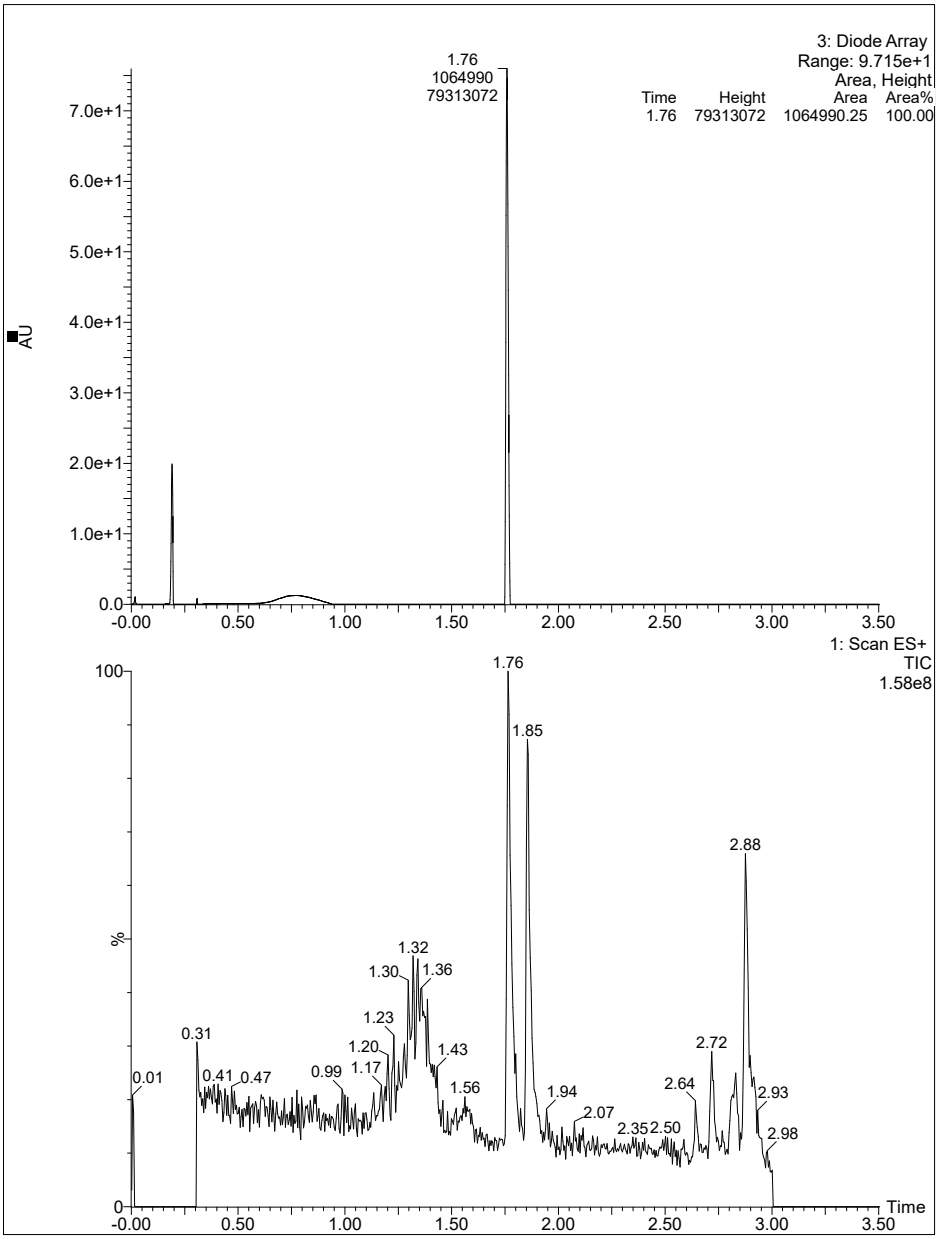
Supporting Figure 31

UPLC-MS spectra of compound 25


3: Diode Array
Range: 5.222e+1
Area, Height
1.90
362030
33839632
Time Height Area Area%
1.90 33839632 362029.72 100.00
AU
3.0e+1
2.75e+1
2.5e+1
2.25e+1
2.0e+1
1.75e+1
1.5e+1
1.25e+1
1.0e+1
7.5
5.0
2.5
0.0
0.50 1.00 1.50 2.00 2.50 3.00 3.50
1: Scan ES+
TIC
1.63e8
100
%
0
1.86
1.90
2.88
1.34
1.39
0.31
1.25
2.10
2.72
0.45
0.61
0.89
1.18
2.64
2.91
0.01
1.59
2.38
2.50
1.62
2.98
Time
0.50 1.00 1.50 2.00 2.50 3.00 3.50

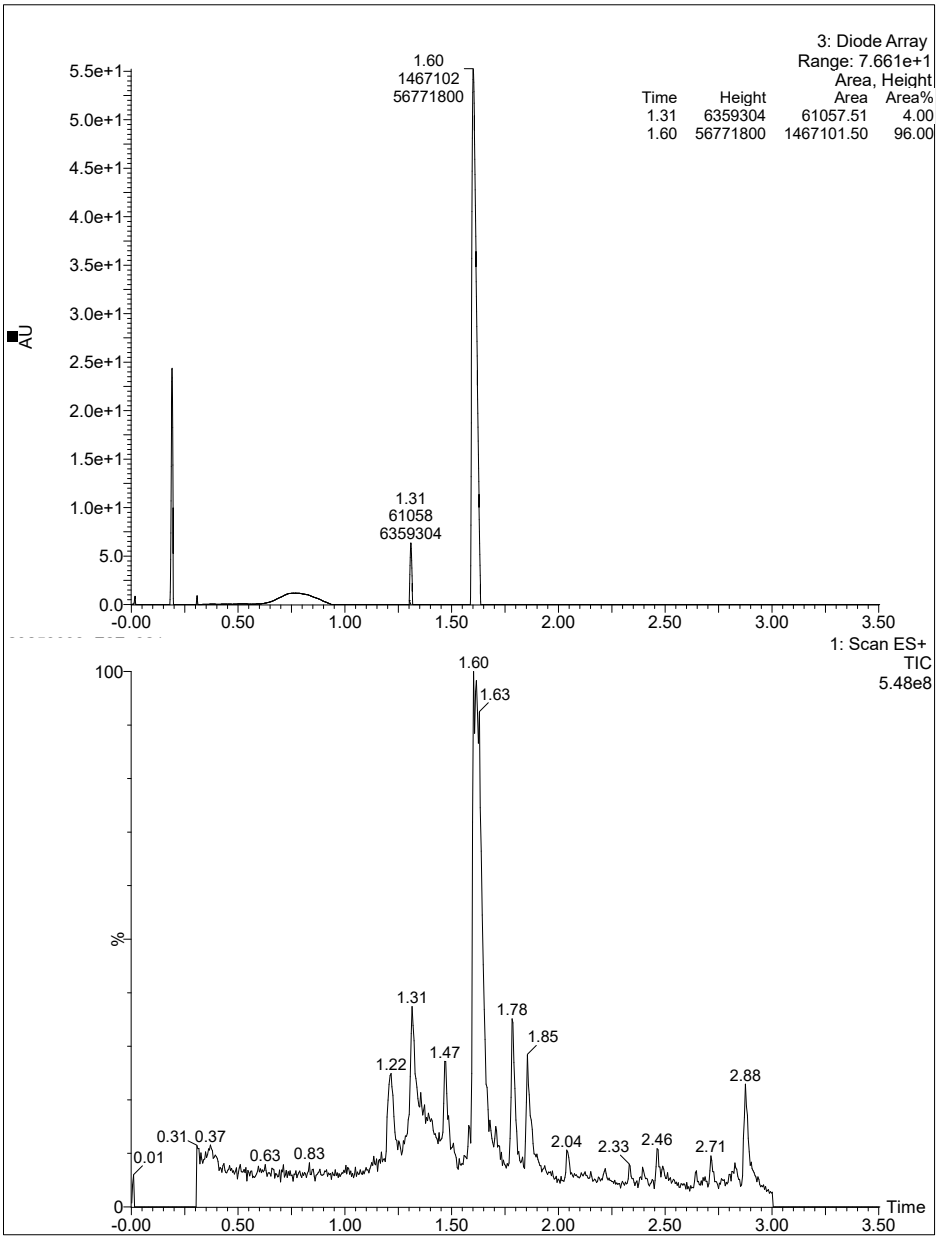
Supporting Figure 32

UPLC-MS spectra of compound 26



Supporting Figure 33

UPLC-MS spectra of compound 27



References

[1] A. De Falco, A.I. Alfano, L. Cutarella, M. Mori, M. Brindisi, J Med Chem 68 (2025) 10556–10576.

[2] N. Reyne, A. McCarron, P. Cmielewski, D. Parsons, M. Donnelley, Front Physiol 14 (2023).

[3] C.S. Thornton, M.D. Parkins, Semin Respir Crit Care Med 44 (2023) 269–286.

[4] J. Singh, M. Solomon, J. Iredell, H. Selvadurai, Antibiotics 14 (2025) 427.

[5] A. Muñoz-Santa, C. López-Causapé, A. Bellés, X. Gómez-Arbonés, S. Cortés-Lara, M. García-González, R. Pifarré-Teixidó, A. Oliver, JAC Antimicrob Resist 7 (2025).

[6] M. Hogardt, J. Heesemann, International Journal of Medical Microbiology 300 (2010) 557–562.

[7] S. Malhotra, D. Hayes, D.J. Wozniak, Clin Microbiol Rev 32 (2019).

[8] A. Bragonzi, D. Worlitzsch, G.B. Pier, P. Timpert, M. Ulrich, M. Hentzer, J.B. Andersen, M. Givskov, M. Conese, G. Döring, J Infect Dis 192 (2005) 410–419.

[9] E. Mahenthiralingam, M.E. Campbell, J. Foster, J.S. Lam, D.P. Speert, J Clin Microbiol 34 (1996) 1129–1135.

[10] M.C. Wolfgang, J. Jyot, A.L. Goodman, R. Ramphal, S. Lory, Proceedings of the National Academy of Sciences 101 (2004) 6664–6668.

[11] E. Mahenthiralingam, M.E. Campbell, D.P. Speert, Infect Immun 62 (1994) 596–605.

[12] J.W. Costerton, P.S. Stewart, E.P. Greenberg, Science (1979) 284 (1999) 1318–1322.

[13] P.K. Singh, A.L. Schaefer, M.R. Parsek, T.O. Moninger, M.J. Welsh, E.P. Greenberg, Nature 407 (2000) 762–764.

[14] J. Lee, L. Zhang, Protein Cell 6 (2015) 26–41.

[15] S. García-Reyes, G. Soberón-Chávez, M. Cocotl-Yanez, J Med Microbiol 69 (2020) 25–34.

[16] E.C. Pesci, J.P. Pearson, P.C. Seed, B.H. Iglewski, J Bacteriol 179 (1997) 3127–3132.

[17] M. Carlsson, S. Shukla, A.C. Petersson, M. Segelmark, T. Hellmark, Journal of Cystic Fibrosis 10 (2011) 265–271.

[18] C.C. Caldwell, Y. Chen, H.S. Goetzmann, Y. Hao, M.T. Borchers, D.J. Hassett, L.R. Young, D. Mavrodi, L. Thomashow, G.W. Lau, Am J Pathol 175 (2009) 2473–2488.

[19] L.Y. Chimi, M. Noubom, B.N. Bisso, G.S. Singor Njateng, J.P. Dzoyem, Int J Microbiol 2024 (2024).

[20] H. Raju, R. Sundararajan, R. Sharma, FEBS Lett 592 (2018) 256–262.

[21] N.C. Caiazza, R.M.Q. Shanks, G.A. O'Toole, J Bacteriol 187 (2005) 7351–7361.

[22] L. Zulianello, C. Canard, T. Köhler, D. Caille, J.-S. Lacroix, P. Meda, Infect Immun 74 (2006) 3134–3147.

[23] A.T. Hastie, S.T. Hingley, M.L. Higgins, F. Kueppers, T. Shryock, Cell Motil 6 (1986) 502–509.

[24] J. Lin, J. Cheng, Y. Wang, X. Shen, Front Cell Infect Microbiol 8 (2018).

[25] A.M. Grabiec, J. Potempa, Crit Rev Microbiol 44 (2018) 336–350.

[26] A. Bandyopadhaya, A. Tsurumi, D. Maura, K.L. Jeffrey, L.G. Rahme, Nat Microbiol 1 (2016) 16174.

[27] M. Mombelli, J. Lugrin, I. Rubino, A.-L. Chanson, M. Giddey, T. Calandra, T. Roger, J Infect Dis 204 (2011) 1367–1374.

[28] M. Brindisi, S. Barone, A. Rossi, E. Cassese, N. Del Gaudio, Á.J. Feliz Morel, G. Filocamo, A. Alberico, I. De Fino, D. Gugliandolo, M. Babaei, G.

Bove, M. Croce, C. Montesano, L. Altucci, A. Bragonzi, V. Summa, Eur J Pharmacol 936 (2022) 175349.

[29] T. Roger, J. Lugrin, D. Le Roy, G. Goy, M. Mombelli, T. Koessler, X.C. Ding, A.-L. Chanson, M.K. Reymond, I. Miconnet, J. Schrenzel, P. François, T. Calandra, Blood 117 (2011) 1205–1217.

[30] J.K. Ariffin, K. das Gupta, R. Kapetanovic, A. Iyer, R.C. Reid, D.P. Fairlie, M.J. Sweet, Antimicrob Agents Chemother 60 (2016) 1521–1529.

[31] S. Barone, E. Cassese, A.I. Alfano, M. Brindisi, V. Summa, J Med Chem 65 (2022) 3080–3097.

[32] J.D. Shrout, D.L. Chopp, C.L. Just, M. Hentzer, M. Givskov, M.R. Parsek, Mol Microbiol 62 (2006) 1264–1277.

[33] T. Zhao, Y. Li, B. Liu, B. Pan, X. Cheng, P. Georgoff, H.B. Alam, Journal of Trauma and Acute Care Surgery 80 (2016) 34–41.

[34] K. Kamemura, M. Ogawa, S. Ohkubo, Y. Ohtsuka, Y. Shitara, T. Komiya, S. Maeda, A. Ito, M. Yoshida, FEBS Lett 586 (2012) 1379–1383.

[35] G.L. Winsor, D.K.W. Lam, L. Fleming, R. Lo, M.D. Whiteside, N.Y. Yu, R.E.W. Hancock, F.S.L. Brinkman, Nucleic Acids Res 39 (2011) D596–D600.

[36] Y.Y. Lenis, M.A. Elmetwally, J.G. Maldonado-Estrada, F.W. Bazer, Zygote 25 (2017) 244–255.

[37] L. Li, J.N. Rao, X. Guo, L. Liu, R. Santora, B.L. Bass, J.-Y. Wang, American Journal of Physiology-Cell Physiology 281 (2001) C941–C953.

[38] I. V. Smirnov, S.I. Dimitrov, V.L. Makarov, J Biomol Struct Dyn 5 (1988) 1149–1161.

[39] K. Thongbhubate, Y. Nakafuji, R. Matsuoka, S. Kakegawa, H. Suzuki, J Bacteriol 203 (2021).

[40] M.W. McGinnis, Z.M. Parker, N.E. Walter, A.C. Rutkovsky, C. Cartaya-Marin, E. Karatan, FEMS Microbiol Lett 299 (2009) 166–174.

[41] S.C. Huang, C.A. Panagiotidis, E.S. Canellakis, Proceedings of the National Academy of Sciences 87 (1990) 3464–3468.

[42] E. Verdin, M. Ott, Nat Rev Mol Cell Biol 16 (2015) 258–264.

[43] M.S. Finnin, J.R. Donigian, A. Cohen, V.M. Richon, R.A. Rifkind, P.A. Marks, R. Breslow, N.P. Pavletich, Nature 401 (1999) 188–193.

[44] Q. Jiang, W. Chen, Y. Qin, L. Huang, X. Xu, L. Zhao, Q. Yan, Microbiologyopen 6 (2017).

[45] P.R. Watson, D.W. Christianson, Biochemistry 62 (2023) 2689–2699.

[46] A. Krämer, T. Wagner, Ö. Yildiz, F.-J. Meyer-Almes, Biochemistry 55 (2016) 6858–6868.

[47] T.K. Nielsen, C. Hildmann, A. Dickmanns, A. Schwienhorst, R. Ficner, J Mol Biol 354 (2005) 107–120.

[48] D. Riester, D. Wegener, C. Hildmann, A. Schwienhorst, Biochem Biophys Res Commun 324 (2004) 1116–1123.

[49] T.K. Nielsen, C. Hildmann, D. Riester, D. Wegener, A. Schwienhorst, R. Ficner, Acta Crystallogr Sect F Struct Biol Cryst Commun 63 (2007) 270–273.

[50] M.J. Bottomley, P. Lo Surdo, P. Di Giovine, A. Cirillo, R. Scarpelli, F. Ferrigno, P. Jones, P. Neddermann, R. De Francesco, C. Steinkühler, P. Gallinari, A. Carfí, Journal of Biological Chemistry 283 (2008) 26694–26704.

[51] S. Barone, I. Bello, A. Guadagni, C. Cerchia, G. Filocamo, E. Cassese, A.I. Alfano, C. Esposito, Á.J. Feliz Morel, M. Brunetti, A. Lavecchia, V. Summa, E. Panza, M. Brindisi, Eur J Med Chem 292 (2025) 117634.

[52] S. Barone, B. Mateu, L. Turco, S. Pelliccia, F. Lembo, V. Summa, E. Buommino, M. Brindisi, Front Microbiol 15 (2024).

Chapter 8

Synergistic antifungal activity of selective HDAC6 inhibitor in combination with Voriconazole agains azole-resistant C. albicans strains

Fungal infections are arising as a public health burden due to the widespread of invasive infections often difficult to diagnose and treat [1,2]. Accordingly, World Health Organization listed fungal priority pathogens for their clinical incidence on healthcare [3]. Among critical priority fungal pathogens, *C. albicans* is a common opportunistic fungal pathogen that normally resides in the human gastrointestinal and genitourinary, and one of the main causes of invasive fungal infections, thus posing a growing healthcare challenge due to its high morbidity and mortality, mainly in immunocompromised patients [4,5]. Nowadays, few classes of drugs have been approved for the treatment of both systemic and superficial fungal infection. Among them, azoles (e.g. voriconazole, **1**, Figure 1), polyenes (e.g. amphotericin B, **2**, Figure 1), echinocandins (e.g. capsofungin, **3**, Figure 1), allylamines (e.g. terbinafine, **4**, Figure 1) and nucleoside analogues (e.g. flucytosine, **5**, Figure 1) – classified according to their chemical structure and mechanism of action - represent the first-line treatment for both systemic and superficial mycoses.

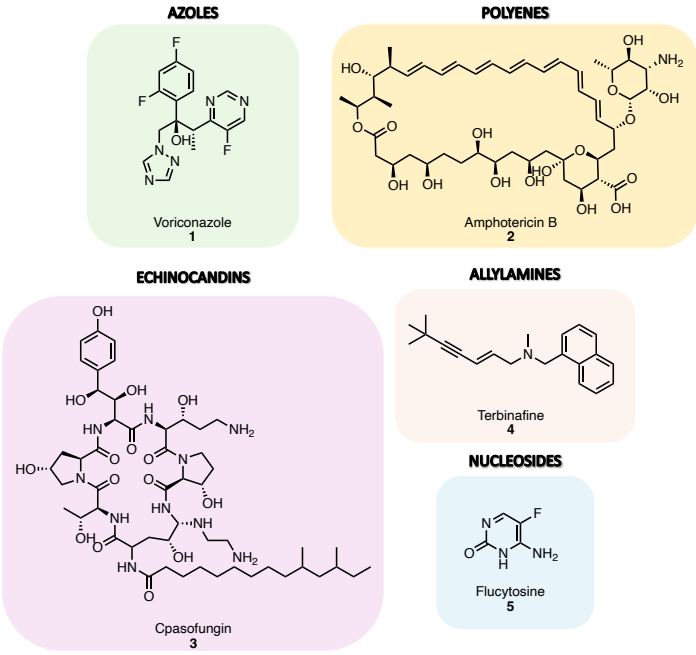


Figure 1. Classification of commonly used antifungal drugs and chemical structures of **1-5**.

Although the broad-spectrum efficacy of these drugs in fighting fungal infections, they are associated to a wide plethora of adverse effects and poor pharmacokinetic properties, while their abuse or misuse led to chemoresistance phenomena, namely the production of drug efflux pumps, target gene mutations, prodrugs inactivation, yeast cells morphological changes, and so on [6-10]. For instance, a main limitation to azoles treatment stands in their fungistatic activity, since surviving yeasts represent a reservoir for the development and selection of azole resistance [11]. Also, trailing effect - usually observed during the treatment of *Candida* spp. - is a common phenomenon in which yeasts treated with azoles maintain a residual growth also at high antifungal concentrations, thus leading to full recovery of the growth in the time [12]. Moreover, external factors such as body temperature, pH or CO_2 levels can trigger the yeast-to-hyphae transition, whereas cells in form of hypha can express virulence factors which facilitate host tissues degradation and invasion and evade immune system [13-15]. Mutations

in *ERG11* gene – which encodes for azoles target enzyme lanosterol-α-demethylase (LDM, involved in ergosterol biosynthesis) are also very common in *C. albicans*, representing the first cause of chemoresistance to azole drugs [16-19]. Accordingly, the treatment of fungal infections has posed significant healthcare challenges, which evidence the need for novel antifungals able to overcome chemoresistance phenomena and effectively manage both localized and systemic fungal infections. In this context, fungi virulence and growth are tightly influenced by PTMs - in which histone modifications play a major role [20-24].

Based on structure homology with *S. cerevisiae* counterparts, 11 HDAC isoforms have been identified in *C. albicans* and *C. glabrata* species, labelled into three main classes, listed below [25-37] (Figure 2):

1. Class I (Rpd3-type): it comprises RPD31, RPD32, HOS1, HOS2 enzymes. RDP31 and RDP 32, along with HOS2 HDA1, have been found to be implicated in azole drugs chemoresistance (*e.g.* trailing effect) and yeast filaments extension [28], while HOS2 is mainly involved in regulating yeast-to-hyphae morphological transition [29], a peculiar phenomenon considered a key virulence trait of *C. albicans,* which can help fungus to escape phagocytosis, increase dissemination during infection stages and favor drug resistance [30]. Although HOS1 role has not been fully elucidated, it is considered to mainly regulate cellular homeostasis and metabolism [31].

2. Class II (Hda1-like): it includes HDA1 and HOS3. *C. albicans* HAD1 is a close analogue of *S. cerevisiae HDA1* which, as previously described, shares high homology sequence with Class II human HDACs [32]. During yeast-to-hyphae transition, HDA1 is recruited to promoters of hypha specific genes by the biofilm regulator 1 (BRG1) transcription factor, which in turns shapes chromatin in an unfavorable configuration to the binding with the transcriptional repressor

NRG1, thereby resulting in hyphal development [33]. HOS3 has been first identified in 2001, while its biological role remains poorly characterized.

3. Class III (sirtuins): SIR2 has been identified in *C. albicans* in 1999, and it exerts deacetylase activity on K16H4, thereby resulting in transcriptional repression [34].

4. Other HDACs: SET3 is a NAD^+-dependent deacetylase. In its active form, SET3 assembles in a multiprotein complex, namely the Set3 histone deacetylase complex (Set3C), which requires HOS1 deacetylase to exert its catalytic activity. Set3C is a key regulator of yeast-to-hyphae transition, modulates biofilm formation and contributes to chemoresistance phenomena [35].

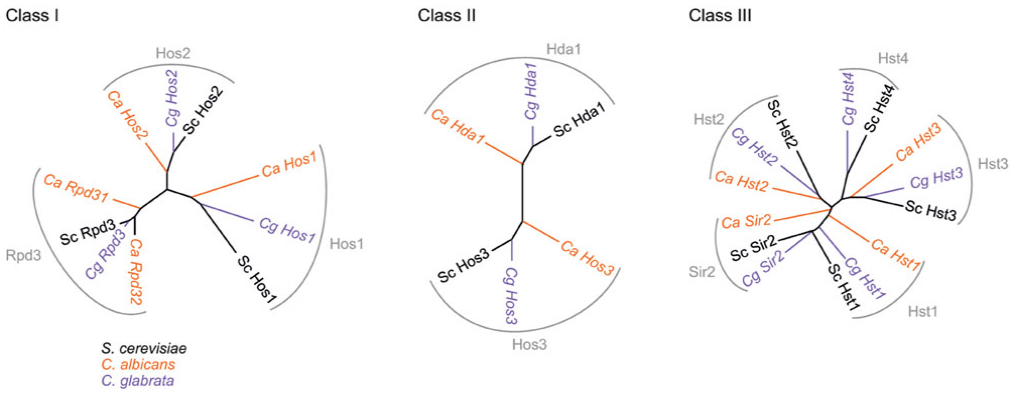


Figure 2. Phylogenetic trees representing *S. cerevisiae*, *C. albicans* and *C. glabrata* HDACs [36].

Interestingly, *HDA1* gene depletion in *C. albicans* cells inhibited hyphal development [37], thereby confirming HDA1 is a key activator of this morphological transition. On the other and, RPD31 can act both as activator and repressor of yeast-to-hyphae transition. In yeast cells RPD31 inhibits the expression of hyphal genes, while, under filament-inducing conditions, it promotes filaments elongation and hyphal genes expression [38]. Accordingly, *C. albicans* yeast defective for RPD31 showed reduced virulence *in vivo* [39]. Likewise, genetic depletion of some Set3C components (*e.g.* SET3 and HOS2) induced hyperfilamentous phenotypes [40]. In a similar manner to what happens

in bacterial cells, yeasts are able to form biofilm to enhance their virulence, persistence in host organism, and resistance to antifungal drugs [41]. Both SET3 and HOS2 genetic depletion reduced biofilm formation [42], while key components or Set3C are repressed during cellular dispersion [43]. According to the enhanced virulence acquired to fungi during biofilm formation, HDA1 and RPD3 were found to be increased during azole-resistance acquisition, probably due to the increase of Hsp90 acetylation degree, responsible for chemoresistance in fungi [43,44]. In line with this data, both HDAC and Hsp90 inhibition were able to restore azole susceptibility in drug resistant *C. albicans* strains [45].

Given the strong epigenetic component underlying *C. albicans* virulence, HDACs have been investigated as potential therapeutic target to counteract fungi pathogenicity. Accordingly, several human HDACis displayed a weak antifungal activity alone, while significantly synergizing azole drugs efficacy, thereby representing a promising therapeutic strategy for the treatment of resistant *C. albicans* infections [46-51]. More recently, fungal HDACis have been developed so far, showing synergistic efficacy with azole drugs in inhibiting morphological transition, biofilm formation and virulence of yeasts [52-54], thereby paving a new avenue in the treatment of mycosis.

8.1 Results and discussion

Taking into account both the key role of fungal HDACs in controlling fungal virulence, and the efficacy of proprietary HDAC6is in attenuating bacterial virulence and biofilm formation (*Chapter 6*), we sought to assess compound **15a** (IC_{50} HDAC6 = 7.1 nM; IC_{50} HDAC1 = 2191 nM, Selectivity Index = 422, *Chapter 6*) in C. albicans 90028 and *C. albicans* 10231 strains in order to evaluate its efficacy in modulating fungal pathogenicity.

8.1.1 Compound 15a in combination with Voriconazole inhibits C. albicans cells growth

We first assessed the effect of compound **15a** on *C. albicans* 90028 and *C. albicans* 10231 cell growth. As expected, compound **15a** alone did not affect yeast cells growth of both strains, with a moderate effect only at 400, 200 and 100 mM 202 on *C. albicans* 10231, with a percentage of growth reduction of 24, 22, and 12%, respectively (Figure 3). This result was perfectly in line with the reported weak intrinsic antifungal activity for HDACis.

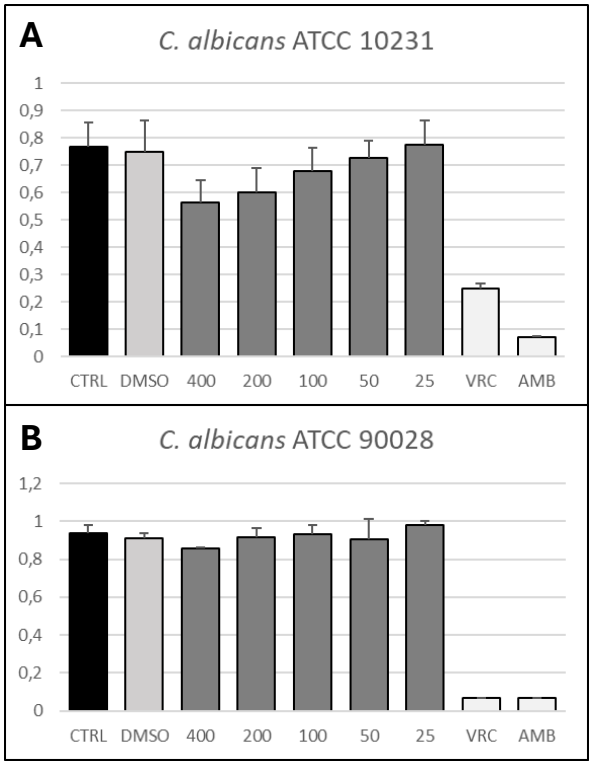


Figure 3. Cell growth inhibition assay *on C. albicans* 120331 (A) and 90028 (B) strains with **15a** at different concentrations. VRC = Voriconazole, AMB = Amphotericin B.

On the next stage, since HDACis have demonstrated to enhance the efficacy antifungals such as azoles, we investigated whether compound **15a** could exploit a synergistic effect in combination with Voriconazole (**1**, Figure 1) on *C. albicans* 120331 strain resistant to Voriconazole itself. Accordingly, compound **15a** (100 mM) showed a fractional inhibitory concentration index (FICI) value of 0.129 in

combination with Voriconazole, indicative of a strong synergistic interaction. Additionally, the synergistic combination completely abrogated the yeast cell growth, compared to untreated and **15a** treated cells (*Table 1*). Conversely, Voriconazole alone partially affected the cell growth of the resistant strain, since after 24 h of treatment we observed a 58% reduction in *C. albicans* 10231 growth (*Table 1*). However, Voriconazole was no longer able to contrast yeast growth after 48 h of treatment, while azole-resistant cells vitality was completely resumed until 6 days of treatment. On contrary, the synergistic interaction between **15a** (100 mM) and Voriconazole (0.125 mg/mL) completely inhibited cell growth until 6 days of treatment. According to these data, we can assume **15a** in combination with Voriconazole was able to contrast *C. albicans* growth after 24 h of treatment, and prolonged treatment (6 days) completely abrogated cell growth, reducing the possibility of acquiring resistance. Similarly, we conducted the same assay on the azole-susceptible *C. albicans* ATCC 90028 strain. Preliminary experiments were performed to establish the activity of Voriconazole on *C. albicans* ATCC 90028 at different drug concentrations and time points. According to literature evidence, lower Voriconazole concentrations were associated with a more pronounced trailing effect (data not shown). More in detail, Voriconazole was able to completely affect the growth of *C. albicans* ATCC 9028 after 24 h of treatment, while during a prolonged treatment (48 h or longer) the drug lost its efficacy, consistent with reported fungistatic activity of azoles.

Table 1. *C. albicans* ATCC 10231 and ATCC 90028 growth at different time points. Yeast counts are given as means in Log_{10} CFU/mL with standard deviations. Each experiment is the result of three independent experiments performed in triplicate. Untreated = Control cells that did not receive the treatment; Vor = Voriconazole; **15a**/Vor = synergistic combination.

C. Albicans strain 10231				
Time	*Untreated*	***15a***[a]	*Vor*[b]	***15a***[a]*/Vor*[b]
0 h	3.47 ± 0.11	3.35 ± 0.21	3.32 ± 0.21	3.38 ± 0.28
24 h	7.00 ± 0.1	6.82 ± 0.12	4.06 ± 0.22	3.54 ± 0.28
48 h	7.18 ± 0.20	6.98 ± 0.15	7.95 ± 0.18	2.90 ± 0.19
72 h	8.30 ± 0.32	8.21 ± 0.24	8.02 ± 0.12	2.53 ± 0.12
6 d	8.42 ± 0.17	8.34 ± 0.11	8.18 ± 0.17	1.08 ± 0.25
C. Albicans strain 10231				
Time	*Untreated*	***15a***[a]	*Vor*[b]	***15a***[a]*/Vor*[b]
0 h	3.47 ± 0.11	3.35 ± 0.21	3.32 ± 0.21	3.38 ± 0.28
24 h	7.00 ± 0.1	6.82 ± 0.12	4.06 ± 0.22	3.54 ± 0.28
48 h	7.18 ± 0.20	6.98 ± 0.15	7.95 ± 0.18	2.90 ± 0.19
72 h	8.30 ± 0.32	8.21 ± 0.24	8.02 ± 0.12	2.53 ± 0.12
6 d	8.42 ± 0.17	8.34 ± 0.11	8.18 ± 0.17	1.08 ± 0.25

a = 100 mM; b = 0.125 mg/mL

8.1.2 Compound 15a in combination with Voriconazole inhibits C. albicans yeast-to- hyphae transition

Given the strong epigenetic component driving yeast phenotypic plasticity, on the next stage we examined the morphological transition of *C. albicans* 10231 following treatments with **15a**, Voriconazole, or their synergistic combination after 2 h and 24 h of treatment, under hyphal induction conditions at 37 °C. As depicted in Figure 4A, *C. albicans* control exhibited the formation of elongated true hyphae after 2 h of observation, with more pronounced elongation after 24 h, thereby confirming yeast-to-hypha transition occurred (Figure 4F). On the contrary, hyphae elongation began by apical extension after 2 h of treatment with **15a** (100 μM), Voriconazole (0.125 mg/ml) or **15a**/Voriconazole combination, although the effect was less pronounced in comparison to control group (Fig 4C-

E). Interestingly, we did not observe a different morphology in the groups receiving **16a** for 2 h, where long hyphae were displayed (Figure 4H), while cells treated with Voriconazole for 2 h showed shorter and sporadic hyphae compared to CTRL or DMSO (Figure 4I). Gratifyingly, the combination **15a**/Voriconazole led to a significant reduction in both number and size of hyphae, with a striking prevalence of yeast forms over hyphal ones (Figure 4L). The results were confirmed by acridine orange (AO) and ethidium bromide (EB) staining, two commonly used dyes in discriminating the living from the death cells. AO stains green live cells, while EB incorporates only in the apoptotic death cell. Both control and treated cells showed a uniform green colour, and no orange-red staining was evident after 24 h of treatment (Figure 4Q).

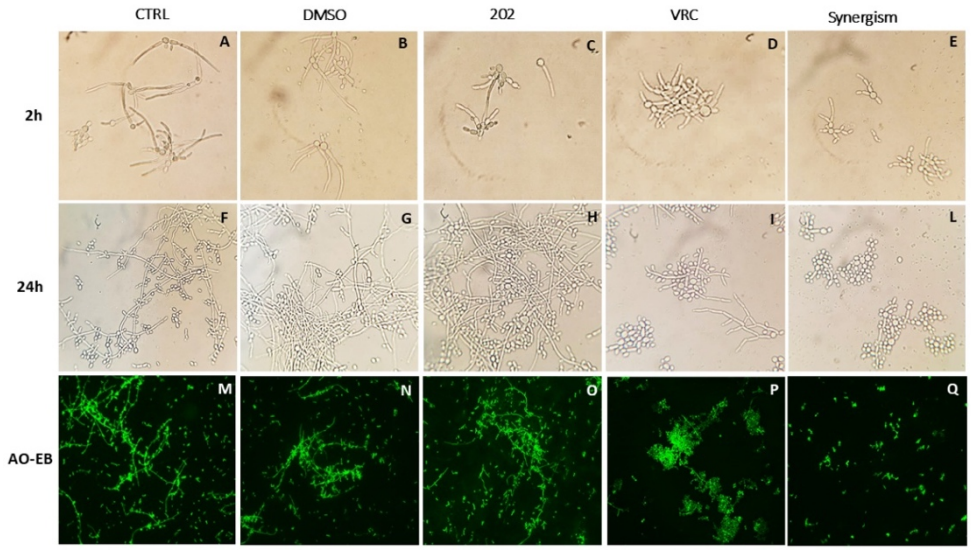


Figure 4. Effect of several treatments on the germination of *C. albicans* 10231, at 2 h and 24 h. CTRL = no treatment; VRC (voriconazole) 0.125 µg/mL; **15a** 100 µM; Synergism: **15a** 100 µM + VRC 0.125 µg/mL. Panel A-E: 2 h treatment; panel F-L: 24 h treatment. Observation under optical microscope with 400x magnification. Panel M-Q: Live/dead imaging of yeasts cells after treatment. Observed at × 200 magnification (Iris Digita System, Twin Helix). After 24 h,

control and treated cells showed uptake of only acridine orange (green fluorescence). No evident uptake of ethidium bromide (red fluorescence), indicative of cell death, was reported.

Taken together, our results suggest that the synergistic interaction between **15a** and Voriconazole is able to inhibit fungal cell growth and effectively reduce the morphological transition to the hyphal phenotype.

8.1.3 Compound 15a in combination with Voriconazole modulates the expression of genes involved in morphogenesis and azole resistance

In order investigate the molecular mechanisms underlying the efficacy of the synergistic combination **15a**/Voriconazole, we first investigated the effect of compound **15a** on the transcriptional expression of the *Hda1* gene in *C. albicans* 10231, upon 2 h and 24 hours of incubation with **15a** alone or in combination with Voriconazole (data not shown). *Hda1* gene expression was not influenced by treatment with either compound **15a** or in combination with Voriconazole, while after 2 h of treatment a not significant decrease in *Nrg1* gene expression was observed compared to the control (Figure 5A). Gratifyingly, the 24 h treatment with **15a** alone induced significant changes of *Nrg1* gene expression relative to the control (52% reduction, $p = 0.09$), while Voriconazole induced a marked increase in *Nrg1* gene expression (Figure 5B). The combined treatment produced a moderate and not significant increase in *Nrg1* gene expression (45%, Figure 5B), suggesting an attenuated effect compared with Voriconazole alone. During morphological transition, TUP1 protein acts as transcriptional repressor, recruiting histone deacetylases and other chromatin-modifying factors. Thus, the effect of compound **15a** on *Tup1* gene expression were evaluated. As shown in Figure 5C,D, preliminary results showed *Tup1* gene expression remained essentially unchanged after 2 h and 24 h of treatment with **15a**, whether tested individually or in combination with Voriconazole.

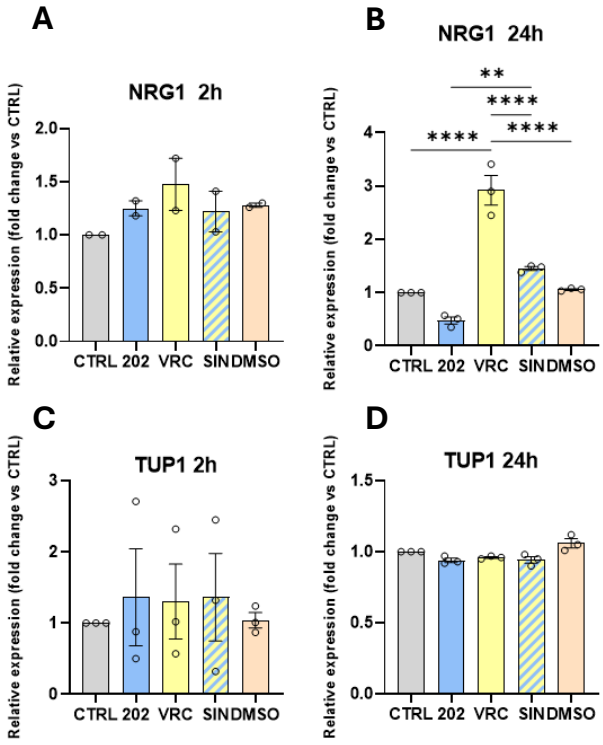


Figure 5. Effect of **16a** on *Nrg1* and *Tup1* gene expression at 2 h and 24 h. CTRL = no treatment; VRC (voriconazole) 0.125 µg/mL; ***15a*** 100 µM; Synergism: ***15a*** 100 µM + VRC 0.125 µg/mL. Panel A/C: 2 h treatment; panel B/D: 24 h treatment.

On the next stage, we analysed the variation in gene expression of *Hwp1* and *Als1*, two key regulators of germination and virulence in *C. albicans* under the negative transcriptional control of *Nrg1* and *Tup1*. Notably, after 2 h of treatment, **15a** induced *Hwp1* gene downregulation (30%), while Voriconazole effect was more marked (40% decrease), and the combination **15a**/Voriconazole yielded a comparable effect (45%, Figure 6A). However, after 24 h of treatment, *Hwp1* expression was strongly suppressed by both Voriconazole (0.24-fold) and the synergistic combination **15a**/Voriconazole (0.21-fold), while **15a** alone had no significant impact (Figure 6B).

Conversely, as shown in Figure 6C, *Als1* expression was significantly downregulated upon treatment with both Voriconazole and **15a**, with 0.32- and 0.59-fold reduction, respectively. When **15a** and Voriconazole were administrated in combination, a more significant effect was observed, with *Als1* expression reduced of 87% compared to the control. After 24 h of treatment, *Als1* downregulation was less pronounced but still significant: Voriconazole alone reduced expression by 56%, the combination by 51%, whereas **15a** alone had only a marginal, non-significant effect (0.82-fold, Figure 6D).

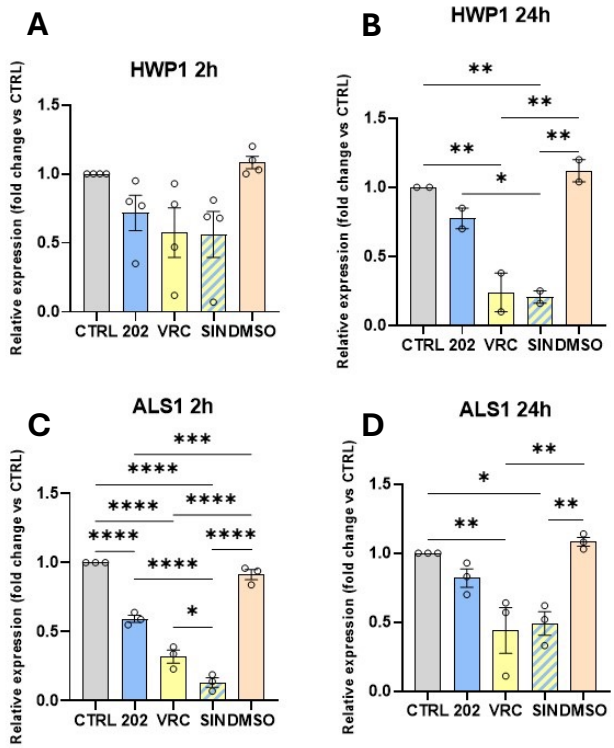


Figure 6. Effect of **15a** on *Hwp1* and *Als1* gene expression at 2 h and 24 h. CTRL = no treatment; VRC (voriconazole) 0.125 µg/mL; ***15a*** 100 µM; Synergism: ***15a*** 100 µM + VRC 0.125 µg/mL. Panel A/C: 2 h treatment; panel B/D: 24 h treatment.

According to obtained results, the combination **15a**/Voriconazole exerts a synergistic effect able to inhibit *C. albicans* cells growth at early stages of infection. Indeed, ALS1 plays a pivotal role in initial phases of adhesion and biofilm development. Thereby, its marked reduction upon **15a** treatment suggests that our HDAC6i may be able to inhibit the initial adhesion to host epithelium. Also, **15a**/Voriconazole was able to block yeast-to-hyphae morphological transition, blocking hyphae formation through the downregulation of key regulator genes (*e.g. Hwp1*) after prolonged treatment (24 h).

8.1.4 Compound 15a in combination with Voriconazole modulates the expression of ERG11 gene

As previously mentioned, *ERG11* gene upregulation usually occurs in azole-resistant *C. albicans*, thereby we have evaluated the effects of **15a**, alone or in combination with Voriconazole, on *ERG11* gene expression. According to literature evidence, we observed a 134% increase in *ERG11* gene expression after 2 h of treatment with Voriconazole, whereas **15a** alone did not show any significant effect. The synergistic combination partially attenuated Voriconazole effect, resulting in a modest, non-significant 36% increase relative to the control (Figure 7A).

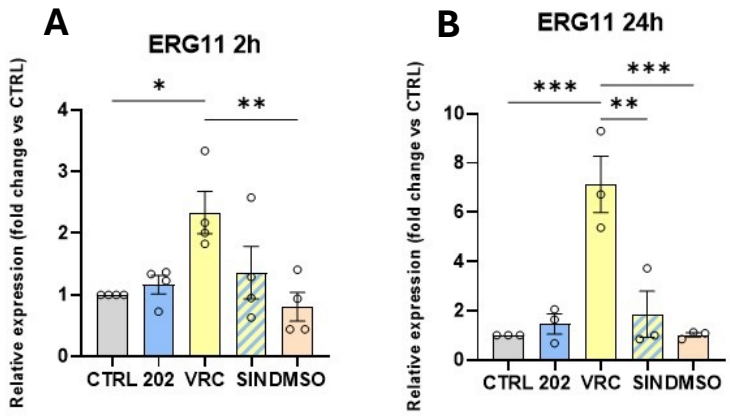


Figure 7. Effect of **15a** on *ERG11* gene expression at 2 h and 24 h. CTRL = no treatment; VRC (voriconazole) 0.125 µg/mL; ***15a*** 100 µM; Synergism: ***15a*** 100 µM + VRC 0.125 µg/mL.

After 24 h, Voriconazole treatment induced a striking ~600% increase in *Erg11* expression, consistent with a compensatory response to pharmacological stress and activation of resistance mechanisms. The synergistic combination induced a modest, non-significant 90% increase relative to the control, effectively attenuating *ERG11* upregulation induced by Voriconazole (Figure 7B).

8.2 Conclusions

Since the abuse or misuse of antifungals led to the rapid onset of multidrug resistant yeast strains, nowadays there is the urgent need for novel effective therapies to tackle both localized and systemic mycosis. Over years, epigenetic mechanisms underlying invasive behaviour in yeasts have been extensively studied, revealing fungal HDACs are key regulators of yeast virulence, including morphological transitions, biofilm formation and tissue dissemination. Accordingly, several HDACis such as Vorinostat have been assessed in *in vivo* infection models, showing a marked synergistic effect in combination with azoles, while few examples of selective yeast HDACis have been reported so far. Considering the efficacy of proprietary HDAC6i **15a** in counteracting *P. aeruginosa* virulence (*Chapter 7*), we sought to investigate its effect also in *C. albicans* cells resistant to azoles. Overall, our results suggest that **15a** may not exerts its action exclusively through direct HDAC inhibition, but it may rather likely engage multiple mechanisms which deserve further investigation and clarification. Accordingly, **15a** did not affect the expression of *Hda1* and *Tup1* genes, while strongly inducing the downregulation of virulence-related genes *Als1* and *Hwp1*, with a more marked effect when administrated in combination with Voriconazole, thereby suggesting a synergistic effect. Moreover, **15a** was able to counteract *ERG11* gene upregulation induced by Voriconazole when

administrated with Voriconazole itself, suggesting that alternative pathways may be activated when **15a** is used in combination with azole drugs. Also, **15a** was able to prevent yeast germination, thus suggesting it may act on cellular stress response, potentially *via* the inhibition of Hsp90-related stress adaptation pathways, including azoles exposure. Supportive of this hypothesis, the trailing effect observed in *C. albicans* strains sensitive to azoles testifies the activation of Hsp90-dependent defence mechanisms to overcome the pharmacological action of Voriconazole. Overall, our results confirmed compound **15a** as an effective compound able to synergize the effect of Voriconazole. Our findings are also in line with previous studies reported for several HDACis, demonstrating the ability in inhibiting morphological changes, cell growth and azoles-induced resistance, through the modulation of *ERG11* gene expression. Currently, we are further investigating molecular mechanisms underlying compound **15a** efficacy in azole-resistant *C. albicans* strains.

8.3 Experimental section

8.3.1 Candida strains and culture conditions

The yeast strains *C. albicans* ATCC 90028 (reference strain) and *C. albicans* ATCC 10231 (azole-resistant strain as reported in the ATCC "*C. albicans* drug resistance panel", Candida albicans (Robin) Berkhout - 10231 | ATCC) were obtained from the American Type Culture Collection (Rockville, MD). Before each experiment, yeast cells were subcultured from the stocks onto Sabouraud dextrose agar (SDA) (Oxoid) at 30 °C for 48 h.

8.3.2 Antifungal susceptibility testing

The antifungal activity of **15a** was determined on *C. albicans* strains by using a standardized broth microdilution method (Clinical and Laboratory Standards Institute (CLSI), Performance Standards for Antifungal Susceptibility Testing of Yeasts. 3rd ed. CLSI supplement M27M44S, 2022). Briefly, the cell suspension was adjusted to 3×10^3 CFU/mL in RPMI 1640 medium (Sigma) supplemented

with 0.2% (w/v) glucose. One hundred microliter aliquots of these cell suspensions were dispensed into 96-well microtiter plates. **15a** was serially diluted using RPMI 1640 medium and added to the wells at a final concentration ranging from 25 to 200 mM, and the plate was incubated for 48 hours at 37 °C. Amphotericin B (AMB, 2 mg/mL) and VRC (0.125 mg/mL for *C. albicans* ATCC 90028 and 30 mg/ml for *C. albicans* ATCC 10231) were chosen as the positive controls. The minimal inhibitory concentration (MIC) was defined as the lowest concentration of the compound that resulted in 100% growth inhibition after 24 h of incubation. Trailing was defined as the presence of residual yeast growth in all wells at supra-MIC concentrations. Voriconazole concentrations ranged from 0.06 to 32 μg/mL, and plates were incubated for 24 hours at 37°C. The trailing growth was assessed at 24 h, 48 h, 72 h, and 6 days. MICs and trailing measurements were performed in triplicates.

8.3.2 Checkerboard assay

To investigate the interaction between **15a** and Voriconazole against *C. albicans* 10231 the checkerboard method in 96-well microtiter plates was used. Briefly, **15a** and Voriconazole were serially diluted along the y and x axes, respectively. The final concentrations ranged from 0.03 to 32 μg/mL (0.03, 0.06, 0.12, 0.25, 0.5, 1, 2, 4, 8, 16, 32) for Voriconazole and from 25 to 200 μg/mL (25, 50, 100, 200) for **15a**. The checkerboard plates were inoculated with yeasts at an approximate concentration of 1 x 10^3 CFU/mL and incubated at 37 °C for 24 h, following which yeasts growth was assessed visually and the turbidity measured by microplate reader at 595 nm. The synergistic effect of **15a** and VRC combination was based on a calculation of the fractional inhibitory concentration index (FICI) for each drug pair. The fractional inhibitory concentration (FIC) for each combination was calculated as follows: FIC of **15a** $= \frac{\text{MIC of 202 in combination}}{\text{MIC of 202 alone}}$; FIC of Voriconazole $= \frac{\text{MIC of VRC in combination}}{\text{MIC of VRC alone}}$. FICI is calculated by the sum of FIC values for each drug. FICI results for each

combination were interpreted as follows: ≤ 0.5: synergistic; > 0.5 to ≤1.0: additive; > 1.0 to ≤ 2.0: indifferent; and >2.0: antagonistic effects. Minimum fungicidal concentration (MFC) was defined as the concentration that caused ≥ $3\log_{10}$ reduction in colony count from the starting inoculum plated on SDA, incubated for 24 h at 37 °C. The MFC was determined by transferring 10 µL aliquots of the synergistic combination, that yielded no fungal growth, on agar plates, and incubating the plates at 37 °C for 24 h. To evaluate the trailing effect the CFU were determined until 6 days of treatment. All the tests were conducted at least three times using independent cell suspensions.

8.3.4 Yeast-to-hyphae morphology studies

C. albicans ATCC 10231 (10^5 cells) was grown in sabouraud medium at 37°C. **15a** and Voriconazole were added to the culture at 100 µM and 0.125 µg/mL, respectively, either alone or in combination for 2 and 24 h. Following incubation the cultures were observed microscopically at x400 magnification and photographed to determine *C. albicans* morphology.

8.3.5 Azoles fungistatic effect determination

To study the fungicidal or fungistatic activity of **15a** and Voriconazole live/dead staining technique was used. Yeast cells were treated with **15a** and Voriconazole at synergistic concentration as above reported. Cells were harvested by centrifugation after 24 h and stained with solution of acridine orange and ethidium bromide (100 µg/mL) and kept in dark for 30 min. Cells were harvested and washed twice with PBS to remove the excess stains. The cells were then observed at × 20 magnification (Iris Digita System, Twin Helix).

8.3.6 RNA isolation and real time PCR

C. albicans was treated with **15a** 100 µM, Voriconazole 0.06 µg/mL or a combination of both for 24 h. Total RNA was isolated by using the GenUp Total RNA kit (BiotechRabbit, Berlin, Germany) according to the manufacturer's instructions. DNA contamination from the total RNA was removed by incubation

with DNase I (RNase-free DNase Set, Qiagen, Hilden, Germany). Measuring the A260/A280 nm ratio assessed the nucleic acid purity. To generate cDNA, total RNA was reverse transcribed by using RevertUP II Reverse Transcriptase (BiotechRabbit, Berlin, Germany) into cDNA using random hexamer primers (Random hexamer, Roche Diagnostics, Monza, Italy) at 48 °C for 1 hour according to the manufacturer's instructions. The real time PCR was carried out using 1 ml of cDNA (5 ng/µl). Gene expression levels were analyzed by quantitative real-time polymerase chain reaction (qRT-PCR) using the CFX96 system (Bio-Rad, Hercules, CA, USA) with the 2xSYBR Green qPCR Mix kit (GDSBio, Guangzhou, China) (Table 3). The thermal cycling parameters were the following: activation of the DNA polymerase at 95 °C for 5 min, 40 cycles comprising 15s at 95 °C for denaturation and 1 min at 58 °C for annealing and extension. The housekeeping *Actin* (*ACT*) gene was used as an internal control to normalize all data. The experiments were carried out in biological triplicate, and in technical duplicate for each data point.

Table 3. Primers sequences used for the qRT-PCR and annealing conditions.

Gene	Sequence (5'-3')		Annealing temperature
ERG11	**Fw**	ACCATTTGGTGGTGGTAGACA	58 °C
	Rev	AGGGTCAGGCACTTTATAACCA	
ACT	**Fw**	CCAGCTTTCTACGTTTCC	54 °C
	Rev	CTGTAACCACGTTCAGAC	

References

[1] D. Seidel, S. Wurster, J.D. Jenks, H. Sati, J.-P. Gangneux, M. Egger, A. Alastruey-Izquierdo, N.P. Ford, A. Chowdhary, R. Sprute, O. Cornely, G.R. Thompson, M. Hoenigl, D.P. Kontoyiannis, Lancet Microbe 5 (2024) e594–e605.

[2] D.W. Denning, Lancet Infect Dis 24 (2024) e428–e438.

[3] (n.d.).

[4] D. Bays, E. Jenkins, M. Lyman, T. Chiller, N. Strong, L. Ostrosky-Zeichner, M. Hoenigl, P. Pappas, G. Thompson, Clin Epidemiol Volume 16 (2024) 549–566.

[5] M. G, S.S.S. Ravi, D. Maheswary, K.V. Leela, R. Harikumar Lathakumari, L.P. K S, Cancer Pathogenesis and Therapy 3 (2025) 402–410.

[6] M.C. Fisher, A. Alastruey-Izquierdo, J. Berman, T. Bicanic, E.M. Bignell, P. Bowyer, M. Bromley, R. Brüggemann, G. Garber, O.A. Cornely, Sarah.J. Gurr, T.S. Harrison, E. Kuijper, J. Rhodes, D.C. Sheppard, A. Warris, P.L. White, J. Xu, B. Zwaan, P.E. Verweij, Nat Rev Microbiol 20 (2022) 557–571.

[7] T. Roemer, D.J. Krysan, Cold Spring Harb Perspect Med 4 (2014) a019703–a019703.

[8] A. Carmo, M. Rocha, P. Pereirinha, R. Tomé, E. Costa, Antibiotics 12 (2023) 884.

[9] R. Bellmann, P. Smuszkiewicz, Infection 45 (2017) 737–779.

[10] S.R. Lockhart, A. Chowdhary, J.A.W. Gold, Nat Rev Microbiol 21 (2023) 818–832.

[11] J.R. Graybill, D.S. Burgess, T.C. Hardin, European Journal of Clinical Microbiology & Infectious Diseases 16 (1997) 42–50.

[12] L.J. Marcos-Zambrano, P. Escribano, C. Sánchez-Carrillo, E. Bouza, J. Guinea, Med Mycol 54 (2016) 733–739.

[13] E.W.L. Chow, L.M. Pang, Y. Wang, Pathogens 10 (2021) 859.

[14] B.J. Chadwick, X. Lin, Curr Opin Microbiol 79 (2024) 102488.

[15] S.G. Nadeem, A. Shafiq, S.T. Hakim, Y. Anjum, S. U. Kazm, Open J Med Microbiol 03 (2013) 185–192.

[16] S.G. Whaley, E.L. Berkow, J.M. Rybak, A.T. Nishimoto, K.S. Barker, P.D. Rogers, Front Microbiol 7 (2017).

[17] P. Navarro-Rodríguez, L. López-Fernández, A. Martin-Vicente, J. Guarro, J. Capilla, Antimicrob Agents Chemother 65 (2020).

[18] M.-J. Xiang, J.-Y. Liu, P.-H. Ni, S. Wang, C. Shi, B. Wei, Y.-X. Ni, H.-L. Ge, FEMS Yeast Res 13 (2013) 386–393.

[19] A.C. Siqueira, G.A. Bernardi, L.N.V.S. Arend, G.T. Cordeiro, D. Rosolen, F.C.B. Berti, A.M.M. Ferreira, T.M. Vasconcelos, B.C. Neves, L.S. Rodrigues, L.M. Dalla-Costa, Journal of Fungi 11 (2025) 24.

[20] A.J.S. Klar, T. Srikantha, D.R. Soll, Genetics 158 (2001) 919–924.

[21] W.L. Smith, T.D. Edlind, Antimicrob Agents Chemother 46 (2002) 3532–3539.

[22] S. Su, X. Li, X. Yang, Y. Li, X. Chen, S. Sun, S. Jia, Future Microbiol 15 (2020) 1075–1090.

[23] J. Kim, J.-E. Lee, J.-S. Lee, Journal of Microbiology 53 (2015) 805–811.

[24] X. Li, Q. Cai, H. Mei, X. Zhou, Y. Shen, D. Li, W. Liu, Journal of Antimicrobial Chemotherapy 70 (2015) 1993–2003.

[25] J. Kim, J.-E. Lee, J.-S. Lee, Journal of Microbiology 53 (2015) 805–811.

[26] P. Trojer, Nucleic Acids Res 31 (2003) 3971–3981.

[27] K.Y. Chou, J.-Y. Lee, K.-B. Kim, E. Kim, H.-S. Lee, H.-Y. Ryu, Comput Struct Biotechnol J 21 (2023) 1843–1850.

[28] X. Li, N. Robbins, T.R. O'Meara, L.E. Cowen, Mol Microbiol 103 (2017) 635–656.

[29] L.F. Zacchi, W.L. Schulz, D.A. Davis, PLoS One 5 (2010) e12171.

[30] H. Chen, X. Zhou, B. Ren, L. Cheng, Virulence 11 (2020) 337–348.

[31] W. Bai, Y. Wang, J. Ma, G. Li, Y. Wang, C. Yang, Q. Zhang, Q. Li, J. Zhang, P. Zhang, Microbiol Res 296 (2025) 128132.

[32] S.-Y. Park, J.-S. Kim, Exp Mol Med 52 (2020) 204–212.

[33] Y. Lu, C. Su, H. Liu, Trends Microbiol 22 (2014) 707–714.

[34] V. Freire-Benéitez, R.J. Price, D. Tarrant, J. Berman, A. Buscaino, Sci Rep 6 (2016) 22989.

[35] C.J. Nobile, E.P. Fox, N. Hartooni, K.F. Mitchell, D. Hnisz, D.R. Andes, K. Kuchler, A.D. Johnson, MBio 5 (2014).

[36] C. Garnaud, M. Champleboux, D. Maubon, M. Cornet, J. Govin, Front Microbiol 7 (2016).

[37] Y. Lu, C. Su, A. Wang, H. Liu, PLoS Biol 9 (2011) e1001105.

[38] J.-E. Lee, J.-H. Oh, M. Ku, J. Kim, J.-S. Lee, S.-O. Kang, FEBS Lett 589 (2015) 513–520.

[39] T. Srikantha, L. Tsai, K. Daniels, A.J.S. Klar, D.R. Soll, J Bacteriol 183 (2001) 4614–4625.

[40] D. Hnisz, O. Majer, I.E. Frohner, V. Komnenovic, K. Kuchler, PLoS Pathog 6 (2010) e1000889.

[41] H.T. Taff, K.F. Mitchell, J.A. Edward, D.R. Andes, Future Microbiol 8 (2013) 1325–1337.

[42] P. Uppuluri, C.G. Pierce, D.P. Thomas, S.S. Bubeck, S.P. Saville, J.L. Lopez-Ribot, Eukaryot Cell 9 (2010) 1531–1537.

[43] N. Robbins, M.D. Leach, L.E. Cowen, Cell Rep 2 (2012) 878–888.

[44] X. Li, Q. Cai, H. Mei, X. Zhou, Y. Shen, D. Li, W. Liu, Journal of Antimicrobial Chemotherapy 70 (2015) 1993–2003.

[45] L.E. Cowen, S. Lindquist, Science (1979) 309 (2005) 2185–2189.

[46] M.A. Pfaller, S.A. Messer, N. Georgopapadakou, L.A. Martell, J.M. Besterman, D.J. Diekema, J Clin Microbiol 47 (2009) 3797–3804.

[47] G. Simonetti, C. Passariello, D. Rotili, A. Mai, E. Garaci, A.T. Palamara, FEMS Yeast Res 7 (2007) 1371–1380.

[48] W.L. Smith, T.D. Edlind, Antimicrob Agents Chemother 46 (2002) 3532–3539.

[49] A. Mai, D. Rotili, S. Massa, G. Brosch, G. Simonetti, C. Passariello, A.T. Palamara, Bioorg Med Chem Lett 17 (2007) 1221–1225.

[50] W.L. Smith, T.D. Edlind, Antimicrob Agents Chemother 46 (2002) 3532–3539.

[51] X. Li, M. Yuan, R. Yin, X. Liu, Y. Zhang, S. Sun, L. Han, S. He, Sci Rep 9 (2019) 9859.

[52] Z. Li, Y. Huang, J. Tu, W. Yang, N. Liu, W. Wang, C. Sheng, J Med Chem 66 (2023) 5950–5964.

[53] N. Pang, J. Sun, S. Che, N. Yang, Journal of Biological Chemistry 298 (2022) 102068.

[54] Z. Li, J. Tu, G. Han, N. Liu, C. Sheng, J Med Chem 64 (2021) 1116–1126.

Chapter 9

Discovery of the first-in-class pyrazole isoxazole based synergistic antifungal agent in combination with voriconazole

A small part of my PhD was also devoted to the identification of novel antiinfective agents with innovative mechanisms of action. In this context, I was involved in the identification of novel classes of antifungals for the treatment of *Candida albicans* strains resistant to azole drugs. During this activity, we identified a novel pyrazole-oxazole based compound, namely SL-38 (**7a**, Table 1) which showed remarkable growth inhibition against the azole resistant *Candida albicans* ATCC 10231 strain in combination with Voriconazole [1].

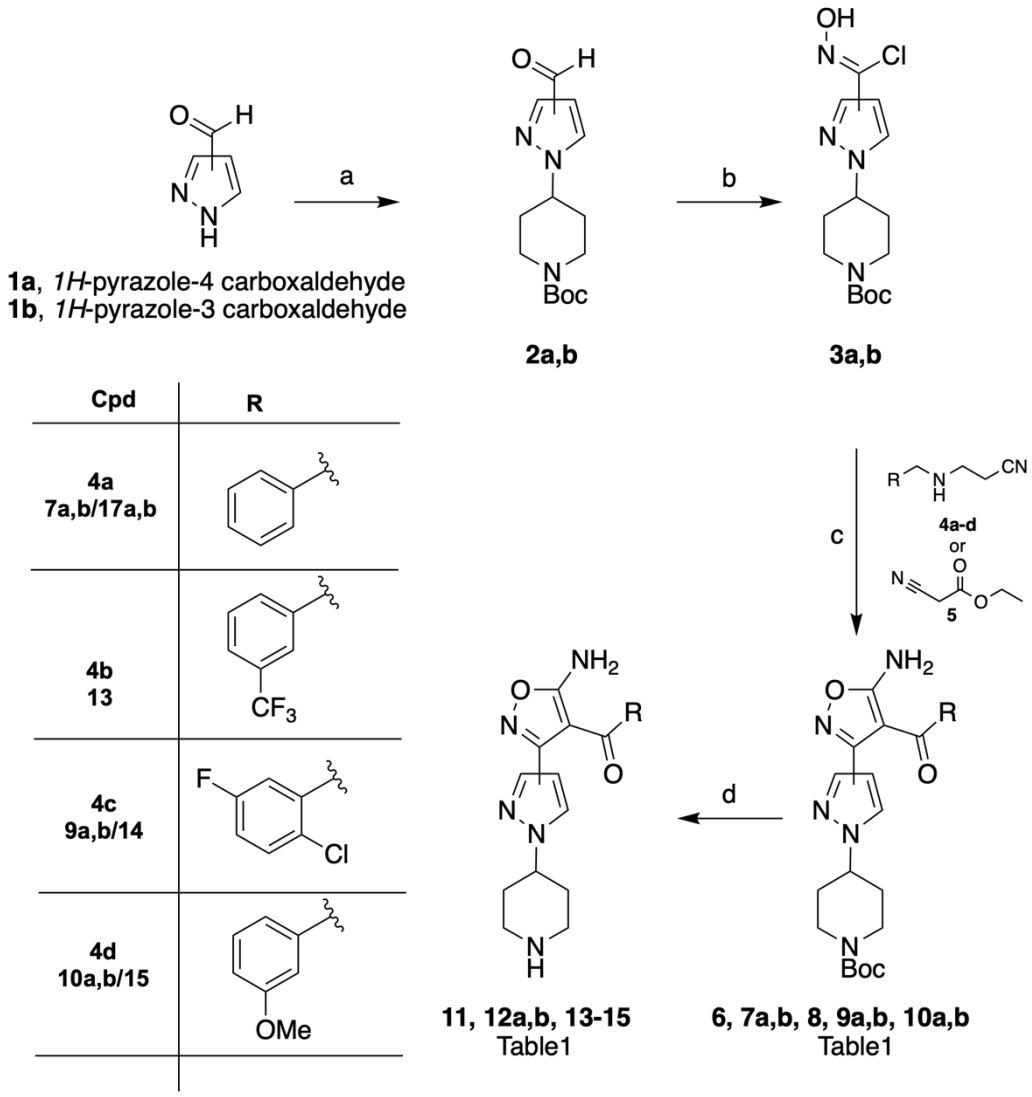
9.1 Results and discussion

9.1.1 Chemistry

Scheme 1 describes the synthesis of 3- and 4- pyrazole-isoxazole containing final compounds. First, an alkylation reaction between 1*H*-pyrazole-4-carboxaldehyde (**1a**) or 1*H*-pyrazole-3-carboxaldehyde (**1b**) and *tert*-butyl 4-(methylsulfonyloxy)piperidine-1-carboxylate in DMF and sodium hydride (60%

dispersion in mineral oil) at 100 °C overnight, yielding the corresponding *N-tert*-butoxycarbonyl-piperidine pyrazole carboxaldehydes **2a,b**. The former were treated with hydroxylamine hydrochloride and Na_2CO_3 in EtOH providing the corresponding pyrazole oximes in good yield and in form of a *E/Z* mixture, subsequently converted into their chloro-oxime counterparts **3a,b** using *N*-chlorosuccinimide in DMF at 25 °C temperature for 2 hours. Chloro-oxime **3a** was subjected to 1,3-dipolar cycloaddition with ethyl-2-cyanoacetate providing the isoxazole ester **6**, easily deprotected from the Boc functionality in the presence of acetyl chloride to afford the corresponding amine in form of the hydrochloride salt **11.** Chloro-oximes **3a,b** were subjected to 1,3-dipolar cycloaddition with differently substituted *N*-benzyl-2-cyanoacetamides (**4a-d**) to provide the final isoxazole pyrazole-based compounds **7-10** with yields ranging from 30% to 70%. Boc removal with acetyl chloride in methanol at room temperature provided the corresponding deprotected amines **12-15** in form of their hydrochloride salts.

Scheme 1. Synthesis of pyrazole-isoxazole based compounds **6-10** and **11-15** [a].

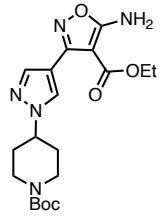
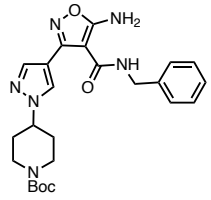
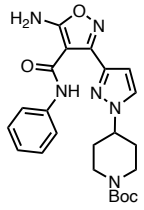


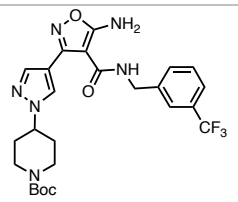
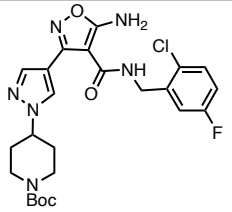
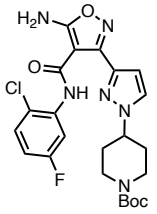
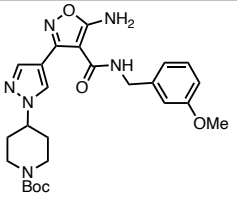
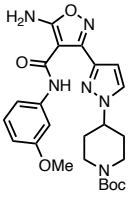
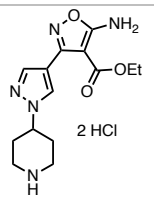
[a]Reagents and conditions: (a) NaH (60 % oil dispersion), *tert*-butyl 4-(methylsulfonyloxy)piperidine-1-carboxylate, dry DMF, 15 h, 0 °C to 100 °C, 75% (for **2a**) and 70% (for **2b**); (b) (i) NH_2OH HCl, Na_2CO_3, EtOH/H_2O, 2 h, 25 °C, quant.; (ii) NCS, DMF, 2 h, 25 °C, quant.; (c) NaOEt, ethyl cyanoacetate or cyanoacetamides (**4a-d**), dry EtOH, 8 h, 0 °C to 80 °C, 39% (for 6), 28-70% (**7-10**); (d) acetyl chloride, MeOH, 4 h, 25 °C, 97% to quant.

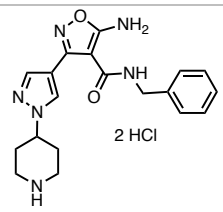
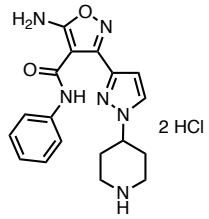
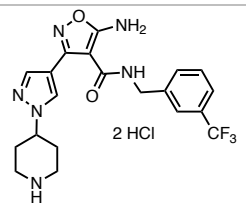
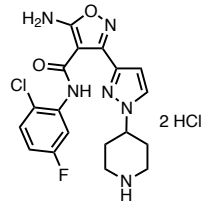
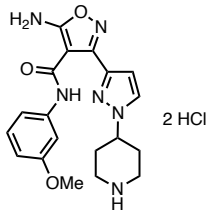
9.1.2 In vitro antifungal activity

All synthesised compounds were assessed on both *C. albicans* ATCC 90028 and azole resistant *C. albicans* ATCC 10231 in order to evaluate their intrinsic antifungal activity. The compounds exhibited no effect in inhibiting yeast growth at the assessed concentrations (*i.e.* 100 and 50 μM), except for compound SL-38 (**17a**, *Table* 1), which demonstrated a 60% reduction in yeast growth at 100 μM. Antifungal drugs Voriconazole (**1**, Figure 1) and amphotericin B (**2**, Figure 1) were used as positive control (*Table* 1) [1].

Table 1. Structures and in *vitro* antifungal activity of compounds **6-15**.

		MIC μM	
Compound	**Structure**	**ATCC 90028**	**ATCC 10231**
6		>100	>100
7a		100 (MIC_{60})	100 (MIC_{60})
7b		>100	>100

8		>100	>100
9a		>100	>100
9b		>100	>100
10a		>100	>100
10b		>100	>100
11		>100	>100

12a		>100	>100
12b		>100	>100
13		>100	>100
14		>100	>100
15		>100	>100
DMSO	-	>100	>100
Voriconazole	-	86	86
Amphotericin B	-	0.13	0.13

MIC = minimum inhibitory concentration

Given the weak antifungal activity of SL-38 (**7a**, *Table* 1) in inhibiting *Candida albicans* cells growth, we decided to further investigate its efficacy in ATCC 10231 strains (resistant to Voriconazole) in combination with Voriconazole itself. The synergistic effect was assessed using the fractional inhibitory concentration index (FICI), with synergism defined as a FICI ≤ 0.5. A significant growth inhibition was observed for compound SL-38 (**7a**, *Table* 1) at 50 μM in combination with 0.125 μg/mL Voriconazole (the MIC of voriconazole is 30 μg/mL on *C. albicans* ATCC 10231), yielding a FICI value of 0.254, indicative of a synergistic interaction. Thereby, although SL-38 (**7a**, *Table* 1) exhibited a weak antifungal activity when used alone (*Table* 1), its combination with voriconazole significantly lowered the required drug concentration to inhibit the growth of azole-resistant strains of *C. albicans*, demonstrating a fungistatic effect, and suggesting SL-38 (**7a**, *Table* 1) may mitigate the risk of drug resistance development [1].

9.1.3 Candida albicans morphological transition

As abovementioned, yeast-to-hypha transition is a pathogenic morphological phenotype, which facilitates host tissue penetration during infection. Acknowledging the importance of dimorphic transition in *Candida albicans* pathogenesis, we examined the morphological transition of ATCC 10231 strain upon treatment with compound SL-38 (**7a**, *Table 1*), Voriconazole (**1**, Figure 1), or their synergistic combination. As depicted in Figure 2, *Candida albicans* control group exhibited elongated hyphae, confirming the transition from yeast to hypha. In contrast, the groups treated with compound SL-38 (**7a**, *Table 1*) at 50 μM concentration or the combination SL-38 (**7a**)/Voriconazole displayed a drastically reduced number and size of hyphae, with a majority of yeast forms, suggesting the synergistic interaction between SL-38 (**7a**) and Voriconazole inhibited fungal cell growth and effectively reduced the morphological transition to the hyphal phenotype [1]. Taken together, these results could suggest an

impaired capacity of the yeast to invade host tissues, supporting the idea of a reduced pathogenicity of *Candida albicans*.

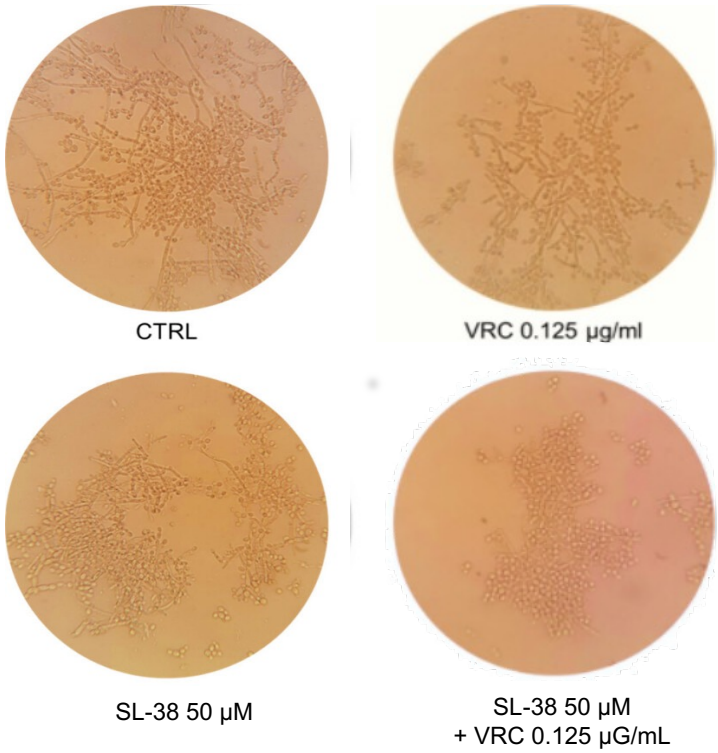


Figure 2. Effect of several treatments on the germination of *C. albicans* 10231 in presence of FBS. CTRL = no treatment; VRC = Voriconazole 0.125 µg/mL; SL-38 50 µM; SL-38 50 µM + VRC 0.125 µg/mL [1].

7.1.4 The combination SL-38/Voriconazole modulates gene associated with resistance in Candida albicans

Since different studies have previously reported the role of *ERG11 gene* (encoding for LDM enzyme) upregulation in azole-resistant *Candida albicans* strains, we investigated the impact of SL-38 (**7a**, *Table 1*) on the transcriptional expression of the *ERG11* gene in treated *Candida albicans* through quantitative real-time polymerase chain reaction (qRT-PCR). Accordingly, the treatment with Voriconazole at 0.125 µg/mL upregulated *ERG11* gene expression (60%

increase, Figure 3), while SL-38 (**7a**) at 50 µM decreased it (68% decrease, Figure 3) [1].

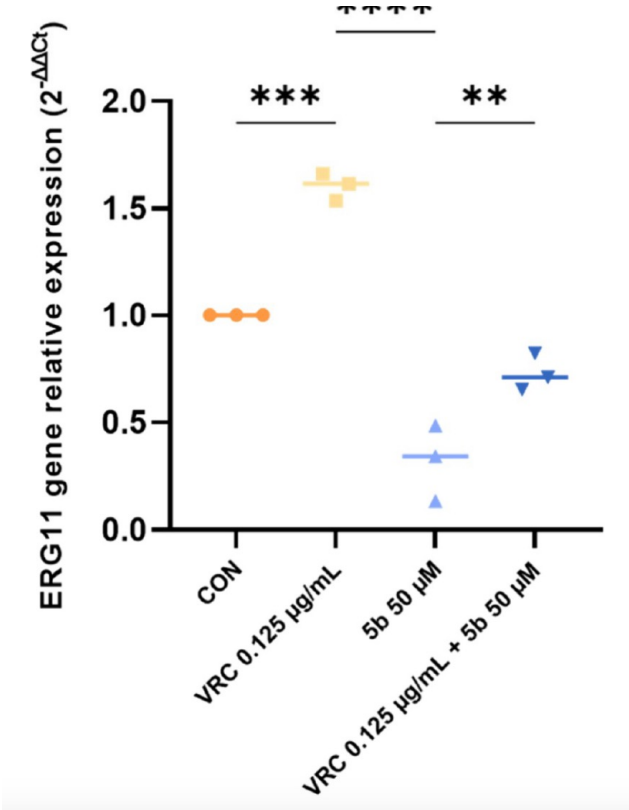


Figure 3. *ERG11* gene relative expression after a 24-hour exposure of *Candida albicans* to different treatments: CON = no treatment; VRC (Voriconazole) 0.125 µg/mL; SL-38 50 µM; VRC = Voriconazole 0.125 µg/mL + SL-38 50 µM [1].

7.1.5 SL-38 assessment in LDM inhibition assay

In order to investigate the mechanism of action of compound SL-38 (**12a**, *Table 1*) and assess target engagement, we embarked *in vitro* experiments aimed to interrogate the ability of the compound to inhibit the *Candida albicans* LDM enzymatic activity (encoded by *ERG11* gene). We first performed spectral titration experiments, by titrating *Candida albicans* LDM with compound SL-38 (**7a**). As expected, we did not register any spectral response (compared to voriconazole), indicating that the compound does not directly interact with LDM

active site, while may indeed be bound next to Voriconazole, closer to the substrate entrance [1].As a further step, we checked the inhibition of *C. albicans* LDM enzymatic activity by Voriconazole in the absence and in the presence of compound SL-38 (**7a**). Gratifyingly, the latter enhances the inhibitory effect of Voriconazole (Figure 4), in agreement with the synergistic effect observed in fungal cells.

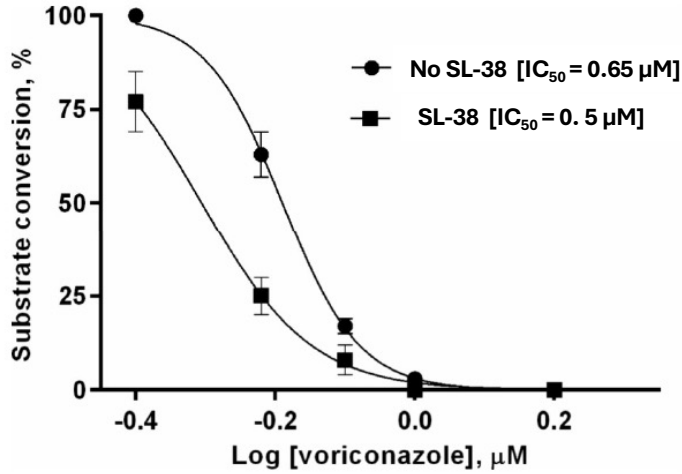


Figure 4. Inhibition of *C. albicans* LDM enzyme by Voriconazole both in absence and in presence of compound SL-38 [443]. VRC = Voriconazole [1].

9.1.6 In silico studies on SL-38 within LDM active site

Given the results for spectral titration experiments - revealing SL-38 does not bind LDM active site - and the synergistic effect of its combination with Voriconazole, molecular modeling studies were carried out into the *Candida albicans* LDM catalytic domain. It is worthy of note that LDM catalytic domain is composed of three different sites, namely the substrate entry channel (SEC), the heme-containing active site and a putative product exit channel (PPEC) (PDB: 5V5Z) [2]. While the triazole ring of Voriconazole binds into the heme-containing active site, the 5-fluoro substituent of the pyrimidine ring projects towards Y118, forcing this residue close enough to interact with the propionate

of the heme group (Figure 5). Similarly, the 2,4-difluorophenyl moiety of Voriconazole is involved in hydrogen bonding G303. The pyrimidine moiety occupies a small portion of the SEC site, forming an aromatic hydrogen bond with M508 [443].

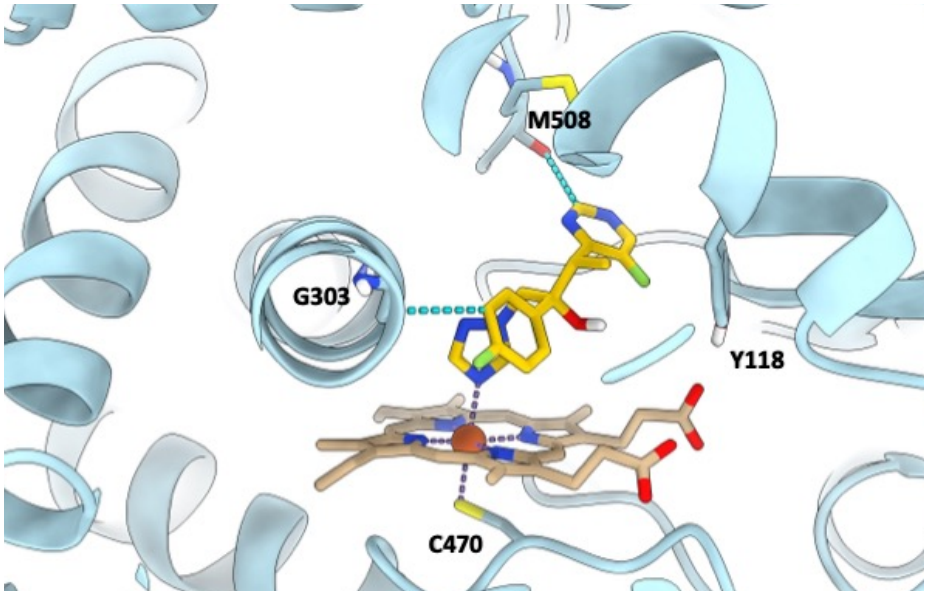


Figure 5. Binding mode of Voriconazole (yellow) in the LDM catalytic domain (PDB: 5V5Z). Protein is depicted as light blue; important residues for ligand binding are shown as sticks. The aromatic hydrogen bonds are indicated with blue dashed lines. The coordination bonds with the metal are indicated with purple dashed lines and non-polar hydrogens are omitted for a better representation of the interactions [1].

Molecular docking of compound SL-38 showed the occupancy of the SEC pocket, similarly to Voriconazole, through the engagement of multiple interactions. More in detail, the amino group of isoxazole forms a hydrogen bond with M508, while the isoxazole ring establishes an additional π-π interaction with H377 and the pyrazole ring forms an aromatic hydrogen bond with Y505 (Figure 6) [1]. Unlike Voriconazole, SL-38 did not bind the heme containing pocket – thus explaining SL-38 lack of activity on LDM in enzymatic assays - rather the

benzyl carbamoyl moiety on the isoxazole ring is able to penetrate into the unoccupied PPEC pocket, with the benzyl ring forming a π-π interaction with F233 and an aromatic H-bonds with P230 and the carbonyl group establishing an aromatic H bond with P230 (Figure 6).

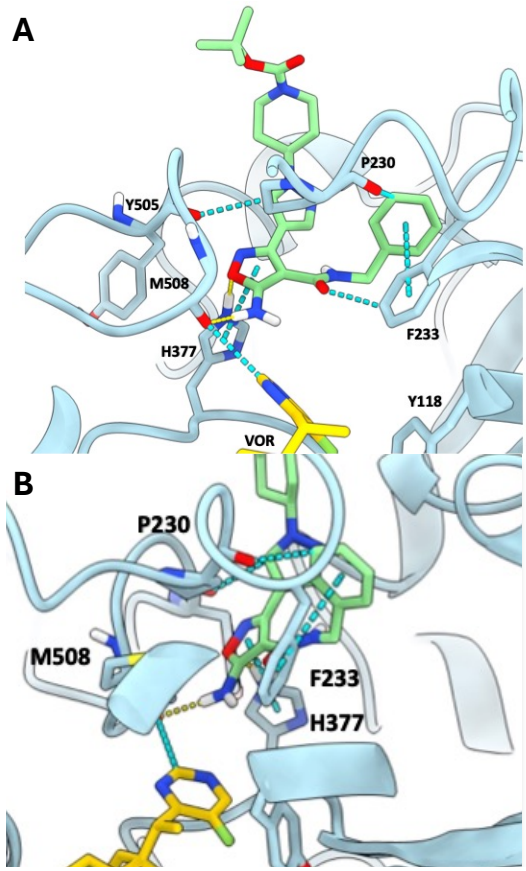


Figure 6. (A) SL-38 interaction within SEC pocket of *Candida albicans* LDM catalytic site. (B) SL-38 interaction within PPEC pocket of *Candida albicans* LDM catalytic site. Protein is depicted as light blue; important residues for ligand binding are shown as sticks. Hydrogen bonds are indicated with yellow dashed lines, the π-stacking and aromatic hydrogen bonds are indicated with blue dashed lines; the coordination bonds with the metal are indicated with purple dashed lines and non-polar hydrogens are omitted for a better representation of the interactions (PDB: 5V5Z) [1].

In silico studies unequivocally unveiled the unique ability of the synergistic combination of SL-38 and Voriconazole to provide a complete occupancy of all the LDM enzyme sites, namely the substrate entry channel (SEC), the heme-containing active site, and a putative product exit channel (PPEC), thereby enhancing the inhibitory potency of VRC itself.

9.1.7 In vivo efficacy of the combination SL-38/Voriconazole

Once confirmed the *in vitro* efficacy of the combination SL-38/ Voriconazole and the putative binding mode in target enzyme LDM, this combination was assessed in an *in vivo* infection model of *Galleria mellonella*. Galleria larvae were infected by intra-haemocoel injection with 10 µL containing 1 x 10^5 *C. albicans* cells and one hour later followed up with a treatment dose. 10 µL of each treatment (Voriconazole, compound **7a** SL-38), and the combinations (Voriconazole + SL-38) were administered. The controls (PBS/DMSO) showed 40% survival at 24 hours but larvae that received 0.5 mg/mL Voriconazole + 50 µM SL-38 had a 70% survival and enhanced survival at 48 and 72 hours. Administration of the lower dose (0.125 µg/mL Voriconazole + 50 µM SL-38) showed slightly increased survival at 24 and 48 hours but increased death with respect to control at 72 hours [1]. Administration of the Voriconazole dose alone did not offer protection to the larvae (Figure 7).

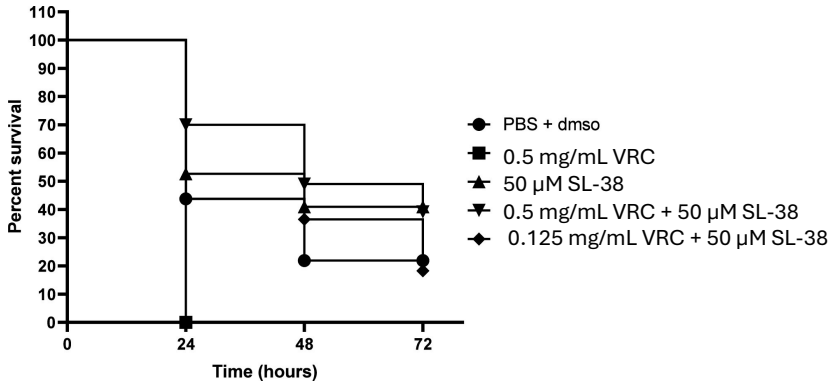


Figure 7. Percentage of survival of *Galleria mellonella* larvae infected with $1x10^5$ *Candida albicans* treated with compound SL-38 and voriconazole [1]. VRC = Voriconazole

9.1.8 Biocompatibility profile of SL-38

HaCaT cells were incubated under controlled experimental conditions for 48 and 96 h with a range of concentrations of SL-38 to then assess the "cell survival index", as thoroughly described in the experimental section. Incubation with SL-38 determines both time-dependent and concentration-dependent biological responses. As shown in Figure 8, cell survival remains acceptable up to incubations with 25 µM of SL-38, showing no significant variations with respect to control cultures (untreated cells). This outcome suggests a fairly good biocompatibility profile of SL-38 when administered in the low micromolar range. Only at higher concentrations (>50 µM), and especially after long contact times (96 h), cytotoxic effects begin to become of biological relevance [1].

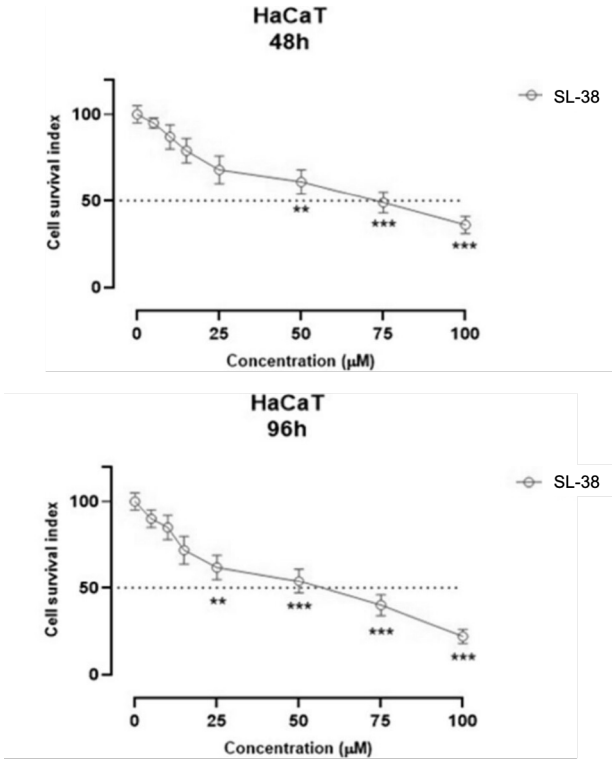


Figure 8. Cell survival index, evaluated by the MTT assay and live/dead automated cell count, for HaCaT cells following 48 and 96 h of incubation with the indicated concentrations (0-100 μM) of the compound SL-38. Data are expressed as percentage compared to control cells and are reported as mean of three independent experiments ± SEM (n = 18). The cell survival index was calculated as described in the experimental section and plotted in line-graphs against the different concentrations of the tested compound. **$p<0.01$ vs. control (untreated cells); ***$p<0.001$ vs. control (untreated cells) [1].

9.2 Conclusions

We have identified a novel class of isoxazole-pyrazole based compounds, namely compound SL-38 (**7a**, *Table 1*), which displayed synergistic activity with VRC, through a novel mechanism of action. Accordingly, SL-38 (**7a**, *Table 1*) induced a remarkable growth inhibition against the azole resistant *C. albicans* ATCC 10231 strain in combination with Voriconazole, in absence of intrinsic antifungal

activity. Indeed, the combination SL-38/Voriconazole led to a significant reduction of the typical yeast-to-hypha morphological transition, a characteristic feature of pathogenic strains. At the transcriptional level, SL-38 (**7a**, *Table 1*) in combination with Voriconazole induced the downregulation of the *ERG11* gene expression in *C. albicans* induced by Voriconazole itself. These results were confirmed in an *in vivo Galleria mellonella* model, where we were able to demonstrate that SL-38 (**7a**, *Table 1*) and Voriconazole can work in synergy also in *in vivo* settings, thereby paving the way for the identification of novel promising therapies in the fight against drug resistance in fungal infections.

In-depth molecular docking studies helped defining the bases of the observed synergistic action of the compounds at the molecular level. In particular, we were able to unveil the unique ability of the synergistic combination of SL-38 (**7a**, *Table 1*)/Voriconazole to provide a complete occupancy of all the LDM sites, namely SEC, the heme-containing active site, and PPEC. *In silico* assessment also highlighted the drug-like nature of our newly conceived derivative SL-38 (**7a**, *Table 1*), thus paving the way to a further optimization of this new class of synergistic agents for antifungal therapy.

9.3 Experimental section

9..3.1 Chemistry

General procedure for the preparation of cyanoacetamides. cyanoacetamides **4a-d** were readily synthesized as reported in literature [2]. To a solution of the opportune amine (benzylamine for **4a**, 3-trifluoromethyl benzylamine for **4b**, 2-chloro-5-fluoro benzylamine for **4c**, 3-methoxy benzylamine for **4d**, 2 eq) in 2-Me-THF (0.8 M), DBU (1 eq) was added and the resulting mixture stirred at 25 °C. After 15 min, ethyl cyanocetate (4 eq) was added and the reaction mixture allowed under stirring at 25 °C for 12 h. Upon completion, the reaction mixture was dissolved with DCM and washed with 0.1 N aqueous HCl and water. The organic layer was collected, dried over Na_2SO_4, filtered and evaporated under

reduced pressure. Crude material was purified by silica gel column chromatography (Hex/EtOAc 90:10 to 30:10 v/v).

General procedure for the preparation of N-substituted pyrazoles. to a stirring solution of 1*H*-pyrazole- 4-carboxaldehyde or 1*H*-pyrazole-3-carboxaldehyde (1 eq) in dry DMF (0.7 M) NaH (60% mineral oil dispersion, 1.8 eq) was added at 0 °C. After 45 min, *tert*-butyl 4-(methylsulfonyloxy)piperidine-1-carboxylate (1.1 eq) was added and the resulting mixture heated at 100 °C and allowed under stirring for 18 h. Reaction was stopped by adding distilled water and washed with EtOAc. Organic layers were collected and washed with NH_4Cl, then dried over Na_2SO_4, filtered and evaporated under reduced pressure.

General procedure the synthesis of chloro-oximes. *Step 1:* a solution of intermediates **2a,b** (1 eq) in EtOH (0.07 M) was added to a solution of hydroxylamine hydrochloride (2.05 eq) and sodium carbonate (1 eq) in a mixture of EtOH/H_2O (5:1 v/v). The resulting mixture was allowed under stirring at 25 °C for 2 h. Upon completion, the reaction mixture was diluted with distilled water and washed with EtOAc. Organic layers were collected, dried over Na_2SO_4, filtered and evaporated under reduced pressure, affording desired *tert*-butyl (*E*)-4-(4-((hydroxyimino)methyl)-1*H*-pyrazol-1-yl)piperidine-1-carboxylate and (*E*)-3-(4-((hydroxyimino)methyl)-1*H*-pyrazol-1-yl)piperidine-1-carboxylate, from **2a** and **2b** respectively, with quantitative yield. *Step 2:* NCS (1.5 eq) was added portiowise to a cooled solution of the corresponding oxime (1 eq) in dry DMF (0.1 M). After 1 h, the mixture was diluted with distilled water and partitioned with EtOAc. Organic layers were collected, dried over Na_2SO_4, filtered and evaporated under reduced pressure to effort corresponding chloro-oximes **3a,b** as a mixture of geometric isomers Z/E 4:1 in quantitative yields. Compounds **3a,b** were employed in the next reaction step without further purification.

General procedure for pyrazole-isoxazole ring formation. To a solution of chloro-oxime **3a,b** (1 eq) in dry ethanol (0.06 M), sodium ethoxide (1.05 eq) and ethyl cyanoacetate or **4a-d** (1.05 eq) were added and the resulting mixture allowed under stirring at 80 °C for 5 h.

General procedure for Boc group deprotection. To a stirring solution of 11-15 in MeOH (0.02 M) acetylchloride was added dropwise (2.3 eq). After 4 h, volatile components were removed under reduced pressure affording desired free amines 16-20 as hydrochloric salts in quantitative yields.

***tert*-Butyl 4-(4-formyl-1*H*-pyrazol-1-yl)piperidine-1-carboxylate (2a).** Compound **2a** was prepared following the general procedure for pyrazole alkylation starting from **1a** (4.68 mmol, 450 mg). The crude residue as purified by silica gel liquid chromatography (Hex/EtOAc 70:30 v/v) providing desired product **2a** with 75% yield (977 mg).

^{1}H NMR (DMSO-d_6, 700 MHz): δ 9.80 (s, 1H), δ 8.55 (s, 1H), δ 8.01 (s, 1H), δ 4.48-4.43 (m, 1H), δ 4.10-3.98 (m, 2 H), δ 3.03-2.81 (m, 2H), δ 2.04-2.02 (m, 2H), δ 1.82-1.76 (m, 2H), δ 1.42 (s, 9H)

***tert*-Butyl 4-(3-formyl-1*H*-pyrazol-1-yl)piperidine-1-carboxylate (2b).** Compound **2b** was prepared following the general procedure for pyrazole alkylation starting from **1b** (5.20 mmol, 500 mg). The crude residue as purified by silica gel liquid chromatography (Hex/EtOAc 60:40 v/v) providing desired product **2b** with 70% yield (1016 mg).

^{1}H NMR (DMSO-d_6, 700 MHz): δ 9.88 (s, 1H), δ 8.04 (s, 1H), δ 6.80 (s, 1H), δ 4.55-4.51 (m, 1H), δ 4.11-4.03 (m, 2 H), δ 3.02-2.82 (m, 2H), δ 2.06-2.04 (m, 2H), δ 1.86-1.80 (m, 2H), δ 1.42 (s, 9H).

Ethyl 5-amino-3-(1-(1-(tert-butoxycarbonyl)piperidin-4-yl)-1*H*-pyrazol-4-yl)isoxazole-4-carboxylate (6). Compound **6** was reported following the general procedure for isoxazole ring formation starting from **3a** (0.176 mmol, 58 mg). Upon completion, the residue was filtered, solvent removed under vacuum, and

the crude material purified by silica gel column chromatography (PE /EtOAc 70:30 v/v) affording desired product **6** with 39% yield (28 mg).

^{1}H NMR (DMSO-d_6, 700 MHz): δ 8.32 (s, 1H), δ 7.88 (s, 1H), δ 7.84 (bs, 2H), δ 4.46-4.41 (m, 1H), δ 4.24-4.21 (m, 2H), δ 4.09-4.00 (m, 2H), δ 3.01-2.83 (m, 2H), δ 2.03-2.01 (m, 2H), δ 1.82-1.76 (m, 2H), δ 1.42 (s, 9H), δ 1.28-1.26 (t, *J*= 7.0 Hz, 3 H).

^{13}C NMR (DMSO-d_6, 176 MHz): δ 179.88, 172.68, 162.73, 154.95, 154.31, 138.84, 129.69, 109.39, 83.79, 79.34, 59.87, 58.66, 29.99. 28.53, 14.80.

***tert*-Butyl 4-(4-(5-amino-4-(benzylcarbamoyl)isoxazol-3-yl)-1*H*-pyrazol-1-yl)piperidine-1-carboxylate (7a).** Compound **7a** was reported following the general procedure for isoxazole ring formation starting from **3a** (0.410 mmol, 137 mg). Upon completion, solvent was evaporated under reduced pressure and the crude material purified by silica gel column chromatography (Hex/EtOAc 60:40 v/v) affording desired product **7a** with 49% yield (96 mg).

^{1}H NMR (DMSO-d_6, 700 MHz): δ 8.11 (s, 1H), δ 7.78 (s, 1H), δ 7.54 (s, 1H), δ 7.39-7.37 (m, 2 H), δ 7.34-7.29 (m, 3H), δ 7.19 (t, *J*= 5.6 Hz, 1H), δ 4.40 (d, *J*= 5.6 Hz, 2H), δ 4.37-4.33 (m, 1H), δ 4.10-4.01 (m, 2 H), δ 3.04-2.83 (m, 2H), δ 1.96-1.94 (m, 2H), δ 1.72-1.66 (m, 2H), δ 1.49 (s, 9H).

^{13}C NMR (DMSO-d_6, 176 MHz): δ 171.41, 162.97, 154.25, 153.85, 139.83, 138.29, 128.86, 128.77, 127.99, 127.25, 109.51, 87.35, 79.34, 58.73, 42.74, 32.15, 28.54.

(ESI) m/z calc. $[M+H]^+$ for $C_{24}H_{31}N_6O_4^+$: 467.24; found: 467.3

***tert*-Butyl 4-(3-(5-amino-4-(benzylcarbamoyl)isoxazol-3-yl)-1*H*-pyrazol-1-yl)piperidine-1-carboxylate (7b).** Compound **7b** was reported following the general procedure for isoxazole ring formation starting from **3b** (0.230 mmol, 75 mg). Upon completion, solvent was evaporated under reduced pressure and the crude material purified by silica gel column chromatography (Hex/EtOAc 70:30 v/v) affording desired product **7b** with 28% yield (30 mg).

^{1}H NMR (DMSO-d_6, 400 MHz): δ 10.24 (t, *J*= 5.6 Hz, 1H), δ 7.95 (d, *J*= 2.8 Hz, 1H), δ 7.91 (s, 2H), δ 7.36-7.25 (m, 5H), δ 6.69 (s, *J*= 2.4 Hz, 1H), δ 4.47 (d, *J*= 5.6 Hz, 2H), δ 4.22-4.14 (m, 2H), δ 3.99-3.92 (m, 2H), δ 2.82-2.70 (m, 2H), δ 1.83-1.80 (m, 2H), δ 1.59-1.49 (m, 2H), δ 1.39 (s, 9H).

^{13}C APT (DMSO-d_6, 176 MHz) δ 173.50, 162.98, 154.25, 152.71, 141.55, 139.70, 131.17, 128.99, 128.14, 127.61, 105.42, 85.41, 79.54, 58.93, 42.73, 32.09, 28.46.

***tert*-Butyl 4-(4-(5-amino-4-(3-(trifluoromethyl)benzylcarbamoyl)isoxazol-3-yl)-1*H*-pyrazol-1-yl)piperidine-1-carboxylate (8).** Compound **8** was reported following the general procedure for isoxazole ring formation starting from **3a** (0.390 mmol, 130 mg). Upon completion, solvent was evaporated under reduced pressure and the crude material purified by silica gel column chromatography (Hex/EtOAc 50:50 v/v) affording desired product **8** with 70% yield (147 mg).

^{1}H NMR (DMSO-d_6, 700 MHz): δ 8.09 (s, 1H), δ 7.23 (s, 1H), δ 7.63 (s, 1H), δ 7.62-7.60 (m, 2H), δ 7.57-7.55 (m, 1H), δ 7.50 (s, 2H), δ 7.41 (t, *J*= 5.6 Hz, 1H), δ 4.42 (d, *J*= 6.3 Hz, 2H), δ 4.34-4.30 (m, 1H), δ 4.06-3.97 (m, 2H), δ 2.99-2.80 (m, 2H), δ 1.93-1.91 (m, 2H), δ 1.69-1.64 (m, 2H), δ 1.42 (s, 9H).

^{13}C NMR (DMSO-d_6, 176 MHz) δ 171.31, 163.18, 154.27, 154.01, 141.63, 138.27, 132.15, 129.77, 128.85, 124.52, 123.97, 109.54, 87.31, 79.33, 58.72, 42.45, 32.16, 28.51.

***tert*-Butyl 4-(4-(5-amino-4-(2-chloro-5-fluorobenzylcarbamoyl)isoxazol-3-yl)-1*H*-pyrazol-1-yl)piperidine-1-carboxylate (19a).** Compound **9a** was reported following the general procedure for isoxazole ring formation starting from **3a** (0.160 mmol, 50 mg). Upon completion, solvent was evaporated under reduced pressure and the crude material purified by silica gel column chromatography (Hex/EtOAc 50:50 v/v) affording desired product **9a** with 30% yield (25 mg).

^{1}H NMR (DMSO-d_6, 400 MHz): δ 8.16 (s, 1H), δ 7.76 (s, 1H), 7.54 (s, 2H), δ 7.50- 7.47 (m, 1H), δ 7.24 (t, *J*= 5.2 Hz, 1H), δ 7.18- 7.13 (m, 2H), δ 4.40-4.33 (m, 3H), δ 4.08- 3.98 (m, 2H), δ 2.99-2.84 (m, 2H), δ 1.99- 1.95 (m, 2H), δ 1.78-1.68 (m, 2H), δ 1.42 (s, 9H).

^{13}C NMR (DMSO-d_6, 101 MHz): δ 171.51, 163.25, 160.11, 154.28, 153.96, 139.48, 138.38, 131.21, 128.97, 116.35 (F), 109.45, 87.22, 79.34, 58.75, 32.23, 28.53

tert-Butyl 4-(3-(5-Amino-4-(2-chloro-5-fluorobenzylcarbamoyl)- isoxazol-3-yl)-4-chloro-1H-pyrazol-1-yl)piperidine-1-carboxylate (9b). Compound **9b** was reported following the general procedure for isoxazole ring formation starting from **3b** (0.250 mmol, 82 mg). Upon completion, solvent was evaporated under reduced pressure and the crude material purified by silica gel column chromatography (Hex/EtOAc 70:30 v/v) affording desired product **9b** with 32% yield (45 mg).

^{1}H NMR (DMSO-*d*6, 400 MHz): *δ* 9.21 (t, *J* = 5.6 Hz, 1H), *δ* 8.38 (s, 1H), *δ* 7.96 (s, 2H), *δ* 7.53−7.50 (m, 1H), *δ* 7.25−7.18 (m, 2H), *δ* 4.50 (d, *J* = 5.6 Hz, 2H), *δ* 4.32−4.25 (m, 1H), *δ* 4.04−3.95 (m, 2H), *δ* 2.87−2.72 (m, 2H), *δ* 1.98−1.91 (m, 2H), *δ* 1.72−1.62 (m, 2H), *δ* 1.39 (s, 9H).

^{13}C APT (DMSO-*d*6, 176 MHz) *δ* 173.11, 162.87, 161.98, 160.60, 154.07, 151.41, 139.34, 137.56, 131.47, 130.29, 127.87, 116.82, 116.35, 109.15, 85.68, 79.40, 60.09, 40.76, 31.83, 28.47.

***tert*-Butyl 4-(4-(5-amino-4-(3-methoxybenzylcarbamoyl)isoxazol-3-yl)-1*H*-pyrazol-1-yl)piperidine-1-carboxylate (10).** Compound **10a** was reported following the general procedure for isoxazole ring formation starting from **3a** (0.180 mmol, 33.7 mg). Upon completion, solvent was evaporated under reduced pressure and the crude material purified by silica gel column chromatography (Hex/EtOAc 50:50 v/v) affording desired product **10a** with 30% yield (24 mg).

^{1}H NMR (DMSO-d_6, 400 MHz): δ 8.05 (s, 1H), δ 7.72 (s, 1H), δ 7.47 (s, 1H), δ 7.30-7.21 (m, 3H), δ 7.11 (t, *J*= 6.0 Hz, 1H), δ 6.85-6.82 (m, 2H), δ 4.32-4.26 (m, 3H), δ 4.05-3.94 (m, 2H), δ 3.73 (s, 3H), δ 2.97-2.81 (m, 2H), δ 1.91-1.88 (m, 2H), δ 1.69-1.62 (m, 2H), δ 1.42 (s, 9H).

^{13}C NMR (DMSO-d_6, 176 MHz): δ 171.34, 162.94, 159.75, 154.26, 153.85, 141.35, 138.30, 129.83, 128.85, 128.76, 128.08, 120.13, 113.57, 112.64, 109.49, 87.38, 79.35, 58.74, 55.42, 42.73, 28.53.

***tert*-Butyl 4-(3-(5-amino-4-(3-methoxybenzylcarbamoyl)isoxazol-3-yl)-1*H*-pyrazol-1-yl)piperidine-1-carboxylate (10b).** Compound **10b** was reported following the general procedure for isoxazole ring formation starting from **3b** (0.240 mmol, 78 mg). Upon completion, solvent was evaporated under reduced pressure and the crude material purified by silica gel column chromatography (Hex/EtOAc 60:40 v/v) affording desired product **10b** with 29% yield (35 mg).

^{1}H NMR (DMSO-d_6, 400 MHz): δ 10.20 (t, *J*= 5.6 Hz, 1H), δ 8.01 (d, *J*= 2.4 Hz, 1H), δ 7.93 (s, 2H), δ 7.26 (t, *J*= 7.6 Hz, 1H), δ 6.91-6.84 (m, 3H), δ 6.71 (d, *J*= 2.4 Hz, 1H), δ 4.45 (d, *J*= 5.2 Hz, 2H), δ 4.20-4.13 (m, 1H), δ 4.01-3.94 (m, 2H), δ 2.82-2.69 (m, 2H), δ 1.88-1.81 (m, 2H), δ 1.66-1.55 (m, 2H), δ 1.40 (s, 9H).

^{13}C APT (DMSO-d_6, 176 MHz) δ 173.54, 162.94, 159.84, 154.15, 152.68, 141.60, 141.35, 130.94, 130.03, 120.27, 113.74, 112.85, 105.48, 85.41, 79.40, 59.06, 55.43, 42.76, 29.99, 28.48.

4-(4-(5-Ammonio-4-(ethoxycarbonyl)isoxazol-3-yl)-1*H*-pyrazol-1-yl)piperidinium dichloride (11). Compound **11** was synthesised following the general procedure for Boc protecting group removal starting from **6** (0.030 mmol, 12 mg) affording desired product **11** with 97% yield (11 mg).

^{1}H NMR (DMSO-d_6, 400 MHz): δ 8.81 (s, 1H), δ 8.57 (s, 1H), δ 8.33 (s, 1H), δ 7.91 (s, 1H), δ 7.83 (s, 2H), δ 4.62-4.53 (m, 1H), δ 4.24-4.19 (m, 2H), δ 4.00-

3.31 (m, 2H, 1 CH_2 under DMSO peak), δ 3.12-3.02 (m, 2H), δ 2.22-2.09 (m, 4H), δ 1.25 (t, *J*= 6.8 Hz, 3H).

^{13}C APT (DMSO-d_6, 176 MHz) δ 172.57, 162.69, 154.92, 139.16, 130.14, 109.55, 83.86, 60.02, 55.74, 42.79, 29.14, 14.81.

4-(4-(5-ammonio-4-(benzylcarbamoyl)isoxazol-3-yl)-1*H*-pyrazol-1-yl)piperidinium (12a). Compound **12a** was synthesised following the general procedure for Boc protecting group removal starting from **7a** (0.033 mmol, 15.5 mg) affording desired product **12a** with 96% yield (14 mg).

^{1}H NMR (DMSO-d_6, 400 MHz): δ 8.73 (s, 1H), δ 8.50 (s, 1H), δ 8.11 (s, 1H), δ 7.76 (s, 1H), δ 7.47 (s, 2H), δ 7.34-7.30 (m, 2H), δ 7.27-7.22 (m, 4H), δ 4.50-4.42 (m, 1H), δ 4.35 (d, *J*= 6.0 Hz, 2 H), δ 3.40-3.36 (m, 2H), δ 3.09-3.00 (m, 2H), 2.13-2.04 (m, 4H).

^{13}C APT (DMSO-d6, 176 MHz) δ 171.16, 162.94, 154.01, 139.78, 138.74, 129.52, 128.79, 127.83, 127.27, 109.65, 87.54, 55.71, 42.77, 42.50, 40.22, 28.98.

4-(3-(5-Ammonio-4-(benzylcarbamoyl)isoxazol-3-yl)-1*H*-pyrazol-1-yl)piperidinium dichloride (12b). Compound **12b** was synthesised following the general procedure for Boc protecting group removal starting from **7b** (0.038 mmol, 18 mg) affording desired product **12b** with quantitative yield (17 mg).

^{1}H NMR (DMSO-d_6, 400 MHz): δ 10.06 (t, *J*= 5.6 Hz, 1H), δ 8.69 (s, 1H), δ 8.51 (s, 1H), δ 7.97 (d, *J*= 2.8 Hz, 1H), δ 7.91 (s, 2H), δ 7.35-7.23 (m, 5H), δ 6.75 (d, *J*= 2.4 Hz, 1H), δ 4.53 (d, *J*= 5.6 Hz, 2H), δ 4.42-4.31 (m, 1H), δ 3.33-3.30 (m, 2H), δ 2.99-2.90 (m, 2H), δ 2.08-2.02 (m, 2H), δ 1.98-1.88 (m, 2H).

^{13}C NMR (DMSO-d_6 ,176 MHz) δ 173.51, 163.05, 152.66, 141.94, 140.07, 131.27, 128.93, 128.00, 127.45, 105.89, 85.42, 56.10, 42.63, 28.87.

4-(4-(5-Ammonio-4-(3-(trifluoromethyl)benzylcarbamoyl)isoxazol-3-yl)-1*H*-pyrazol-1-yl)piperidinium dichloride (13). Compound **13** was synthesised following the general procedure for Boc protecting group removal starting from

8 (0.014 mmol, 7.5 mg) affording desired product **13** with quantitative yield (7 mg).

^{1}H NMR (DMSO-d_6, 700 MHz): δ 8.88 (bs, 1H), δ 8.62 (bs, 1H), δ 8.18 (s, 1H), δ 7.78 (s, 1H), δ 7.64 (s, 1H), δ 7.61-7.56 (m, 4H), δ 7.50 (s, 2H), δ 4.52-4.48 (m, 1H), δ 4.44 (d, *J*= 5.6 Hz, 2H), δ 3.39-3.37 (m, 2H), δ 3.09-3.01 (m, 2H), δ 2.16-2.09 (m, 4H).

^{13}C NMR (DMSO-d_6, 176 MHz) δ 171.02, 163.10, 154.17, 141.72, 138.72, 131.98, 129.78, 129.48, 124.37, 123.90, 109.84, 87.51, 55.70, 42.58, 42.52, 29.02.

4-(3-(5-Ammonio-4-(2-chloro-5-fluorobenzylcarbamoyl)- isoxazol-3-yl)-4-chloro-1H-pyrazol-1-yl)piperidinium Dichloride (14). Compound **14** was synthesised following the general procedure for Boc protecting group removal starting from **9b** (0.047 mmol, 26 mg) affording desired product **14** with quantitative yield (26 mg).

^{1}H NMR (DMSO-*d*6, 400 MHz): *δ* 9.00 (t, *J* = 5.6 Hz, 1H), *δ* 8.70 (s, 2H), *δ* 8.39 (s, 1H), *δ* 7.95 (s, 2H), *δ* 7.52−7.48 (m, 1H), *δ* 7.20− 7.13 (m, 2H), *δ* 4.53−4.47 (m, 3H), *δ* 3.33- 3.31 (m, 2 H, 1 CH2 under DMSO peak), *δ* 3.03−2.97 (m, 2H), *δ* 2.24−2.18 (m, 2H), *δ* 2.10−1.99 (m, 2H).

^{13}C APT (DMSO-*d*6, 176 MHz) *δ* 173.06, 162.88, 162.00, 160.62, 151.45, 139.78, 139.74, 138.03, 131.44, 131.39, 130.52, 127.62, 116.34, 116.20, 116.08, 115.95, 109.35, 85.79, 57.06, 42.37, 40.82, 28.64.

4-(3-(5-Ammonio-4-(3-methoxybenzylcarbamoyl)isoxazol-3-yl)-1*H*-pyrazol-1-yl)piperidinium (15). Compound **15** was synthesised following the general procedure for Boc protecting group removal starting from **10b** (0.011 mmol, 5.5 mg) affording desired product **15** with 97% yield (5 mg).

^{1}H NMR (DMSO-d_6, 400 MHz): δ 10.03 (t, *J*= 6.0 Hz, 1H), δ 8.74 (s, 1H), δ 8.58 (s, 1H), δ 7.97 (s, 1H), δ 7.90 (s, 2H), δ 7.26-7.21 (m, 1H), δ 6.87-6.80 (m, 3H),

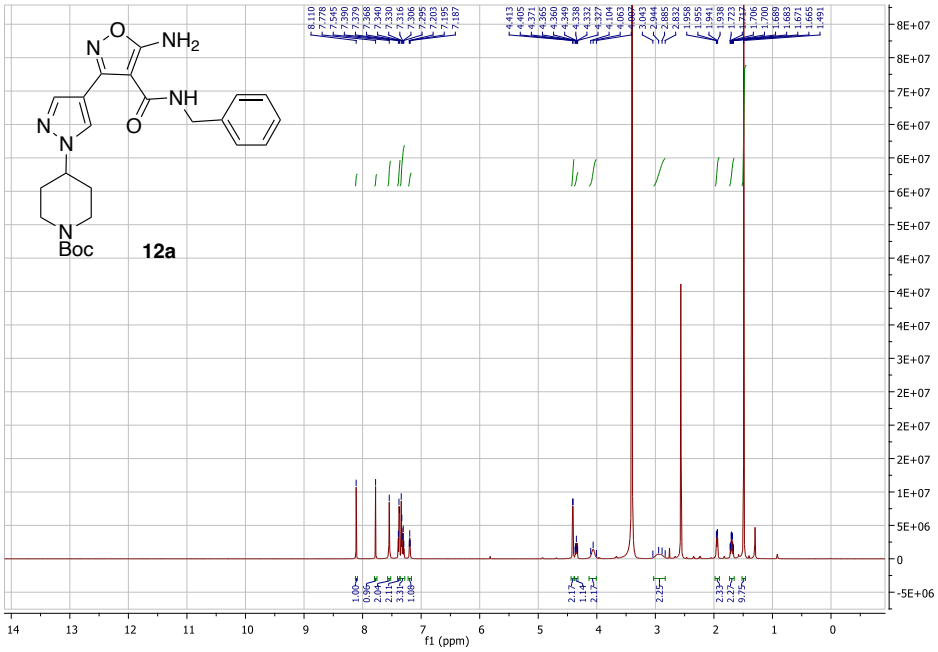
δ 6.75 (s, 1H), δ 4.49 (d, *J*= 5.2 Hz, 2H), δ 4.42-4.35 (m, 1H), δ 4.00- 3.31 (m, 5H, CH_3 of OCH_3 and 1 CH_2 under DMSO peak), δ 2.97-2.91 (m, 2H), δ 2.06-1.97 (m, 4H).

^{13}C APT (DMSO-d_6, 176 MHz) δ 173.50, 163.04, 159.72, 152.66, 151.30, 141.92, 141.71, 131.24, 130.10, 120.15, 113.80, 112.53, 105.91, 85.42, 56.13, 55.48, 42.63, 42.53, 29.97, 28.88.

7.3.2 Supporting Figures

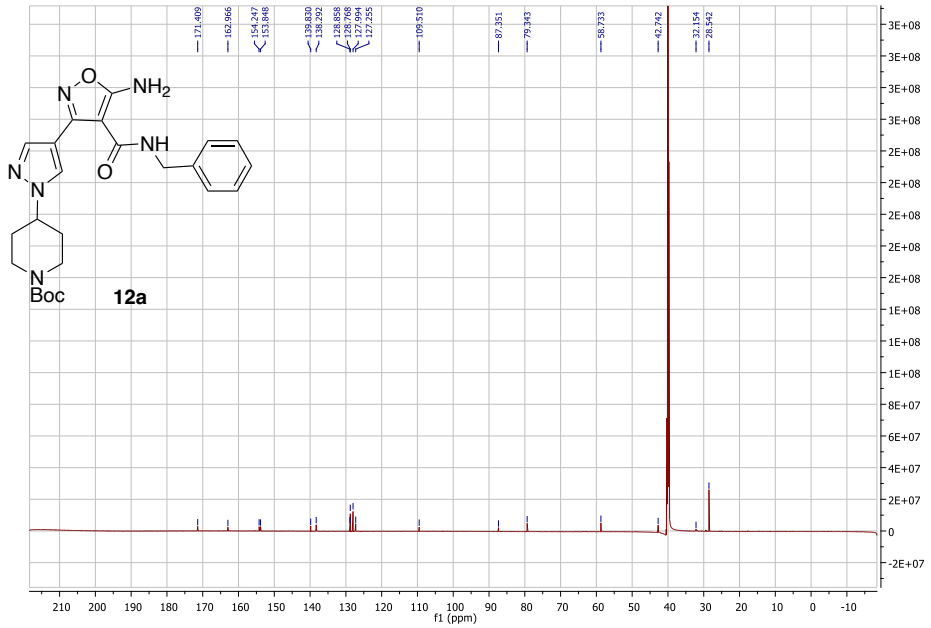
Supporting Figure 1

^{1}H spectrum of compound 7a (SL-38)

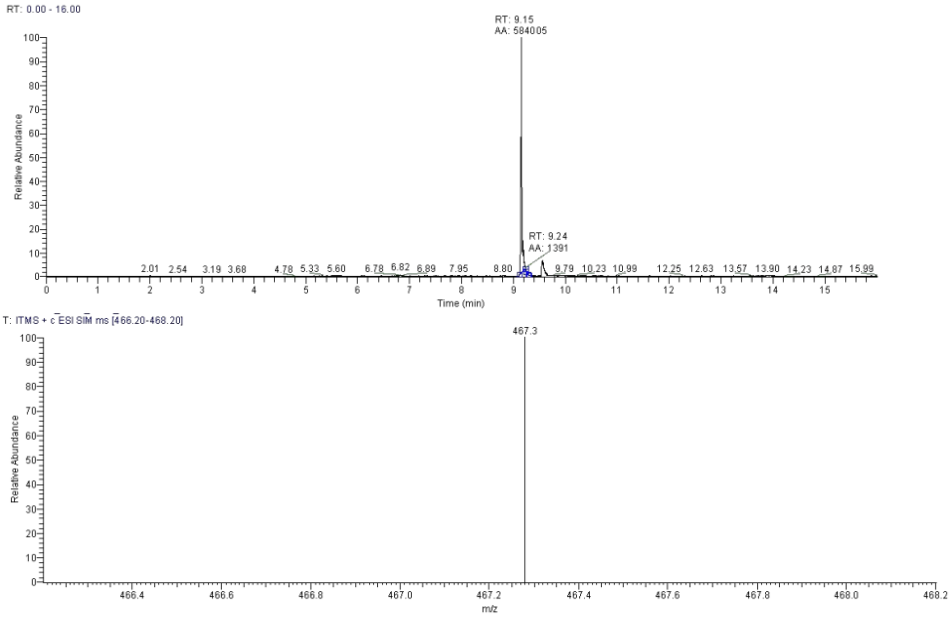


Supporting Figure 2

^{13}C spectrum of compound 7a (SL-38)



Supporting Figure 3
UPLC-MS spectrum of compound 7a (SL-38)



References

[1] S. Pelliccia, P. Russomanno, S. Barone, B. Mateu, A.I. Alfano, M. Miranda, L. Coretti, F. Lembo, M. Piccolo, C. Irace, L. Friggeri, T.Y. Hargrove, A. Curtis, G.I. Lepesheva, K. Kavanagh, E. Buommino, M. Brindisi, J Med Chem 67 (2024) 14256–14276.

[2] M. V. Keniya, M. Sabherwal, R.K. Wilson, M.A. Woods, A.A. Sagatova, J.D.A. Tyndall, B.C. Monk, Antimicrob Agents Chemother 62 (2018).

Chapter 10

Conclusions and Perspectives

In conclusion, during my PhD, my research efforts were aimed to the development of novel high potent and selective HDAC6is, while ensuring enhanced pharmacokinetic properties compared to existing inhibitors, in order to address both cancer, inflammatory and infectious diseases. For this purpose, spirocyclic scaffolds have been introduced in designed inhibitors, since these motifs have been extensively reported in literature as promising strategy for the success of developed drugs, in order to increase water solubility, bioavailability and reducing off-target interactions, while guaranteeing versatile modifications to rapidly explore structure-activity relationships. In the design of the proprietary inhibitors, the general structural features of HDAC6is were taken into account, namely (i) a rigid and bulky cap group (represented by spirocyclic scaffold), (ii) an aromatic linker, and (iii) ZBG for enzyme inhibition. Driven by *in silico* studies, we first identified *1-phenyl-1,3,8-triazaspiro[4.5]decan-4-one* cap group, able to interact with L1 pocket, while minimizing the binding affinity over nuclear HDACs. In this design, both amines, amides, ureas and oxalamides were introduced on the spiro-piperidine nitrogen of the cap group, while the aromatic linker bringing the hydroxamate ZBG was introduced on the amide portion. This design led to the identification of high potent and selective

HDAC6is, which showed efficacy in both *in vitro* and *ex vivo* on MDA-MB-231 TNBC cells culture. On the next stage, I investigated the effect of single-point modifications on *1-phenyl-1,3,8-triazaspiro[4.5]decan-4-one* cap group on HDAC6 isoform selectivity and potency. First, a strategic linker overturning was performed from the imidazolidine to the piperidine ring. X-ray studies on compound **7b** (*Chapter 5*) revealed a key interaction of the linker moiety with S531 residue L2 loop (unique on HDAC6), thus confirming the reliability of this strategy to enhance isoform selectivity. Also, during the second year of my PhD I had the opportunity to spent six-months in Finn K. Hansen research group, were I worked on the effect of fine-tuning the cap group and ZBG moieties on HDAC6 potency and selectivity. For this purpose, a simpler *1-thia-4,8-diazaspiro[4.5]decan-3-one* cap group was introduced. Designed inhibitors, bearing the canonical hydroxamate ZBG, while retaining nM potency on HDAC6, lacked isoform specificity towards HDAC1, while the substitution of the hydroxamate with DFMOs as ZBGs, lead to completely inactive compounds on HDAC1, thereby confirming the importance of ZBGs in driving isoform selectivity. On the next stage, given the strong epigenetic component in inflammatory and infective states, coupled with our previous results for the efficacy of selective HDAC6is in counteracting inflammatory state in a chronic murine model of *P. aeruginosa* infection, a second subset of inhibitors was developed through strategic cap group modifications to the interaction with key aminoacidic residues in *P. aeruginosa* HDAC PA3771. Gratifyingly, compound **15a** (*Chapter 7*) was able to reduce the production of *P. aeruginosa* virulence factors and disrupted biofilm formation. Similarly, compound **15a** showed synergistic effect in combination with Voriconazole in *C. albicans* strains resistant to Voriconazole itself, counteracting azole-induced resistance and inhibiting yeast-to-hyphae morphological transition. These data, coupled to literature evidence, strongly support deeper investigation of molecular

underpinnings at the basis of the antibacterial and antifungal effect for HDACs inhibitors, in order to find novel efficient anti-infective drugs for the treatment of multidrug resistant infections. In parallel, a small part of my Phd was devoted to the identification of anti-infective agents with innovative mechanisms of action. In this frame, I was involved in the design and synthesis of oxazole-pyrazole synergistic compounds for the treatment of azole-resistant mycosis.

In conclusion, this thesis work provided key insights in selective HDAC6 modulation for the treatment of both solid cancers and infectious diseases, ultimately advancing the design of epigenetic modulators.